Politecnico di Bari

Repository Istituzionale dei Prodotti della Ricerca del Politecnico di Bari

Evolution of the clay micro-structure in compression and shearing loading paths

This is a PhD Thesis

Original Citation:
Evolution of the clay micro-structure in compression and shearing loading paths / Guglielmi, Simona. - (2018). [10.60576/poliba/iris/guglielmi-simona_phd2018]

Availability:
This version is available at http://hdl.handle.net/11589/120653 since: 2018-01-22

Published version
DOI:10.60576/poliba/iris/guglielmi-simona_phd2018

Publisher: Politecnico di Bari

Terms of use:

(Article begins on next page)

13 August 2026

D.R.R.S

POLITECNICO DI BARI

06

2018

Doctor of Philosophy in Environmental and Building Risk and Development

Coordinator: Prof. Michele Mossa

XXX CYCLE
Curriculum: Environment and Natural Resources

DICATECh
Department of Civil, Environmental, Building Engineering and Chemistry

Evolution of the clay micro-structure in compression and shearing loading paths

Prof. Federica Cotecchia
DICATECh
Polytechnic University of Bari

Dr. Francesco Cafaro
DICATECh
Polytechnic University of Bari

Prof. Antonio Gens
Department of Civil and Environmental Engineering
Universitat Politècnica de Catalunya

Simona Guglielmi

Politecnico di Bari

LIBERATORIA PER L'ARCHIVIAZIONE DELLA TESI DI DOTTORATO

Al Magnifico Rettore
del Politecnico di Bari

La sottoscritta GUGLIELMI SIMONA nata a ANDRIA (BAT) il 07/01/1990

residente a ANDRIA (BAT) in via GIOVANNI PASCOLI, 25 e-mail simona.guglielmi90@gmail.com

iscritta al 3° anno di Corso di Dottorato di Ricerca in RISCHIO E SVILUPPO AMBIENTALE, TERRITORIALE ED EDILIZIO ciclo XXX

ed essendo stata ammessa a sostenere l'esame finale con la prevista discussione della tesi dal titolo:

"EVOLUTION OF THE CLAY MICRO-STRUCTURE IN COMPRESSION AND SHEARING LOADING PATHS"

DICHIARA

1) di essere consapevole che, ai sensi del D.P.R. n. 445 del 28.12.2000, le dichiarazioni mendaci, la falsità negli atti e l'uso di atti falsi sono puniti ai sensi del codice penale e delle Leggi speciali in materia, e che nel caso ricorressero dette ipotesi, decade fin dall'inizio e senza necessità di nessuna formalità dai benefici conseguenti al provvedimento emanato sulla base di tali dichiarazioni;
2) di essere iscritto al Corso di Dottorato di ricerca RISCHIO E SVILUPPO AMBIENTALE, TERRITORIALE ED EDILIZIO ciclo XXX, corso attivato ai sensi del *"Regolamento dei Corsi di Dottorato di ricerca del Politecnico di Bari"*, emanato con D.R. n.286 del 01.07.2013;
3) di essere pienamente a conoscenza delle disposizioni contenute nel predetto Regolamento in merito alla procedura di deposito, pubblicazione e autoarchiviazione della tesi di dottorato nell'Archivio Istituzionale ad accesso aperto alla letteratura scientifica;
4) di essere consapevole che attraverso l'autoarchiviazione delle tesi nell'Archivio Istituzionale ad accesso aperto alla letteratura scientifica del Politecnico di Bari (IRIS-POLIBA), l'Ateneo archivierà e renderà consultabile in rete (nel rispetto della Policy di Ateneo di cui al D.R. 642 del 13.11.2015) il testo completo della tesi di dottorato, fatta salva la possibilità di sottoscrizione di apposite licenze per le relative condizioni di utilizzo (di cui al sito http://www.creativecommons.it/Licenze), e fatte salve, altresì, le eventuali esigenze di "embargo", legate a strette considerazioni sulla tutelabilità e sfruttamento industriale/commerciale dei contenuti della tesi, da rappresentarsi mediante compilazione e sottoscrizione del modulo in calce (Richiesta di embargo);
5) che la tesi da depositare in IRIS-POLIBA, in formato digitale (PDF/A) sarà del tutto identica a quelle **consegnate**/inviate/da inviarsi ai componenti della commissione per l'esame finale e a qualsiasi altra copia depositata presso gli Uffici del Politecnico di Bari in forma cartacea o digitale, ovvero a quella da discutere in sede di esame finale, a quella da depositare, a cura dell'Ateneo, presso le Biblioteche Nazionali Centrali di Roma e Firenze e presso tutti gli Uffici competenti per legge al momento del deposito stesso, e che di conseguenza va esclusa qualsiasi responsabilità del Politecnico di Bari per quanto riguarda eventuali errori, imprecisioni o omissioni nei contenuti della tesi;
6) che il contenuto e l'organizzazione della tesi è opera originale realizzata dal sottoscritto e non compromette in alcun modo i diritti di terzi, ivi compresi quelli relativi alla sicurezza dei dati personali; che pertanto il Politecnico di Bari ed i suoi funzionari sono in ogni caso esenti da responsabilità di qualsivoglia natura: civile, amministrativa e penale e saranno dal sottoscritto tenuti indenni da qualsiasi richiesta o rivendicazione da parte di terzi;
7) che il contenuto della tesi non infrange in alcun modo il diritto d'Autore né gli obblighi connessi alla salvaguardia di diritti morali od economici di altri autori o di altri aventi diritto, sia per testi, immagini, foto, tabelle, o altre parti di cui la tesi è composta.

Luogo e data 20/12/2017, Bari Firma Simona Guglielmi

La sottoscritta, con l'autoarchiviazione della propria tesi di dottorato nell'Archivio Istituzionale ad accesso aperto del Politecnico di Bari (POLIBA-IRIS), pur mantenendo su di essa tutti i diritti d'autore, morali ed economici, ai sensi della normativa vigente (Legge 633/1941 e ss.mm.ii.),

CONCEDE

- al Politecnico di Bari il permesso di trasferire l'opera su qualsiasi supporto e di convertirla in qualsiasi formato al fine di una corretta conservazione nel tempo. Il Politecnico di Bari garantisce che non verrà effettuata alcuna modifica al contenuto e alla struttura dell'opera.
- al Politecnico di Bari la possibilità di riprodurre l'opera in più di una copia per fini di sicurezza, back-up e conservazione.

Luogo e data Bari, 20/12/2017 Firma Simona Guglielmi

EXTENDED ABSTRACT

The work presents a research approach in which the investigation of the macro-behaviour through element testing is systematically combined with the observation of processes and changes taking place at the micro-scale. The approach is aimed at identifying the main physical factors and internal features which control, at the micro-scale, the material response, causing given behavioural facets. The research final aim is at assessing the influence of the different aspects of behaviour on model parameter values, hence supporting constitutive modelling and finding a relation between classes of behaviour and corresponding models and classes of clays.

The tested materials are two illitic stiff clays of marine origin, Pappadai clay and Lucera clay, that are investigated both when natural and when reconstituted and one-dimensionally consolidated in the laboratory.

The microstructural analyses are carried out by means of different techniques. Scanning electron microscopy (SEM) is used to provide a qualitative investigation of the clay fabric and is combined with image processing, which allows to assess quantitatively the fabric orientation by means of a statistical analysis of the orientation of particles and particle domains. This microstructure investigation involves different levels of magnification, hence different scales of analysis.

The clay bonding is directly investigated through mineralogical and geo-chemical investigations at the micro-scale and, indirectly, through the analysis of its effects on the clay behaviour during strain paths while probing the clay swelling capacity.

The pore size distribution is analysed by means of mercury intrusion porosimetry (MIP), which provides information about the geometry and distribution of pores.

The microstructure is first analysed for both Pappadai and Lucera clay at initial state, i.e., in the undisturbed state for the natural clay and after consolidation in consolidometer for the reconstituted clay. Then, the evolution of microstructure is

explored after 1D and isotropic compression to states pre- and post- gross-yield, up to large pressures. A comparison is made between microstructures of specimens 1D and isotropically compressed to the same void ratio. The evolution of both the natural and the reconstituted clay microstructure is also investigated under shearing loading paths, in both drained and undrained conditions, starting from different isotropic compression states pre- and post- isotropic gross-yield. To explore the microstructure evolution both before and after reaching the current SBS, two shear tests are stopped half way through the stress path.

The microstructural features underlying the macro-response exhibited by the clay are also compared with those recognized in the literature for other natural and reconstituted clays.

The constitutive laws adopted by some advanced constitutive models to simulate the effects of structure are evaluated in the light of the observation and interpretation of the features and processes acting at the micro-scale and of their evolution under the different loading paths.

key words: clays, fabric, porosimetry, microstructure, micro-macro, constitutive modelling

INDEX

INDEX 5
LIST OF FIGURES 11
LIST OF TABLES 39
LIST OF SYMBOLS 41
1 INTRODUCTION 45
1.1 Introduction 45
1.2 Structure of the thesis 47
2 MICROSTRUCTURE AND MICRO-BEHAVIOUR OF CLAYS 51
2.1 Introduction 51
2.2 Clay minerals and particles 51
2.3 Interaction between clay particles and water 53
2.4 Interaction between clay particles 55
2.5 Soil structure and remoulding 57
2.6 Classification of fabrics 63
2.7 Fabrics of remoulded clays 65
2.8 Effects of deposition conditions on the clay fabric and structural changes under burial 68
2.9 Types of clay structure 71
2.10 Effects of 1D compression on the clay microstructure 72
2.11 Effects of isotropic compression on the clay microstructure 92
2.12 Effects of shear on the clay microstructure 99
2.13 Microstructural analysis of strain localisation in clays 105
3 MACRO-MECHANICAL BEHAVIOUR OF CLAYS 111
3.1 Introduction 111
3.2 The behaviour of reconstituted clays 111

3.2.1 The Critical State Framework 111
3.2.2 The Cam Clay model 121
3.3 Advanced Constitutive models for reconstituted clays 125
3.3.1 The model of Al-Tabbaa and Wood (1989) 125
3.3.2 The model of Stallebrass and Taylor (1997) 128
3.3.3 The model of Wheeler et al. (2003) 133
3.4 The behaviour of natural clays 137
3.4.1 Behaviour of clays with a sedimentation structure 139
3.4.2 Behaviour of clays having a post-sedimentation structure 148
3.4.3 Shape of gross-yield and state boundary curves 151
3.4.4 A general normalized gross yield curve for clays 155
3.4.5 Behaviour of Pappadai clay 159
3.4.6 Application of the sensitivity framework to other natural clays 162
3.4.7 Plastic strain increment ratios 169
3.5 Constitutive models for natural clays 174
3.5.1 The model of Rouainia and Wood (2000) 174
3.5.2 The model of Kavvadas and Amorosi (2000) 177
3.5.3 The model of Baudet and Stallebrass (2004) 182
3.5.4 The model of Koskinen et al. (2002) 185
4 GEOLOGICAL FEATURES OF PAPPADAI AND LUCERA CLAYS 189
4.1 Introduction 189
4.2 Geological background and sampling 192
4.3 Physical and mineralogical properties of Pappadai and Lucera clays 199
5 TESTING PROGRAMME, EQUIPMENT AND PROCEDURES 211

5.1 Testing programme 211
5.2 Mechanical testing equipment 216
5.2.1 Oedometer apparatus 217
5.2.2 Triaxial and stress path apparatuses 219
5.3 Microstructural analyses 228
5.3.1 Scanning electron microscopy 230
5.3.2 Mercury intrusion porosimetry 232
5.3.3 Image processing 236
5.4 Testing procedures 241
5.4.1 Reconstituted material preparation 241
5.4.2 Measurement of suction by filter-paper technique and high capacity IC tensiometers 244
5.4.3 Oedometer tests 249
5.4.4 Triaxial tests 253
6 MECHANICAL TEST RESULTS 261
6.1 Introduction 261
6.2 One-dimensional compression tests 261
6.2.1 Compression curves and gross yield stresses 262
6.2.2 Primary and secondary oedometric consolidation 274
6.2.3 Coefficient of permeability 282
6.3 Isotropic compression tests 287
6.4 Shear tests 294
6.4.1 Stress-strain behaviour 297
6.4.2 Flow rules and stress ratios at critical state 320

6.4.3 Critical states 325
6.4.4 Shear stiffness 330
6.5 State boundary surface 334
7 RESULTS OF THE MICROSTRUCTURAL ANALYSES 343
7.1 Introduction 343
7.2 Initial clay microstructure 344
7.2.1 Microstructure of the undisturbed clay 344
7.2.2 Microstructure of the reconstituted clay after consolidation in the consolidometer 376
7.3 Evolution of microstructure in 1D and isotropic compression 391
7.3.1 Microstructural changes in 1D compression for the natural clay 391
7.3.2 Microstructural changes in swelling for the natural clay 420
7.3.3 Microstructural changes in 1D compression for the reconstituted clay 427
7.3.4 Microstructural changes in isotropic compression for the natural clay 435
7.3.5 Microstructural changes in isotropic compression for the reconstituted clay 448
7.4 Evolution of microstructure in shear 451
7.4.1 Microstructural changes for the natural clay under drained shear 451
7.4.2 Microstructural changes for the natural clay under undrained shear 469
7.4.3 Microstructural changes for the reconstituted clay under shear 494
8 DISCUSSION OF THE RESULTS 505
8.1 Introduction 505
8.2 Factors controlling the current clay microstructure 508

8.3 A novel microstructural interpretation of sensitivity 528
8.4 Micro to macro compression behaviour 532
8.4.1 One-dimensional compression 532
8.4.2 Isotropic compression 547
8.5 Micro to macro shear behaviour 554
8.6 Possible further advancements of clay constitutive modelling 564
8.6.1 Role and shape of the gross yield surface for the natural soil 564
8.6.2 Modelling of Pappadai clay 571
9 CONCLUSIONS 587
10 ACKNOWLEDGEMENTS 603
11 REFERENCES 605
12 CURRICULUM 625

LIST OF FIGURES

Fig. 2.1 – Synthesis pattern for the clay minerals (after Mitchell and Soga, 2005)....52
Fig. 2.2 - (a) Charge distribution on the clay particle surface; (b) Internal surface structure of a structural unit of kaolinite (after Mitchell and Soga, 2005). 53
Fig. 2.3 - Scheme of the different water layers surrounding the clay particle (after Veniale, 1983).....54
Fig. 2.4 – Distribution of ions adjacent to a clay surface according to the concept of the diffuse double layer (after Mitchell and Soga, 2005).....55
Fig. 2.5 - (a) Terzaghi-Casagrande honeycomb fabric (after Terzaghi, 1925); (b) Open fabric of undisturbed marine clay (after Casagrande, 1936-a). 57
Fig. 2.6- (a) Relation between liquidity index and undrained shear strength of remoulded clays; (b) Relation between liquidity index and consolidation pressure for natural and remoulded clays (after Skempton and Northey, 1952) and constant sensitivity lines. 62
Fig. 2.7- (a) Cardhouse fabric in saltwater deposit (b) cardhouse fabric in freshwater deposit; (c) remoulded fabric (after Lambe, 1953). 63
Fig. 2.8 - Idealized clay fabrics (after Sides and Barden, 1970).....65
Fig. 2.9 - Assemblages and pore classes in the open fabric of a reconstituted clay (after Griffiths and Joshi, 1990). 66
Fig. 2.10 - (a) Kaolin slurry (w=117%); (b) "bridge" between domains (after V. Cotecchia et al.,1982-b).....67
Fig. 2.11 - Pyrite framboids (after O'Brien and Slatt, 1990). 69
Fig. 2.12 - SEM micrographs of intact St Marcel clay on a vertical plane at (a) 3000x, (b) 7000x and (c) 15000x magnification (after Delage and Lefebvre, 1984).....73
Fig. 2.13 – SEM micrographs of a remoulded sample of St Marcel clay (after Delage and Lefebvre, 1984).....74
Fig. 2.14 – Change in PSD curves of St Marcel clay during oedometer compression (after Delage and Lefebvre, 1984 and Delage, 2010).....75
Fig. 2.15 – Pore size distribution of intact Louiseville clay compressed at increasing volumetric strain (after Lapierre et al., 1990).....76

Fig. 2.16 - Pore size distribution of reconstituted Louiseville clay compressed at increasing volumetric strain (after Lapierre et al., 1990)..... 76
Fig. 2.17 – Natural and reconstituted microstructures of Gulf of Guinea clay at initial state: (a) cumulative and (b) differential volume results (after Hattab and Fleureau, 2013)..... 77
Fig. 2.18 - Natural and reconstituted microstructures of Gulf of Guinea clay after oedometric loading: (a) cumulative and (b) differential volume results (after Hattab and Fleureau, 2013). 78
Fig. 2.19 – Pore-size changes as a function of vertical stress on a Osaka Bay clay sample (after Tanaka and Locat, 1999 modified)..... 79
Fig. 2.20 – Change of pore diameter distribution curves of Osaka Bay clay taken at (a) 10m, (b)95 m, (c) 175 m due to consolidation (after Rito et al., 2003). 80
Fig. 2.21 - Fiumicino clay, normally consolidated in situ: (a) fabric on a vertical fracture through an undisturbed sample from 18m depth; (b) fabric on a vertical fracture through a sample compressed to σ'_v = 4704 kPa; (e) fabric scheme applying to the clay compressed to very high stresses (after F.Cotecchia 1996, pictures after Sfondrini 1975)..... 83
Fig. 2.22 - Oedometer compression of a kaolin slurry (w_0=63%=wLL): (a) σ'_v = 4.9kPa; (b) σ'_v = 49 kPa; (e) σ'_v = 490 kPa; (d) σ'_v = 4900 kPa; (e) scheme of the complex architecture of the fabric in (a); after F. Cotecchia (1996), pictures after V. Cotecchia et al.(1982-b)..... 85
Fig. 2.23 – Fabric orientation of a kaolin specimen at initial state after consolidation in consolidometer to σ'_v=120 kPa, along a vertical plane (after Hattab and Fleureau, 2010)..... 87
Fig. 2.24 - Observation of kaolinite specimen 1D compressed to 6.3MPa: (a) horizontal plane, (b) vertical plane (after Hicher et al., 2000). 88
Fig. 2.25 - Observation of bentonite specimen 1D compressed to 1 MPa: (a) horizontal plane, (b) vertical plane (after Hicher et al., 2000). 89
Fig. 2.26 – Orientation histograms of a bentonite specimen 1D compressed to 6.3 MPa (after Hicher et al., 2000 modified)..... 89

Fig. 2.27 - SEM micrographs of reconstituted Lucera clay (a)at the end of consolidometer stage and (b) after K_0 compression to p'=1350 kPa (after Mitaritonna et al., 2014). 91
Fig. 2.28 – Comparison of orientation curves for kaolinite at initial state (σ'_v =120 kPa) and after isotropic compression to p'=1400 kPa (after Hattab and Fleureau, 2010).93
Fig. 2.29 - (a) Kaolin consolidated to around 80 kPa in a consolidometer and (b) after isotropic consolidation to p'=300 kPa with fabric orientation quantification (after Hicher et al., 2000 modified). 94
Fig. 2.30 – Pore size changes in a kaolinite specimen after isotropic compression to 100 and 400 kPa: (a) cumulative and (b) incremental pore volume vs. entrance pore diameter (after Yu et al., 2016). 95
Fig. 2.31 - (a) Bentonite consolidated in a consolidometer and (b) after isotropic consolidation to p'=6 MPa with fabric orientation quantification (after Hicher et al., 2000 modified). 96
Fig. 2.32 – Microstructure of Gulf of Guinea clay after isotropic loading: (a) cumulative volume results, (b) incremental volume results, (c) SEM photo of natural sediment at 900 kPa and (d) SEM photo of reconstituted sediment at 1000 kPa (after Hattab and Fleureau, 2013)....97
Fig. 2.33 – SEM image and direction histogram of reconstituted Lucera clay compressed under a stress path η=0.3 (Mitaritonna et al., 2014). 98
Fig. 2.34 – Comparison of orientation curves for different axial strains in drained triaxial loading (after Hattab and Fleureau, 2010). 100
Fig. 2.35 – Microfabric after triaxial loading to ε_a=25% along a vertical plane (after Hattab and Fleureau, 2010). 100
Fig. 2.36 - Fabric orientation quantifications of kaolin after drained triaxial shear to 9.1% and 19.5 % axial strain (after Hicher et al., 2000 modified). 101
Fig. 2.37 – SEM micrographs of a kaolinite specimen after drained shear to ε_a=19.5% along a vertical plane (after Hicher et al., 2000). 101
Fig. 2.38 – Pore size changes of a normally consolidated specimen of kaolin after drained triaxial shearing (after Yu et al., 2016 modified). 102

Fig. 2.39 – Microstructure of reconstituted specimen of Gulf of Guinea clay after triaxial loading from p'=100, 200 and 600 kPa. (a) cumulative volume results, (b) incremental volume results, (c) SEM photo at 100 kPa, (d) SEM photo at 200 kPa and (e) SEM photo at 600 kPa (after Hattab and Fleureau, 2013). 103
Fig. 2.40 - Microstructure of natural specimen of Gulf of Guinea clay after triaxial loading from p'=40, 200 and 800 kPa. (a) cumulative volume results, (b) incremental volume results, (c) SEM photo at 40 kPa, (d) SEM photo at 200 kPa and (e) SEM photo at 800 kPa (after Hattab and Fleureau, 2013). 104
Fig. 2.41 – Sequential development of Riedel shears in a specimen of consolidated kaolin with vertical bedding; half arrows indicate the direction of shear (after Morgenstern and Tchalenko, 1967). 106
Fig. 2.42 – Measurements of water content inside samples of kaolinite after drained triaxial tests; A: normally consolidated sample, B: overconsolidated sample. Percentages are calculated as $dw = w_{LOCAL} - w_{AVERAGE}$ (after Hicher et al., 1994). 108
Fig. 2.43 – SEM observation of the failure zone in a normally consolidated specimen of kaolinite after drained shear (after Hicher et al., 1994). 109
Fig. 2.44 – TEM observation of microscopic failure zones with the same orientation as the macroscopic principal failure zone in an OC sample of bentonite after drained shear (after Hicher et al., 1994). 109
Fig. 3.1 - Reconstituted London clay: isotropic compression and swelling curves (data from Henkel 1956; after Schofield and Wroth, 1968). 113
Fig. 3.2 - Normally consolidated reconstituted Weald Clay: failure states in drained and undrained shearing (data from Parry 1960; after Atkinson and Bransby, 1978). 115
Fig. 3.3 - Overconsolidatcd rcconstituted kaolin: nomialized undraincd stress paths (data from Loudon, 1967; after Atkinson and Bransby, 1978). 116
Fig. 3.4 - Remoulded London Clay at failure (data from Parry, 1958; after. Schofield and Wroth, 1968). 117
Fig. 3.5 - Condition of specimens at yield in relation to the critical state line (after Schofield and Wroth, 1968). 118

Fig. 3.6 - Normally consolidated reconstituted kaolin: normalized stress paths (data from Balasubramaniam, 1969; after Atkinson and Bransby, 1978). 119
Fig. 3.7 - The state boundary surface and the elastic wall in the Critical State Framework (after Atkinson and Bransby, 1978). 121
Fig. 3.8 – Plastic potentials: (1) Modified Cam Clay, (2) original Cam Clay and (3) Rowe's stress-dilatancy (drawn for M=1) (after Wood, 1994).....123
Fig. 3.9 – Elliptical yield locus for Cam Clay model in q-p' plane (after Wood, 1994). 124
Fig. 3.10 – Sketch of the 3-SKH model in triaxial stress space (after Stallebrass and Taylor, 1997). 130
Fig. 3.11 – Sketch illustrating the principle of the translation rule for the kinematic surfaces of the 3-SKH model (after Stallebrass and Taylor, 1997).....131
Fig. 3.12 – Diagrammatic representation of the variation of stiffness with recent stress history and loading predicted by the model as the kinematic surfaces translate (after Stallebrass and Taylor, 1997).....133
Fig. 3.13 – S-CLAY 1 yield curve (after Wheeler et al., 2003). 135
Fig. 3.14 – In situ I_v-σ'_v state for natural clays (after Burland, 1990). 141
Fig. 3.15 - SC curves for clays of different sensitivities and yield states, and S_t values for post-sedimentation structure clays (data from Graham et al. (1983) and Lacasse et al. (1985); after Cotecchia and Chandler (2000)). 143
Fig. 3.16 – Sedimentation compression curves in the idealized sensitivity framework; the ICL is taken from Burland (1990) (after Cotecchia and Chandler, 2000).....144
Fig. 3.17 – (a) In situ states of normally consolidated natural clays (Skempton, 1970) and (b) the corresponding SC curves (after Cotecchia and Chandler, 2000). 145
Fig. 3.18 - Idealized behaviour of a natural clay and of the same clay when reconstituted (after Cotecchia and Chandler, 2000). 146
Fig. 3.19 – Undrained stress-paths for clay samples consolidated to gross-yield (after Cotecchia and Chandler, 2000). 147
Fig. 3.20 – Idealized normalized behaviour of different natural clays of given strength sensitivity and of reconstituted clays (after Cotecchia and Chandler, 2000). 148

Fig. 3.21 - Response to one-dimensional compression of reconstituted clay and of natural clay overconsolidated with a post-sedimentation structure at gross yield (after Cotecchia and Chandler (2000)). 149
Fig. 3.22 - One-dimensional compression of natural and reconstituted clays plotted against the void index (data from Samuels, 1975; Bishop et al., 1965; Burland, 1990; Smith, 1992; Coop et al., 1995; 151
Fig. 3.23 - Stress path test data for reconstituted Thames alluvium (from Pickles (1989)). 153
Fig. 3.24 – Stress path data for Bothkennar clay normalized for volume (after Smith, 1992). 154
Fig. 3.25 - Gross yield data for Saint Alban clay samples from two depths (from Leroueil et al. (1979)) normalized for volume (after Cotecchia and Chandler, 2000). 155
Fig. 3.26 – General normalized gross-yield locus for clays (after Cotecchia and Chandler, 2000)..... 157
Fig. 3.27 – Normalizing factors for volume p^*_e and structure (Stress Sensitivity S_σ) (after Cotecchia and Chandler, 2000). 158
Fig. 3.28 - Pappadai clay: gross yield states of the natural clay, stress paths of the clay compressed beyond isotropic gross yield, and stress paths of the reconstituted clay (from Cotecchia & Chandler (1997)). 161
Fig. 3.29 - Pappadai clay behaviour normalized for both volume and structure: gross yield data of the natural clay, post-gross yield stress paths of the natural clay (U, undrained; D, drained), and stress paths for the reconstituted clay (after Cotecchia and Chandler, 2000)..... 162
Fig. 3.30 – Gross yield data for Winnipeg clay normalized for both volume and strength sensitivity (after Graham et al., 1988)..... 163
Fig. 3.31 –Shear tests data for natural and reconstituted Sibari clay samples normalized (a) for volume and composition and (b) for volume and structure (after Cotecchia and Chandler, 2000)..... 164
Fig. 3.32 - Bothkennar clay: gross yield states (after Cotecchia and Chandler, 2000). 165

Fig. 3.33 - Behaviour of both Pappadai and Bothkennar clay normalized for volume, composition and structure (after Cotecchia and Chandler, 2000).....166
Fig. 3.34 – Compression curves for Saint Alban clay samples (from Leroueil et al. (1979). 168
Fig. 3.35 – Compression curves for Bothkennar clay samples (from Smith, 1992).169
Fig. 3.36 – Reconstituted Pappadai clay: flow rules during shear for isotropically (TR1, TR4) and K_0 (TR5) normal consolidated samples (after Cotecchia and Chandler, 1997). 170
Fig. 3.37 - Flow rule for natural Pappadai clay (from Cotecchia & Chandler (1997)) (a) and (b) drained tests (c) undrained tests.....171
Fig. 3.38 - Pappadai clay: stress paths of the natural clay specimens consolidated to states before gross isotropic yield (from Cotecchia & Chandler (1997)). 172
Fig. 3.39 - Idealized behaviour of natural sensitive clays.....173
Fig. 3.40 – Bubble surface, structure surface and reference surface in the model of Rouainia and Wood (2000). 175
Fig. 3.41 – Characteristic surfaces of the MSS model (after Kavvadas and Amorosi, 2000). 178
Fig. 3.42 – Diagram showing the three surfaces of the S3-SKH model in triaxial stress space (after Baudet and Stallebrass, 2004).....183
Fig. 3.43 – Yield curves of S-CLAY1S model (after Koskinen et al., 2002a). 186
Fig. 4.1 - Simplified geological scheme of Southern Italy.....189
Fig. 4.2 - Schematic geological map of Pappadai area (after Cotecchia et al., 1995) with indication of boreholes. Key: 1, alluvium; 2, Quaternary calcarenites; 3, Pappadai clay; 4, lines of section; 5, Borehole A; 6, shaft; 7, individual boreholes. 190
Fig. 4.3 - Geological-geomorphological map of the northern slope of Lucera hill, showing also some of the field investigations carried out in the area. Key: 1) fill of the quarry, 2) terraced alluvial deposits, 3) Sub-Apennine Clays, 4) landslide (a -crowns of landslides A and B; b – body of landslide A), 5) fractured zones, 6) flexures and deep cracks related to landslide C in 1998, 7) foot of the slope (a-1954, b-1975), 8) quarry

front, 9) boreholes drilled in the area (a – inclinometer, b – piezometer), 10) the initials of the continuous coring boreholes, their lithological logs are shown in Fig. 4.8. ... 191
Fig. 4.4 - Geology of the study area, showing the Bradano Trough and Pleistocene marine terraces (from Ciaranfi et al. 1988). Key: 1, Middle-Upper Pleistocene calcarenites; 2, Monte Marano Sands; 3, upper-cycle blue clays; 4, Gravina Calcarenites; 5, palaeocoastline; 6, location of Pappadai; 7, Cretaceous limestone (after Cotecchia and Chandler, 1995). 193
Fig. 4.5 - Sections A-A and B-B, see Fig. 4.2. 195
Fig. 4.6 - Block sampling of Pappadai clay. 196
Fig. 4.7 - Schematic geological map of Lucera area (after National Geological Map, modified). Key: 1) Alluvial deposits, 2) Terraced alluvial deposits, 3) Sub-Apennine Clays, 4) strata attitude, 5) stratigraphic contact, 6) quarry, 7) Lucera town, 8) road. 197
Fig. 4.8 - Lithological profiles of the continuous coring boreholes drilled within the northern slope of the town of Lucera, lying below the hospital. Key: 1) Top soil and/or fill, 2) Sandy-gravely landslide block, 3) Yellow sandy silt with sandy levels, locally pebbly and/or clayey; Sub-Apennine Clay Formation: 4) Yellow sandy-clayey silt or sandy clays with grey sandy or silty levels, 5) Grey silty-sandy clay with yellow sandy or silty levels, 6) Grey silty clay, locally sandy-silty clays, with grey sandy-silty levels; 7) undisturbed sample. 198
Fig. 4.9 - Panoramic view of the Fiamma quarry from the slope below the hospital. 198
Fig. 4.10 - Block sampling of Lucera clay on a wall of the Fiamma quarry. 199
Fig. 4.11 - Geotechnical profiles, borehole A (after Cotecchia and Chandler, 1995). 201
Fig. 4.12 - Casagrande plasticity chart of the block samples of Pappadai clay. 203
Fig. 4.13 - Grading curves of the block samples of Pappadai clay. 203
Fig. 4.14 - Mineralogy of Pappadai clay, data from borehole A (after Cotecchia and Chandler, 1995) 205

Fig. 4.15 - Index properties of Lucera clays from borehole and block samples (CF=clay fraction; wL=Liquid limit; IP=Plasticity index; A=Activity; LI=Liquidity index). 208
Fig. 4.16 - Casagrande plasticity chart of both borehole and block samples.....209
Fig. 4.17 - Grading curves of the block samples of Lucera clay. 209
Fig. 4.18 - Comparison of the grading curves of the second block sample of Pappadai clay and the new block sample of Lucera clay. 210
Fig. 5.1 – Pictures of specimens of Lucera clay at the end of shear tests (those of the upper row are natural clay specimens; those of the bottom row are reconstituted clay specimens). 216
Fig. 5.2 - Schematic design of the oedometer cell. 217
Fig. 5.3 - Modified oedometer apparatus of the Geotechnical Laboratory at the Technical University of Bari. 218
Fig. 5.4 - Triaxial apparatus TRX B at geotechnical laboratory at the Technical University of Bari. 220
Fig. 5.5 – High Pressure Stress-Path System (HPSPS) of the geotechnical laboratory of the Technical University of Bari. 223
Fig. 5.6 – Set up of a specimen inside the cell of the HPSPS. 224
Fig. 5.7 - Volume gauge (Head, 1980). 226
Fig. 5.8 - Sketch of axial LVDT with adjustable screw (Rolo, 2003) and example of application on a triaxial specimen. 227
Fig. 5.9 - Load cell-specimen connection by means of the half ball. 228
Fig. 5.10 - Schematic diagram of an electron microscope (manual of Cambridge 500 SEM). 231
Fig. 5.11 - FESEM Zeiss Supra 40 at CNR Institute of Methodologies for Environmental Analysis at Tito Scalo (PZ).....232
Fig. 5.12 - Porosimeter AutoPore IV (Micromeritics Instr. Corp.) at the geotechnical laboratory of UPC (Universitat Politècnica de Catalunya). 235
Fig. 5.13 - Example of 'fabric orientation' calculation on a sample of Pappadai clay subjected to 22 MPa vertical pressure in oedometer. a) SEM picture; b) polygonal approximation of the 'thinned' image; c) values of the vector orientations, grouped in

intervals of 10°; d) corresponding direction histogram: index $L = 0.277$ (between 1 and 0.21), indicating a very oriented fabric (after Martinez-Nistal et al., 1999). 237
Fig. 5.14 - Method of image processing proposed by Hattab and Fleureau (2010). Example of orientation curve (after Hattab and Fleureau, 2010). 239
Fig. 5.15 - Example of orientation curve (after Hattab and Fleureau, 2010). 240
Fig. 5.16 - One dimensional compression of reconstituted Pappadai (red) and Lucera (black) clays from slurry in the consolidometer. 243
Fig. 5.17 - One dimensional compression of reconstituted Pappadai: batch prepared by Cotecchia (1996) and batch P (see Table 5.5)..... 243
Fig. 5.18 - Suction probe (Imperial College tensiometer). 244
Fig. 5.19 - Suction measured by IC tensiometers for Pappadai clay. 247
Fig. 5.20 - Comparison of suction measured on block 2 of Pappadai clay and suction resulting from a drying path on block sample 1 (after Cotecchia (1996) and Cafaro and Cotecchia (2015) modified). 248
Fig. 5.21 – Terzaghi's model: U%-T_v relationship (after Head, 1986). 252
Fig. 5.22 – Casagrande curve fitting method (after Head, 1986)..... 253
Fig. 5.23 - Specimen with preformed failure plane at axial displacement Δh (eq.(5.20); after Chandler, ... 258
Fig. 5.24 - Bulging and progressive shear band formation before the development of a failure surface (after Cotecchia (1996)). 259
Fig. 6.1 – 1D compression tests on undisturbed (red) and reconstituted (light blue) Pappadai clay from block sample 2. 264
Fig. 6.2 - 1D compression tests on undisturbed and reconstituted Pappadai clay: comparison of tests from this experimental programme (red for the natural clay, light blue for the reconstituted clay) and tests from Cotecchia (1996) (green for the natural clay, blue for the reconstituted clay). 265
Fig. 6.3 - 1D compression tests on undisturbed (black) and reconstituted (light blue) Lucera clay..... 267
Fig. 6.4 - 1D compression tests on undisturbed and reconstituted Lucera clay: comparison of tests from this experimental programme (light blue for the reconstituted

clay, black for the natural clay) and tests from Longo (2003) (blue for the reconstituted clay, green for the natural clay).....268
Fig. 6.5 - Effects of swelling on the compression behaviour of natural Pappadai (red) and Lucera (black) clays. 269
Fig. 6.6 – C_c values from tests on undisturbed and reconstituted Pappadai clay. Data from new tests (red for natural and light blue for reconstituted) compared with data from Cotecchia (1996) (green for natural and blue for reconstituted).....271
Fig. 6.7 - C_c values from tests on undisturbed and reconstituted Lucera clay. Data from new tests (black for natural and light blue for reconstituted) compared with data from Longo (2003) (green for natural and blue for reconstituted). 272
Fig. 6.8 – C_s values from tests on undisturbed and reconstituted Pappadai clay. Data from new tests (red for natural) are compared with data from Cotecchia (1996) (green for natural and blue for reconstituted). 273
Fig. 6.9 - C_s values from tests on undisturbed and reconstituted Lucera clay. Data from new tests (red for natural and light blue for reconstituted) are compared with data from Longo (2003) (green for natural and blue for reconstituted). 274
Fig. 6.10 – Oedometric stiffnesses M measured in oedometer tests and CRS tests on natural and reconstituted Pappadai clay. Data from new tests (red for natural and light blue for reconstituted) are compared with data from Cotecchia (1996) (green for natural and blue for reconstituted).....275
Fig. 6.11 - Oedometric stiffnesses M measured in oedometer tests on natural and reconstituted Lucera clay. Data from new tests (black for natural and light blue for reconstituted) are compared with data from Longo (2003) (green for natural and blue for reconstituted).....276
Fig. 6.12 - Values of c_v of natural and reconstituted Pappadai clay measured in oedometer and CRS tests. Data from new tests (red for natural and light blue for reconstituted) are compared with data from Cotecchia (1996) (green for natural and blue for reconstituted). 277
Fig. 6.13 - Values of c_v of natural and reconstituted Lucera clay measured in oedometer tests. Data from new tests (black for natural and light blue for reconstituted) are

compared with data from Longo (2003) (green for natural and blue for reconstituted). 278
Fig. 6.14 – c_α values measured from oedometer tests on natural and reconstituted Pappadai clay. Data from new tests (red for natural and light blue for reconstituted) are compared with data from Cotecchia (1996) (green for natural and blue for reconstituted). 280
Fig. 6.15 - c_α values measured from oedometer tests on natural and reconstituted Lucera clay..... 281
Fig. 6.16 - - c_α values measured from swelling tests on natural and reconstituted Lucera clay. 281
Fig. 6.17 – k values measured from oedometer and CRS tests on natural and reconstituted Pappadai clay. Data from new tests (red for natural and light blue for reconstituted) are compared with data from Cotecchia (1996) (green for natural and blue for reconstituted)..... 283
Fig. 6.18 - k values measured from oedometer tests on natural and reconstituted Lucera clay. Data from new tests (black for natural and light blue for reconstituted) are compared with data from Longo (2003) (green for natural and blue for reconstituted). 284
Fig. 6.19 - k values measured in compression and swelling paths on Lucera clay. 285
Fig. 6.20 - k values measured from oedometer tests on Lucera and Pappadai clays. 286
Fig. 6.21 – Isotropic compression and swelling states for Pappadai clay. Data from the new test in light blue are compared with data from Cotecchia (1996) (green for natural and blue for reconstituted). 288
Fig. 6.22 – Isotropic (dashed lines) and 1D (full lines) compression behaviour of Pappadai clay. 1D compression data on the natural clay from the new test in red are compared with data from Cotecchia (1996) (green for natural and blue for reconstituted). 289

Fig. 6.23 - Isotropic compression curves for natural and reconstituted Lucera clay. Data from new tests (black for natural and light blue for reconstituted) are compared with data from Longo (2003) (green for natural and blue for reconstituted). 291
Fig. 6.24 - Isotropic (dashed lines) and 1D (full lines) compression behaviour of Lucera clay (only new test data). 293
Fig. 6.25 – Pictures of specimens of Lucera clay at the end of shear tests (those of the upper row are natural clay specimens; those of the bottom row are reconstituted clay specimens). 296
Fig. 6.26 – Specimens of Lucera clay from Longo (2003) and Losacco (2004) at the end of the tests. 297
Fig. 6.27 - v-p' states of shear tests on reconstituted Lucera clay: data from both the new experimental programme and from Longo (2003) and Losacco (2004). 298
Fig. 6.28 - Reconstituted clay: stress-strain behaviour of isotropically consolidated drained test TRL1 (R=1.8) 300
Fig. 6.29 - Reconstituted clay: stress-strain behaviour of isotropically consolidated drained test TRL5 (R=2.8) 301
Fig. 6.30 - Reconstituted clay: stress-strain behaviour of isotropically consolidated undrained test TRL2 (R=4). 302
Fig. 6.31 - Reconstituted clay: stress-strain behaviour of isotropically normally consolidated undrained test TRL3. 303
Fig. 6.32 – Comparison of stress- strain behaviour of reconstituted Lucera clay: data from both the new experimental programme and from Longo (2003) and Losacco (2004). 305
Fig. 6.33 - Comparison of pore pressure increase in undrained tests on reconstituted Lucera clay. 306
Fig. 6.34 – Comparison of volumetric strain in drained tests on reconstituted Lucera clay. 306
Fig. 6.35 - v-p' states of shear tests on natural Lucera clay: data from both the new experimental programme and from Longo (2003) and Losacco (2004). 308

Fig. 6.36 - Natural clay: stress-strain behaviour of isotropically normally consolidated undrained tests TNL1(grey) and TNL10(black) (YSR=3). 310
Fig. 6.37 - Natural clay: stress-strain behaviour of isotropically normally consolidated drained tests TNL4 (YSR=3). 311
Fig. 6.38 - Natural clay: stress-strain behaviour of isotropically normally consolidated undrained tests TNL7 (grey) and TNL11 (black) (YSR=1.6). 313
Fig. 6.39 - Natural clay: stress-strain behaviour of isotropically normally consolidated drained tests TNL6 (YSR=1.6). 314
Fig. 6.40 - Natural clay: stress-strain behaviour of isotropically normally consolidated undrained test TNL12..... 315
Fig. 6.41 – Comparison of stress-strain behaviour for natural Lucera clay in q-ε_a plane and indication of failure surface formation. Data from the new shear tests and from Longo (2003) and Losacco (2004). 317
Fig. 6.42 - Comparison of stress- strain behaviour of natural Lucera clay in q/p'-ε_a plane Data from the new shear tests and from Longo (2003) and Losacco (2004).. 318
Fig. 6.43 - Comparison of pore pressure increase in undrained tests on natural Lucera clay. 319
Fig. 6.44 - Comparison of volumetric strain in drained tests on natural Lucera clay. 319
Fig. 6.45 – Reconstituted Lucera clay: flow rules for tests TRXA, TRXC and TRL2. 321
Fig. 6.46 - Reconstituted Lucera clay: flow rules for tests TRL1 and TRL3. 322
Fig. 6.47 – Natural Lucera clay: flow rules for undrained tests pre-gross-yield. 323
Fig. 6.48 - Natural Lucera clay: flow rules for drained tests pre-gross-yield. 324
Fig. 6.49 - Natural Lucera clay: flow rules for undrained tests post-gross-yield. 324
Fig. 6.50 – Reconstituted clay: stress paths (enlarged in the upper graph) and critical state line..... 326
Fig. 6.51 – Reconstituted clay: v-p' state paths and critical state line. 327
Fig. 6.52 - Natural clay: stress paths and critical state line. 328
Fig. 6.53 - Natural clay: v-p' state paths and critical states..... 330

Fig. 6.54 – Comparison of shear stiffness measured by local and external displacement transducers (test TRL2 on reconstituted Lucera clay).....331
Fig. 6.55 - Comparison of shear stiffness measured by local and external displacement transducers (test TNL7 on natural Lucera clay). 332
Fig. 6.56 - Shear stiffness of reconstituted Lucera clay. 333
Fig. 6.57 - Shear stiffness of natural Lucera clay.....334
Fig. 6.58 – Definition of a curvilinear isotropic compression line for normalization. 335
Fig. 6.59 – Reconstituted clay: normalized stress paths and state boundary surface. 337
Fig. 6.60 – Stress paths normalized with respect to the equivalent pressure p*e: (a) natural clay specimens consolidated to states before isotropic yield; (b) natural clay specimens consolidated to states beyond isotropic yield and reconstituted clay specimens. 340
Fig. 6.61 – Normalized stress paths of the natural clay consolidated to states before isotropic yield and dry and wet sides of natural clay framework of behaviour.....341
Fig. 6.62 – Comparison of natural and reconstituted state boundary surfaces for Pappadai and Lucera clay (data for Pappadai after Cotecchia, 1996).....342
Fig. 7.1 - SEM micrographs along a vertical fracture of undisturbed Pappadai clay at low magnification (after Cotecchia, 1996).....346
Fig. 7.2 - Image processing of the SEM micrograph in Fig. 7.1b: a) 'thinned' image and b) resulting direction histogram. 347
Fig. 7.3 - SEM micrograph along a vertical fracture of undisturbed Pappadai clay at medium magnification (after Cotecchia, 1996).....348
Fig. 7.4 – SEM micrographs along a vertical fracture of undisturbed Pappadai clay at medium magnification. 349
Fig. 7.5 – Image processing of the SEM micrograph in Fig. 7.4a: a) 'thinned' image and b) resulting direction histogram. 350
Fig. 7.6 – SEM micrographs along a vertical fracture of undisturbed Pappadai clay. a) Fossil shells and pyrite crystals; b) Foraminifera. 351

Fig. 7.7 – SEM micrographs along a vertical fracture of undisturbed Pappadai clay: framboid pyrite crystals. 352
Fig. 7.8 – SEM micrographs along a vertical fracture of undisturbed Pappadai clay: large grains of a) quartz and b) calcite. 353
Fig. 7.9 - SEM micrographs along a horizontal fracture of undisturbed Pappadai clay. 356
Fig. 7.10 - SEM micrographs along a vertical fracture of undisturbed Pappadai clay at high magnification (after Cotecchia, 1996). 357
Fig. 7.11 - Direction histograms of the SEM micrographs in Fig. 7.10 on undisturbed Pappadai clay. 358
Fig. 7.12 – SEM micrograph along a vertical fracture of undisturbed Pappadai clay at high magnification. 359
Fig. 7.13 - SEM micrograph along a vertical fracture of undisturbed Pappadai clay at high magnification 360
Fig. 7.14 - MIP tests on natural Pappadai clay at undisturbed state (state P_1, $e=0.82$). a) cumulative and b) derivative curve. 362
Fig. 7.15 – SEM pictures of undisturbed Pappadai at high magnification: pores having size equal to the DPS can be recognized. 365
Fig. 7.16 – Enlargement of the micrograph in Fig. 7.13. 366
Fig. 7.17 – SEM micrograph of undisturbed Lucera clay along a vertical fracture at low magnification (after Mitaritonna, 2006 on block sample 1). 369
Fig. 7.18 – Direction histogram of the micrograph shown in Fig. 7.17 of undisturbed Lucera clay. 369
Fig. 7.19 - SEM micrographs along a vertical fracture of undisturbed Lucera clay at medium-low magnification (after Mitaritonna, 2006 on block sample 1). 370
Fig. 7.20 - SEM of undisturbed Lucera clay along a vertical fracture at high magnification (after Mitaritonna, 2006 on block sample 1). 371
Fig. 7.21 - SEM of undisturbed Lucera clay along a vertical fracture at medium magnification: areas of chaotic fabric with particles mainly in edge-to-face contact (after Mitaritonna, 2006 on block sample 1). 371

Fig. 7.22 - SEM micrograph of undisturbed Lucera clay along a horizontal fracture (after Mitaritonna, 2006 on block sample 1).....372
Fig. 7.23 – SEM micrograph of undisturbed Lucera clay: detail of Globigerinae (after Mitaritonna, 2006 on block sample 1).....372
Fig. 7.24 – Fossils in natural Lucera clay. 373
Fig. 7.25 - MIP test on undisturbed Lucera clay (state L_1, e=0.55): a) cumulative and b) derivative curves. 375
Fig. 7.26 – SEM of reconstituted Pappadai Clay: global view of the fabric on a vertical fracture (after Cotecchia, 1996).....378
Fig. 7.27 - SEM of reconstituted Pappadai Clay on a vertical fracture at medium magnification (after Cotecchia, 1996). 378
Fig. 7.28 – Direction histogram of the SEM micrograph in Fig. 7.27.....379
Fig. 7.29 – SEM of reconstituted Pappadai Clay on a sub-horizontal fracture at medium magnification (after Cotecchia, 1996). 379
Fig. 7.30 - SEM of reconstituted Pappadai Clay on a vertical fracture at medium magnification (after Cotecchia, 1996). 380
Fig. 7.31 – Direction histograms of the SEM micrographs in Fig. 7.30 381
Fig. 7.32 - MIP test on reconstituted Pappadai clay (state PR, e=1.245): a) cumulative and b) derivative curves. 382
Fig. 7.33 - SEM of reconstituted Lucera clay along a vertical fracture at medium magnification. 384
Fig. 7.34 - Direction histogram of reconstituted Lucera clay on the picture in Fig. 7.33a. 385
Fig. 7.35 - SEM of undisturbed Lucera clay along a vertical fracture at medium-high magnification. 385
Fig. 7.36 - SEM of undisturbed Lucera clay along a vertical fracture at medium-high magnification. 386
Fig. 7.37 -Direction histograms of the SEM micrographs in (a) Fig. 7.35 and (b) Fig. 7.36b.....387
Fig. 7.38 – SEM in reconstituted Lucera clay: fossil shells.....387

Fig. 7.39 - MIP test on reconstituted Lucera clay (state LR, e=0.92): a) cumulative and b) derivative curves..... 389
Fig. 7.40 – SEM of reconstituted Lucera clay: identification of the DPS. 390
Fig. 7.41 – Microstructural analyses on specimens 1D and isotropically compressed. 392
Fig. 7.42 - MIP tests on natural Pappadai clay in 1D compression. a) cumulative and b) derivative curves..... 396
Fig. 7.43 - Natural clay compressed to a σ'_v of 3 MPa: the fabric is more open and flocculated in the centre of the picture; "chaotic masses" of particles are seen in the bottom half and in the top right of the picture..... 397
Fig. 7.44 - Natural clay compressed to a σ'_v of 3 MPa: chaotic densely packed fabric (after Cotecchia, 1996)..... 397
Fig. 7.45 - SEM micrograph along a vertical fracture of Pappadai clay 1D compressed σ'_v=3 MPa at medium magnification. 398
Fig. 7.46 – SEM on natural Pappadai clay compressed to σ'_v=3 MPa: undamaged shells of globigerinae. 398
Fig. 7.47 - SEM on natural Pappadai clay compressed to σ'_v=3 MPa: undamaged pyrite crystals. 399
Fig. 7.48 – SEM micrograph along a vertical fracture of natural Pappadai clay compressed σ'_v of 3 MPa; two stacks of iso-orientated particles confine a chaotic mass of particles (after Cotecchia, 1996). 399
Fig. 7.49 –SEM micrograph along a vertical fracture of Pappadai clay 1D compressed to σ'_v=3 MPa at high magnification. 400
Fig. 7.50 - SEM micrographs along a vertical fracture at medium magnification of Pappadai clay 1D compressed to σ'_v=5 MPa. 402
Fig. 7.51 - Direction histograms of the SEM micrographs in Fig. 7.50a. 403
Fig. 7.52 - SEM micrograph along a vertical fracture of Pappadai clay 1D compressed to σ'_v=5 MPa: undamaged calcite crystal. 403
Fig. 7.53 - SEM micrograph along a vertical fracture of Pappadai clay 1D compressed to σ'_v=5 MPa: undamaged pyrite crystal. 404

Fig. 7.54 - Natural clay compressed to aσ'_v of 22 MPa: vertical fracture; stacks of c.p.o. fabric within less oriented fabric (after Cotecchia, 1996). 406
Fig. 7.55 - Natural clay compressed to a σ'_v of 22 MPa: vertical fracture; the fabric is highly oriented, with many stack s of c.p.o. fabric (after Cotecchia, 1996). 406
Fig. 7.56 - SEM micrographs along a vertical fracture of Pappadai clay 1D compressed to σ'_v=18.5 MPa at medium magnification. 407
Fig. 7.57 - Natural clay compressed to a σ'_v of 22 MPa: vertical fracture; detail of flocculated fabric (after Cotecchia, 1996). 408
Fig. 7.58 –SEM micrograph along a vertical fracture of Pappadai clay 1D compressed to σ'_v=18.5 MPa at high magnification. 408
Fig. 7.59 - SEM micrograph along a vertical fracture of Pappadai clay 1D compressed to σ'_v=18.5 MPa at high magnification: evidence of zones of flocculated fabric. ...409
Fig. 7.60 - SEM micrograph along a vertical fracture of Pappadai clay 1D compressed to σ'_v=18.5 MPa: undamaged pyrite framboids. 410
Fig. 7.61 - MIP tests on natural Lucera clay in 1D compression: a) cumulative, b) enlarged cumulative and c) derivative curves. 416
Fig. 7.62 - SEM micrograph along a vertical fracture of Lucera clay 1D compressed to σ'_v=5 MPa at medium magnification. 417
Fig. 7.63 - SEM micrograph along a vertical fracture of Lucera clay 1D compressed to σ'_v=5 MPa at medium-high magnification. 417
Fig. 7.64 - SEM micrograph along a vertical fracture of natural Lucera clay 1D compressed to σ'_v=5 MPa: areas of flocculated fabric. 418
Fig. 7.65 – SEM micrograph along a vertical fracture of natural Lucera clay 1D compressed to σ'_v=5 MPa: view of a c.p.o. domain. 418
Fig. 7.66 – Direction histograms of natural Lucera clay 1D compressed to σ'_v=5 MPa, referred to a) Fig. 7.62, b) Fig. 7.63 and c) Fig. 7.65. 419
Fig. 7.67 - SEM micrograph along a vertical fracture of natural Pappadai clay 1D swelled to σ'_v=20 kPa at medium magnification. 423
Fig. 7.68 - SEM micrograph along a vertical fracture of natural Pappadai clay 1D swelled to σ'_v=20 kPa: enlargement of Fig. 7.67. 423

Fig. 7.69 - SEM micrograph along a vertical fracture of Pappadai clay after swelling to σ'_v=20 kPa at high magnification. 424
Fig. 7.70 - SEM micrograph along a vertical fracture of Pappadai clay after swelling to σ'_v=20 kPa: pores between particles approaching the DPS. 424
Fig. 7.71 – Direction histograms of Pappadai clay after swelling to σ'_v=20 kPa of the micrographs in a) Fig. 7.67, b) Fig. 7.68 and c) Fig. 7.69 425
Fig. 7.72 – Orientation curves from SEM micrographs at the same magnification (3000x) for natural Pappadai clay under 1D compression. 426
Fig. 7.73 - MIP tests on reconstituted Pappadai in 1D compression. a) cumulative and b) derivative curves..... 430
Fig. 7.74 – SEM micrographs of reconstituted Pappadai clay compressed to a σ'_v of 22 MPa: fabric on fractures inclined to the horizontal (after Cotecchia, 1996). 431
Fig. 7.75 - SEM micrographs of reconstituted Pappadai clay compressed to σ'_v of 22 MPa: fabric on vertical fractures at medium magnification (after Cotecchia, 1996). 432
Fig. 7.76 – SEM micrograph on reconstituted Pappadai clay compressed to σ'_v of 22 MPa: areas of chaotic fabric where the small particles are either stuck on the surface of the domains or penetrate into them (after Cotecchia, 1996). 433
Fig. 7.77 – Direction histograms of reconstituted Pappadai clay compressed to σ'_v of 22 MPa of a) Fig. 7.75a, b)Fig. 7.75b and c) Fig. 7.76. 433
Fig. 7.78 – MIP tests on reconstituted Lucera clay in 1D compression. a) cumulative and b) derivative curves. 434
Fig. 7.79 – MIP tests on natural Lucera clay after isotropic compression: a) cumulative and b) derivative curves. 437
Fig. 7.80 – Comparison of incremental curves for specimens of natural Lucera clay 1D and isotropically compressed to states pre- and post- gross-yield to approximately the same void ratios. 438
Fig. 7.81 – SEM micrograph of natural Lucera clay isotropically compressed to pre-gross-yield state LI_2 along a vertical fracture at medium magnification. 438
Fig. 7.82 - SEM micrographs of natural Lucera clay isotropically compressed to pre-gross-yield state LI_2 along a vertical fracture at medium-high magnification. 439

Fig. 7.83 – Direction histograms of natural Lucera clay under isotropic loading to pre-gross-yield state LI_2 of a) Fig. 7.81, b) Fig. 7.82a and c) Fig. 7.82b. 440
Fig. 7.84 – Enlargement of the micrograph in Fig. 7.82b showing a nucleus formed by clay particles. 441
Fig. 7.85 - SEM on natural Lucera clay at state LI_2 along a vertical fracture: example of a particular particle domain. 441
Fig. 7.86 – SEM on natural Lucera clay at state LI_2 showing two nuclei separated by a c.p.o. strata. 442
Fig. 7.87 – SEM micrograph along a vertical fracture of natural Lucera clay isotropically compressed to state LI_3 at medium magnification. 444
Fig. 7.88 - SEM micrograph along a vertical fracture of natural Lucera clay isotropically compressed to state LI_3 at medium magnification. 445
Fig. 7.89 - SEM micrograph along a vertical fracture of natural Lucera clay isotropically compressed to state LI_3 at medium magnification. 445
Fig. 7.90 – Enlargement of the micrograph in Fig. 7.88. 446
Fig. 7.91 - Enlargement of the micrograph in Fig. 7.89 446
Fig. 7.92 – Direction histograms of the micrographs in a) Fig. 7.87, b) Fig. 7.88 and c) Fig. 7.89. 447
Fig. 7.93 – Orientation curves for natural Lucera clay under 1D and isotropic compression (all curves refer to micrographs of magnification 1000x). 447
Fig. 7.94 - MIP tests on reconstituted Pappadai clay 1D and isotropically compressed. a) cumulative and b) derivative curves. 450
Fig. 7.95 – a) v-p' states and b) stress paths of shear tests on natural Lucera clay: indication of states of microstructural analyses. 453
Fig. 7.96 - Specimens TNL4 and TNL6 at the end of the drained shear tests and corresponding final void ratios. The position of the MIP specimens is indicated, inside the band of strain localization for specimen TNL4, inside (pink) and outside (purple) the zone of strain localization for specimen TNL6. 454

Fig. 7.97 - MIP tests on natural Lucera clay in drained shear TNL4 (R=3, e=0.53) inside the shear band compared to undisturbed state. a) cumulative and b) derivative curves. 457
Fig. 7.98 - SEM micrograph of natural Lucera clay specimen TNL4 sheared drained along a vertical fracture: global view and indication of the incipient shear band location. 458
Fig. 7.99 - SEM micrograph of natural Lucera clay specimen TNL4 sheared drained along a vertical fracture at low magnification: enlargement of the incipient shear band. 458
Fig. 7.100 - SEM micrograph of natural Lucera clay specimen TNL4 sheared drained along a vertical fracture at medium- low magnification: enlargement of Fig. 7.99... 459
Fig. 7.101 - SEM micrograph of natural Lucera clay specimen TNL4 sheared drained along a vertical fracture at medium-low magnification..... 459
Fig. 7.102 - SEM micrograph of natural Lucera clay specimen TNL4 sheared drained along a vertical fracture at medium-high magnification. 460
Fig. 7.103 – Direction histograms of specimen TNL4 inside the incipient shear band on micrographs in a) Fig. 7.101 and b) Fig. 7.102. 460
Fig. 7.104 - SEM micrograph of natural Lucera clay specimen TNL4 sheared drained along a vertical fracture outside the shear band zone at a) low and b) medium magnification. 461
Fig. 7.105 - Direction histograms of specimen TNL4 outside the incipient shear band on micrographs in a) Fig. 7.104a and b) Fig. 7.104b. 462
Fig. 7.106 - MIP tests on natural Lucera clay in drained shear TNL6(R=1.6, e=0.455), both inside (SB) and outside (OB) the localization zone, compared to state LI2. a) cumulative and b) derivative curves..... 465
Fig. 7.107 - SEM micrographs of natural Lucera clay specimen TNL6 sheared drained along a vertical fracture at low magnification. 466
Fig. 7.108 - Direction histograms of specimen TNL6 inside the incipient shear band on micrographs in a) Fig. 7.107a and b) Fig. 7.107b. 467

Fig. 7.109 – Enlargement of Fig. 7.107a showing a fissure along the direction of the shear band. 467
Fig. 7.110 – Enlargement of Fig. 7.109 showing highly oriented strata interbedding areas of random fabric. 468
Fig. 7.111 - SEM micrographs of natural Lucera clay specimen TNL6 sheared drained along a vertical fracture at medium magnification. 468
Fig. 7.112 – Orientation curves for natural Lucera clay under drained shear (all curves refer to micrographs of magnification 300x) 469
Fig. 7.113 - Specimens TNL1 and TNL7 at the end of the undrained shear tests. The position of the specimens taken for microstructural analyses is indicated, inside the shear bands (SB, pink) and outside the shear bands (OB, green) 470
Fig. 7.114 - MIP tests on natural Lucera clay in undrained shear test TNL1 (R=3, e=0.546) inside (SB) and outside (OB) the shear band compared to specimen at undisturbed state. a) cumulative, b) enlarged cumulative and c) derivative curves. 475
Fig. 7.115 - SEM micrographs of natural Lucera clay specimen TNL1 sheared undrained along a vertical fracture across the shear band at medium magnification. 476
Fig. 7.116 – Enlargements of micrographs in Fig. 7.115. 477
Fig. 7.117 . Enlargement of Fig. 7.116b showing very small domains of edge-to-face particles. 478
Fig. 7.118 - SEM micrograph of natural Lucera clay specimen TNL1 sheared undrained along a vertical fracture across the shear band at medium-high magnification: highly oriented particles confining with honeycomb arrangements. 478
Fig. 7.119 - - SEM micrograph of natural Lucera clay specimen TNL1 sheared undrained along the failure surface. 479
Fig. 7.120 - SEM micrograph of natural Lucera clay specimen TNL1 sheared undrained along the failure surface: intersection with the failure surface of the symmetrical shear band. 479
Fig. 7.121 – Enlargement of the micrograph in Fig. 7.120: a perfectly oriented stack of particles emerges from the failure surface of the investigated shear band. 480

Fig. 7.122 - SEM micrograph of natural Lucera clay specimen TNL1 sheared undrained outside the shear band at low magnification. 480
Fig. 7.123 - SEM micrograph of natural Lucera clay specimen TNL1 sheared undrained outside the shear band at medium magnification. 481
Fig. 7.124 - SEM micrograph of natural Lucera clay specimen TNL1 sheared undrained outside the shear band at medium-high magnification. 481
Fig. 7.125 – Direction histograms for the micrographs on specimen TNL1 OB shown in a) Fig. 7.122, b) Fig. 7.123 and c) Fig. 7.124. 482
Fig. 7.126 - MIP tests on natural Lucera clay at undisturbed state, in undrained shear TNL1, inside (SB) and outside (OB) the shear band, and at $q_{peak}/2$ (TNL10). a) cumulative and b) derivative curves..... 484
Fig. 7.127 - MIP tests on natural Lucera clay in undrained shear test TNL7 (R=1.6, e=0.518) inside (SB) and outside (OB) the shear band compared to specimen at state LI2. a) cumulative, b) enlarged cumulative and c) derivative curves. 487
Fig. 7.128 - SEM micrograph of natural Lucera clay specimen TNL7 sheared undrained inside the shear band: detail of the shear band observed on a vertical fracture. 489
Fig. 7.129 - SEM micrograph of natural Lucera clay specimen TNL7 sheared undrained inside the shear band: detail of a highly oriented band parallel to the shear band. .. 490
Fig. 7.130 – Enlargement of the micrograph in Fig. 7.128. 490
Fig. 7.131 – Enlargement of the micrograph in Fig. 7.129. 491
Fig. 7.132 – Enlargement of the micrograph in Fig. 7.130. 491
Fig. 7.133 - SEM micrograph of natural Lucera clay specimen TNL7 sheared undrained inside the shear band at medium-high magnification..... 492
Fig. 7.134 – Direction histograms of the SEM micrographs in (a) Fig. 7.131 and (b) Fig. 7.133 492
Fig. 7.135 - MIP tests on natural Lucera clay at state LI2, in undrained shear TNL7 (R=1.6, e=0.518) inside (SB) and outside (OB) the shear band, and at $q_{peak}/2$ (TNL11). a) cumulative and b) derivative curves..... 493
Fig. 7.136 – a) v-p' states and b) stress paths of shear tests on reconstituted Lucera clay: indication of states of microstructural analyses. 495

Fig. 7.137 – Specimens TRL1 and TRL2 (from which the extremities were cut for measurements of w) at the end of the drained and undrained shear tests respectively. Position of MIP specimens is indicated. 496
Fig. 7.138 – MIP tests on reconstituted Lucera clay at state LR and in undrained shear TRL2 (R=4, e=0.926), both inside (SB) and outside (OB) the shear band. a) cumulative and b) derivative curves. 498
Fig. 7.139 - MIP tests on reconstituted Lucera clay at state LR and in drained shear TRL1 (R=1.8, e=0.85), both inside (SB) and outside (OB) the shear band. a) cumulative and b) derivative curves. 501
Fig. 7.140 - SEM micrograph of reconstituted Lucera clay specimen TRL1 sheared drained at low magnification. 502
Fig. 7.141 - SEM micrograph of reconstituted Lucera clay specimen TRL1 sheared drained at medium magnification. 502
Fig. 7.142 – Enlargement of the micrograph in Fig. 7.141, showing the fabric generated by drained shear at high magnification. 503
Fig. 7.143 – Direction histograms of specimen TRL1 on the micrographs in a) Fig. 7.140, b)Fig. 7.141 and c) Fig. 7.142. 503
Fig. 8.1 – Comparison of PSD curves for stiff Pappadai, Lucera and Boom clay at undisturbed state (data on Boom clay after Lima et al., 2008). 510
Fig. 8.2 –High magnification SEM micrographs of a) undisturbed Pappadai clay and b) natural Lucera clay at state LI_2, in which pores having the size of the DPS are recognized. 512
Fig. 8.3 - SEM micrographs of undisturbed Boom clay (after Lima et al., 2008)....513
Fig. 8.4 - Comparison of PSD curves for soft St Marcel, Gulf of Guinea and Bothkennar clay at undisturbed state (after Delage and Lefevbre, 1984; Hattab et al., 2013; Tanaka, 2003 respectively). 516
Fig. 8.5 - SEM micrograph of undisturbed Gulf of Guinea clay on a vertical plane (after Hattab et al., 2013). 521
Fig. 8.6 - SEM micrograph of undisturbed St Marcel clay on a vertical plane at high magnification (after Delage and Lefebvre, 1984). 521

Fig. 8.7 – Pore-size changes of a kaolin slurry, prepared at twice the LL, after 1D consolidation to 50 and 100 kPa (after Yu et al., 2016). 522
Fig. 8.8 - Comparison of PSD curves for remoulded St Marcel clay and reconstituted Gulf of Guinea clay (after Delage and Lefebvre, 1984 and Hattab et al., 2013)..... 522
Fig. 8.9 - SEM micrograph of reconstituted GoG clay consolidated at σ'_v=80 kPa (after Hattab et al., 2013)..... 523
Fig. 8.10 – Comparison of PSD curves for reconstituted stiff Pappadai, Lucera and London clay after compression in consolidometer (data for London clay after Monroy et al., 2006)..... 526
Fig. 8.11 - SEM micrographs of reconstituted London clay consolidated to σ'_v=108 kPa at a) 1000x and b) 3000x magnification (after Monroy et al., 2006). 527
Fig. 8.12 - Comparison of PSD curves for the undisturbed and reconstituted soft clays of St Marcel and GoG (after Delage and Lefebvre, 1984 and Hattab et al., 2013)... 531
Fig. 8.13 – Comparison of PSD curves for the undisturbed and reconstituted stiff clays of Pappadai and Lucera. 531
Fig. 8.14 - Evolution in 1D compression of PSD curves of natural stiff Pappadai clay (e and σ'_v in standard character) and Lucera clay (e and σ'_v in italics). 534
Fig. 8.15 - Evolution in 1D compression of PSD curves of natural and reconstituted Pappadai clay. 539
Fig. 8.16 - Evolution in 1D compression of PSD curves of natural and reconstituted Lucera clay..... 539
Fig. 8.17 - Evolution in 1D compression of PSD curves of natural soft St Marcel clay (replotted after Delage and Lefebvre, 1984). 540
Fig. 8.18 - Evolution in 1D compression of PSD curves of natural soft GoG clay (after Hattab et al., 2013). Note that $e_{(MIP)}$ is the maximum void ratio measured in the MIP test, reported in case the actual void ratio is unknown. 540
Fig. 8.19 – Evolution in 1D compression of PSD curves of natural and reconstituted GoG clay (after Hattab et al., 2013). Note that $e_{(MIP)}$ is the maximum void ratio measured in the MIP test, reported in case the actual void ratio is unknown. 541

Fig. 8.20 – Dominant pore size against vertical effective stress in 1D compression for Pappadai, Lucera, GoG and St Marcel clay. The threshold pressure for microstructural re-organization is indicated with an arrow. 543
Fig. 8.21 – Frequency of the DPS against vertical effective stress in 1D compression for Pappadai, Lucera, GoG and St Marcel clay. 546
Fig. 8.22 – Width of the pore size distribution curve against vertical effective stress in 1D compression for Pappadai, Lucera, GoG and St Marcel clay. 546
Fig. 8.23 – Dominant pore size against sensitivity in 1D compression for Pappadai, Lucera and GoG clay. 547
Fig. 8.24 - Comparison of natural GoG specimens 1D and isotropically compressed (after Hattab et al., 2013). 553
Fig. 8.25 – Evolution of DPS with volumetric strain for natural GoG clay in 1D and isotropic compression. 553
Fig. 8.26 – State boundary surfaces of the natural and reconstituted sediments of Gulf of Guinea (after Le, 2008). 554
Fig. 8.27 – Comparison of the undisturbed specimen of Gulf of Guinea clay and the specimen sheared drained from a lightly over-consolidated state (after Hattab et al., 2013). 563
Fig. 8.28 – Evolution in drained shear of natural and reconstituted Gulf of Guinea clay compressed isotropically beyond gross-yield (after Hattab et al., 2013). 563
Fig. 8.29 - Evolution in drained shear of natural Lucera clay in drained shears TNL4 and TNL6, compared to isotropic pre-yield compression states prior to shearing, respectively L1 and LI2 (Fig. 7.41). 564
Fig. 8.30 – Stress paths of the drained and undrained shear tests on natural Pappadai clay used for the calibration of the model of Rouainia and Wood (2000) (test data after Cotecchia, 1996). 572
Fig. 8.31 – v-lnp' state paths of the drained and undrained shear tests on natural Pappadai clay used for the calibration of the model of Rouainia and Wood (2000) (test data after Cotecchia, 1996). 573

Fig. 8.32 – Bubble surface, structure surface and reference surface in the model of Rouainia and Wood (2000). 573
Fig. 8.33 – One dimensional compression curves for natural Pappadai clay: experimental data in full lines (after Cotecchia, 1996) and numerical results in dashed lines. 577
Fig. 8.34 - Stress-strain curves for the shear tests on natural Pappadai clay: experimental data in full lines (after Cotecchia, 1996) and numerical results in dashed lines. 578
Fig. 8.35 – Excess pore water pressure against deviatoric strain for the shear tests on natural Pappadai clay: experimental data in full lines (after Cotecchia, 1996) and numerical results in dashed lines..... 578
Fig. 8.36 – Volumetric strains against deviatoric strains for the shear tests on natural Pappadai clay: experimental data in full lines (after Cotecchia, 1996) and numerical results in dashed lines. 579
Fig. 8.37 - Stress paths for the shear tests on natural Pappadai clay: experimental data in full lines (after Cotecchia, 1996) and numerical results in dashed lines. 579
Fig. 8.38 – State paths for the shear tests on natural Pappadai clay: experimental data in full lines (after Cotecchia, 1996) and numerical results in dashed lines. 580
Fig. 8.39 – Evolution of the parameter r in a one-dimensional compression test simulation..... 581
Fig. 8.40 – Comparison between isotropic compression curves from experimental and numerical data (after Amorosi et al., 2001)..... 584
Fig. 8.41 – Comparison between stress-strain curves from experimental and numerical data (after Amorosi et al., 2001). 585
Fig. 8.42 - Comparison between excess pore water pressure and volumetric strains against axial strain from experimental and numerical data (after Amorosi et al., 2001). 585

LIST OF TABLES

Table 4.1- Summary of the index properties of the Pappadai clay, borehole A (after Cotecchia and Chan-dler,1995). 201
Table 4.2 - Index properties of the two Pappadai block samples: block sample 1 is that of Cotecchia (1996), block sample 2 is that used in this experimental programme. w_n = natural water content; e_0 = natural void ratio; G_s = particle specific gravity; S_r = saturation degree; w_L=liquid limit; w_P=plastic limit; IP = plasticity index; CF = clay fraction; A = activity; IC = consistency index. 202
Table 4.3 - Mineralogical composition of the Pappadai undisturbed sample from block sample 1 (Cotecchia, 1996). 206
Table 4.4 - Index properties of Lucera block samples: for block sample 1, data from Longo (2003), denoted as L_1, and from Mitaritonna (2006), denoted as L_2 and L_3, are shown. w_n = natural water content; e_0 = natural void ratio; G_s = particle specific gravity; S_r = saturation degree; w_L=liquid limit; w_P=plastic limit; IP = plasticity index; CF = clay fraction; A = activity; IC = consistency index. 207
Table 4.5 - Mineralogical composition (weight %) of the clay block sampled at the Fiamma quarry. Bulk sample: phyllosilicate (ΣPh), quartz (Q), K-feldspar (K-Fd), plagioclase (P), calcite (Cc), dolomite (D); Clay fraction sample: mixed-layers illite/smectite (I/S; the illite content, as %, in the interlayers is specified in brackets), illite (I), kaolinite (K), chlorite (Ch); tr = in traces. 210
Table 5.1 - 1D compression tests on Pappadai and Lucera clays. 213
Table 5.2 – Isotropic compression tests on Pappadai and Lucera clays. 214
Table 5.3 – Shear tests on reconstituted Lucera clay. 215
Table 5.4 – Shear tests on natural Lucera clay. 215
Table 5.5 - Reconstituted Pappadai and Lucera clays: water content, initial and final void ratios. 242
Table 5.6 - Results of filter paper measurements on natural Pappadai clay soon after block sampling. 247
Table 5.7 - Results of filter paper and triaxial suction measurements on natural Lucera clay soon after block sampling. 249

Table 6.1 – Values of soil constants for Pappadai (after Cotecchia, 1996) and Lucera clays. 294
Table 6.2 – Shear tests on natural and reconstituted Lucera clay carried out by Longo (2003) and Losacco (2004)..... 296
Table 6.3 – Summary of shear tests results on natural Lucera clay. 320
Table 6.4 – Natural clay: pseudo-critical states..... 328
Table 7.1 – Synthesis of microstructural analyses on specimens 1D and isotropically compressed. 393
Table 8.1 – Summary of the properties of the analysed clays..... 507
Table 8.2 – Rouainia and Wood (2000) model parameters for Pappadai clay. 577
Table 8.3 – Kavvadas and Amorosi (2000) model parameters for Pappadai clay... 583

LIST OF SYMBOLS

1-D	one-dimensional
c_α	coefficient of secondary compression: $\Delta e/\log(t)$
Cc	compression index
CF	clay fraction
C_k	permeability index
CS	critical state
Cs	swelling index
CSL	Critical State Line
C_u	undrained shear strength
C_u^R	remoulded undrained shear strength
Cv	coefficient of 1 D consolidation
d	diameter of the specimen
Dol	dolomite
Dr	relative density
d_0	immediate oedometer settlement (Casagrande curve fitting)
e	voids ratio
e_0	initial void ratio
Feld	feldspar
Gs	soil specific gravity
H	longest drainage path at the start of consolidation
h	initial height of the specimen
I	Illite
k	coefficient of hydraulic conductivity
K	Kaolinite
K_0	at-rest earth pressure coefficient
LI	liquidity index
M	stress ratio q/p' at critical state
MF	silt fraction

mv	coefficient of oedometric compressibility
NC	normally consolidated
OC	overconsolidated
OCR	overconsolidation ratio: σ'p / σ'v
PI	plasticity index
p'	mean normal effective stress: $(\sigma'_1 + 2\,\sigma'_3)/3$ for axial symmetry
	mean effective stress at the start of shearing in triaxial testing
p'_{cs}	mean effective stress at critical state
p'_y	mean effective stress at yield in isotropic compression
q	deviatoric stress: $\sigma'_1 - \sigma'_3$ for axial symmetry
q_{CS}	deviatoric stress at critical state
q_t	cone resistance from CPTU test
Qz	quartz
r	pore fluid salinity
R	overconsolidation ratio: p'_p/p'
SCC	sedimentation compression line (Skempton 1970)
Sm	Smectite
S_t	sensitivity
SF	sand fraction
t	time in minutes
Tv	Terzaghi's time factor
Δu	excess pore water pressure
w	water content
w_L	liquid limit
w_P	plastic limit
ε_r	radial strain
ε_s	shear strain: $2(\varepsilon 1 - \varepsilon 3)/3$ for axial symmetry
ε_v	volumetric strain: $(\varepsilon 1 + 2\,\varepsilon 3)$
φ'_{CS}	critical state friction angle
γ	bulk unit weight

γ_d	dry bulk unit weight
γ_w	unit weight of water
γ_s	unit weight of the soil grains
σ	total stress
σ'	effective stress
σ'_h	in situ horizontal stress
σ'_n	normal effective stress
σ'_r	radial effective stress
σ'_v	vertical effective stress
σ'_p	one-dimensional preconsolidation stress
σ'_{v0}	in situ horizontal stress
σ'_y	vertical effective stress at gross yield in one-dimensional compression
τ	shear stress

1 INTRODUCTION

1.1 Introduction

The present research work has been developed in the field of the interpretation and modeling of the mechanical response of soils, in particular of clays, and has used the approach which combines the investigation of the soil element macro-behaviour, through laboratory experimental testing, with the observation of the soil features and processes at the micro-scale.

One of the broadest field of interest of geotechnical research, since its early development, has been concerned with the assessment and modelling of the mechanical behaviour of natural soils. In nature, these materials are of varying composition and experience variable geological histories, during which several processes can occur (e.g., thixotropy, diagenesis, weathering), determining the variability of the soil response. Several are the chemo-physical processes that may affect the clay microstructure and, consequently, control the clay state and macro-response.

The complexity of the whole series of phenomena occurring at the micro-scale, which are also the subject of clay sciences, e.g., mineralogy, micro-morphology and crystallography, make the prediction of the clay macro-behaviour through the modelling of such processes a major challenge. For coarse granular soils, deducing the macro-behaviour from the modelling of the micro-processes, generally according to micro-mechanics, is nowadays widely developed (Cundall and Strack, 1979; Li et al., 2009). Conversely, attempts of incorporating in continuous mechanics models for clays local mechanisms that occur at the micro-scale, adequate for coarse materials (Oda, 1993; Wan and Al-Mamum, 2005), may oversimplify the complexity of the microstructural processes. Therefore, the modelling of clays through the representation of the micro-phenomena requires adequately modelling of thermo-chemo-mechanical coupled phenomena taking place at the micro-scale (e.g., Alonso and Navarro, 2002; Gajo et

al., 2002; Manassero et al., 2002). The present research work has been, therefore, intended to contribute to the knowledge of these phenomena, by developing a rational investigation of their occurrence by means of the most advanced procedures available nowadays, thanks to the recently pursued technological advancements in the direct observation of material features at the micro to nano scales.

Since the fifties, the macro behaviour of clays has been addressed as effect of the combination of its nature and its structure (e.g., Skempton and Northey, 1952; Skempton, 1970; Delage and Lefebvre, 1984; Griffiths and Joshi, 1989; Burland, 1990; Leroueil and Vaughan, 1990; Cotecchia and Chandler, 1997, 1998). The strategy adopted to assess the correlations between the clay micro-features and its macro-behaviour has been to study systematically the clay composition and micro-features and the corresponding macro-response. The investigation at the micro-level has allowed to explore the possible factors generating given aspect of the macro-response, without attempting to model the macro-behaviour by simulating the micro-processes. Therefore, the research approach adopted in the research presented in this thesis has been consistent with this historical background, aimed at assessing the micro-scale processes for varying stress-strain conditions, along given stress-strain paths (i.e. while the clay exhibits given macro-responses). The research results have allowed to relate different micro-features and their evolutions to different facets of clay macro-behaviour. In this way, classes of clays, distinguished on the basis of their micro-structural features, can be hence connected to classes of macro-responses and, hence, to constitutive laws and parameter values.

The availability of a correspondence between clay typologies, constitutive models and parameter values should prompt a wider use of the constitutive models in practice, since it would support the engineer in the selection of the model and of the parameter values most appropriate for the clay involved in the design of interest.

The research has addressed the micro to macro behaviour of two Italian clays, Pappadai clay and Lucera clay, both in their natural and reconstituted states. The experimental programme has entailed macro-mechanical tests and micro-structural analyses on the specimens both before and at different stages of several loading paths. The macro-behaviour of the clay has been investigated both in compression and shearing. The analysis of the clay microstructure has made use of greatly advanced technical procedures that, to date, can explore materials at the micro-scale. The fabric analyses have been carried out by means of scanning electron microscopy (SEM), combined with an image processing technique delivering quantitative assessment of the fabric orientation. At the same time, the bonding strength has been characterized indirectly, through swelling tests, and the porosimetry of the clay has been assessed by means of mercury intrusion porosimetry (MIP) tests.

The microstructural features and the main physical processes underlying the macro-response exhibited by the clay have been explored and also compared with those recognized in the literature for other natural and reconstituted clays.
The constitutive laws and algorithms used by some advanced constitutive models to simulate the effects of structure on the clay macro-behaviour have been evaluated in the light of the observation and interpretation of the features and processes acting at the micro-scale, and of the microstructural evolution recorded under the different loading paths.

1.2 Structure of the thesis

A detailed literature review of both the microstructure and micro-behaviour of clays and of the macro-behaviour of clays has been carried out in Chapter 2 and Chapter 3.
In Chapter 2, the microstructural features of clays are described and the modifications induced to clay minerals as a result of geological processes are discussed, being among the factors determining the structure of the clay and the clay behaviour. The microstructural effects of the application of given loading paths are also described.

A literature review of the mechanical behaviour of both reconstituted clays and natural clays is carried out in Chapter 3, and the general framework for the behaviour of clays proposed by Cotecchia and Chandler (2000) is recalled. A review of some constitutive models for both reconstituted and natural clay, all originating in the framework of Critical State Soil Mechanics, is made. Advanced models for "structured" soils are particularly addressed, to achieve a deeper knowledge of the laws adopted to simulate the effects of structure on the clay behaviour.

Chapter 3 describes the two clays of reference for the research, Pappadai clay and Lucera clay. The the lithological characteristics, the index properties and the mineralogy of the clays are presented. Using data from previous research works on the same clays, the deposition conditions and geological history of Pappadai clay and Lucera clay are described. The physical properties of the block samples used in this research are compared with those previously measured on the same clays by Cotecchia (1996) on Pappadai clay and Longo (2003) and Mitaritonna (2006) on Lucera clay.

The experimental programme carried out in the research, including both mechanical tests and microstructural analyses on both Pappadai and Lucera clays, in their natural and reconstituted states, is described in Chapter 5. Compression and shear tests were carried out and microstructural analyses were performed on the specimens at the end of the tests. The techniques of microstructural analysis, consisting in SEM, combined with image processing, and MIP, are also discussed.

In Chapter 6, the investigation of the macro-response of Pappadai clay and Lucera clay is described, with reference to both the compression and the shear testing programme. The results of the mechanical tests carried out on both the natural and the reconstituted clay are shown and compared with previous tests carried out by Cotecchia (1996) on Pappadai clay and by Longo (2003) and Losacco (2004) on Lucera clay, which improved the understanding of the clay behaviour.

The results of the microstructural analyses carried out on the specimens before and after loading are examined in Chapter 7. The main features and the changes occurred to the clay microstructure under loading are recognized.

Chapter 8 discusses the micro and macro testing results, outlining some common features of behaviour recognized for the two clays, both in their natural and reconstituted states. The microstructural changes recorded in other clays from the literature are analysed and interpreted, in the light of the comparison with the clays of reference in the research. Suggestions for advanced constitutive modelling of natural clay behaviour are also given.

The main conclusions drawn from the research work described are summarised in Chapter 9. Future developments for the research are finally envisaged.

2 MICROSTRUCTURE AND MICRO-BEHAVIOUR OF CLAYS

2.1 Introduction

In most branches of engineering, materials are regarded as continua and their behaviour is modelled in the framework of continuum mechanics. This is generally the case also in soil mechanics. However, the understanding of the particulate nature of the soil and of the phenomena occurring at the micro-level, is important, because the soil behaviour is the expression of both its particulate nature and its geological history. For clays, this approach implies the investigation and assessment of the complex interaction between the small sized clay particles.

The present chapter reviews the nature of both the clay particles and the microstructure of clays. The nature of the clay minerals and their modification as a result of geological processes are among the main factors which determine the structure of the clay and the clay behaviour. The modifications of clay microstructure that can be determined under loading are also discussed.

2.2 Clay minerals and particles

Clay minerals are hydrated layered silicates of aluminium and magnesium. The mineral structural units have an alternating crystalline structure consisting of siliceous layers and aluminium-magnesium layers (Fig. 2.1), in which substitution of some of the cations with other isomorphous ones (e.g. Al3+ with Fe2+, Fe3+) can occur. The sequence of layers in the structural unit will differ for different clay minerals as indicated in Fig. 2.1.

The clay particle is formed of a sequence of structural units whose distance (basal spacing) is more or less stable depending on the strength of the link between the units. Kaolinite is the most stable as hydroxal links exist between the units.

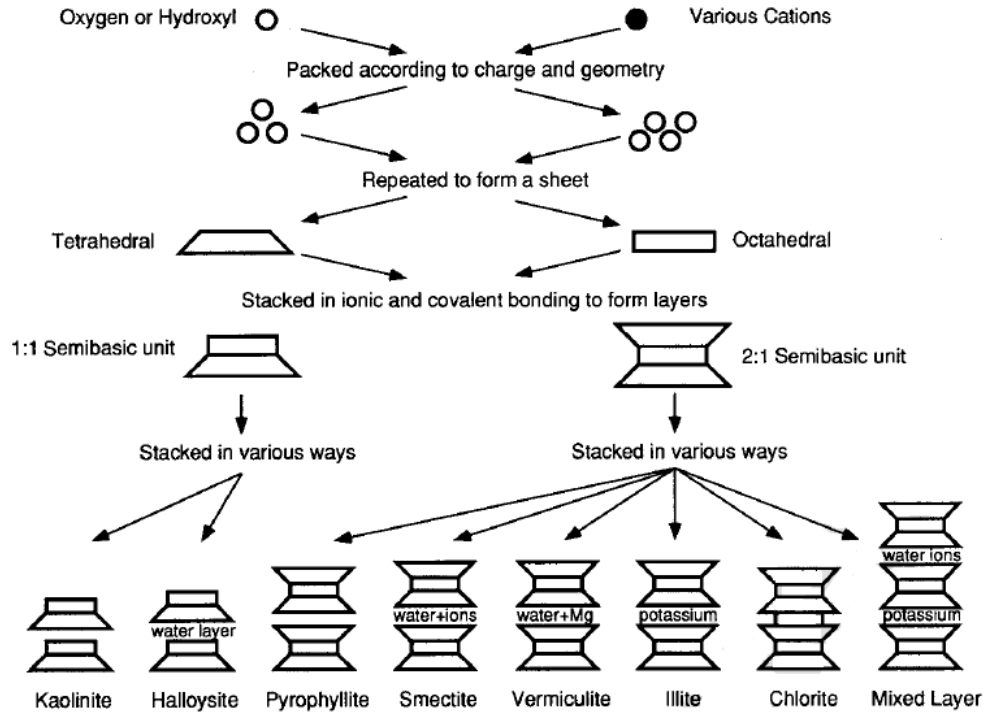

Fig. 2.1 – Synthesis pattern for the clay minerals (after Mitchell and Soga, 2005).

Illites are sedimentary micas in which potassium links are present in the basal spacing inducing a rather stable base dimension. They show different possible degradation and stability levels in relation to different levels of interlayer potassium hydration. Also chlorites have a rather stable base dimension, because of brucite-octohedral links. Smectites, derived from the extreme degradation of rock silicates, are the least stable clay minerals, as the basal link is provided by hydrated cations, e.g. Na+, Ca+, Mg+ (Fig. 2.1) (Veniale, 1983; Mitchell and Soga, 2005).

With extreme degradation processes, illites and chlorites can become smectites. Conversely, through diagenetic processes (aggradation), smectites can lose their swelling capacity acquiring a stronger inter-unit link and becoming "intergrades" or "mixed-layer" minerals. These are the results of an intermediate stage in the diagenetic process that can finally transform smectites into illites and chlorites (Fig. 2.1). Aggradation and degradation of the clay minerals typically occur respectively during

deposition-compaction and unloading-weathering processes, and these phenomena can modify significantly the clay behaviour.

Theoretically fine-grained soils possess greater free energy than a soil formed of larger crystals of the same composition (Veniale, 1983). Consequently, a clay does not represent a potential equilibrium condition, the particle behaviour being governed by particle surface forces rather than gravity. Moreover, a clay particle is a "non-perfect" crystal: unbalanced links can be present along the edges due to fracturing, while the basal planes are negatively charged as result of isomorphous substitutions of structural cations with cations of different valence which do not preserve electrostatic neutrality in the structural units (Fig. 2.2). These unbalanced charges govern the behaviour of the clay particles and their bonding.

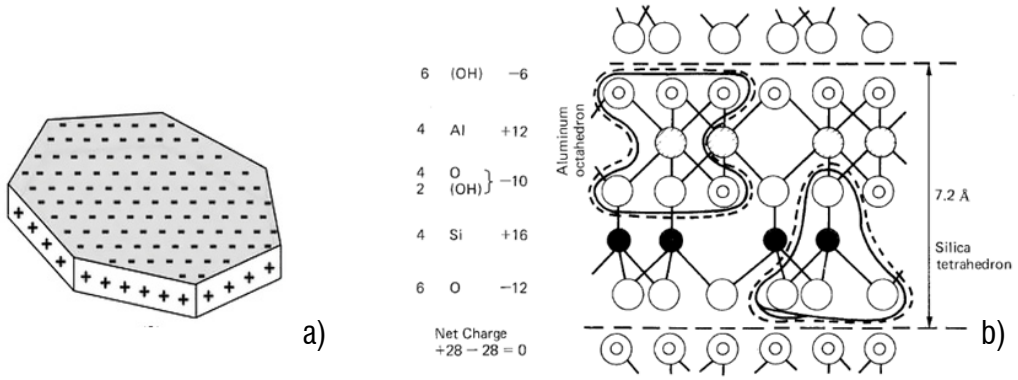

Fig. 2.2 - (a) Charge distribution on the clay particle surface; (b) Internal surface structure of a structural unit of kaolinite (after Mitchell and Soga, 2005).

2.3 Interaction between clay particles and water

When submerged, the clay particles interact with the pore water, i.e., with an electrolyte solution. The closest water molecules are attracted by the surface of the clay particles and form a thin "bound" or solid layer of water molecules which cannot be removed even by heating (Fig. 2.3). Beyond the bound-water film, water molecules and hydrated cations are attracted by the particle and form a layer of high viscosity water: the absorbed water (Fig. 2.3). This can be removed by heating, but because of its high

viscosity it is not moved by hydraulic gradients. The charged particle surface and the cations located in the absorbed water layer together form the "diffuse double layer". Both the thickness of the double layer and the unbalanced nature of the particle surface charges depend on the mineralogy of the particle and the pore water chemistry.

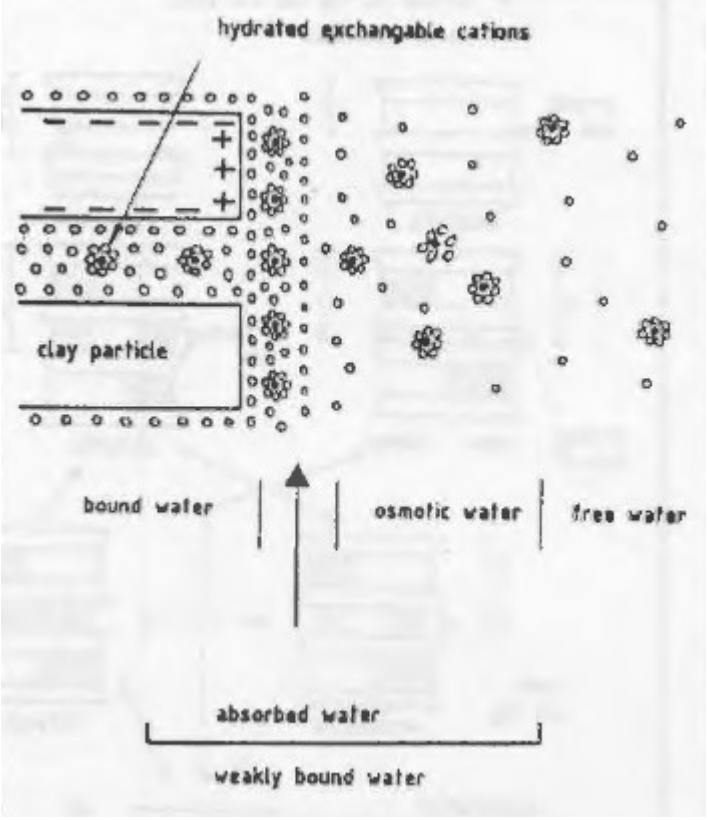

Fig. 2.3 - Scheme of the different water layers surrounding the clay particle (after Veniale, 1983).

Because the adsorbed cations are responsible for a much higher concentration near the surfaces of the particles, there is a tendency for them to diffuse away in order to equalize concentration throughout. Their freedom to do so, however, is restricted by the negative electric field originating at the particle surfaces. The escaping tendency due to diffusion and the opposing electrostatic attraction lead to a cation distribution adjacent to a clay particle in suspension, as shown in Fig. 2.4.

Anions, however, are excluded from the negative force fields of the particles, giving the distribution shown in Fig. 2.4 and a phenomenon termed negative adsorption. Several

theories have been proposed for the description of ion distributions adjacent to charged surfaces in colloids (e.g., Gouy, 1910; Chapman, 1913).

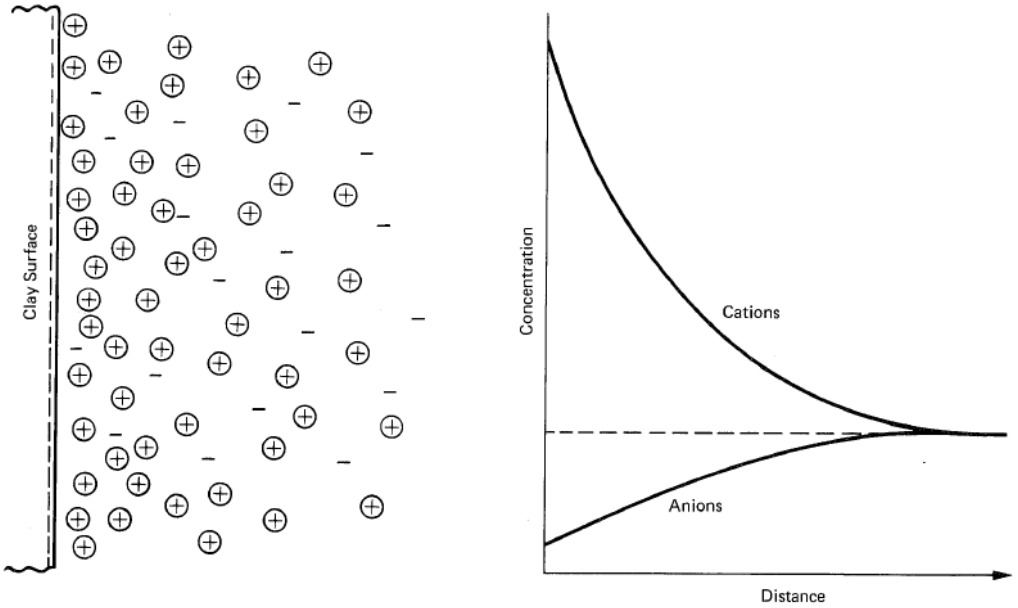

Fig. 2.4 – Distribution of ions adjacent to a clay surface according to the concept of the diffuse double layer (after Mitchell and Soga, 2005).

2.4 Interaction between clay particles

The clay particles do not interact directly. It is the association of the single clay particle with its own double layer, called the "single particle-water system" here-after, which controls the interaction between each other of the single particle-water systems at deposition. Such interaction is governed by the combined effect of gravity, electrostatic forces, Van der Waal forces, osmotic pressures and pore water surface tension (Sfondrini, 1975). The electrostatic forces are related to the charge distribution within the particle-water systems, while the Van der Waal forces depend on the dielectric constant of the soil-water system (Sides and Barden, 1970). The complexity of the particle interactions in clays is thus evident.

When an increment of overburden pressure or other external stress is applied to the clay sediment, the particle interactions change as the soil mass reaches a new equilibrium state. Models have been proposed which assume that the clay particles are

not in contact and the external forces are equilibrated by the repulsion between the particles (Bolt, 1956; Leroux, 1975). In the last decades instruments, such as the Transmission Electron Microscope (TEM) and the Scanning Electron Microscope (SEM), have allowed two and three-dimensional imaging of clay particle arrangements (e.g., Smart and Tovey, 1981). The existence of direct contacts between clay particles and groups of particles has been assessed, so that also a mechanical stress can be transmitted at the interparticle contacts. But even if the available models provide theoretical descriptions of the interparticle stresses, how the physico-chemical interactions and the mechanical stresses are actually combined to provide equilibrium in clays has not been yet formulated (V. Cotecchia et al., 1982-a).

As early as 1925, Terzaghi postulated that during consolidation highly viscous absorbed water, coating the clay particle surface, is squeezed out from between points of contact (Fig. 2.5(a)), and the resulting close approach of particles leads to high attractive forces. In this way Terzaghi addressed the microstructure of naturally sedimented clays. He accounted for remoulding as disruption of the interparticle contacts, by which absorbed water fills in around the old contacts and the strength of the clay is reduced. This "breakage of contacts" was seen as the cause of different strengths between the natural and the remoulded clay. Terzaghi later (1944) defined as sensitivity S_t the ratio between the undrained strength of the undisturbed clay and the undrained strength of the remoulded clay at the same water content. Since then, sensitivity has been regarded as the parameter embodying the differences of the microstructures of the natural and the remoulded clay.

Casagrande (1936-a) (Fig. 2.5(b)) explained marine clay sensitivity on the basis of a load-carrying skeleton consisting of highly compressed bond clay trapped between silt and fine sand particles during consolidation. Remoulding was visualized by Casagrande as the destruction of the load carrying skeleton.

Skempton and Northey (1952) carried out an experimental study of the effects of the leaching action of fresh water on the volume and strength of natural clays. Leaching of marine clays had been recognized as cause of sensitivity in the Norwegian and Canadian quick clays. Skempton and Northey inferred that the change in chemistry of

the pore water at leaching was affecting the double layers, and they measured a variation of the liquid limit of the clay after leaching. But since they observed that the leaching process was not affecting either the volume or the strength of the clay, they deduced that the clay particles had to be in effective contact before leaching. So Skempton and Northey (1952), as had earlier Terzaghi (1925) and Casagrande (1936-a), considered that the strength of the natural clay was related to a microstructure formed of particles in open arrangement and effectively in solid contact, established through the interpenetration of the films of bound water.

Nowadays,as will be shown later, the clay particles are recognized to be either in contact, or not, and the forces between clay particles are seen to occur both as mechanical, when a direct contact between the particles actually exists, and as electrostatic, electromagnetic, osmotic and chemical, which can apply also between particles that are not in contact. In this respect, the clay micro-structure is recognized to be more complex than as schematized in Fig. 2.5.

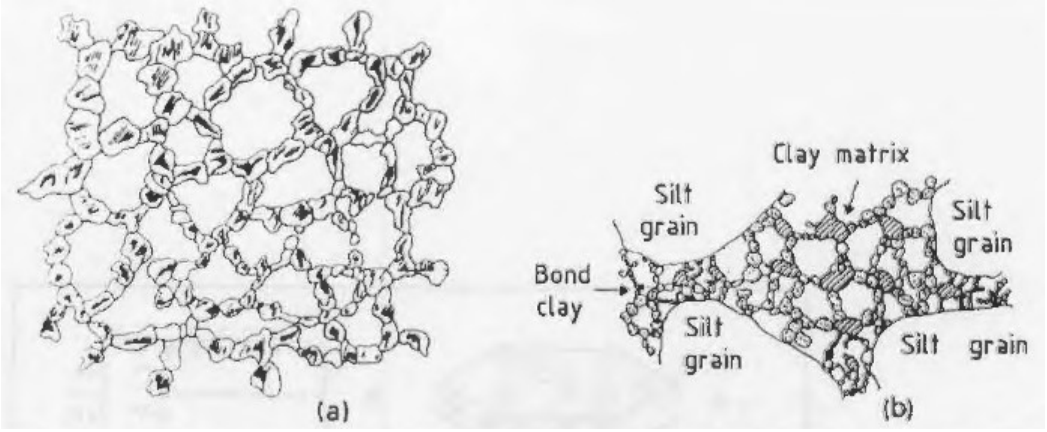

Fig. 2.5 - (a) Terzaghi-Casagrande honeycomb fabric (after Terzaghi, 1925); (b) Open fabric of undisturbed marine clay (after Casagrande, 1936-a).

2.5 Soil structure and remoulding

According to the definition of Lambe and Whitmann (1969), soil microstructure (referred to also as structure hereafter) is considered as the combination of the orientation and distribution of the particles in a soil mass, called *fabric*, and the forces

between adjacent soil particles. Cotecchia & Chandler (2000) have readdressed bonding as only that part of the inter-particle forces which are not of mechanical nature, to distinguish it from the mechanical contact stresses and the cemented bonding applying to rocks (e.g. cemented sands, cemented clays etc.).

While the fabric of a clay can be visualized through electron microscopy and quantified through processing of the SEM images, the particle interactions cannot be easily investigated. If a saturated clay is under positive effective stresses, normal and tangential frictional stresses can be transmitted at the inter-particle contacts. In addition, electrostatic and Van der Waal forces, and viscous stresses within the absorbed water layer, will act between uncemented particles. If cemented links exist between the particles, part of the load may be concentrated at these links. The combination of all the interparticle forces which are not of purely frictional nature, e.g., normal and tangential frictional contact stresses, will be defined as *bonding* (Cotecchia & Chandler 2000). It follows that bonding is not necessarily a solid link, and should be considered as a field of forces. Differences in bonding are highly effective on the behaviour of clays of different structure.

The bonding which develops in a clay depends on the physico-chemical environment, e.g., chemistry of the suspension, pressure, temperature, organic content, and on the mechanical boundary conditions, e.g., the consolidation strain path and the deposition and consolidation rate (Mitchell, 1976; Sides and Barden, 1970; Sfondrini, 1975; Mitchell and Soga, 2005).

Following the definition of structure given above, the term remoulding should now be discussed. To remould a clay, the material is worked to weaken its bonding. Remoulding can require the clay to be mixed with water; for stiff clays it is in general necessary to create a slurry. The Atterberg limits are measured on the heavìly remoulded clay and reflect both the amount and type of minerals present in the clay, and such properties as cation-exchange capacity and total surface area (Skempton, 1953). Skempton and Northey (1952) referred to clays consolidated from a slurry and they considered that the process of formation of the clay slurry (reconstitution) and very rapid consolidation of the slurry in the laboratory created non-sensitive clays. By

consolidating and shearing these reconstituted clays, Skempton and Northey demonstrated that the curves relating the undrained strength and the liquidity index (LI) for the different clays were very close (Fig. 2.6a). They so observed that the strength of clays normally consolidated from a slurry in the laboratory is a function only of the liquidity index of the clay. This reinforced the distinction between the stable microstructure created in the laboratory by reconsolidating the clay from slurry and that resulting from the natural deposition process.

Cotecchia (1996), concurring with the definitions applying within the literature about mineralogy of clays and clay micro-morphology (Veniale, 1983; Sides & Barden, 1970), highlights that reconstituted clays possess a structure as any other clay and that reconstituted clays, having sensitivity 1, possess a structure, i.e. fabric with bonding, which is "stable", as the clay strength does not change with disturbance.

Skempton and Northey found that various sensitive natural clays from different environments had a more open structure than the clays consolidated from slurry in the laboratory, showing that the liquidity index of the natural clays is always higher than that of remoulded clay compressed to the same vertical pressure (Fig. 2.6b). The Authors concluded that factors other than leaching and thixotropy account for the state of natural clays. It appears that the bonding created during the very slow process of the natural formation of clays can be so strong as to impart to the intact clay a more open fabric and higher sensitivity than that of the reconstituted clay under the same load (Fig. 2.6b).

Clays consolidated from slurry in the laboratory, however, can exhibit a sensitivity higher than 1 as the sensitivity of a one-dimensionally consolidated reconstituted clay depends on the initial water content, the load increment ratio and the loading rate (Mitchell and Houston, 1969). In general, though, clays generated in the laboratory should be defined as resedimented, if subjected to low loading rates (Leroueil et al., 1984). When loading rates are high, as applied in conventional oedometer tests, though, the sensitivities are very low, approaching 1, and only these should be considered as reconstituted clays, following Burland (1990).

Burland (1990) defined as "reconstituted" the clays remoulded to form a slurry at water contents between the liquid limit and 1.5 times the liquid limit (preferably 1.25) and consolidated using the conventionally high laboratory loading rates. He thus distinguished the reconstituted clays, which then have S_t about 1, from the resedimented clays (Leroueil et al.,1984), where the consolidation process is much slower, and from the remoulded clays disturbed to perhaps only to a limited extent. The term reconstituted clay will be used in the following as suggested by Burland (1990).

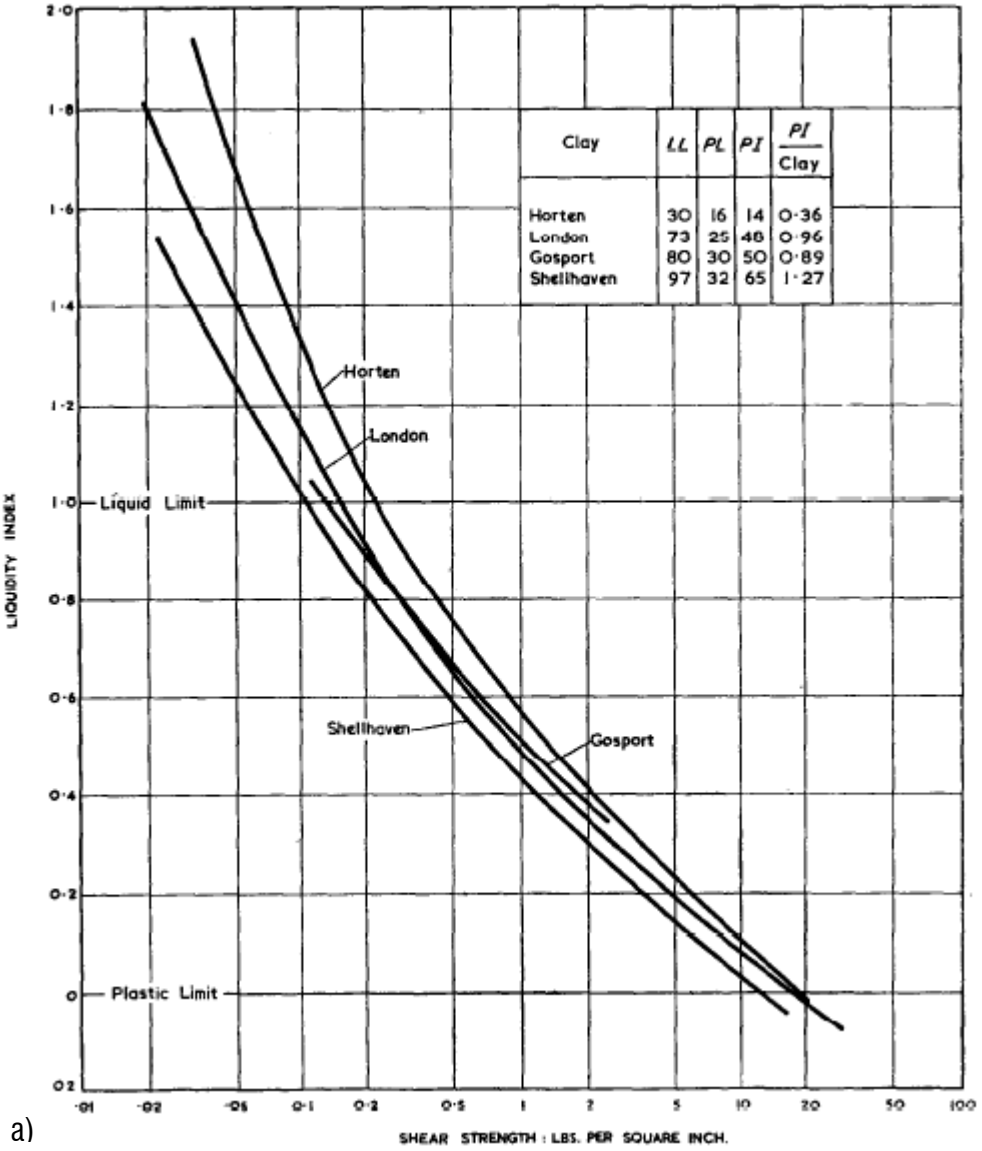
Clay | LL | PL | PI | PI/Clay
Horten | 30 | 16 | 14 | 0·36
London | 73 | 25 | 48 | 0·96
Gosport | 80 | 30 | 50 | 0·89
Shellhaven | 97 | 32 | 65 | 1·27
Horten
London
Liquid Limit
Shellhaven
Gosport
Plastic Limit
LIQUIDITY INDEX
2·0
1·8
1·6
1·4
1·2
1·0
0·8
0·6
0·4
0·2
0
0·2
·01
·02
·05
0·1
0·2
0·5
1
2
5
10
20
50
100
SHEAR STRENGTH : LBS. PER SQUARE INCH.

a)

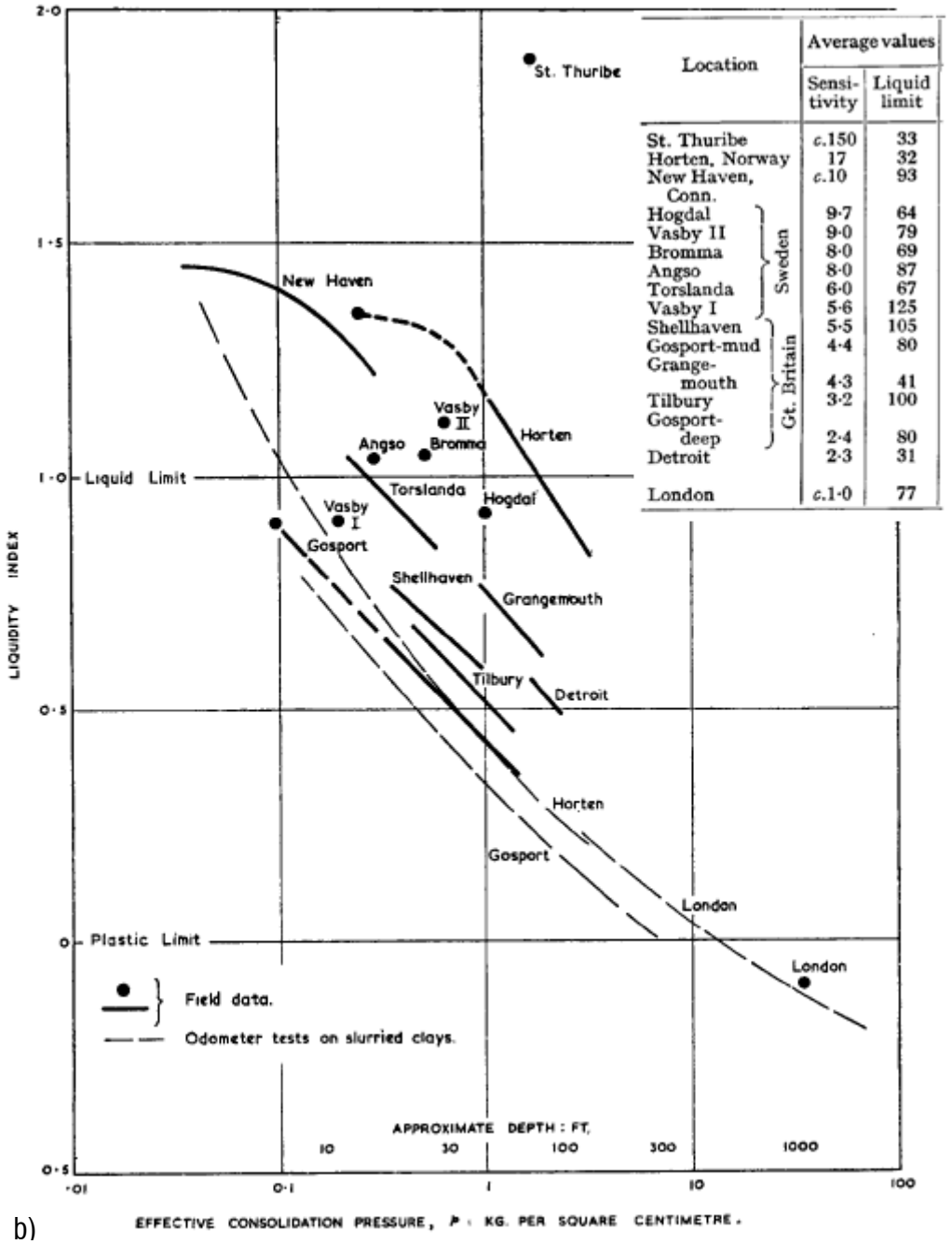

Location		Average values: Sensitivity	Average values: Liquid limit
St. Thuribe		c.150	33
Horten, Norway		17	32
New Haven, Conn.		c.10	93
Hogdal	Sweden	9·7	64
Vasby II	Sweden	9·0	79
Bromma	Sweden	8·0	69
Angso	Sweden	8·0	87
Torslanda	Sweden	6·0	67
Vasby I	Sweden	5·6	125
Shellhaven	Gt. Britain	5·5	105
Gosport-mud	Gt. Britain	4·4	80
Grange-mouth	Gt. Britain	4·3	41
Tilbury	Gt. Britain	3·2	100
Gosport-deep	Gt. Britain	2·4	80
Detroit		2·3	31
London		c.1·0	77

b)

Fig. 2.6- (a) Relation between liquidity index and undrained shear strength of remoulded clays; (b) Relation between liquidity index and consolidation pressure for natural and remoulded clays (after Skempton and Northey, 1952) and constant sensitivity lines.

2.6 Classification of fabrics

The models of microstructure were for too long oversimplistic, until the first use of polarizing and transmission electron microscopes. The models gave great emphasis to the existence of flocculated particle arrangements that were then considered a general feature of sensitive clays.

Rosenqvist (1963) observed that the undisturbed fabric of Norwegian marine clays corresponded closely to the schematic picture of a clay mineral network dominated by edge to face contacts. Both edge to face and edge to edge particle contacts were observed by Push (1966), which were similar to the card-house scheme (Fig. 2.7a) already proposed by Lambe in 1953. The flocculated arrangement was considered responsible for the stronger and less compressible behaviour of natural clays and the deflocculated state was associated with remoulded clay (Fig. 2.7c).

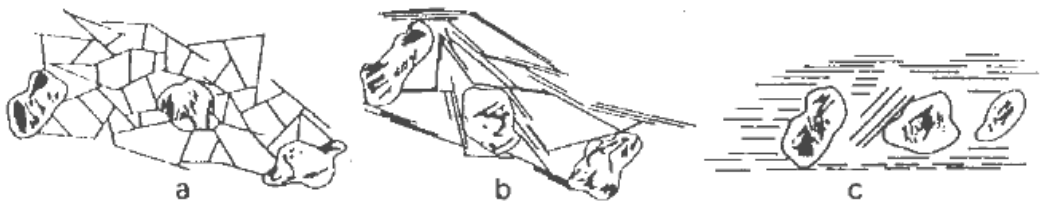

Fig. 2.7- (a) Cardhouse fabric in saltwater deposit (b) cardhouse fabric in freshwater deposit; (c) remoulded fabric (after Lambe, 1953).

These rather simple schemes did not discern the typologies of interparticle forces. However, many purely theoretical studies were carried out to quantify the interparticle forces and deduce the resulting clay particle arrangements in given colloidal suspensions, as reviewed by V. Cotecchia et al.(1982-a). The results of these studies, which also implemented improved applications of electron microscopy, revealed that the generally accepted concepts of flocculated and dispersed structures were too simple (Sides and Barden, 1970). Nowadays, because of the increasingly sophisticated techniques and theoretical analyses involved in the study of the micromorphology of clays, this has become a specialism distinct from classic Soil Mechanics. Many fabric classifications are proposed in the literature, and quantitative interpretations of the

fabric of clays are now possible using image processing of SEM pictures (see Chapter 5).

Sides and Barden (1970) provided a classification of the fundamental fabrics that, because it is concise, is considered helpful and will be referred to subsequently.

Fig. 2.8 shows schemes (a), (b) and (c), which represent flocculated fabrics, the term flocculated referring to a soil in which the net electrical force between the adjacent particles during deposition was attractive. The term "cardhouse" refers to the essentially single-particle arrangement of Fig. 2.8a, but little evidence of it is reported in the literature. The term "bookhouse" (Fig. 2.8b) refers to a much more common structure. The groups or aggregates of particles, in which the particles are approximately parallel, are called domains. Domains are nowadays generally recognized as the fundamental unit of the clay fabric, as they are casually formed in the suspension during deposition (V. Cotecchia et al.,1982-a). Salt flocculated implies small domains containing few particles. An even more open fabric is the “honeycomb” (Fig. 2.8c).

The term "dispersed" is used by Sides and Barden for a soil in which the net electrical force between adjacent particles during deposition was one of repulsion. Thus, dispersed implies a rather close packed fabric, as in Fig. 2.8d. However, Sides and Barden considered that a more realistic representation of a dispersed fabric is the “turbostratic” fabric (Fig. 2.8e), in which some edge to face contacts between domains are present. Areas of high degree of overall orientation, complete preferred orientation (c.p.o.), is the “stack” represented in Fig. 2.8f.

The simple two-dimensional schemes of fabric are often difficult to recognize in the three-dimensional visualisation given by the SEM. Moreover, the clay fabric is strongly affected by the presence of sand and silt grains, which induce turbulence even in a dispersed fabric (O'Brien and Slatt, 1990; Lupini et al.,1983; Hawkins and McDonald, 1992).

Sides and Barden pointed out that the main difficulty in classifying fabrics is to distinguish a turbostratic from a compressed bookhouse fabric. The first implies large domains with a gradual change in orientation, with the boundary between domains often diffuse and indistinct and with no inter-domain macro-voids. The compressed

bookhouse fabric is formed of smaller domains having rather well-defined boundaries with sudden and marked changes in orientation and large inter-domain macro-voids.

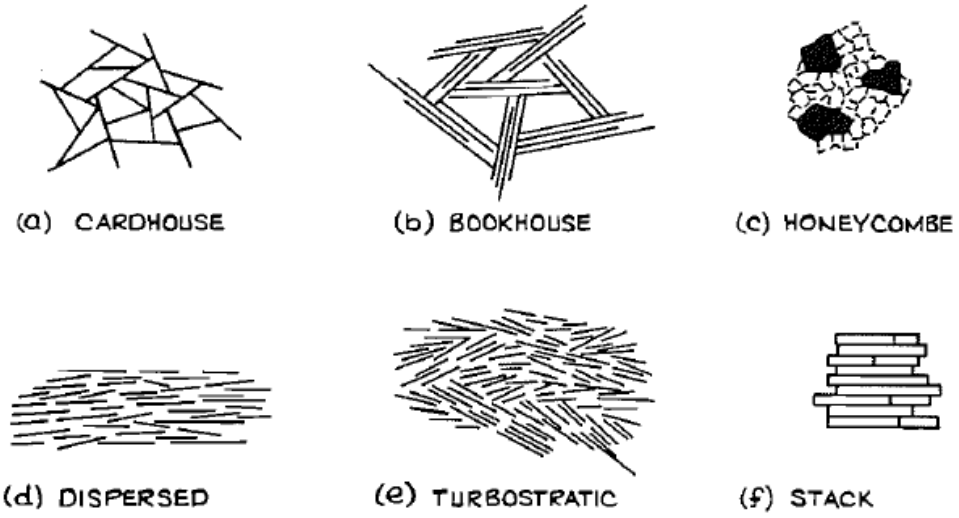

Fig. 2.8 - Idealized clay fabrics (after Sides and Barden, 1970).

2.7 Fabrics of remoulded clays

Griffiths and Joshi (1990) observed with the SEM the fabric of an illitic clay slurry at the liquid limit. They described it as formed by three orders of aggregates and pores in a flocculated arrangement (Fig. 2.9). In this scheme, the assemblages of domains interact through connectors which give the entire fabric a honeycomb appearance. Such a fabric is very distant from the simplified scheme of the fabric of the remoulded clay reported by Lambe (1953), Fig. 2.7(c).

According to the schemes in Fig. 2.7, widely accepted in the past, the fabric of the remoulded clay was considered not to be aggregated and the intact fabric of sensitive clays was considered flocculated. But the intact sensitive and the remoulded clay can both have flocculated particle arrangements (Griffiths and Joshi, 1990; V. Cotecchia et al.,1982-b). In fact, what is fundamentally different between the structure of the remoulded clay and that of the intact sensitive clay is not necessarily the type of fabric, but the nature, stability and strength of the bonding. V. Cotecchia et al.(1982-b) recognized flocculated domains in both a slurry of kaolin and a slurry of bentonite in

distilled water; the flocculated fabric of the kaolin slurry is shown in Fig. 2.10. They showed how the dimensions of the domains decrease with increasing mixing water content; a connecting bridge between assemblages, formed by smaller domains and sometimes by single particles, is shown in the SEM pictures (Fig. 2.10(b)). The fabric of the slurried kaolin in Fig. 2.10b resembles that reported for reconstituted clay by Griffiths and Joshi (1990).

Differences between the natural and the remoulded clay fabric also arise from the distribution of the sand and silt grains. In well graded clayey soils one fraction does not dominate the fabric and clay bands flow around the sand and silt grains. When the clay fraction is small with respect to the silt and sand fractions, remoulding can give rise to segregation of the sand and clay. Lupini et al. (1983) showed that segregation occurred in remoulded Lower Cromer Till, producing unusual effects on the stiffness and strength of the soil.

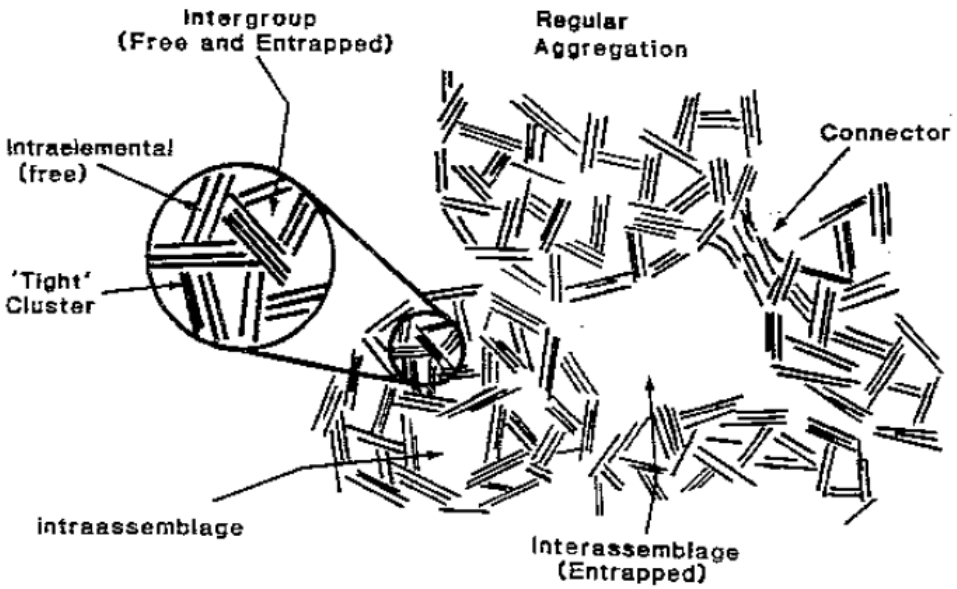

Fig. 2.9 - Assemblages and pore classes in the open fabric of a reconstituted clay (after Griffiths and Joshi, 1990).

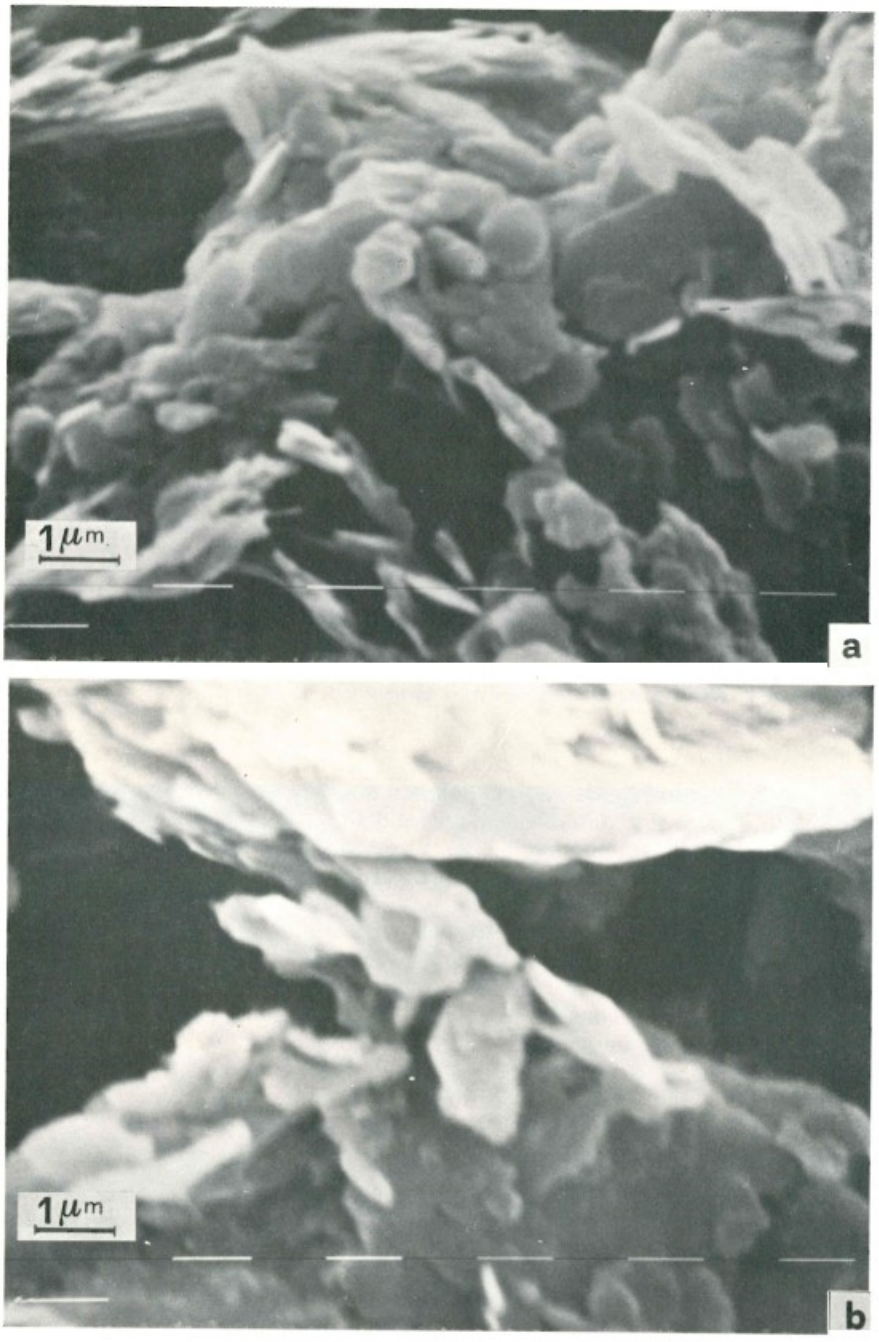

Fig. 2.10 - (a) Kaolin slurry (w=117%); (b) "bridge" between domains (after V. Cotecchia et al.,1982-b).

2.8 *Effects of deposition conditions on the clay fabric and structural changes under burial*

Reviewing now the fabrics and the sensitivities observed for sedimented clays as the effects of particular deposition conditions, it may be observed that identical clay particles sedimented in solutions of different salinity form clays of different activity. In this case, not only are the fabrics and the strengths of the sedimented clays different, but also the strengths of the equivalent remoulded clays are different, giving rise to different sensitivities (Leroueil et al.,1984).

Sides and Barden (1970) studied the fabrics of kaolinite, illite and montmorillonite resulting from slurries containing chemical dispersing and flocculating agents. They observed that kaolinite formed in a flocculating environment at 30 kPa vertical pressure was not very different from that formed in a dispersing environment, both having a high degree of orientation. The fabric of the flocculated illite was far more random than the flocculated kaolin. So, Sides and Barden concluded that the dispersing and the flocculating agents have a much greater influence on the arrangement of smaller colloidally active particles. They recalled cases of illitic clays deposited in a saline marine environment for which fairly random open fabrics had been observed and a case of illitic clay deposited in dispersing conditions created by the presence of organic matter whose fabric was highly oriented.

Distinguishing the origins of the features of a natural fabric is a very complex task, even for a sediment of recent deposition. The fabric at deposition will be here termed "primary fabric". Confined areas of different primary fabric can exist as a consequence of either the local presence of chemical agents, organic matter, or a local perturbation of the mechanical deposition. O' Brien and Slatt (1990) showed that lamination indicates that deposition occurred in still conditions, with no post-depositional mixing, while the existence of pyrite framboids (Fig. 2.11) is an indicator of anaerobic sulphide diagenesis developing in the early stages of consolidation, implying the existence of a confined, reducing environment.

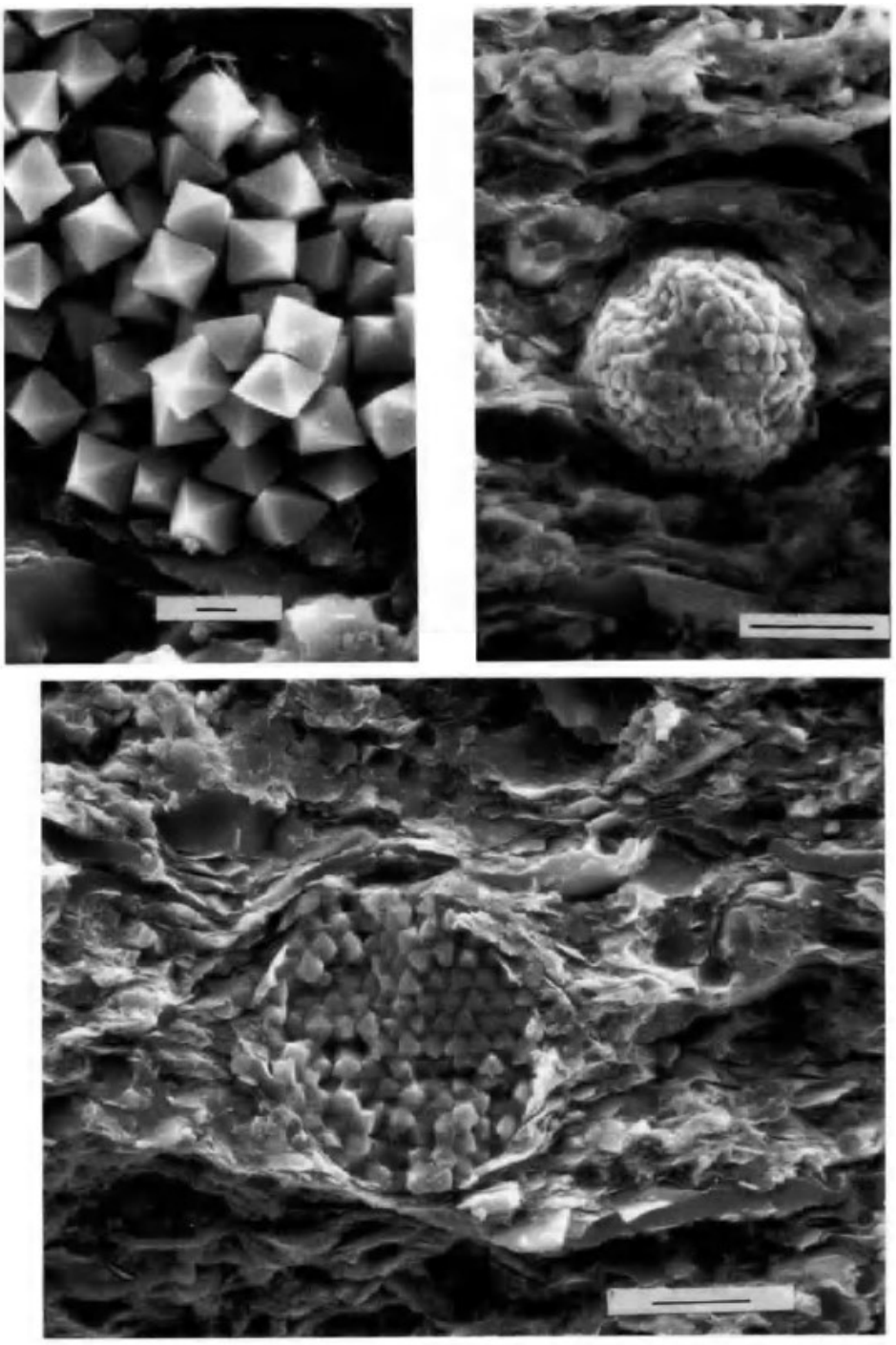

Fig. 2.11 - Pyrite framboids (after O'Brien and Slatt, 1990).

Variations of such factors as the electrostatic and the magnetic interactions between crystals, the ion concentration in the pore water, the vapour tension, the osmotic pressure, temperature and the conditions of the buried organic material can cause substantial changes of both the bonding and the fabric of the clay with time.

"Ageing" is defined as the stage in which the clay rests after burial following primary consolidation. The main phenomena occurring during ageing are considered to be creep deformations and the thixotropic processes. Thixotropy is a reversible process (Skempton and Northey, 1952) which develops in nature for any clay during periods of rest and induces an increase of strength and sensitivity (generally up to 1.5-2) that develops mostly in the first year of rest of the sediment and is lost on remoulding.
Higher sensitivities may be induced in marine or estuarine clays by leaching, a process in which the salt concentration in the pore water is reduced, subsequent to deposition, by the leaching action of fresh water (Skempton and Northey, 1952). This is for example the case for Canadian soft clays (Quigley, 1980; Torrance, 1975; Locat, 1995).

Differently from thixotropy, diagenetic phenomena require a longer time to develop and are predominantly irreversible. Diagenesis can produce modifications and creation of crystals, the alteration and crystallisation of organic matter, the strengthening of the clay bonding and changes of fabric. Mild diagenesis can start in the early stages of burial, as the vertical pressure increases and the soil-water system becomes hydraulically confined. Some diagenesis can also occur in clay under high pressures while it is still consolidating. Generally, the diagenetic processes which cause the major structural changes, strengthen the clay bonding and increase the clay strength, all develop at high pressures after consolidation, i.e., in the clay at rest, and are referred to as long-term diagenesis (Cotecchia, 1996). The aggradation of the swelling minerals, previously discussed, is a common diagenetic process.
The formation of authigenic cement between the clay particles can also occur after consolidation at high pressures as part of the long-term diagenesis. Cement can

precipitate if a supersaturated solution fills the pores (Sfondrini, 1975), as in clays rich of either calcareous fossils or detritus, when an authigenic carbonate cement can be formed as a result of the segregation of calcite in either its crystalline or amorphous forms (Veniale, 1985). Long-term diagenesis can modify the clay fabric and bonding to such an extent as to significantly affect its mechanical behaviour.

The occurrence of diagenetic phenomena can be identified if the mineralogy and chemical composition of the soil is seen in the context of the geological history of the deposit. The direct visualisation of the fabric of the clay greatly helps this reconstruction (O'Brien and Slatt, 1990).

Cotecchia and Chandler (1997) observed for Pappadai clay a decrease in the proportion of smectites with depth, along with an increase in the proportions of non-swelling minerals and a decrease in activity, suggesting that diagenesis had occurred. Using chemical micro-analyses within the SEM, they demonstrated the presence of a film of amorphous calcite coating both the clay particles and their contacts. Being amorphous, this calcite is likely to be authigenic, and thus the result of diagenesis.

Seiphoori et al. (2017) investigated the effects of diagenetic cementation on the pore structure of natural Opalinus shale by comparison with reconstituted specimens. The reconstituted shale, consolidated under an effective stress comparable to the maximum effective stress undergone by the natural sample in situ, shows a larger porosity than that of natural shale, indicating that diagenetic cementation had a role in reducing the porosity of the natural shale, for example by means of an infilling of pore space as a consequence of chemical or chemo-mechanical processes.

2.9 Types of clay structure

It is apparent from the above discussion that the structure of a clay is the result of all the geological phenomena that have occurred since deposition and that a description of all the processes affecting the microstructure of a clay can never be complete. The soil structure should be thought of as continuously developing, being affected by most of the environmental factors involving the clay.

According to Cotecchia (1996), two basic classes of clay structure can be distinguished. The first is defined “sedimentation structure” and includes all structures that develop during and after deposition as a result solely of one-dimensional consolidation. This structure is present only in normally consolidated clays and can include many different fabrics and degrees of bonding. It exists also in one-dimensionally normally consolidated reconstituted clays.
The second, the “post-sedimentation structure”, develops when some geological process subsequent to normal consolidation intervenes to modify the sedimentation structure. Such processes might be simple mechanical unloading, for example due to erosion or a rising water table, or other geological processes, such as creep, thixotropy, post-deposition bonding or, more generally, diagenesis.

The processes giving rise to the sedimentation structure give rise to the "sedimentation sensitivity", which is the sensitivity that a normally consolidated clay has if its structure has not undergone changes after virgin compression. The processes acting after virgin compression, which change the structure from a sedimentation to a post-sedimentation structure, give rise to an "acquired sensitivity", which adds to the sedimentation sensitivity and generates a "post-sedimentation sensitivity".

2.10 Effects of 1D compression on the clay microstructure

The effects of compression on clay microstructure are complex and have been investigated through the last decades with different techniques and data interpretation methods. SEM and MIP have often been used in conjunction, to get both a qualitative and quantitative characterization of microstructure evolution.
For clays with aggregated microstructures, the reduction in void ratio caused by compression has often been related to a reduction in the volume of larger pores, i.e., the inter-aggregate pores, with minor or no modification of the intra-aggregate pore structure.
Delage and Lefebvre (1984) analysed the evolution of microstructure under 1D compression of soft highly sensitive St Marcel clay. The SEM observation of the

undisturbed clay (Fig. 2.12) shows an aggregated structure, in which aggregates and clay bridges crossing interaggregate pores can be identified (Fig. 2.12c). The fabric of natural St Marcel clay in Fig. 2.12c resembles the scheme proposed by Griffiths and Joshi (1990), shown in Fig.2.9, but for a reconstituted clay. Hence, being recognized for either a high water content reconstituted kaolin (Fig. 2.10), or for natural very soft clay (Fig. 2.12), the scheme from Griffiths and Joshy might apply to a high water content clay under initial loading from slurry (early virgin compression), either in situ or in the laboratory. Also the remoulded sample of St Marcel clay (Fig. 2.13) is seen to have an aggregated structure, so remoulding has not destroyed the aggregates.

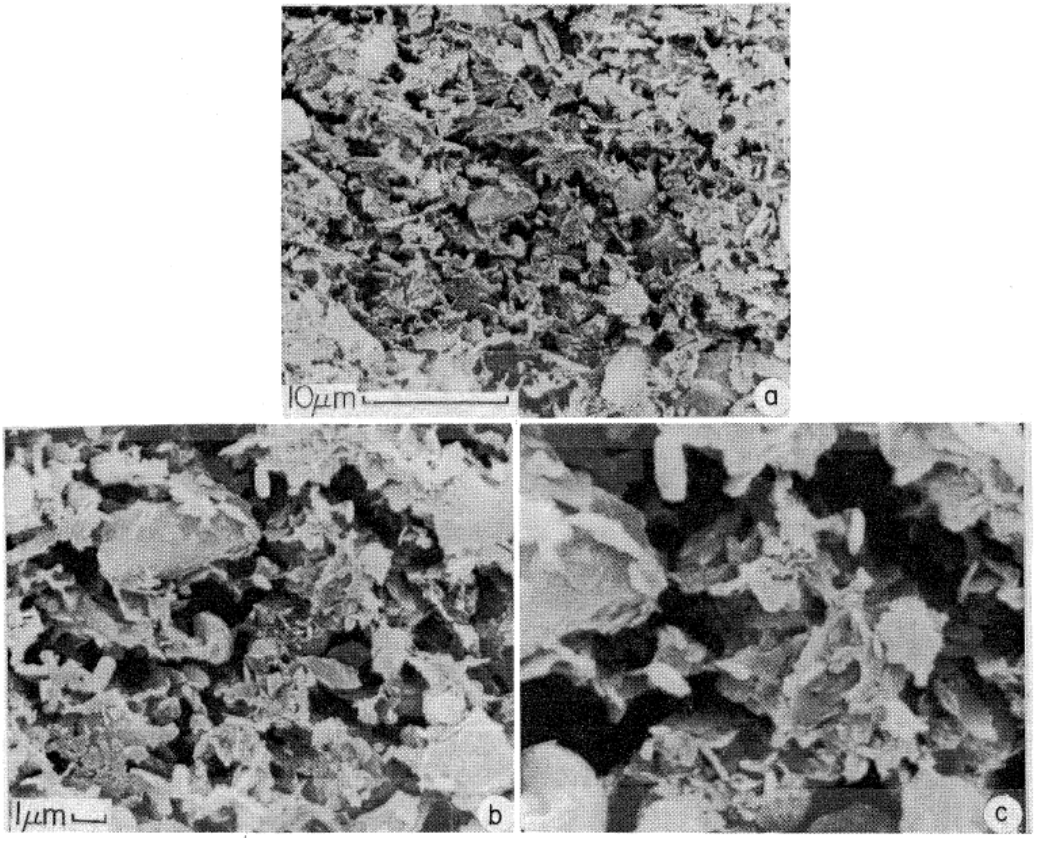

Fig. 2.12 - SEM micrographs of intact St Marcel clay on a vertical plane at (a) 3000x, (b) 7000x and (c) 15000x magnification (after Delage and Lefebvre, 1984).

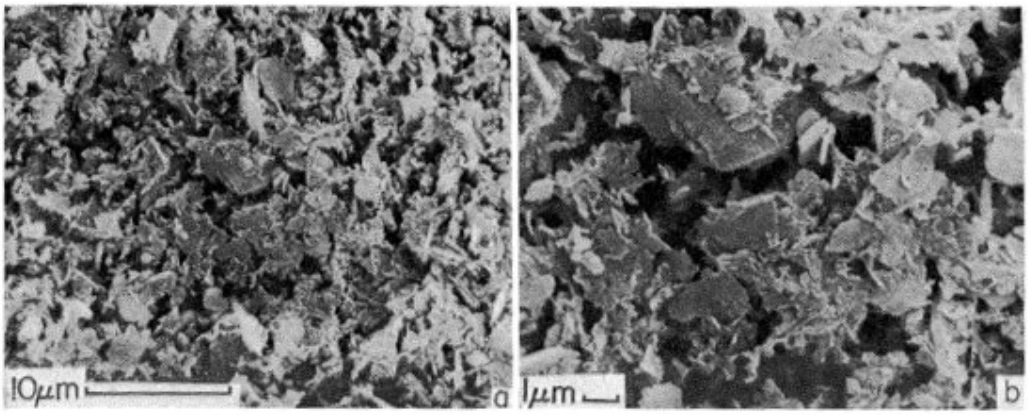

Fig. 2.13 – SEM micrographs of a remoulded sample of St Marcel clay (after Delage and Lefebvre, 1984).

St Marcel clay is then 1D compressed to 23, 124, 421 and 1452 kPa and MIP tests are carried out on each specimen after unloading in several stages to 4 kPa. The results of the MIP tests are plotted as the reverse of the cumulative intruded volume curve: the volume plotted at entrance radius r equals the total volume intruded for the specimen minus the volume intruded down to radius r.

The pore size distribution curves (Fig. 2.14) indicate a progressive collapse of the largest pores with increasing pressure; on the contrary, the intra-aggregate pores seem not to be affected by compression in the range of the applied pressures, as suggested by the overlapping of the intrusion curves for the smaller pore sizes. Therefore, 1D compression seems to have deformed the aggregates without compressing them and with no variation of intra-aggregate porosity (Delage, 2010).

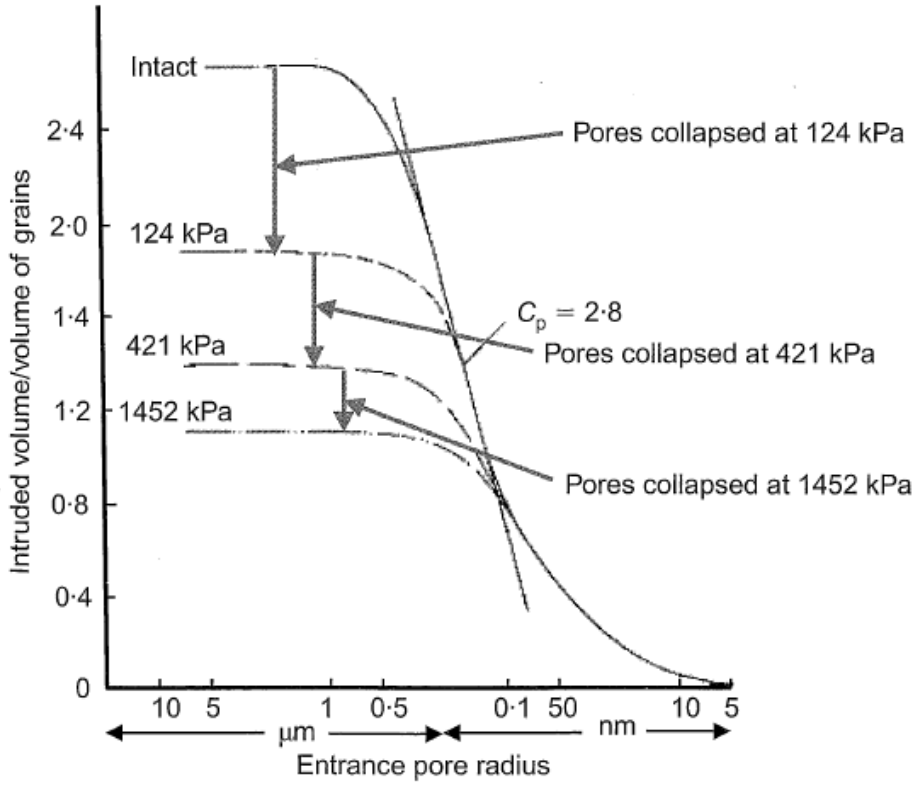

Fig. 2.14 – Change in PSD curves of St Marcel clay during oedometer compression (after Delage and Lefebvre, 1984 and Delage, 2010).

Similar results were found by Lapierre et al. (1990) on soft Louiseville clay. With increasing volumetric strain in 1D compression (Fig. 2.15), the results of MIP tests on the natural clay seem to show a reduction of the volume of the largest (inter-aggregate) pores. Minor changes are seen in the intra-aggregate porosity up to 30% strain, but the specimen strained to 41% exhibits a major change in the small pores distribution.
The MIP analyses on the reconstituted clay 1D compressed (Fig. 2.16) show a change of slope in the pore volume distribution curve, which can be related to the presence of a double family of pores. With compression the double porosity is progressively lost, hence the largest pores are closing and the pore system is becoming more uniform.

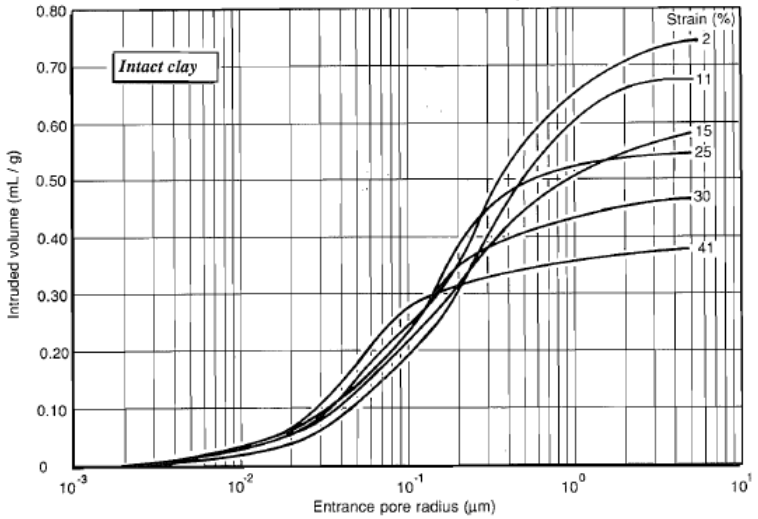

Fig. 2.15 – Pore size distribution of intact Louiseville clay compressed at increasing volumetric strain (after Lapierre et al., 1990).

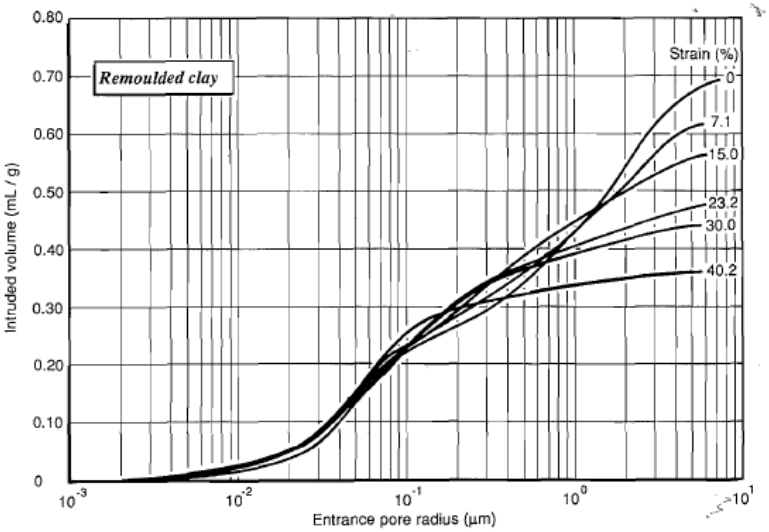

Fig. 2.16 - Pore size distribution of reconstituted Louiseville clay compressed at increasing volumetric strain (after Lapierre et al., 1990).

It should be outlined that the difference between inter-aggregate and intra-aggregate porosity is not univocally recognized in the literature. In this research work, the term inter-aggregate will be generally referred to larger “macro” pores, with sizes above 1

μm, whereas intra-aggregate porosity will be generally associated to “micro” pores of sizes below 1 μm.

Hattab and Fleureau (2013) observed the microstructural evolution of soft Gulf of Guinea clay, which is characterized by the presence of two pore families corresponding to two peaks in the MIP incremental curve, which can be attributed to the inter- and intra-aggregate porosity, in both natural and reconstituted initial states (Fig. 2.17). Oedometric loading up to 1000 kPa (Fig. 2.18) reduces the average diameter of the inter-aggregate pores, while the intra-aggregate porosity remains almost unchanged.

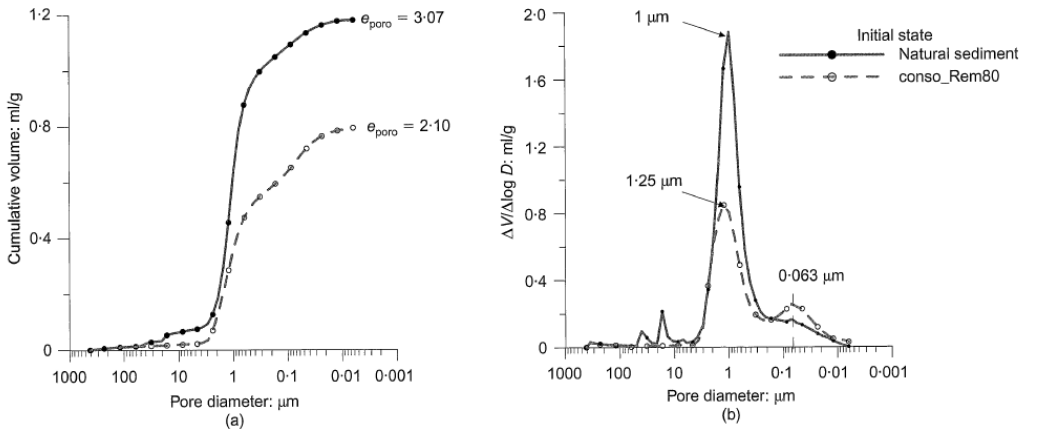

Fig. 2.17 – Natural and reconstituted microstructures of Gulf of Guinea clay at initial state: (a) cumulative and (b) differential volume results (after Hattab and Fleureau, 2013).

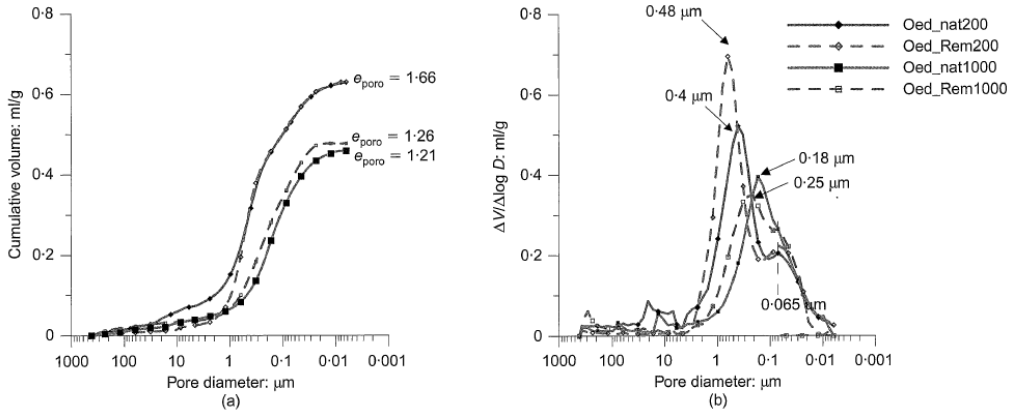

Fig. 2.18 - Natural and reconstituted microstructures of Gulf of Guinea clay after oedometric loading: (a) cumulative and (b) differential volume results (after Hattab and Fleureau, 2013).

Also for Osaka Bay clay (Tanaka and Locat, 1999), the decrease in void ratio due to compression is related to the progressive closing of the inter-aggregate pore space (line B, Fig. 2.19) and the shift of the dominant mode, i.e., the peak of the pore size distribution curve, towards the intra-aggregate line (A, Fig. 2.19). The value of the differential curve at line A remains almost unaffected with increasing pressure, indicating that intra-aggregate pore space is not altered by compression. Hence, based on this analysis of these data from the literature, it is here deduced that a seemingly general structure evolution takes place at very early stages of compression of the normally consolidated clay. Where the initial clay fabric, at high water contents and low pressures, tends to resemble that from Griffiths and Joshi (1990), for either reconstituted and natural clays, then the inter-aggregate set-up is the first to be lost with compression, with a corresponding tendency to lose the eventual bi-modality of the pore size distribution. This aspect of the structure evolution with compression will be further discussed in Chapter 7.

However, analysing samples of Osaka Bay clay taken at different depths, Rito et al. (2003) observed that with increasing in situ pressure (1D conditions), the pore diameter distribution curves progressively move to the smaller-sized diameter region. At pressures higher than 3 MPa all pores larger than 10-20 nm are influenced by

compression (Fig. 2.20). Hence, these data provide evidence of the possible reduction in intra-aggregate porosimetry with large compression.

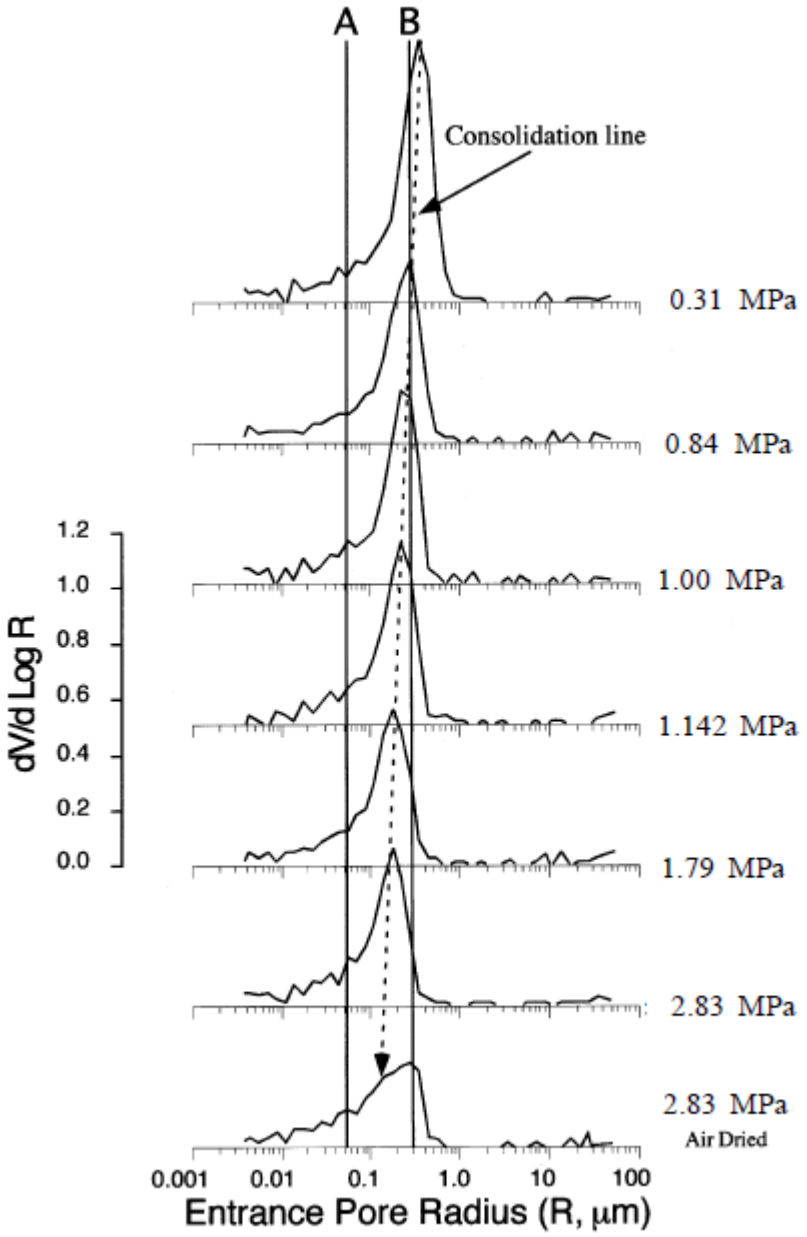

Fig. 2.19 – Pore-size changes as a function of vertical stress on a Osaka Bay clay sample (after Tanaka and Locat, 1999 modified).

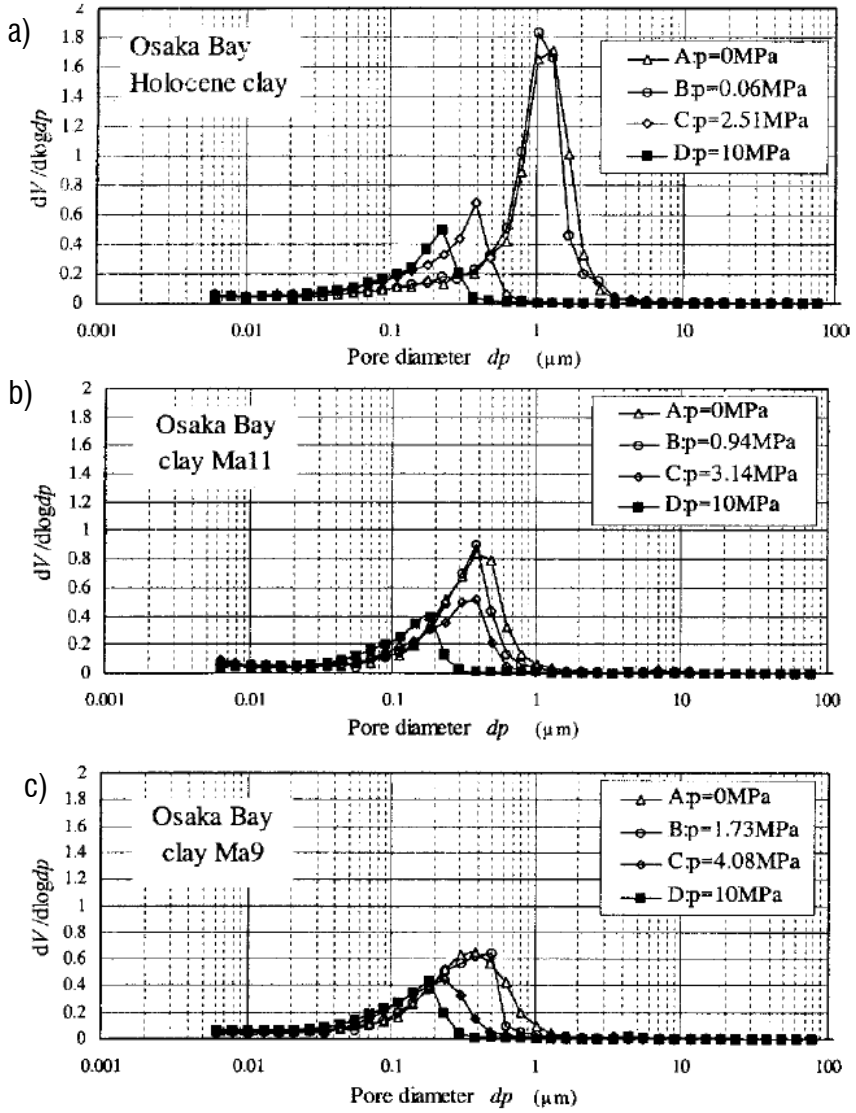

Fig. 2.20 – Change of pore diameter distribution curves of Osaka Bay clay taken at (a) 10m, (b)95 m, (c) 175 m due to consolidation (after Rito et al., 2003).

Griffiths and Joshi (1989; 1990) investigated the microstructural changes due to one-dimensional consolidation of four artificial clays of different composition (including kaolinite) reconstituted in the laboratory and compressed up to 1500 kPa. The

increasing consolidation stress resulted for all soils in a reduction of the total intruded volume, which especially affected the inter-assemblage (Fig. 2.9) pore space.

In addition to the change in pore structure, 1D compression is generally believed to orientate the clay particles to lie normally to the maximum principle stress (Tchalenko, 1967), and an increase in the average degree of orientation of the clay particles is observed in many clays with increasing vertical stress.
From SEM micrographs of St. Marcel clay at different loading pressures, Delage and Lefebvre (1984) observe a progressive stretching of large pores and of aggregates along the horizontal direction, relating to the progressive increase of structure anisotropy. Areas of more random orientation, with an arrangement of particles similar to the intact structure can still be found in the specimen compressed to 124 kPa, but they are not observed in subsequent loading. Similarly, for Louiseville clay Lapierre et al. (1990) notice a decrease in the size of inter-aggregate pores with increasing volumetric strain and a clear orientation of particles in the horizontal direction.
SEM images of reconstituted Gulf of Guinea clay after compression (Hattab and Fleureau, 2013) show a structural organisation of particles towards the horizontal direction which, however, is far less evident in the natural clay after compression.
Therefore, the overall increase in the particle orientation may be considered as a result of the development of areas of highly oriented fabric and the preservation of areas of non-oriented fabric.
As reported by Cotecchia (1996), Sfondrini (1975) proposed a scheme for fabric development in oedometric compression. First, the author suggested that there exists a lower bound stress below which the fabric of the clay is determined by the internal forces. Above this value the extemal forces determine the fabric of the clay. Sfondrini discussed the case of Fiumicino clay, an illitic clay that after deposition in a brackish lagoon and normal consolidation to 180 kPa still has a bookhouse fabric (Fig. 2.21(a)), showing that the in-situ consolidation preserved much of the primary fabric. Sfondrini found that under oedometric compression in the laboratory the strain was concentrated in some areas of the sample, preserving the porosity of others. Sfondrini identified a

stage when strata of c.p.o. fabric, referred to as "stacks" above and that Sfondrini called "complex laminae", formed between a honeycomb fabric (Fig. 2.21 (b)). The picture and the scheme in Fig. 2.21(b) resemble the fabric architecture described for compressed kaolin. The complex laminae are predominantly formed of particles in face contact, which progressively grow with increased loading. Similar fabrics develop in stiff clays which have been subject to both high consolidation and high shearing stresses in situ. Sfondrini (1975) observed that samples of Scaly Clays are crossed by frequent slip surfaces which cut strata of c.p.o. particles. These strata are interbedded in a more random fabric.

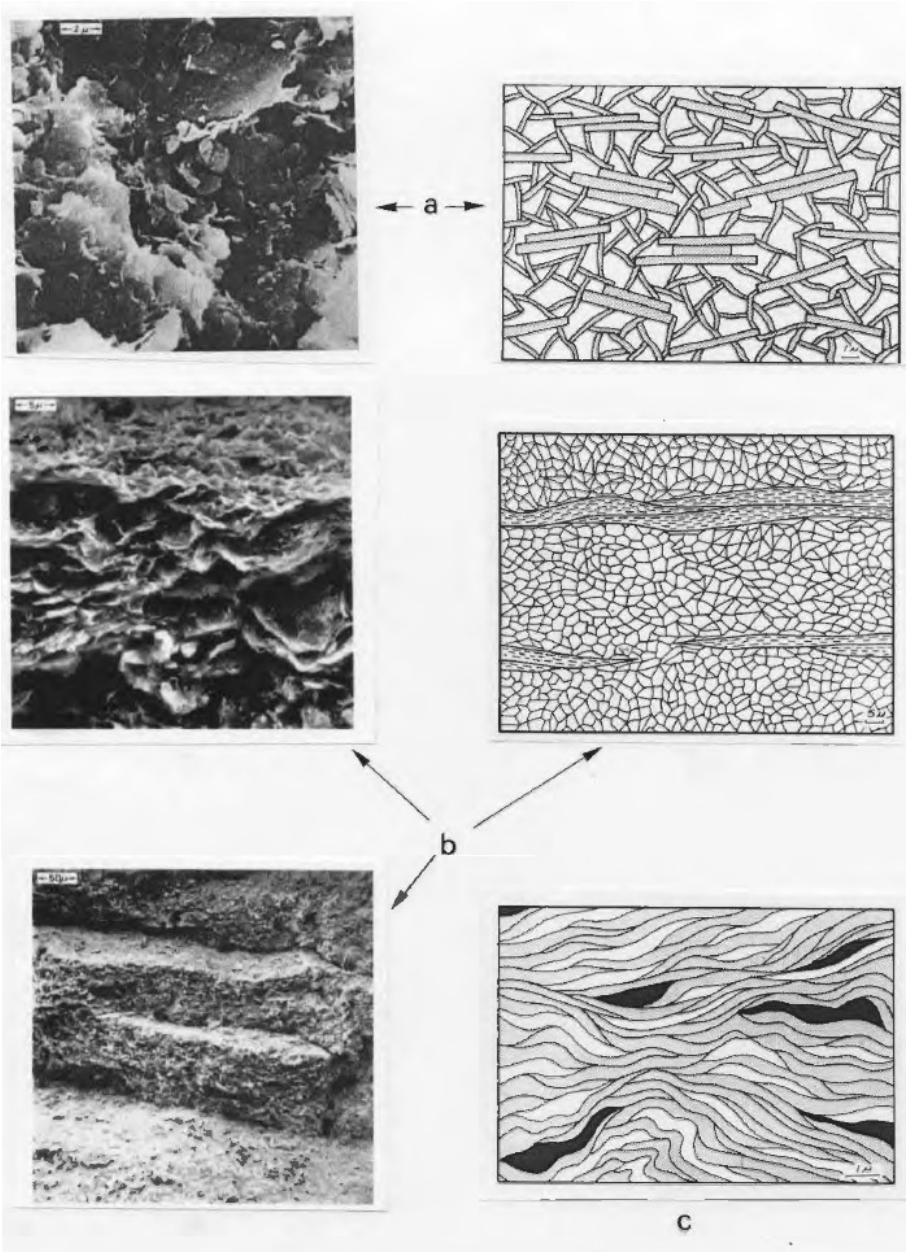

Fig. 2.21 - Fiumicino clay, normally consolidated in situ: (a) fabric on a vertical fracture through an undisturbed sample from 18m depth; (b) fabric on a vertical fracture through a sample compressed to σ'_v *= 4704 kPa; (e) fabric scheme applying to the clay compressed to very high stresses (after F.Cotecchia 1996, pictures after Sfondrini 1975).*

V. Cotecchia et al. (1982-b) reported SEM pictures (Fig. 2.22) showing the effects of one-dimensional consolidation on a kaolin slurry. At 4.9 kPa (Fig. 2.22(a)) the fabric was already much more compacted than that at the liquid limit although, not discussed by the authors, a complex fabric architecture can be identified consisting of horizontal strata of c.p.o. fabric interbedded between areas of flocculated fabric. As discussed by Cotecchia (1996) and Cotecchia & Chandler (1997 and 1998), these strata resemble horizontal slabs sustained by a truss of domains in edge to face contacts (Fig. 2.22(e)). Further compression induced further development of the strata of c.p.o. fabric, the stacks, and the fabric developed through interpenetration of the domains (V. Cotecchia et al., 1982-b). The level of orientation achieved by compression to 490 kPa seems not to be increased significantly with compression to 4900 kPa. The further loading seems only to increase the density of the clay, while edge-to-face contacts between domains are preserved.

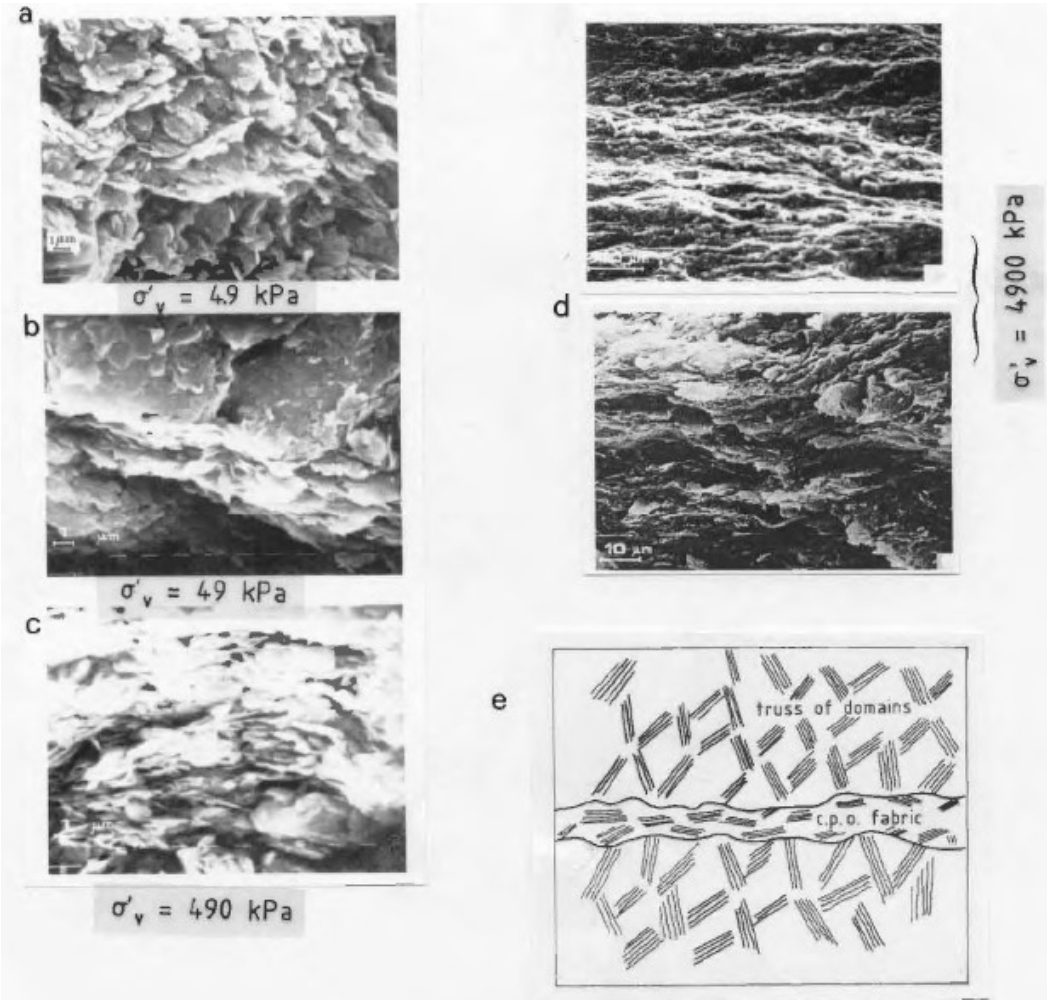

Fig. 2.22 - Oedometer compression of a kaolin slurry (w_0=63%=wLL): (a) σ'_v = 4.9kPa; (b) σ'_v = 49 kPa; (e) σ'_v = 490 kPa; (d) σ'_v = 4900 kPa; (e) scheme of the complex architecture of the fabric in (a); after F. Cotecchia (1996), pictures after V. Cotecchia et al.(1982-b).

Also Griffiths and Joshi (1990) observed that after the compression of kaolinite to 490 kPa vertical stress, much of the inter-assemblage porosity was lost and showed that the connectors in the fabric had been destroyed. However, at this pressure the reorientation involved only part of the fabric, and a random fabric was still preserved inside the assemblages. Consolidation to 1500 kPa vertical stress induced reorientation

of the particles within the aggregations, though some areas of random orientation could still be recognized.
Cotecchia and Chandler (1998) analysed SEM pictures of stiff Pappadai clay 1D compressed to large pressures, observing that stacks of well oriented domains are interbedded with areas of medium oriented to honeycomb fabric, which can be quite open, sometimes as open as the random fabric locally noticed in the undisturbed clay. Thus, 1D compression of the natural clay is seen to increase the orientation of fabric at the medium scale, but areas of flocculated fabric are preserved, causing a non-uniform fabric orientation. Similarly, in the reconstituted clay, 1D compression to large pressures does not give rise to a fabric as oriented as recognized with normal consolidation to medium pressures of monomineralic clays (V. Cotecchia et al., 1982). The variety of minerals, as well as the presence of coarser components, may have affected the fabric orientation process. These data on Pappadai clay will be recalled and developed with further data in the following Chapters.

In recent years, thanks to the availability of advanced technical instruments and software, the qualitative observation of SEM micrographs has often been aided by image processing techniques, which aim at quantifying the degree of particle orientation using different methods. This will be discussed in further detail in Chapter 5.
Although the technique adopted is thought to influence significantly the results of image processing (see Chapter 5), the finding that 1D compression increases the degree of fabric orientation has found confirmation in many works.
Hattab & Fleureau (2010) analysed and processed SEM images of kaolin after reconstitution in the laboratory and consolidation to 120 kPa in the consolidometer. The technique used will be discussed in detail in Chapter 5. The results show that kaolin has a structural anisotropy (Fig. 2.23) with a preferential orientation of particles along vertical fractures towards the horizontal direction (0-15°).

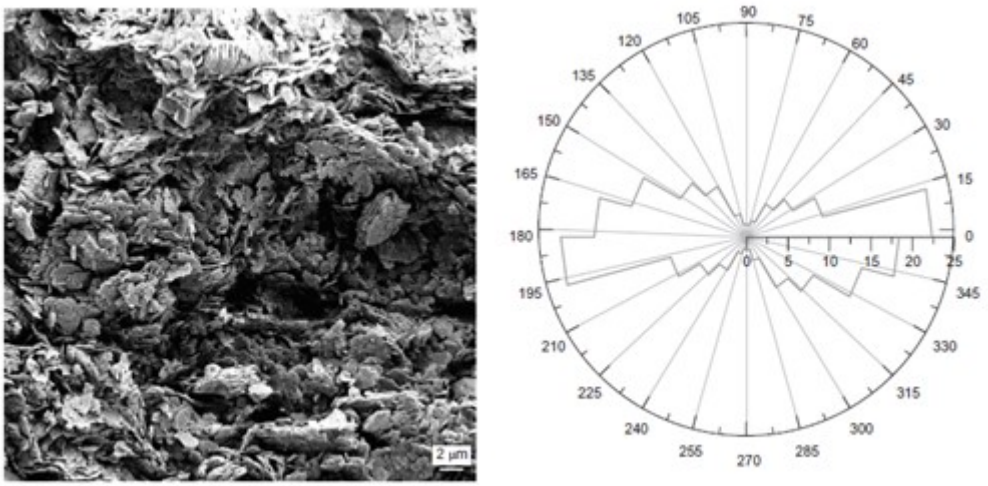

Fig. 2.23 – Fabric orientation of a kaolin specimen at initial state after consolidation in consolidometer to σ'_v=120 kPa, along a vertical plane (after Hattab and Fleureau, 2010).

Using a similar image processing technique (see Chapter 5), Hicher et al. (2000) observed that under 1D compression up to 6.3 MPa kaolinite exhibits a very strong structural anisotropy due to the reorientation of particles in the direction perpendicular to the direction of loading (Fig. 2.24). Similarly, in a bentonite specimen 1D compressed to 1 MPa (Fig. 2.25) and to 6.3 MPa (Fig. 2.26) a strongly marked orientation of the particles is observed in vertical fractures. In this case, the long and flexible shape of bentonite particles is considered to allow for a higher possibility of reorientation and structural anisotropy.

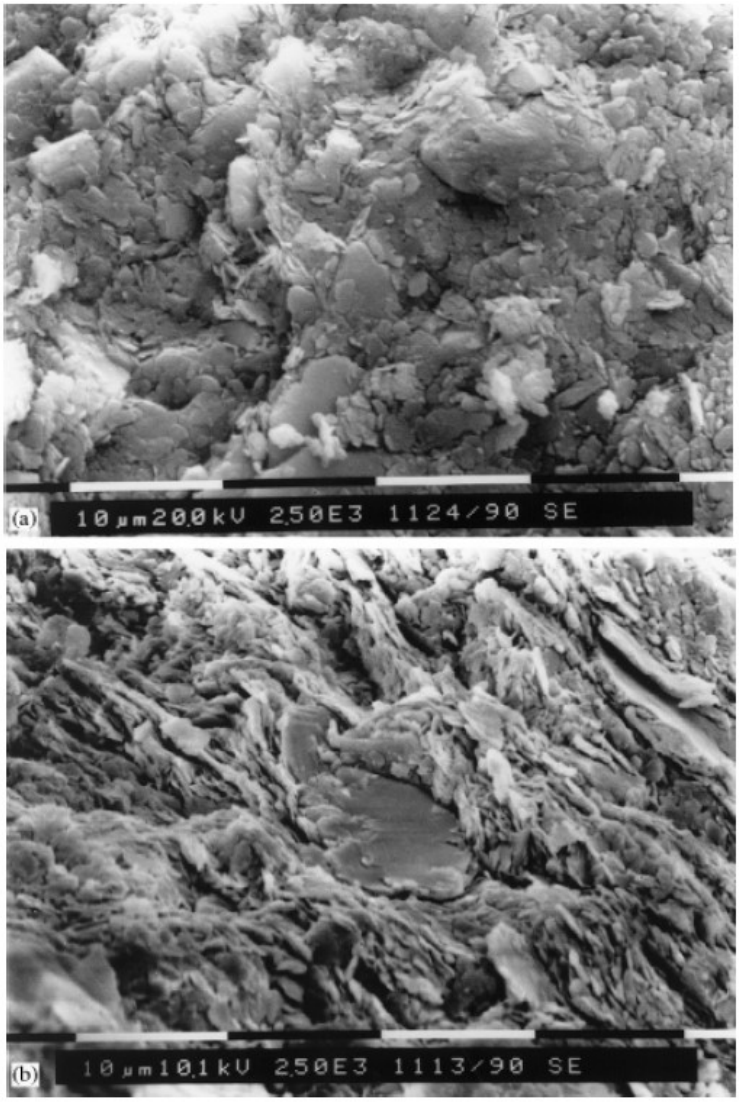

Fig. 2.24 - Observation of kaolinite specimen 1D compressed to 6.3MPa: (a) horizontal plane, (b) vertical plane (after Hicher et al., 2000).

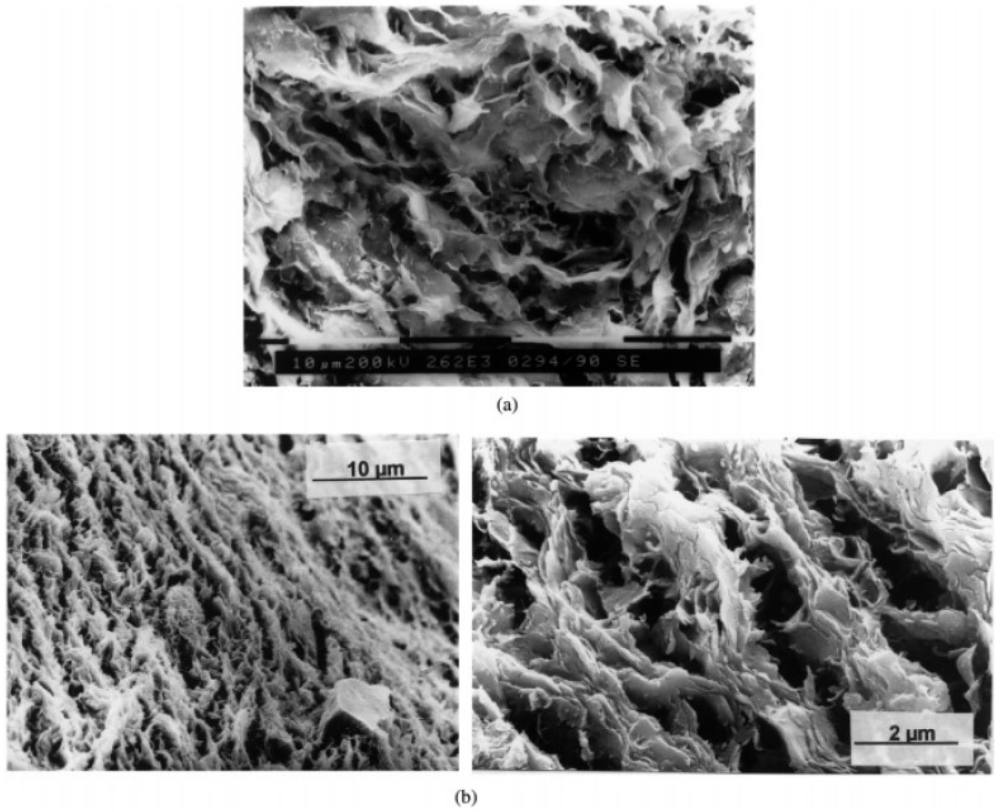

Fig. 2.25 - Observation of bentonite specimen 1D compressed to 1 MPa: (a) horizontal plane, (b) vertical plane (after Hicher et al., 2000).

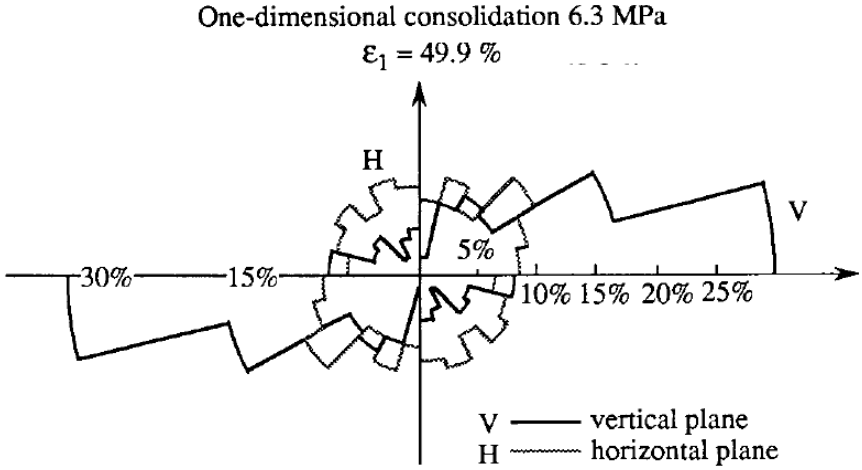

Fig. 2.26 – Orientation histograms of a bentonite specimen 1D compressed to 6.3 MPa (after Hicher et al., 2000 modified).

Mitaritonna et al. (2014) observed the fabric of reconstituted Lucera clay at initial state (σ'_v=100 kPa) and after K_0 compression to medium pressures. As found for Pappadai clay by Cotecchia et al. (1998), alternating stacks of domains and honeycomb particle arrangements are recognized both prior to testing, i.e., after consolidometer loading, and after further 1D compression, despite the fabric being more densely packed in the latter case. Qualitative observations are confirmed by image processing, carried out according to the technique proposed by Martinez-Nistal et al. (1999), which gives similar values of fabric orientation degree (indicated as L in Fig. 2.27) for the specimens before and after compression. Furthermore, this result is found to be consistent with the constant value of the anisotropy degree G_{hh}/G_{hv} recorded by means of horizontal bender elements mounted in the stress path apparatus.

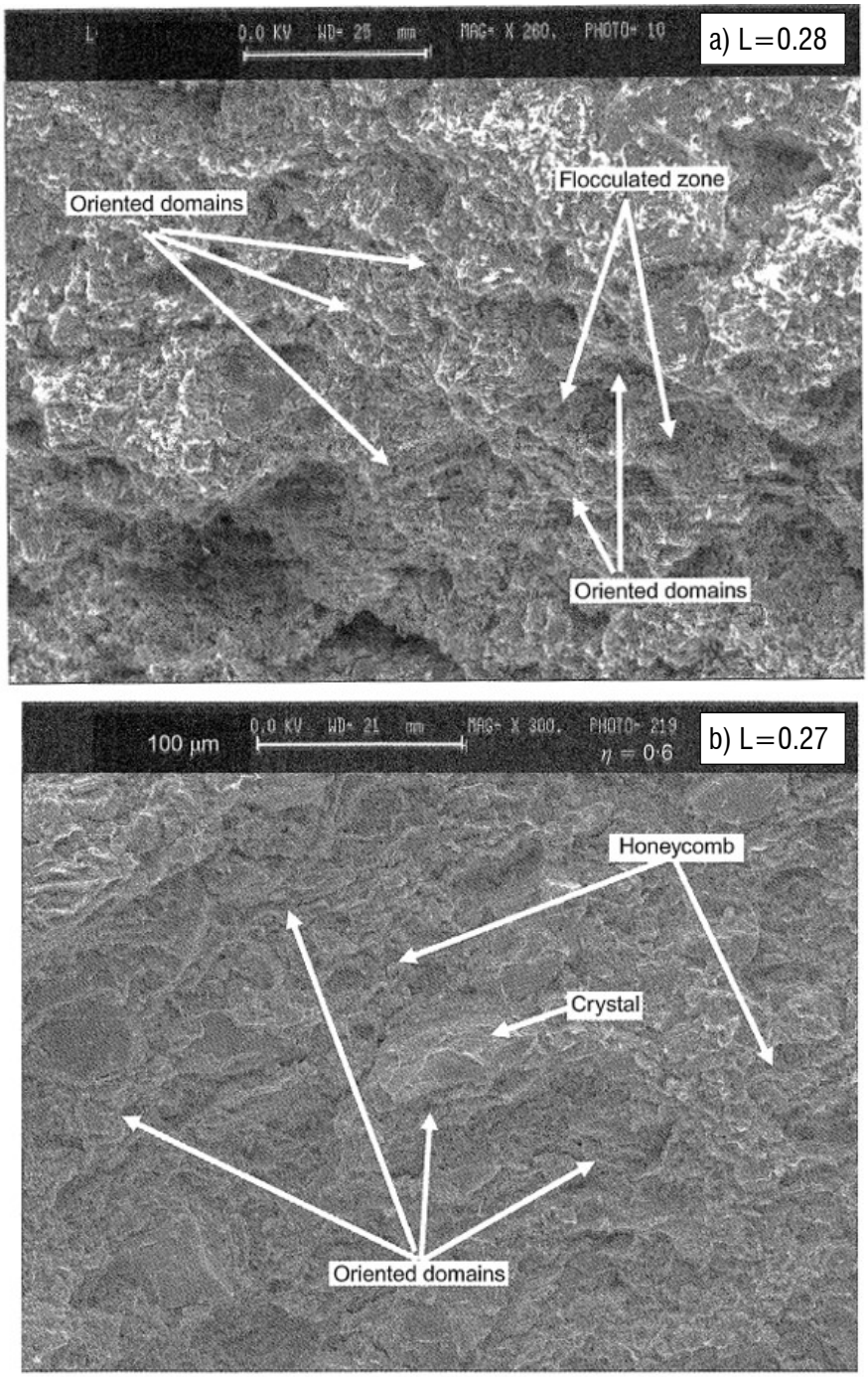

Fig. 2.27 - SEM micrographs of reconstituted Lucera clay (a)at the end of consolidometer stage and (b) after K_0 compression to p'=1350 kPa (after Mitaritonna et al., 2014).

2.11 Effects of isotropic compression on the clay microstructure

Contrarily to 1D compression, isotropic compression is generally considered to induce randomness of the particle arrangement and, thus, to reduce the overall degree of fabric orientation. With reference to pore size distribution, isotropic compression has often been seen to reduce inter-aggregate pores with minor changes of intra-aggregate porosity.

Hattab and Fleureau (2010) observed that when reconstituted kaolinite after consolidation in the consolidometer is compressed isotropically to medium pressures (1400 kPa), the corresponding decrease in pore space is related to a more random orientation of the particles. In fact, the initially U-shaped curve in the plot of the orientation angle to the horizontal against percentage of particles oriented along that direction (see Chapter 5) is replaced by a line closer to the depolarisation line, that indicates randomness, showing a tendency towards the development of an isotropic fabric through a depolarization mechanism (Fig. 2.28).

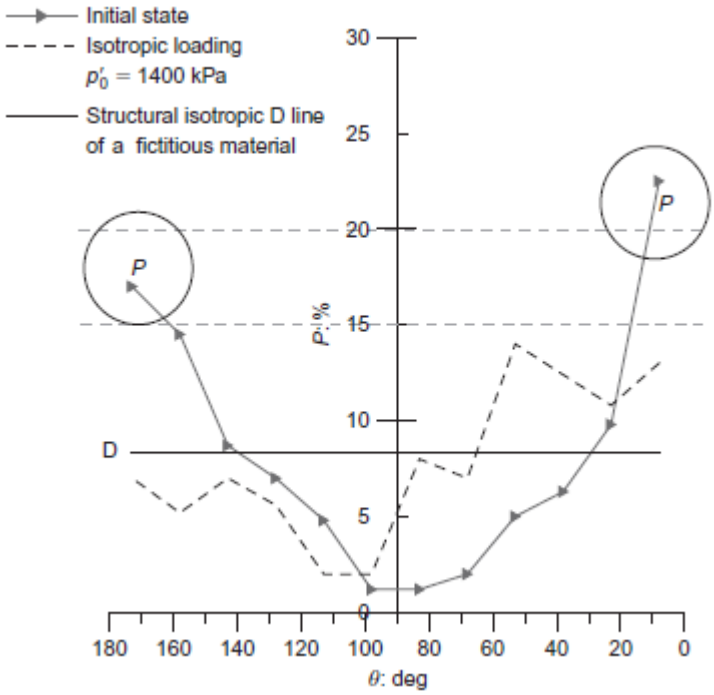

Fig. 2.28 – Comparison of orientation curves for kaolinite at initial state (σ'_v =120 kPa) and after isotropic compression to p'=1400 kPa (after Hattab and Fleureau, 2010).

The behaviour of reconstituted kaolinite under isotropic compression was also investigated by Hicher et al. (2000), who found that the application of an isotropic loading around 3 times larger than the initial pressure generates an isotropic particle orientation (Fig. 2.29).

Yu et al. (2016) investigated the evolution of porosimetry under isotropic compression of kaolinite. As shown in Fig. 2.30, isotropic compression shifts the dominant pore size from 500 nm (initial state), to 270 nm (at 100 kPa) and finally to 220 nm (at 400 kPa), with a subsequent compression of the larger inter-aggregate pores. On the other hand, the smaller intra-aggregate pores remain almost unchanged at 100 kPa and slightly increase at 400 kPa, suggesting that more intra-aggregate pores are produced after some of the inter-aggregate pores are compressed.

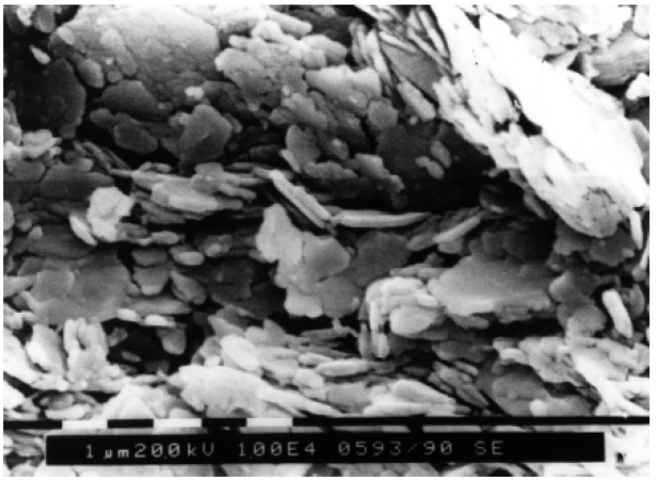

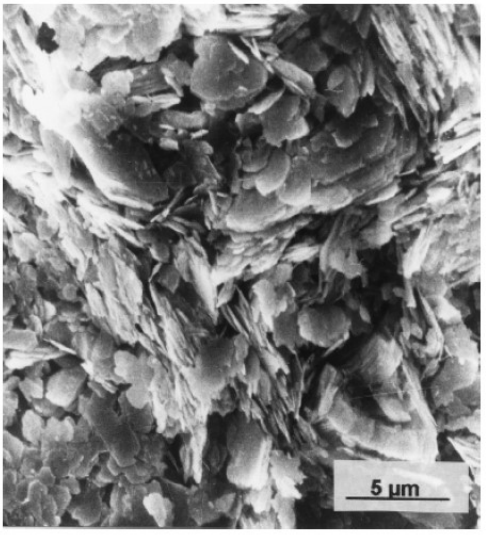

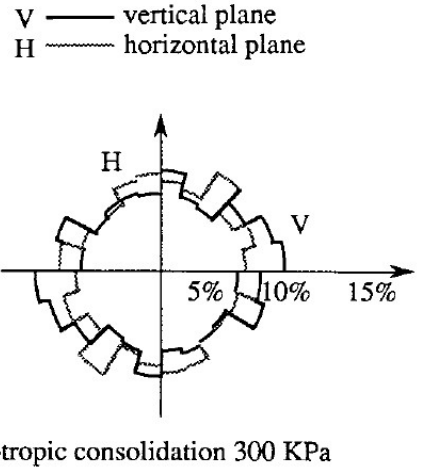

Fig. 2.29 - (a) Kaolin consolidated to around 80 kPa in a consolidometer and (b) after isotropic consolidation to p'=300 kPa with fabric orientation quantification (after Hicher et al., 2000 modified).

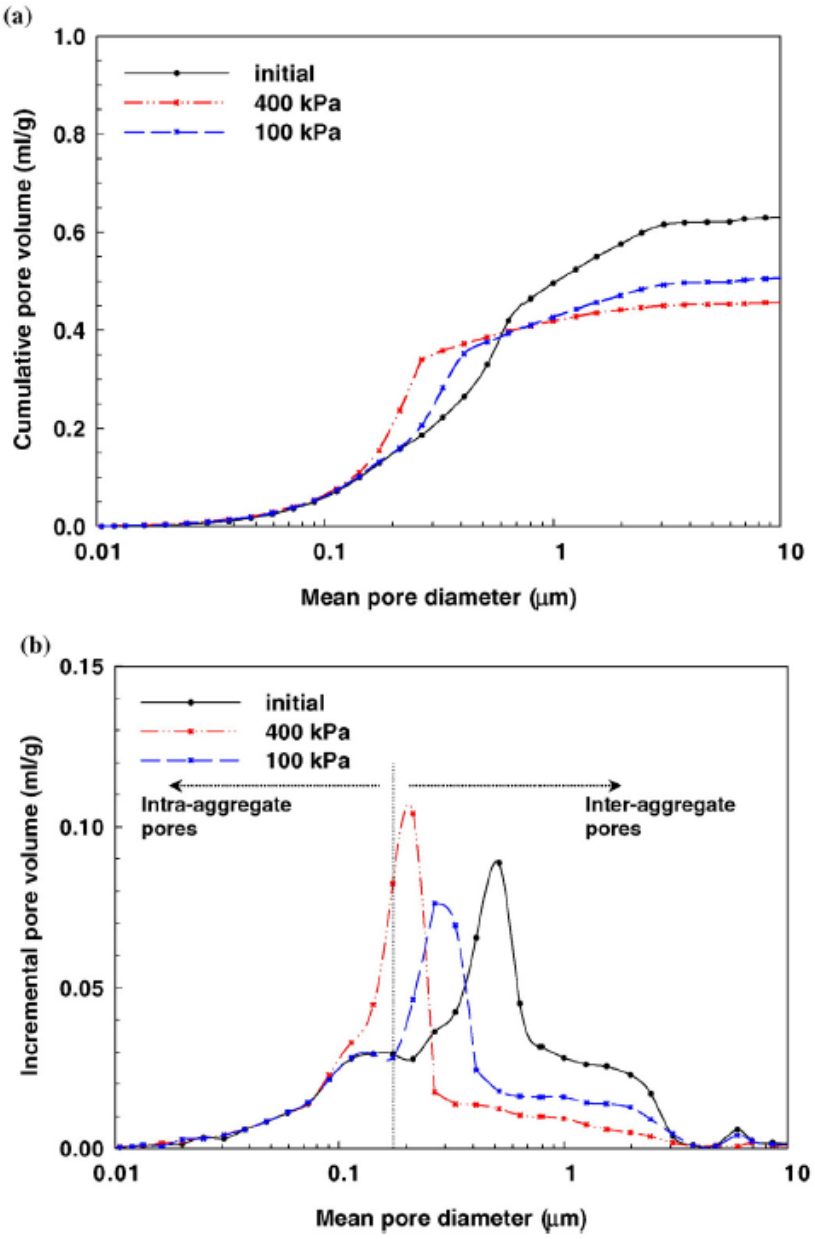

Fig. 2.30 – Pore size changes in a kaolinite specimen after isotropic compression to 100 and 400 kPa: (a) cumulative and (b) incremental pore volume vs. entrance pore diameter (after Yu et al., 2016).

Similarly to kaolinite, according to Hicher et al. (2000) bentonite isotropically loaded to 6 MPa shows a denser particle arrangement with fully isotropic orientation, seen in both horizontal and vertical planes (Fig. 2.31).

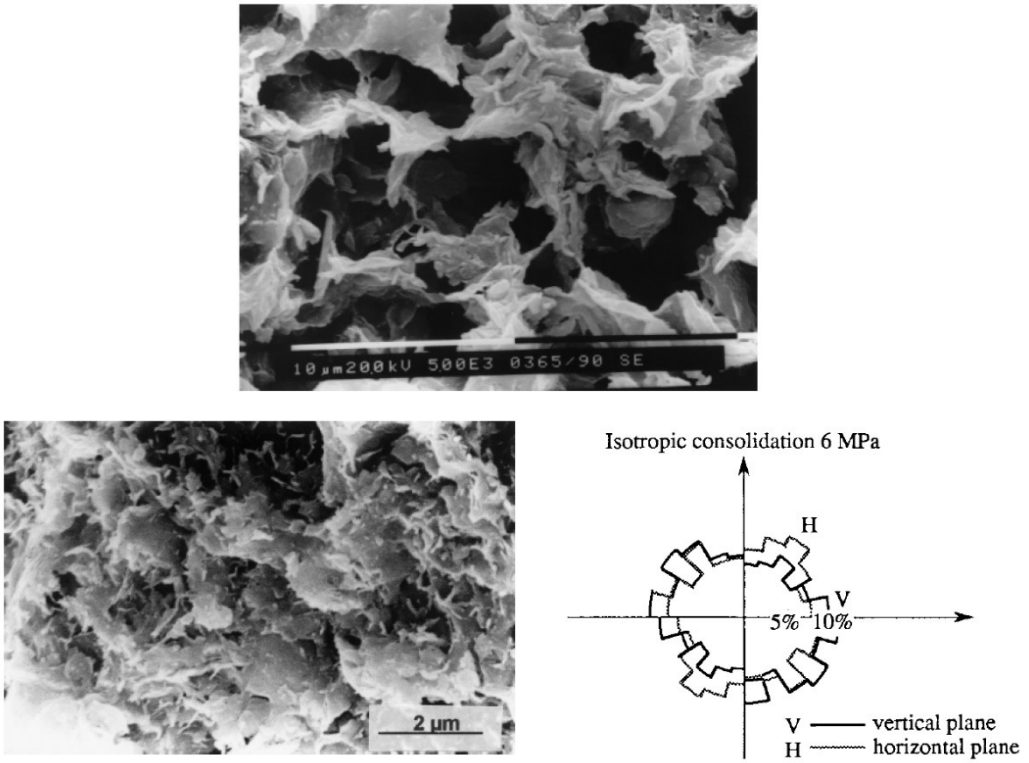

Fig. 2.31 - (a) Bentonite consolidated in a consolidometer and (b) after isotropic consolidation to p'=6 MPa with fabric orientation quantification (after Hicher et al., 2000 modified).

For natural Gulf of Guinea clay isotropically compressed from undisturbed state (≈36 kPa) to p'=1000 kPa, Hattab and Fleureau (2013) observed a significant reduction of inter-aggregate pores and a completely random orientation of particles (Fig. 2.32(a,b,c)). In the reconstituted material compressed from initial state (80 kPa) to p'=900 kPa, a similar collapse of macro pores occurs but particles appear still mainly oriented towards the horizontal direction, indicating that the effect of initial 1D consolidation in the consolidometer has not been completely erased yet (Fig. 2.32(d)).

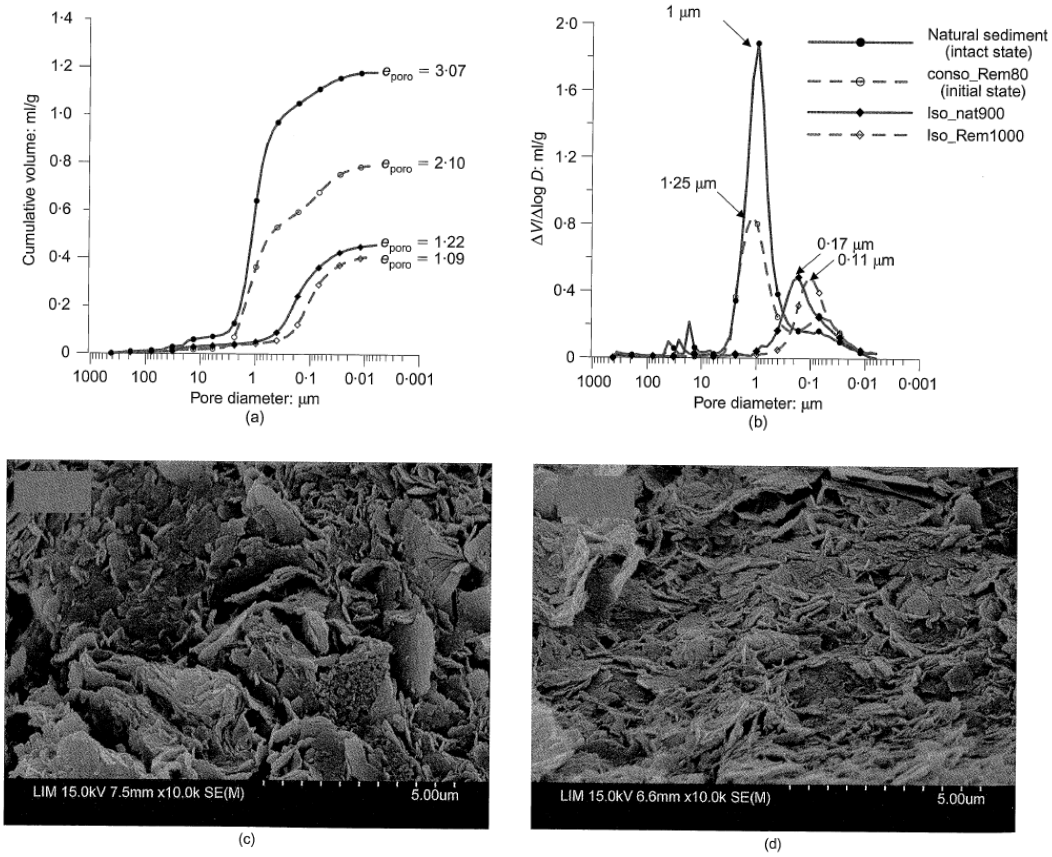

Fig. 2.32 – Microstructure of Gulf of Guinea clay after isotropic loading: (a) cumulative volume results, (b) incremental volume results, (c) SEM photo of natural sediment at 900 kPa and (d) SEM photo of reconstituted sediment at 1000 kPa (after Hattab and Fleureau, 2013).

Mitaritonna et al. (2014) observed that the application of an isotropic stress path from around 70 kPa to reconstituted Lucera clay up to 1350 kPa causes a reduction in stiffness anisotropy ratio G_{hh}/G_{hv} with respect to the value measured in K_0 compression. Accordingly, the initially well oriented fabric (L=0.28; Fig. 2.27a) is evidently undergoing a severe rearrangement into a far less oriented fabric. As a confirmation, the SEM images (Fig. 2.33) of a specimen subjected to a stress ratio $\eta=0.3$, being very close to an isotropic stress path, do not show a preferred orientation and are characterized by a degree of fabric orientation L lower than 0.15, which corresponds to random orientation (Martinez-Nistal, 1999; see Chapter 5).

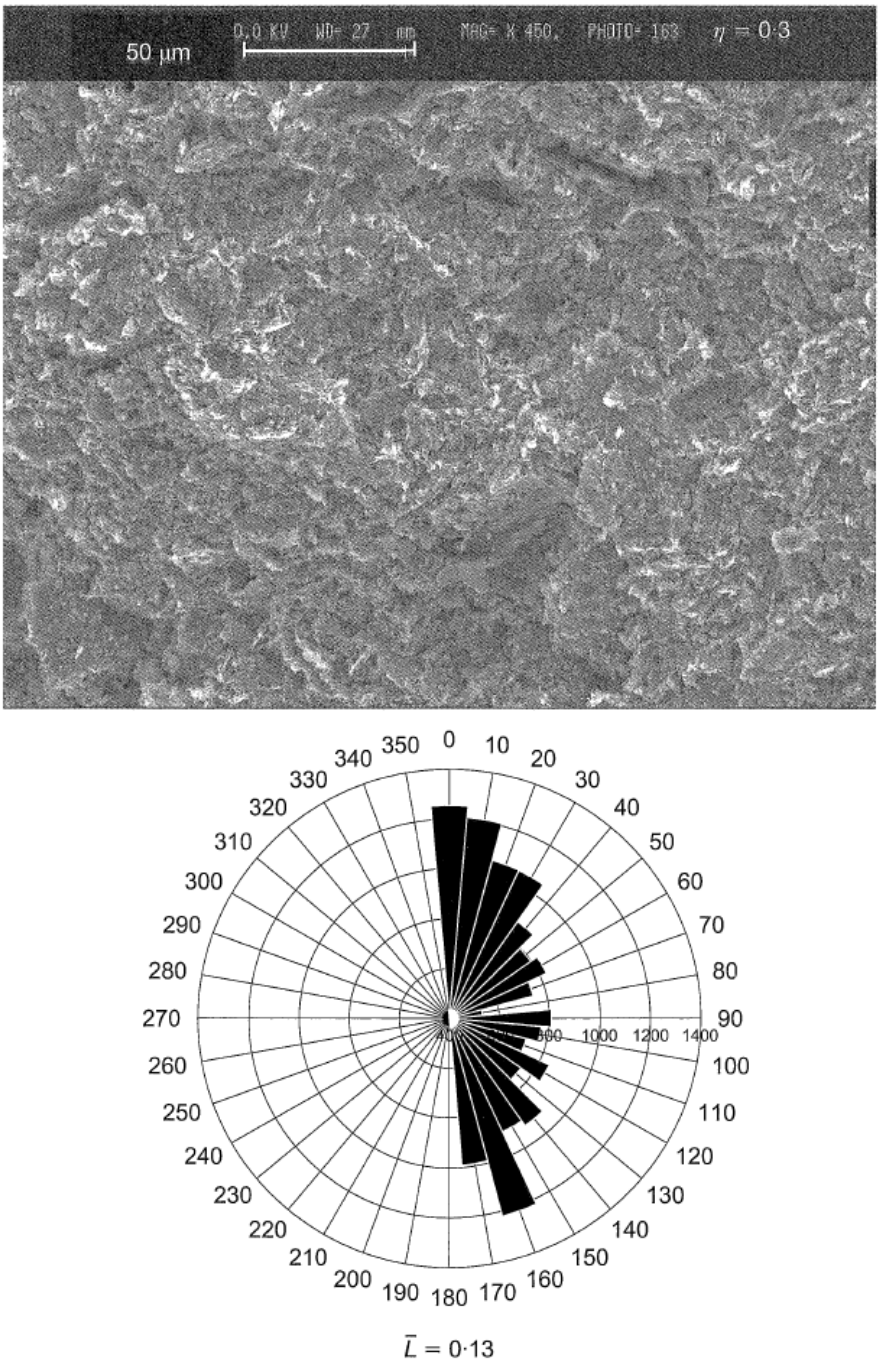

Fig. 2.33 – SEM image and direction histogram of reconstituted Lucera clay compressed under a stress path η=0.3 (Mitaritonna et al., 2014).

2.12 Effects of shear on the clay microstructure

The effects of shear on the clay microstructure have been often investigated in drained conditions on specimens exhibiting a contractant behaviour, in which the reduction in pore volume is related to a reduction in the inter-aggregate pores.
Recent works report an increase in particle orientation along the direction of the shear band in specimens subjected to shearing. In clay samples sheared to residual V. Cotecchia et al.(1982-b) observed the presence of strata of c.p.o. fabric on the sides of the shearing plane, interbedded in a honeycomb fabric, hence resulting in heterogeneous straining similar to that induced by 1D compression.

For kaolin, Hattab and Fleureau (2010) examined the evolution of particle orientation under drained shear at three values of axial strain ε_a, i.e., 5%, 15% and 25%. The specimen was isotropically loaded to p'=1400 kPa (see Section 2.11 and Fig. 2.28) and then unloaded to 1000 kPa (R=1.4), resulting in a lightly overconsolidated sample, and exhibiting contractant behaviour. As shown in Fig. 2.34, at the beginning of triaxial loading (ε_a=5%), the orientation curve approaches the depolarisation line D, indicating that the depolarisation mechanism causing fabric randomness induced by the previous isotropic path is still active. At ε_a=15%, the SEM micrographs along vertical fractures show that some groups of particles acquire a preferential orientation; the orientation curve assumes a U-shape with principal orientation modes towards the horizontal and also towards 20-40° to the horizontal. At ε_a=25%, the strong orientation of particles with face to face contacts appearing in SEM micrographs (Fig. 2.35) is confirmed by an orientation curve which is no longer U-shaped, but has a strong anisotropy towards 20-40°.
So, the triaxial shear path induces fabric depolarisation up to a critical threshold, which the Authors identify as the limit of the pseudo-elastic domain (ε_a=5%). Once this threshold has been overcome, particles tend to acquire a preferential orientation, even though no shear plane is observed at the macro-scale.

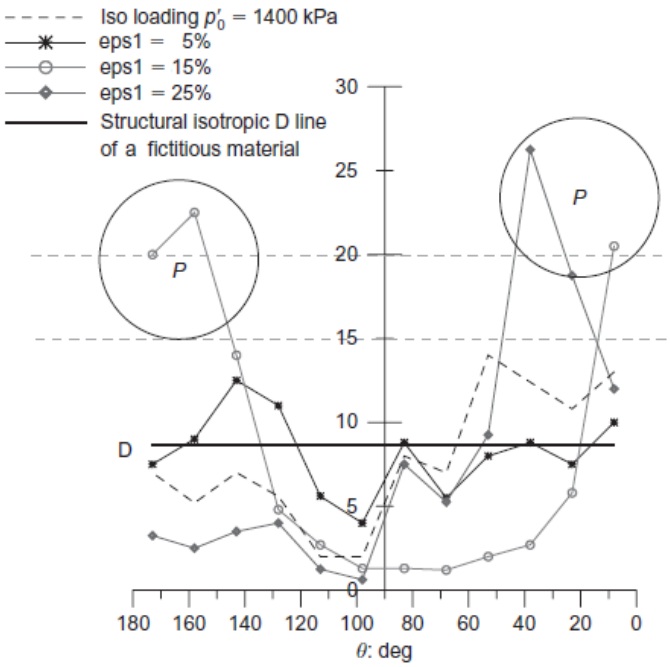

Fig. 2.34 – Comparison of orientation curves for different axial strains in drained triaxial loading (after Hattab and Fleureau, 2010).

Fig. 2.35 – Microfabric after triaxial loading to ε_a=25% along a vertical plane (after Hattab and Fleureau, 2010).

Hicher et al. (2000) also observed on a kaolin specimen normally consolidated isotropically to 300 kPa and sheared in drained conditions, that the particle orientation, which is still almost random at ε_a=9%, becomes clearly anisotropic at ε_a=19.5% (Fig. 2.36). SEM micrographs taken along a vertical fracture next to the failure surface show that the orientation of particles is parallel to the direction of the shear band (Fig. 2.37).

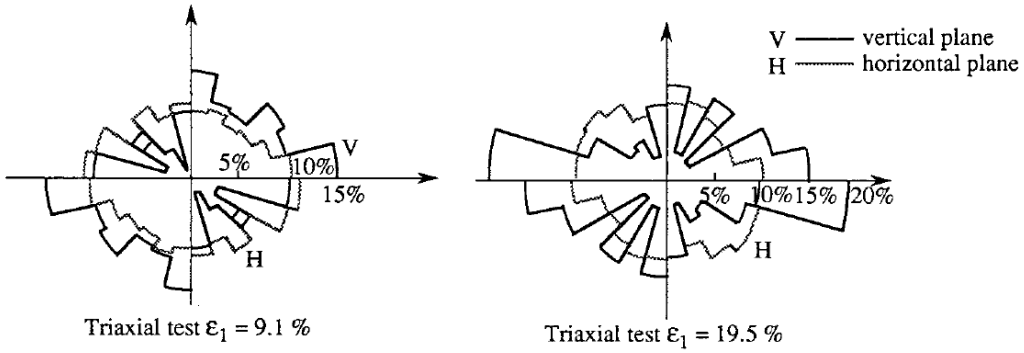

Fig. 2.36 - Fabric orientation quantifications of kaolin after drained triaxial shear to 9.1% and 19.5 % axial strain (after Hicher et al., 2000 modified).

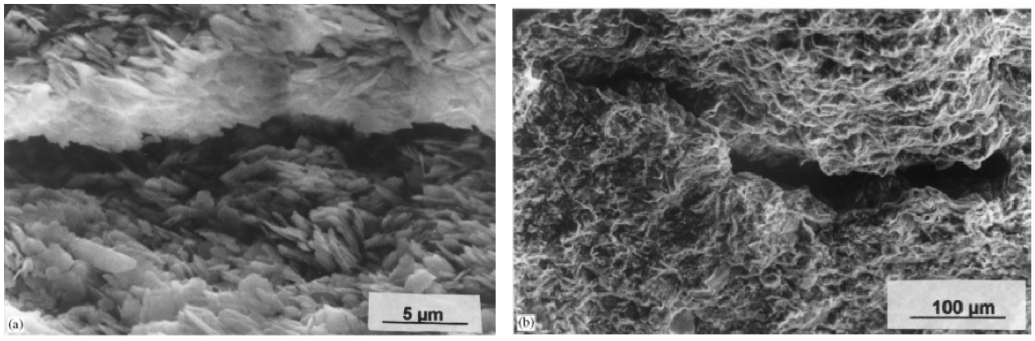

Fig. 2.37 – SEM micrographs of a kaolinite specimen after drained shear to ε_a=19.5% along a vertical plane (after Hicher et al., 2000).

Yu et al. (2016) carried out MIP tests on a kaolin specimen subjected to drained shears under a confining pressure of 100 kPa, which had been divided into three different sections (upper, middle and lower) after shear testing. For the applied confining

pressure, shearing reduces the size of the inter-aggregate pores, leaving the intra-aggregate almost unchanged (Fig. 2.38).

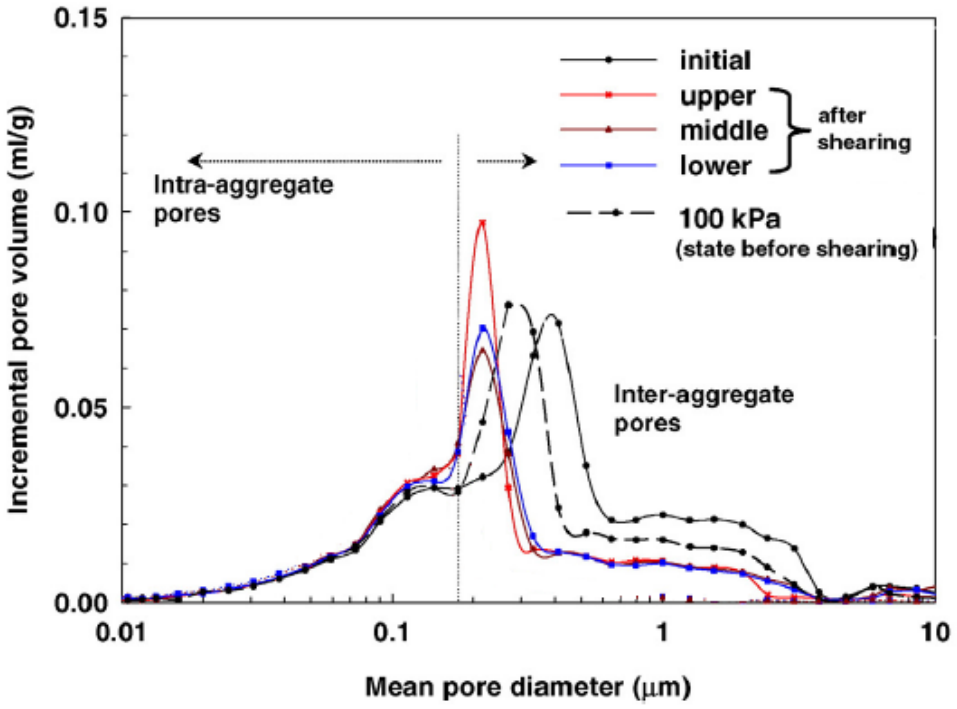

Fig. 2.38 – Pore size changes of a normally consolidated specimen of kaolin after drained triaxial shearing (after Yu et al., 2016 modified).

The behaviour of the natural soft Gulf of Guinea clay was investigated in drained shear by Hattab and Fleureau (2013), and for comparison also specimens of the reconstituted clay were sheared in drained conditions at increasing values of confining stress. In both cases, a decrease in the inter-aggregate pore space with increasing confining pressure occur, while the intra-aggregate pores remained not affected (Fig. 2.39a, b; Fig. 2.40a, b). SEM micrographs of reconstituted specimens after shearing (Fig. 2.39c, d, e) clearly show preferential directions of particle groups. In the intact sediment, only a few areas appear oriented (Fig. 2.40c, d, e), maybe as a consequence of bonding between aggregates which contrasts the reorientation mechanism.

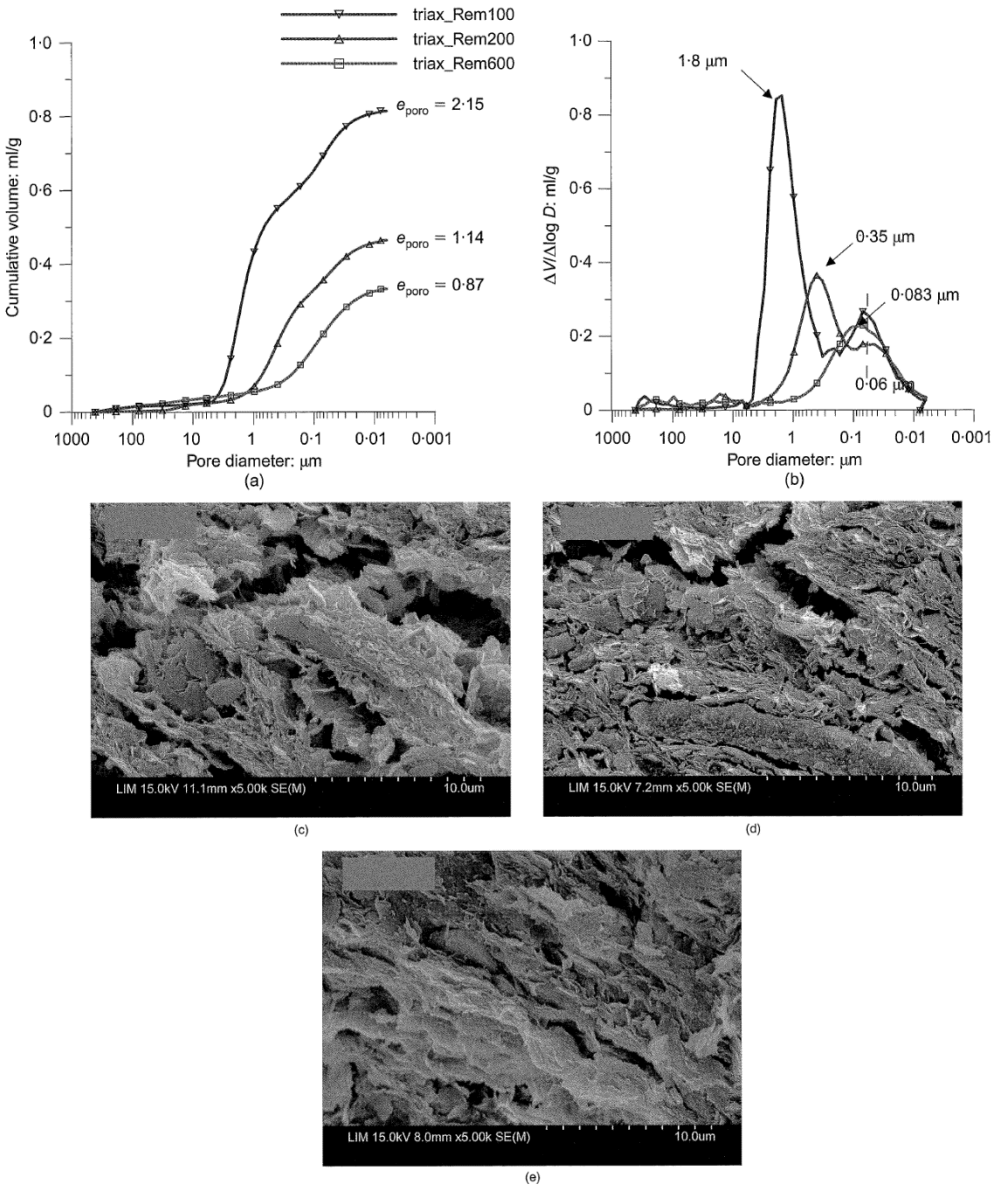

Fig. 2.39 – Microstructure of reconstituted specimen of Gulf of Guinea clay after triaxial loading from p'=100, 200 and 600 kPa. (a) cumulative volume results, (b) incremental volume results, (c) SEM photo at 100 kPa, (d) SEM photo at 200 kPa and (e) SEM photo at 600 kPa (after Hattab and Fleureau, 2013).

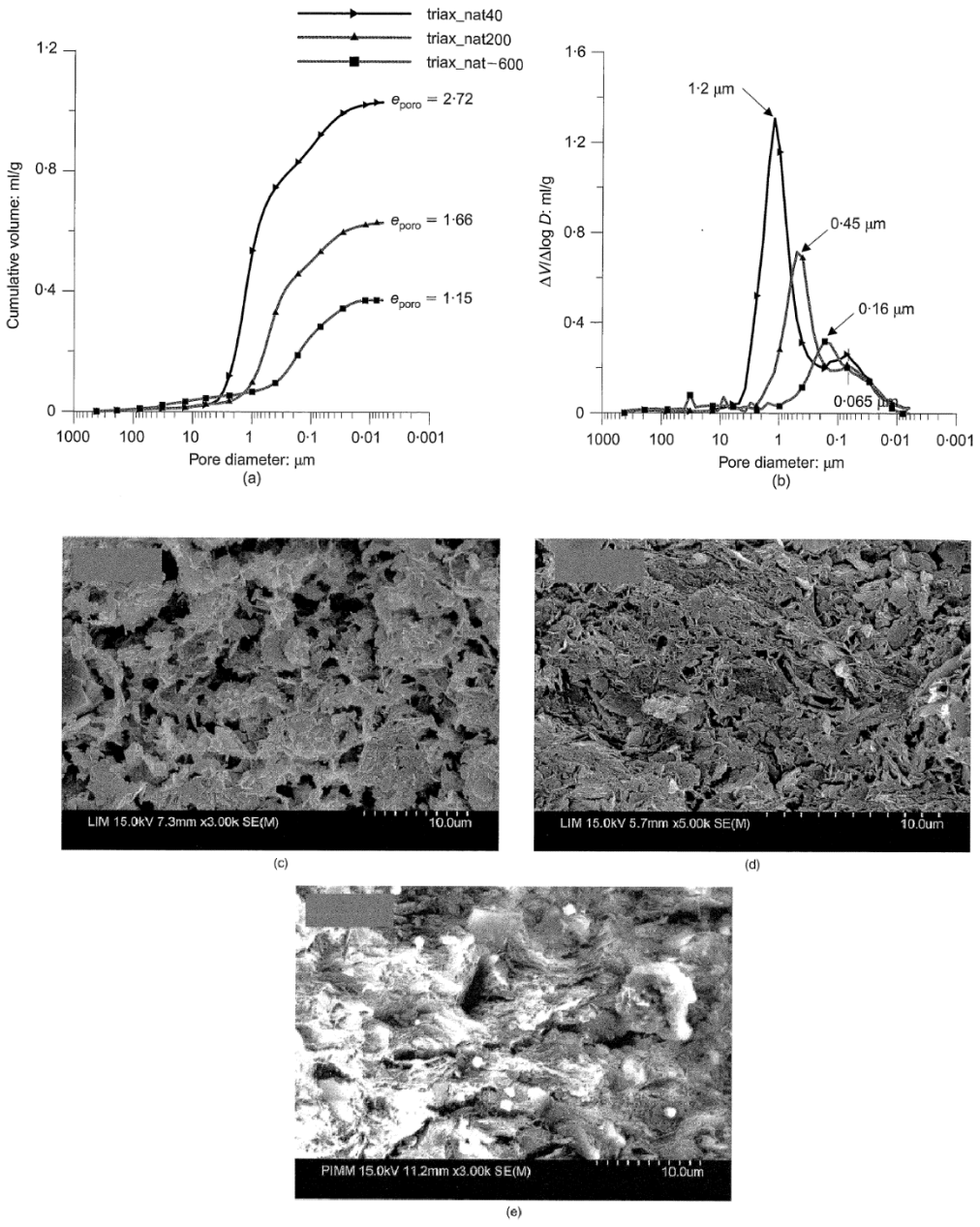

Fig. 2.40 - Microstructure of natural specimen of Gulf of Guinea clay after triaxial loading from p'=40, 200 and 800 kPa. (a) cumulative volume results, (b) incremental volume results, (c) SEM photo at 40 kPa, (d) SEM photo at 200 kPa and (e) SEM photo at 800 kPa (after Hattab and Fleureau, 2013).

2.13 Microstructural analysis of strain localisation in clays

The first studies on the evolution of microstructure of clays in shear were carried out after direct shear experiments on thin sections observed with the help of optical microscopy. Monomineralic clays were preferred for the sake of simplicity.

Morgenstern and Tchalenko (1967) took direct shear specimens from a kaolin slurry after consolidation to around 400 kPa, which resulted in a high degree of orientation. Samples with original bedding normal and parallel to the shearing direction were interrupted at various displacements and thin sections prepared and observed by means of optical microscopy (Fig. 2.41). During yield to peak strength, no discontinuities appear but a quasi-homogeneous rotation of the structures constituting the original fabric orientation is observed in the direction of the imposed motion. At peak strength the major structures which appear are Riedel shears (Riedel, 1929) and simple shear conditions are believed to occur in the central portion of the specimen; a continuous horizontal structure generates only towards the residual stage. Some intermediate structures are seen to develop, as a consequence of the kinematic restraints imposed by the box configuration.

Later Tchalenko (1970) analysed the formation and development of shear structures in clays and mainly distinguished three characteristic stages in the evolution of a shear zone. The first is the peak stage, during which the shear resistance is maximum and the structures formed are Riedel shears and conjugate Riedel shears. In direct shear tests, the width and the length of the shear zone varies from a few microns to millimetres. The post-peak stage is characterized by a decrease of shear resistance and the formation of new shears, termed “P-shears”, symmetrically to the Riedel shears with respect to the general direction of movement. The last stage is the residual stage, during which the shear resistance attains a constant value smaller than the peak value and one or more parallel principal displacement shears are seen in the direction of movement.

More recent studies on the evolution of the clay structure inside the shear band were carried out by Hicher et al. (1994) and could take advantage of more advanced technical instrumentation, such as electron microscopy and X-ray scanning.

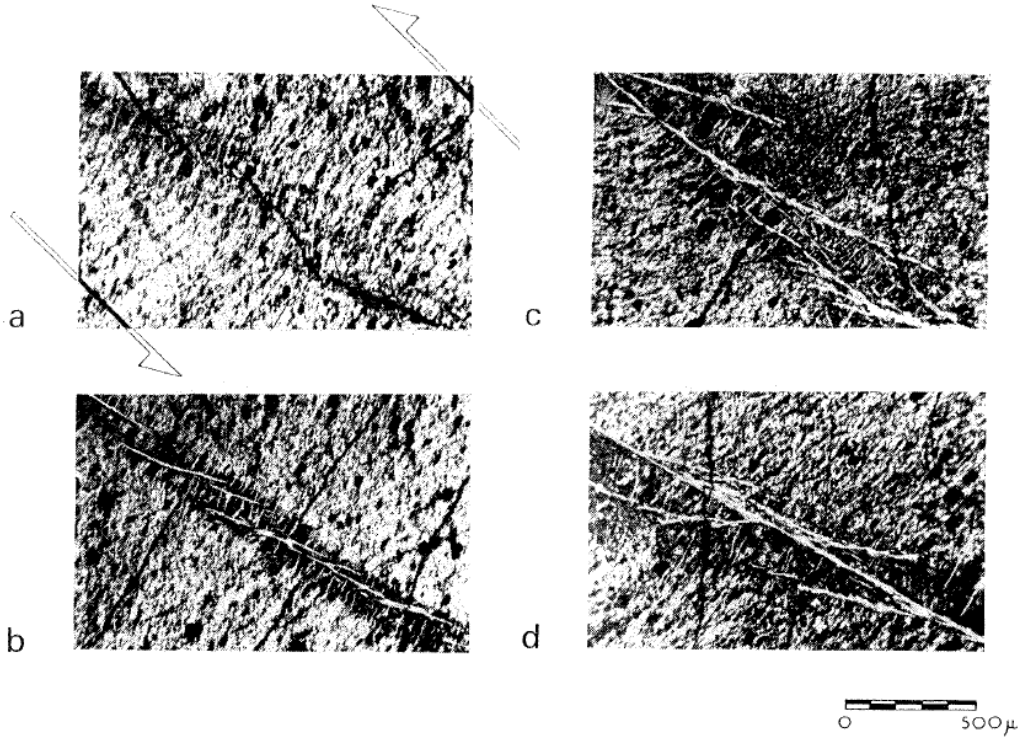

Fig. 2.41 – Sequential development of Riedel shears in a specimen of consolidated kaolin with vertical bedding; half arrows indicate the direction of shear (after Morgenstern and Tchalenko, 1967).

Carrying out triaxial shear tests on reconstituted kaolinite and bentonite consolidated to around 100 kPa, the Authors observe that testing conditions influence significantly the development of shear bands during both drained and undrained tests. Indeed, shear bands are seen to develop in specimens of NC kaolin with size ratio (height/diameter) of 2 which do not exhibit dilative behaviour. The orientation of the shear band is found not to vary for a given clay, independently of the test conditions and of the OCR; the shear band orientations found for kaolin and bentonite are seen to be in accordance with those calculated using a Coulomb criterion as $\pi/4+\phi'/2$.

Hicher et al. also carried out measurements of water content on small portions of specimen after triaxial testing, with particular attention to the parts near the shear bands (Fig. 2.42). For a NC specimen of kaolinite after drained shear, with an overall

contractant behaviour, the water content outside the shear band is fairly homogeneous and reveals a reduction in w, indicative of a contractant behaviour. Inside the shear band, more contraction is seen, especially for central thin elements on both sides of the shear band. A highly OC specimen of kaolinite (OCR=10) with an overall dilative behaviour shows more dispersion in local values of w; inside the shear band the behaviour is dilative, whereas outside the shear band the material is contracting. The Authors find that when a shear band mechanism is completely developed in a specimen, the volume change is limited to the localised zone which, under large distortions, continues to contract in the case of a NC clay or dilate in the case of a highly OC clay. The results of the water content measurements are also confirmed by X-ray scanning (computed tomography) on the same specimens after shear testing.

As expected from the optical microscopy observations, the SEM observations on parts of specimen inside the shear band (Fig. 2.43) show that the orientation of particles next to the failure surface is parallel to the shear band direction. Thus, large displacements in the shear band appear to be associated to large rotations of the particles and the creation of large anisotropy of the structure in a narrow zone along the failure surface. Comparing this zone with other zones of the specimens, the mean size of the particles is found to be smaller and their shape more angular, indicating the breaking of aggregates and even particles.

Transmission electron microscopy (TEM) observations at larger magnification revealed the presence of several microscopic discontinuities inside the shear band parallel to the failure surface (Fig. 2.44).

Hicher et al. also found that the thickness of the shear band, i.e., of the zone of large particle reorientation, was generally around 2-7 mm and was proportional to the amount of vertical displacement of the top of the sample.

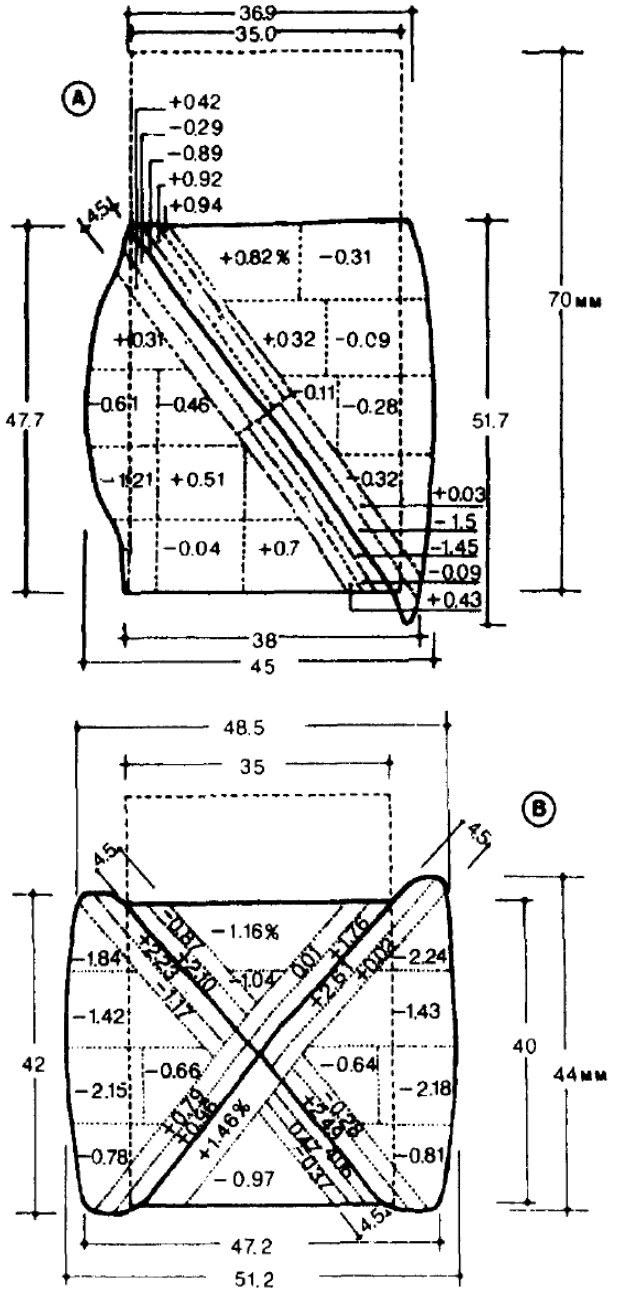

Fig. 2.42 – Measurements of water content inside samples of kaolinite after drained triaxial tests; A: normally consolidated sample, B: overconsolidated sample. Percentages are calculated as $dw = w_{LOCAL} - w_{AVERAGE}$ *(after Hicher et al., 1994).*

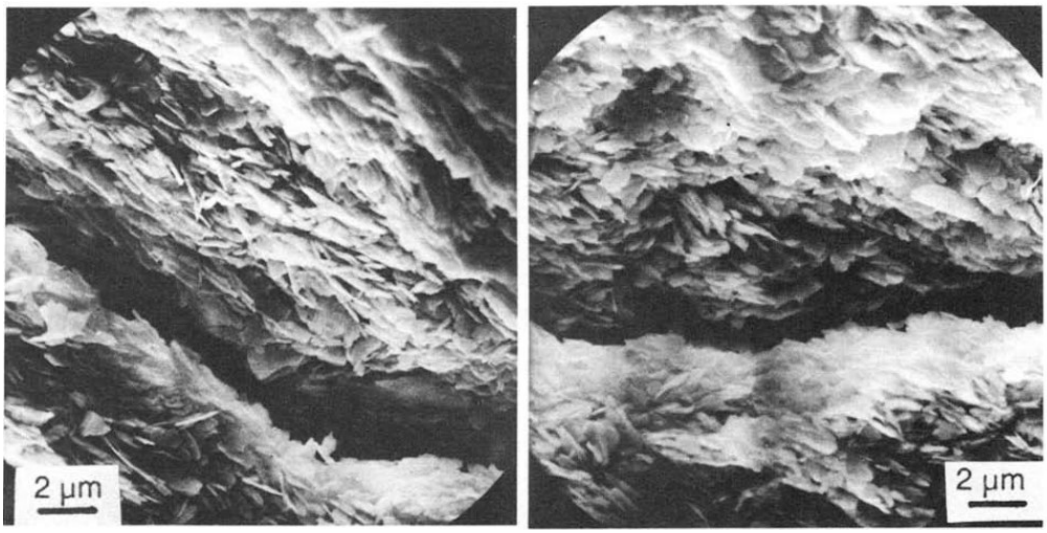

Fig. 2.43 – SEM observation of the failure zone in a normally consolidated specimen of kaolinite after drained shear (after Hicher et al., 1994).

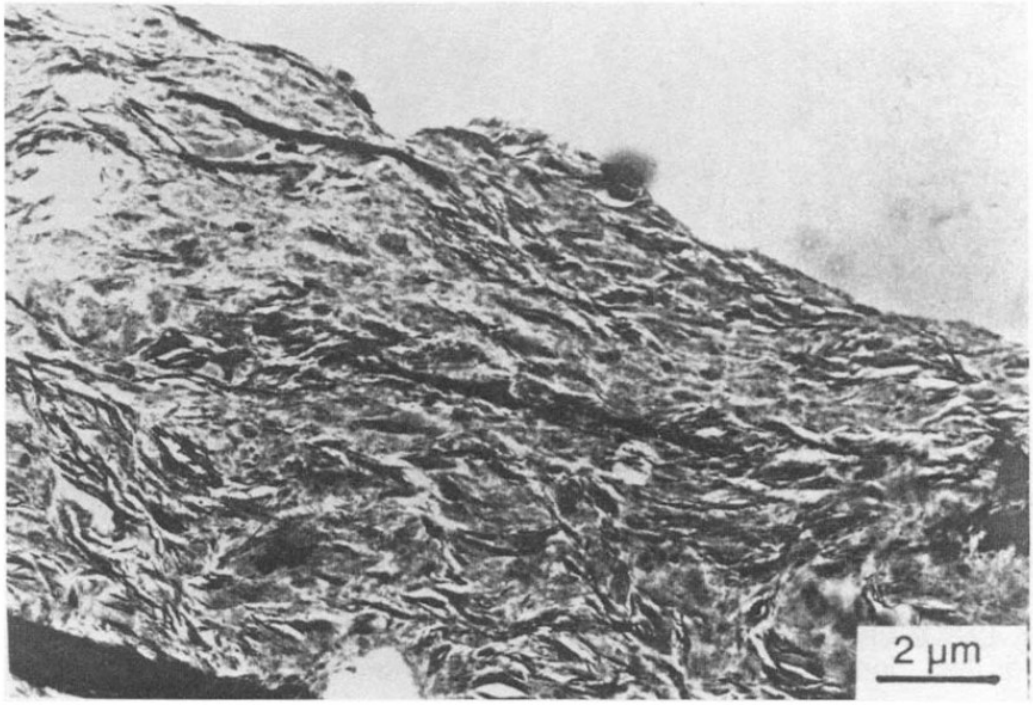

Fig. 2.44 – TEM observation of microscopic failure zones with the same orientation as the macroscopic principal failure zone in an OC sample of bentonite after drained shear (after Hicher et al., 1994).

3 MACRO-MECHANICAL BEHAVIOUR OF CLAYS

3.1 Introduction

In this chapter, a literature review of the mechanical behaviour of both reconstituted clays and natural clays is carried out and the general framework for the behaviour of clays proposed by Cotecchia and Chandler (2000) is recalled. Also, some of the constitutive models for reconstituted and natural clay behaviour, in the framework of Critical State Soil Mechanics, are described.

A lot of constitutive models for clays originate from the Cam Clay model, inheriting its basic principles and adding new laws to better describe the behaviour of natural clays. Since Gens and Nova (1993), models for natural clays account for the effects of structure on the mechanical behaviour, although disregarding a specific knowledge about the microstructural processes corresponding to the exhibited response. The investigation of these micro-processes and the diagnosis of which phenomena occur in the background of the macro-response exhibited by the material could possibly represent a great support for a further development of the constitutive modelling of clays.

3.2 The behaviour of reconstituted clays

3.2.1 The Critical State Framework

Most of the research on the mechanical behaviour of clays has been based on laboratory testing on either reconstituted or remoulded clay. The features of the structure of reconstituted clays have been discussed in Chapter 2. In this case, series of specimens of equal mechanical properties can be created on which a defined stress-strain history can be applied. So, the testing of reconstituted clay specimens was a rational start to investigate the clay behaviour. A large part of this research investigated the clay response for axially-symmetric stress paths.

The Critical State Framework (Roscoe et al.,1958; Roscoe and Poorooshabs, 1963; Schofield and Wroth, 1968) was the first rationalization of the results of the research

on reconstituted clays, and it addressed concepts fundamental to the general behaviour of soils. The most important concept underlying the framework is that the soil behaviour depends both on specific volume (v) and the effective stress invariants (q; p'). The state of the clay is represented as a point in the v-q-p' space at any stage of its state history. The framework considers the clay behaviour along axi-symmetric stress paths and shows that the clay behaviour with respect to the effective stresses is the same for different constant volumes, apart from a scaling factor depending on specific volume, since the clay behaviour can be normalized with respect to specific volume (Rendulic, 1936; Hvorslev, 1937; Roscoe et al., 1958; Roscoe and Poorooshabs, 1963; Schofield and Wroth, 1968).

Using results of the type shown in Fig. 3.1, the isotropic virgin compression and the isotropic swelling of the reconstituted clay were represented in the v-lnp' plane as straight lines, of gradient λ and κ respectively. The volumetric behaviour was described as elasto-plastic during virgin compression and as non-linear elastic during isotropic swelling (Schofield and Wroth, 1968). In one-dimensional compression the linearity of the virgin compression line in the v-logσ'_v plane and the constant value of K_0 ($=\sigma'_h/\sigma'_v$) (Jaky, 1944; Brooker and Ireland, 1965; Schmidt, 1966) were both consistent with a state path plotting as a straight line in the v-lnp' plane. The one-dimensional compression line:

$$\eta = \frac{q}{p'} = \frac{3(1 - K_0)}{(1 + 2K_0)} \qquad (3.1)$$

appeared to be closely parallel to the isotropic compression line. All the lines at constant stress ratio η ($=q/p'$) were assumed parallel in the v-lnp' plane, so as to plot positions which are geometrically similar for changing volume, and the swelling from any η line was considered to be uniquely related to the change of p' and to follow lines of constant gradient κ. The experimental results obtained by Gens (1982) for reconstituted Lower Cromer Till are an example of later experimental evidence that confirmed that these CSF assumptions were well justified.

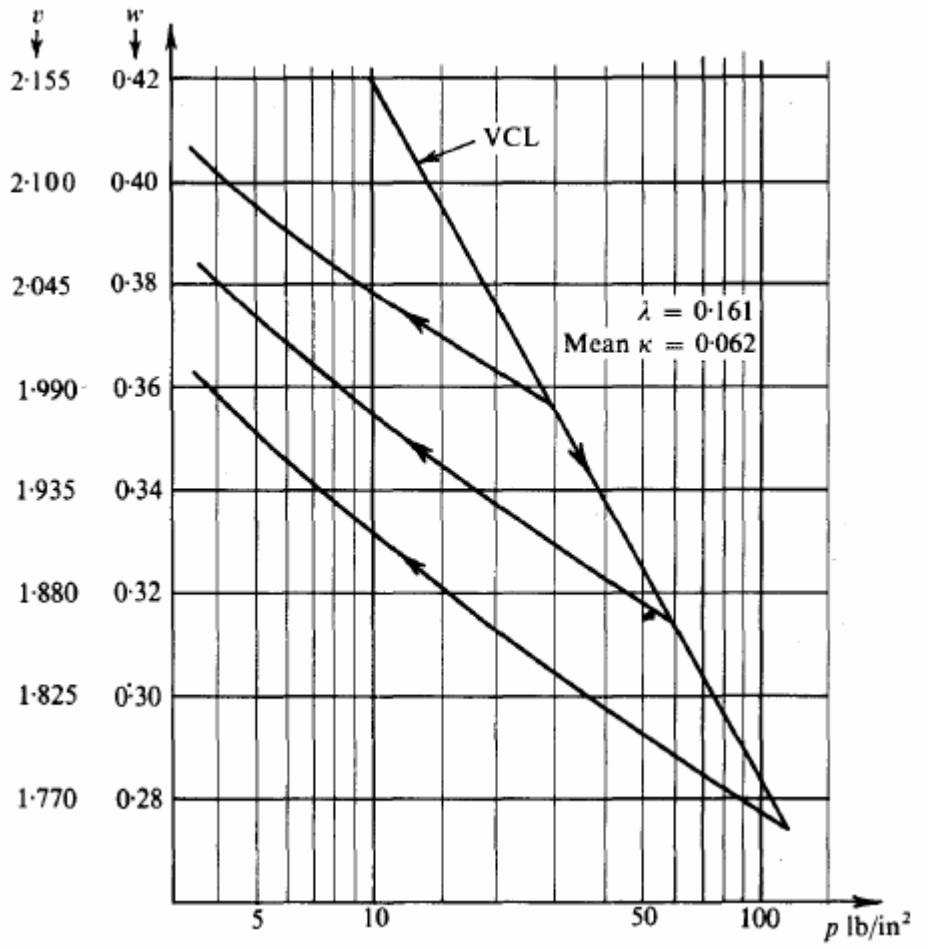

Fig. 3.1 - Reconstituted London clay: isotropic compression and swelling curves (data from Henkel 1956; after Schofield and Wroth, 1968).

The existence of a critical state (CS), reached by the soil at large shear strains, at which the soil can undergo distortion at both constant volume and effective stress, was first defined by Casagrande (1936-a). Roscoe et al. (1958) also observed critical states at large strains in simple shear tests. Results of triaxial tests on isotropically normally consolidated reconstituted clay (Parry, 1960) also showed that the clay reached a final state of constant volume and effective stress. For a given specific volume, the critical

state was found to occur at a unique effective stress and the locus of the critical states in v-q-p' space coincided with the line $q/p' = M$; $v = \Gamma - \lambda \ln p'$ (Parry 1960; Fig. 3.2).
The gradient of the critical state line in the q-p' plane, M, is a simple constant modelling frictional behaviour at the macroscopic scale. It defines the deviatoric stress, q_{cs}, needed to keep the soil flowing at the critical state for a given p'_{cs}.
The data in Fig. 3.2 are for both undrained and drained shearing tests on isotropically normally consolidated clay. The framework assumed that the critical state is reached during shearing of both isotropically normally consolidated and overconsolidated specimens, as shown in Fig. 3.3 and Fig. 3.4.
The stress paths in Fig. 3.3 are normalized with respect to volume by means of an equivalent pressure p'_e. The $\eta = M$ line lies parallel to the other constant η lines.
Contractant and strain hardening behaviour is shown by the soil yielding in shear on the right side of the critical state line, and dilation with strain softening is exhibited by the soil yielding on the left side of the critical state line (Fig. 3.4 and Fig. 3.5(d)). Thus, the critical state line is a key locus, separating two different shear behaviour modes.
Schofield and Wroth claimed that the ultimate fully remoulded condition at the critical state would always occur if the process of uniform distortion were carried out until the soil flowed as a frictional fluid. However, they acknowledged that specimens only approach the critical state after severe distortion, when strain may no longer be homogeneous, so that the average soil state across the specimen may not define accurately the critical state. Only those portions of the specimen where strain localizes reach the critical state.

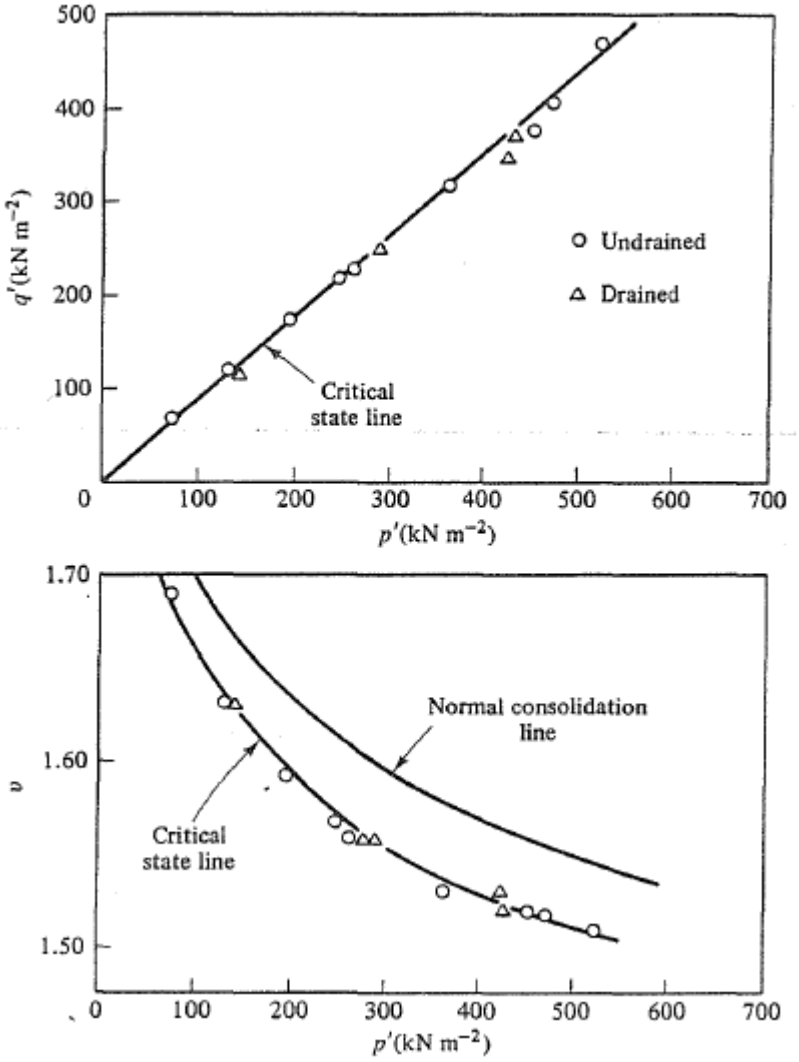

Fig. 3.2 - Normally consolidated reconstituted Weald Clay: failure states in drained and undrained shearing (data from Parry 1960; after Atkinson and Bransby, 1978).

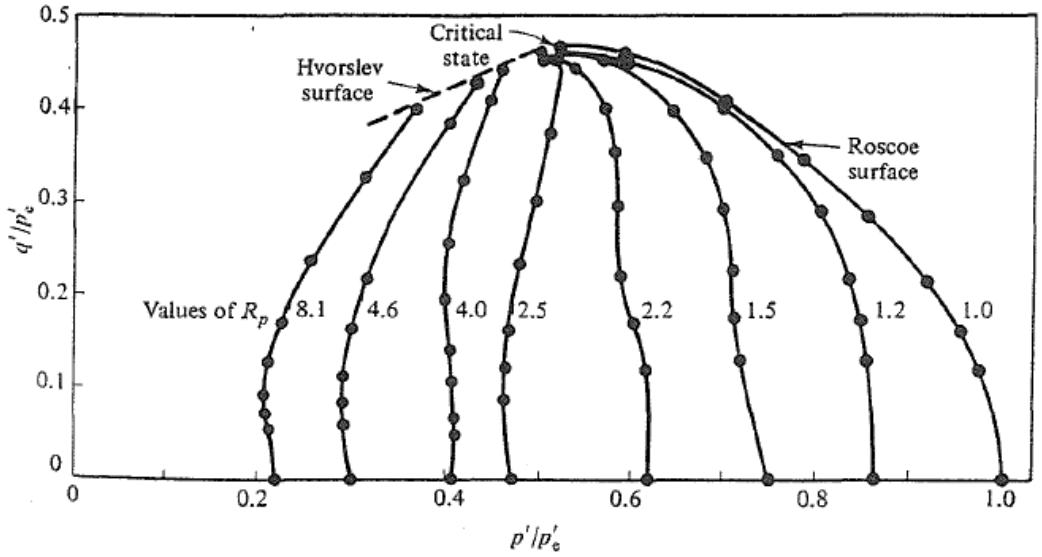

Fig. 3.3 - Overconsolidatcd rcconstituted kaolin: nomialized undraincd stress paths (data from Loudon, 1967; after Atkinson and Bransby, 1978).

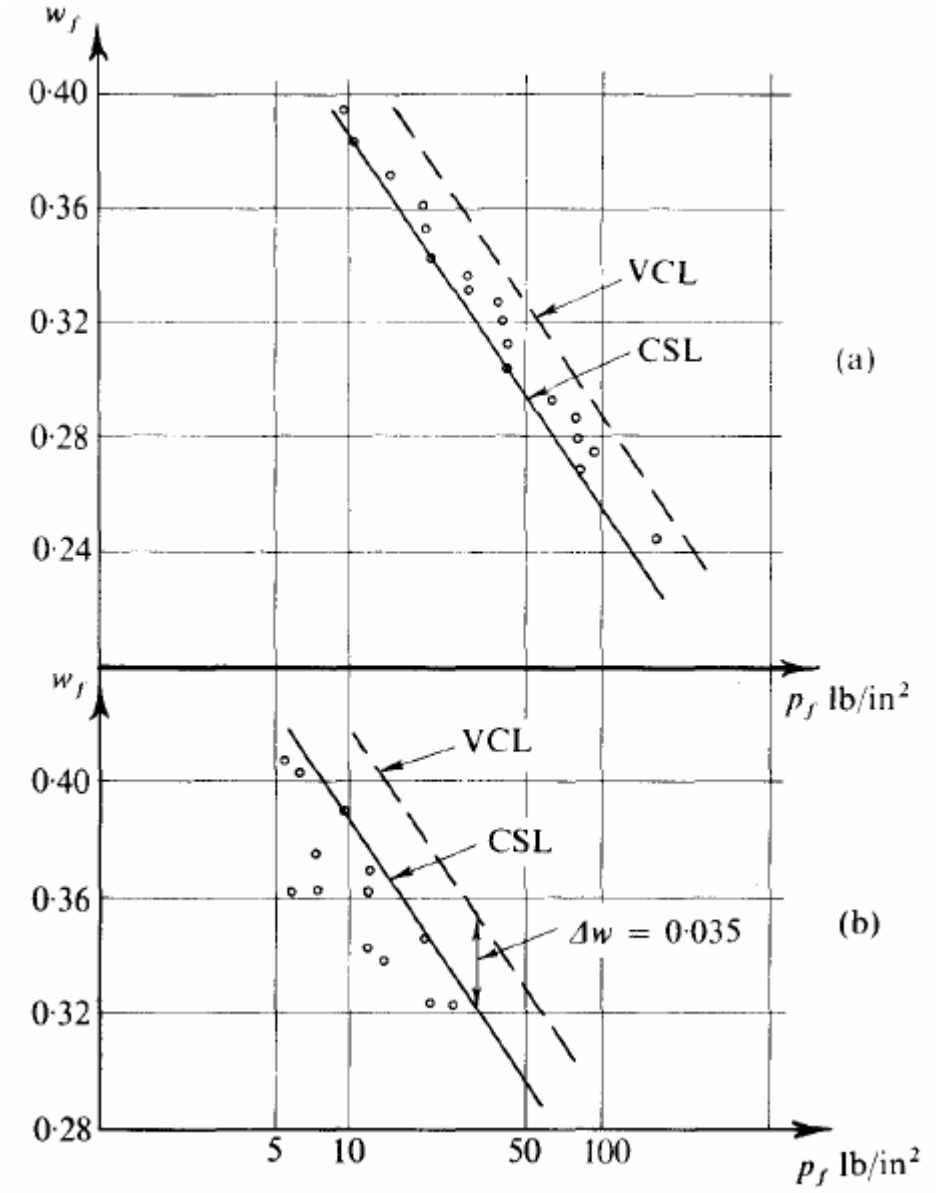

Fig. 3.4 - Remoulded London Clay at failure (data from Parry, 1958; after. Schofield and Wroth, 1968).

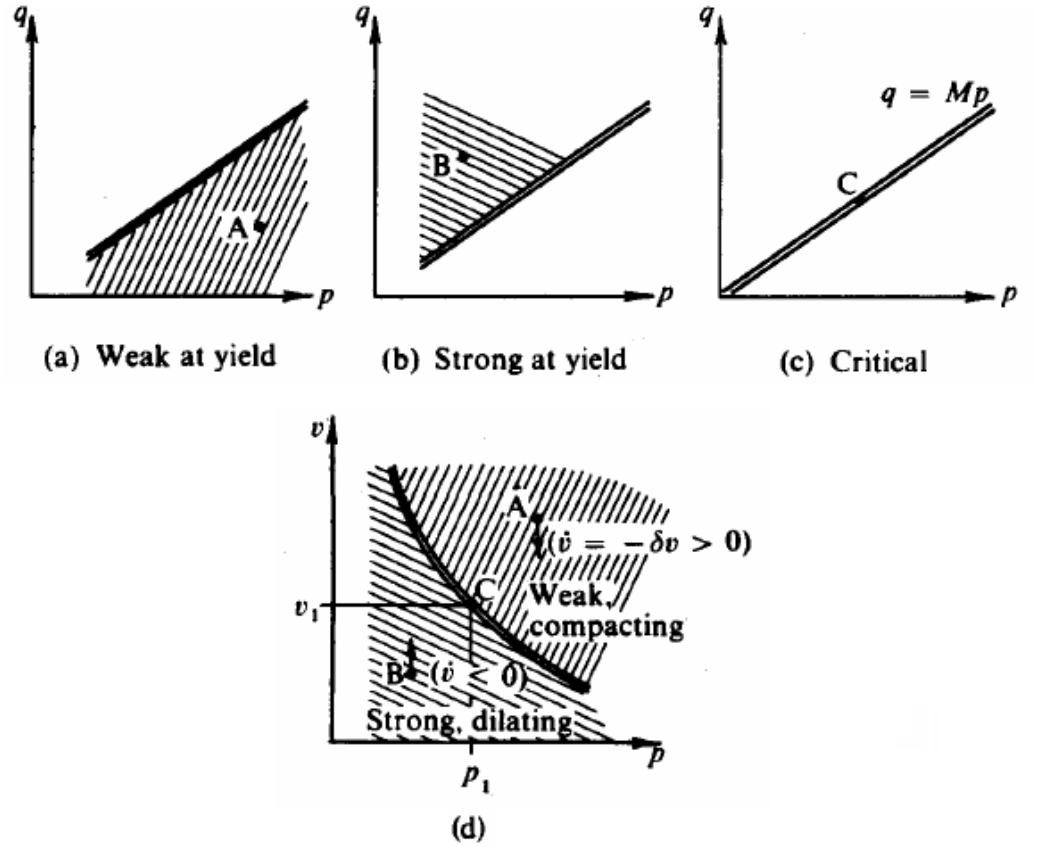

Fig. 3.5 - Condition of specimens at yield in relation to the critical state line (after Schofield and Wroth, 1968).

Rendulic (1936) and later Henkel (1960) showed that the stress-strain behaviour during shearing of isotropically normally consolidated clay can be normalized with respect to volume. Undrained stress paths for normally consolidated specimens consolidated to different volumes and constant volume contours from drained stress path data were found to have a similar shape in the effective stress plane. It was inferred that, in the v-q-p' space, the stress paths during shearing of the isotropically normally consolidated clay lie on a unique surface, the "Roscoe" surface, that stretches from the virgin isotropic compression line to the critical state line. The η lines were assumed to lie on the Roscoe surface as it was presumed that no stress path crossed it. This surface was then termed the "state boundary surface" (SBS) by Roscoe and Poorooshabs

(1963), as it was considered to confine the domain of the possible states for the clay. Normalizing the stress states on the boundary surface with respect to volume by means of the mean effective stress p'_e on the isotropic compression line corresponding to the same volume, Roscoe and Poorooshasb (1963) defined a two-dimensional representation of the Roscoe surface.

The normalized Roscoe surface for kaolin is shown in Fig. 3.6 (Balasubramaniam, 1969).

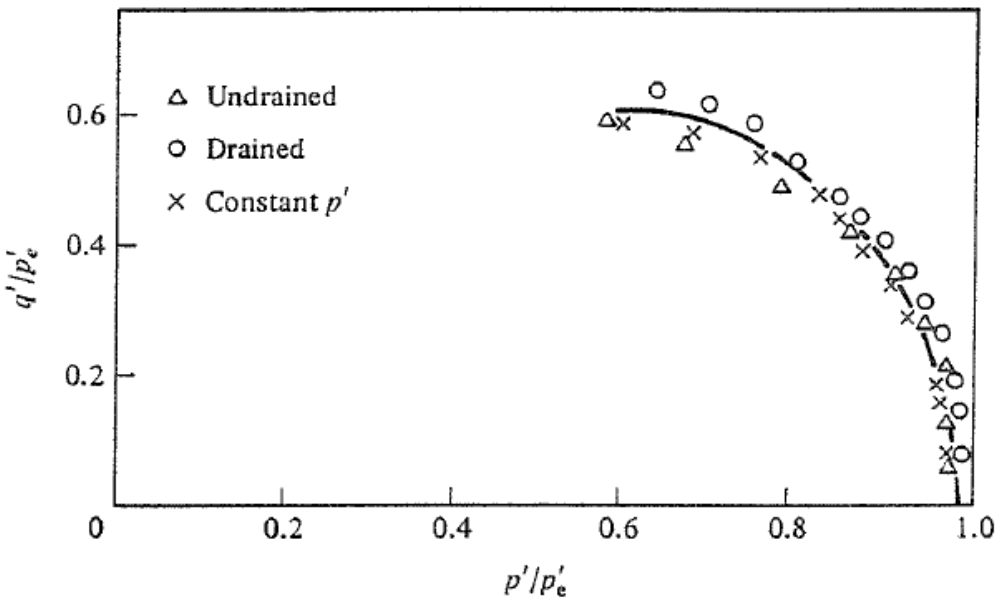

Fig. 3.6 - Normally consolidated reconstituted kaolin: normalized stress paths (data from Balasubramaniam, 1969; after Atkinson and Bransby, 1978).

On the dry side of the framework, the difficulty of observing stress paths approaching critical state was attributed by Schofield and Wroth to the instability triggered by strain softening. As heterogeneous strains usually occur in specimens, they considered strain softening to prompt important localization of strain, which causes the difficulties to recognize the arrival to critical state on the dry side through element testing.

The effects of dilation on the peak strength of granular soils were analysed by Rowe (1962), who assumed friction to be the property of the soil which governs its strength, and chose the friction between the mineral surfaces at the interparticle contacts as the

friction constant ϕ_μ for the soil. He modelled mathematically the sliding of particles during the deformations of the assemblage and, following Taylor (1948) and Skempton and Bishop (1950), he calculated the work done by the effective stresses as dissipated in frictional heat. So, Rowe derived the stress-dilatancy equation:

$$\frac{\sigma'_1}{\sigma'_3\left(1+\frac{dV/V}{d\varepsilon_1}\right)} = tan^2\left(45° + \frac{\phi_\mu}{2}\right) \qquad (3.2)$$

which shows that both friction and the dilation rate determine the peak strength, the peak occurring when the dilation rate is maximum. The stress-dilatancy theory explained the peak failure, although it did not explain how the dilation rates vary in the v-q-p' space. For dense packings at low confining stresses, eq.(3.2) was shown to work with ϕ_μ, but with increasing void ratio or confining pressure, dilatancy at failure gradually reduces and a parameter ϕ_f had to be considered, which accounted for overall frictional effects. For a range of soils that would plot on the wet side of the critical state framework, Rowe recognized the occurrence of failure at constant volume and stress. Therefore, Rowe identified a critical state, which he described as a state when continuous local dilations and contractions occur.

From the experimental observations reported by Rowe, heterogeneity of strain appears always to be active in the soil during large distortions, as strain is continuously redistributed among particle groups. The peak strength can therefore be seen as the maximum average of the strengths exhibited by differently strained particle groups. When strain softening starts in some of the particle groups, the redistribution of strain tends to strain localization. Therefore Rowe, in agreement with Schofield and Wroth (1968), regarded the strain softening behaviour as the trigger of the formation of the failure surface post-peak, and not vice-versa.

The normalization that Hvorslev (1937) applied to the direct shear strengths showed that the peak strength behaviour in the v-q-p' space can be normalized with respect to the volume at failure. Parry (1960) found that a similar normalization was successful for peak strength values recorded for triaxial stress paths on isotropically consolidated clay. In the v-q-p' space the peak states lie on the "Hvorslev" surface (Fig. 3.7).

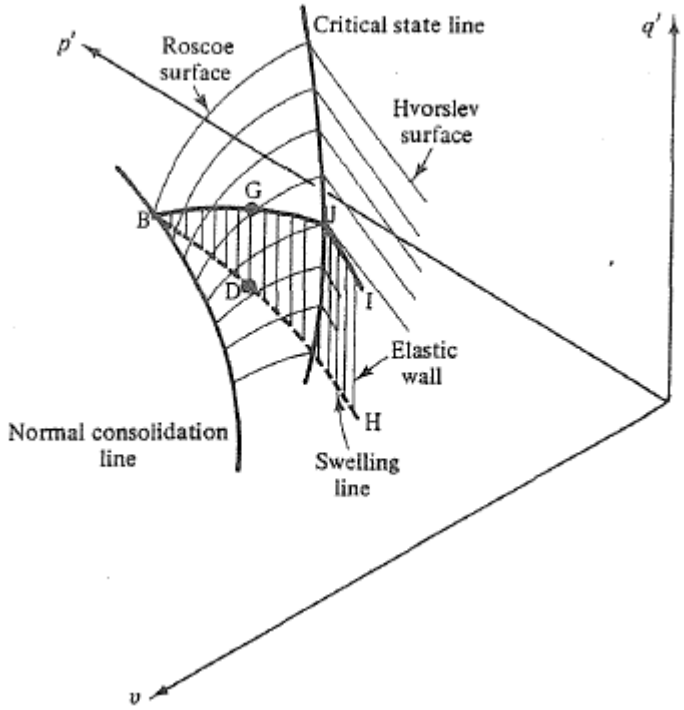

Fig. 3.7 - The state boundary surface and the elastic wall in the Critical State Framework (after Atkinson and Bransby, 1978).

The Hvorslev normalization demonstrates that the effects of dilatancy on the peak strength outlined by Rowe (1962) can be normalized with respect to the specific volume at peak. Within the CSF, state paths for overconsolidated soils are assumed to reach the Hvorslev surface and then travel on it towards the critical state, while exhibiting large plastic deformations. The Roscoe surface and the Hvorslev surface together thus define the complete state boundary surface (SBS) (Roscoe et al., 1958; Roscoe and Poorooshabs, 1963) for reconstituted clay (Fig. 3.7).

3.2.2 The Cam Clay model

The Cam Clay model was intended to be a simple model to interpret soil behaviour at large strains within the critical state framework. The model was first proposed by

Roscoe and Schofield (1963) and later in Schofield and Wroth (968), and was afterwards revised by Roscoe and Burland (1968), who called it 'modified' Cam Clay (MCC) to distinguish it from the earlier one, which today is generally referred to as 'original' Cam Clay (OCC).

The model assumed isotropic elastic behaviour below the SBS, where the state paths move along elastic walls defined by the κ lines as shown in Fig. 3.7, and the elastic strain increments are defined as:

$$\delta\varepsilon_v^e = \frac{\delta p'}{K'} \tag{3.3}$$

$$\delta\varepsilon_s^e = \frac{\delta q}{3G'} \tag{3.4}$$

where K' is the bulk modulus and G' is the shear modulus. The bulk modulus is expressed as follows:

$$K' = \frac{vp'}{\kappa *} \tag{3.5}$$

The assumption of elastic behaviour below the SBS implies that no permanent modifications are expected to occur to the soil specimen when the current state is inside the SBS, hence no changes are believed to take place to its microstructure. As will be discussed in the following Chapters, the experimental programme carried out in this research has entailed some microstructural analyses specifically aimed at exploring if microstructural changes are recorded or not below the SBS.

The model considers the soil behaviour to be isotropically hardening with plastic volumetric strains after yield, according to the following hardening rule:

$$\delta p'_0 = \frac{p'_0}{(\lambda - \kappa)} \delta\varepsilon_v^p \tag{3.6}$$

in which evidently the scalar p'_0 is the hardening function.

As a consequence of the dependency only on volumetric strains, the yield curves in the v-q-p' space are similar and can be normalized with respect to volume.

Differently from Modified Cam Clay, Original Cam Clay model assumed that the soil plastic flow was governed by Taylor's (1948) dilatancy law, according to a purely frictional mechanism:

$$\frac{q}{p'} = M - \frac{d\varepsilon_v^p}{d\varepsilon_s^p} \qquad (3.7)$$

If it is assumed that a soil which follows eq.(3.7) also obeys the principle of normality, the yield locus will have equation:

$$\frac{\eta}{M} = ln\frac{p'_0}{p'} \qquad (3.8)$$

corresponding to the shape shown in Fig. 3.8. The discontinuous plastic potential function is seen to cause many computational difficulties in numerical modelling, that is the reason that prompted a wider use of MCC for numerical predictions.

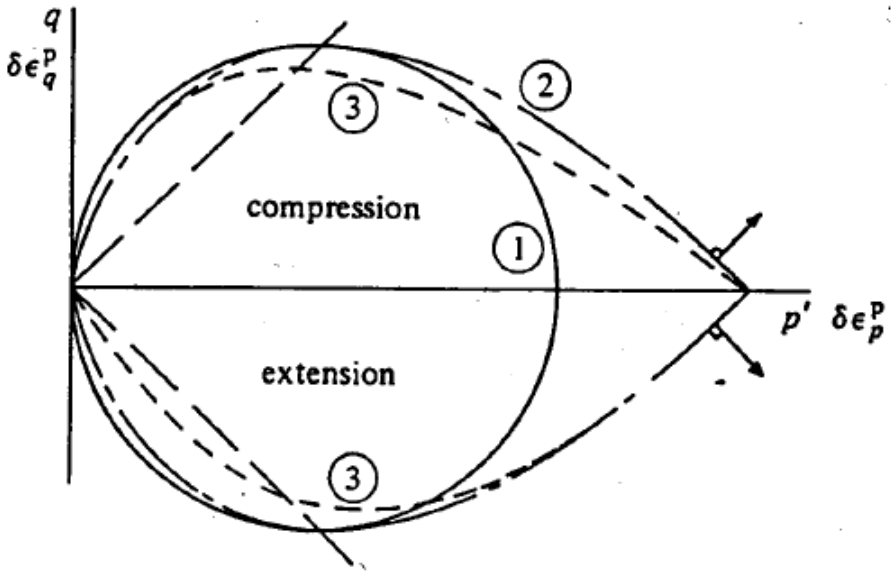

Fig. 3.8 – Plastic potentials: (1) Modified Cam Clay, (2) original Cam Clay and (3) Rowe's stress-dilatancy (drawn for M=1) (after Wood, 1994).

The MCC assumes an elliptical yield locus in q-p' plane (Fig. 3.9), of equation:

$$f = q^2 - M^2 p'(p'_0 - p') \qquad (3.9)$$

in which M controls the shape and p'_0 controls the size of the ellipse. Yield is assumed to occur on the SBS.

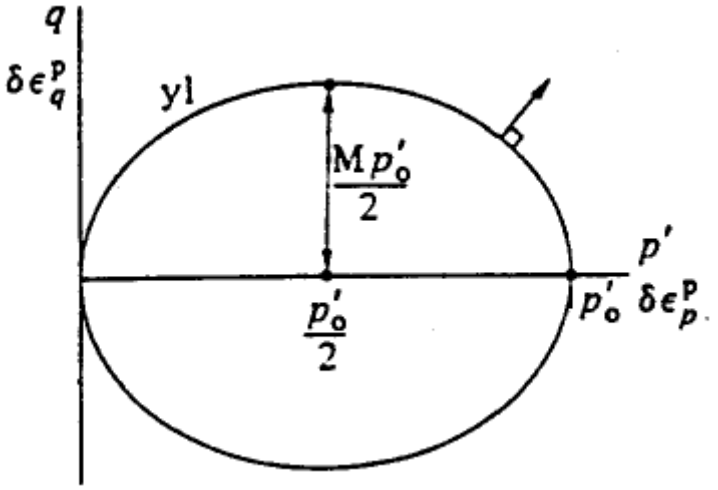

Fig. 3.9 – Elliptical yield locus for Cam Clay model in q-p' plane (after Wood, 1994).

Disregarding the frictional mechanism predicted by OCC, MCC assumes that the soil obeys the normality condition, so the vector of plastic strain increment is in the direction of the outward normal to the yield locus. As the yield function is known, so is the plastic potential. Therefore:

$$\frac{\delta\varepsilon_v^p}{\delta\varepsilon_s^p} = \frac{M^2(2p' - p'_0)}{2q} = \frac{M^2 - \eta^2}{2\eta} \qquad (3.10)$$

On the right side of the critical state line, the soil yields at q/p' less than M. If a frictional mechanism of deformation applies, then for equation (3.7) the soil necessarily has to contract and strain harden, and indeed soils yielding on the right side exhibit this behaviour. Schofield and Wroth (1968) termed the domain where the soil yields at stress ratios q/p' lower than the critical stress ratio M and where the soil contracts, as the "wet zone", using the expression "weak at yield" (Fig. 3.5(a)). For reconstituted clays, in the v-p' plane the wet domain happens to be concentrated to the right of the critical state line (Fig. 3.5(d)).

On the left side of the critical state line, the soil yields at q/p' values higher than M, and the constitutive law then requires the soil to dilate, as actually observed. Schofield and Wroth termed “dry zone” the domain where the soil yields at stress ratios higher than the stress ratio at critical state. The wet and dry behaviour modes are then truly related only to the difference between the yield stress ratio q/p' and the basic friction ratio M (Fig. 3.5(a) and (b)).
Four parameters are required to fully describe the stress-strain behaviour of the soil: λ, κ, Γ, M.

3.3 Advanced Constitutive models for reconstituted clays

Nowadays it is generally accepted that the soil is already at yield after very small strains, and that its true yield surface involves a region of very small extent (Atkinson et al.,1990; Jardine, 1992; Gasparre et al., 2005). Atkinson et al. (1990) and Jardine (1992) have shown that the elastic boundary of soils is a kinematic yield surface inside the SBS, which is dragged with the current stress point through the stress space. This achievement has been indeed included in many kinematic hardening constitutive models, which introduce more realistic representations of the soil stress-strain behaviour, which are still formulated according to the critical state framework. Some of them will be discussed in the following Section.
For some soils, which exhibit low yield pressures, the elastic strain region is considered less important and, for the sake of simplicity, the use of a yield surface analogous to that of Cam Clay is preferred.

3.3.1 The model of Al-Tabbaa and Wood (1989)

As discussed, the Cam Clay model assumes the soil behaviour below the SBS to be elastic. To improve the simulation of real soil behaviour, an inner kinematic hardening “bubble” was implemented by Al-Tabbaa and Wood (1989) in the framework of Cam Clay, developing the so-called “bubble” model.

Following the original paper, the model is described for axially symmetric conditions in the following. A basic feature of the model is that it should degenerate to the Cam Clay model for given parameter values corresponding to a soil which keeps being elastic under loading up to the SBS.

The model includes two surfaces of elliptical shape:

- a Cam Clay yield locus of size p'_0, which corresponds to half the isotropic yield pressure, centred around point (p'_0, 0):

$$\left(p' - p'_0\right)^2 + \frac{q^2}{M^2} = p'^2_0 \qquad (3.11)$$

- an inner yield surface of size R (being Rp'_0 equivalent to half the horizontal axis) and centre (p'_α, q_α), bounding the truly elastic domain:

$$\left(p' - p'_\alpha\right) + \frac{(q - q_\alpha)^2}{M^2} = R^2 p'^2_0 \qquad (3.12)$$

Initially, the soil state is assumed to be at the centre of the inner yield locus; when loaded, the state moves inside the elastic domain until reaching the boundary of the inner yield locus: from this point onwards, plastic deformations occur and the inner yield locus is dragged by the current state inside the Cam Clay yield locus.
An isotropic volumetric hardening rule controls the change in size of both the inner yield locus and the Cam Clay yield locus with plastic volumetric strains $\delta\varepsilon_v^p$:

$$\delta p'_0 = \frac{p'_0}{(\lambda * - \kappa *)} \delta\varepsilon_v^p \qquad (3.13)$$

where λ^* and κ^* represent the slope of the normal compression line and of the swelling line in the lnv-lnp' plane (Butterfield, 1979).
This hardening law is identical to that of Cam Clay, but it applies not only when the stress state is on the Cam Clay yield locus, but also when the current state is inside the Cam Clay yield locus, on the boundary of the inner yield locus. This implies that the Cam Clay yield locus, and consequently also the inner yield locus having a size related to that of the Cam Clay yield locus, start to experience isotropic hardening due to the

small plastic strains generated inside the outer yield locus, which should correspond to changes recorded at the microstructural level.

A kinematic hardening law governs the translation of the inner yield locus inside the Cam Clay yield locus, which occurs in the direction of the vector β joining the point representing the current state on the inner yield locus to its conjugate on the Cam Clay yield locus, the latter being the point having same outward normal to the yield locus (Mroz, 1967; Mroz et al., 1979; Hashiguchi, 1985):

$$\begin{bmatrix} \delta p'_{\alpha} \\ \delta q_{\alpha} \end{bmatrix} = \frac{\delta p'_0}{p'_0} \begin{bmatrix} p'_{\alpha} \\ q_{\alpha} \end{bmatrix} + S \begin{bmatrix} \frac{p' - p'_{\alpha}}{R} - (p' - p'_0) \\ \frac{q - q_{\alpha}}{R} - q \end{bmatrix} \tag{3.14}$$

In eq.(3.14) the first term represents the change in position of the centre of the inner yield locus due to a change in p'_0 due to hardening, while the second part describes the translation along vector β. The scalar quantity S can be derived from the consistency condition (Prager, 1949). For strain-hardening materials, consistency means that the stress state at yield must belong to the yield locus and remain on the subsequent yield loci, i.e., follow it (Yu, 2006).
Evidently, the change of the inner yield locus, that occurs when plastic strains are being generated, can be separated into two components: one part is associated to the translation of the yield locus, the other is associated with the change in size of both the Cam Clay and the inner yield locus.

The behaviour inside the inner yield locus obeys the same elastic law of Modified Cam Clay, i.e., isotropic elastic behaviour.
The flow is associated and the flow rule is the same as that of Modified Cam Clay.

To calculate plastic strains, whether or not the yield locus and the Cam Clay yield locus are in contact, the Authors propose the following equation:

$$\begin{bmatrix}\delta\varepsilon_v^p\\ \delta\varepsilon_s^p\end{bmatrix} = \frac{1}{h}\begin{bmatrix}(p'-p'_\alpha)^2 & (p'-p'_\alpha)\frac{q-q_\alpha}{M^2}\\ (p'-p'_\alpha)\frac{q-q_\alpha}{M^2} & \frac{q-q_\alpha}{M^2}\end{bmatrix}\begin{bmatrix}\delta p'\\ \delta q\end{bmatrix} \quad (3.15)$$

where the plastic modulus $h=h_0+H$ is a positive scalar hardening quantity.
For states on the Cam Clay yield locus, i.e., when the current state belongs to both yield surfaces, $h=h_0$ and $H=0$. For states inside the Cam Clay yield locus, h will be considered as a function depending on the component b of the vector β, connecting the current state to its conjugate state, along the direction of the outward normal to the yield locus at the current state. The following interpolation function is thus defined:

$$H = \left[\frac{1}{\lambda * -\kappa *}\right]\left(\frac{b}{b_{max}}\right)^{\psi} p'^3_0 \quad (3.16)$$

where b_{max} is the maximum value of b and ψ is a positive exponent, which can be determined experimentally. It must be noticed that the ratio b/b_{max} is maximum when the current state touches the yield locus, corresponding to the lowest $\delta\varepsilon_v^p$.

The model requires six parameters, two more than Modified Cam Clay: κ^* initial slope of the swelling lines in (lnp'; lnv); λ^* slope of the NCL in the (lnp'; lnv) plane; the M slope of the critical state line, representing the ultimate failure conditions in the (p'; q) plane; R the ratio of the size of the inner yield locus to that of the Cam Clay locus; ψ exponent of the hardening function H; υ Poisson's ratio.
In addition, three initial state variables need to be defined: the initial current state, the initial void ratio and N or Γ, as reference points on the INCL or CSL.

3.3.2 The model of Stallebrass and Taylor (1997)

The model of Stallebrass and Taylor (1997) accounts for the influence on the stress-strain response of the loading history experienced by the soil to reach a specific current state, in particular the relative directions of the current and previous loading paths.

This is done by introducing two kinematic hardening surfaces inside the conventional Modified Cam Clay SBS. The model is also known as the *three surface kinematic hardening* (3-SKH) model.
Indeed, the loading history experienced by the clay, among other factors, is believed to significantly influences the microstructural features recorded in the clay, hence the algorithms adopted by the model to simulate its effects are considered of interest.

The three characteristic surfaces of elliptical shape are shown in Fig. 3.10.
Their equations are:

- the Cam Clay bounding surface of radius p'_0 and centre (p'_0; 0):

$$\left(p' - p'_0\right)^2 + \frac{q^2}{M^2} = p'^2_0 \qquad (3.17)$$

- a History surface of radius Tp'_0, which describes the effect of recent stress history and defines the limit to the influence of recent stress history:

$$\left(p' - p'_a\right) + \frac{(q - q_a)^2}{M^2} = T^2 p'^2_0 \qquad (3.18)$$

- a Yield surface of radius TSp'_0, delimiting the elastic domain:

$$\left(p' - p'_b\right) + \frac{(q - q_b)^2}{M^2} = T^2 S^2 p'^2_0 \qquad (3.19)$$

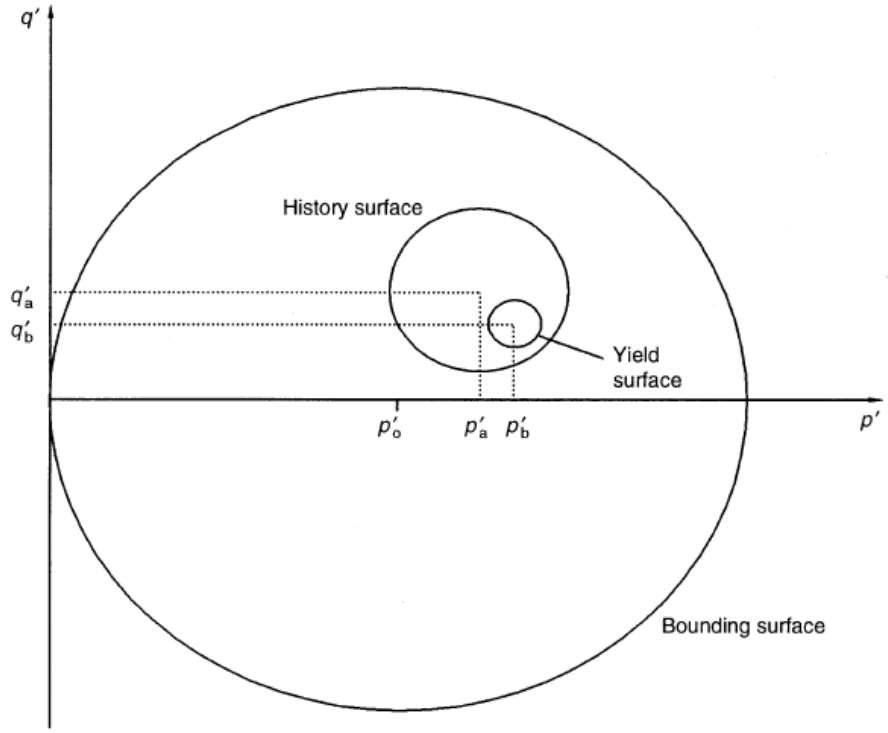

Fig. 3.10 – Sketch of the 3-SKH model in triaxial stress space (after Stallebrass and Taylor, 1997).

An isotropic volumetric hardening rule identical to that of MCC and of Al-Tabbaa and Wood (1989) controls the hardening occurring with $\delta\varepsilon_v^p$ of all the three surfaces, whose dimensions are related by p'_0.

The kinematic surfaces move when the current stress state lies on one or more surface, one of which must be the inner yield surface, and the load increment is in the range $\pm 90°$ to the outward normal to the surface. The magnitude and direction of the movement is controlled by the translation laws of the same form as those used in the "bubble" model (Mroz et al., 1979; Hashiguchi, 1985). So, when the current state is inside the inner yield surface, only elastic strains develop and no surface change is seen. When the current state reaches the inner yield surface, the centre of the surface starts moving along vector γ (Fig. 3.11), while the inner yield surface is dragged by the current state and the other two kinematic surfaces do not translate, but start changing

size because of the onset of plastic strains; when the current state reaches point B, then both the inner yield and the History surface start translating along vector β.
The translation rule allows the model to provide a memory of previous loading history when the loading direction is changed.
The flow is associated and the flow rule is the same as that of Modified Cam Clay; when the stress state is within the Yield surface, deformations are governed by the isotropic elastic constitutive equation of MCC.

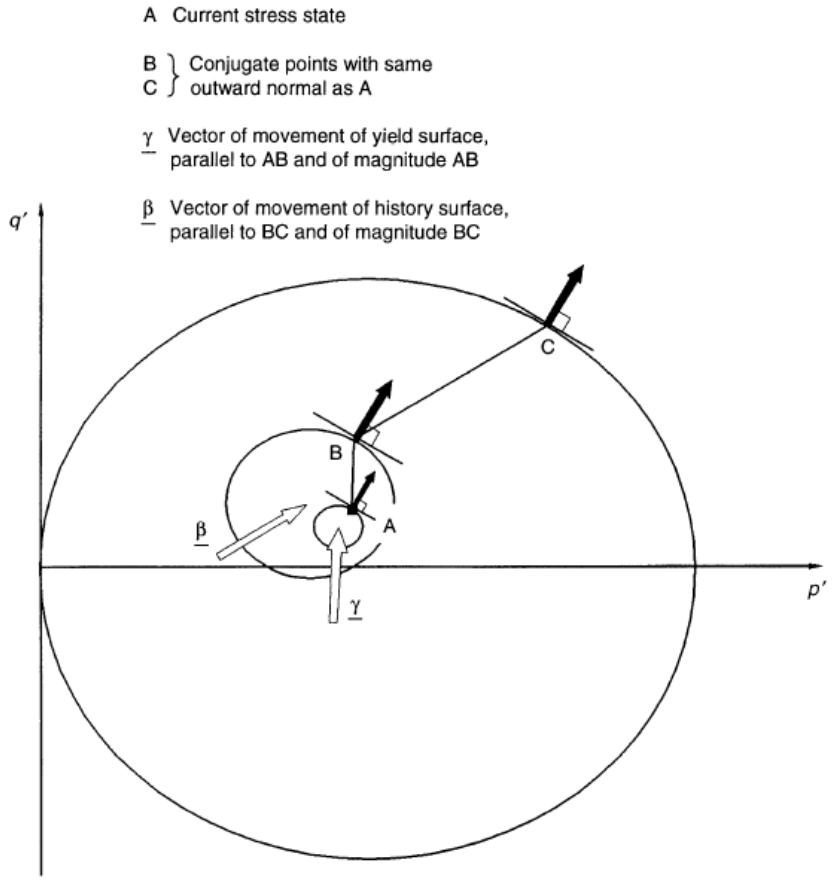

Fig. 3.11 – Sketch illustrating the principle of the translation rule for the kinematic surfaces of the 3-SKH model (after Stallebrass and Taylor, 1997).

Following Al-Tabbaa and Wood (1989), the plastic modulus h is written as $h = h_0 + H_1 + H_2$, where h_0 is the value on the yield surface, H_1 and H_2 are interpolation functions of

the position of the History and Yield surfaces respectively. The elasto-plastic constitutive law of the model is:

$$\begin{bmatrix}\delta\varepsilon_v^p\\ \delta\varepsilon_s^p\end{bmatrix} = \frac{1}{h}\begin{bmatrix}(p'-p'_b)^2 & (p'-p'_b)\frac{q-q_b}{M^2}\\ (p'-p'_b)\frac{q-q_b}{M^2} & \frac{q-q_b}{M^2}\end{bmatrix}\begin{bmatrix}\delta p'\\ \delta q\end{bmatrix} \qquad (3.20)$$

where:

$$h = \left[\frac{1}{\lambda* - \kappa*}\right]\left[(p'-p'_b)\left(p'(p'-p'_b) + q\frac{(q-q'_b)}{M^2}\right) + \left(\frac{b_1}{b_{1max}}\right)^{\psi} p'^3_0 S^2 + \left(\frac{b_2}{b_{2max}}\right)^{\psi} p'^3_0\right] \qquad (3.21)$$

In eq. (3.21) the three terms h_0, H_1, H_2 can be distinguished; b_1 is the scalar product of the outward normal at B and the vector β, b_2 is the scalar product of the outward normal at A and the vector γ (Fig. 3.11).

The effect of recent stress history can be observed in Fig. 3.12, in which the link between the stiffness predicted by the model and the configuration of the three surfaces is illustrated. Fig. 3.12(a) and (b) show the configuration of the kinematic surfaces before constant p' shearing along BE, following two different stress paths AB and CB. At B the kinematic surfaces have become aligned with the initial stress path and the position of the surfaces means that the initial stiffness, when the soil is sheared after path AB, is less than the stiffness for the soil loaded from C to B (Fig. 3.12(c)), since in the latter case when shearing begins the stress state initially moves across the yield surface, so that deformations are elastic and the stiffness is at maximum. This higher stiffness corresponds to the path which constitutes the greatest stress path rotation (180°) (Stallebrass, 1990; Stallebrass and Taylor, 1997).

The exponent ψ changes the rate of decay of stiffness with the stress change and is identical for H_1 and H_2.

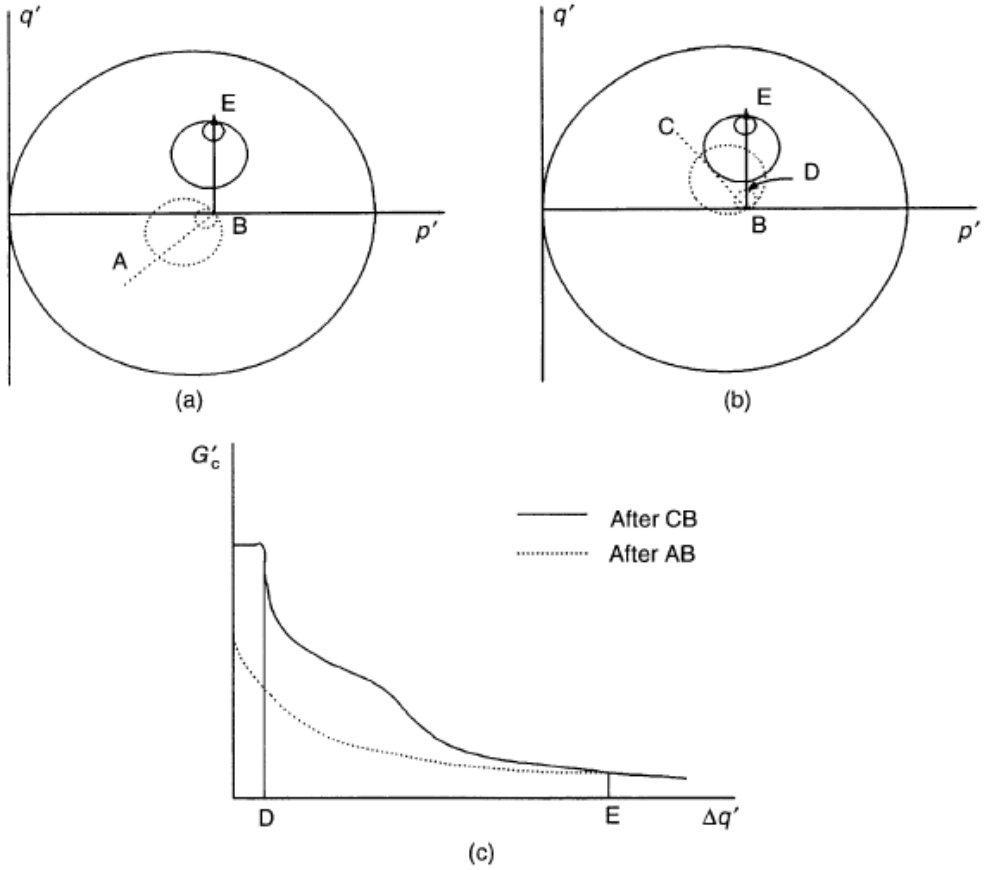

Fig. 3.12 – Diagrammatic representation of the variation of stiffness with recent stress history and loading predicted by the model as the kinematic surfaces translate (after Stallebrass and Taylor, 1997).

The model includes eight parameters, five of which come from MCC: κ^* initial slope of the swelling lines in (lnp'; lnv); λ^* slope of the INCL in (lnp'; lnv); N reference point on the INCL; M slope of the critical state line representing the ultimate failure conditions in (p'; q); G elastic shear modulus; T size of the history surface; S size of the yield surface; ψ exponent of the hardening function H.

3.3.3 The model of Wheeler et al. (2003)

The model of Wheeler et al. (2003), also known as S-CLAY1, was initially developed for natural soft clays. However, the model proved successful in predicting the behaviour

of reconstituted clays rather than natural clays, and hence was later extended to model S-CLAY1S, which allows to account for the effects of structure and structure degradation according to the suggestions of Gens and Nova (1993). The latter model will be described in Section 3.5.4.

The model was conceived as an extension of the critical state models, especially developed to simulate the behaviour of soft clays, which according to the Authors present an important initial and a strain induced anisotropy. The latter term is used to represent a directional feature associated to the suspected fabric anisotropy developed by soft clays during deposition, implemented by using an inclined yield surface and a rotational component of hardening, of use to model the evolution of the plastic yielding due to changes in the material, again assumed to be changes in the material anisotropy with plastic straining (Wheeler et al., 2003). As will be further discussed in Section 3.4.6, Cotecchia and Chandler (2000) and Cotecchia et al. (2011) formulated an hypothesis to explain the particular shape observed for the gross yield surfaces of soft clays which is not concerned with particular directional properties of the soft clays.
Moreover, in Chapter 8 the microstructural features for some soft clays from the literature will be analysed and a particular microstructural behaviour will be found to characterize this class of clays, that however will be found not to be oriented at the in situ state.

The yield surface of the model is an inclined ellipse, identical to that proposed by Dafalias (1987) and Korhonen and Lojander (1987):

$$f = (q - \alpha p')^2 - (M^2 - \alpha^2)\left(p'_m - p'\right)p' = 0 \qquad (3.22)$$

where M is the critical state stress ratio, p'_m is the size of the yield curve and α is the inclination of the yield curve (Fig. 3.13). Assuming $\alpha=0$ corresponds to assuming the yield curve of MCC.
As shown in Fig. 3.13, the proposed yield curve has vertical tangents at the origin and at point A (where $\eta = \alpha$) and horizontal tangents at B and C, the points of intersection with the critical state lines in triaxial compression and extension.

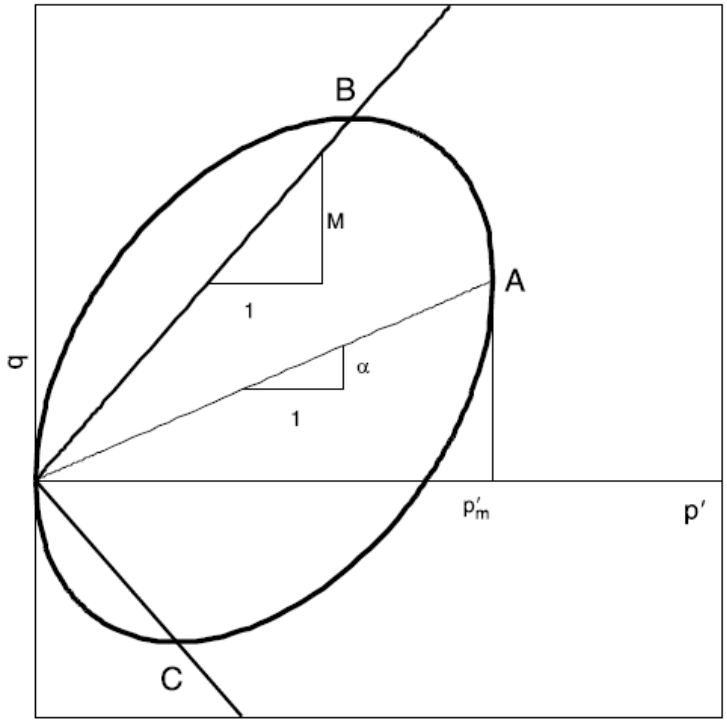

Fig. 3.13 – S-CLAY 1 yield curve (after Wheeler et al., 2003).

Differently from the models previously presented for reconstituted clays, S-CLAY1 predicts isotropic elastic behaviour inside the yield surface, analogously to MCC.

For simplicity, S-CLAY 1 assumes an associated flow rule, which is analogous to that of MCC but accounts for the degree of anisotropy α:

$$\frac{d\varepsilon_d^p}{d\varepsilon_v^p} = \frac{1}{M^2 - \eta^2} 2(\eta - \alpha) \qquad (3.23)$$

Experimental evidence confirms that the use of an associated flow rule provides a reasonable approximation (Graham et al., 1983; Korhonen and Lojander, 1987).

The model includes two hardening laws. The isotropic hardening law governs the change in size dp'_m of the yield curve, which is only related to plastic volumetric strains ε_{vol}^P as in MCC:

$$dp'_m = \frac{vp'_m d\varepsilon_v^P}{(\lambda * - \kappa *)} \quad (3.24)$$

where λ and κ are the slopes of the isotropic normal compression line and of the swelling line in v-lnp' plane.

The second hardening law, that is that of rotational hardening, describes the change of inclination $d\alpha$ of the yield curve produced by plastic volumetric and deviatoric straining, representing the evolution of the yield behaviour with plastic straining:

$$d\alpha = \mu\left[(\chi_v(\eta) - \alpha)\langle d\varepsilon_v^p\rangle + \beta(\chi_d(\eta) - \alpha)\left|d\varepsilon_d^p\right|\right] \quad (3.25)$$

The notation $<>$ represents the Macaulay brackets, which render null the term $<d\varepsilon_v^p>$ when $d\varepsilon_v^p$ is negative, thus neglecting in this case the effect of the change in plastic volumetric strain on the change of inclination $d\alpha$.

Volumetric and deviatoric plastic strains are considered to induce different rearrangement of fabric, then to modify the inclination α of the yield surface differently and to make it tend to different instantaneous target values, $\chi_v(\eta)$ and $\chi_d(\eta)$ respectively, both depending on the current stress ratio. Expressions for $\chi_v(\eta)$ and $\chi_d(\eta)$ are proposed by the Authors in the light of experimental results:

$$\chi_v(\eta) = \frac{3}{4}\eta \qquad \chi_d(\eta) = \frac{1}{3}\eta \quad (3.26)$$

The soil constant β in eq.(3.25) controls the relative effectiveness of plastic shear strains and plastic volumetric strains in determining the overall current target value for α, i.e., in rotating the yield curve. The soil constant μ of eq. (3.25) controls the rate at which α approaches its current target value, i.e., the rate of change of α with plastic strains.

It should be noted that the suspected fabric orientation and successive fabric evolution associated to both the initial inclination and the rotation of the yield surface are not supported by any direct observation of soft clay fabrics. By means of data on natural and reconstituted soft clays from the literature (e.g., Delage and Lefebvre, 1984; Delage, 2010; Hattab et al., 2013), microstructural features and changes occurring

under different loading paths will be recognized for soft clays and compared to the assumptions of the model. This will be discussed in Chapter 8.

In model S-CLAY1, as in model MIT-S1 by Pestana and Whittle (1999), the rotational hardening depends on both volumetric and deviatoric strains, differently from other models in which it is only related to volumetric strains (Dafalias, 1987; Whittle and Kavvadas, 1994). As a consequence, S-CLAY1 predicts only one final inclination of the yield curve, corresponding to a critical state value of α equal to χ_d(M). The final yield curve depends only on the stress conditions and it is independent of both the initial yield curve inclination and of the stress-path followed to critical state. Hence, S-CLAY1 predicts a unique critical state line, differently from many constitutive models including rotational hardening.
It must be noted that the use of Macaulay brackets in eq. (3.25) is used by the Authors to keep the model stable in case of negative plastic volumetric strains, i.e., when yielding occurs on the dry side of critical (Pestana and Whittle, 1999). However, model predictions in this case are expected to be poor. In fact, the model is intended for normally consolidated or at least lightly overconsolidated clays.

The model includes six parameters, four of which come from MCC: κ^* initial slope of the swelling lines in (lnp'; v); λ^* slope of the INCL in (lnp'; v); M slope of the critical state line representing the ultimate failure conditions in (p'; q); G (or ν') elastic shear modulus; β and μ, parameters of the rotational hardening law. Three initial state parameters are required: stress state and specific volume, p'_m, initial size of the yield curve, and α, inclination of the yield curve.

3.4 The behaviour of natural clays

The microstructure of natural clays is the result of their composition and geological history, as explained in Chapter 2. Consequently, studies of their mechanical behaviour have typically treated individual materials as special cases, reflecting their variable and complex origins. Leroueil and Vaughan (1990) gave an extensive review of natural soil

behaviour to support the idea that, while the origins of natural structures may be complex, the effects themselves are repetitive for different soils. Similarly, Burland (1990) considered the general effects of structure on soil behaviour with the objective of interpreting the response of natural materials within an overall pattern.
According to Cotecchia and Chandler (1997; 1998), the structure of all clays includes basic common elements as a result of which similar basic mechanisms of deformation take place at the microlevel. So, many patterns of behaviour are common to different clays. The Authors suggest that these common patterns can be modelled similarly for clays of different structure. However, some differences in behaviour due to differences in microstructure exist among clays, as for example between natural and reconstituted clays, which should be modelled according to the class of difference. They also assess that the main difference in behaviour between natural and reconstituted clays is the size of the response, which represents the overall effect of the various structural elements on the behaviour of the clay and may be related to a scalar parameter, that is the clay sensitivity.
Reviewing the relationships between clay structure and clay behaviour, Cotecchia and Chandler (2000) developed a behavioural framework applicable to many different clays, as will be explained in the following.

The behavioural differences between clays having a sedimentation and a post-sedimentation structure will be described. The term “gross-yield” will be used to refer to a state in the effective stress space, which may be reached after the initial yield (e.g. the inner yield of the bubble models) beyond which soil stiffness falls significantly. Beyond gross-yield, the plastic strain increments become substantially larger as a result of onset of degradation of the soil structure that the authors assess to be far larger than pre-gross yield. Generally, a substantial change in the hardening relationship occurs at gross-yield, which is reflected in changes in the relationships of both strength and stiffness with the consolidation v-p’ state (e.g., Graham et al., 1988; Leroueil and Vaughan, 1990). As a consequence, soil behaviour might be distinguished as either

pre- and post- gross-yield. In the following, the subscript y will be used to denote gross yield.
Clays with a sedimentation structure at gross yield will have a Yield Stress Ratio (YSR $= \sigma'_{vy}/\sigma'_{v0}$; Burland, 1990) equal to the overconsolidation ratio (OCR$= \sigma'_{vc}/\sigma'_{v0}$). Clays which possess a post-sedimentation structure, at gross yield have a yield stress ratio which exceeds the overconsolidation ratio. In general, it is the yield stress ratio, rather than the geological overconsolidation ratio, which controls the compression and the strength behaviour of clays.

As anticipated in Chapter 1, it will be seen that since the fifties the macro behaviour of clays has been addressed as effect of the combination of its nature and its structure (e.g., Skempton and Northey, 1952; Skempton, 1970; Delage and Lefebvre, 1984; Griffiths and Joshi, 1989; Burland, 1990; Leroueil and Vaughan, 1990; Cotecchia and Chandler, 1997, 1998). To assess the correlations between the clay micro-features and its macro-behaviour, the strategy was adopted of studying systematically the clay composition and micro-features and the corresponding macro-response.

Following this historical background, the research work is intended to associate the clay-macro-response to different classes of clays, distinguished on the basis of their geological and mechanical history. In the light of this, the objective will be pursued to try and associate microstructural processes to classes of clays and, then, macro-behavioural facets to micro-features and classes. Through the assessment of the influence of these microstructural processes on the algorithms and parameter values adopted by the models, classes of behaviour and corresponding models could be finally connected to classes of clays.

3.4.1 Behaviour of clays with a sedimentation structure

Terzaghi (1944) defined the e-σ'_v curve followed by the clay during virgin compression in situ as the sedimentation compression curve (SCC) of the clay. The SCC of a clay reflects the response of the structure developing in the clay during virgin compression,

that is the sedimentation structure defined in Chapter 2. When reconstituted and consolidated in the laboratory, the clay moves along a different SCC, controlled by a stable sedimentation structure, which gives the clay a sensitivity of about 1 (Skempton and Northey, 1952; Skempton, 1970; Cotecchia and Chandler, 1997, 1998).

Skempton & Northey (1952) showed that normalizing the clay water contents with respect to composition by means of the liquidity index, the SCCs of reconstituted clays of different mineralogy coincide (see Section 2.5), indicating that they have a similar structural response to one-dimensional loading. The stability of the reconstituted clay structure is such that the SCC always plots to the left of the corresponding natural SCC, as shown in Fig.2.6b. The SCCs of the natural clays plot to the right and their different locations reflect differences in response of their sedimentation structures. The average values of sensitivity are reported for each natural clay in Fig.2.6b. As can be seen from the graph, each of the natural clays lies on a SCC which has a position corresponding approximately to the clay's sensitivity.

Leroueil and Vaughan (1990) defined the space to the right of the ICL as “structure permitted” space, to point out that the ‘structure’ allows the natural soil to exist outside the SBS of the reconstituted clay. Hereafter in this Chapter, the term ‘structure’ will be intended according to Leroueil and Vaughan (1990) as the difference between the structure of the natural and that of the reconstituted clay

Burland (1990) used the void index:

$$I_v = \frac{e - e^*_{100}}{e^*_{100} - e^*_{1000}} \qquad (3.27)$$

rather than the liquidity index to normalize the clay state with respect to composition, being the two parameters conceptually similar. He thus defined the “Intrinsic Compression Line” (ICL) as the unique SCC of the reconstituted clays in the I_v-σ'_v plane and gave an equation for it (Fig. 3.14).

Replotting many natural clay states from Skempton (1970) together with the ICL and other field data in the I_v-σ'_v plot, Burland also defined the "Sedimentation Compression Line" (SCL), representing the trend of in situ states of natural clays (Fig. 3.14).

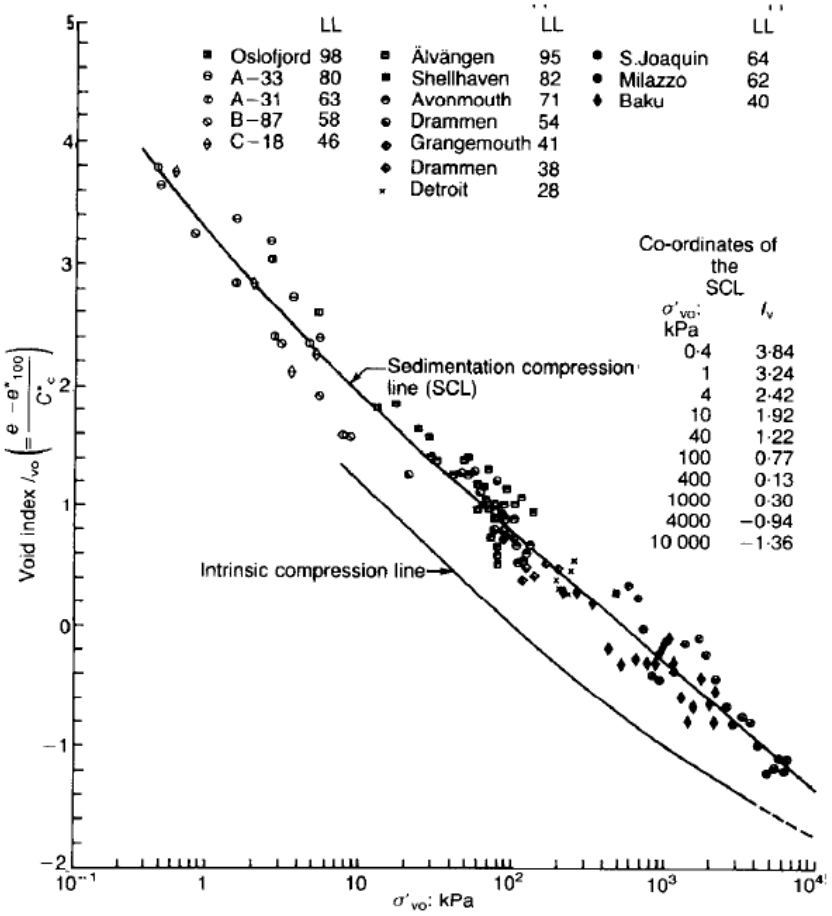

Fig. 3.14 – In situ I_v-σ'_v state for natural clays (after Burland, 1990).

Cotecchia and Chandler (2000) reported SC curves based on the in-situ data and each relating to a single value of sensitivity (Fig. 3.15). These SC curves appear to be parallel to the reconstituted SCC. Cotecchia and Chandler define *strength sensitivity* S_t, of clays with either sedimentation or post-sedimentation structure, as the ratio of the undrained strength after consolidation to gross yield to that of the reconstituted clay normally consolidated to the same water content as the natural clay at gross yield. Then, by

definition, $S_t=1$ for reconstituted clays. For the natural sedimentation structure clays in Fig.2.6b, the sensitivities shown are values of strength sensitivity S_t; sedimentation structure clays which have close values of S_t appear to follow close SC curves. Thus, their IL-σ'_v states appear to reflect their strength sensitivity, which may be regarded as a numerical parameter representing the influence of sedimentation structure on the one-dimensional normal compression behaviour of the clay. The SC curve of a clay will depend on its strength sensitivity during normal consolidation, irrespective of its exact origin or sedimentation structure.

An overall behavioural pattern is then suggested, called Sensitivity Framework, which is shown in Fig. 3.16 as I_v versus σ'_v. The SC curves are all quasi-parallel, with the curve for reconstituted clays ($S_t=1$) lying to the left. The SC curves for which $S_t>1$ lie to the right, the distance increasing with sensitivity. Doing so, Cotecchia and Chandler (2000) wished to provide a picture of the main effect of the differences in microstructure among clays (so far with a sedimentation structure) on the clay macro-response. They addressed first the similarities in behaviour among clays and the main difference, lying in the size of the clay SBS, in order to approach the analysis of more specific differences for specific classes of clays later on.

The pattern of clay behaviour in Fig. 3.16 is consistent with in situ data for clays with sedimentation structures presented by Skempton (1970) (Fig. 3.17(a)). The 13 clays show nearly parallel SC curves, occupying a narrow band which includes sensitivities in the range 1-10 (Fig. 3.17(b)). Although the strength sensitivity is not known for all the clays, it can be seen that Gosport clay ($S_t = 2.4$) and Tilbury clay ($S_t = 3.2$) (Skempton & Northey, 1952) lie to the left of the range of curves, while those with high sensitivity (e.g., Alvängen clay, Sweden, and Drammen clay, Norway; Bjerrum, 1967) lie to the right.

Burland's SCL (Fig. 3.14) can now be recognized as the average SCC for sedimentation structure clays of sensitivities $S_t \approx 5$. The SCL is approximately parallel to the ICL, at stresses five times those of the ICL. It appears that Burland's SCL is consistent with the conceptual framework shown in Fig. 3.16.

Any of the SC curves in Fig. 3.16 is a curve of gross yield stresses σ'_{vy}, providing the clays have a sedimentation structure. If this is the case $\sigma'_{v0}=\sigma'_{vy}$. The ratio of σ'_{vy} to the equivalent stress σ^*_{ey} on the ICL is defined as the stress sensitivity $S_\sigma= \sigma'_{vy}/ \sigma^*_{ey}$. (Cotecchia and Chandler, 2000).

On the basis of data for many different clays, Cotecchia and Chandler suggested that the stress sensitivity is, for all practical purposes, numerically equal to the strength sensitivity S_t, so that $S_t = S_\sigma= \sigma'_{vy}/ \sigma^*_{ey}$.

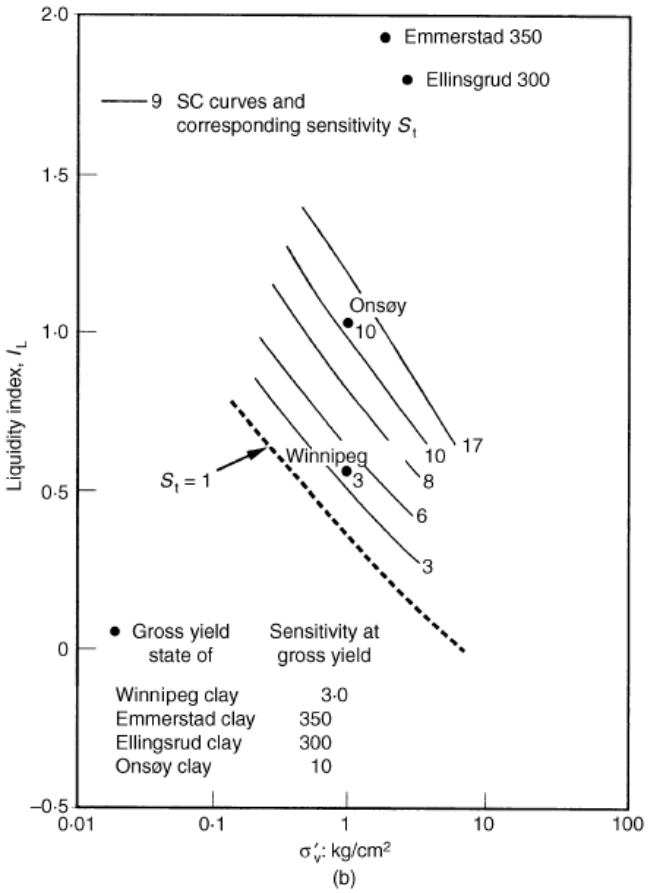

Fig. 3.15 - SC curves for clays of different sensitivities and yield states, and S_t values for post-sedimentation structure clays (data from Graham et al. (1983) and Lacasse et al. (1985); after Cotecchia and Chandler (2000)).

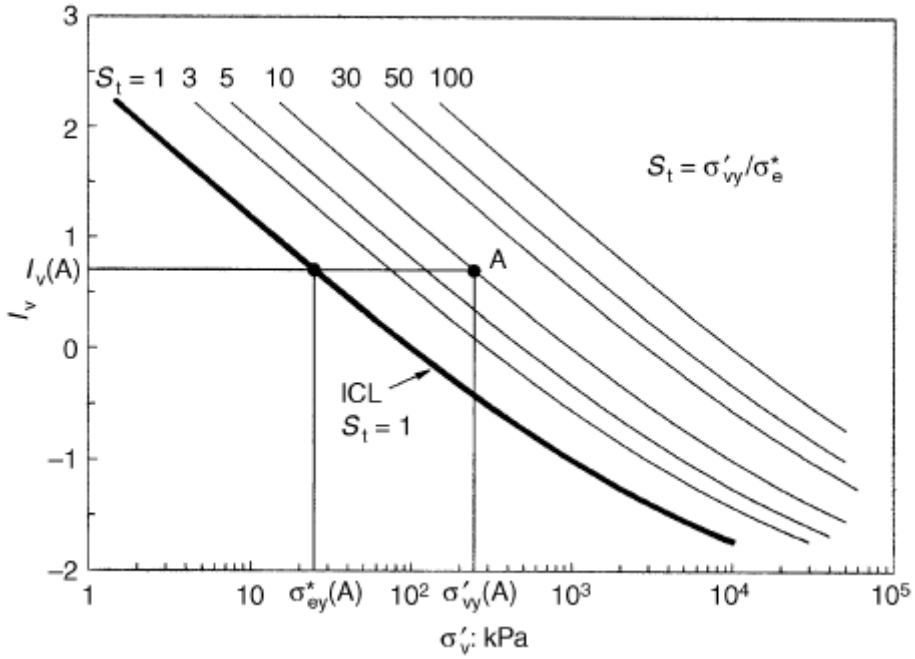

Fig. 3.16 – Sedimentation compression curves in the idealized sensitivity framework; the ICL is taken from Burland (1990) (after Cotecchia and Chandler, 2000).

This relationship also applies to clays overconsolidated by simple mechanical unloading, not altered by diagenesis, as for the case of Winnipeg clay (Graham et al., 1983). The gross yield state in one-dimensional compression for Winnipeg clay samples from a single depth is shown in Fig. 3.15(b) and implies a strength sensitivity S_t of 3-4, close to the sensitivity reported by Graham et al., fitting well with the suggested behaviour.

It will be seen later that the same relationship applies to clays having a post-sedimentation structure, although in this case the gross yield stress will be greater than the in-situ stress.

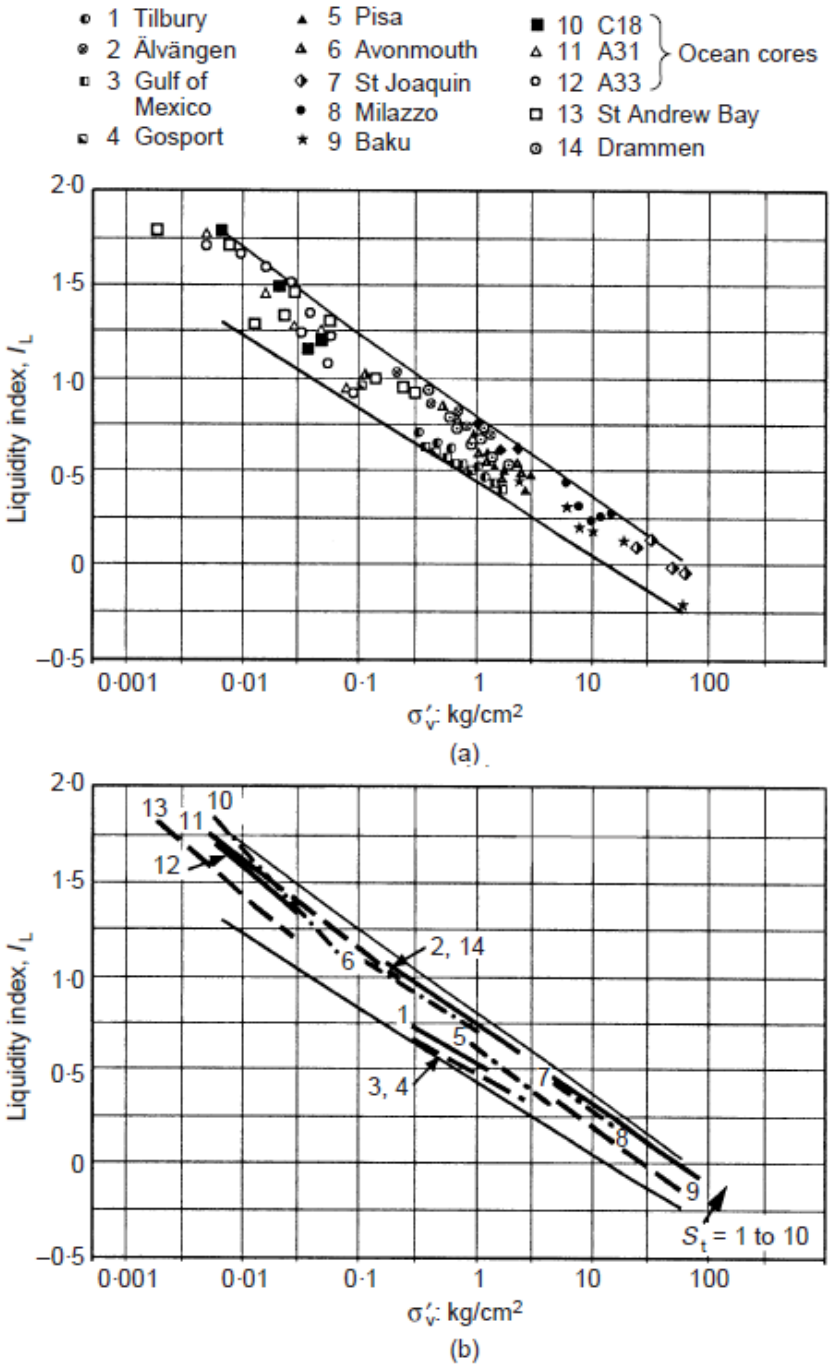

Fig. 3.17 – (a) In situ states of normally consolidated natural clays (Skempton, 1970) and (b) the corresponding SC curves (after Cotecchia and Chandler, 2000).

In Fig. 3.18 the sensitivity framework is represented in the q-p'-v space for a natural clay with a sedimentation structure, compared to the same clay when reconstituted. For simplicity, only axisymmetric compression is considered. The natural SC curve is the locus of the gross yield states in one-dimensional compression of samples of equal strength sensitivity S_t, and its projection in the v-lnp' plane lies parallel to the ICL, at a distance $S_\sigma = S_t$. In this case, the stress sensitivity $S_\sigma = \sigma'_{vy}/\sigma^*_{ey}$ is presumed to equal the ratio p'_{K0y}/p^*_{K0y} (the subscript K_0 denotes one-dimensional conditions). If S_σ is also equal to p'_{iy}/p^*_{iy} (the subscript i denotes isotropic conditions), the SC curve in Fig. 3.18 is also parallel to the isotropic gross yield locus in the v-lnp' projection.

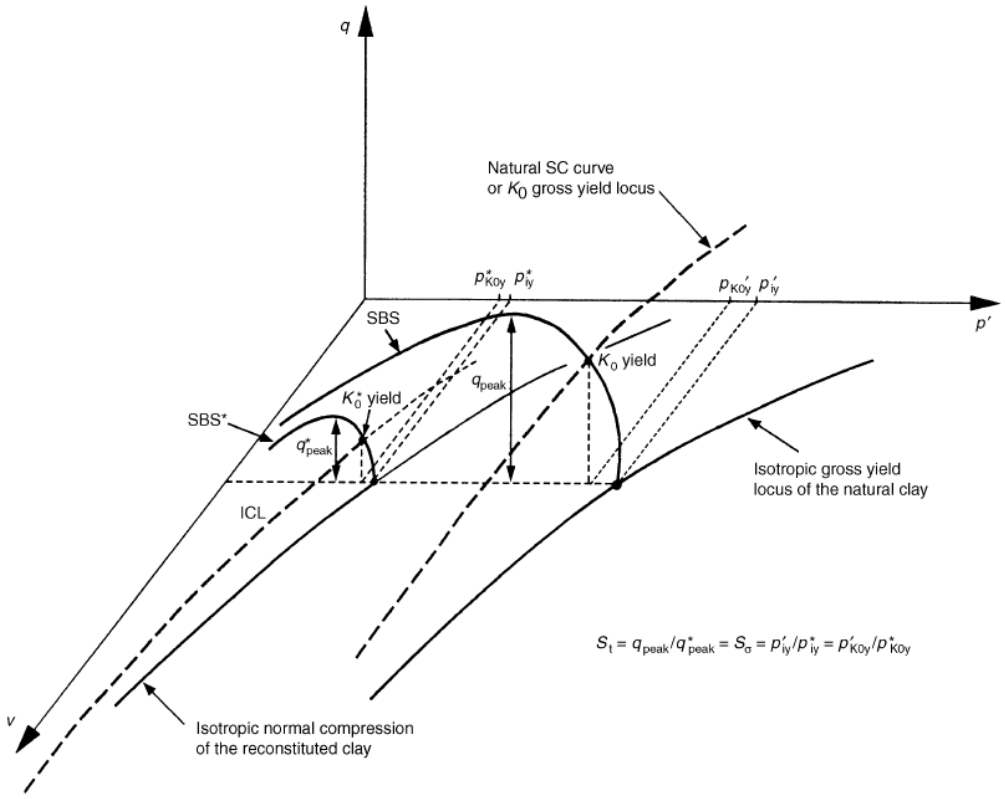

Fig. 3.18 - Idealized behaviour of a natural clay and of the same clay when reconstituted (after Cotecchia and Chandler, 2000).

As will be shown later, natural clays sheared from a YSR of 1.0, typically exhibit their peak undrained strength at the apex of the state boundary surface (SBS), with a strength

q_{peak} as can be seen in Fig. 3.19. Thus, as said before, the strength sensitivity S_t is ridefined by Cotecchia and Chandler (2000) as the ratio of the vertical size of the SBS of the natural clay to the corresponding size of the SBS* of the reconstituted clay at the same specific volume (Cotecchia and Chandler, 2000). The equality of S_t and S_σ implies that there is geometric similarity between the natural clay SBS and the SBS* of the corresponding reconstituted clay.

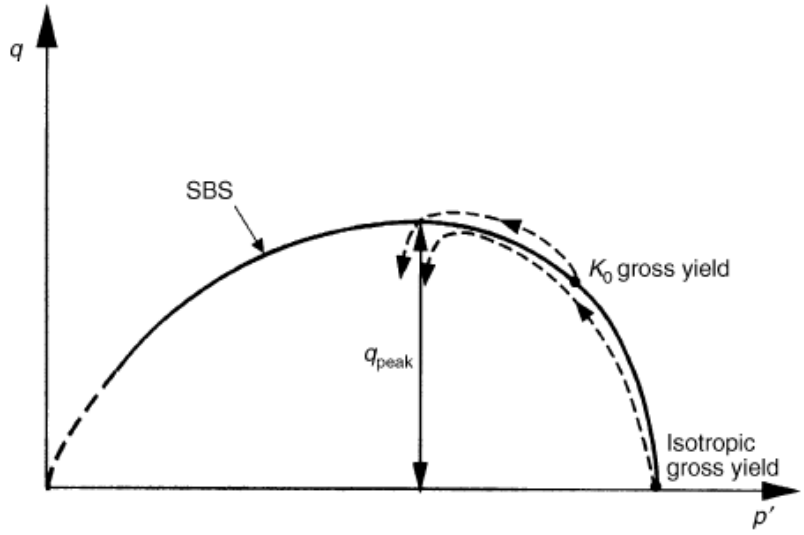

Fig. 3.19 – Undrained stress-paths for clay samples consolidated to gross-yield (after Cotecchia and Chandler, 2000).

The friction ratio at the critical state M can be considered as a normalizing factor for the effects of composition on soil strength (Graham et al., 1988; Coop et al., 1995). Following this assumption, the state boundary surface, normalized for the influence of composition on both specific volume and strength in I_v-q/M-p' space, should be the same for clays of different composition and structure, but of equal strength sensitivity S_t, as shown in Fig. 3.20. Therefore, Fig. 3.20 represents the general behaviour of different natural clays of equal strength sensitivity.

A and B are samples, overconsolidated only by unloading, of two different clays consolidated in situ to different specific volumes, but with sedimentation structures at gross yield having similar strength sensitivities S_t. As such, their gross yield points in

isotropic compression are located on the same isotropic gross yield locus, and they have the same SBS. Given the relatively high loading rates of laboratory compression tests compared with geological time-scale rates, the compression curve for samples A and B is represented in Fig. 3.20 as a curve falling below the SCC after gross yield.

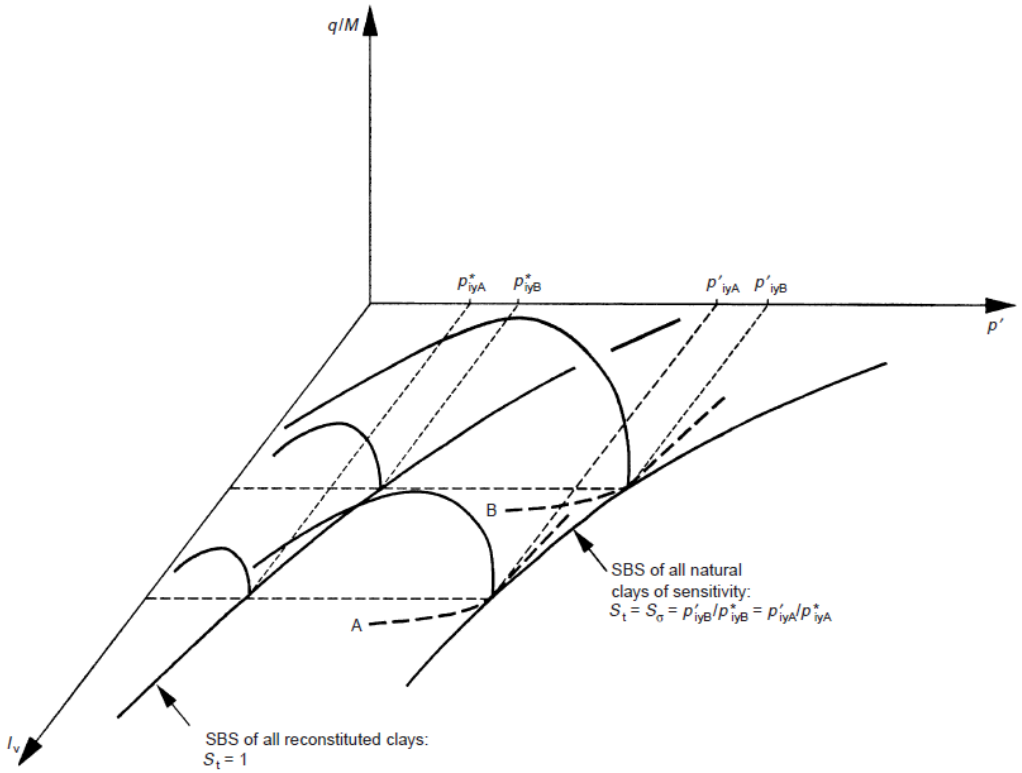

Fig. 3.20 – Idealized normalized behaviour of different natural clays of given strength sensitivity and of reconstituted clays (after Cotecchia and Chandler, 2000).

3.4.2 Behaviour of clays having a post-sedimentation structure

Cotecchia and Chandler (2000), still aiming at connecting clay history to classes of clay response, reported the schemes of response of clays possessing either a sedimentation structure, or a post-sedimeattion structure, or a reconstituted structure, in schemes, as that shown in Fig. 3.21. Many natural clays possess a post-

sedimentation structure that reflects some diagenesis, so that with oedometer reloading they retain post-sedimentation structural elements and cross the SCC, moving some distance to the right before gross yielding (path O-Y, Fig. 3.21). In this case, the post-sedimentation structure still dominates the clay behaviour at stress levels greater than the previous geological loading. After gross yield (path Y-Z_3), the sample follows a path steeper than the SCC, its gradient depending on the subsequent structural changes. Thus, the behaviour at gross yield of a clay depends on whether, at that point, it possesses solely a sedimentation structure, or if in addition retains elements of a post-sedimentation structure.

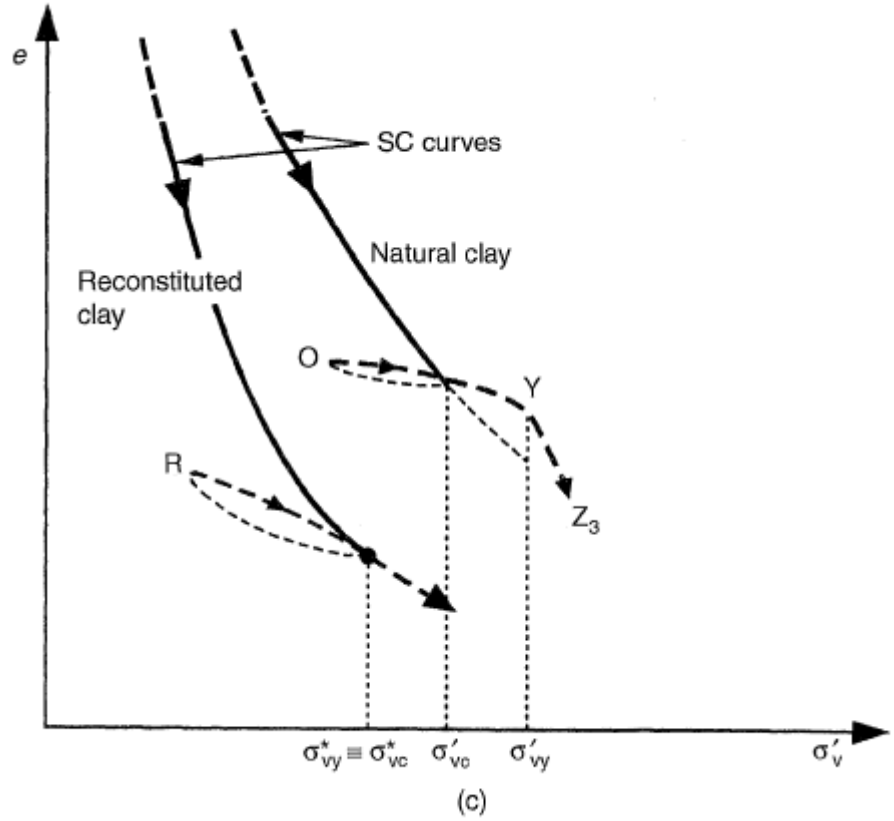

Fig. 3.21 - Response to one-dimensional compression of reconstituted clay and of natural clay overconsolidated with a post-sedimentation structure at gross yield (after Cotecchia and Chandler (2000)).

One-dimensional laboratory compression curves for clays with post-sedimentation structure have been plotted by Cotecchia and Chandler (2000), together with the compression curve of reconstituted Pappadai clay (Fig. 3.22). The compression curve for Bothkennar clay, which appears to have a sedimentation structure, is also shown.
The YSR of natural Pappadai clay is about 6, compared to the geological OCR of about 3, as the result of diagenesis (Cotecchia, 1996; Cotecchia and Chandler, 1997, 1998). Todi and Boom clay also have YSR values which exceed the OCR, and thus have post-sedimentation structures at gross yield. With Gault and London clay the OCR is not known, so that it cannot be established if these clays retain a post-sedimentation structure at yield, but it is likely that they do.
For the clays shown in Fig. 3.22, Cotecchia and Chandler (2000) compared the stress sensitivity ratios S_σ with the strength sensitivities S_t calculated as the ratio of the vertical size of the natural SBS to that of the reconstituted clay. They showed that, in general, $S_t \approx S_\sigma$, indicating that the behaviour of post-sedimentation structure clays is also in accordance with the sensitivity framework shown in Fig. 3.16, the constant S_t lines in the figure being the loci of the one-dimensional compression gross yield points of clay samples of equal strength sensitivity S_t.
Further assessment of the sensitivity framework is provided by the soft highly sensitive post-sedimentation structure clays from Onsøy, Ellingsrud and Emmerstad. The one-dimensional yield data for these clays are shown in Fig. 3.15(b), along with the strength sensitivity values derived from triaxial tests (Lacasse et al., 1985), and it is seen that their position in the IL-σ'_v plane is consistent with the framework. It follows that, as with sedimentation structure clays, clays with different post-sedimentation structures, but having equal strength sensitivity S_t, will have the same state boundary surface in I_v-q/M-p' space (see Fig. 3.20), although clays with a post-sedimentation structure at gross yield have an SC curve that lies within, not on, the SBS.

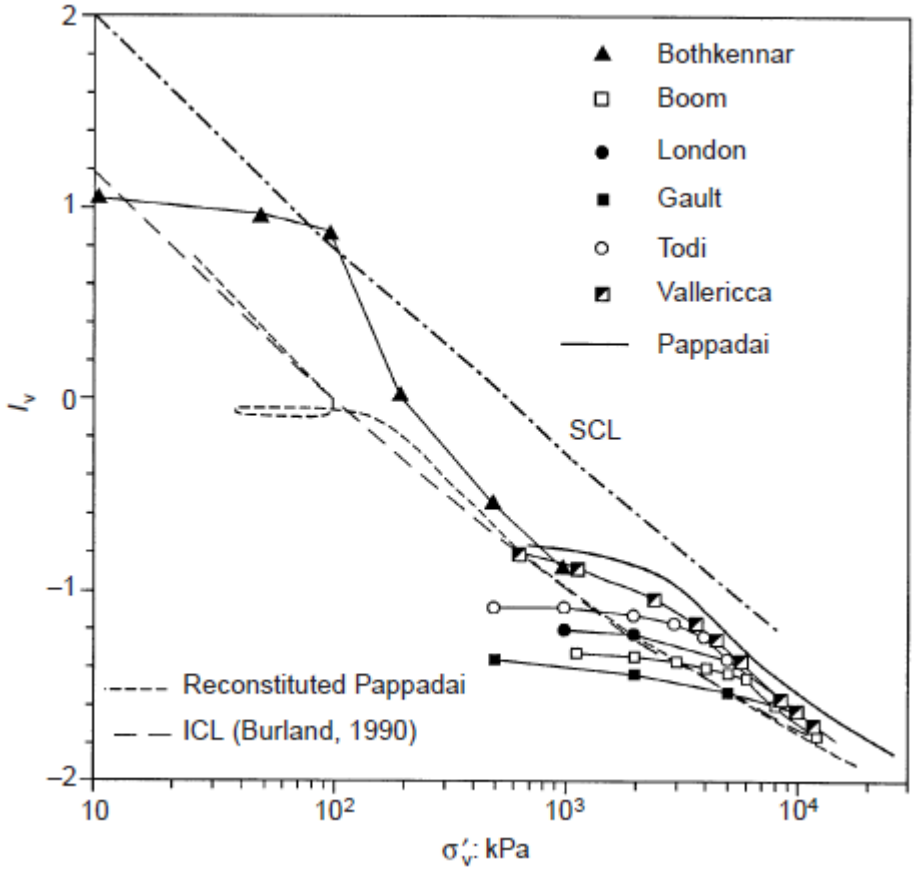

Fig. 3.22 - One-dimensional compression of natural and reconstituted clays plotted against the void index (data from Samuels, 1975; Bishop et al., 1965; Burland, 1990; Smith, 1992; Coop et al., 1995; Burland et al., 1996; Cotecchia, 1996)

3.4.3 Shape of gross-yield and state boundary curves

As assumed by Wheeler et al. (2003), inherent anisotropy may be reflected in the shape of the stress-strain curves (i.e. in the clay stiffness), in the gross yield and state boundary curves, which may differ from those applying to samples consolidated isotropically.

For example, a marked peak in the deviatoric stress is observed in undrained shear with both normally consolidated natural clays (e.g., Leroueil et al., 1979; Tavenas et al.,

1979; Jamiolkowski et al., 1985; Smith et al., 1992) and reconstituted K_0 consolidated clays (Pickles, 1989; Rossato et al., 1992), and also with reconstituted samples initially K_0 consolidated but subsequently further consolidated isotropically (Cotecchia, 1996). This peak is not so evident with samples isotropically consolidated from low pressures (Parry, 1956; Gens, 1982).

Stress-path data from Pickles (1989) show this aspect of behaviour for a K_0 consolidated reconstituted clay (Thames alluvium) (Fig. 3.23). The data are normalized by the mean effective stress at isotropic gross yield p'_{iy}. Irrespective of the test type or loading sequence, the normalized stress paths for the K_0 normally consolidated clay samples are all characterized by a peak q value, which occurs at the apex of the SBS. Note that the SBS is more elongated vertically than predicted by the modified Cam Clay model, a feature of K_0 consolidated reconstituted clays. The shape of the SBS in Fig. 3.23 resembles an "arch" in the plane of stresses normalized for p'_{iy} with positive values of q. For reconstituted clays, the gross yield states are generally close to the SBS and, assuming that the gross yield curves lie on the SBS, the gross yield curves of K_0 consolidated reconstituted clays may also be assumed to be arch shaped.

It has been suggested (Leroueil et al., 1979; Tavenas et al., 1979; Tavenas, 1981; Leroueil and Vaughan, 1990), and later applied in some constitutive models as S-CLAY1 (Section 3.3.3), that the shape of the gross-yield and limit state curves of soft natural clays, in both t-s' and q-p' planes, are approximately symmetric about the K_0 line, reflecting the anisotropic stress conditions. This can be seen in Fig. 3.24 for Bothkennar clay (Hight et al., 1992; Smith, 1992), a soft clay having medium to high strength sensitivity and lightly overconsolidated. The stress paths in Fig. 3.24 are normalized by the equivalent pressure on the reconstituted K_0 normal compression line.

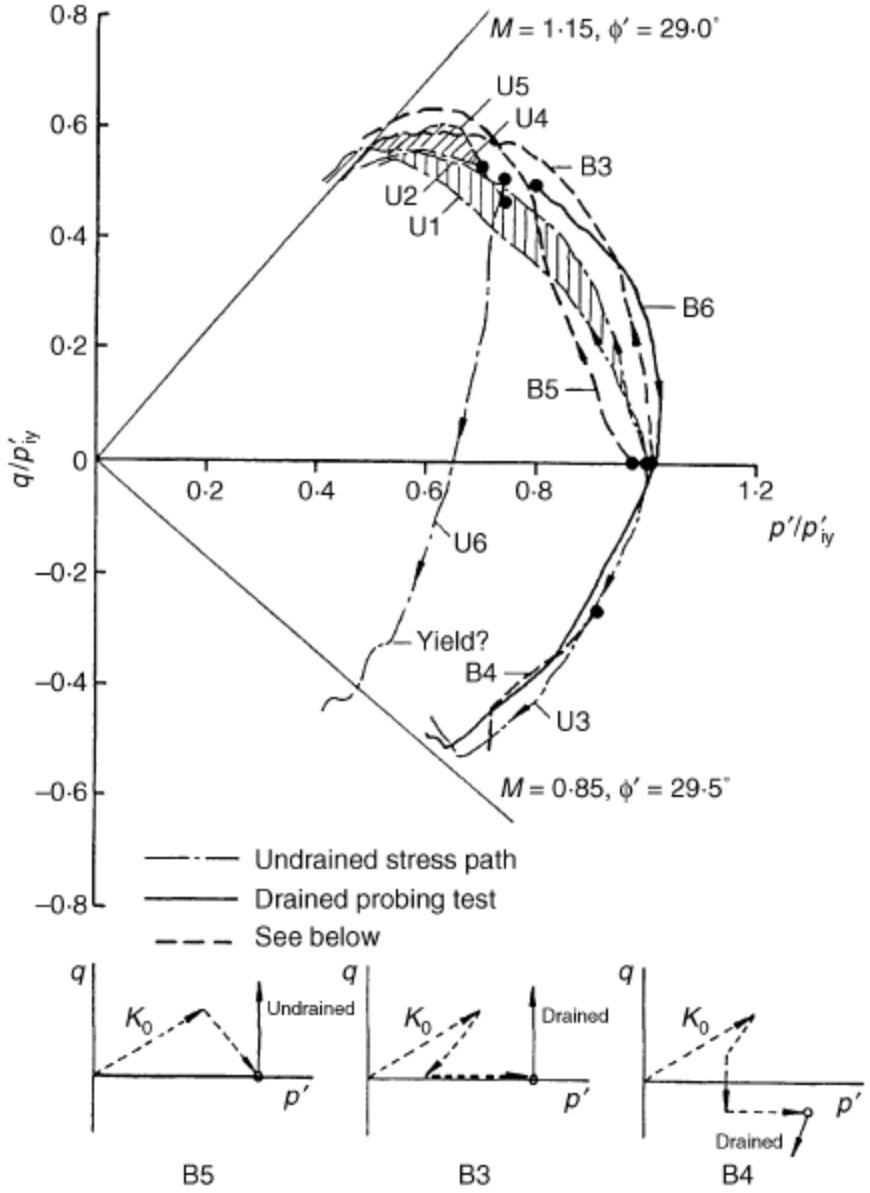

Fig. 3.23 - Stress path test data for reconstituted Thames alluvium (from Pickles (1989)).

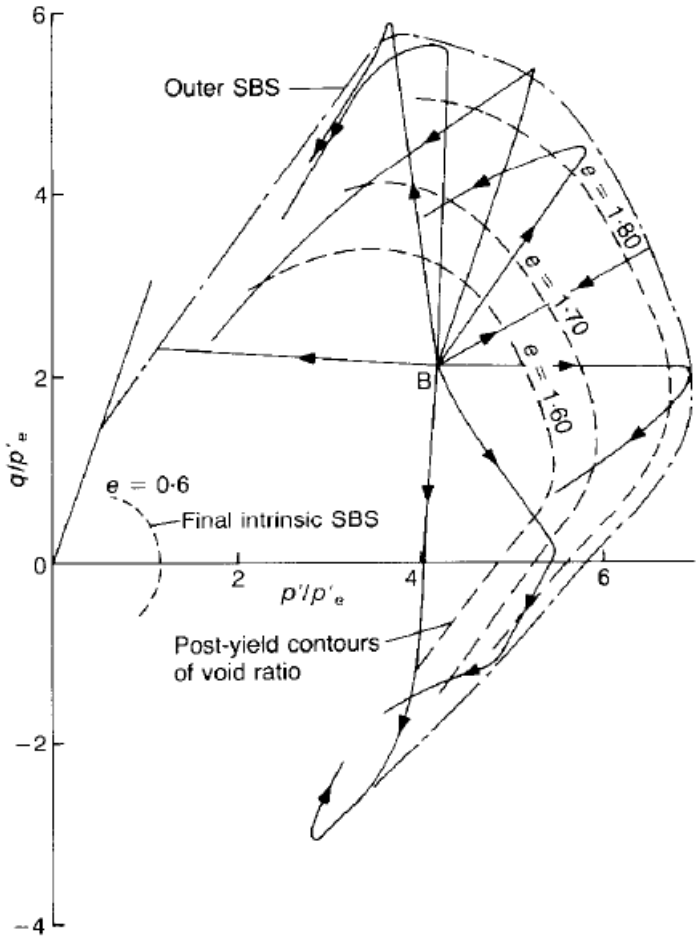

Fig. 3.24 – Stress path data for Bothkennar clay normalized for volume (after Smith, 1992).

A similar behaviour is shown by the very soft sensitive Saint Alban clay, of sensitivity higher than 14 (Leroueil et al., 1979). Fig. 3.25 shows the gross yield data from two depths, normalized by the gross yield stress σ'_{vy}. The gross-yield curve appears vertically elongated, with an evident symmetry about the K_0 line.

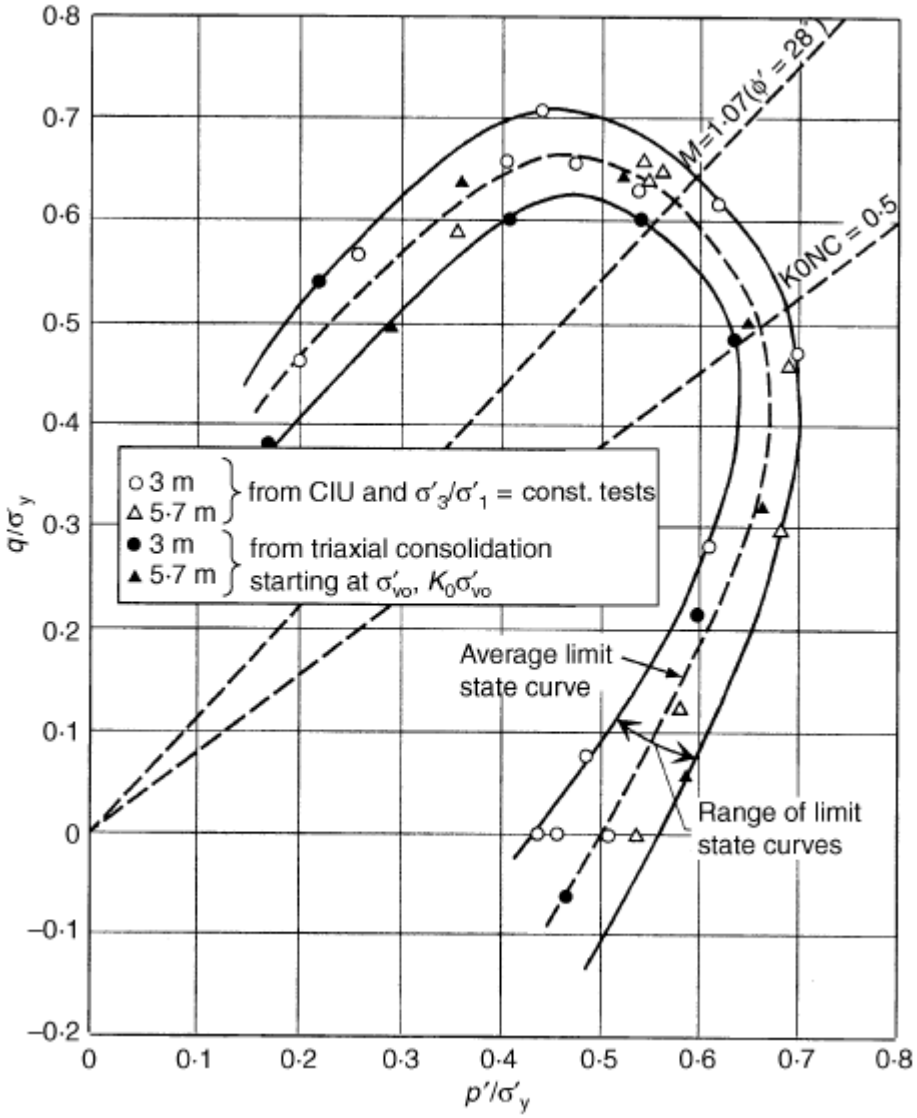

Fig. 3.25 - Gross yield data for Saint Alban clay samples from two depths (from Leroueil et al. (1979)) normalized for volume (after Cotecchia and Chandler, 2000).

3.4.4 A general normalized gross yield curve for clays

The sensitivity framework implies that samples from different depths of a given natural clay, of the same sensitivity, have gross yield states, in both compression and shear,

which lie on a state boundary surface, in the v-q-p' space, which can be normalized for volume. For undisturbed samples of a clay of given strength sensitivity S_t, the gross yield curves will have a constant size-ratio to the corresponding reconstituted curves, equal to S_t. Consequently, the gross yield curves of the natural clay can be normalized for volume by the equivalent pressure p^*_e, defined as the equivalent pressure on the INCL for the reconstituted clay, as with the reconstituted gross yield curves. In fact, Cotecchia and Chandler (2000) show that if q_{peak} is the deviatoric stress at the apex of the natural clay SBS and q^*_{peak} is the equivalent reconstituted value (see Fig. 3.18), then:

$$\frac{q_{peak}}{S_t p^*_e} = \frac{q^*_{peak}}{p^*_e} = constant \qquad (3.28)$$

This relationship assumes that p^*_e is the normalizing factor for the effect of volume on the clay strength, and thus shows that S_t is the normalizing factor for structure. If these normalizations apply to the complete gross yield behaviour, then all the gross yield curves of a given clay and of the same clay reconstituted should reduce to a unique curve in plane $[q/(S_t p^*_e)\text{-}p'/(S_t p^*_e)]$.

If the deviatoric stress is further normalized for composition by means of the intrinsic strength parameter M, which is a normalising parameter for the effects of composition on strength, the gross yield curves for clays of different structure and composition should all reduce to a unique curve in plane $[q/(MS_t p^*_e)\text{-}p'/(S_t p^*_e)]$.

Replacing strength sensitivity S_t by stress sensitivity S_σ, a unique general gross yield locus can then be postulated for all clays, in either plane $[q/(Mp^*_e p'_{iy}/p^*_{iy})\text{-}p'/(p^*_e p'_{iy}/p^*_{iy})]$ or plane $[q/(Mp^*_e p'_{K0y}/p^*_{K0y})\text{-}p'/(p^*_e p'_{K0y}/p^*_{K0y})]$, as p^*_e can be taken either on the isotropic compression line or on the K_0 normal compression line. The unique general gross yield locus is shown in the latter plane in Fig. 3.26.

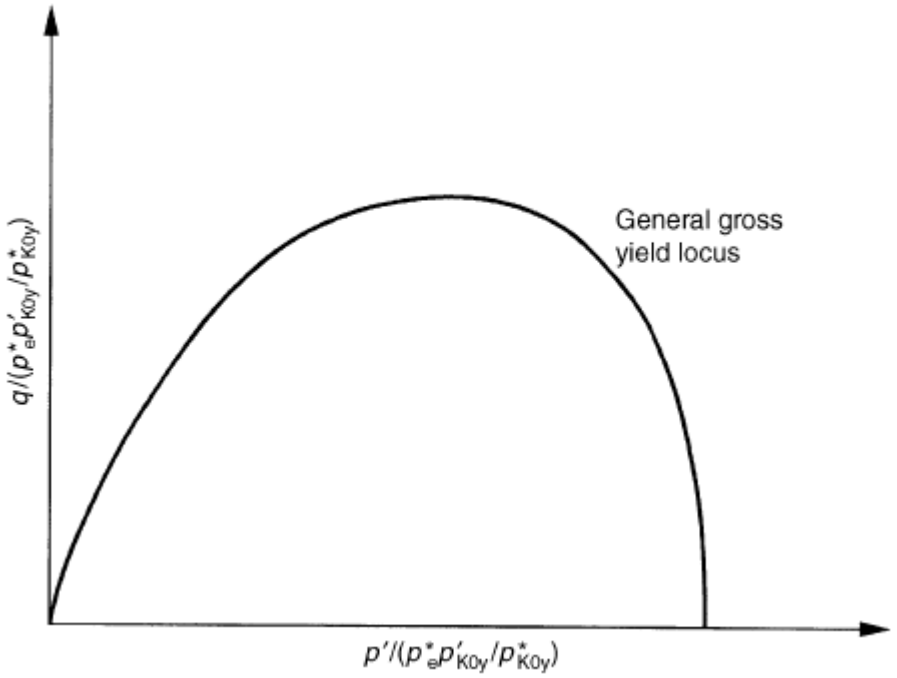

Fig. 3.26 – General normalized gross-yield locus for clays (after Cotecchia and Chandler, 2000).

These various normalizing factors are defined in Fig. 3.27. Two samples of the same clay, but at different specific volumes, A and A', are shown in Fig. 3.27. Y_{iA} is the isotropic gross yield state of sample A and $Y_{K0A'}$ is the K_0 gross yield state of sample A'. Note that p^*_e changes with the specific volume of the clay samples, whereas the sensitivity ratio is the same for specimens on the same swelling line, since these all have the same gross yield curve. The ratios $S_\sigma = p'_{iy}/p^*_{iy} = p'_{K0y}/p^*_{K0y}$ are equal to the ratios p'_{iNC}/p^*_e and p'_{K0NC}/p^*_e, respectively, where p'_{iNC} and p'_{K0NC} are taken on the isotropic and the K0 gross yield locus of the undisturbed clay, respectively, for the same specific volume as the consolidation state (A or A') being considered. Substituting the latter ratios in the expressions used for planes 3 and 4, a unique gross yield locus should be found in both plane $q/(Mp'_{iNC})$-$p'/(p'_{iNC})$ and plane $q/(Mp'_{K0NC})$-$p'/(p'_{K0NC})$.

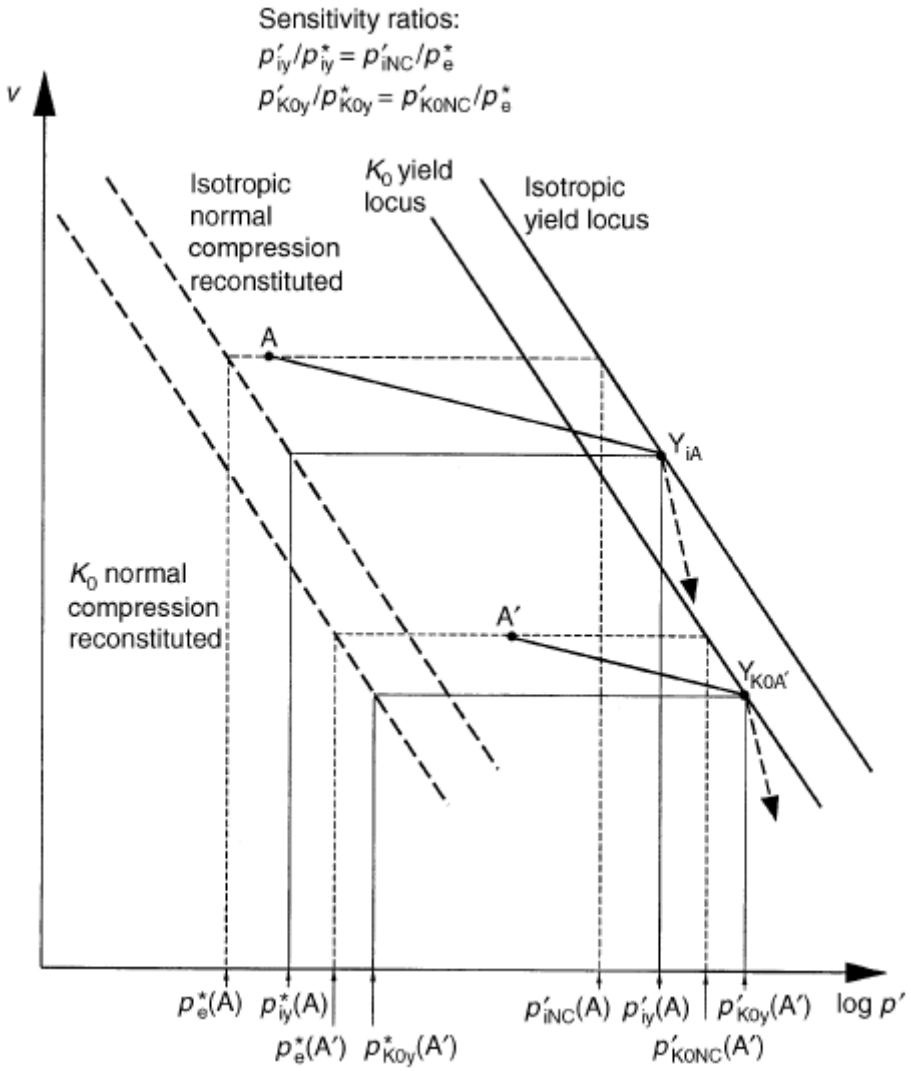

Fig. 3.27 – Normalizing factors for volume p^*_e and structure (Stress Sensitivity S_σ) (after Cotecchia and Chandler, 2000).

For many natural clays, after gross-yield the behaviour is different from that observed before gross-yield and from that of reconstituted clays post gross-yield.
For example, in one-dimensional compression the natural clay after gross yield follows a path falling below the SCC, which represents the K_0 gross yield locus of the pre-gross yield behaviour, as shown in Fig. 3.21. In this case, the clay strength sensitivity S_t is

progressively reduced with compression after gross yield, crossing successive loci of K_0 gross yield states, of different strength sensitivities S_t (see Fig. 3.16). Similarly, in shear for many natural clays (Tavenas and Leroueil, 1985; Jamiolkowsky et al., 1985; Smith, 1992; Cotecchia, 1996) stress paths are seen to move inwards from the state boundary envelope in the normalized stress plane. An example is shown in Fig. 3.24 for soft Bothkennar clay (Smith, 1992).
Reconstituted clays, having constant strength sensitivity S_t (=1) both before and after gross yield, have similar pre- and post-gross yield behavioural frameworks.

The main consequence of the post-gross yield change in strength sensitivity of the natural clay is that, with straining post gross yield, the size of the current gross yield curve is not controlled solely by the plastic volumetric strains, as for reconstituted clays, but also by the change in strength sensitivity. The latter hence becomes a parameter of structure evolution.
Thus, it is necessary to normalize both for volume (using p^*_e) and for strength sensitivity, using the stress sensitivities p'_{iy}/p^*_{iy} or p'_{K0y}/p^*_{K0y}, which both reduce with compression after gross yield.

3.4.5 Behaviour of Pappadai clay

The stress paths followed by reconstituted Pappadai clay, together with the gross yield states of natural Pappadai clay specimens trimmed from a block sample, consolidated to different values of p' before gross yield, are shown in Fig. 3.28.
The reconstituted clay samples were consolidated in a consolidometer up to 200 kPa vertical stress, and then either consolidated isotropically or under K_0 conditions before shearing. When normalized, these stress paths appear to be bounded by an arch-shaped state boundary surface.
Also the gross yield data for the natural clay consolidated before gross-yield before shear define an arch-shaped gross yield locus. Since the natural clay stress paths are seen to reverse in direction after gross yield in shear, the gross yield locus is also a

SBS for the undisturbed clay, and is apparently geometrically similar to that of the reconstituted clay. Thus, the main difference between the natural and the reconstituted state boundary surfaces is one of scale, as implied in Fig. 3.18 and Fig. 3.20.
In Chapter 8, the microstructural features giving rise to the SBS of Pappadai clay will be discussed, and the SBS will be seen to embody the microstructure observed for a given clay. Following this, it will be also shown that conceptually the SBS differs from the "structure" yield surface used to represent the effects of structure in some advanced constitutive models (Section 3.5).

Also shown in Fig. 3.28 are the stress paths for two natural samples isotropically compressed beyond gross-yield before shear. These indicate the position and size of the SBS of the clay compressed after gross yield. These stress paths lie within the initial gross yield locus, implying a lower strength sensitivity than the initial (before gross yield) value of 3.2, due to the weakening of structure in post-gross yield straining.
The undrained stress path indicates a strength sensitivity S_t of $\approx$2.5, and corresponds to a stress sensitivity before shear $S_\sigma = p'_{iy}/p^*_{iy}$ of 2.7, S_t and S_σ being approximately equal as expected.
The Pappadai reconstituted stress paths, the natural gross yield data and the post-gross yield stress paths were further normalized by S_σ, as shown in Fig. 3.29.
The post-gross yield undrained stress path is now seen to follow the SBS of samples consolidated before gross yield to its apex, before falling towards a pseudo-critical state (Cotecchia & Chandler, 1997), as will be discussed later in further detail. The post-gross yield drained stress path also follows the same SBS, but diverges from it before reaching the apex, probably as a consequence of the uncertainties in the stresses due to the large strains at the final stage of the test.
The consistency of both the natural and the reconstituted clay data about the same gross yield locus and state boundary surface seen in Fig. 3.29 demonstrates that the gross yield states, of either natural clays sheared from pre- or post-gross yield states, or of reconstituted clays, exhibit common behaviour when normalized by consideration of both volume and strength sensitivity. Only at very large shear strains, when the stress

paths diverge from the state boundary surface, this normalization is no more effective. This normalization also show that the gross yield curves are isotropically hardening.

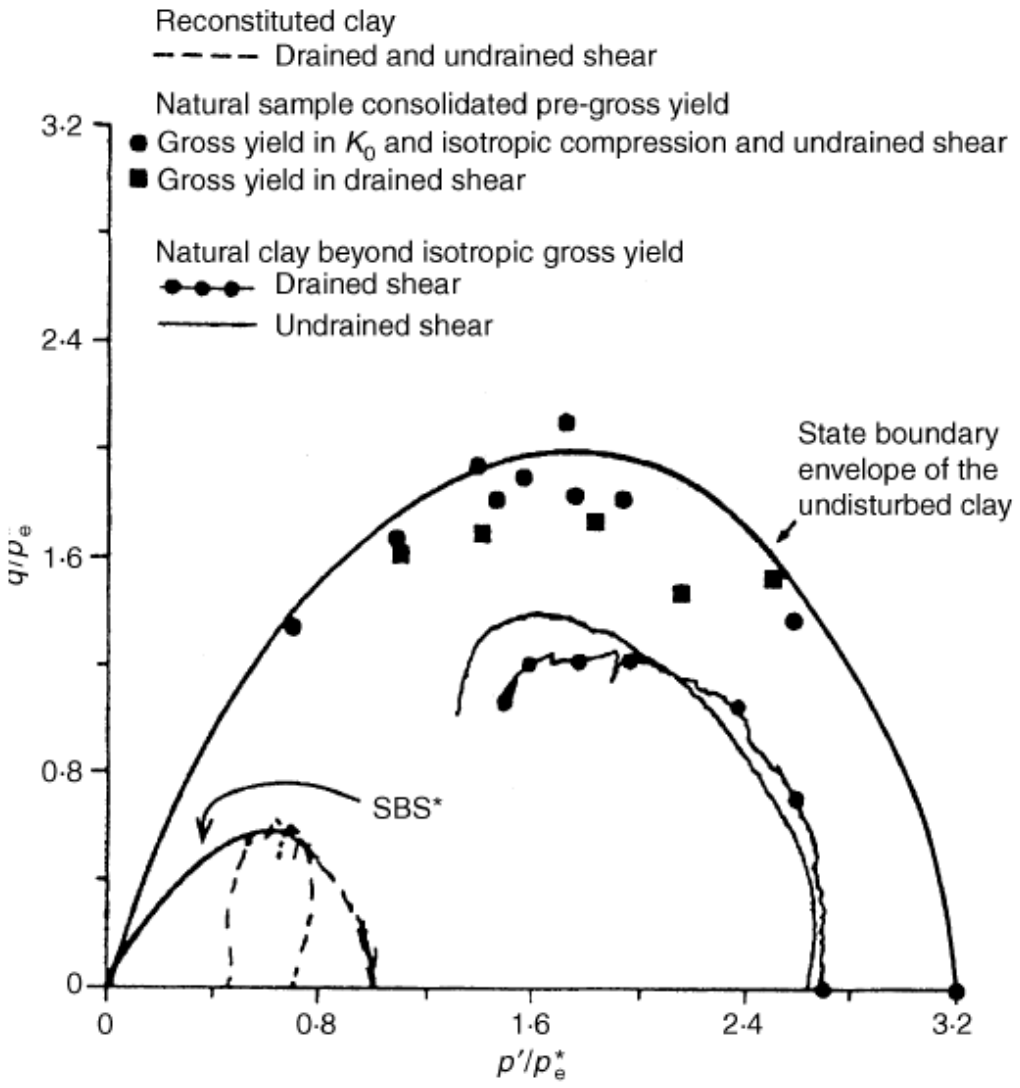

Fig. 3.28 - Pappadai clay: gross yield states of the natural clay, stress paths of the clay compressed beyond isotropic gross yield, and stress paths of the reconstituted clay (from Cotecchia & Chandler (1997)).

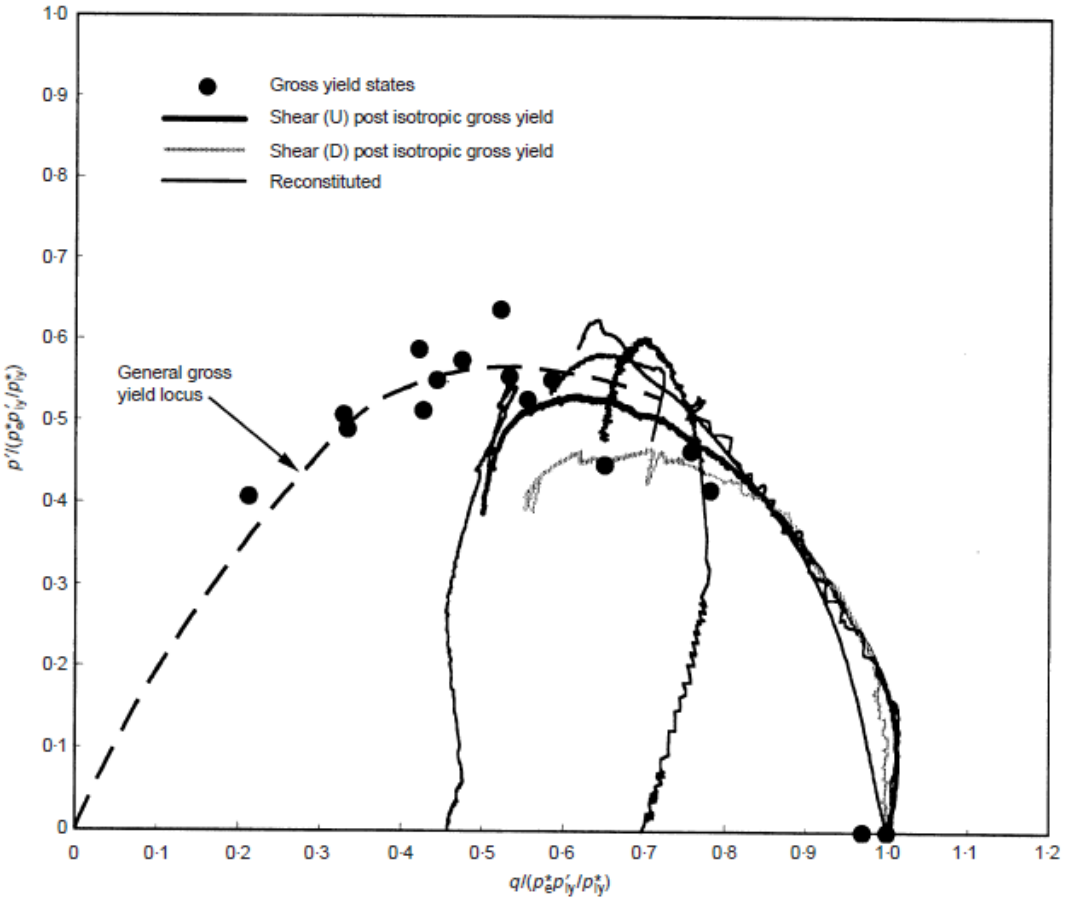

Fig. 3.29 - Pappadai clay behaviour normalized for both volume and structure: gross yield data of the natural clay, post-gross yield stress paths of the natural clay (U, undrained; D, drained), and stress paths for the reconstituted clay (after Cotecchia and Chandler, 2000).

3.4.6 Application of the sensitivity framework to other natural clays

Cotecchia and Chandler (2000) have shown that many natural clays fit the sensitivity framework.

This is for example the case of Winnipeg clay (Graham et al., 1988), for which it is shown that the gross yield states of undisturbed samples from four different depths reduce to a single curve once normalized using the equivalent pressure p'_{KONC} (Fig. 3.30). This curve represents at the same time the normalized gross yield and the state

boundary locus for undisturbed Winnipeg clay, since the natural clay stress paths reverse in direction having yielded at the state boundary surface.

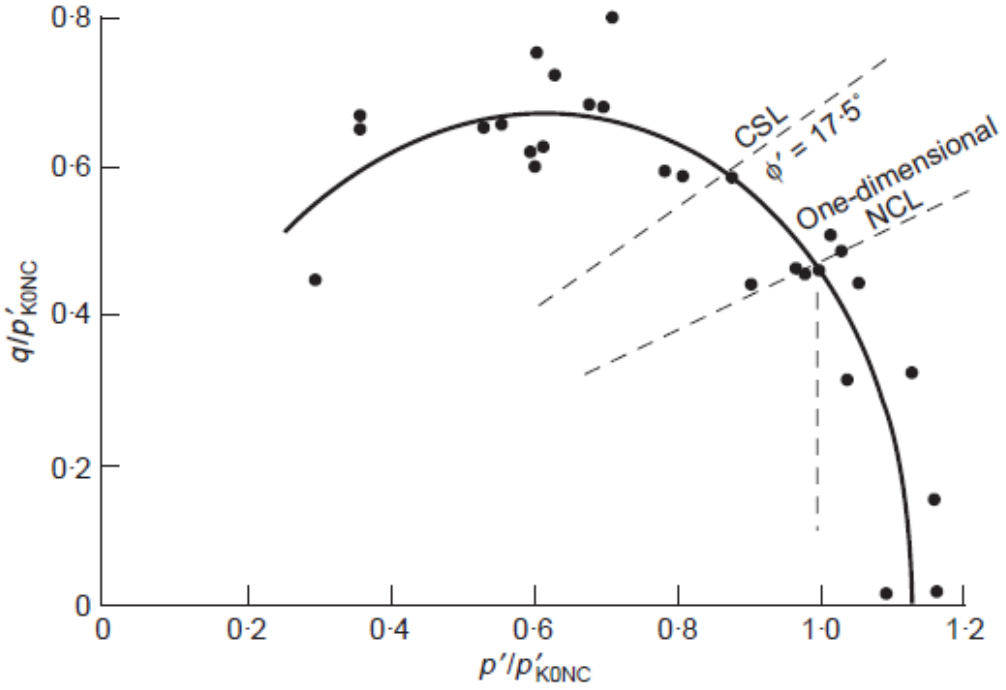

Fig. 3.30 – Gross yield data for Winnipeg clay normalized for both volume and strength sensitivity (after Graham et al., 1988).

Shear tests from states K_0 consolidated to a stress beyond gross-yield were carried out on Sibary clay, a layered clay with thin intercalations of silt and fine sand, of sensitivity around 3 (Coop and Cotecchia, 1995).

For natural samples and corresponding reconstituted samples, the stresses are normalized for volume by p^*_e, the equivalent stress on the reconstituted isotropic compression line, and the deviator stress is also normalized for the stress ratio M at the critical state (Fig. 3.31a). The stress paths follow the wet side of the corresponding state boundary surface, rising to the apex of the surface, and reach the critical state to its left. The normalization for structure has been applied to the Sibari clay data in Fig. 3.31a, resulting in the curves shown in Fig. 3.31b. Sibari clay behaves in agreement with the sensitivity framework, as the stress paths for the normally consolidated natural

specimens reduce to a single curve, which is close to the state boundary surface of the reconstituted clay.

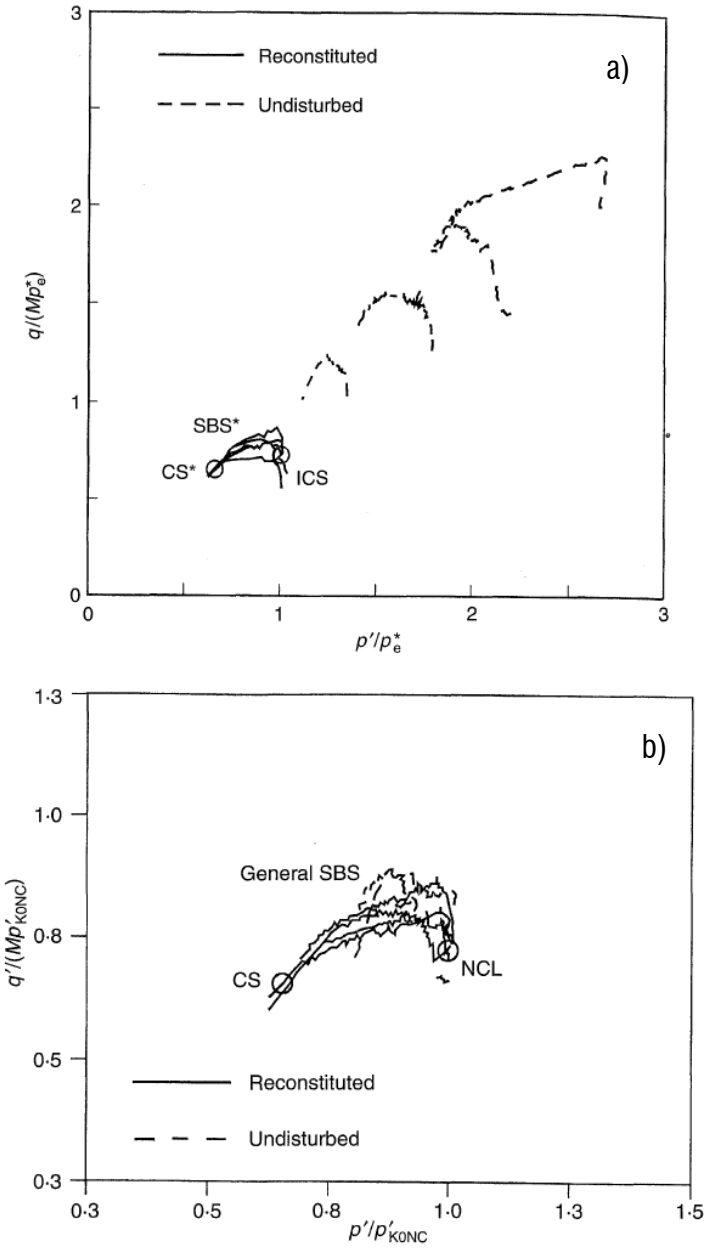

Fig. 3.31 –Shear tests data for natural and reconstituted Sibari clay samples normalized (a) for volume and composition and (b) for volume and structure (after Cotecchia and Chandler, 2000).

For Bothkennar clay (Smith et al., 1992), the gross yield points corresponding to the stress paths shown in Fig. 3.24 are plotted in Fig. 3.32, in terms of both q and p' taken from Smith et al. (1992), and also as determined using the same criteria adopted for the Pappadai clay gross yield data shown in Fig. 3.29.

There is correspondence between both sets of gross yield data and the SBS of the clay for stress paths where there is an increase in deviator stress. Although the exact shape of the gross-yield curve is dependent on the criterion used to determine yield, the Bothkennar gross yield curve does not have the expected arch shape in the region of the p' axis.

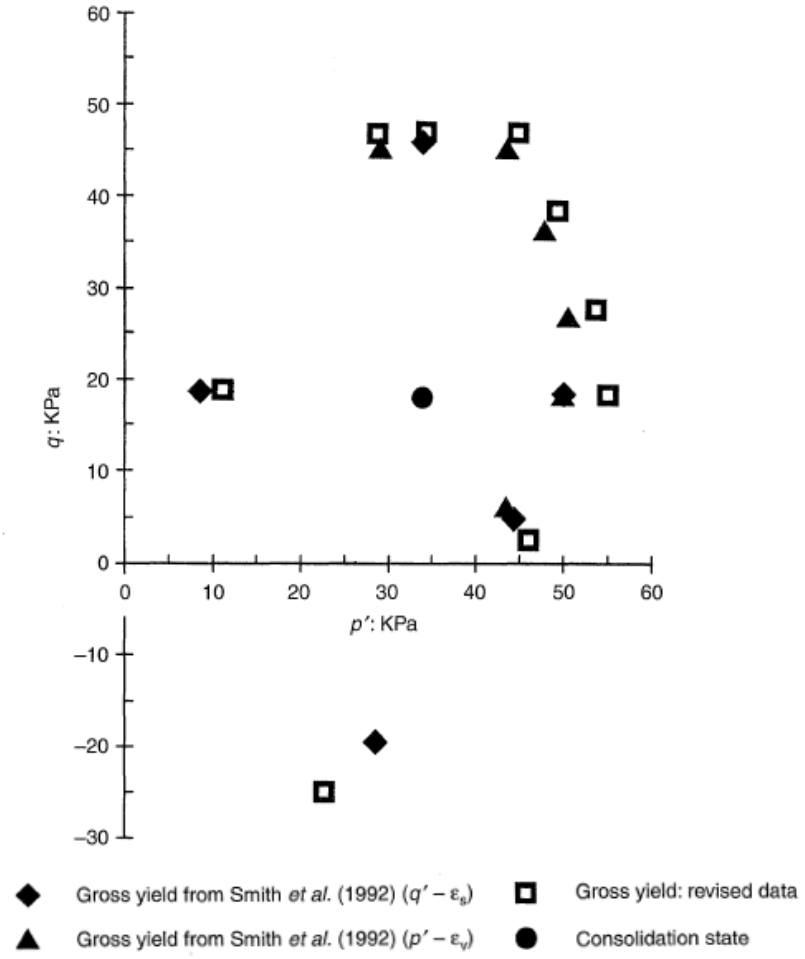

Fig. 3.32 - Bothkennar clay: gross yield states (after Cotecchia and Chandler, 2000).

In Fig. 3.33, Bothkennar and Pappadai clay gross yield data, as well as a reconstituted Pappadai clay stress path, are plotted together to show the general applicability of the proposed normalizations to define a single gross yield locus. The data are normalized for volume (p^*_e on the K_0 normal compression line), for structure (p'_{K0y}/p^*_{K0y}), and for composition (by means of the critical state stress ratio M).

There is considerable similarity between the locus of gross yield states of both Pappadai and Bothkennar clay. A further check of these normalizations is provided by a test on a specimen of Bothkennar clay K_0 consolidated after gross yield (Smith et al., 1992; test CK_0U). Owing to creep during consolidation, the normalized stress path for this test starts within the general SBS, but it soon reaches and follows the SBS.

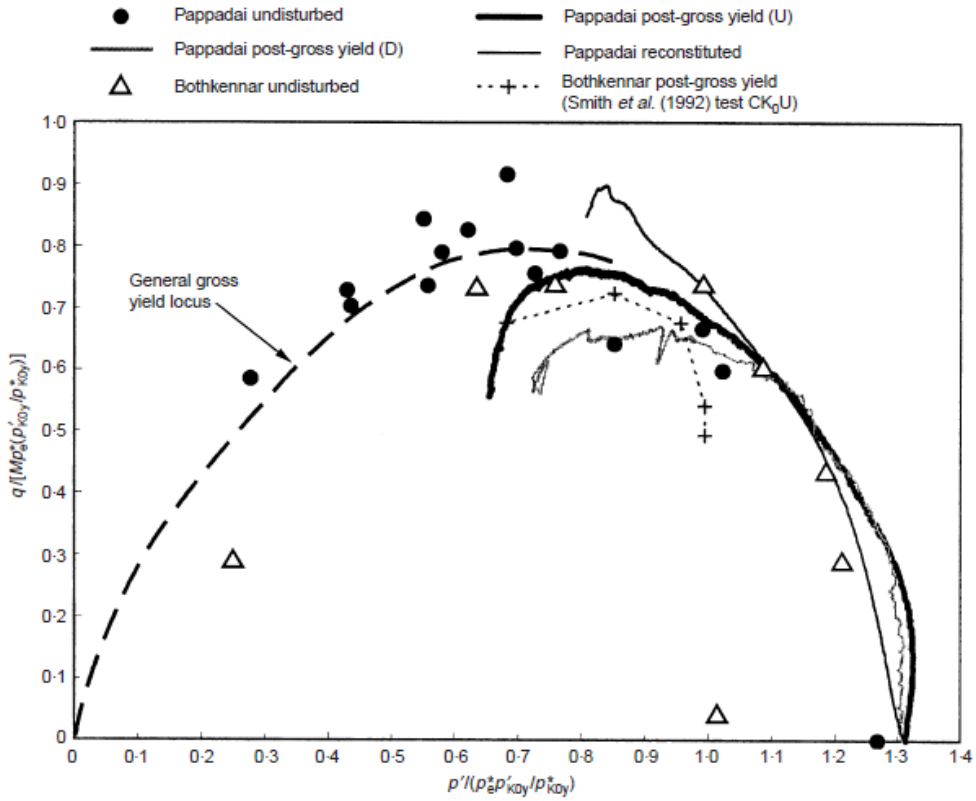

Fig. 3.33 - Behaviour of both Pappadai and Bothkennar clay normalized for volume, composition and structure (after Cotecchia and Chandler, 2000).

The SBS in Fig. 3.33 is arch shaped, although the comparison between the gross yield locus and the SBS is not very satisfactory for Bothkennar clay in the region of the p' axis. This behaviour appears in agreement with the gross-yield data shown in Fig. 3.32 for Bothkennar clay and also with gross yield states shown in Fig. 3.25 for the very soft Saint Alban clay. For Saint Alban clay, the gross-yield curve is seen to diverge from an arch shape in the region where $q/\sigma'_{vy} < 0.4$.

However, this symmetry of the gross-yield curve about the K_0 line contrasts with the gross yield behaviour of the other one-dimensionally consolidated clays discussed earlier (Cotecchia et al., 2011).
A possible explanation of the difference between the shape of the gross yield curves of soft natural clays and that of reconstituted clays and stiff natural clays, is that the natural soft clays, which are the most sensitive, possess a structure which is disturbed by the imposition of isotropic stresses on initially anisotropic samples. Consequently, they develop large plastic strains, even with small increments in isotropic stress. This behaviour is shown in Fig. 3.34 and Fig. 3.35, where isotropic and K_0 compression curves are compared for both Saint Alban and Bothkennar clay. Both these sensitive clays are initially much less stiff in isotropic compression, have a poorly defined isotropic gross yield, and the isotropic compression curves cross the K_0 compression curves at large strains. Thus, for soft sensitive clays, the gross yield curve lies close to the state boundary surface in the region where the deviatoric stress q is increasing, as it does with stiffer natural clays and with reconstituted clays. With reducing values of q, the gross yield points are less clearly defined, and it is possible that, with increasing strength sensitivity, they lie progressively further from the SBS.

It is concluded that, in compression, the inherent anisotropy of natural and K_0 consolidated clays is the dominant factor giving rise to an arch-shaped gross yield curve. An appropriate mathematical expression for the gross yield curve would be one that approximately fits the majority of the data.

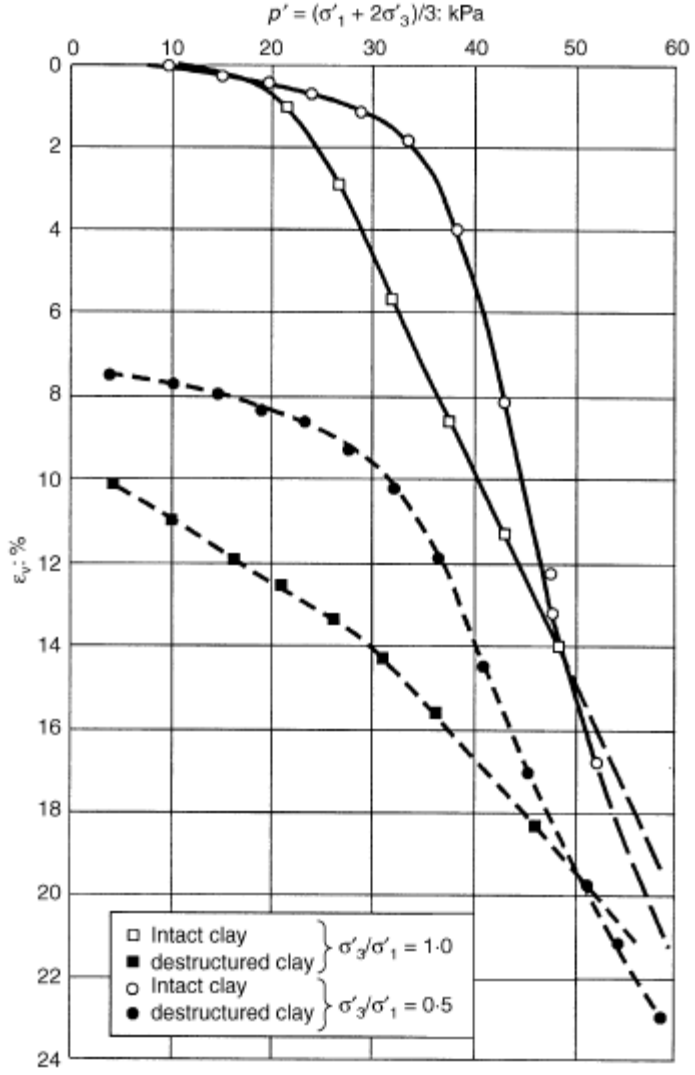

Fig. 3.34 – Compression curves for Saint Alban clay samples (from Leroueil et al. (1979).

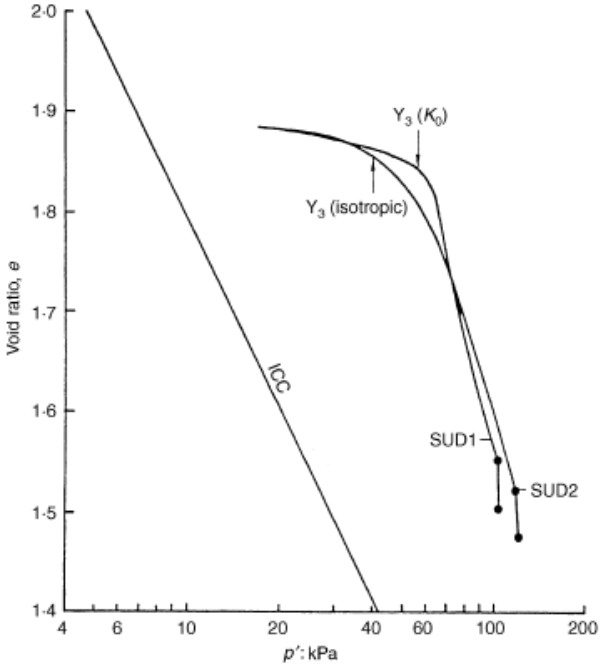

Fig. 3.35 – Compression curves for Bothkennar clay samples (from Smith, 1992).

3.4.7 Plastic strain increment ratios

The linear nature of the Cam Clay flow rule (eq. 3.7) is preserved if it is written in more general terms as:

$$\frac{q}{p'} = Q - A\frac{\delta\varepsilon_v^p}{\delta\varepsilon_s^p} \qquad (3.29)$$

where $\delta\varepsilon_v^p/\delta\varepsilon_s^p$ is the plastic strain increment ratio. In the Cam Clay model, Q would take the value M, while A is unity, suggesting "purely frictional" behaviour. If $A \neq 1$ in equation (3.29), the behaviour may be described as "basically frictional", applying to the soil in the q-p' plane on either side of the critical state line, meaning that the frictional deformation mechanism applies, although the deformation is influenced by structure and is not therefore solely frictional (Cotecchia and Chandler, 1997; 2000).

Cotecchia & Chandler (1997) showed that plastic strain increment ratios of reconstituted Pappadai clay satisfy equation (3.29), with a value of A which differs from unity and which is stress-path dependent, being about 0.5 in drained tests and about 1.5 in undrained tests (Fig. 3.36). So, the reconstituted clay appears to have a "basically frictional", rather than purely frictional, behaviour. The difference of A from unity reflects structural degradation with strain in addition to pure friction. The stress-path dependence of these effects is plausible since structural changes along different stress-path types are likely to differ.

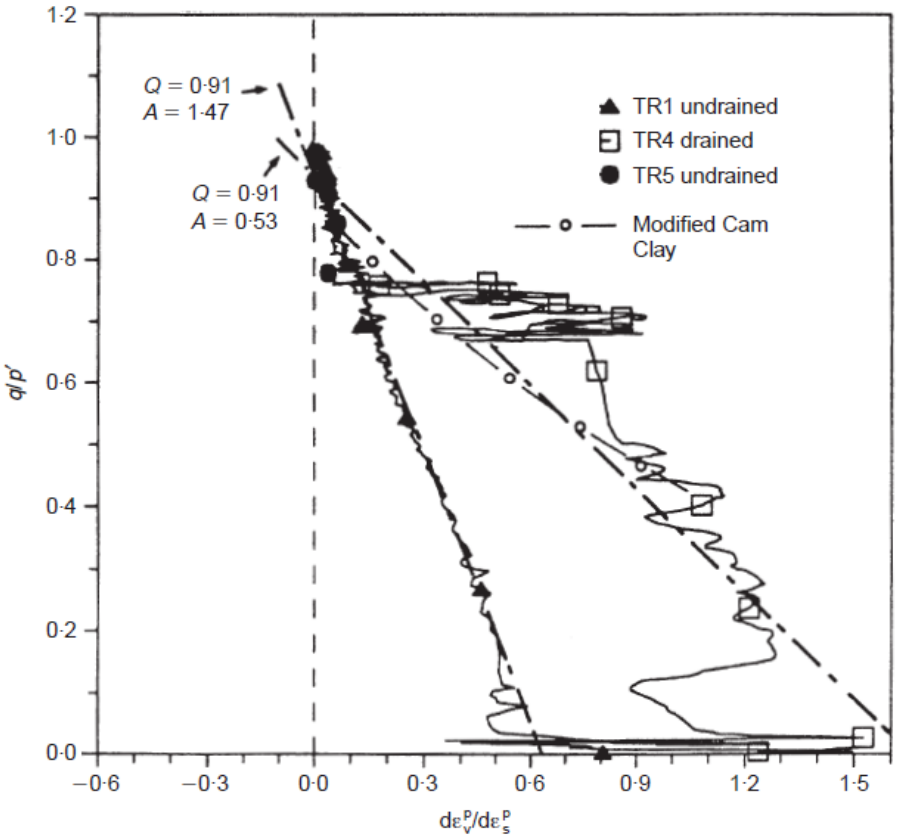

Fig. 3.36 – Reconstituted Pappadai clay: flow rules during shear for isotropically (TR1, TR4) and K_0 (TR5) normal consolidated samples (after Cotecchia and Chandler, 1997).

Natural Pappadai clay data in the q/p'-$\delta\varepsilon_v^p/\delta\varepsilon_s^p$ plane are shown in Fig. 3.37 for specimens consolidated isotropically to states both before and after gross yield. The

elastic volumetric strains have been calculated using the gradient of the swelling lines κ, the elastic shear strains being considered to be negligible since shear moduli as high as 100 MPa have been measured for natural Pappadai clay in the laboratory during triaxial tests (Cotecchia & Chandler, 1997). The data in Fig. 3.37 fit the linear equation (3.29) to beyond gross yield, with values of A which differ in undrained and drained shear, although they are close to those measured for reconstituted Pappadai clay.

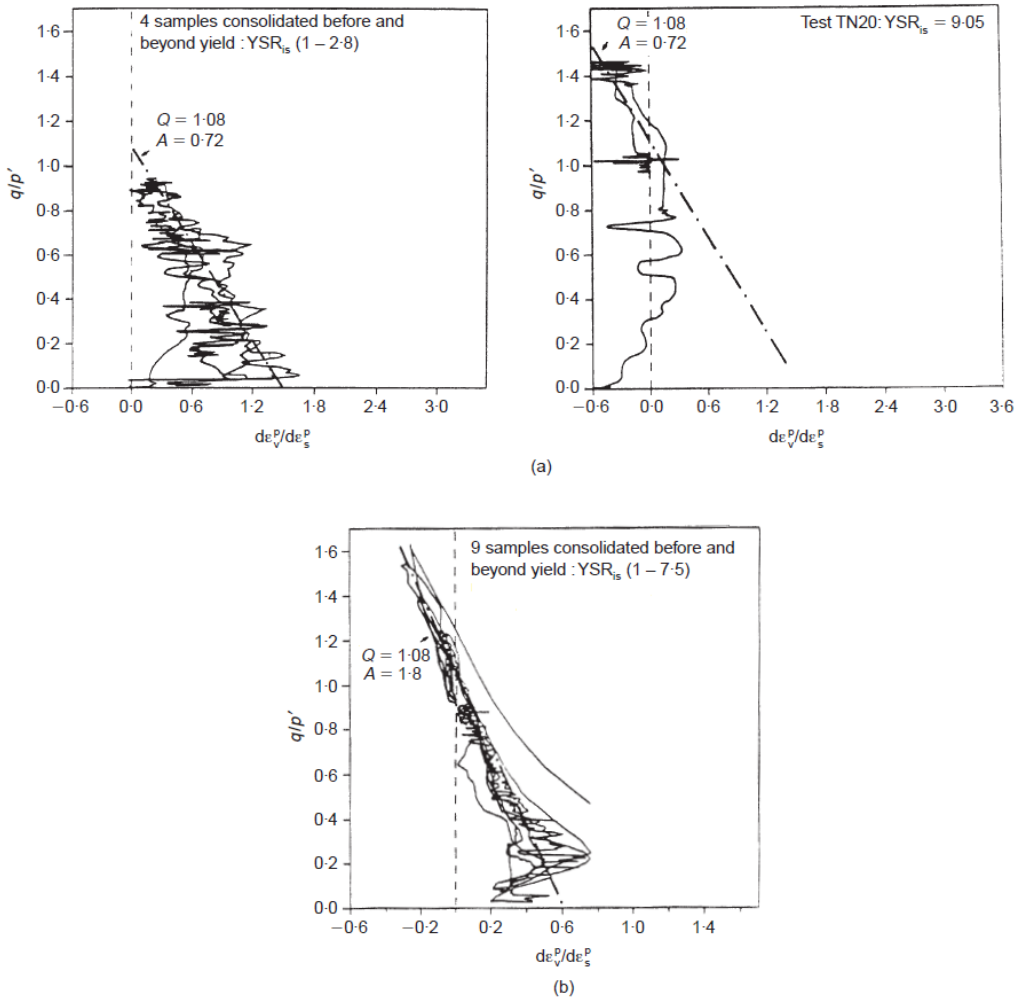

Fig. 3.37 - Flow rule for natural Pappadai clay (from Cotecchia & Chandler (1997)) (a) and (b) drained tests (c) undrained tests.

The value of the intercept Q (=M_{nat}; Cotecchia and Chandler, 1997) is 1.08 in all plots in Fig. 3.37, higher than the final stress ratio M=0.85 reached after gross yield by all the natural specimens, at a state of constant volume and strength, which may be considered a "pseudo-critical state" (Cotecchia & Chandler, 1997; 2000).

Thus, as with the reconstituted Pappadai clay, the natural clay exhibits basically frictional behaviour to large strains, although with a friction parameter M_{nat}>M.

A consequence of this behaviour is that the natural clay in the q-p' plane shows a "wet" (contractant) and a "dry" (dilatant) side, separated by a straight line of gradient M_{nat} (Fig. 3.38), differently from the reconstituted clay, in which the critical state line itself separates the two sides. The straight line of gradient M_{nat} crosses the gross yield locus about at its apex (Fig. 3.38). This behaviour is shown in idealized form in Fig. 3.39.

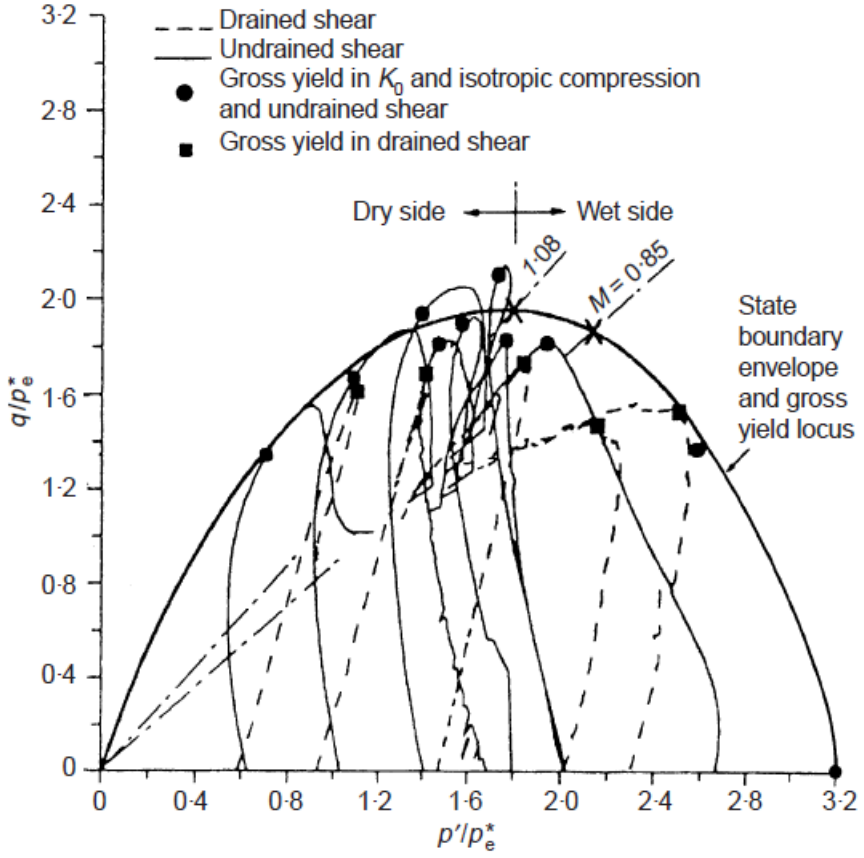

Fig. 3.38 - Pappadai clay: stress paths of the natural clay specimens consolidated to states before gross isotropic yield (from Cotecchia & Chandler (1997)).

The data in Fig. 3.37 appear to suggest that the linearity of the relationship between the stress ratio and the plastic strain increment ratio may be generally applicable, irrespective of the stress path, and that the value of A is related only to the stress path followed, and not to the consolidation state of the soil, either before or after gross yield. There is further evidence of the applicability of equation (3.29) to clays (Amorosi, 1996) and also to sands and weakly cemented rocks (Coop & Atkinson, 1993; Lagioia, 1993). The applicability of equation (3.29) to Lucera clay will be discussed in Chapter 6.

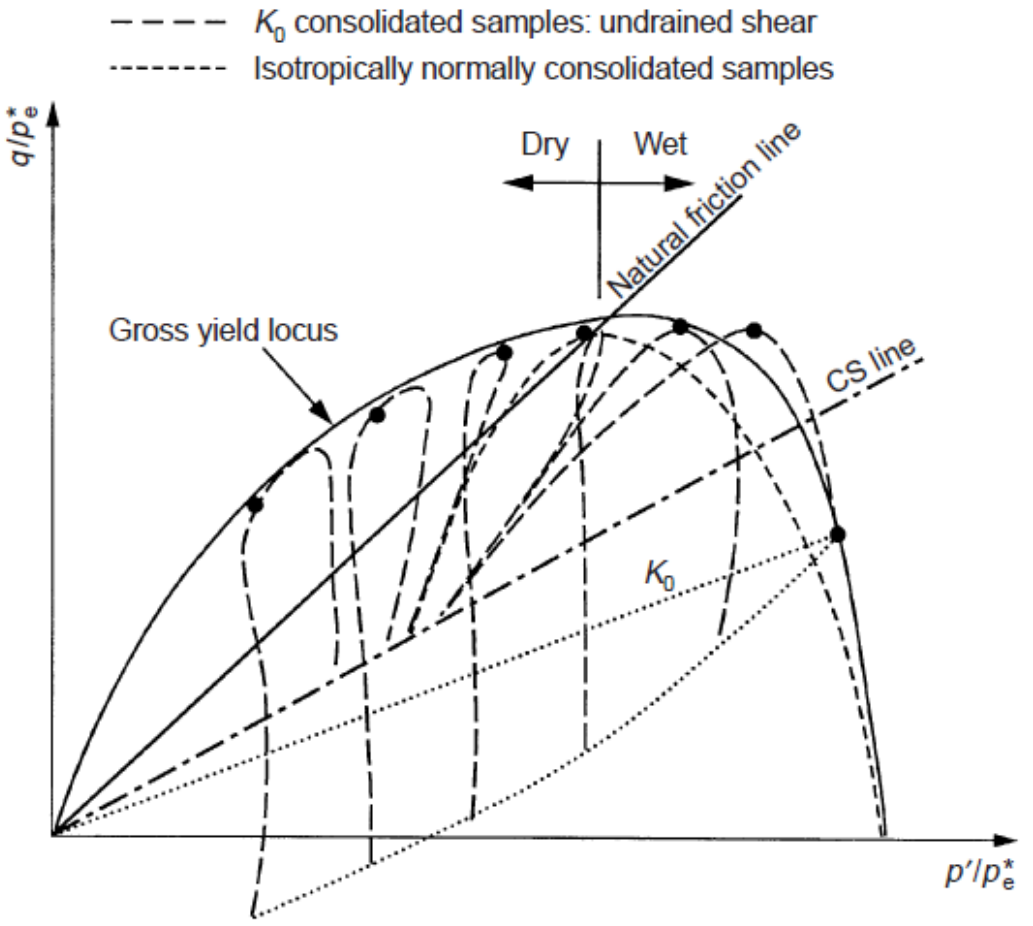

Fig. 3.39 - Idealized behaviour of natural sensitive clays.

3.5 Constitutive models for natural clays

3.5.1 The model of Rouainia and Wood (2000)

Rouainia and Wood (2000) proposed a constitutive model for natural clays formulated within the framework of kinematic hardening with elements of bounding surface plasticity. The model can be considered an extension of the Cam Clay model to account for the effects of structure in natural clays and for the plastic straining inside the SBS. As a consequence, the model can degenerate to the Modified Cam Clay by means of a proper combination of parameters.

In the following, the constitutive model will be presented in the general stress space, as formulated by the Authors. The mean pressure and the deviatoric stress are therefore given by:

$$p = \frac{1}{3} tr[\boldsymbol{\sigma}] \qquad \boldsymbol{s} = \boldsymbol{\sigma} - p\boldsymbol{I} \tag{3.30}$$

where **I** is the second-rank identity tensor and tr is the trace operator.

The model includes three elliptical surfaces (Fig. 3.40):

- the "reference" surface, which represents the behaviour of the reconstituted soil, of centre $\tilde{\alpha} = (p_c, 0)^T$ and size p_c:

$$f = \frac{3}{2M_\theta^2}(\boldsymbol{s}) : (\boldsymbol{s}) + (p - p_c)^2 - (p_c)^2 = 0 \tag{3.31}$$

where M_θ is a dimensionless scaling function which depends on the critical state stress ratio M;

- the "bubble" surface, which encloses the elastic domain, of centre $\bar{\alpha} = (p_{\bar{\alpha}}, \boldsymbol{s}_{\bar{\alpha}})^T$ in the stress space and size Rp_c:

$$f_b = \frac{3}{2M_\theta^2}(\boldsymbol{s} - \boldsymbol{s}_{\bar{\alpha}}) : (\boldsymbol{s} - \boldsymbol{s}_{\bar{\alpha}}) + (p - p_{\bar{\alpha}})^2 - (Rp_c)^2 = 0 \tag{3.32}$$

- the "structure" surface, which acts like a bounding surface, of $\hat{\alpha} = (rp_c, (r-1)\boldsymbol{\eta_0} p_c)^T$ and size rp_c:

$$F = \frac{3}{2M_\theta^2}[\boldsymbol{s} - (r-1)\boldsymbol{\eta_0} p_c]:[\boldsymbol{s} - (r-1)\boldsymbol{\eta_0} p_c] + (p - rp_c)^2 - (rp_c)^2 = 0 \quad (3.33)$$

where $\boldsymbol{\eta_0}$ is a dimensionless deviatoric tensor representing the anisotropy of the material.

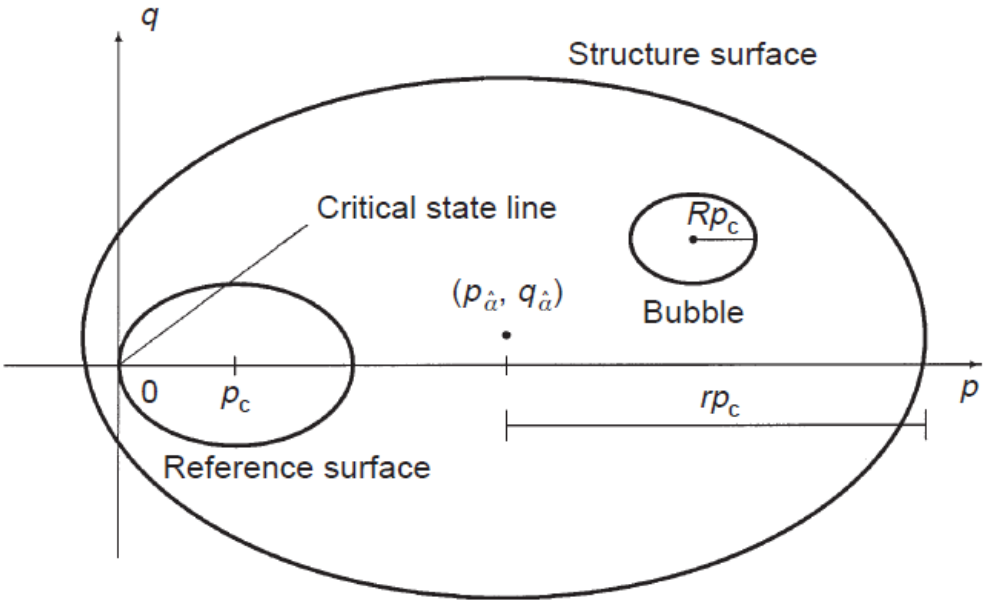

Fig. 3.40 – Bubble surface, structure surface and reference surface in the model of Rouainia and Wood (2000).

As for the Cam Clay model, an isotropic volumetric hardening rule controls the change in size of all the three surfaces (depending on p_c) occurring with $\dot{\varepsilon}_v^p$:

$$\frac{\dot{p_c}}{p_c} = \frac{\dot{\varepsilon}_v^p}{(\lambda * - \kappa *)} \quad (3.34)$$

where, as seen in the previous constitutive models, λ^* and κ^* are the slopes of the normal compression line and of the swelling line in lnv-lnp'.

For the structure surface, this isotropic hardening contribution is combined with another isotropic hardening contribution of opposite sign relating to changes in the structure parameter r, due to both volumetric and deviatoric plastic strains $\dot{\varepsilon}_v^p$, $\dot{\varepsilon}_s^p$:

$$\dot{r} = -\frac{k}{(\lambda * - \kappa *)}(r_0 - 1)\dot{\varepsilon_d} \quad (3.35)$$

where r_0 is the initial parameter for structure, k is the rate of destructuration with strain through $\dot{\varepsilon_d}$ that is a combination of the volumetric and the deviatoric plastic strain rates $\dot{\varepsilon_v^p}$, $\dot{\varepsilon_s^p}$:

$$\dot{\varepsilon_d} = \sqrt{(1-A)\dot{\varepsilon_v^p}^2 + A\dot{\varepsilon_q^p}^2} \quad (3.36)$$

It should be noted that assuming r_0=1 and η_0=0, the model reduces to the model of Al-Tabbaa and Wood (1989). If R=1, the model reduces to Modified Cam Clay (Roscoe and Burland, 1968).

The kinematic hardening law governs the translation of the bubble surface, which is the only one which translates according to the translation rule by Mroz (1967). The translation rule of the centre of the bubble, combined with the consistency condition that the current state must belong to the bubble, gives:

$$\dot{\bar{\boldsymbol{\alpha}}} = \dot{\hat{\boldsymbol{\alpha}}} + (\bar{\boldsymbol{\alpha}} - \hat{\boldsymbol{\alpha}})\left(\frac{\dot{r}}{r} + \frac{\dot{p_c}}{p_c}\right) + \frac{\bar{\boldsymbol{n}}:\left\{\dot{\hat{\boldsymbol{\sigma}}} - \hat{\boldsymbol{\sigma}}\left(\frac{\dot{r}}{r} + \frac{\dot{p_c}}{p_c}\right) + \bar{\boldsymbol{\sigma}}\frac{\dot{r}}{r}\right\}}{\bar{\boldsymbol{n}}:(\boldsymbol{\sigma_c} - \boldsymbol{\sigma})}(\boldsymbol{\sigma_c} - \boldsymbol{\sigma}) \quad (3.37)$$

where the three terms represent respectively: the shift of the centre of the structure surface, the scaling of the space inside the structure surface according to the changes in r and p_c, the translation along the line joining the conjugate points.

As for MCC, the response inside the bubble is elastic and expressed in terms of bulk and shear moduli, K and G, which are assumed to be linearly related to the pressure p:

$$K = \frac{p}{\kappa *} \qquad G = \frac{3(1-2\nu)}{2(1+\nu)}K \quad (3.38)$$

where κ* is the slope of the swelling line in lnv-lnp'.

The flow rule is identical to that of MCC and is associated with the yield function of the bubble.

The plastic modulus H necessary for the calculation of plastic strains is assumed to depend on the distance between the current stress and the conjugate point on the structure surface. The value of H equals H_c at the conjugate point when the bubble and the structure surface are in contact at the current stress.
For current stress inside the structure surface, H can be derived from the following interpolation rule:

$$H = H_c + \frac{1}{\|\bar{\boldsymbol{n}}\|^2} \frac{B p_c^3}{(\lambda * - \kappa *) R} \left(\frac{b}{b_{max}}\right)^{\psi} \quad (3.39)$$

where b is the normalized distance between current stress and conjugate stress and b_{max} is the value at the distance at a point diametrically opposite to the conjugate point. The rule interpolates between a value of H that is significantly high when $b=b_{max}$ (current state far from the structure surface) and $H=H_c$ ($b=0$, the bubble and structure surfaces are in contact), with intermediate states where $b/b_{max}<1$. B and ψ are positive stiffness interpolation parameters, as they describe the rate of decay of stiffness. In fact, increasing the value of ψ and reducing the value of B, a reduction in H is provoked with consequent increase in plastic strains.

The model requires the definition of ten parameters: κ^* initial slope of the swelling lines in (lnp'; lnv); λ^* slope of the INCL in (lnp'; lnv); ν Poisson's ratio; M slope of the critical state line; m, parameter controlling the shape of the yield surfaces in deviatoric plane; R size of the bubble; B and ψ, stiffness interpolation parameters; k rate of loss of structure; A proportion of distorsional and volumetric destructuration.
It must be noted that κ^*, λ^*, M must be referred to the reconstituted material.

In Chapter 8, the calibration of the model of Rouainia and Wood for some experimental test results from Cotecchia (1996) will be discussed.

3.5.2 The model of Kavvadas and Amorosi (2000)

The model for structured soils (MSS), based on the critical state concepts and on the MCC model, can account for the effects of structure and degradation of structure and

for the stress- and structure-induced anisotropy. The model is formulated in the general tensorial space.

MSS introduces two characteristic yield surfaces of elliptical shape (Fig. 3.41):

- the Bond Strength Envelope (BSE) of centre K(σ_K, $\mathbf{s_K}$) and size of the isotropic and deviatoric axes (α,cα) respectively:

$$F(\boldsymbol{\sigma}, \boldsymbol{\sigma_K}, \alpha) = \frac{1}{c^2}(\boldsymbol{s} - \boldsymbol{s_K}) : (\boldsymbol{s} - \boldsymbol{s_K}) + (\sigma - \sigma_K)^2 - (\alpha)^2 = 0 \qquad (3.40)$$

- the Plastic Yield Envelope (PYE), enclosing the elastic domain and fully contained inside the BSE, of centre L(σ_L, $\mathbf{s_L}$) and size of the isotropic and deviatoric axes ($\xi\alpha$,c$\xi\alpha$) respectively:

$$f(\boldsymbol{\sigma}, \boldsymbol{\sigma_L}, \alpha) = \frac{1}{c^2}(\boldsymbol{s} - \boldsymbol{s_L}) : (\boldsymbol{s} - \boldsymbol{s_L}) + (\sigma - \sigma_L)^2 - (\xi\alpha)^2 = 0 \qquad (3.41)$$

The scalar ξ, representing the ratio between the size of the PYE and the BSE, is generally very small (of the order of 0.001).

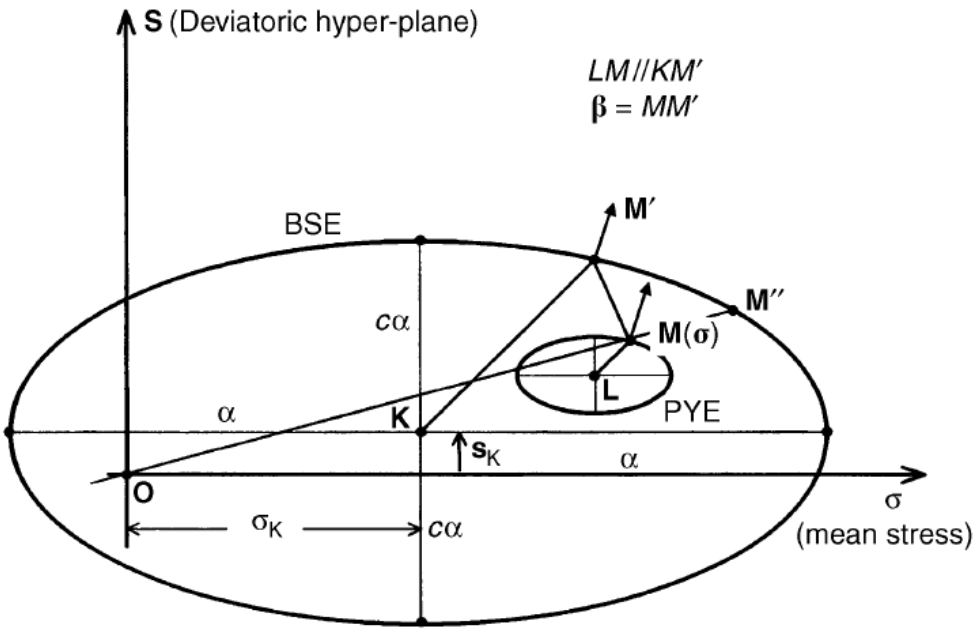

Fig. 3.41 – Characteristic surfaces of the MSS model (after Kavvadas and Amorosi, 2000).

An isotropic hardening law governs the change in size of the BSE and, consequently, of the PYE since their sizes are related by the parameter α:

$$\dot{\alpha} = \alpha \left[\left(\frac{1+e}{\lambda - \kappa} \right) \dot{\varepsilon}_v^p + \left\{ -\zeta_V e^{-\eta_v \varepsilon_v^p} \right\} \dot{\varepsilon}_v^p + \left\{ \theta_q - \zeta_q e^{-\eta_q \varepsilon_q^p} \right\} \dot{\varepsilon}_q^p \right] \qquad (3.42)$$

where λ and κ are the intrinsic compressibility parameters in v-lnp' plane, (ζ_v, η_v) are the volumetric structure degradation parameters and (ζ_q, η_q) are the deviatoric structure degradation parameters. θ_q represents permanent structure degradation (if positive) or hardening (if negative), although it is most often assumed equal to 0 (Kavvadas and Amorosi, 2000).

The isotropic hardening thus depends on both volumetric and deviatoric plastic strains and includes a negative component related to structure. According to eq.(3.42), the hardening law is made of two components: the first term in the square brackets is the positive isotropic volumetric hardening common to the MCC model and also present in all the other models discussed so far; the other two terms are representing the negative isotropic hardening, both volumetric and deviatoric, due to degradation of structure. In particular, the second term represents the volumetric-strain-induced structure degradation and the third term defines the deviatoric-strain-induced structure degradation. The rate of structure degradation is defined by an exponential damage type form, which expresses a decay at large plastic strains, with a rate depending on the positive parameters η_v and η_q. Positive values of parameters ζ_v and ζ_q tend to reduce the size of the BSE (and of the PYE) with increasing volumetric and deviatoric strains respectively.

Eq.(3.42) reduces to the hardening rule of MCC if all the structure degradation parameters are zero.

The kinematic hardening rule of the model governs the translation of the characteristic surfaces, BSE and PYE, by controlling the motion of their centres K and L, thus describing the evolution of anisotropy with plastic strains.

With reference to the centre K of the BSE assumed to be on the isotropic axis, when the current state is inside the BSE the centre K moves along a radial path passing through the origin:

$$\dot{\boldsymbol{\sigma}}_{\boldsymbol{K}} = \frac{\dot{\alpha}}{\alpha}\boldsymbol{\sigma}_{\boldsymbol{K}} \tag{3.43}$$

If the current state is on the BSE, the centre K moves according to the following equation:

$$\dot{\boldsymbol{\sigma}}_{\boldsymbol{K}} = \frac{\dot{\alpha}}{\alpha}\boldsymbol{\sigma}_{\boldsymbol{K}} + \psi\frac{\dot{\alpha}}{\alpha}\left(\boldsymbol{s} - \chi\frac{\sigma}{\sigma_K}\boldsymbol{s}_{\boldsymbol{K}}\right) \tag{3.44}$$

in which the second term represents the deviation from radial direction, that is a change in anisotropy. χ represents the angle of deviation from the radial stress path, ψ is the rate of movement of the BSE in stress space, $\mathbf{b_K}=\mathbf{s_K}/\sigma_K$ is the "primary anisotropy tensor", which corresponds to the tangent of the angle of segment OK with the isotropic axis (Fig. 3.41).

With reference to the centre L of the PYE, when the current state is on the BSE, i.e., the two surfaces are in contact at the point corresponding to current state, the position of L depends on the position of K, according to equation:

$$\frac{\boldsymbol{\sigma} - \boldsymbol{\sigma}_{\boldsymbol{L}}}{\xi\alpha} = \frac{\boldsymbol{\sigma} - \boldsymbol{\sigma}_{\boldsymbol{K}}}{\alpha} \Rightarrow \boldsymbol{\sigma}_{\boldsymbol{L}} = (1-\xi)\boldsymbol{\sigma} + \xi\boldsymbol{\sigma}_{\boldsymbol{K}} \tag{3.45}$$

For current states inside the BSE, the current state M (Fig. 3.41) moves towards the conjugate point M', such that the normal vectors to the surfaces at these points are parallel (Mroz, 1967):

$$\dot{\boldsymbol{\sigma}}_{\boldsymbol{L}} = \frac{\dot{\alpha}}{\alpha}\boldsymbol{\sigma}_{\boldsymbol{L}} + \dot{\mu}\boldsymbol{\beta} \tag{3.46}$$

where $\boldsymbol{\beta}=\overrightarrow{\mathrm{MM'}}$ and the factor m is determined from the consistency condition that the stress point remains on the PYE ($\dot{\mathrm{f}} = 0$).

Elastic behaviour characterises the material inside the PYE. In critical state models, such as those seen so far, both the bulk K and the shear moduli G are assumed to be pressure dependent; in this case, elasticity reveals to be non-conservative (Houlsby, 1985). Hyper-elasticity can be used in this model, as it preserves the pressure dependency of K and G and maintains the conservative nature of elasticity.

Moreover, hyper-elasticity introduces coupling between the volumetric and the deviatoric components in stress-strain behaviour:

$$\dot{\sigma} = p_r e^{\frac{\varepsilon_v^e}{\kappa^*}} \left\{ \frac{1}{\kappa^*} \left[1 + \left(\frac{3\alpha^*}{2\kappa^*} \right) \left(\varepsilon_q^e \right)^2 \right] \dot{\boldsymbol{\varepsilon}}_{\boldsymbol{v}}^{\boldsymbol{e}} + \left(\frac{2\alpha^*}{\kappa^*} \right) (\boldsymbol{e}^{\boldsymbol{e}} \cdot \dot{\boldsymbol{e}}^{\boldsymbol{e}}) \right\} \qquad (3.47)$$

$$\dot{s} = p_r e^{\frac{\varepsilon_v^e}{\kappa^*}} \left\{ \left(\frac{2\alpha^*}{\kappa^*} \right) \boldsymbol{e}^{\boldsymbol{e}} \dot{\varepsilon}_v^e + 2\alpha^* \dot{\boldsymbol{e}}^{\boldsymbol{e}} \right\}$$

where κ^* is the slope of the swelling line of the reconstituted material in the lnv-lnp' plane.

The flow rule is associated and is the same as for MCC model.

For material states inside the BSE (current state M), the plastic modulus H can be derived from the following interpolation rule:

$$H = \quad H'' + |H''| \left\{ \left[1 - \left(\frac{\delta}{\delta_0} \right) \right]^{-\gamma} - 1 \right\} \qquad (3.48)$$

where H'' is the value of the plastic modulus at point M'' (Fig. 3.41), in which vector $\overrightarrow{\mathrm{OM}}$ intersects the BSE; δ is the normalized length of MM'' and δ_0 is the value of d at the initiation of yielding. The rule interpolates between $H=\infty$ (when the current state reaches the PYE, $\delta/\delta_0=1$) and $H=H''$ (when the stress state reaches the BSE at point M'', $\delta=0$), with intermediate stages where $\delta/\delta_0<1$. $\gamma>0$ is the rate of variation of H in the range $[\infty; H'']$. The value of H'' can be determined from the consistency condition that the current state is on the BSE $\dot{\mathrm{F}} = 0$.

The model requires twelve parameters: κ^* slope of the swelling line in (lnp'; lnv); G/K or α^* elastic shear parameter for poro- or hyper-elasticity respectively; λ^* intrinsic compressibility; c dimension of the minor axis of the BSE; ζ_v, η_v, ζ_q, η_q isotropic hardening parameters; χ, ψ kinematic hardening and primary anisotropy parameters; γ interpolation law for the plastic modulus H; ξ size of the PYE.

The calibration of the model on the experimental data of Pappadai clay carried out by Amorosi et al. (2001) will be discussed in Chapter 8.

3.5.3 The model of Baudet and Stallebrass (2004)

This model, also known as S3-SKH (*Sensitivity Three Surfaces Kinematic Hardening*) is based on the previously presented model of Stallebrass and Taylor (1997) for reconstituted clays, which is extended to model the behaviour of natural clays. To simulate structure, the model refers to the Sensitivity Framework and uses a single parameter, sensitivity, to represent current structure, plus an expression to describe the degradation of structure or sensitivity with strain.

The model introduces three surfaces, a history and a yield surface lying within a natural state boundary surface, called "sensitivity surface" (Fig. 3.42). According to the Sensitivity Framework (Cotecchia and Chandler, 2000), the natural state boundary surface and the intrinsic surface have the same shape, that is elliptical as for MCC.
The three yield surfaces, having sizes related by constant ratios, are:

- the sensitivity surface, of radius sp'_0 and centre (sp'_0; 0), representing the intersection of the natural bounding surface with an elastic wall:

$$\left(p' - sp'_0\right) + \frac{q^2}{M^2} = (sp'_0)^2 \qquad (3.49)$$

where s is the current sensitivity;

- the history surface, of radius Tsp'_0 and centre (p'_a, q_a), which describes the effect and defines a limit to the influence of recent stress history:

$$\left(p' - p'_a\right) + \frac{(q - q_a)^2}{M^2} = T^2(sp'_0)^2 \qquad (3.50)$$

- the yield surface, of radius $TSsp'_0$ and centre (p'_b, q_b), which delimits the elastic domain:

$$\left(p' - p'_b\right) + \frac{(q - q_b)^2}{M^2} = T^2S^2(sp'_0)^2 \qquad (3.51)$$

As suggested by Gens and Nova (1993), the hardening rule is made up of two terms. The first term describes an isotropic volumetric hardening identical to that of MCC (the same as Al-Tabbaa and Wood (1989) and Stallebrass and Taylor (1997)), which

controls the hardening occurring with $\delta\varepsilon_v^p$ of all the three surfaces, which have dimensions related by p'_0 (see equation (3.13)).

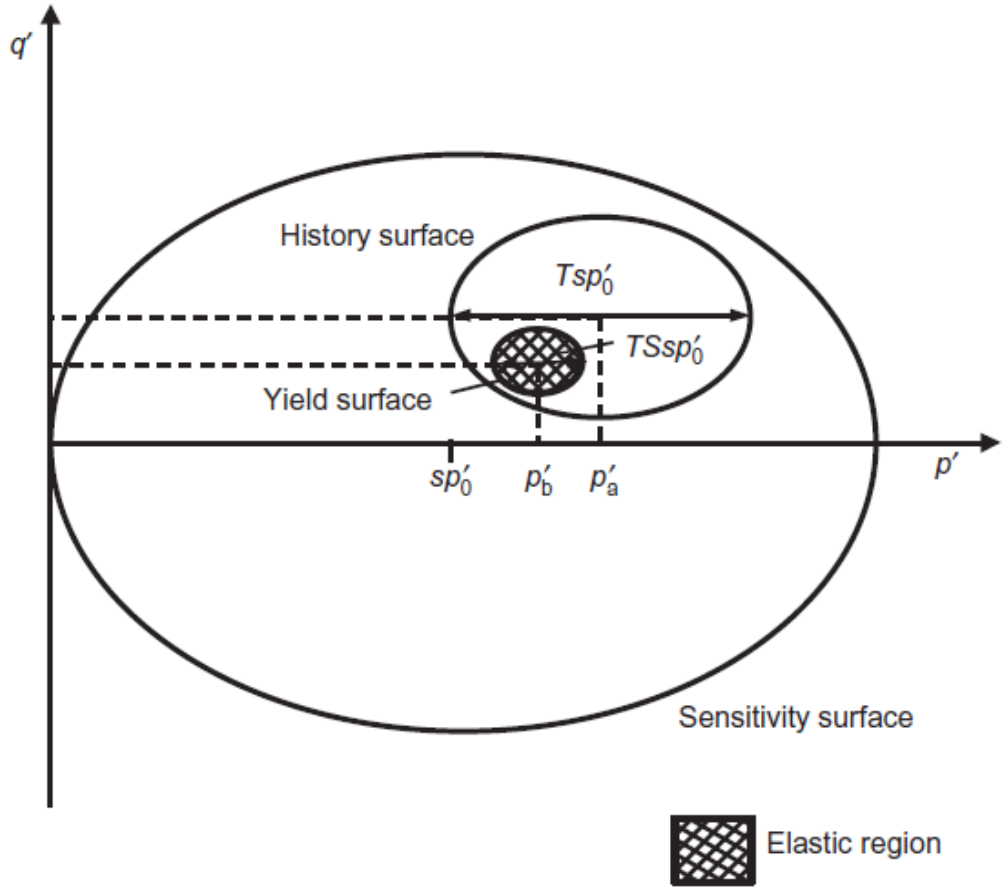

Fig. 3.42 – Diagram showing the three surfaces of the S3-SKH model in triaxial stress space (after Baudet and Stallebrass, 2004).

The second term is the destructuration law, which describes the change in size of the sensitivity surface due to the reduction in sensitivity s; since all the surfaces have a size dependent on s, this law actually involves all of them.

$$\dot{s} = -\frac{k}{(\lambda - \kappa)}(s - s_f)\dot{\varepsilon_d} \qquad (3.52)$$

where λ and κ refer to the reconstituted material, k controls the rate of destructuration and s_f is the ultimate sensitivity. When $s=s_f$, destructuration stops independently of k. In this model, the damage strain accounts for the entire effects of both volumetric and deviatoric plastic strains on destructuration, differently from Rouainia and Wood (2000) and Kavvadas and Amorosi (2000):

$$\dot{\varepsilon_d} = \sqrt{\dot{\varepsilon_v^p}^2 + \dot{\varepsilon_q^p}^2} \qquad (3.53)$$

The kinematic hardening of the yield and history surfaces involves the same translation rules of model 3-SKH (Mroz (1967); Stallebrass (1990); Stallebrass and Taylor (1997); see Fig. 3.11): the kinematic surfaces move when the current stress state lies on one of the surfaces and the load increment is in the range $\pm 90°$ to the outward normal to the surface. Similarly to model 3-SKH, the translation rules of S3-SKH allow the model to provide a memory of previous loading history when the loading direction is changed.

As for the model 3-SKH of Stallebrass and Taylor (1997), when the current stress state lies within the yield surface, the deformation of the soil is isotropic and elastic.

The flow is associated on all the three surfaces and the flow rule, as for model 3-SKH, is that of MCC.

As in model 3-SKH, the plastic modulus is given by $h=h_0+H_1+H_2$, where h_0 is the value on the yield surface (derived for the case in which all the yield surfaces are in contact), H_1 and H_2 are interpolation functions of the position of the history and yield surfaces respectively:

$$h_0 = \left(\frac{p' - p'_b}{\lambda - \kappa}\right)\left[p'(p' - p'_b) + q\frac{(q - q'_b)}{M^2}\right] * \left[1 - \frac{k}{p' - p'_b}\left(1 - \frac{s_f}{s}\right)\sqrt{(p' - p'_b)^2 + \left(\frac{q - q'_b}{M^2}\right)^2}\right] \quad (3.54)$$

$$H_1 + H_2 = \left[\frac{1}{\lambda - \kappa}\right]\left[\left(\frac{b_1}{b_{1max}}\right)^{\psi}(sp'_0)^3 S^2 + \left(\frac{b_2}{b_{2max}}\right)^{\psi}(sp'_0)^3\right] \quad (3.55)$$

where b_1 and b_2 have the same meaning as for model 3-SKH, the exponent ψ controls the rate of decay of stiffness with stress change and is the same for H_1 and H_2.

The model requires the same parameters of 3-SKH (eight parameters) and three structure parameters: s_0, representing the initial sensitivity or initial degree of structure; s_f, ultimate sensitivity (not necessarily 1); k rate of destructuration with plastic strains. For simplicity, the model does not account for the effects of structure on stiffness (Cafaro and Cotecchia, 2001) and the elastic part of the swelling line has the same slope as for the reconstituted soil; the Authors explain that the stiffer behaviour of natural soil due to structure is displayed through plastic deformations. However, the model can incorporate the law proposed by Viggiani and Atkinson (1995) for the calculation of G_0.

3.5.4 The model of Koskinen et al. (2002)

The model, also known as S-CLAY1S, is an extension of model S-CLAY1 (Wheeler, 1997; Näätänen et al., 1999; Wheeler et al., 2003) realized to include the effects of destructuration and change of anisotropy observed in natural clays (Gens and Nova, 1993). In fact, model S-CLAY1 is seen to successfully predict the behaviour of

reconstituted clays which present an important initial and a strain induced anisotropy, but in which bonding and destructuration are absent (Koskinen et al., 2002b).

The model includes two yield surfaces (Fig. 3.43), both elliptical and with the same orientation. The yield surface of the natural soil is identical to that of S-CLAY1 (eq.3.22). As bonding provides additional resistance to yielding, the yielding behaviour of an equivalent "unbonded" soil is represented by an intrinsic yield surface (Gens and Nova, 1993), of size p'_{mi}, smaller than the yield curve for the natural soil, of pize p'_{m}:

$$p'_m = (1 + x)p'_{mi} \qquad (3.56)$$

where x is the parameter defining the current degree of bonding.

As in model S-CLAY1, the flow rule is associated. The behaviour inside the largest yield surface is isotropic elastic, identically to S-CLAY1; the smaller yield surface is a reference and target surface for the largest one.

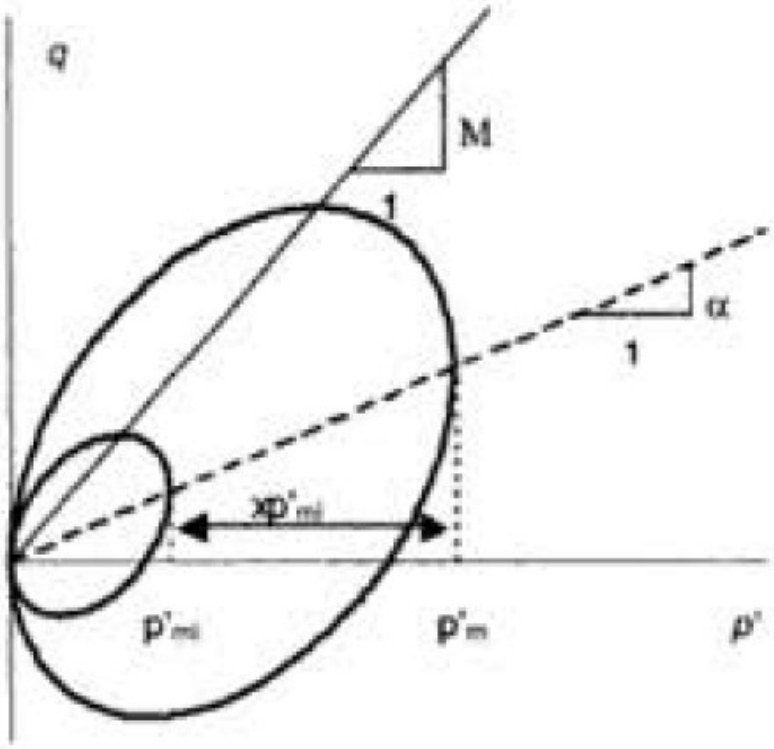

Fig. 3.43 – Yield curves of S-CLAY1S model (after Koskinen et al., 2002a).

S-CLAY1S incorporates three hardening laws. The first is the isotropic hardening law of the intrinsic yield curve, driven by plastic volumetric strains, as in S-CLAY1:

$$dp'_{mi} = \frac{vp'_{mi}d\varepsilon_v^P}{(\lambda_i^* - \kappa_i^*)} \qquad (3.57)$$

where λ_i and κ_i are the slope of the INCL* and swelling line for the reconstituted clay in plane (lnp'; v). It should be noticed that this law also induces isotropic hardening to the "structure" yield curve, the size of which depends on the size of the intrinsic yield curve p'_{mi} (see eq.3.56).

The rotation of the two yield curves is controlled by the rotational hardening law and depends on both volumetric and deviatoric plastic strains; the law is identical to that of S-CLAY1 and can be written as:

$$d\alpha = \mu\left[\left(\frac{3}{4}\eta - \alpha\right)\langle d\varepsilon_v^p\rangle + \beta\left(\frac{\eta}{3} - \alpha\right)\left|d\varepsilon_d^p\right|\right] \qquad (3.58)$$

Similarly to model S-CLAY1, μ is the absolute rate of change of α with $d\varepsilon^p$ and β controls the relative effectiveness of volumetric and deviatoric plastic strains in rotating the yield curve.

The size of the structure yield surface changes with both volumetric and deviatoric plastic strains, independently from the size of the intrinsic yield curve, according to an isotropic hardening law:

$$dx = a\left[(0-x)\left|d\varepsilon_v^p\right| + b(0-x)\left|d\varepsilon_d^p\right|\right] = -ax\left[\left|d\varepsilon_v^p\right| + b\left|d\varepsilon_d^p\right|\right] \qquad (3.59)$$

in which a and b are additional soil parameters: a is the absolute rate of destructuration, b represents the relative effectiveness of $d\varepsilon_v^p$ and $d\varepsilon_d^p$ in destroying bonding. The use of the modulus operator ensures that the contribution of destructuring to isotropic hardening is negative. With the same aim, Rouainia and Wood (2000) and Baudet and Stallebrass (2004) use the squares of $d\varepsilon_v^p$ and $d\varepsilon_d^p$.

The model includes nine parameters, six of which are identical to S-CLAY1: κ_i initial slope of the intrinsic swelling lines in (lnp'; v); λ_i slope of the intrinsic INCL in (lnp'; v); M slope of the critical state line representing the ultimate failure conditions in (p'; q); G (or ν') elastic shear modulus; β and μ, parameters of the rotational hardening law; a

and b, destructuration parameters; x_0, initial value of bonding. Three initial state parameters are required: stress state and specific volume, p'_{m0}, initial size of the structure yield curve, and α_0, inclination of the yield curves.

Compared to model S-CLAY1, S-CLAY1S gives better predictions for natural soft clays, as the rate at which destructuration progresses and hence the gradient of the post-yield compression curves varies with the stress path and with the amount of degradation that has already occurred. S-CLAY1 could not account for different rates of destructuration on different stress paths.

4 GEOLOGICAL FEATURES OF PAPPADAI AND LUCERA CLAYS

4.1 Introduction

The present chapter describes the geological origins, the mineralogical composition and the basic geotechnical properties of the two tested clays, Pappadai and Lucera clays.

Both the clays studied are natural stiff clays part of the Sub-Apennine Blue Clay formation. Pappadai clay comes from the Pappadai valley, located in the Montemesola basin near Taranto, in Southern Apulia in the South of Italy (Fig. 4.1). This valley was the subject of intensive field investigations for the construction of a dam across the valley (V. Cotecchia et al., 1993) and the lithological profile of the clay deposit was examined in great detail. Undisturbed samples taken at various depths in several boreholes (locations indicated in Fig. 4.2) provided an indication of the variation of properties within the deposit (Cotecchia, 1996), as will be later described in this chapter.

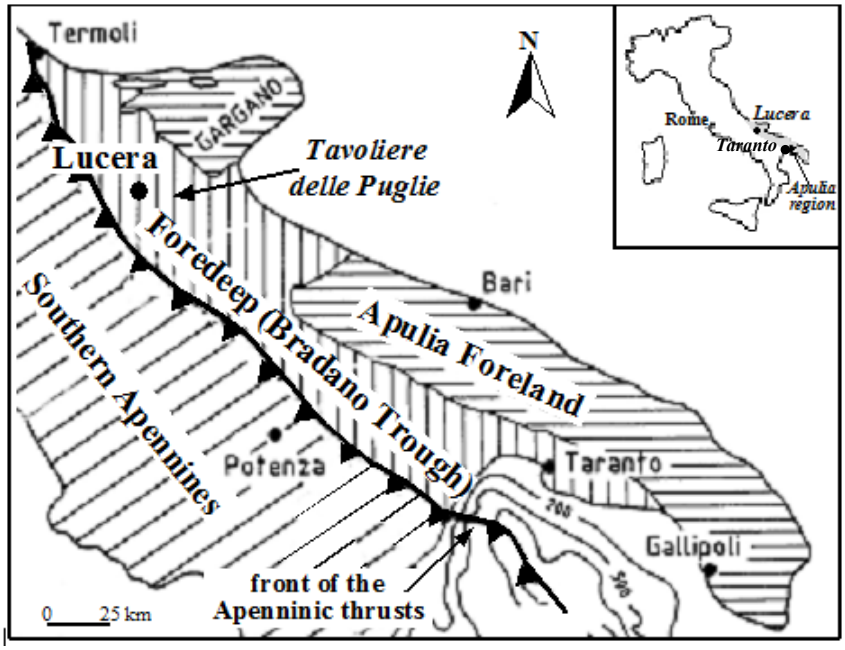

Fig. 4.1 - Simplified geological scheme of Southern Italy.

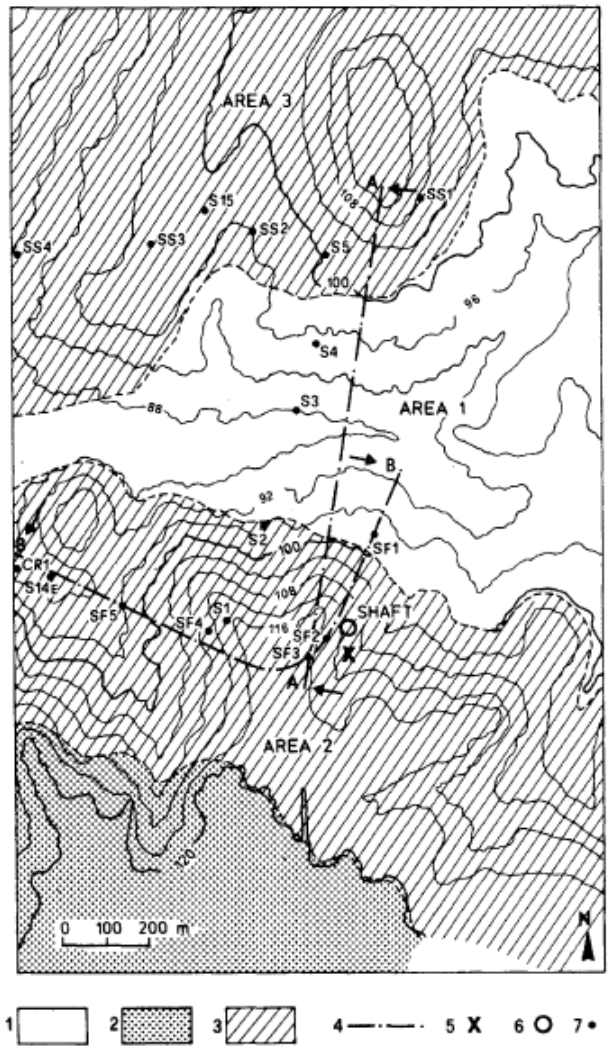

Fig. 4.2 - Schematic geological map of Pappadai area (after Cotecchia et al., 1995) with indication of boreholes. Key: 1, alluvium; 2, Quaternary calcarenites; 3, Pappadai clay; 4, lines of section; 5, Borehole A; 6, shaft; 7, individual boreholes.

Lucera clay outcrops on the hilly slopes of the town of Lucera, in Northern Apulia (Fig. 4.1**Errore. L'origine riferimento non è stata trovata.**). In the last century, the stiff clayey slopes of this hill have been subjected to intensive quarry excavation, which changed their morphology and severely affected their stability.

Two of these quarries are located at the toe of the northern slope of Lucera hill, as shown in Fig. 4.3; the Fiamma quarry is still active, while the slope excavation at the Ilca quarry was stopped by the end of seventies (Santaloia et al., 2004). To investigate instability processes involving the slope below the hospital, where the Ilca quarry was located (at the toe), the cut slope (Fig. 4.3) has been analysed during different research programmes supported both by PRIN (2001-2003) and CNR-GNDCI (2002). Several continuous coring boreholes, of depth ranging between 10 and 75 m, were drilled throughout the slope. Some of these boreholes are located on the map in Fig. 4.3.

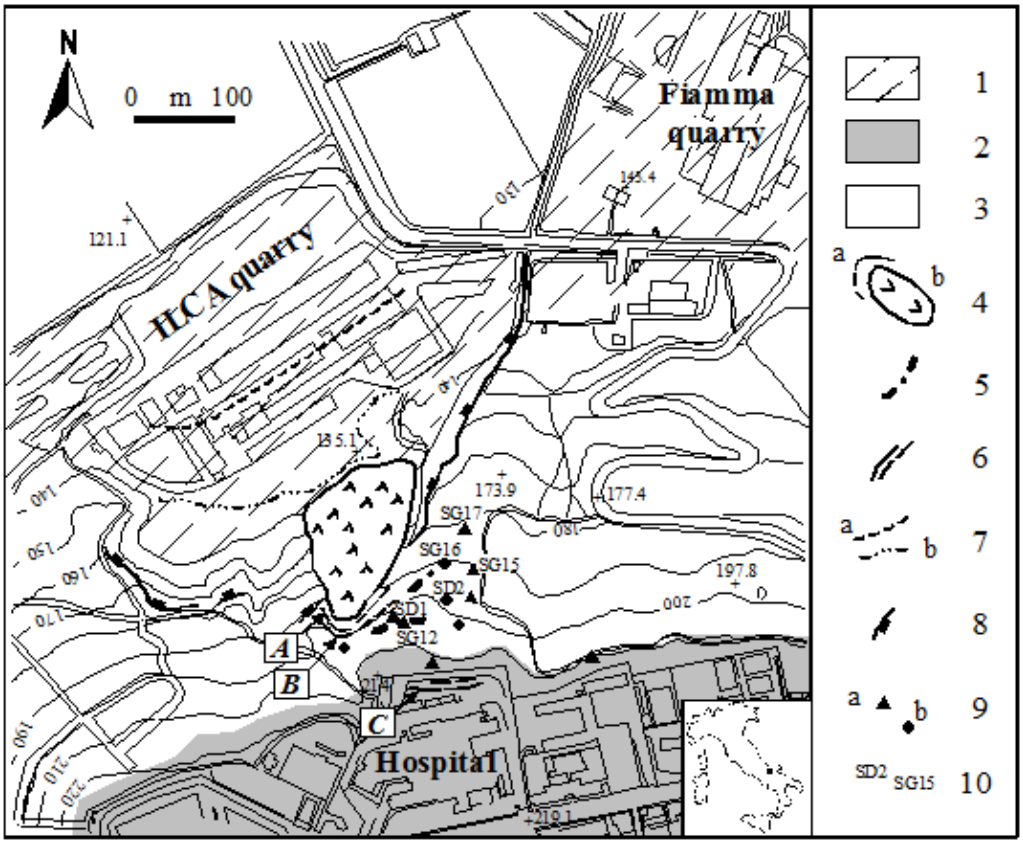

Fig. 4.3 - Geological-geomorphological map of the northern slope of Lucera hill, showing also some of the field investigations carried out in the area. Key: 1) fill of the quarry, 2) terraced alluvial deposits, 3) Sub-Apennine Clays, 4) landslide (a -crowns of landslides A and B; b – body of landslide A), 5) fractured zones, 6) flexures and deep cracks related to landslide C in 1998, 7) foot of the slope (a-1954, b-1975), 8) quarry front, 9) boreholes drilled in the area (a – inclinometer, b – piezometer), 10) the initials of the continuous coring boreholes, their lithological logs are shown in Fig. 4.8.

The geotechnical properties and the mechanical behaviour of some natural clayey undisturbed samples, taken in the boreholes and discussed by Amorosi et al. (2003), Santaloia et al. (2004) and Lollino et al. (2005), are also summarised later in this chapter.

The first failure of the slope, landslide A in Fig. 4.3, was triggered by the significant morphological changes resulting from the excavation works. The slope failure was delayed with respect to the excavation works, stopped some years before the landslide event, due to the consolidation processes, as demonstrated by means of finite differences analyses (Amorosi et al., 2003; Santaloia et al., 2004; Lollino et al., 2005). In 1998, the retrogression and widening of the sliding process occurred with the development of landslide C (Fig. 4.3). For this body, the slope collapse occurred in the long term, i.e., about twenty years after excavation, due to progressive failure.
The progressive failure mechanism is generally influenced by several factors, such as the soil stiffness, the in-situ permeability, the change of slope geometry, the initial distribution of the pore pressures within the slope, the initial in-situ stress state, the suctions at ground level and the drainage paths (Chandler, 1984; Potts at al., 1997).

4.2 Geological background and sampling

The Sub-Apennine Blue Clays are marine deposits of widespread distribution in Southern Italy, that were deposited in two sedimentary cycles (Del Prete and Valentini, 1971). The lower-cycle blue clays are of Lower or Middle Pleistocene age and are found in basins within the Apennine Chain, where the tectonical activity has been responsible for significant disturbance in situ. Upper-cycle blue clays occur in the Bradano Trough, which is the Apennine foredeep located between the Southern Apennines and the Apulia foreland (Fig. 4.1), and also on the Apulian Cretaceous platform to the east. They were deposited during a marine transgression in Upper Pliocene-Lower Pleistocene times, following the formation of the Bradano Trough during the Upper Pliocene (Ogniben, 1969). These upper-cycle clays differ from those of the lower-cycle, typically having higher proportions of clay and being far less disturbed tectonically.

In the south-eastern part of the Bradano Trough and in Apulia the upper-cycle Blue clays lie on a dolomite basement of Cretaceous age. Directly overlying the Cretaceous bedrock are the Gravina Calcarenites, fine to coarse weakly cemented sands, on which the Sub-Apennine blue clays deposited. The blue clays are composed of sediments derived from the erosion of Apennine rocks and were deposited continuously throughout the upper-cycle transgression. Subsequently, uplift resulted in a regression, and, where the uplift was more rapid, sands and conglomerates (i.e., Monte Marano sands, Irsina conglomerates) were deposited (Fig. 4.4).

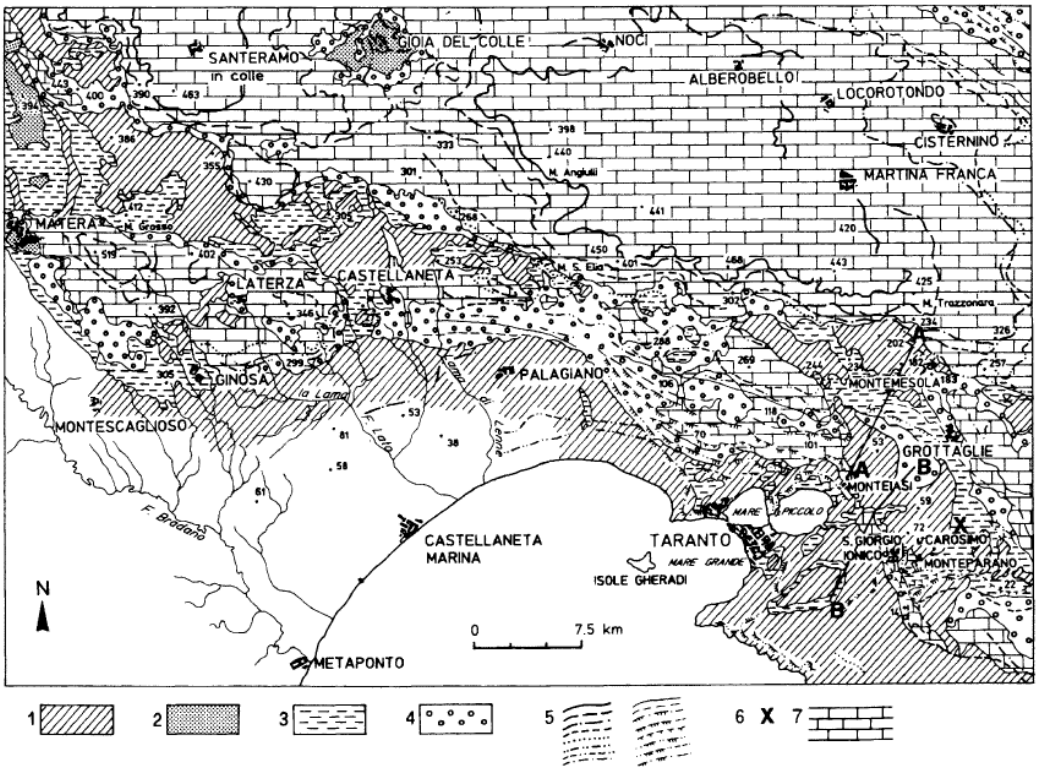

Fig. 4.4 - Geology of the study area, showing the Bradano Trough and Pleistocene marine terraces (from Ciaranfi et al. 1988). Key: 1, Middle-Upper Pleistocene calcarenites; 2, Monte Marano Sands; 3, upper-cycle blue clays; 4, Gravina Calcarenites; 5, palaeocoastline; 6, location of Pappadai; 7, Cretaceous limestone (after Cotecchia and Chandler, 1995).

This marks the start of the regression and the top of the sedimentary cycle, though still within the Lower-Middle Pleistocene, with an age of 1.0-1.1 million years. At this time

some of the depositional basins, notably those of Taranto and Montemesola, were still submerged, and the sands and conglomerates were not deposited. This regression eventually resulted in the erosion of a sequence of Upper Pleistocene marine terraces on which calcarenites were deposited.

Ciaranfi et al. (1971) show that the depositional conditions in the Montemesola basin at the time of deposition of Pappadai clay were those of a protected and still sea, resulting in a reducing environment at the sea bed. The presence in the clay of authigenic sulphates (greigite and pyrite; Cotecchia, 1996) confirms that there was organic matter present in a reducing environment with little water circulation at the time of deposition. The deposition of Pappadai clay thus occurred in comparatively deep and still marine reducing conditions.

A continuously-cored deep borehole (borehole A, Fig. 4.2) allowed for a detailed reconstruction of the lithological profile (Cotecchia, 1996) and for samples to be taken at various depths to identify the variation of the properties within the deposit. The reconstruction of sections AA and BB of Fig. 4.5 shows that the Gravina Calcarenites outcrop at a depth of 50 m below ground level, that is the base for a thick layer of grey clay. Between depths 33-25 m the grey clay is particularly uniform, massive and stiff. Marked horizontal laminations can be seen, the occurrence of which can be correlated to a quiet deposition environment with little water circulation. The clay in this layer exhibits comparatively uniform mechanical properties (Cotecchia, 1996). With decreasing depth, around 20 m depth, a gradual lack of uniformity and increasing oxidation is seen as the ground surface is approached, as shown by a gradual colour change of the clay from grey to yellow-brown.

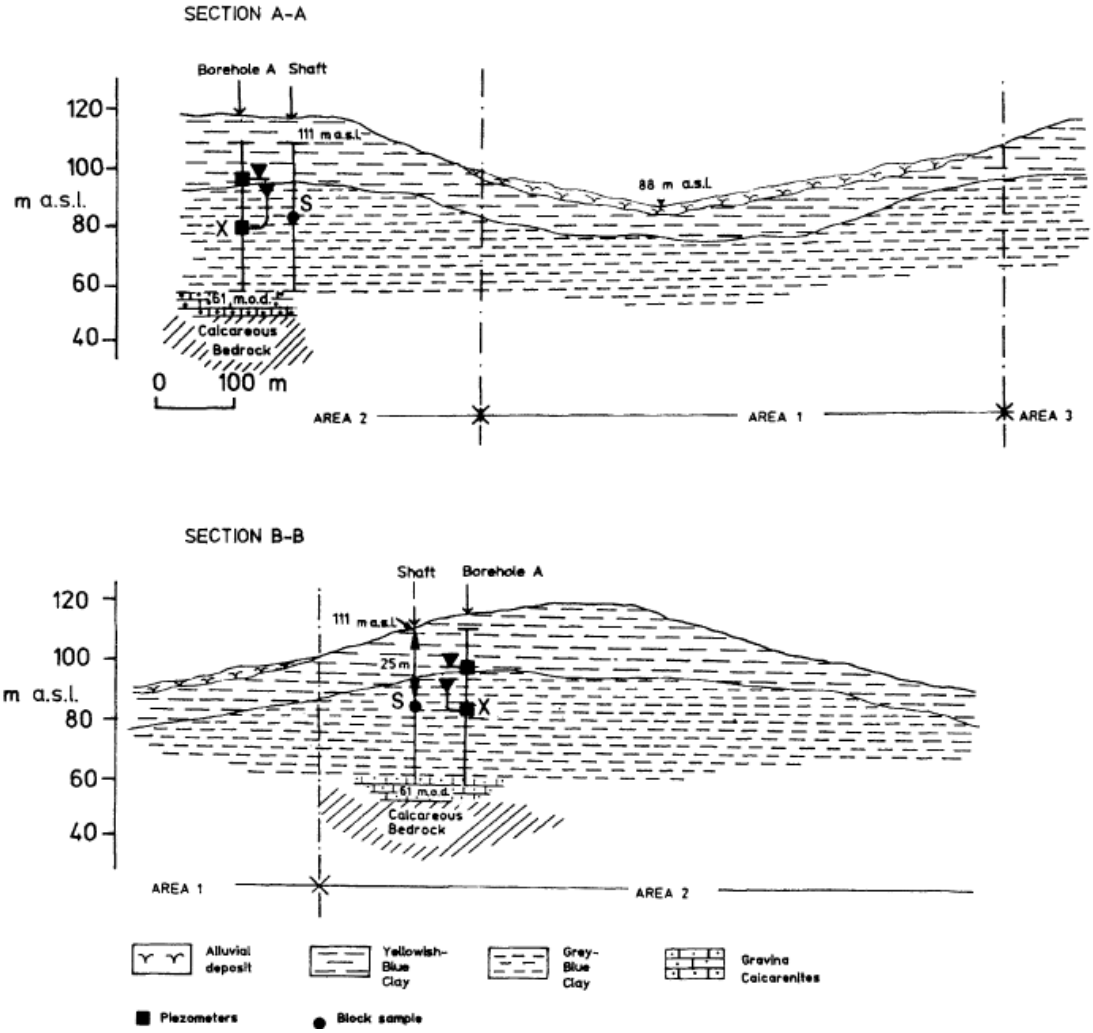

Fig. 4.5 - Sections A-A and B-B, see Fig. 4.2.

In a shaft excavated close to borehole A, two high quality undisturbed block samples of clay were taken at about 25 m depth (Fig. 4.6). One of them was used by Cotecchia (1996) for an intensive mechanical testing programme; the other one was stored in a high humidity cellar and used for the mechanical and microstructural tests part of this research, as will be discussed in the following.

Fig. 4.6 - Block sampling of Pappadai clay.

The soils forming the Lucera hill are also part of the Sub-Apennine Blue Clay Formation. In the area studied, this marine succession is overlain by alluvial sands and conglomerates (terraced alluvial deposits of Pleistocene age; Gallicchio et al., 2003) which lie at the top of Lucera hill (Fig. 4.7). The bedding of these geological formations is either sub-horizontal or it dips gently towards NE (Fig. 4.7).

As resulted from both the field surveys carried out in the area and the analysis of the soil corings and their lithological profiles (Fig. 4.8), the Sub-Apennine Blue Clays in this area are mainly represented by stiff and silty clays, grey in colour, interbedded with sandy and silty strata. Moreover, the upper part of these clays, about 6 m thick, is often weathered, yellow in colour and with a higher silty and sandy content (Amorosi et al., 2003; Santaloia et al., 2004).
In detail, Lucera clay belongs to the grey lower succession of the Sub-Apennine Blue Clays.

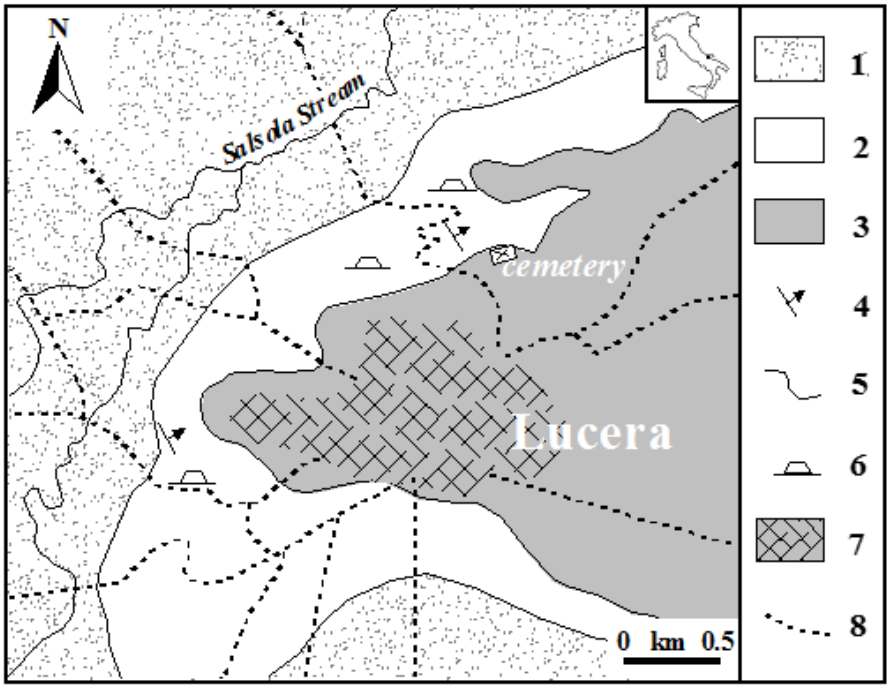

Fig. 4.7 - Schematic geological map of Lucera area (after National Geological Map, modified). Key: 1) Alluvial deposits, 2) Terraced alluvial deposits, 3) Sub-Apennine Clays, 4) strata attitude, 5) stratigraphic contact, 6) quarry, 7) Lucera town, 8) road.

Two undisturbed block samplings of the grey clay were carried out at the front of the active Fiamma quarry (Fig. 4.9). The first block sample was taken by Longo (2003) at almost 170 m a.s.l.; then, a second sampling was made in February 2016 (Fig. 4.10). Two undisturbed block samples of around 40 cm side were taken by means of a hand operated chain-saw (Fig. 4.10) from the quarry wall at a depth of around 40 m below ground level, corresponding to almost 150 m a.s.l.. Soon after sampling, the block samples were wrapped in cling film and waxed. Once in the laboratory, layers of clay a few cm thick were removed from the sides of the blocks. One block was again wrapped in cling film, waxed and stored in an underground cellar at low temperature and high humidity. The other block was first subjected to a suction test using the filter paper technique, as described in Chapter 5. Then, prisms were cut from it to be used for trimming oedometer and triaxial specimens.

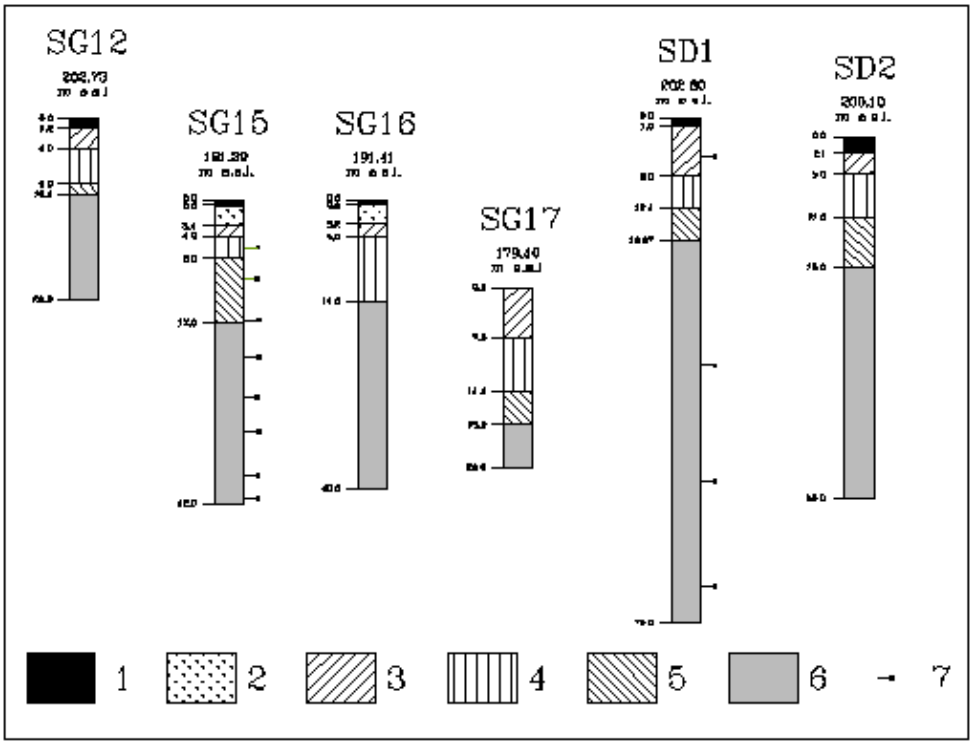

Fig. 4.8 - Lithological profiles of the continuous coring boreholes drilled within the northern slope of the town of Lucera, lying below the hospital. Key: 1) Top soil and/or fill, 2) Sandy-gravely landslide block, 3) Yellow sandy silt with sandy levels, locally pebbly and/or clayey; Sub-Apennine Clay Formation: 4) Yellow sandy-clayey silt or sandy clays with grey sandy or silty levels, 5) Grey silty-sandy clay with yellow sandy or silty levels, 6) Grey silty clay, locally sandy-silty clays, with grey sandy-silty levels; 7) undisturbed sample.

Fig. 4.9 - Panoramic view of the Fiamma quarry from the slope below the hospital.

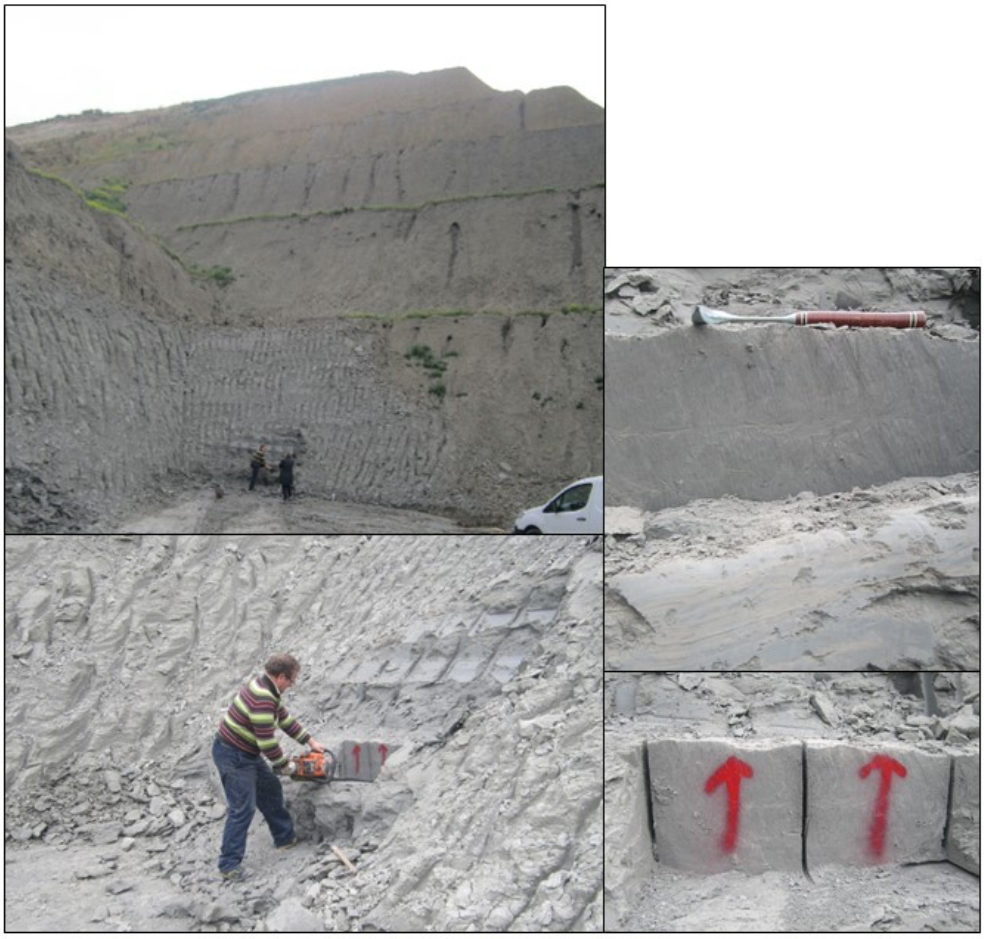

Fig. 4.10 - Block sampling of Lucera clay on a wall of the Fiamma quarry.

4.3 Physical and mineralogical properties of Pappadai and Lucera clays

Cotecchia (1996) took various undisturbed samples of Pappadai clay at various depths along borehole A (Fig. 4.2, Fig. 4.5) to get an indication of the variation of the properties within the deposit. The natural water contents, index properties, particle-size distributions and specific gravities were measured in the laboratory. In addition, the carbonate contents were measured by gasometric techniques using a calcimeter. These laboratory investigations were carried out in the geotechnical laboratory at the Technical University of Bari. The mineralogical analysis was carried out at the

Mineralogy Department of the University of Pavia by X-ray diffractometry on dry powder at 60°C and also after both glycolation and heating to 550°C.

The profiles of Atterberg limits, specific gravity G_s, carbonate content, clay fraction CF and activity in borehole A are reported in Fig. 4.11 and Table 4.1. It can be seen that the liquid and plastic limits vary in parallel with the clay fraction, and that the activity of the clay gradually decreases down the profile, while carbonate content increases. It appears that there was a general reduction in the quantity of calcareous sediment with time, presumably reflecting the gradually changing nature of the source of the sediment. There is no indication of significantly different physical properties between the grey clay and the yellow-brown clay, the average liquid and plastic limits of both being 55% and 30% respectively. In the more clayey strata the liquid and plastic limits are respectively about 63% and 33% (Table 4.1). A general decrease of carbonate content is observed up the profile.
As explained in Chapter 2, the nature of this high carbonate content was explored by Cotecchia (1996) and Cotecchia and Chandler (1997) using chemical micro-analyses within the SEM. They demonstrated the presence of a film of amorphous calcite coating both the clay particles and their contacts. Being amorphous, this calcite is likely to be authigenic, and thus the result of long-term diagenesis.
As might be expected, the variations of specific gravity with depth follow the variations in carbonate content, though the values of specific gravity reflect the dominance of the clay fraction.

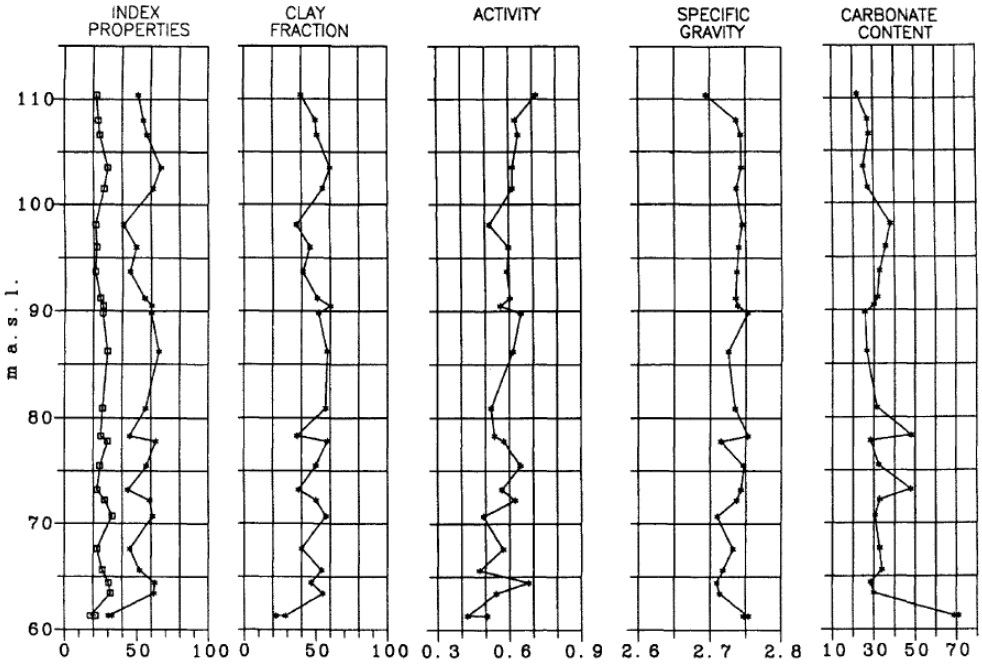

Fig. 4.11 - Geotechnical profiles, borehole A (after Cotecchia and Chandler, 1995).

Table 4.1- Summary of the index properties of the Pappadai clay, borehole A (after Cotecchia and Chandler,1995).

Depth (m)	Liquid limit (%)	Plasticity index (%)	Clay fraction (%)	G_s	Activity	Carbonate content
1.6	51	29	40	2.70	0.72	22.4
4.0	55	32	50	2.74	0.63	27.2
5.4	57	33	51	2.74	0.64	27.2
8.5	67	37	60	2.74	0.62	25.1
10.5	61	34	55	2.74	0.62	27.1
13.9	41	19	37	2.75	0.52	38.1
16.0	50	28	46	2.74	0.60	35.6
18.3	45	24	41	2.74	0.59	32.9
20.8	55	31	51	2.74	0.60	31.6
21.5	60	34	60	2.74	0.56	29.8
22.2	60	34	52	2.75	0.65	25.6
25.8	66	36	58	2.73	0.62	26.3
31.0	56	30	57	2.74	0.52	31.5
33.7	45	20	37	2.75	0.54	47.6
34.2	63	33	58	2.72	0.58	28.4
36.5	57	32	50	2.75	0.65	32.5
38.8	44	22	38	2.74	0.57	48.2
39.8	59	31	50	2.74	0.62	33.0
41.3	61	28	57	2.71	0.49	30.6
44.4	45	23	40	2.73	0.57	32.8
46.4	52	26	54	2.72	0.47	34.0
47.6	63	32	47	2.71	0.68	28.5
48.6	62	30	55	2.71	0.54	30.0
50.7	31	12	29	2.75	0.42	68.8
50.8	33	11	22	2.75	0.51	71.1

The index properties of the first block sample (Cotecchia, 1996) are compared with those measured on the second block sample in Table 4.2. In the latter case, the long-term storage had caused drying of the more external part of the block, so only the core of the sample was used in the laboratory. The comparison in Table 4.2 reveals that the storage of the second block sample seems not to have altered the clay properties in the core of the block. A small reduction in water content and degree of saturation is observed, but index properties remained almost unchanged. Further elements for the analysis of the effects of storage will be discussed in Chapter 5.
In both the block samples, Pappadai clay shows a clay fraction around 60% (Table 4.2) and is of high plasticity (PI=35%; Fig. 4.12). The grading curves of the block samples are compared in Fig. 4.13, showing very little difference.

Table 4.2 - Index properties of the two Pappadai block samples: block sample 1 is that of Cotecchia (1996), block sample 2 is that used in this experimental programme. w_n = natural water content; e_0 = natural void ratio; G_s = particle specific gravity; S_r = saturation degree; w_L=liquid limit; w_P=plastic limit; IP = plasticity index; CF = clay fraction; A = activity; IC = consistency index.

Sample	Depth (m)	w_n (%)	e_0	G_s	S_r (%)	w_L (%)	w_P (%)	IP (%)	CF (%)	A	IC
block 1	25	30.00	0.88	2.746	100	64.8	29.8	35	58	0.60	1
block 2	25	28.97	0.82	2.746	97.3	65.9	31.52	34.38	58.9	0.58	1.07

The mineralogical composition of clay samples from borehole A, determined by X-ray diffractometry on powdered clay by Cotecchia (1996), is shown in Fig. 4.14. If the calcite and dolomite contents given are summed they are in good agreement with the values of carbonate content measured by gasometric technique shown in Fig. 4.11. Table 4.3 reports the detail of the mineralogical composition of the clay at 25 m depth in borehole A. In the table, the term smectite refers to all the swelling minerals present in the clay, including the intergrades.

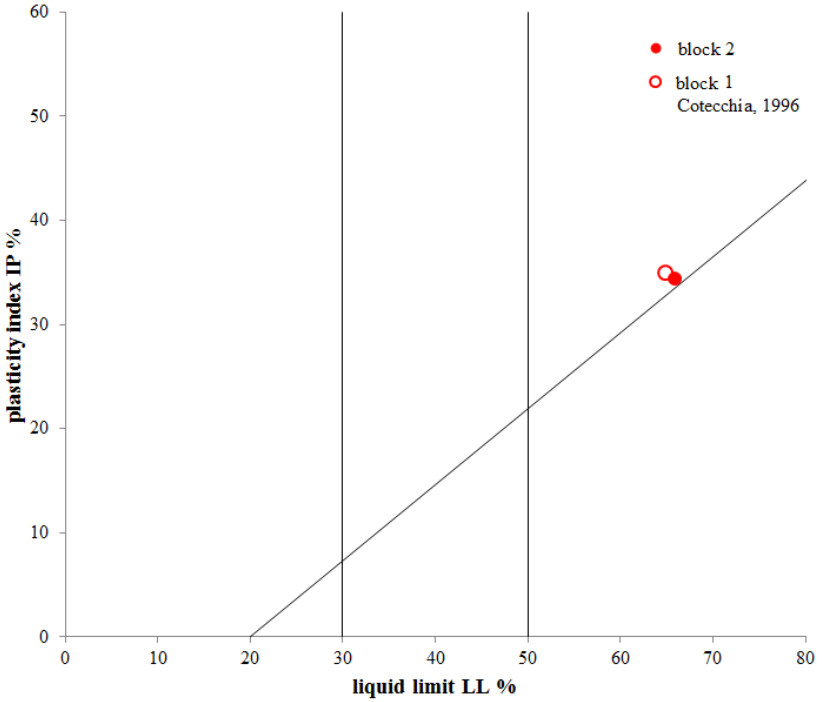

Fig. 4.12 - Casagrande plasticity chart of the block samples of Pappadai clay.

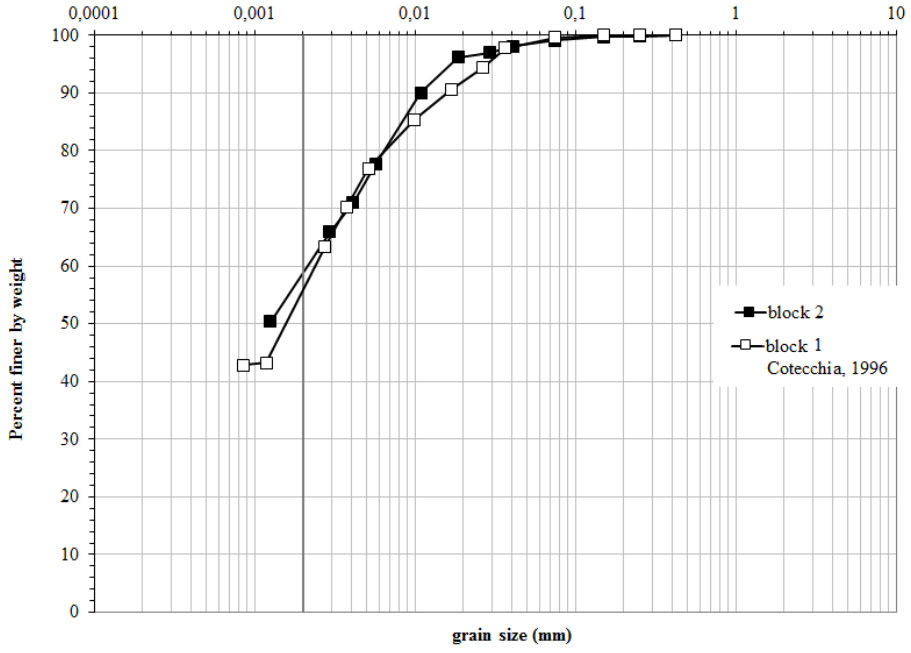

Fig. 4.13 - Grading curves of the block samples of Pappadai clay.

It can be seen from Fig. 4.14 that the dominant clay minerals are illite and kaolinite, with subordinate chlorite and smectite. The amount of smectite is quite large at shallow depths (Ciaranfi et al., 1971; De Marco et al.1981; Dell'Anna and Laviano, 1991), but it reduces below 10m depth (100 m a.s.l.), while the proportion of mixed-layer minerals, together with chlorite and illite, increases with depth. Reduction with depth of the proportion of swelling minerals is generally recognized as the effect of geological compaction (e.g. O'Brien and Slatt, 1990), a major physical diagenetic process responsible for the final structure of many argillaceous rocks.

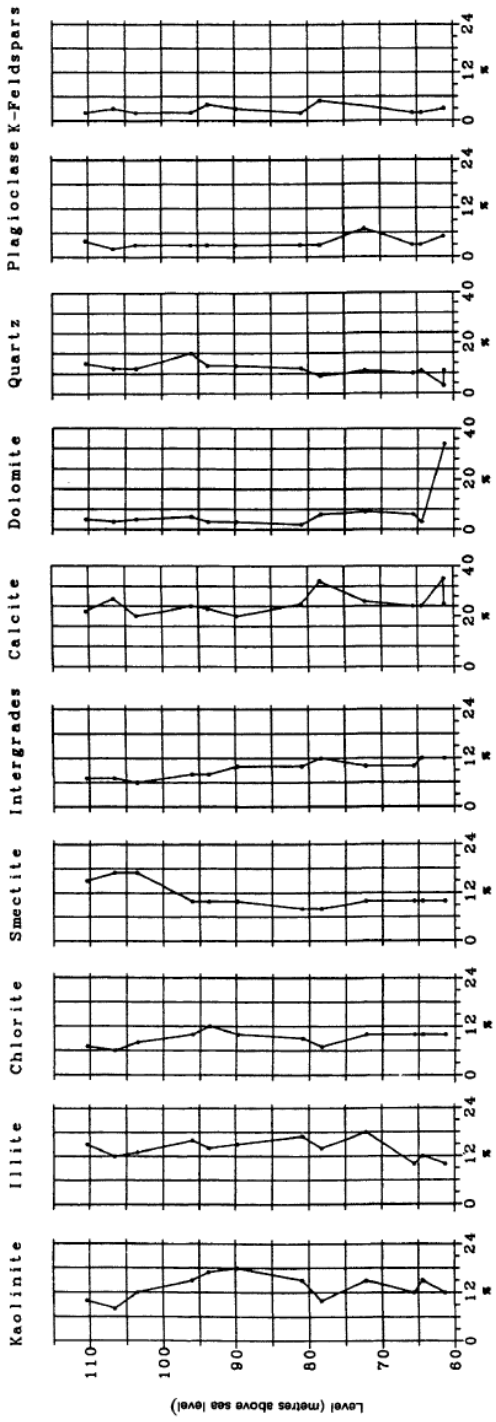

Fig. 4.14 - Mineralogy of Pappadai clay, data from borehole A (after Cotecchia and Chandler, 1995)

Table 4.3 - Mineralogical composition of the Pappadai undisturbed sample from block sample 1 (Cotecchia, 1996).

Qz	Fd	Ca	Dol	K	Cl	I	Sm
3	1	22	6	12	14	20	22

For Lucera clay, the physical and mechanical properties of the first block sample (that of 2003) are compared with those of the second block sample (that of 2016), and both are compared with existing data characterizing the borehole samples, taken at various depth down borehole SG15 (Fig. 4.8).

For both block samples, the natural water contents, index properties, particle-size distributions and specific gravities of the soil particles have been measured in the laboratory of the Technical University of Bari; the data are reported in Table 4.4.

The index properties for the borehole samples compared with data for the block samples are plotted in Fig. 4.15. They show that the variability in the stiff grey clay layer of the liquid limit, plasticity index, clay fraction and activity with depth is quite limited and that the differences in index properties between the sample taken in the slope (borehole SG15) and the block samples from the Fiamma quarry, at about 500 m distance, are negligible. Therefore, the site can be considered as a stiff grey clay deposit of noticeably uniform geotechnical properties; in Chapter 6, this feature will be seen to be reflected in the very similar macro-behaviour exhibited by the specimens from the two block samples, thus allowing the comparison of the results of the tests from Longo (2003) and Losacco (2004) with those included in the new experimental programme.

It is an overconsolidated clay deposit, but it is rather difficult to estimate the value of the overconsolidation ratio because there are many doubts on the thickness of the eroded stratum. From a preliminary analysis, an overconsolidation degree (OCR) of about 7.5 near to ground level has been calculated. The OCR decreases with depth down to a value of 4 at 40 m below ground level (Lollino et al., 2005).

Lucera clay has a clay fraction (CF) generally around 45% (Fig. 4.15) and is of medium plasticity (PI= 24-25%) (Fig. 4.16). The grading curve of the block samples is shown in Fig. 4.17. Its void ratio is relatively low (e = 0.55).

The mineralogical composition of the clayey blocks sampled on the wall of the Fiamma quarry, was determined by X-ray diffractometry on powders of both the whole sample and solely the clay fraction by Mitaritonna (2006). With reference to the clay fraction, the diffractometry was carried out on three oriented specimens differently prepared: air dried, glicolated at 60°C for eight hours and heated at 375° for one hour.
The results are shown in Table 4.5, both as bulk sample composition and as the percentage of the clay minerals within the clay fraction. The investigated samples are mainly formed of phyllosilicates, followed by quartz and calcite, with subordinate feldspars. The dominant clay minerals are the interstratified illite/smectite, with 40-45% of illite layers, followed by kaolinite, illite and chlorite.

Table 4.4 - Index properties of Lucera block samples: for block sample 1, data from Longo (2003), denoted as L_1, and from Mitaritonna (2006), denoted as L_2 and L_3, are shown. w_n = natural water content; e_0 = natural void ratio; G_s = particle specific gravity; S_r = saturation degree; w_L=liquid limit; w_P=plastic limit; IP = plasticity index; CF = clay fraction; A = activity; IC = consistency index.

Sample	Position (m a.s.l)	w_n (%)	e_0	G_s	S_r (%)	w_L (%)	w_P (%)	IP (%)	CF (%)	A	IC
block 1 (L_1)	170	21.1	0.578	2.73	99	41.3	21.08	20.22	42.8	0.47	1
block 1 (L_2)	170	20.3	0.556	2.738	100	48.11	24.12	23.98	42.8	0.56	1.16
block 1 (L_3)	170	19.07	0.521	2.738	100	47.57	22.61	24.95	42.8	0.58	1.14
block 2	150	19.88	0.557	2.716	97	47.86	23.36	24.50	48.5	0.50	1.13

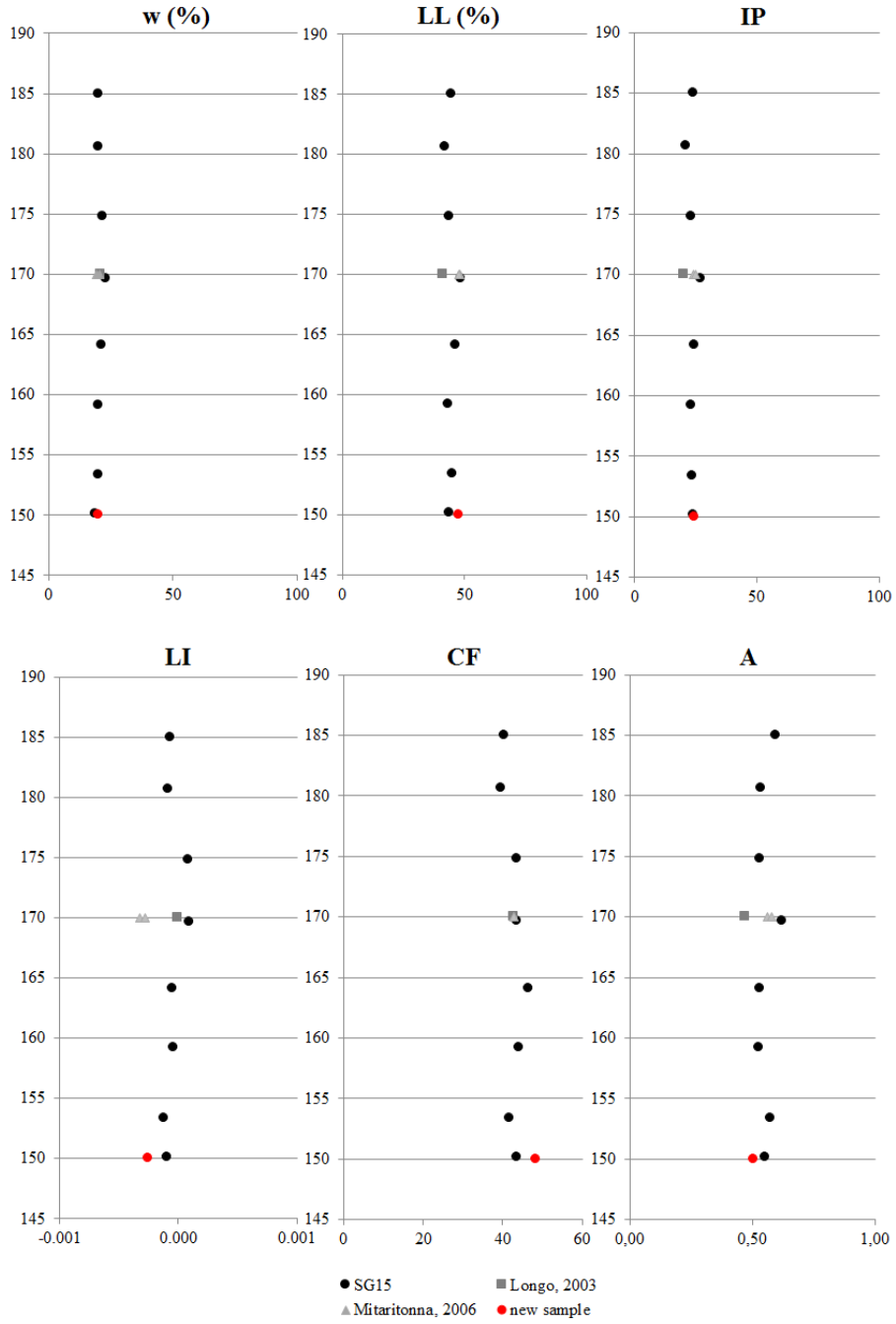

Fig. 4.15 - Index properties of Lucera clays from borehole and block samples (CF=clay fraction; wL=Liquid limit; IP=Plasticity index; A=Activity; LI=Liquidity index).

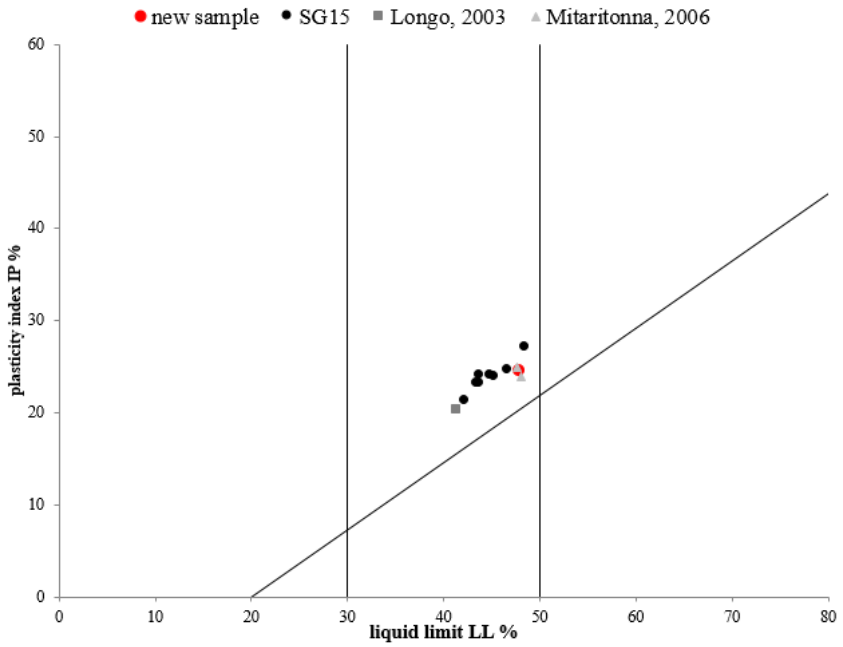

Fig. 4.16 - Casagrande plasticity chart of both borehole and block samples.

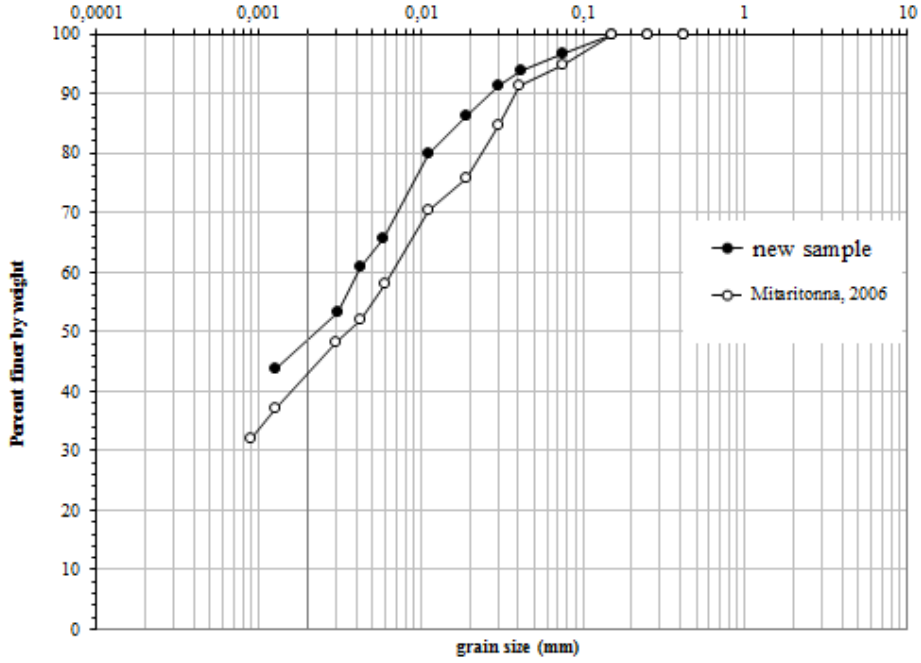

Fig. 4.17 - Grading curves of the block samples of Lucera clay.

Table 4.5 - Mineralogical composition (weight %) of the clay block sampled at the Fiamma quarry. Bulk sample: phyllosilicate (ΣPh), quartz (Q), K-feldspar (K-Fd), plagioclase (P), calcite (Cc), dolomite (D); Clay fraction sample: mixed-layers illite/smectite (I/S; the illite content, as %, in the interlayers is specified in brackets), illite (I), kaolinite (K), chlorite (Ch); tr = in traces.

Bulk composition						*Clay fraction*			
ΣPh	Q	K-Fd	P	Cc	D	I/S	I	K	Ch
70	15	1	3	11	tr	77 (40-45)	8	9	6

The comparison of the two studied clays shows that Pappadai clay has higher clay fraction, plasticity and activity, while Lucera is more silty, of medium plasticity and medium activity. For both the clays, the mineralogical analyses show a dominant presence of illite/smectite interlayers and a medium-high carbonate content.

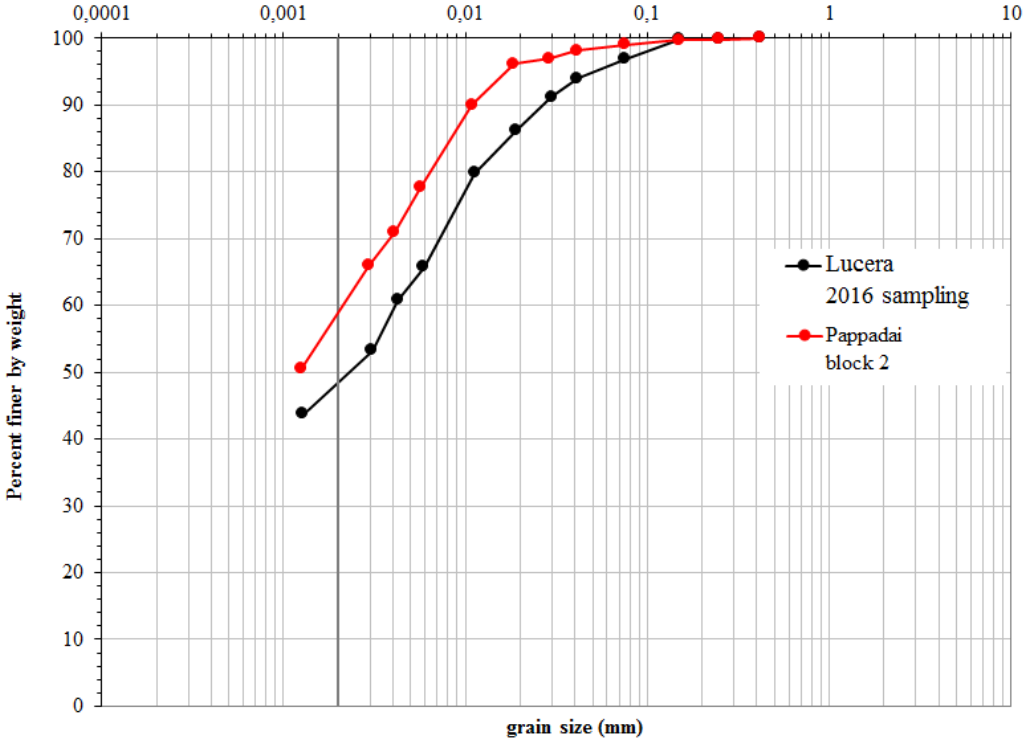

Fig. 4.18 - Comparison of the grading curves of the second block sample of Pappadai clay and the new block sample of Lucera clay.

5 TESTING PROGRAMME, EQUIPMENT AND PROCEDURES

5.1 Testing programme

The testing programme includes mechanical tests and microstructural analyses, that were carried out on both Pappadai and Lucera clays, in their natural and reconstituted states. Compression and shear tests were carried out and microstructural analyses consisting in SEM, MIP and image processing were performed on the specimens at the end of the tests.

Given the limited quantity of material available from the second block sample of Pappadai clay and the extensive investigation of Cotecchia (1996), a few mechanical tests were programmed on Pappadai clay, especially with the aim of exploring the evolution in porosimetry which accompanies the evolution of fabric with 1D loading already seen in the SEM (Cotecchia, 1996; Cotecchia and Chandler, 1998).

For this purpose, four one-dimensional oedometer compression tests were carried out on natural Pappadai clay from the second block sample (indicated as P_nat in Table 5.1): one swelling test from undisturbed state to low pressures (test S to σ'_v=20 kPa) and three compression tests, to immediately post-yield (test R2 to σ'_v=3000 kPa;), to medium pressures (test R to σ'_v=5000 kPa) and to large pressures (test HP to σ'_v=18500 kPa).

Two one-dimensional and one isotropic compression tests have been carried out on reconstituted Pappadai clay (indicated as P_rec in Table 5.1 and Table 5.2): one oedometer test (test EDOR1 to σ'_v=600 kPa) and the isotropic compression test (test PRI4 to p'=600 kPa) were stopped at the same void ratio, in order to investigate the differences in microstructure induced by different compression stress-path; the other oedometer test (test EDOR2 to σ'_v=5000 kPa) was brought to large pressures.

A more extensive macro and micro testing programme was planned for Lucera clay. For this clay, the writer could take advantage of some mechanical tests carried out by Longo (2003) and Losacco (2004) on both natural and reconstituted Lucera clay, and of the study of evolution of elastic stiffness anisotropy carried out by Mitaritonna (2006)

on reconstituted Lucera clay, in which also SEM pictures of the clay had been taken at various states. All these studies will be often recalled in the following.
1D and isotropic compression tests were carried out on natural Lucera clay (indicated as L_nat in Table 5.1 and Table 5.2) to investigate the clay behaviour under different loading paths and to different strain levels both before and beyond gross-yield. For comparison, also the reconstituted clay was compressed both isotropically and one-dimensionally.
Two compression tests were performed to medium pressures (tests EDOL1 and EDOL4 to σ'_v=5000 kPa), one compression test to large pressures (test EDOL2 to σ'_v=18500 kPa), one swelling test from undisturbed state (test EDOL7 to σ'_v=20 kPa), one swelling (to σ'_v=10 kPa) - recompression (to σ'_v=5000 kPa) – swelling (to σ'_v=10 kPa) test (EDOL6) and one compression test to a state pre-gross-yield (test EDOL3 to σ'_v=1440 kPa). The latter was stopped at the same void ratio of the isotropic compression test TNL8 to p'=1640 kPa (Table 5.2). Another compression test TNL5 was carried out to larger pressures (p'=4200 kPa).
Two oedometer compression tests were carried out on reconstituted Lucera clay (indicated as L_rec in Table 5.1): one consisted in loading from initial state to σ'_v=5000 kPa and swelling to 10 kPa (test EDORS), the other was a compression test to large pressures (σ'_v=15000 kPa, test LUCR1). An isotropic compression was also carried out to p'=1200 kPa (test LUCRISO).

Four triaxial shear tests to large strains were carried out on reconstituted Lucera clay from different isotropic compression states (Table 5.3), both pre-and post-yield in compression. The undrained test TRL2 and the drained test TRL5 started from an overconsolidation ratio of around 3, while the specimen subjected to the drained test TRL1 was lightly overconsolidated to R≈1.8. The undrained test TRL3 was carried out on a normally consolidated specimen.

The shear tests on natural Lucera clay (Table 5.4) were intendend to explore the behaviour of the clay both inside and outside its state boundary surface and to

investigate differences in microstructural evolution occurring under drained and undrained shear.

A couple of undrained (TNL1) and drained (TNL4) shear tests were performed on specimens having YSR≈3. Analogously, one undrained (TNL7) and one drained (TNL6) tests were carried out on specimen of YSR≈1.6.

Two undrained shear tests (TNL10 and TNL11) were carried out on specimens consolidated to the same isotropic states and then sheared until half the peak deviatoric stresses observed in the tests TNL1 and TNL7 respectively. The aim of these tests was that of analysing the microstructural changes taking place inside the SBS of the natural clay. Only one undrained shear test was performed on a specimen consolidated isotropically to large pressures beyond gross-yield (p'=4200 kPa, test TNL12). On this specimen, no microstructural analyses were carried out.

Table 5.1 - 1D compression tests on Pappadai and Lucera clays.

Test	**Sample**	**w_0 (%)**	**e_0**	**S_r (%)**	**σ'_{v0} (kPa)**	**Loading path**	**σ'_{vmax} or σ'_{vmin} (kPa)**	**stress before unloading**	**SEM**	**MIP**	**IP**
S	P_nat	28.29	0.839	92.56	1200	U	*20*	1200	•	•	•
R	P_nat	29.00	0.831	95.76	1200	L	3000	-	•	•	•
R2	P_nat	29.00	0.826	96.38	1200	L	5000	-	•	•	•
HP	P_nat	29.00	0.867	91.80	1200	L	18450	-	•	•	•
EDOR1	P_rec	44.28	1.216	98.11	200	L	600	-		•	
EDOR2	P_rec	43.82	1.203	96.54	200	L	5000	-		•	
EDOL1	L_nat	19.86	0.563	95.73	800	L	5000	-	•	•	•
EDOL2	L_nat	19.71	0.564	94.91	800	L	18450	-		•	

EDOL3	L_nat	19.42	0.545	96.69	800	L	1440	-		•	
EDOL4	L_nat	19.60	0.565	94.14	840	L	5000	-			
EDOL6	L_nat	18.08	0.545	95.30	800	U-L-U	*10*-5000	880-5000			
EDOL7	L_nat	18.08	0.534	92.04	880	U	*20*	880		•	
LUCR1	L_rec	33.36	0.936	96.79	100	L	15000	-		•	
EDORS	L_rec	31.97	0.890	97.57	60	L-U	5000-*10*	5000			

N.B. U=unloading, L=loading

Table 5.2 – Isotropic compression tests on Pappadai and Lucera clays.

Test	**Sample**	**w_0 (%)**	**e_0**	**S_r (%)**	**p'_0 (kPa)**	**p'_f (kPa)**	**Loading path**	**Apparatus**	**SEM**	**MIP**	**IP**
PRI4	P_rec	43.89	1.205	100	85	600	L	B		•	
TNL5	L_nat	19.76	0.549	97.78	1000	4200	L	HPSPS	•	•	•
TNL8	L_nat	19.70	0.547	97.85	1000	1640	L	E	•	•	•
LUCRISO	L_rec	33.55	0.928	98.19	27	1186	L	B			

Table 5.3 – Shear tests on reconstituted Lucera clay.

Test	w_0 (%)	e_0	S_r (%)	p'_p (kPa)	R	e before shearing	shear	axial strain rate (%/min)	Apparatus	SEM	MIP	IP
TRL1	34.16	0.936	99	65	1.8	0.878	D	0.0003	D	•	•	•
TRL2	33.50	0.926	99	30	4	0.926	U	0.003	E(*)		•	
TRL3	32.97	0.900	99	442	1	0.657	U	0.003	E			
TRL5	32.83	0.897	99	43	2.8	0.859	D	0.0003	B			

(*) equipped with local transducers

Table 5.4 – Shear tests on natural Lucera clay.

Test	w_0 (%)	e_0	S_r (%)	p'_p (kPa)	YSR	e before shearing	shear	axial strain rate (%/min)	Apparatus	SEM	MIP	IP
TNL1	19.87	0.544	99	881	3	0.546	U	0.003	B	•	•	•
TNL4	19.86	0.544	99	879	3	0.544	D	0.0003	B	•	•	•
TNL6	20.11	0.547	100	1637	1.6	0.523	U	0.003	D	•	•	•
TNL7	18.64	0.528	96	1590	1.6	0.518	D	0.0003	E(*)	•	•	•
TNL10	18.87	0.531	96	878	3	0.569	U	0.003	D	•	•	
TNL11	18.51	0.531	95	1675	1.6	0.529	U	0.003	D	•	•	
TNL12	18.12	0.524	94	4004	1	0.431	U	0.003	HPSPS			

(**) anisotropic consolidation

(*) equipped with local transducers

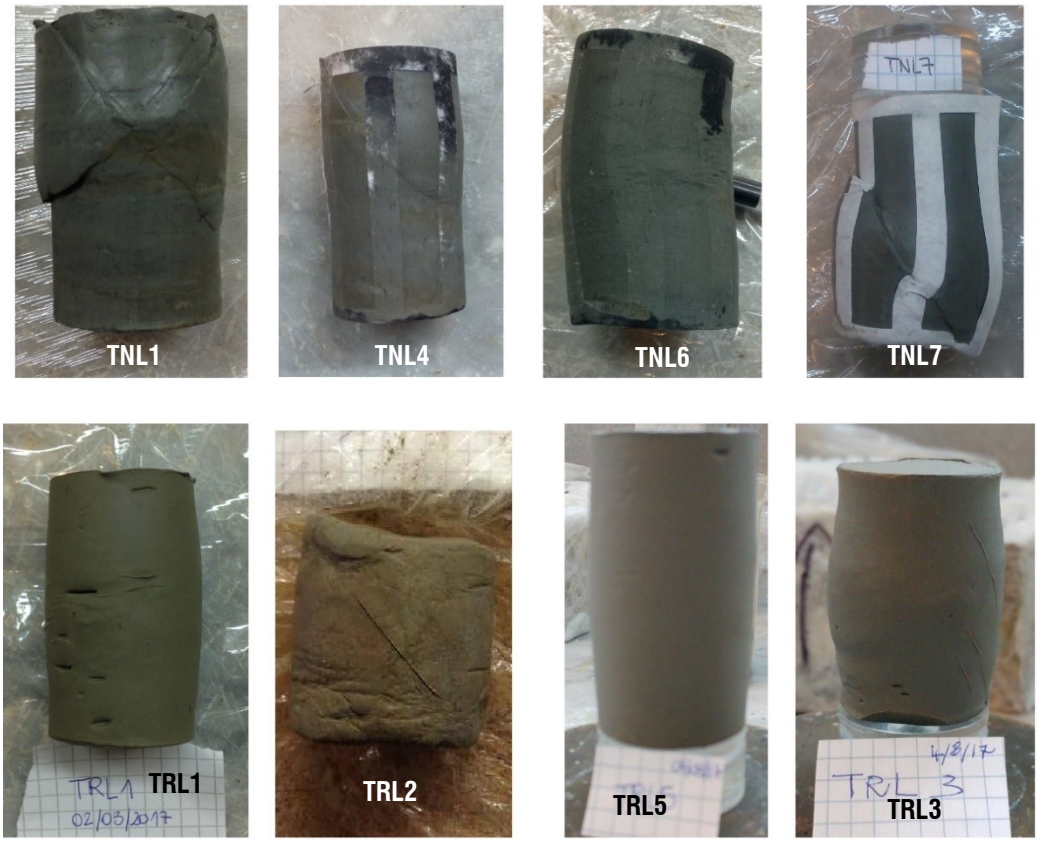

Fig. 5.1 – Pictures of specimens of Lucera clay at the end of shear tests (those of the upper row are natural clay specimens; those of the bottom row are reconstituted clay specimens).

5.2 Mechanical testing equipment

All the compression and shear tests included in the experimental programme were carried out at the geotechnical laboratory of the Technical University of Bari.
Four oedometer apparatuses, of two different types, three stress-path systems and one conventional triaxial apparatus were used. Their characteristics will be described in detail in the following. All the tests were carried out in a temperature controlled room at 20°C.

5.2.1 Oedometer apparatus

The oedometer test reproduces, in the laboratory, one-dimensional compression conditions. The basic version of this test consists of applying a sequence of loads on a specimen laterally confined, so that strain and water flow are allowed only in the vertical direction. A sketch of the oedometer apparatus is given in Fig. 5.2.

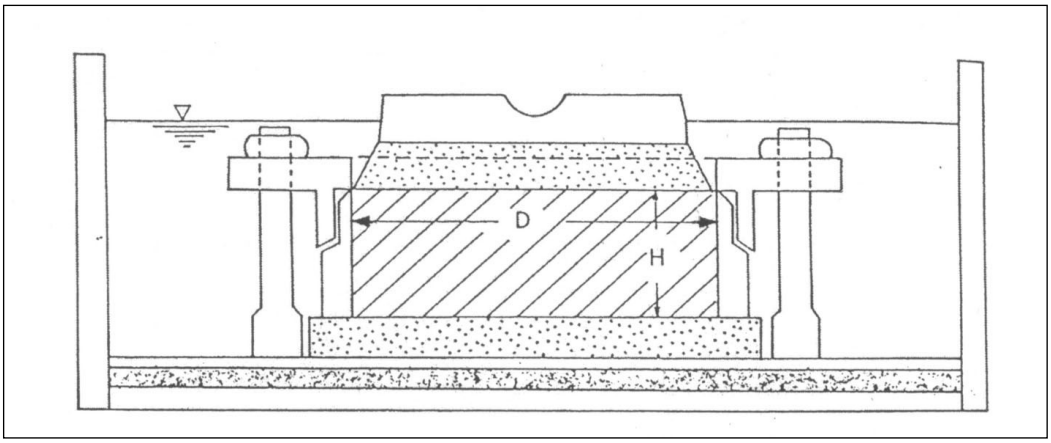

Fig. 5.2 - Schematic design of the oedometer cell.

The conventional oedometer cell consists of a rigid ring containing the specimen, which is in contact with two porous stones at the top and bottom surface to allow double drainage. The dimensions of the specimen are designed so as to make the ratio of the diameter to the height greater than two, in order to reduce the effects of side friction (Bishop and Henkel, 1962). In this work, specimens of 56 mm diameter x 20 mm height and 50 mm diameter x 20 mm height have been used. The latter allow to reach larger vertical pressures for a given applied force by means of the smaller transmission surface area.

The oedometer cell lies on a rigid aluminium base and a loading yoke allows the transmission of load from a lever arm carrying the weights to the sample top cap.

In this work, both classical oedometer apparatuses and a modified oedometer apparatus have been used. With respect to the classical apparatus, the modified one

allows to attain a maximum vertical stress $\sigma'_v = 15$ MPa instead of 5 MPa, by means of a tri-multiplier stress system placed at the end of the lever arm, as shown in Fig. 5.3.

Fig. 5.3 - Modified oedometer apparatus of the Geotechnical Laboratory at the Technical University of Bari.

The sample and the rigid ring are located in a water bath to prevent drying of the sample during consolidation and allow for the absorption of water during swelling. The stress and strain conditions are assumed to be axi-symmetric and friction at the contact between the soil and the ring is assumed to be zero. The soil-steel contact on the inner surface of the ring is lightly lubricated with grease before testing.

When the axial stress σ_v is applied, the sample of initial height h_0 deforms vertically with time. It ultimately settles of an amount Δh when the excess pore-water pressure is completely dissipated, that is when the internal effective stress σ'_v equals the externally total applied stress σ_v.

A linear displacement transducer, placed on the top platen, measures the vertical displacements Δh_i at each loading step *i*. As lateral strain is restricted by the stiff ring ($\varepsilon_x = \varepsilon_y = 0$), the volumetric strain ε_{vol} is equal to the axial strain ε_z:

$$\varepsilon_{vol} = \varepsilon_x + \varepsilon_y + \varepsilon_z = \varepsilon_z = -\frac{\Delta h}{h_0} \qquad (5.1)$$

During the trimming of the sample, flat and parallel surfaces are ensured to minimize the error due to the imperfect alignment of the top platen with the ring, which can cause misreading of the displacements. The main source of error is derived from the bedding error due to the roughness or other imperfections of both the top and base of the sample.

5.2.2 Triaxial and stress path apparatuses

5.2.2.1 General description

The experimental programme includes tests conducted using one triaxial apparatus, TRX D, and three computer-controlled stress path cells (Taylor & Coop, 1993), TRX B, TRX E, and the HPSPS (High Pressure Stress-Path System). Each apparatus is named after its label in the laboratory. The stress-path systems are equipped with actuators mounted on the crossbeam and connected to a piston transferring a vertical force to the ram connected to the load cell. In these systems the axial load can be applied to the specimen by means of a *controlled rate of strain* or a *controlled loading* operating mode, increasing the pressure in the upper chamber of the actuator to transfer it to the loading ram at a user-defined rate. In this work, all the stress path cells have been used in the first cited operating mode. As an example, Fig. 5.4 shows the TRX B stress-path system.

The HPSPS (Fig. 5.5) has been designed and developed by Lagioia (1998) and modified by Cotecchia (1999) in order to reach cell pressures as high as 10 MPa.
All the apparatuses are equipped with conventional transducers; in addition, TRXE is fitted with two submersible linear variable differential transformers (LVDT) for local axial strain measurements.
All the cells have data-logging systems which monitor the transducers measuring force, pressure and displacement. The specimen sizes are in all cases 76 mm height and 38 mm diameter. The cylindrical specimen is enclosed in a latex membrane, placed on a base platen and sealed at the top and bottom by o-rings. The specimen is located in a cylindrical cell full of water under confining pressure σ_r, within which there is also a load cell of Imperial College type, which can measure the axial force F_a applied to the specimen in addition to the cell pressure. The drainage is allowed from the base of the specimen.

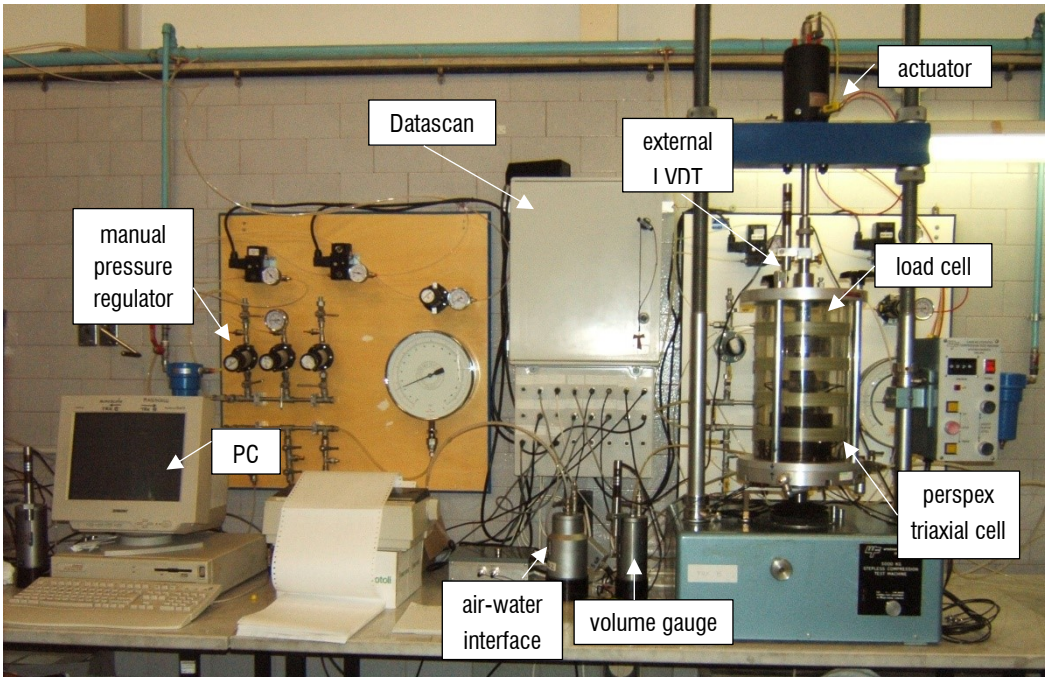

Fig. 5.4 - Triaxial apparatus TRX B at geotechnical laboratory at the Technical University of Bari.

Three of the apparatuses used, TRX B, E and D, include Wykeham Farrance triaxial cells made of reinforced Perspex, with different capacity, and are all equipped with pedestals for 38 mm diameter samples. Each apparatus has both cell and pore water pressure transducers, of a semi-conductor type.
The triaxial cell of TRXD has capacity of 3500 kPa. The system is equipped with cell and pore water pressure transducers manufactured by Wykeham Farrance with capacity of 3300 kPa, together with an internal load cell of Imperial College type of capacity 25 kN manufactured by Wykeham Farrance.
TRXE has a cell of capacity of 2000 kPa, a cell pressure transducer manufactured by Wykeham Farrance with capacity of 3000 kPa and a pore water pressure transducer manufactured by Druck with capacity of 1500 kPa, together with an internal load cell of Imperial College type of capacity 10 kN manufactured by Wykeham Farrance.
TRXB is equipped with a cell of 1700 kPa capacity, cell and pore water pressure transducers both manufactured by Wykeham Farrance with capacity of 1700 kPa, and an internal load cell of Imperial College type of capacity 3 kN manufactured by Wykeham Farrance.

The cell and the back pressures are supplied by a compressor operating at a maximum pressure of 1500 kPa. The air pressure provided by the compressor is reduced to 800 kPa through a valve before being conveyed to the different users. Manual pressure regulators are used in TRX B, E and D to control the air pressure sent to air-water interfaces connected to both the pore water, in order to apply the back pressure during the drained stages, and the cell pressure. For TRX B, E and D, the interfaces double the pressure, so that the pressure of the water in the cell is twice that exiting the valve.

For the HPSPS (Fig. 5.5), the triaxial cell is made of stainless steel with internal steel rods, which allow the mounting of the specimen and its connection with the load cell before positioning the cell, with the aim to avoid alignment errors (Fig. 5.6).
The system is equipped with a pedestal for 38 mm diameter samples, which includes two drainage tubes connected by means of stainless steel lines to two pressure blocks

placed outside the triaxial cell. Both the cell and the pore water pressure can be automatically controlled by means of stepper motors controlled air pressure regulators. The cell pressure is measured by means of a pressure transducer manufactured by Keller with a capacity of 10 MPa and is applied by means of a high-pressure water pump, with screw piston, controlled by a stepper motor. The brass pump has a capacity of 100 cm^3 and can provide up to 14 MPa cell pressure.

The pore water pressure transducer is of the same type and capacity as that used for the measurement of the cell pressure; the pore pressure is applied by means of an electro-valve connected to a stepper motor. The internal load cell is of Imperial College type manufactured by Wykeham Farrance and has a capacity of 25 kN.

The control of the pressure applied to the actuator is made through an electro-valve connected to a stepper motor. In this work, however, the system has not been used in this operating mode.

Fig. 5.5 – High Pressure Stress-Path System (HPSPS) of the geotechnical laboratory of the Technical University of Bari.

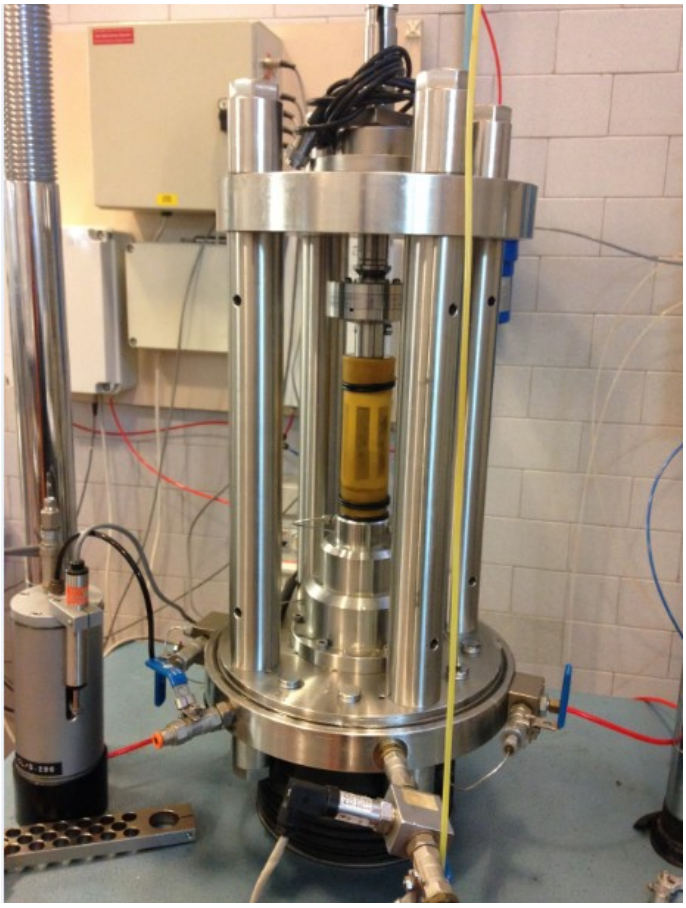

Fig. 5.6 – Set up of a specimen inside the cell of the HPSPS.

In all the cells the axial displacements are measured externally by a LVDT of type RDP LDC 500/A which is connected to the ram outside the cell and measures the vertical displacements. The volumetric strains are measured in all systems by means of 50 cm^3 volume gauges. The volume gauges are fitted with a LVDT of the same type as that used for the external measurement of the axial displacement.

All the transducers are connected to a digital/analogue converter of Datascan Technology, which provides 16 analog input channels and is used for logging the input signals coming from all the transducers.

The acquisition and control software is written in GWBASIC for TRX E and B and in BBCBASIC for the HPSPS. The acquisition software for TRX D is written in LabVIEW.

The accuracy of the measurements depends not only on the particular transducer being used, but also on the design of the apparatus, the stability of the temperature of the laboratory and the characteristics of the data-logger system.
The instruments were carefully calibrated before testing within their linear range. The load cells and pressure transducers were calibrated against a Budenberg dead-weight tester, while the displacement transducers were calibrated against a micrometer. For the volume gauges a previously calibrated Bishop ram was used. The calibration constants have been checked routinely between the tests.

5.2.2.2 Volume strain measurement

Standard Imperial College volume gauges of 50 cm^3 capacity were used for measuring the volumetric changes of the triaxial samples (Fig. 5.7). The volume gauge (Fig. 5.7) also acts as an air-water interface for the back-pressure system, the base chamber being filled with air and connected to the back-pressure valve, while the top chamber is filled with water and connected to the sample drainage system. The movement of a piston occurs with the movement of water from/into the specimen and such movement is monitored using a linear variable differential transformer (LVDT). The resolution of the measuring device is 0.001 cm^3, that represents a resolution in the volume strain measurement of around 10^{-3} % for the 38 mm diameter samples.
The drainage and the pore pressure measuring systems are connected only to the base pedestal. The base pedestal in each apparatus has two drainage ports, one connected to the volume gauge through the pore pressure transducer block and the other one to a drainage tap. This arrangement allows the base drainage system to be flushed before the test and also during the test if air is suspected to have been entrapped within it. All drained tests have been conducted under a constant back pressure to avoid errors due to compliances of the drainage ducts and volume gauges.

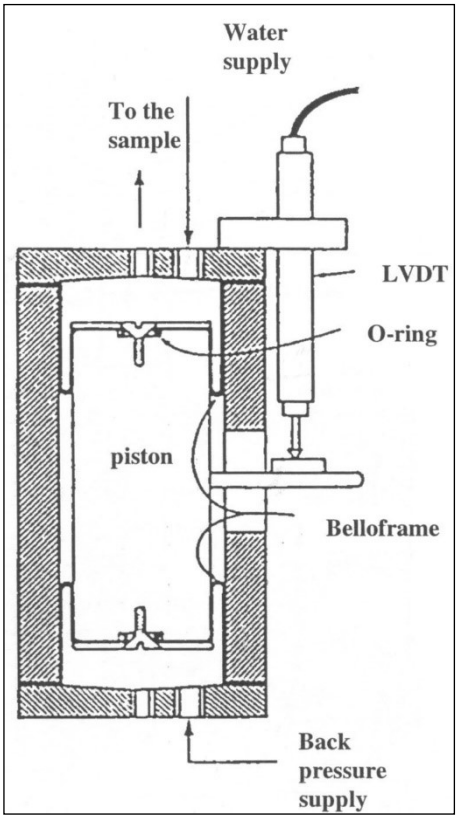

Fig. 5.7 - Volume gauge (Head, 1980).

5.2.2.3 Axial strain measurement

The axial strains of the triaxial specimens were measured through the measurement of axial displacements carried out outside the cell and sometimes also locally on the specimen, with local transducers inside the cell.

External measurements were taken using a standard displacement transducer with a maximum travel length of 25 mm; its body is fixed to the loading ram, while the piston is allowed to move jointly to the cell and measures its movement. Accounting for corrections for the compliances of the apparatus, the accuracy of such displacement measurements is about 0.05%.

However, reliable measurements of the soil stiffness throughout the small strain-region, from strains of about 0.001% up to about 0.1%, can be made only using local strain gauges, which are attached directly to the specimen (Jardine et al., 1984).
Small submersible LVDTs of type RDP D5/200WRA were used to measure local axial strain. The use and operation of these transducers is described in detail by Cuccovillo et al. (1997) (Fig. 5.8). Two transducers are mounted on opposite sides of the specimen inside the cell by using mounts (which are glued to the membrane using loctite) and each transducer has a resolution of 0.05 μm. The armature rests on the lower mount, as represented in Fig. 5.8.
This kind of transducer has a linear calibration over a range of displacements of about ±5 mm. In order to achieve high resolution strain measurements, the LVDTs are set at their electrical zero by adjusting the zero potentiometer in the transducer amplifier; this allows the data logger to work in the most sensitive range.

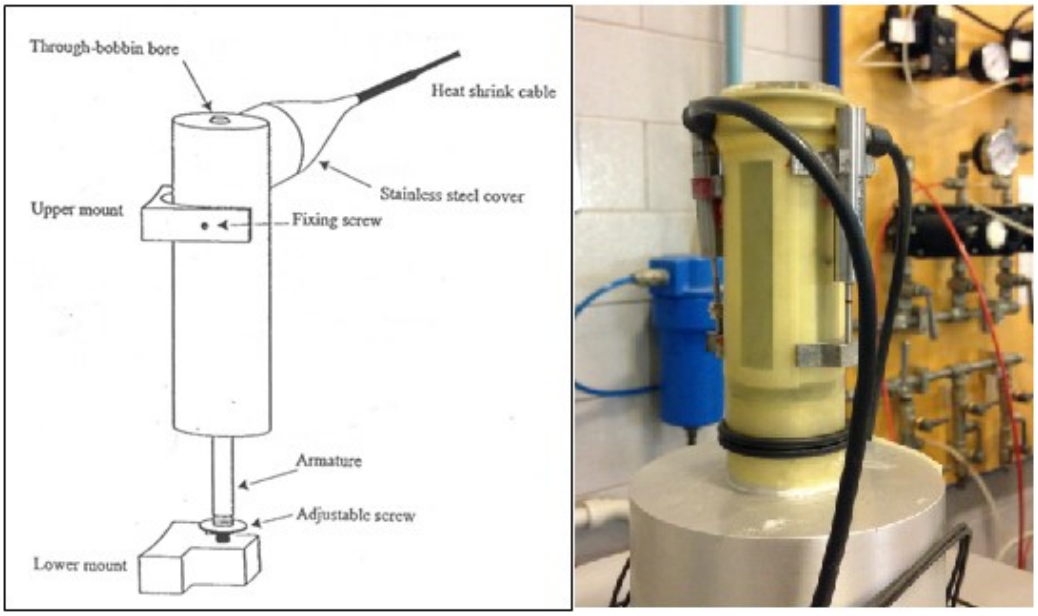

Fig. 5.8 - Sketch of axial LVDT with adjustable screw (Rolo, 2003) and example of application on a triaxial specimen.

The interaction between the specimen top platen and the load cell was realized by means of a half ball seated in a notch on the top platen, as illustrated in Fig. 5.9.

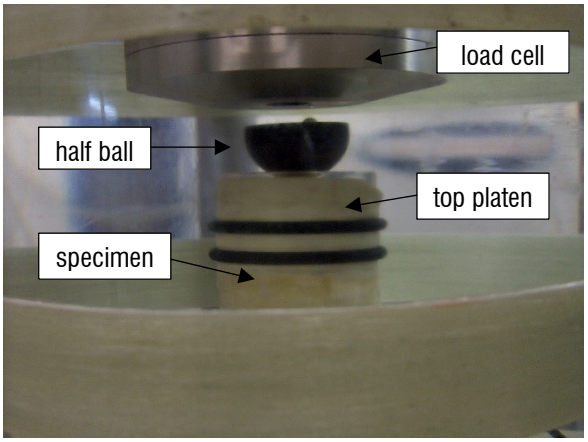

Fig. 5.9 - Load cell-specimen connection by means of the half ball.

5.3 Microstructural analyses

Microstructural analyses were carried out on portions of specimens subjected to both oedometer and triaxial tests after fast undrained unloading. The microstructural analyses consisted in mercury intrusion porosimetry tests and scanning electron microscopy observations on the freeze-dried specimens. The sample preparation and the MIP tests have been carried out at the geotechnical laboratory of the Universitat Politècnica de Catalunya (UPC-Barcelona) The SEM analyses have been carried out using the Field Emission Scanning Electron Microscope (FESEM) at the laboratory of the CNR (National Research Council) Institute of Methodologies for Environmental Analysis at Tito Scalo (Potenza). The qualitative observation of the resulting SEM micrographs has been aided by a quantitative image processing analysis, aimed at determining the degree of fabric orientation using the technique proposed by Martinez-Nistal et al., 1999. For this purpose, selected micrographs have been sent for image analysis to the Unidad de Microscopía Fotónica y Proceso de Imágenes of the University of Oviedo (Spain).

All the samples subjected to microstructural analyses were prepared by means of freeze-drying, in order to remove all the pore water prior to testing. The clay at original water content was immersed into nitrogen (-196°C) and then transferred to a vacuum pump so that the water could sublimate and the clay could dry with no significant volume change.

Sample dehydration can also be achieved by means of other techniques including air or oven drying, or critical point drying (Delage and Pellerin, 1984); an effective drying method should impose minimum disturbance to the soil structure. Gillot (1970) investigated the fabric of Leda clay and compared different drying techniques, showing that although all had detectable effects on fabric, air drying caused the greatest disturbance. Air-drying also significantly disturbs the fabric of saturated clays at high water contents, since it determines considerable pore shrinkage in the material (Mitchell and Soga, 2005). Oven drying may result in less fabric changes, as the shorter drying time limits the particle rearrangement (Sasanian and Newson, 2013). However, thermal stresses induced by oven-drying may cause breakage of particle clusters (Mitchell and Soga, 2005). Delage and Lefebvre (1984) showed that oven-drying significantly modified the microstructure of soft Champlain sea clays, resulting in a denser particle packing. Cuisinier and Laloui (2004) also reported that oven drying induced a significant porosity reduction in specimens of compacted silt. However, the disturbance to clay microstructure is seen to be minimized by freeze drying, which in fact nowadays is the most commonly used method. Freeze drying processes manipulate temperature and pressure conditions to eliminate the surface tension forces caused by air-water interfaces, and thus it is assumed that no shrinkage occurs on drying which could alter soil structure (Romero and Simms, 2007).

Prior to freeze drying, soil samples have been cut into cubes less than 1 cm^3 in size to maximize heat transfer. For each sample, two small cubes were prepared so that one could be used for MIP and the other for SEM. In the latter case, the cube was fractured along sub-horizontal and sub-vertical surfaces which were then carbon coated (10 nm

thick) in order to avoid charging of the surface and allow chemical micro-analyses during the SEM application.

5.3.1 Scanning electron microscopy

The physical principles background of SEM as well as the system and techniques used for SEM applications are amply documented in the literature (Smart and Tovey, 1981;1982; Wenk, 1976).

Basically, in the scanning electron microscope an electron gun shoots a focused electron beam generated by a thermic electron source against a sample surface under vacuum, thus delivering images with information about the sample topography and composition. Three magnetic lenses compress the size of the beam so that the size of the area being scanned is reduced. Due to the impact of the electrons with the sample constituents, secondary electrons leave the sample in a way that depends on the topography of the constituents being hit, as schematically shown in Fig. 5.10. A receiver-decoder of the reflected electrons produces a message which is then converted into magnified images of the area being scanned.

In this work, a field emission scanning electron microscope (Zeiss Supra 40; Fig. 5.11) has been used, equipped with a Schottky emitter: the electron beam is produced by thermal field emission and can deliver a finer and more stable beam, resulting in higher resolution than in the conventional SEM. Elemental analyses were performed with an energy-dispersive X-ray spectrometer (EDS, Oxford Inca Energy 350).

The SEM techniques are so sophisticated that specialized operators have to carry out the SEM application, though the objectives may require the method to be used in different ways. In this work the SEM observations have been carried out in a specialized laboratory, the writer preparing the clay samples to be scanned and supervising the specialized operator during the observation.

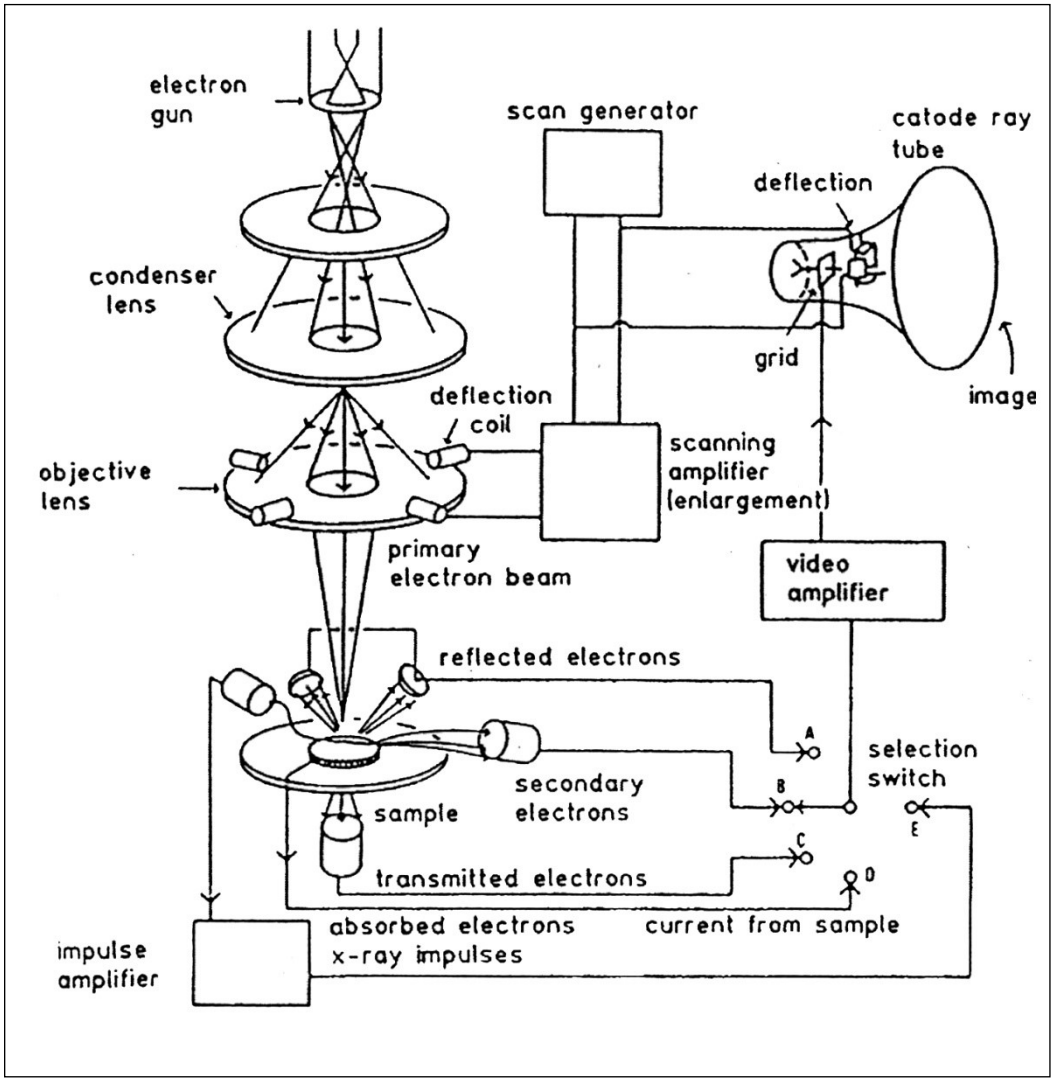

Fig. 5.10 - Schematic diagram of an electron microscope (manual of Cambridge 500 SEM).

Fig. 5.11 - FESEM Zeiss Supra 40 at CNR Institute of Methodologies for Environmental Analysis at Tito Scalo (PZ).

5.3.2 Mercury intrusion porosimetry

Mercury intrusion porosimetry has been widely used for investigating the microfabric and pore distribution of various porous media, including compacted and natural clays and shales previously subjected to different hydraulic and mechanical stress paths (e.g. Delage and Lefevbre, 1984; Delage, 2010; Griffiths and Joshi, 1989; Howard, 1991; Hattab and Fleureau, 2010; 2013; 2015; Ninjgarav et al., 2007; Romero and Simms, 2007; Sasanian and Newson, 2013; Seiphoori et al., 2014; 2017; Yu et al., 2016).

In the MIP technique an absolute pressure p is applied to a non-wetting liquid (mercury) in order to enter the empty pores. The following Washburn equation applies (Diamond, 1970; Juang and Holtz, 1986b; Webb and Orr, 1997) for idealized pores of cylindrical shape and parallel infinite plates (fissure-like microstructure):

$$p_{Hg} = -\frac{n\sigma_{Hg}\theta_{nw}}{x} \quad (5.2)$$

where σ_{Hg} is the surface tension of mercury ($\sigma_{Hg} = 0.484$ N/m at 25°C), θ_{nw} the contact angle between mercury and the pore wall, and x the entrance or throat pore diameter ($n = 4$) or the entrance width between parallel plates ($n = 2$). The value $n = 4$ is used in MIP. The contact angle, which is very sensitive to surface roughness, is usually taken between 139° (smectites) and 147° (kaolinite and illite) for clay minerals (Diamond, 1970), although Penumadu and Dean (2000) have reported higher values with kaolin clay using the sessile drop technique (advancing angle of 162° and receding angle 158°).

MIP implicitly assumes a constant contact angle at equilibrium and does not check the applicability of (5.2), which is an equation for equilibrium state with zero penetration velocity of mercury. In fact, the contact angle varies as a function of the flow dynamic conditions, as shown experimentally by Hoffman (1975). However, Aït-Mokhtar et al. (2004) showed that for a given value of pressure, the contact angle between the mercury and the capillary wall starts to change significantly only from a 'critical' value of capillary radius. For this reason, sufficient time must be let in the pressure rising to allow for the quasi-static state condition to be reached (Romero and Simms, 2007)

The main limitations of MIP are: (a) isolated pores are not measured, although this enclosed porosity reveals not to be significant in soils; (b) pores that are accessible only through smaller ones (constricted porosity) are not detected until the smaller pores are penetrated ("bottle-neck effect"); (c) due to the maximum practical applicable pressure, the apparatus may not have the capacity to enter the smallest pores of the sample (non-intruded porosity); and (d) the minimum practical pressure of the apparatus limits the maximum pore size to be detected (non-detected porosity). As a consequence, when the clay sample is intruded by mercury, the intruded void ratio estimated under the maximum applied pressure does not coincide with the estimated void ratio of the sample. Differences mainly arise due to the non-intruded porosity with entrance pore sizes lower than 10 nm and the non-detectable porosity for pore sizes larger than 400 μm.

In addition, if two intrusions are applied successively (Pellerin, 1979), a difference in the volume of intruded mercury is seen, indicating that some mercury has been permanently entrapped. The corresponding pore volume is defined "constricted" pore volume and can be calculated as the difference between the first and second intrusion. Similarly, an intrusion (pressure increase) and subsequent extrusion (pressure decrease) cycle does not close when the initial pressure is restored, and the extruded volume gives an indication of the non-constricted porosity.
Delage and Lefebvre (1984) and later Delage (2010) attributed the non-constricted or "free" porosity to the intra-aggregate pores and the entrapped porosity to the inter-aggregate pores, because of the presence of clay bridges and irregularities in the aggregates.

Another aspect of the test is the alteration in pore geometry caused by pressure application (Romero and Simms, 2007). It has been reported that the soil structure is not affected during the high-pressure intrusion (Sills et al. 1973; Lawrence 1978; Reed et al. 1979), since the pore system is mostly filled with incompressible mercury. However, this cannot be the case during low-pressure application and before the initial intrusion takes place in compressible materials.

Mercury intrusion allows to determine the entrance pore-size distribution, by means of the relation between the volume of intruded pores and the pressure applied for intrusion. Typically, the test results are displayed in a cumulative intrusion curve representing the entrance pore size against the equivalent void ratio e_{nw} computed from the volume of the specimens intruded by the non-wetting fluid. Another typical representation includes a derivative intrusion curve representing the entrance pore size plotted against the log differential intrusion curve ($-de_{nw}/dlogx$), called pore size density function or frequency distribution, PSD. This graph aids the visual detection of the dominant pore modes. As discussed, such a PSD is not necessarily the true distribution of pores, due to various issues including pore accessibility and sample treatment, but gives a useful quantitative characterisation of microstructure.

For this work the MIP tests were carried out using an AutoPore IV (Micromeritics Instrument Corp.), shown in Fig. 5.12, which attains a maximum pressure of 230 MPa, corresponding to a pore entrance diameter of approximately 7 nm according to equation (5.2). To carry out the test, the cube of dried soil was placed in a penetrometer and then the sealed penetrometer was inserted into the low-pressure port of the equipment. In the first phase, air was evacuated and replaced by mercury in increments until a mercury pressure of around 200 kPa was reached. Then the penetrometer, filled with mercury, was removed from the low-pressure port, weighed and the placed in the high-pressure port, where it was pressurized incrementally up to the maximum pressure of 222 MPa. Depending on the expected total pore volume of the sample, two different penetrometers were used with different stem volumes.

Fig. 5.12 - Porosimeter AutoPore IV (Micromeritics Instr. Corp.) at the geotechnical laboratory of UPC (Universitat Politècnica de Catalunya).

5.3.3 Image processing

Methods to quantify the fabric of argillaceous geomaterials from scanning electron microscopy images have been presented by several authors. Tovey and Sokolov (1980) and Sergeev et al. (1985) used Fourier analysis for particle orientation. Tovey (1980), Russ (1990) and Tovey et al. (1992) described a method to calculate the fabric orientation from digitized images, examining the gradient of the intensity variations in two orthogonal directions and displaying a rosette diagram after computing the gradient intensity of each point in the image. Sokolov and O'Brien (1990) proposed a fabric index to classify argillaceous rocks, sediments and soils.

The technique adopted in this work is that proposed by Martinez-Nistal et al. (1999), which had already proved successful in the analysis of other clays (e.g. Pisa clay and Pappadai clay; Veniale et al., 1993; 1995; Cotecchia and Chandler, 1997; 1998).

The procedure (Fig. 5.13), based on the digital processing of the SEM images, entails the analysis of the brightness intensity of the pixels.

Elongated bright regions in the image are interactively thinned to line-shaped regions. These are processed through filtering to derive, based on a brightness threshold, a binary image in which lines complying with the threshold are considered of interest (ON). These are thinned to a pixel width and the fabric orientation is calculated from the texture line map. The calculation of the fabric orientation is based on the texture line map using a line-following algorithm, to obtain polygonal lines, whose segments are logged in terms of length and orientation (vectors). A rose histogram is then used to represent the vector lengths l_i, for each direction range, θ_i (10° interval). A statistical analysis of the vector lengths results in both the mean direction of all the vectors, θ, and a scalar statistical expression of the dispersion of the vectors with respect to the mean direction $\bar{L}$:

$$\theta = tan^{-1}\left[\frac{\sum_{i=1}^{n} l_i sin\theta_i}{\sum_{i=1}^{n} l_i cos\theta_i}\right] \qquad (5.3)$$

$$\boldsymbol{L} = \sqrt{\left(\sum_{i=1}^{n} l_i cos\theta_i\right)^2 + \left(\sum_{i=1}^{n} l_i sin\theta_i\right)^2} \qquad (5.4)$$

$$\bar{L} = \frac{\boldsymbol{L}}{\sum_{i=1}^{n} l_i} \qquad (5.5)$$

Given the expression of $\bar{L}$, its values characterising different degrees of orientation are not of uniform size. For example, $\bar{L}=1$ means maximum degree of iso-orientation; $0{,}21<\bar{L}<1$ means fabric with low degree of orientation; $\bar{L}<0.15$ means fabric with random orientation.

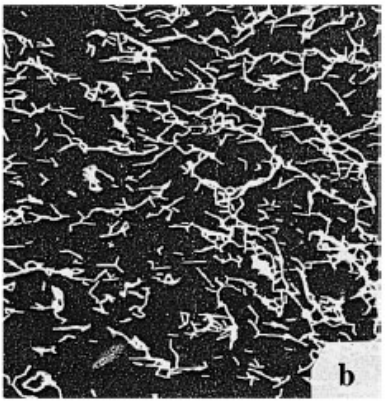

(c)

vector orientation	pixel amount
0 - 9°	1230.273
10 - 19	615.617
20 - 29	706.483
30 - 39	612.502
40 - 49	569.244
50 - 59	412.946
60 - 69	505.664
70 - 79	436.922
80 - 89	259.597
90 - 99	447.034
100 - 109	368.720
110 - 119	600.564
120 - 129	644.110
130 - 139	712.442
140 - 149	1025.191
150 - 159	1160.159
160 - 169	1192.857
170 - 179°	909.174

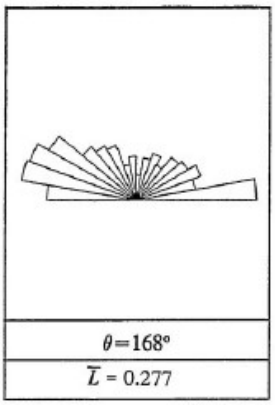

(d)

Fig. 5.13 - Example of 'fabric orientation' calculation on a sample of Pappadai clay subjected to 22 MPa vertical pressure in oedometer. a) SEM picture; b) polygonal approximation of the 'thinned' image; c) values of the vector orientations, grouped in intervals of 10°; d) corresponding direction histogram: index $\bar{L}$ =0.277 (between 1 and 0.21), indicating a very oriented fabric (after Martinez-Nistal et al., 1999).

To quantify particle orientation, Hicher et al. (2000) adopted a different technique based on the operator manual identification of particles in the SEM pictures. For each photo, the plane was divided into a given number of quadrants (15° amplitude each); then, the number of particles having the long axis oriented along a given quadrant was calculated for each quadrant and divided by the total number of particles found in the image. A percentage of particles was then obtained for a given orientation, allowing for the construction of a rose diagram. This procedure was repeated for ten photos at the same mechanical state and then a final overall rose diagram was constructed by superposing the results obtained from all the photos.

A similar procedure was developed by Hattab and Fleureau (2010). The method (Fig. 5.14) consists in randomly extracting from a low magnitude photo representative surfaces (20x20 μm), seen at higher magnification, and isolate them. Then, each particle seen sideways is identified and a segment having the same dimension and orientation is manually drawn on it. Image processing of the diagram thus obtained allows to calculate the orientation of all the represented particles with respect to the horizontal direction and then, an angular distribution diagram can be drawn as a rose diagram, giving the percentage of side particles as a function of their orientation.

A global rose diagram is then plotted superimposing the results of at least six isolated pictures randomly taken from different observation points.

As anticipated in Chapter 2, the Authors also suggest plotting the angular distribution rose diagram as *orientation curves* (Fig. 5.15), giving the percentage P of particles as a function of their orientation θ. This kind of representation allows the curves corresponding to different loading conditions to be superimposed and compared. Two modes of orientation can thus be defined: a) the depolarization (D) mode, corresponding to a random orientation mechanism in which all the orientations are represented by the same percentage; b) the principal (P) orientation mode, that is the preferential orientation for which the percentage of particles oriented in that direction is significant.

A U-shaped curve, such as that represented in Fig. 5.15 corresponding to kaolinite consolidated under a vertical effective stress of 120 kPa, clearly shows the structural anisotropy of the fabric with the principal mode of orientation towards the horizontal.

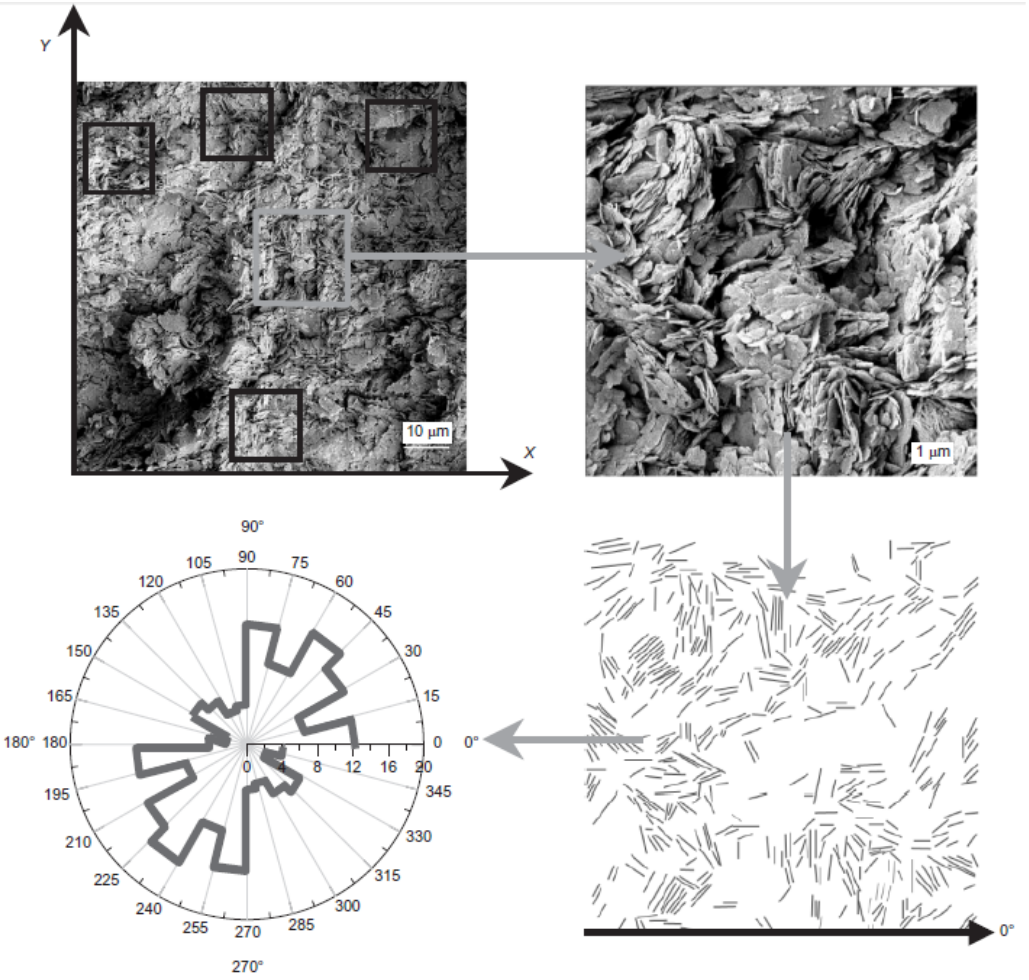

Fig. 5.14 - Method of image processing proposed by Hattab and Fleureau (2010). Example of orientation curve (after Hattab and Fleureau, 2010).

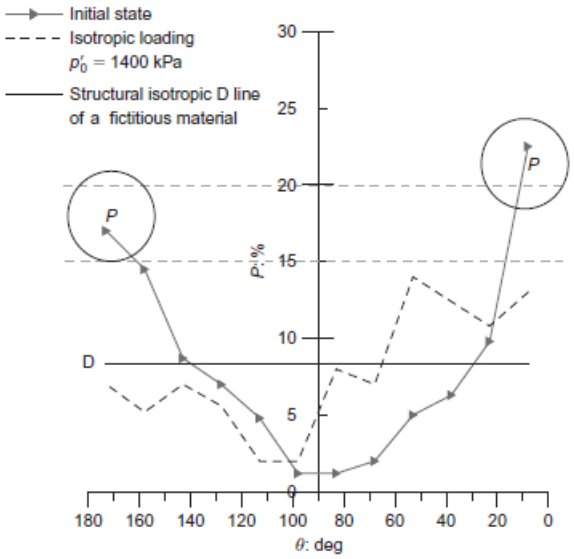

Fig. 5.15 - Example of orientation curve (after Hattab and Fleureau, 2010).

Both the techniques used by Hicher et al. (2000) and Hattab and Fleureau (2010) are based on the decomposition of a low magnification image into representative surfaces; the latter are observed at higher magnification and the individual clay particles are manually recognized by the operator. The partial results are finally averaged by superimposing histograms and an overall degree of orientation for the initial image is conveyed.

Other than being time-consuming, the visual identification of particles is thought to be feasible only at medium-high levels of magnification and more easily for clays made of particles that can be clearly distinguished, e.g., kaolinite.

Conversely, the procedure adopted in this work (Martinez-Nistal et al., 1999) is operator-independent, since it is based on the digital analysis of the images and is automatic. The method can thus be applied on micrographs taken at more complex microstructures and at different levels of magnification, thus conveying different information depending on the level of magnification investigated.

The differences between the two techniques of image processing are related to the adoption of different approaches to the characterization of fabric orientation.

In Chapter 7, direction histograms and corresponding values of $\bar{L}$ achieved by means of image processing (Martinez-Nistal et al., 1999) of SEM images of both Pappadai and Lucera clay will be shown at different states, together with orientation curves, as described by Hattab and Fleureau (2010).

5.4 Testing procedures

5.4.1 Reconstituted material preparation

In this work, both Pappadai and Lucera clay were reconstituted and one-dimensionally consolidated. Firstly, the undisturbed natural clay was heavily remoulded and mixed with water to form a slurry. Thereafter, the slurry was consolidated in a consolidometer. In the following the procedure adopted to create the slurry and consolidate it are discussed.

Large pieces of undisturbed clay are cut into very small pieces and are set in demineralized water to swell. Following the procedure suggested by Burland (1990), the water content of the clay slurry is planned to be about 1.25 times the liquid limit of the clay. The clay-water mixture is thoroughly worked to complete the disaggregation of the clay pieces.

The clay slurry is poured into the consolidometer of around 140 cm^2 cross sectional area and 26 cm height. In order to ensure one-dimensional deformation of the clay in the consolidometer, its internal surface is covered with grease, reducing the side friction. The slurry is then compressed by incremental loading up to a nominal vertical effective stress of 200 kPa for Pappadai clay and of 100 kPa for Lucera clay. This choice was made to reach the same final pressure attained in the consolidation of reconstituted Pappadai clay and Lucera clay, prepared following the same procedure used here by Cotecchia (1996) and by Longo (2003) respectively, thus reproducing the same history in terms of fabric creation.

One Pappadai clay and two Lucera clay reconstituted batches, named respectively P, L1 and L2, were prepared and all reconstituted specimens used in this work were trimmed from these batches. The water contents, the initial void ratios and the void

ratios at the end of compression in the consolidometer are reported in Table 5.5. The compression curves from slurry are reported in Fig. 5.16.
In Fig. 5.17, the comparison is shown between the compression curve obtained by Cotecchia (1996) and that of batch P. Given the difficulty of obtaining a slurry at the same void ratio, differences are seen in the compression curves and in the final void ratios.
For reconstituted Lucera clay, although Longo (2003) did not provide the compression curve for the consolidometer stage, the void ratio after consolidation is known to have been 0.82, lower than that found for the new batches L1 and L2.

At the end of the consolidometer stage, the free water is removed from the top of the consolidometer and the clay is quickly unloaded. Although swelling is restrained, a small void ratio increase is recorded after unloading, as will be shown in the following Chapter.

Table 5.5 - Reconstituted Pappadai and Lucera clays: water content, initial and final void ratios.

	P	L1	L2
w (%)	84.28 (1.28*LL)	56.00 (1.17*LL)	64.39 (1.34*LL)
e_i	2.31	1.53	1.78
e_f	1.21	0.93	0.90

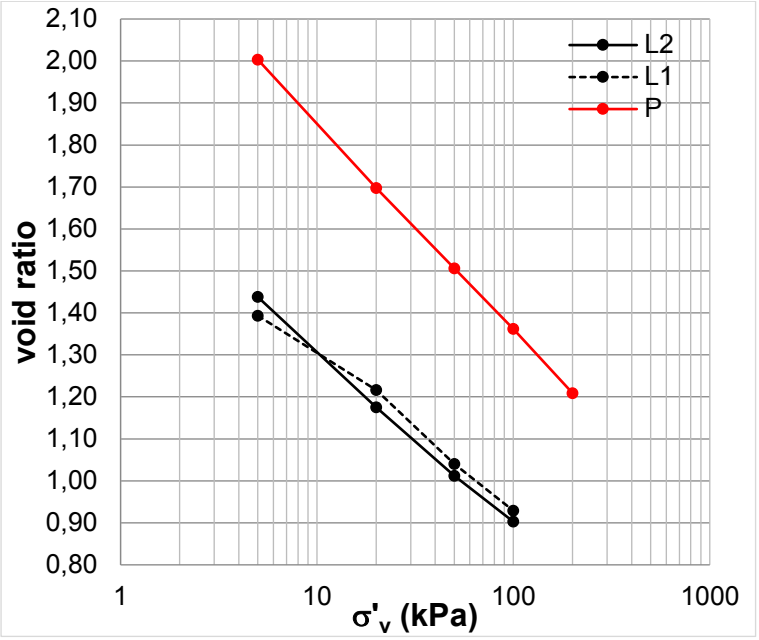

Fig. 5.16 - One dimensional compression of reconstituted Pappadai (red) and Lucera (black) clays from slurry in the consolidometer.

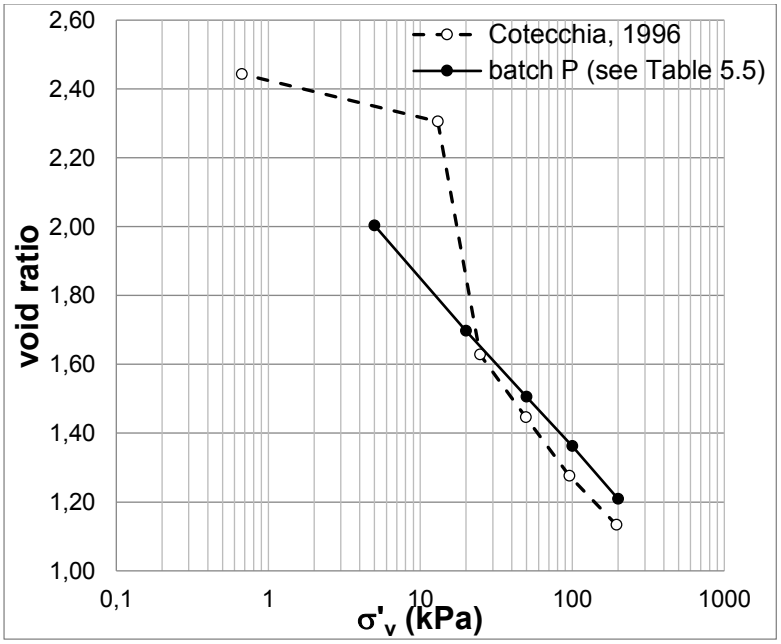

Fig. 5.17 - One dimensional compression of reconstituted Pappadai: batch prepared by Cotecchia (1996) and batch P (see Table 5.5).

5.4.2 *Measurement of suction by filter-paper technique and high capacity IC tensiometers*

High capacity IC tensiometers, described by Ridley and Burland (1993) and available in the geotechnical laboratory of Technical University of Bari, were used to measure the matrix suction s of the block sample of Pappadai clay that had been stored for a long time inside a high-humidity cellar, as described in Section 4.3.
Then, also the filter paper technique, described by Chandler and Gutierrez (1986), was used to repeat the matrix suction measurement on Pappadai block sample and make a measurement on Lucera block sample.

The high capacity IC tensiometers are capable of measuring matrix suctions higher than 100 kPa (Fig. 5.18) and work in a large range of pressures thanks to a technique of pre-pressurization of the water inside the water reservoir of the tensiometer (Harvey et al., 1994); this procedure prevents the formation of air bubbles inside the tensiometer that could be due to vapour entrapped within the instrument imperfections. A pressure of 3500 kPa can thus be applied to the water inside the system, that is closed and protected from cavitation (Richards and Trevena, 1976). However, since the system is provided with porous filters, the maximum measurable suction is related to the filter "air entry value", that corresponds to around 1600 kPa. If the suction value is greater that the filter air entry value, air passes through the filter, affecting the suction measurement. Another issue related to the use of this instrument is the quick desaturation, that requires frequent re-saturation of the porous filter (Bottiglieri, 2009).

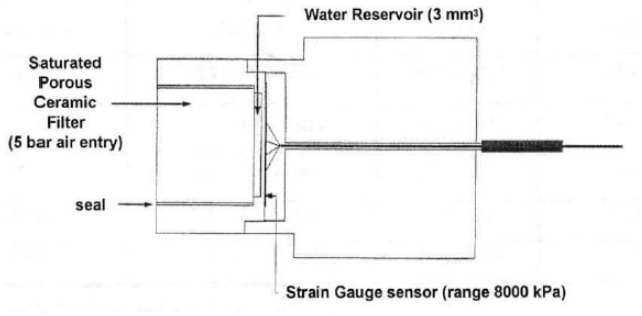

Fig. 5.18 - Suction probe (Imperial College tensiometer).

The filter paper technique can be used to measure a wide range of suctions. The method consists in putting in contact the soil sample with filter paper discs, sealing them and keeping the system in a constant temperature room. The system tends to reach the thermodynamic equilibrium. After some days, during which the filter paper absorbs water from the soil sample (assuming that this amount of water causes negligible variations of the soil water content), the filter paper water content can be determined. Finally, by means of a calibration curve, the value of suction in the filter paper can be determined, which is equal to that of the soil sample. The validity of Kelvin's law ensures this condition. Since the filter paper and the soil sample are in the same place, with the same temperature and relative humidity, the value of suction of the two elements must be the same; conversely, the water content will be different, as the two materials have different porosity.

The filter paper method can be used for both matrix and total suction measurements. For matrix suction measurements, direct contact between filter paper and sample is required and the equilibrium is achieved by transfer of humidity from the soil sample to the filter paper, water being in its liquid phase; at equilibrium, a small change in soil humidity (and then suction) due to this transfer will have developed, but it can be considered negligible.

To measure total suction, no direct contact is required between filter paper and soil sample; the thermodynamic equilibrium is obtained through transfer of humidity as vapour. Since the soil sample, air and filter paper have different humidity, molecules of water sublimate while passing from the sample to air and then from air to the filter paper. At equilibrium, soil and filter paper will incorporate water at the same suction.

For high degrees of saturation, the in-contact filter paper technique measures the matrix suction (Chandler and Gutierrez, 1986; Ridley, 1993), but for both clays of low saturation degree and clays with very high suctions ($>$1000 kPa), continuity of the filter paper with the soil pore water may be affected (Schreiner, 1988; Ridley, 1993); if this happens, a suction intermediate between the matrix and the total suction is measured.

Various calibration equations are presented in the literature, depending on the type of filter paper used and the time for reaching thermodynamic equilibrium (Cafaro, 1998; Bottiglieri, 2009). In the following, two equations for the Whatman No.42 filter paper have been used:

Chandler, Crilly and Montgomery-Smith (1991)

$$log_{10}s = 4.842 - 0.0622w \quad (w<47\%) \tag{5.6}$$

Leong et al. (2002)

$$log_{10}s = 4.95 - 0.067w \quad (w<47\%) \tag{5.7}$$

The matrix suction of the first Pappadai block sample was measured by Cotecchia (1996) at Imperial College by means of filter paper, giving an average value of 650 kPa for the clay soon after sampling (S_r=100%).

For the second Pappadai block sample, the value of suction was firstly measured by means of two high capacity IC tensiometers applied to a sample of void ratio 0,823 (w=29.55%) and degree of saturation S_r=98.6% and kept in contact with the sample until equalization or cavitation was seen. As shown in Fig. 5.19, the first measure (IC1) gave a value of suction of around 890 kPa, while the second measure (IC2) did not seem to reach an equalization stage, probably as a consequence of bad contact between the sample and the tensiometer. In the latter case, it is suspected that progressive evaporation occurred during the measurement, not allowing to attribute the suction value recorded before cavitation (1590 kPa) to the soil sample.

The measurement of suction was then repeated using filter paper (FP1) on a sample of water content 25.02% that was kept sealed for one-month. The same was left to slowly air-dry at controlled temperature; then, after one-month sealing with filter paper, the measure of suction was repeated (FP2) on the sample that had reached w=21.21%. The values of suction obtained are reported in Table 5.6. For this specimen, the void ratio was unknown as the measure of the volume of the specimen through immersion into mercury revealed unsuccessful.

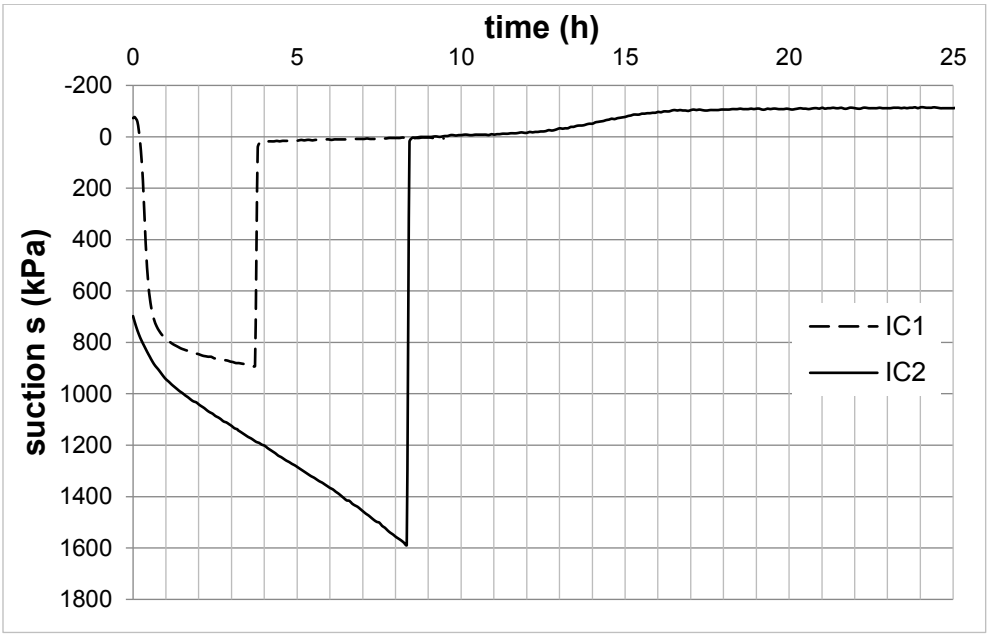

Fig. 5.19 - Suction measured by IC tensiometers for Pappadai clay.

Table 5.6 - Results of filter paper measurements on natural Pappadai clay soon after block sampling.

sample	w (%)	e	s (kPa) suction probe	s (kPa) *(Chandler et al., 1991)*	s (kPa) *Leong et al. (2002)*
IC1 (tensiometer)	29.55	0.823	891		
IC2 (tensiometer)	29.55	0.823	1588		
FP1 (filter paper)	25.02	-		2174	2135
FP2 (filter paper)	21.21	-		2821	2825

The measured values of suction on the undisturbed and on the air-dried specimen were compared to those determined on Pappadai clay (Cotecchia, 1996; Cafaro and Cotecchia, 2015) subjected to a drying path. The values of suction are plotted against water contents in Fig. 5.20.

The new data are seen to plot on a line parallel to that relative to the previous tests. So the plot suggests that the specimens from the second block sample of Pappadai clay

have undergone a pre-consolidation due to drying. On drying, the same drying path of the tests from Cotecchia (1996) seems to be followed. Although having experienced some drying due to prolonged storage, the second block sample is believed not to have undergone significant degradation of structure.
This will be further confirmed by mechanical test results in the following Chapter.
For reconstituted Pappadai clay, only one measurement of suction was made in a triaxial test, resulting in a value of 85 kPa.

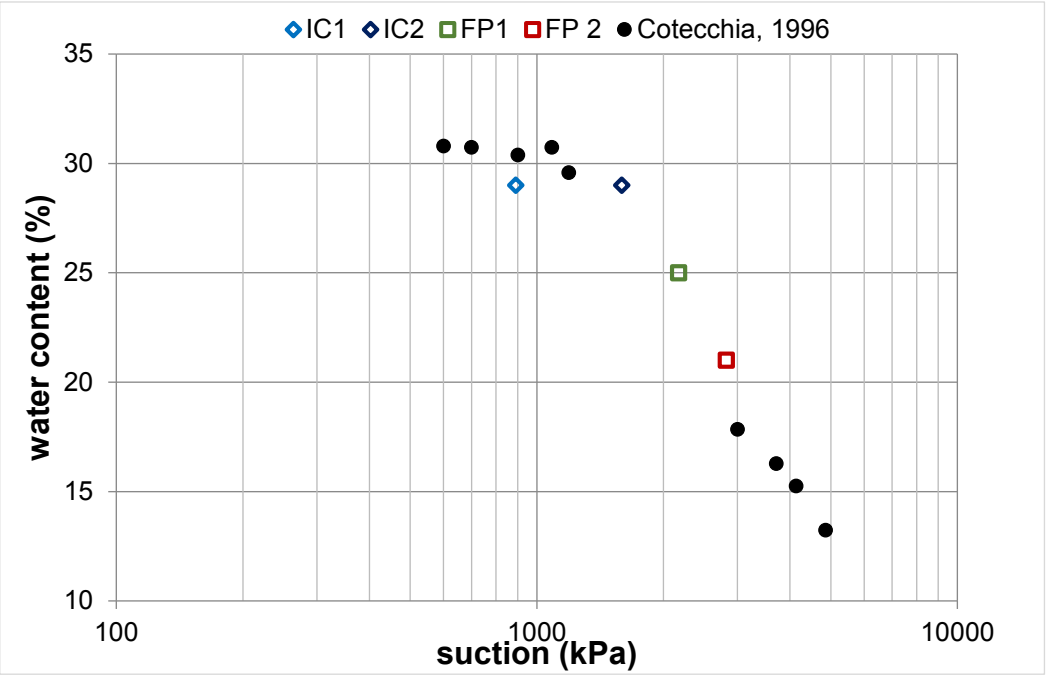

Fig. 5.20 - Comparison of suction measured on block 2 of Pappadai clay and suction resulting from a drying path on block sample 1 (after Cotecchia (1996) and Cafaro and Cotecchia (2015) modified).

The measurement of suction was also made on undisturbed Lucera clay by means of the filter paper technique. Three discs of filter paper Whatman No.42 (fpL1, fpL2, fpL3) were applied to a prism of 5 cm height, 5 cm depth and 15 cm length, sealed for one month. The average value of suction measured is reported in Table 5.7, together with the values measured in the triaxial specimens. Noticeably, the values of suction measured through the different techniques are very similar.

For reconstituted Lucera clay, suction was only measured in triaxial test and resulted in values of suction of around 25-30 kPa.

Table 5.7 - Results of filter paper and triaxial suction measurements on natural Lucera clay soon after block sampling.

sample	s (kPa) *(Chandler et al., 1991)*	s (kPa) *(Leong et al., 2002)*	s (kPa) triaxial tests
fpL1 (filter paper)	970	895	
fpL2 (filter paper)	853	779	
fpL3 (filter paper)	1392	1320	
Average filter paper	*1072*	*998*	
Natural trx specimens			900-1000

5.4.3 Oedometer tests

The reconstituted clay specimens for oedometer testing were hand trimmed with the help of the oedometer ring. The natural clay specimens, instead, were hand trimmed on a lathe from larger prisms previously cut from the block samples. While trimming the specimen, some adjacent pieces of material were isolated, weighed and placed in the oven at 105°C for at least 24h to determine the initial water content attributable to the specimen. The weight of the specimen was also measured for the calculation of initial void ratio.

Compression tests have been performed on samples of both natural and reconstituted Pappadai clay, trimmed from block sample 2 and from batch P respectively, and on samples of both natural and reconstituted Lucera clay, trimmed from the block sample and from batches L1 and L2 respectively (Table 5.1).
All the oedometer tests have been carried out as of step-loading type, the duration of each loading step being related to the reaching of a very low rate of settlement (around 0.003-0.005 mm/h) that is when the primary consolidation could be considered to have finished.

For both Pappadai and Lucera clay, for each loading step, the primary consolidation took about 48-72 hours.
At the end of each test the water in the oedometer cell was removed and the specimen was quickly unloaded, in order to restrain swelling by means of an undrained unload. At the end of the test, the extremities of each specimen were cut to measure the final water content, whereas the core of the specimen was wrapped in cling film and wax, stored in a high humidity cellar and preserved for micro-analyses.

When compressing the clay in an oedometer test, the measured settlements include not only soil compression, but also bedding compressions and the apparatus compliance. Cotecchia (1996) carried out compliance tests on a number of oedometer apparatuses and observed that, given the insufficient repeatability, the compliance test results could be difficultly considered reliable.
As both the bedding and the compliance settlements occur immediately after the application of the stress increment $\Delta\sigma_v$, that is at the commencement of primary consolidation, when the Terzaghi theory of 1D consolidation (Terzaghi, 1936) best fits the soil behaviour, the Terzaghi theory has been preferred in this work to distinguish the soil compression from the compliance and bedding settlements. Accordingly, the curve-fitting method proposed by Casagrande (1936) was applied to compute the starting value for the settlements (d_0) in the oedometer tests, both in loading and in unloading.

In the following the equations of Terzaghi's model of 1D consolidation are briefly reviewed as they have been considered of reference in the analysis of the oedometer test data.
Based upon the hypotheses of Terzaghi's model (Terzaghi and Peck, 1967), the consolidation process is expressed by the differential equation:

$$c_v \frac{\partial^2 u(z;t)}{\partial z^2} = \frac{\partial u(z;t)}{\partial t} \qquad (5.8)$$

where t is time, z is the depth from the drainage boundary and u(z;t) is the excess pore water pressure. The coefficient of consolidation c_v is equal to:

$$c_v = \frac{Mk}{\gamma_w} \tag{5.9}$$

and is assumed to be constant according to the hypotheses of Terzaghi's model. The solution u(z;t) of eq. (5.8) by separation of variables (Taylor, 1948) for consolidation under a stress increment $\Delta\sigma_v$ and constant water pressure at the drainage boundaries, emerged as a Fourier series:

$$u(X;T_v) = \frac{\sum_{n=0}^{\infty} 2\Delta\sigma_v}{Msin(MX)} e^{-M^2 T_v} \tag{5.10}$$

where M equals $(2n+1)\pi/2$. In eq.(5.10), X and T_v (Terzaghi and Pech, 1967; Taylor, 1948) are:

$$X = \frac{z}{H} \text{ and } T_v = \frac{c_v t}{H^2} \tag{5.11}$$

where H is the distance of the undrained boundary from the free drainage boundary (z=0). If Terzaghi's assumptions that the soil behaviour is linear elastic, not strain-rate dependant and of constant permeability do not hold in reality, then c_v may change during consolidation and the solution of the consolidation problem in eq.(5.10) may be not accurate enough.

According to eq. (5.10), the average consolidation degree in terms of pore water pressures $U_p(T_v)$ is:

$$U_p(T_v) = \frac{\int_0^1 (\Delta\sigma_v - u(X;T_v)dX}{\Delta\sigma_v} = 1 - \frac{\sum_{n=0}^{\infty} 2}{M^2} e^{-M^2 T_v} \tag{5.12}$$

and because of the assumption of linear soil behaviour, it is equal to the average degree of consolidation in terms of settlements $U_s(T_v)$:

$$U_s(T_v) = \frac{\int_0^1 m_v(\Delta\sigma_v - u(X;T_v)dX}{m_v\Delta\sigma_v} = U_p(T_v) \tag{5.13}$$

where S is the soil compression and m_v is the coefficient of 1D compressibility. So, for given boundary conditions, the model gives a unique expression of the average degree of consolidation of the soil stratum with time $U(T_v)$ ($=U_p(T_v)=U_s(T_v)$; Fig. 5.21) and the soil compression completely defines the process of consolidation, controlled solely by the coefficient of consolidation c_v.

Terzaghi's model was applied to the oedometer test data using the Casagrande curve fitting method (Head, 1986). For each loading step, the initial compression d_0 due to apparatus compliance and the settlement related to the average consolidation degree of 50% was calculated as shown in Fig. 5.22 (Head, 1986). The coefficient of consolidation for U% equal to 50% was calculated as:

$$c_v = \frac{0.197H^2}{t_{50}} \qquad \left[\frac{m^2}{year}\right] \tag{5.14}$$

where H is the one defined above and is expressed in mm and t is time in minutes.
The oedometric stiffness M ($=1/m_v$), was calculated as:

$$M = \frac{\Delta\sigma_v}{\Delta\varepsilon_v} \tag{5.15}$$

where ε_v is the vertical strain at the end of the compression step. The corresponding coefficient of permeability k was derived from eq.(5.9).
During the oedometer tests the creep coefficient c_α was calculated as:

$$c_\alpha = \frac{\Delta e}{\Delta log t} \tag{5.16}$$

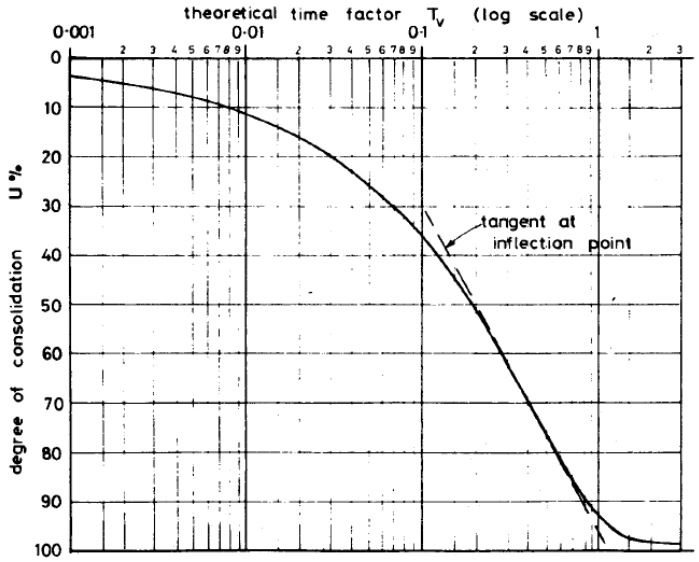

Degree of consolidation U%	Time factor T_v	$\sqrt{T_v}$
0	0	0
10	0.0077	0.0877
20	0.031	0.176
30	0.071	0.266
40	0.126	0.355
50	0.196	0.443
60	0.286	0.535
70	0.403	0.635
80	0.567	0.753
90	0.848	0.921
95	1.129	1.063
100	∞	∞

Fig. 5.21 – Terzaghi's model: U%-T_v relationship (after Head, 1986).

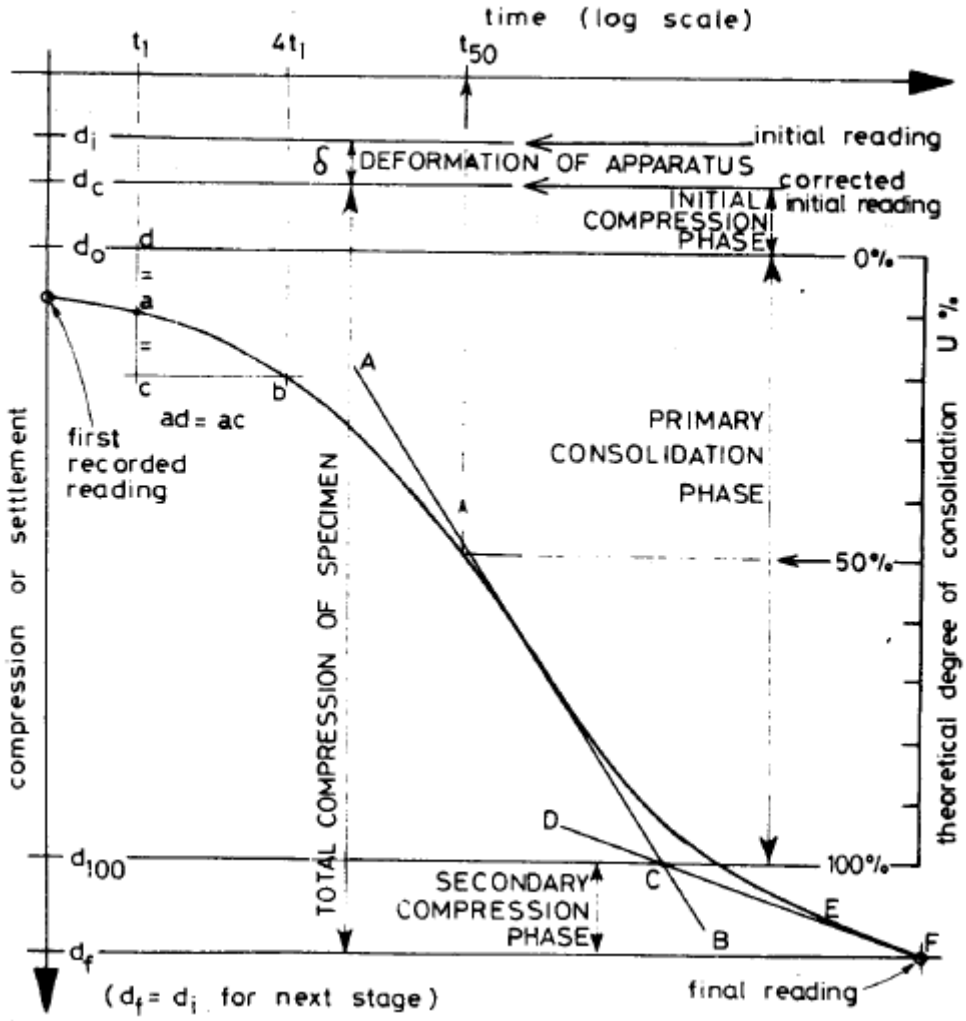

Fig. 5.22 – Casagrande curve fitting method (after Head, 1986).

5.4.4 Triaxial tests

Triaxial tests were carried out on reconstituted Pappadai and Lucera clay and on natural Lucera clay. No triaxial tests were carried out on natural Pappadai clay, because of the small quantity of material available from the block sample. Indeed, a large experimental programme was available from Cotecchia (1996) on Pappadai clay.

All the triaxial tests were carried out in the geotechnical laboratory at Technical University of Bari, using apparatuses TRX D, TRX E, TRX B and HPSPS, as discussed in Section 5.2.
All the triaxial specimens of reconstituted clay (both Pappadai and Lucera) have been trimmed manually from the batches using sharp knives to a size slightly bigger than the final size 76x38mm, then extruded onto an aluminium cradle previously greased to prevent sample sticking. While resting in the cradle the sample ends were carefully trimmed using a wire saw. As for oedometer specimens, the initial water content and the sample dimensions were carefully measured before setting up the specimen in the apparatus.
A maximum time of 30 minutes was spent to prepare the sample, in order to avoid significant drying of the sample.
Filter paper discs, which were damped before use, were placed at the bottom of the sample between the specimen base and the porous stone, which had been previously saturated.

The undisturbed triaxial specimens, all taken from Lucera clay, were hand trimmed on a lathe from prisms cut from the block sample. This was done within one hour to minimise drying of the sample. The moisture content of the trimmings was measured to determine the initial water content of the specimen and the initial weight and dimensions of the trimmed specimen were also measured, similarly to the reconstituted triaxial specimens. Filter paper, damped before use, was put at the bottom of the specimen, between the base and the saturated porous stone, and along the lateral surface of the specimen to facilitate drainage and re-saturation.
At the end of the test, the top and bottom extremities of the cylindrical specimens (around 1 cm thick) were cut, separately weighed and oven dried for the measurement of final water content. The core of the triaxial specimen, as for the oedometer specimens, was covered in cling film, waxed and stored for microstructural analyses in a high humidity cellar of the geotechnical laboratory in Bari. In fact, the cubes subjected to freeze-drying were cut from the stored specimens at UPC, at the specimen

preparation for microstructural analyses, in order to limit the change in water content. Moreover, at the extrusion of cubes for microanalyses, adjacent material resulting from the cutting was used for local and more accurate measurements of water content, to be directly attributed to the cube to be tested.

Before setting up the specimen, the triaxial cell was prepared for the test. The pore water circuit was flushed and saturated with demineralized water; zero readings for the pressure transducers and load cell were taken prior to setting up the specimen. These readings were checked after the test to determine if there had been some significant electrical drift of the transducer readings. The base pedestal was greased with wax to ensure a good sealing between the membrane and the metal once the sample is mounted.
The porous stone was first de-aired, by boiling it for a few minutes, and then kept in demineralized water to ensure complete saturation. At this stage, the porous stone was placed on the pedestal with previously dampened filter paper on the top of it. The specimen was placed on the triaxial pedestal very carefully, the membrane was folded both at the top and at the bottom to adhere to the top cap and to the pedestal respectively. O-rings are then put both at the top and at the bottom to guarantee a proper sealing of the specimen from the cell filling water.
A pair of local axial LVDTs in TRX E has been mounted on the opposite sides of the specimen in some of the tests (Fig. 5.8; see Table 5.3, Table 5.4).
At this stage, the cell could be mounted and screwed to the pedestal and then filled with water.

Some triaxial tests on both natural and reconstituted clay started with a measurement of suction during isotropic undrained loading, which is feasible if both the clay and the pore pressure measuring system are saturated. For reconstituted clays, a cell pressure of about 200 kPa was applied and a suction of about 85 kPa for Pappadai clay and of about 25-30 kPa for Lucera clay was measured. For natural clay tests (only on Lucera clay), a cell pressure of about 1500 kPa was applied and a suction of about 900-1000

kPa was measured in several tests. These suction values were close to those measured with the filter paper technique, as discussed in Section 5.4.2.

The saturation of the specimen was always checked by measuring the Skempton parameter B:

$$B = \frac{\Delta u}{\Delta \sigma_r} \qquad (5.17)$$

where $\Delta\sigma_r$ and Δu are respectively the change in cell and in the pore pressure in isotropic undrained loading.

For natural specimens of Lucera clay which were known to be incompletely saturated, a back pressure of 300 kPa was applied, giving an isotropic effective stress of 1000 kPa which was approximately the suction that should have been measured. This re-saturation stage was maintained until a B value greater than 90% was achieved, which was generally checked after 3 days. If a lower B value was obtained the base drainage system was flushed through under pressure using freshly de-aired water.

The reconstituted specimens generally had higher degrees of saturation and were not subjected to a saturation phase. Instead, a total stress of around 200 kPa was usually applied and the pore pressure allowed to stabilise. The test then commenced from whatever effective stress was measured.

The specimens were isotropically consolidated in step-loading mode, each loading/unloading step lasting until the volume strain rate dropped below 0.05%/day. Undrained and drained shears were carried out at a constant rate of strain of 0.003 mm/min and 0.0003 mm/min respectively with a constant cell pressure until an axial strain of at least 15% was reached. Undrained shear tests generally lasted around one week, whereas drained shear tests took no shorter than one month. In this case, the very low strain rate was selected to allow drainage and avoid pore pressure increase, according to mid-height suction probe measurements on stiff Pappadai and Montemesola clays by Cotecchia (1996) and Cafaro (1998).

The average axial strain during shearing ε_a was calculated as the ratio of the measured displacement Δh to the height of the specimen at the start of shearing h_0. The value of

h_0 was calculated assuming isotropic strain during the isotropic compression prior to shearing. In the shearing stages, where local strain gauges were present, the axial strain was also calculated from the local strain measurements, which were not affected by the small strain-related errors in the measurement made by the external displacement transducers. In the following sections mention will be made of the cases where the axial strain is determined from the local strain measurements.

The volumetric shearing strains, ε_v, were calculated as the ratio between the volume changes and the volume of the specimen V_0 before shearing. The shearing strain ε_s was calculated as:

$$\varepsilon_s = \varepsilon_a - \frac{\varepsilon_v}{3} \qquad (5.18)$$

The current area of the specimen during shearing was calculated applying the right-cylinder correction (Bishop and Henkel, 1957):

$$A = A_0 \frac{1 - \varepsilon_v}{1 - \varepsilon_a} \qquad (5.19)$$

where A_0 is the initial cross-sectional area, ε_a and ε_v are the axial and volumetric strain. The corrected area was used to calculate the q-p' state.

The area correction was applied until a complete cinematically-compatible mechanism of localized deformation emerged. In all the tests, a failure surface formed rapidly and the prior formation of a shear band was not observed. After the formation of the failure surface the displacement mechanism consisted primarily of the sliding of two blocks along the failure surface. Thus, the q-p' state was calculated using the expression proposed by Chandler (1966) for the cross-sectional area under the conditions shown in Fig. 5.23:

$$Area = \frac{{D_{fs}}^2}{2}\left[\frac{\pi}{2} - \arcsin\left(\frac{\Delta h - \Delta h_{fs}}{D_{fs}}\right)\right] - \left(\Delta h - \Delta h_{fs}\right) cotg\alpha \sqrt{\frac{{D_{fs}}^4}{4} - \frac{\left(\Delta h - \Delta h_{fs}\right)^2 (cotg\alpha)^2}{4}} \qquad (5.20)$$

where D_{fs} and Δh_{fs} are the diameter of the specimen and the displacement at the time of formation of the failure surface, respectively. Eq.(5.20) does not account for changes in volume of the clay blocks, so it should be used in undrained tests only. However, it

was used also for the drained tests because of the limited extent of volume changes after failure surface formation.

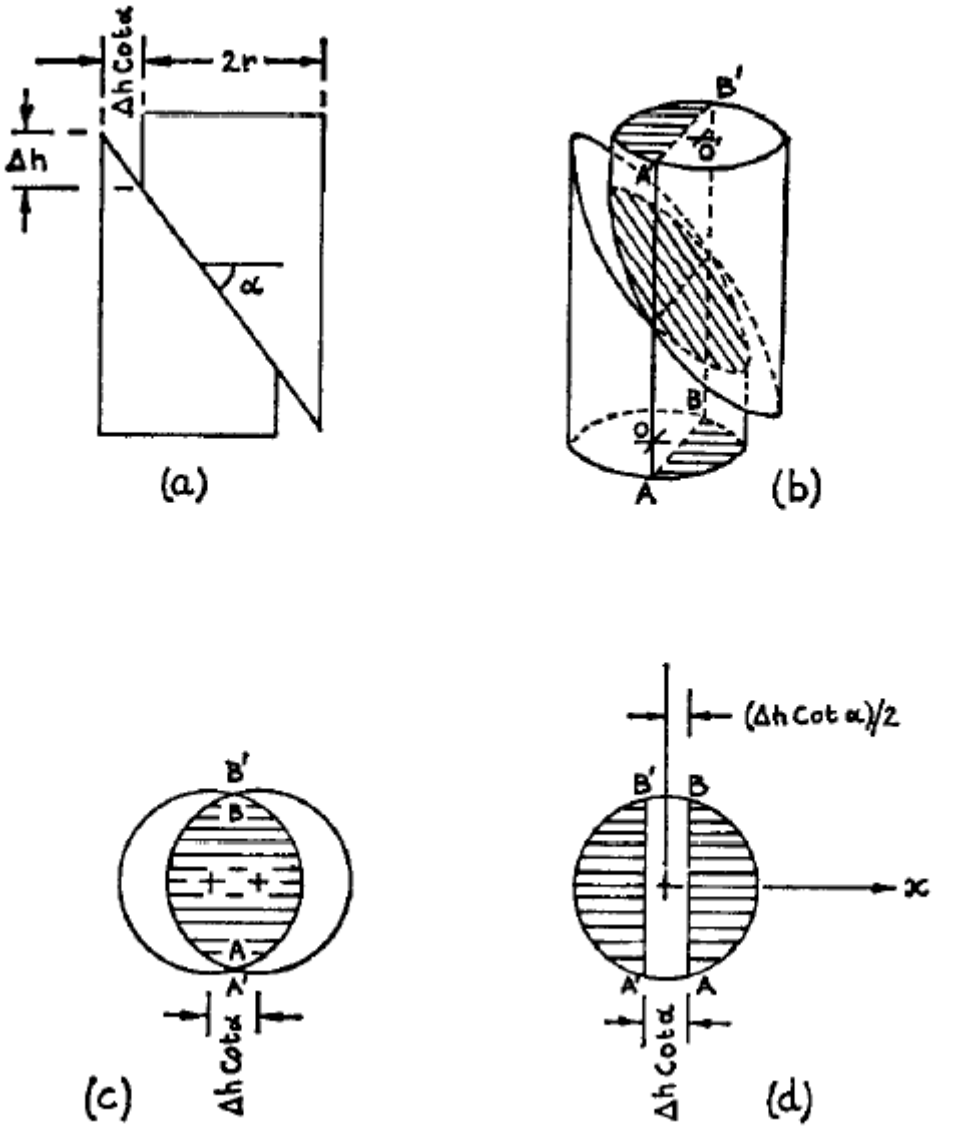

Fig. 5.23 - Specimen with preformed failure plane at axial displacement ⊿h (eq.(5.20); after Chandler, 1966).

The error in the overall calculation of the area during the test stems essentially from the assumption that the specimen was suddenly split into two sliding blocks when the failure surface was formed. By contrast, although the formation of the failure surface appeared brittle, there might have been a stage in the test when the specimen underwent a deformation as shown in Fig. 5.24, though this deformation mode cannot easily be modelled. The expression used to calculate the vertical strain ε_a and the shearing strain ε_s was the same before and after the failure surface formation. Thus, the shearing strains ε_s were thereafter underestimated (Cotecchia, 1996).

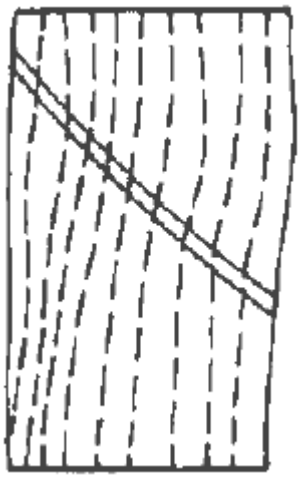

Fig. 5.24 - Bulging and progressive shear band formation before the development of a failure surface (after Cotecchia (1996)).

In the following the data corrected for localization as above will be distinguished with the suffix "loc". In some of the tests, the values of q_{loc} and q/p'_{loc} tend to increase with increasing axial strain. Chandler (1968) showed this to be the effect of the restraint of the membrane to continued deformation of the specimen. He obtained a correction to the deviatoric stress which depended on the cell pressure and the deformation of the specimen after the formation of the failure surface. After the correction of the data, the adjusted values of q_{loc} and q/p'_{loc} remain almost constant after the drop resulting from the formation of the failure surface.

The plastic volumetric strain ε_v^p was calculated as the difference between the total volumetric strain ε_v and the elastic volumetric strain ε_v^e. For the calculation of ε_v^e, isotropic non-linear elasticity was assumed along the swelling lines (κ lines) in the v-lnp' plane. Consequently, ε_v^p is equal to:

$$\varepsilon_v^p = \varepsilon_v - \frac{\kappa}{v_0} ln\left(\frac{p'}{p'_0}\right) \qquad (5.21)$$

v_0 and p'_0 being the specific volume and the mean effective pressure at the start of shearing, respectively.

The elastic shear strains ε_s^e were regarded as negligiblethus the plastic shear strains ε_s^p coincided with ε_s. The plastic strain increment ratio $d\varepsilon_v^p/d\varepsilon_s^p$ was derived from linear regression of the data. Similarly, the stiffness G was calculated from linear regression of the q-ε_s data.

6 MECHANICAL TEST RESULTS

6.1 Introduction

In the present Chapter, the investigation of the macro-response of the clay will be described and the results of mechanical tests carried out on both the natural and the reconstituted Pappadai clay and Lucera clay will be discussed.

As explained in Section 5.1, the testing programme was intended to explore the clay mechanical behaviour under different loading paths, both before and beyond gross-yield, in compression and shearing. Also, testing was repeated and stopped at different stages in order to explore the evolution in microstructure generated by the loading path. Previous tests carried out by Cotecchia (1996) on Pappadai clay and by Longo (2003) and Losacco (2004) on Lucera clay were compared with the new results in order to improve the understanding of the clay behaviour.

One-dimensional compression tests will be analysed first; the compression curves of the clays in the e-σ'_v plane will be derived and a comparison will be made between the curves of the natural and of the corresponding reconstituted clay. The stress corresponding to gross-yield for the natural clay will be characterized.

Then, the behaviour of the clays in isotropic compression will be analysed and the normal compression lines in both isotropic and oedometric compression will be identified and compared.

The triaxial tests performed to investigate the macro-behavioural framework in shear of both the natural and the reconstituted clay will be analysed. The stress-strain behaviour and the strength of the clays will be examined and a state boundary surface will be defined. The effects on the clay response of structure and of its evolution in shear will be particularly addressed.

6.2 One-dimensional compression tests

The results of the oedometer tests listed in Section 5.1 and Table 5.1 are discussed in the following. In particular, the relation of the parameters: oedometric stiffness, M, coefficient of consolidation, c_v, coefficient of permeability, k, creep coefficient, c_α,

compression and swelling indexes C_c and C_s, with the yield stress ratio, YSR $= \sigma'_{vy}/\sigma'_{v0}$ (Burland, 1990), will be analysed.

The oedometer test results for the second block sample of Pappadai clay will be compared to the results of some oedometer and CRS (constant rate of strain) tests carried out on Pappadai clay by Cotecchia (1996). Compression tests from the undisturbed state to either medium pressures (OED5 to 5000 kPa) or to large pressures (CRSnat to 22 MPa), together with swelling tests from the undisturbed state (OED7) and from post-yield compression states (OED8 from 3000 kPa) to very low pressures will be discussed. For reconstituted Pappadai clay, tests OEDR of compression and swelling and test CRSrec of compression to very large pressures will be replotted.
Analogously, the oedometer tests on Lucera clay will be compared with those carried out on the same clay by Longo (2003), consisting in two compression tests on the natural clay and one on the reconstituted clay: EDMP, for swelling from the undisturbed state and compression to post-yield and swelling; EDHP, for compression to large pressures and swelling; EDR, for compression of the reconstituted clay to large pressures and swelling.

6.2.1 Compression curves and gross yield stresses

The compression curves for the oedometer tests carried out in this experimental programme on Pappadai and Lucera clay are shown in the following.
The sole compression tests on Pappadai clay are shown in Fig. 6.1, along with the compression curve of the clay in the consolidometer; these are compared to the above-mentioned tests from Cotecchia (1996) in Fig. 6.2. For clarity, only the first stage of swelling from the undisturbed state is reported for test OED7, which also includes a compression stage to medium pressures that will be shown later. The compression curves from the consolidometer stage, i.e., from slurry to $\sigma'_v = 200$ kPa, are also plotted for both the batches of the previous and of the more recent investigations.
For both the new and the previous tests the compressibility of the natural clay increases dramatically at about $\sigma'_v = 1500$ kPa and the gross-yield state, σ'_{vy} (Y in Fig. 6.2), can

be identified at a vertical effective stress of around 2600 kPa and a void ratio around 0.8, similarly to what found by Cotecchia (1996).

Casagrande construction (1936) was used to identify the gross yield point; the distinction between σ'_p and σ'_{vy} has been defined in Chapter 3.

Tests R and R2 start from a lower void ratio, probably due to light drying undergone by the specimens, so they are seen to be initially parallel to tests OED5 and CRSnat; then they join a common compression line beyond gross yield.

Cotecchia (1996) found that the value of σ'_{vy} for natural Pappadai clay was higher than its geological pre-consolidation pressure σ'_p, which was about 1310 kPa. This resulted in Pappadai clay having a YSR higher than its OCR, the former being about 6 and the latter about 3.2; this was considered a consequence of the long-term diagenesis that the clay had undergone, causing YSR>OCR. Undisturbed Pappadai clay from block sample 2 has been shown to have undergone a light pre-consolidation due to drying occurred during the long-term storage (Section 5.4.2). This has caused a higher suction in the undisturbed clay and then a higher swelling pressure in the oedometer tests, which reduces the YSR of the clay after drying to around 2. However, no change has occurred to the gross-yield pressure, confirming that little alteration occurred to the microstructure of the second block sample.

With reference to the reconstituted clay, the tests EDOR1 and EDOR2 started with the application of a pressure equal to that of the last consolidometer compression step, i.e., 200 kPa. The first point in the compression curves corresponds in both cases to a void ratio smaller than that at the end of the consolidometer stage, as effect of the unloading reloading path the clay has been subjected to. The compression curves resulting from the new tests on the reconstituted clay are seen to differ from those obtained by Cotecchia (1996), mainly because of the differences in the final void ratios reached at the end of consolidation in the consolidometer (Section 5.4.1). In fact, as discussed in Chapter 5, although the procedure followed for the preparation of the slurry was the same (Burland, 1990), differences arose in the void ratio of the slurry and, accordingly, in the compression curves of the consolidometer stage.

The ratio of the vertical effective stress at gross-yield σ'_{vy} to the equivalent pressure taken on the compression curve of the reconstituted clay σ^*_e defines the stress sensitivity S_σ (Cotecchia and Chandler, 2000; see Chapter 3). In this case, S_σ is equal to 3.5.

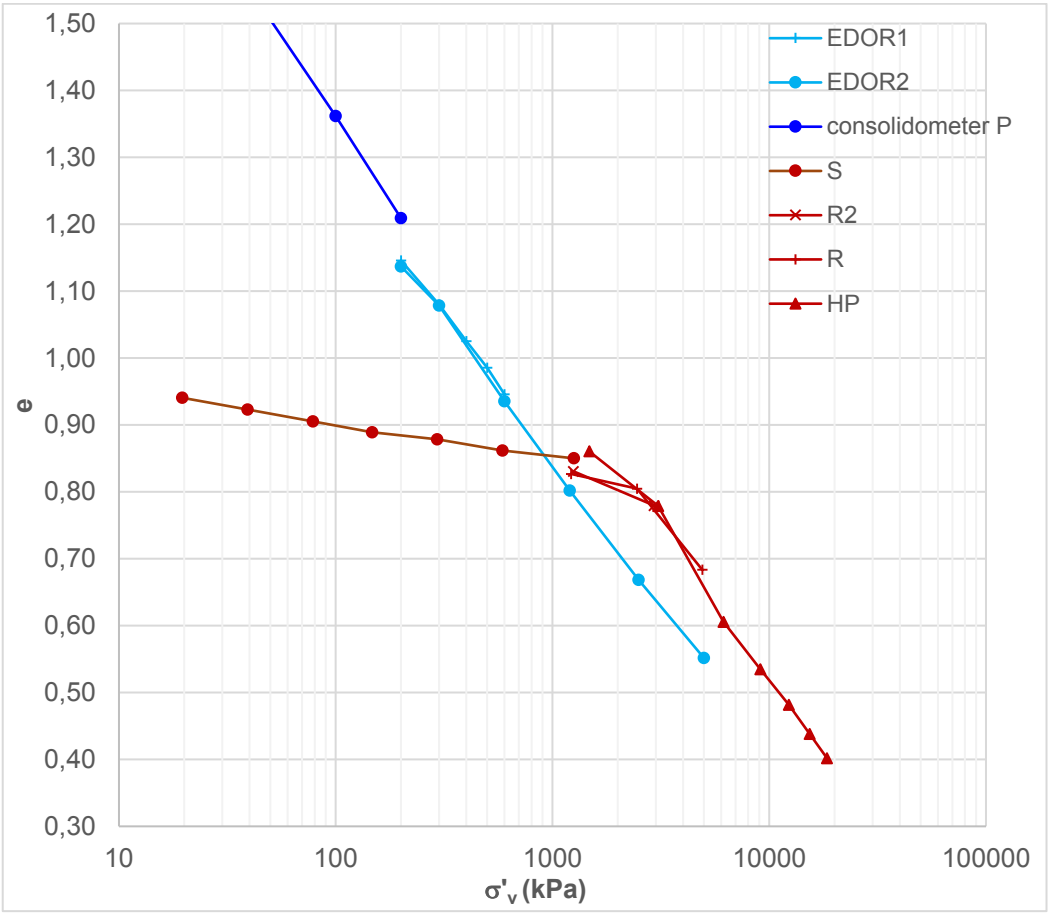

Fig. 6.1 – 1D compression tests on undisturbed (red) and reconstituted (light blue) Pappadai clay from block sample 2.

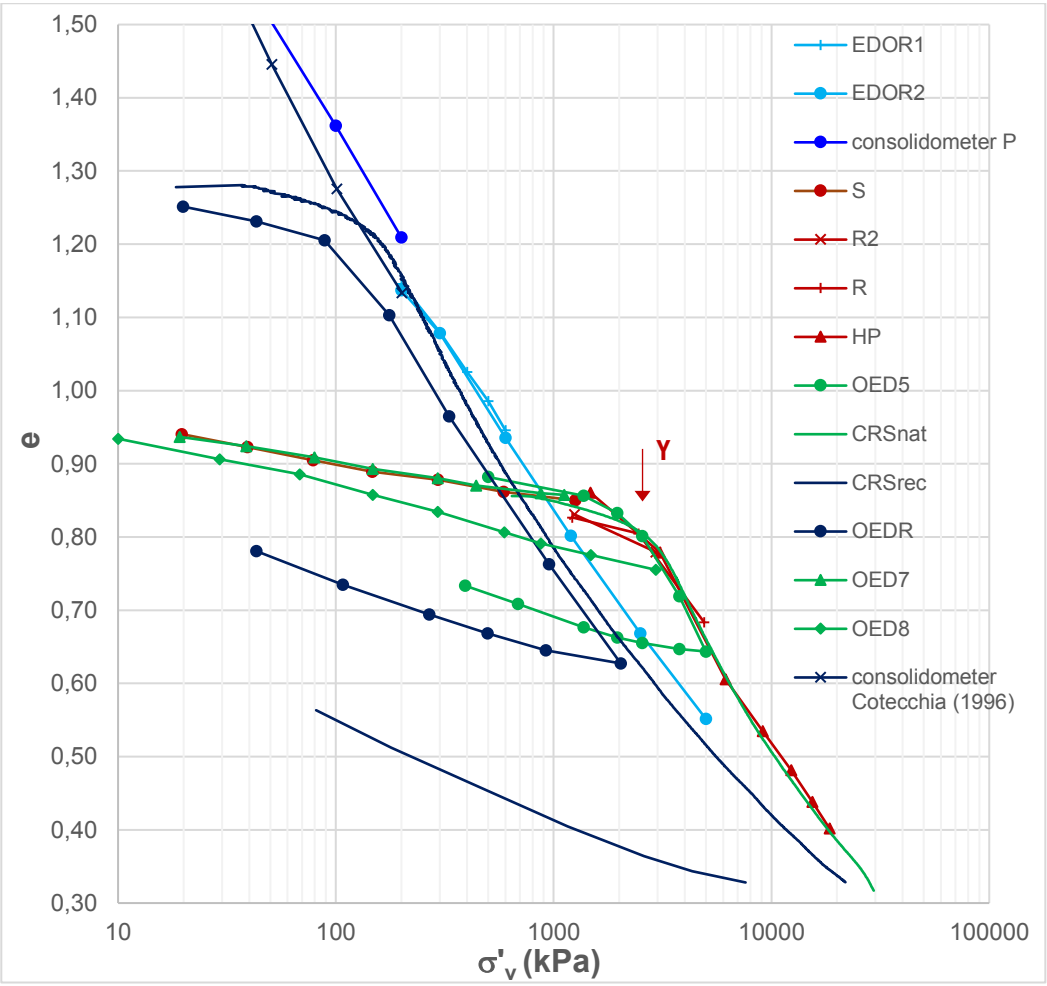

Fig. 6.2 - 1D compression tests on undisturbed and reconstituted Pappadai clay: comparison of tests from this experimental programme (red for the natural clay, light blue for the reconstituted clay) and tests from Cotecchia (1996) (green for the natural clay, blue for the reconstituted clay).

The one-dimensional compression curves for Lucera clay are plotted in Fig. 6.3 and then compared to those of Longo (2003) in Fig. 6.4.

In the same figures, the compression curves resulting from the consolidation from slurry to σ'_v=100 kPa for both batches L1 and L2 (Section 5.4.1) are also plotted.

The reconstituted specimens from batches L1 and L2 were initially lightly overconsolidated due to the decrease in suction as a consequence of unloading in the consolidometer (Section 5.4.1).
At σ'_v higher than 100 kPa the data appear to converge to a straight line. A difference is seen in Fig. 6.4 between the compression curves of the reconstituted clay from the former and the new investigation. As for the case of reconstituted Pappadai clay, the differences between the slurries are reflected in differences between the compression curves.

As for Pappadai, the Casagrande construction is used to identify the gross yield stress of the natural Lucera clay, which is found at σ'_y=2700-2800 kPa, at a void ratio of around 0.51. The stress sensitivity S_σ in this case is seen to be 1.93.

The state path followed by the clay during recompression after significant swelling in test EDOL6 is seen to intercept the initial state (e_0; σ'_{v0}) and then continue towards the gross-yield point. The curve (Fig. 6.5) is seen to superimpose to that of test EDOL2 compressed from undisturbed state and to be in good agreement with test EDOL1, also compressed from undisturbed state, plotting lightly below its state path. The similarity with this and the other compression curves seems to suggest that limited structural degradation should occur during swelling, despite the unloading path being very large. It should be noticed that greater, although not dramatic, differences were found by Cotecchia (1996) between recompression stress paths occurring after either limited or greater swelling from undisturbed state. In the latter case, the state path was seen to pass below the initial state (e_0; σ'_{v0}) and a light reduction of σ'_{vy} by comparison with the yield stress of the clay in the other oedometer tests was observed. Not only the swelling process was seen to reduce the yield stress, but it also resulted in the post-gross yield compression line differing from that of the undisturbed clay (Fig. 6.5). Despite being limited, this effect suggests that although limited, some weakening is induced by swelling for the structure of Pappadai clay (Cotecchia and Chandler, 1998) and not as much for Lucera clay. This is probably because Pappadai clay possesses a

more sensitive bonding than Lucera clay, due to the quiet deposition conditions in which it generated with respect to Lucera clay. It is likely that the more turbulent and chaotic deposition environment of Lucera clay did not allow for the formation of the amorphous calcite bonding which was instead recognized for Pappadai clay as the result of diagenesis (Section 2.8).

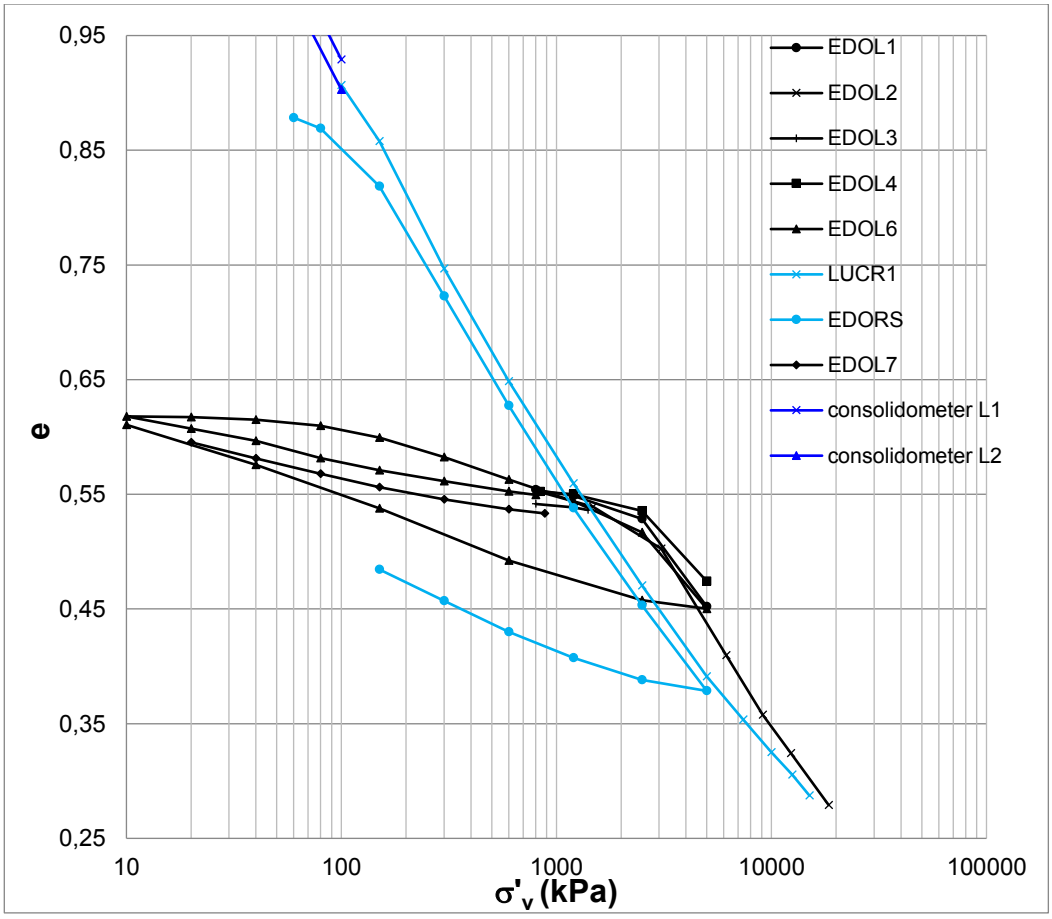

Fig. 6.3 - 1D compression tests on undisturbed (black) and reconstituted (light blue) Lucera clay.

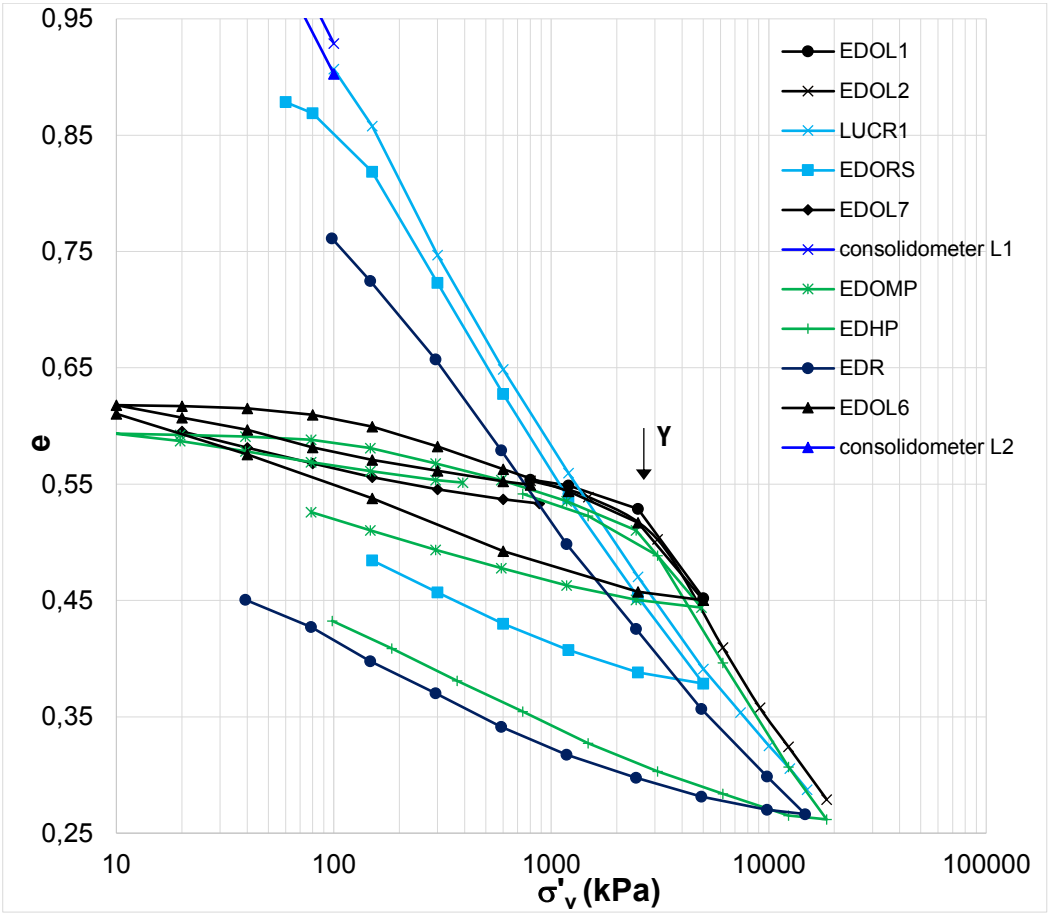

Fig. 6.4 - 1D compression tests on undisturbed and reconstituted Lucera clay: comparison of tests from this experimental programme (light blue for the reconstituted clay, black for the natural clay) and tests from Longo (2003) (blue for the reconstituted clay, green for the natural clay).

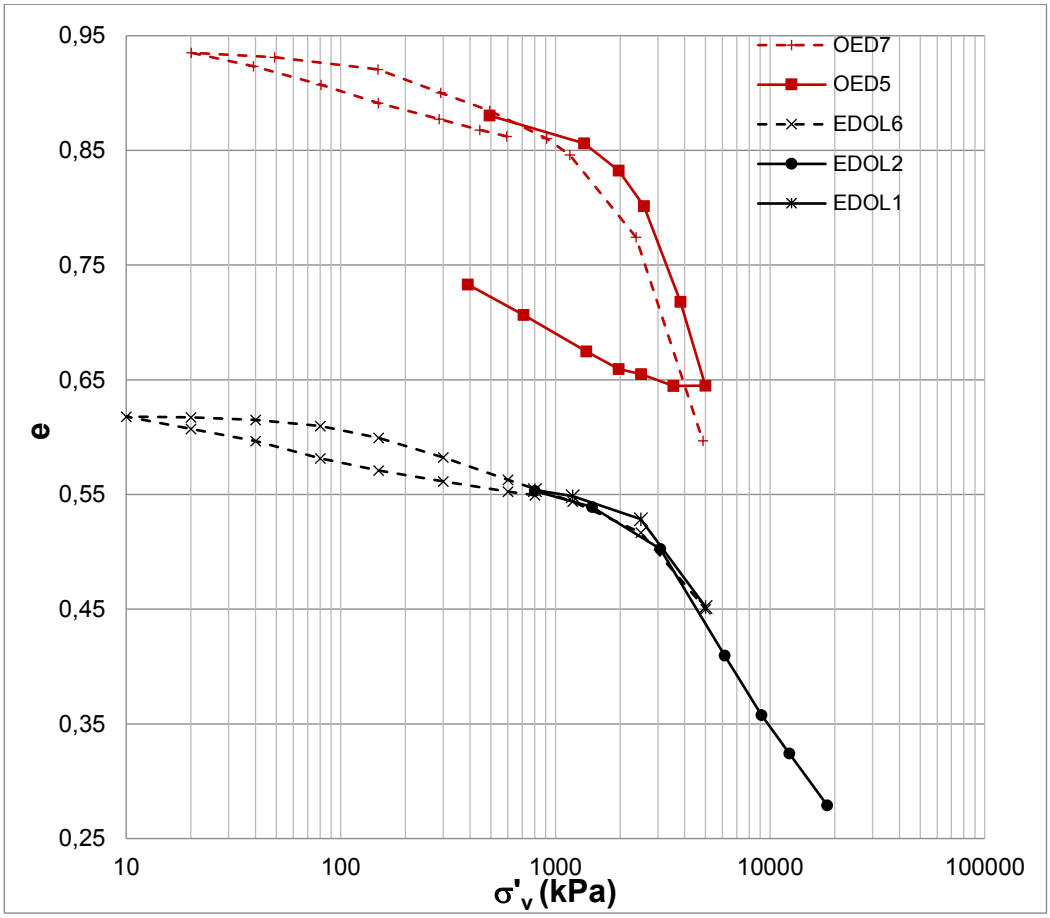

Fig. 6.5 - Effects of swelling on the compression behaviour of natural Pappadai (red) and Lucera (black) clays.

The compression indices C_c, calculated for the tests shown in Fig. 6.2 and Fig. 6.4, are plotted against σ'_v in Fig. 6.6 and in Fig. 6.7 for Pappadai and Lucera clay respectively. The location of the gross yield stresses is also shown for both the natural and the reconstituted clay.

Pappadai clay data show that the compression index is lower than 0.05 below 1000 kPa, but it increases to 0.54 over the stress range 1000-3000 kPa. For the new tests, the C_c - σ'_v curves are initially parallel to those of tests OED5 and OED7 (Cotecchia, 1996) and then join that of test CRSnat beyond gross yield, around σ'_v=6000 kPa.

Similarly, for Lucera clay the value of C_c increases over the stress range which includes σ'_y, thereafter it is first constant and then decreases.
The lower compression index found for Lucera clay is considered to be an effect of the less sensitive bonding characterizing the clay, which determines a less pronounced structure degradation in one-dimensional compression post-gross-yield, other than lower structure weakening in recompression after swelling.
The different bonding sensitivity recognized in the two clays, in agreement with the different stress sensitivity showed in one-dimensional compression, will be seen to determine also differences in the microstructural features of undisturbed Pappadai clay and Lucera clay

The values of $C_c^* \approx 0.5$ for reconstituted Pappadai ($200 < \sigma'_y < 600$ kPa) and $C_c^* \approx 0.32$ for reconstituted Lucera ($120 < \sigma'_y < 600$ kPa) can be derived from the horizontal parts of the C_c - σ'_v curves shown in Fig. 6.6 and Fig. 6.7. These values appear to be in both cases in good agreement with the empirical relationship value derived from Schofield and Wroth (1968):

$$C_c = G_s \frac{IP}{2} \qquad (6.1)$$

which gives 0.48 for reconstituted Pappadai clay and 0.32 for reconstituted Lucera clay. As expected, the compressibility calculated using eq. (6.1) is for reconstituted soils and is lower than that observed for undisturbed soils (Wood, 1994).

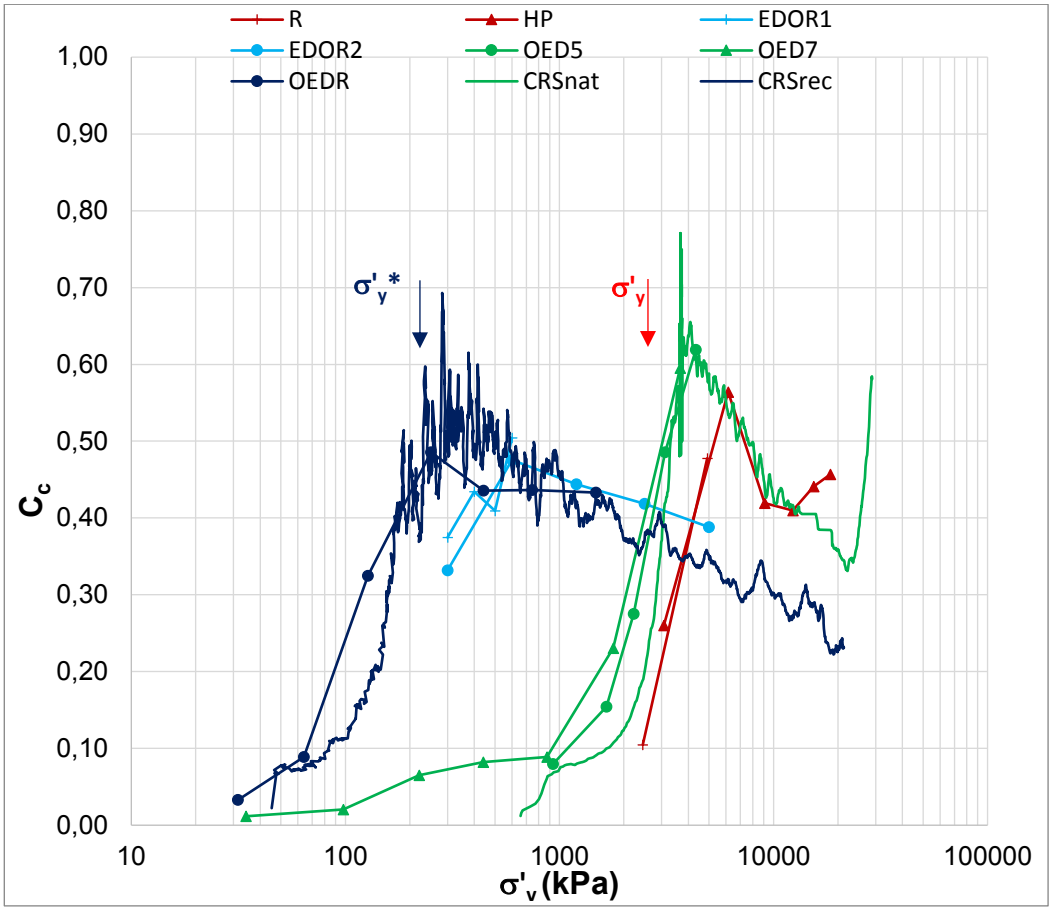

Fig. 6.6 – C_c values from tests on undisturbed and reconstituted Pappadai clay. Data from new tests (red for natural and light blue for reconstituted) compared with data from Cotecchia (1996) (green for natural and blue for reconstituted).

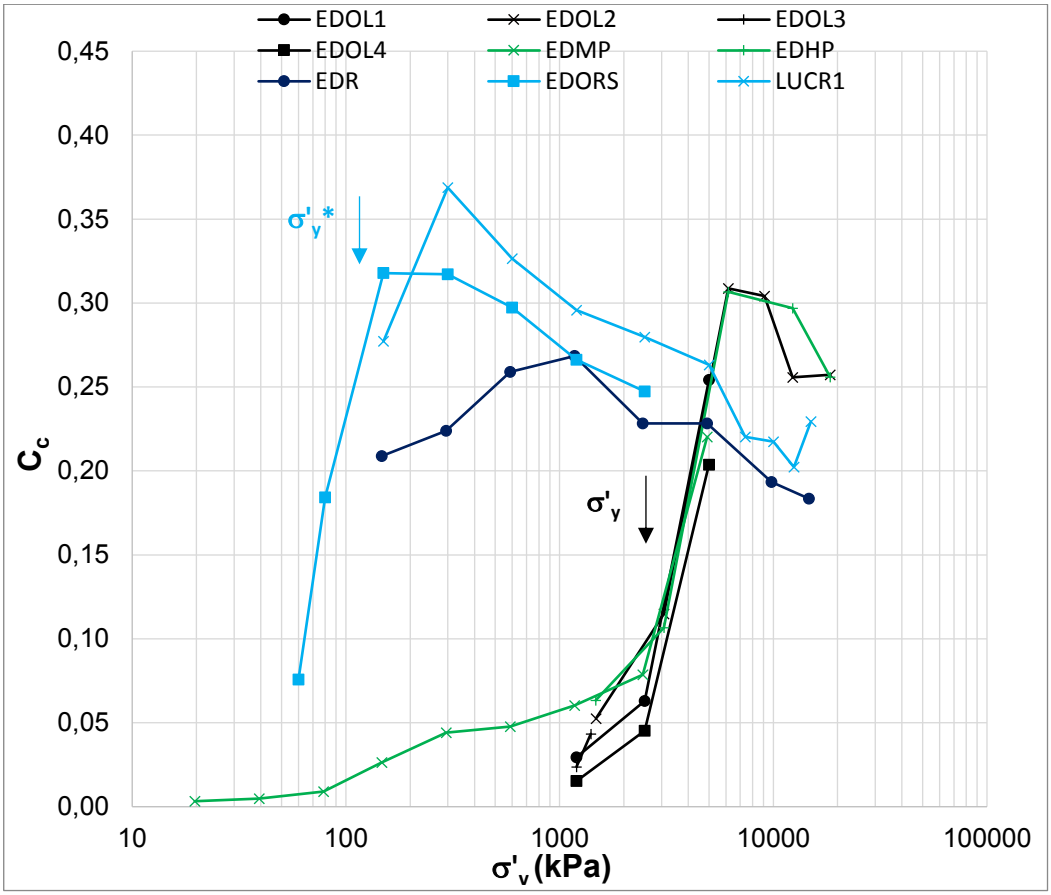

Fig. 6.7 - C_c values from tests on undisturbed and reconstituted Lucera clay. Data from new tests (black for natural and light blue for reconstituted) compared with data from Longo (2003) (green for natural and blue for reconstituted).

In Fig. 6.8 and Fig. 6.9, the swelling indices C_s measured in swelling tests are plotted against σ'_v for Pappadai and Lucera clay respectively.

For the natural clay, the swelling index is seen to vary depending on the starting point of the swelling path on the NCL. Swelling of Pappadai clay from the undisturbed state (tests S and OED7, full symbols) determines an average swelling index of 0.06, which increases to around 0.08 in the swelling paths post-gross yield (OED5 and OED8, empty symbols), getting closer to the value exhibited by the reconstituted clay (OEDR). Reconstituted Pappadai, in fact, has an average C_s* of around 0.08.

In Fig. 6.9 the curves C_s-σ'_v are plotted for reconstituted and natural Lucera clay. In the latter case, full symbols indicate swelling from undisturbed state and empty symbols indicate swelling after compression beyond gross yield.

Similarly to Pappadai clay, swelling of Lucera clay from the undisturbed state determines an average C_s of 0.04, which increases to around 0.06 post-gross-yield. Reconstituted Lucera clay has an average C_s* that is around 0.08.

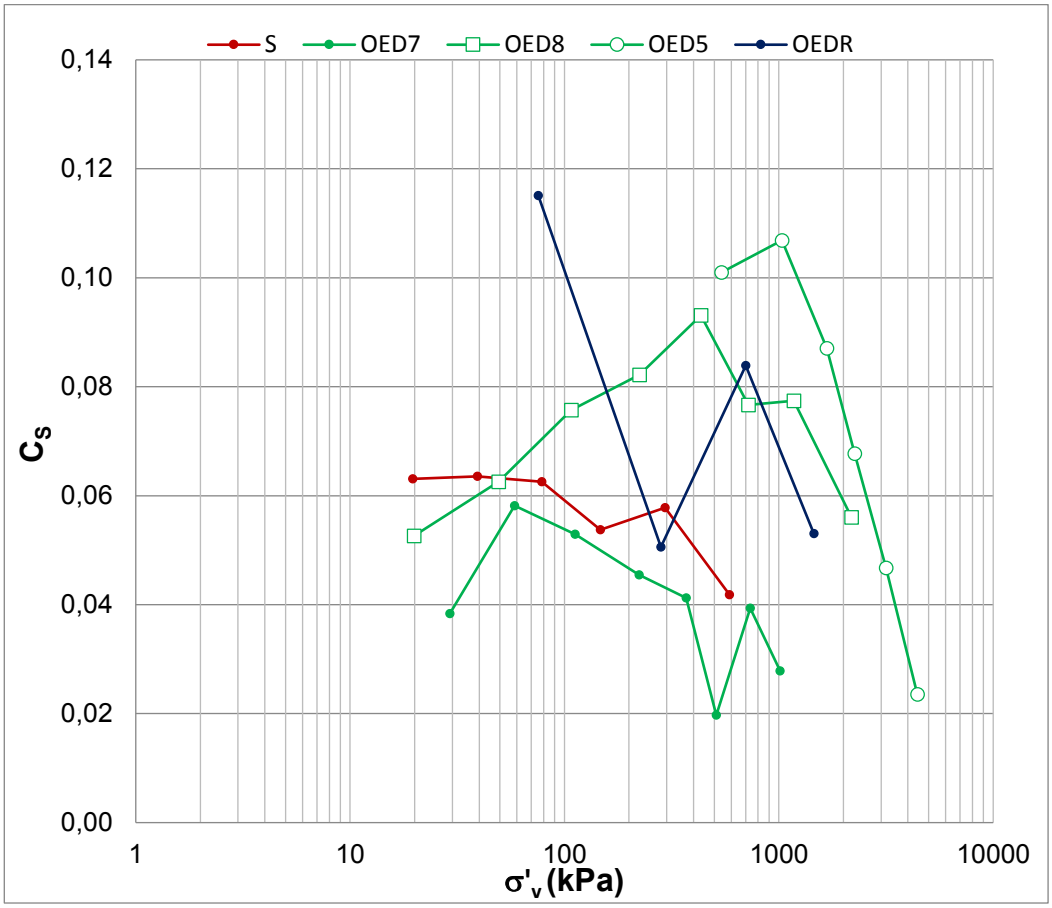

Fig. 6.8 – C_s values from tests on undisturbed and reconstituted Pappadai clay. Data from new tests (red for natural) are compared with data from Cotecchia (1996) (green for natural and blue for reconstituted).

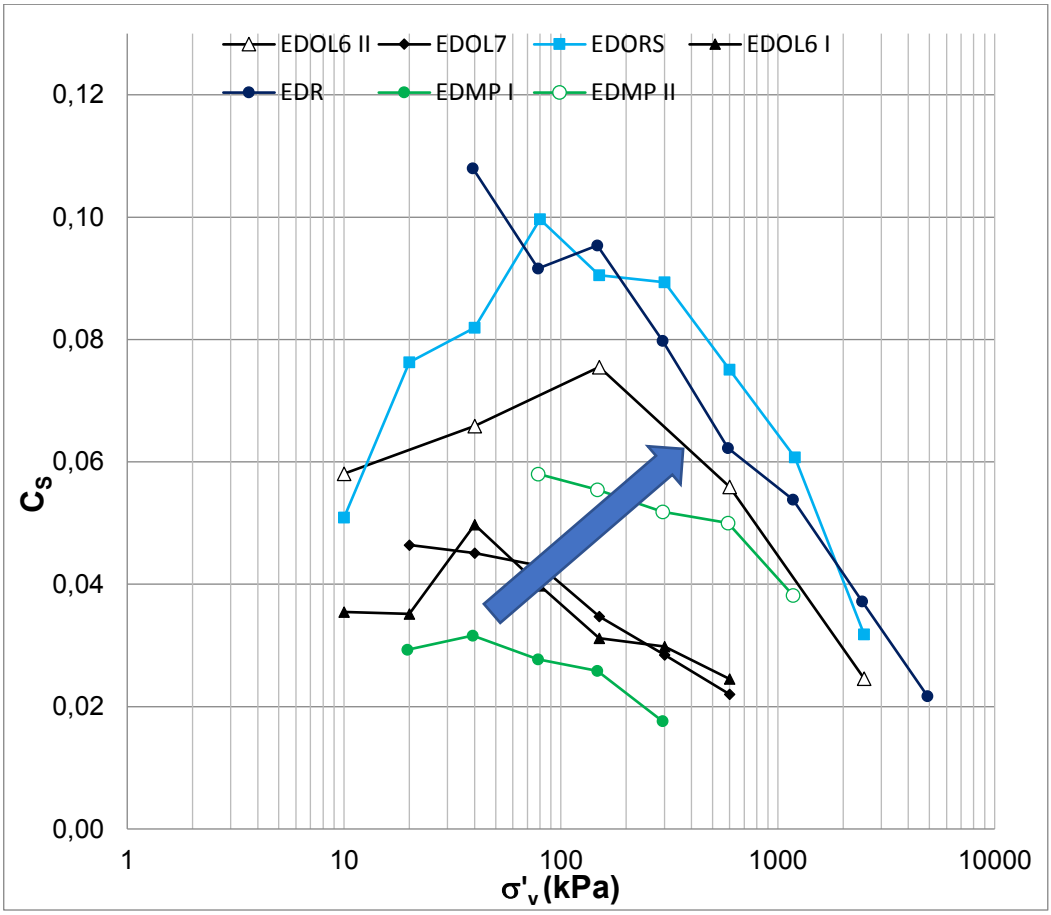

Fig. 6.9 - C_s values from tests on undisturbed and reconstituted Lucera clay. Data from new tests (red for natural and light blue for reconstituted) are compared with data from Longo (2003) (green for natural and blue for reconstituted).

6.2.2 Primary and secondary oedometric consolidation

The Casagrande curve fitting technique could be satisfactorily applied to all consolidation curves of both tests on Pappadai clay and Lucera clay to compute both d_0, the immediate oedometer compliance settlement, used to correct the data for compliances, and the Terzaghi coefficient of consolidation, c_v.

The values of oedometric stiffness M are plotted against σ'_v for Pappadai and Lucera clay in Fig. 6.10 and Fig. 6.11 respectively.

The oedometric stiffness for the undisturbed Pappadai clay is seen to be about 70 MPa, whereas when reloaded after large swelling (OED7), the clay exhibits a lightly lower value of M (Cotecchia, 1996). With compression, the values of stiffness recorded in the different tests reduce and become progressively closer. The minimum values of M are recorded at σ'_v just beyond gross yield. Post-gross yield the clay specimens seem to exhibit equal stiffness for equal σ'_v, independent of their stress history. Reconstituted Pappadai clay initially shows a value of M of around 30 MPa, which is kept constant until just beyond gross yield. For increasing pressure, the values of M, for both the natural and the reconstituted clay, are seen to follow a straight line in the bi-logarithmic plane, similarly to what observed by Cotecchia (1996). Thus, in general, whatever type of structure present in the clay, the stiffness beyond gross yield increases exponentially with the vertical stress.

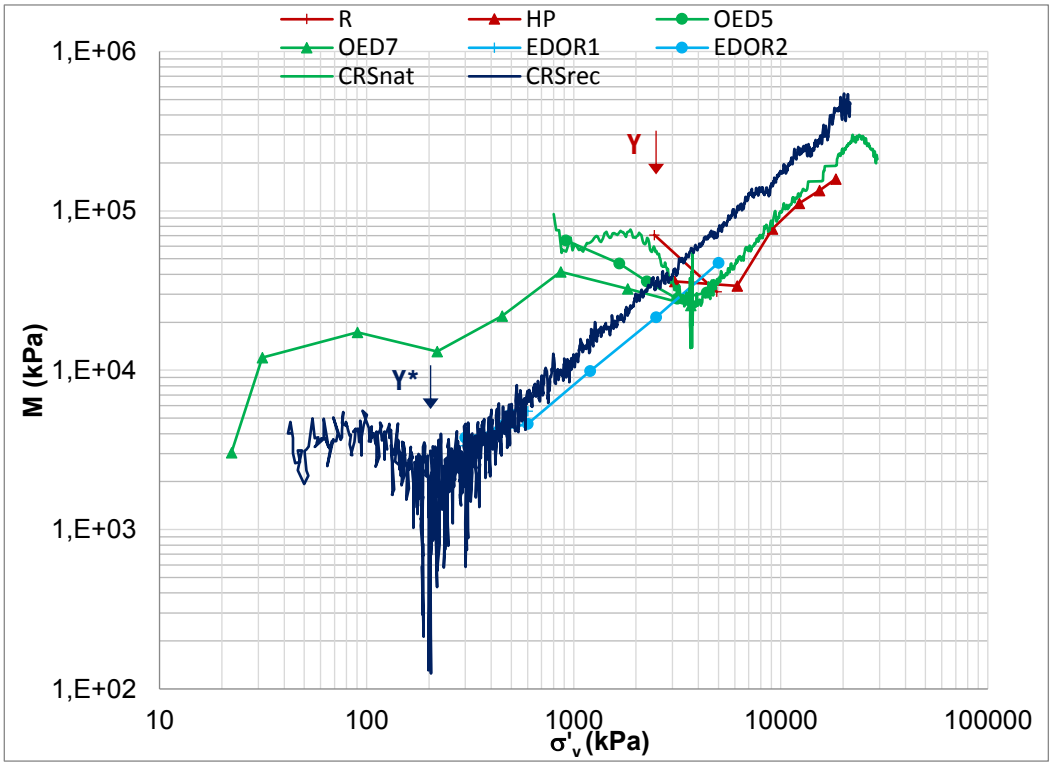

Fig. 6.10 – Oedometric stiffnesses M measured in oedometer tests and CRS tests on natural and reconstituted Pappadai clay. Data from new tests (red for natural and light blue for reconstituted) are compared with data from Cotecchia (1996) (green for natural and blue for reconstituted).

A similar trend is observed for Lucera clay (Fig. 6.11); the stiffness of the clay in the undisturbed state is seen to range from 80 to 200 MPa, with lower values corresponding to compression after swelling. Then, the curves converge to similar values just beyond gross-yield and, after a minimum value of around 50 MPa, the stiffness starts increasing according to an exponential law. The reconstituted clay stiffness has an initial value of around 30 MPa, which increases soon after gross yield, following a linear trend almost parallel to that of the natural clay.

For both Pappadai and Lucera clay, the natural clay disturbed by swelling before compression is still stiffer than the reconstituted clay before gross yield, indicating that the structural features giving rise to the current strength and stiffness of the natural clay are stable and are not altered significantly by swelling.

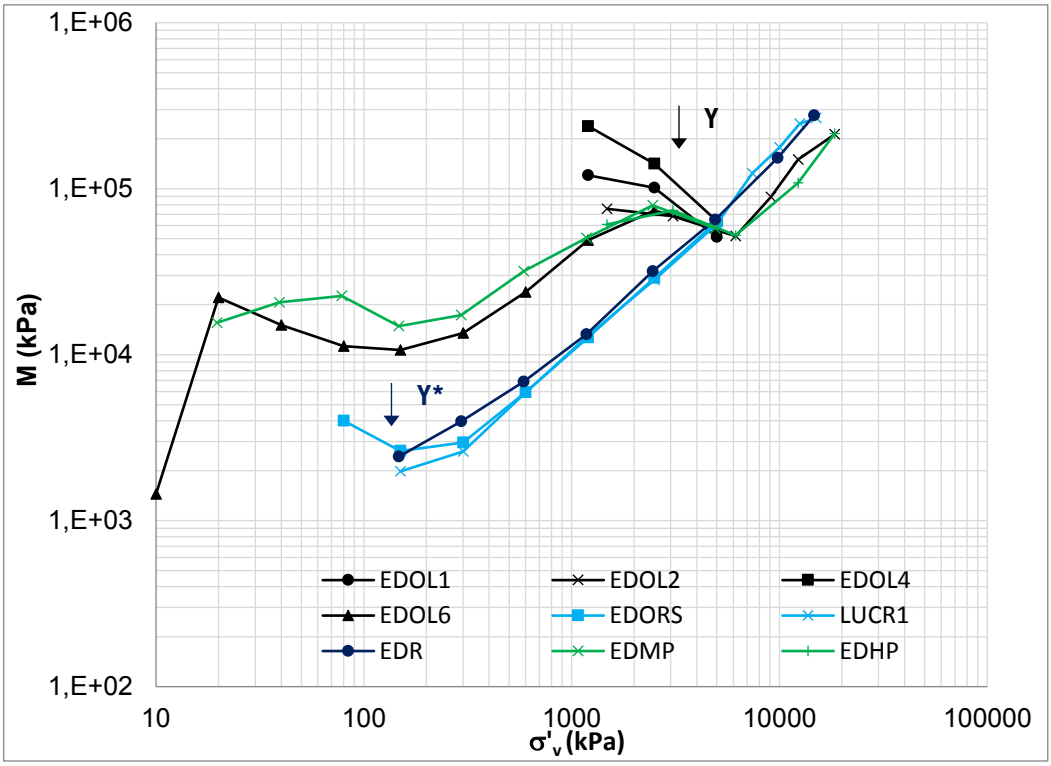

Fig. 6.11 - Oedometric stiffnesses M measured in oedometer tests on natural and reconstituted Lucera clay. Data from new tests (black for natural and light blue for reconstituted) are compared with data from Longo (2003) (green for natural and blue for reconstituted).

The c_v values corresponding to the M values shown in Fig. 6.10 and Fig. 6.11 are plotted in Fig. 6.12 and Fig. 6.13.

For natural Pappadai clay, c_v values are seen to be high at the initial state and then decrease when yield is approached, until a constant value is reached. CRS tests are seen to give higher values of c_v than those recorded in oedometer tests, which however rapidly drop to values which are consistent with those measured in oedometer tests.

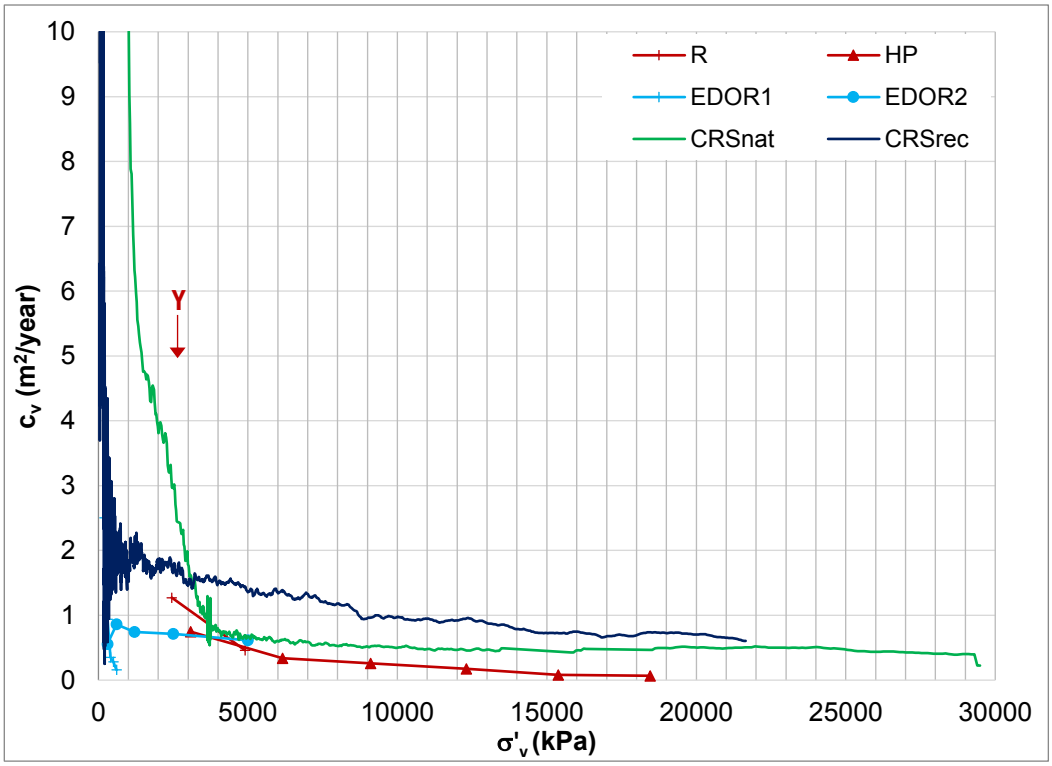

Fig. 6.12 - Values of c_v of natural and reconstituted Pappadai clay measured in oedometer and CRS tests. Data from new tests (red for natural and light blue for reconstituted) are compared with data from Cotecchia (1996) (green for natural and blue for reconstituted).

For the reconstituted clay, the c_v values rise to a maximum before dropping to a minimum around gross yield.

Just beyond gross yield the c_v value of the natural clay is already very low, and it reduces further only slightly with increasing σ'_v. The c_v value for the reconstituted clay

is similar to that of the natural clay in the oedometer tests, although it keeps being higher than that of the natural clay in CRS tests. For the reconstituted clay, compression beyond gross yield causes a decrease in c_v, which reduces to that of the natural clay at high stresses.

Similarly, for Lucera clay (Fig. 6.13) the values of c_v are maximum before gross yield and then slowly decrease until reaching a constant value in both natural and reconstituted clay. However, in this case the c_v values for the reconstituted clay are found to be lower than those for the natural clay, until the natural clay values decrease to that of the reconstituted at very large stresses.

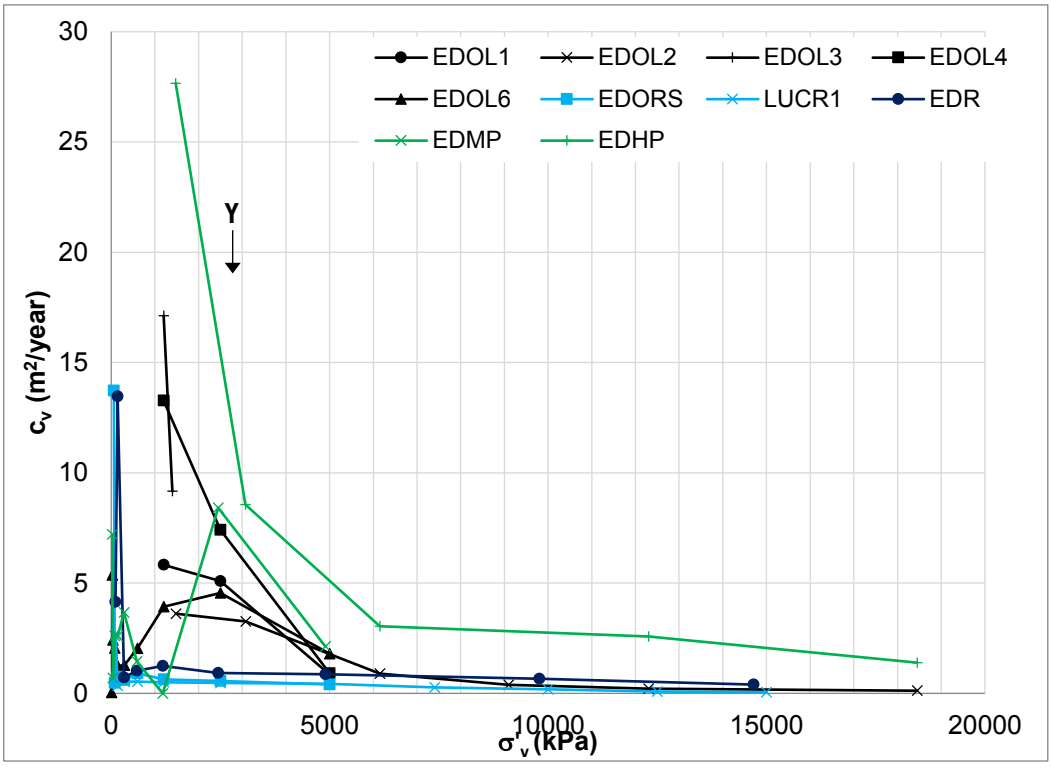

Fig. 6.13 - Values of c_v of natural and reconstituted Lucera clay measured in oedometer tests. Data from new tests (black for natural and light blue for reconstituted) are compared with data from Longo (2003) (green for natural and blue for reconstituted).

Creep coefficients c_α have been measured for both Pappadai and Lucera clay and are plotted against σ'_v in Fig. 6.14 and Fig. 6.15.

For natural Pappadai clay, the values of c_α of the clay compressed from its undisturbed state are seen to be lower than 0.0025 at σ'_v below 2000 kPa, and progressively increase with increasing σ'_v reaching a maximum of 0.025 at σ'_v of 1.5-2σ'_{vy}. The clay structure weakened by the unloading path prior to compression (OED7) exhibited similar c_α values to those of the natural undisturbed clay for equal σ'_v.
After reaching the maximum value, the values of c_α are seen to decrease and finally reach a constant value of around 0.016-0.018.

For Lucera clay, the values of c_α were not available for the oedometer tests of Longo (2003), so in Fig. 6.15 only the data from the new oedometer tests are plotted.
The natural clay exhibits values of c_α lower than 0.002 before gross-yield, which increase with σ'_v reaching a maximum of 0.012 at σ'_v of 2σ'_{vy}, then decrease to the initial value for very large stresses. No significant difference is seen between the clay compressed from undisturbed state (EDOL2) and the clay swelled before compression (EDOL6), as noted for Pappadai clay. However, the c_α values of Lucera clay are quite smaller than for Pappadai clay.

As for reconstituted Pappadai clay, the value of c_α for reconstituted Lucera clay increases rapidly over yield and then reaches a constant value lower than that of the natural clay.
The values of c_α were also measured in unloading paths, as shown in Fig. 6.16, where they are plotted as negative values to be distinguished from those calculated in loading paths. The values for both the swelling path from undisturbed state and the swelling path from beyond gross-yield are reported for test EDOL6. The natural clay is seen to exhibit low creep coefficients (intended as absolute values) at the beginning of the unloading path, which however rapidly increase with decreasing σ'_v, indicating that creep becomes more significant with advancing swelling. The reconstituted clay has a similar trend. Noticeably, when swelled from beyond gross-yield, the natural clay shows c_α values as high as for the reconstituted clay and their curves superimpose.

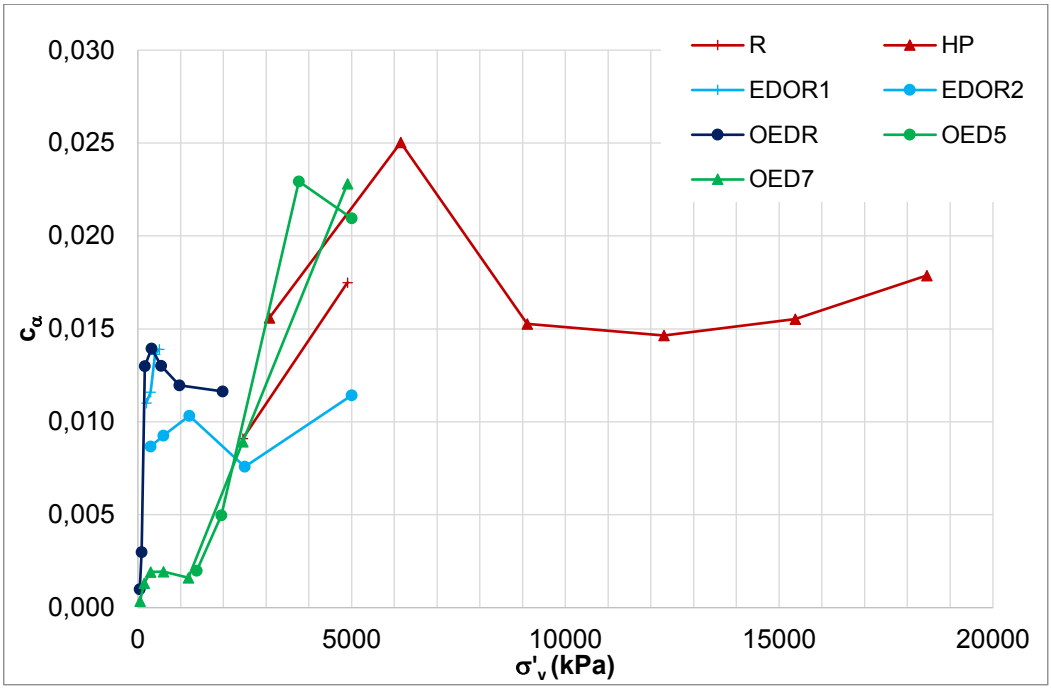

Fig. 6.14 – c_α values measured from oedometer tests on natural and reconstituted Pappadai clay. Data from new tests (red for natural and light blue for reconstituted) are compared with data from Cotecchia (1996) (green for natural and blue for reconstituted).

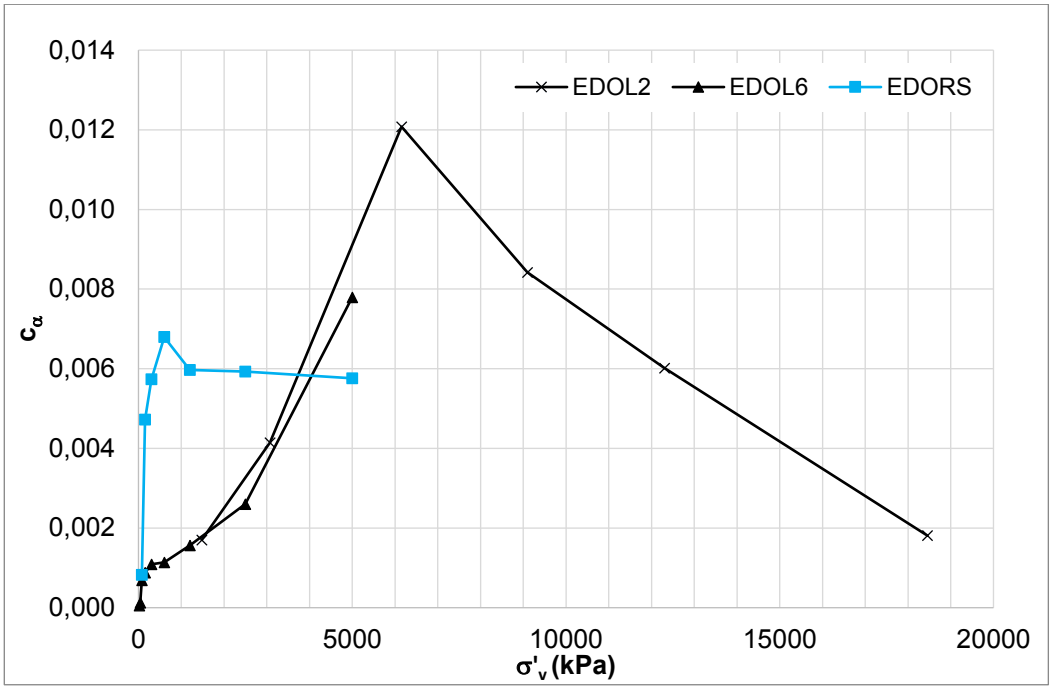

Fig. 6.15 - c_α values measured from oedometer tests on natural and reconstituted Lucera clay.

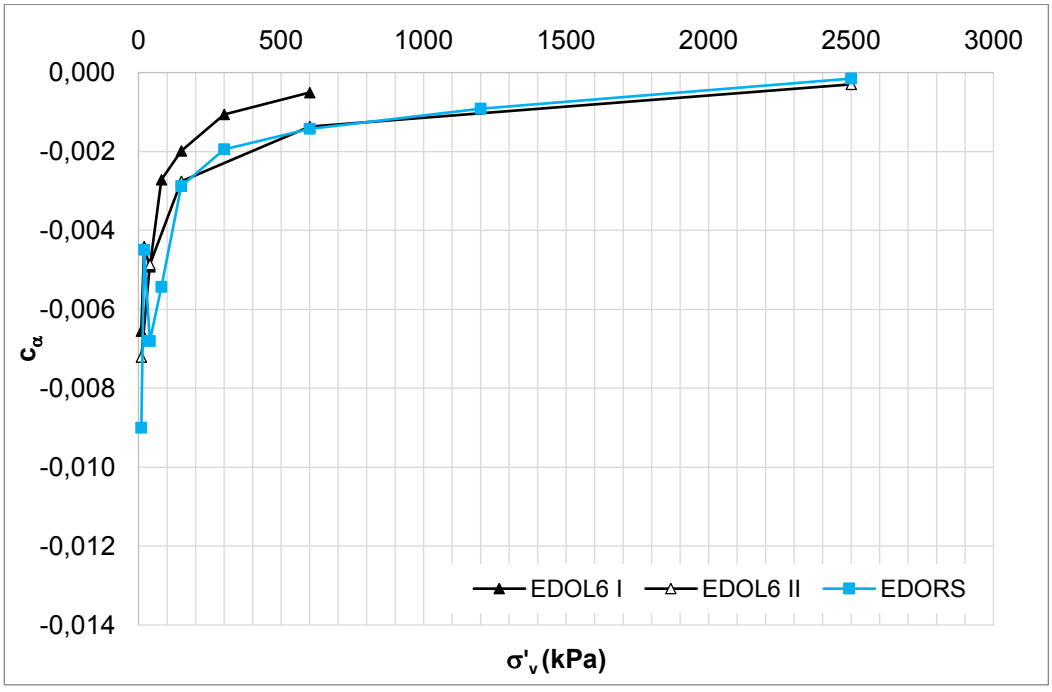

Fig. 6.16 - - c_α values measured from swelling tests on natural and reconstituted Lucera clay.

6.2.3 Coefficient of permeability

The coefficients of permeability measured indirectly from the oedometer tests are plotted against void ratio in Fig. 6.17 and Fig. 6.18, for Pappadai clay and Lucera clay respectively.

The logk-e curves recorded by Cotecchia (1996) on Pappadai block sample 1 show lightly higher permeability for both the tests on the natural and on the reconstituted clay than those recorded in tests on block sample 2. Being recorded on both the natural and the reconstituted specimens, this difference is believed to be due to light differences in the calculation technique adopted (although in both case the Terzaghi theory (1936) was used), rather than to differences in the pore size distribution of the specimens from the two block samples.

Compression paths of natural Pappadai clay from block sample 1 show a linear reduction of the logarithm of k with decreasing void ratio for values of e below 0.8, that is from about the void ratio at gross yield. For higher values of e, k is seen not to vary much. Although test HP on natural Pappadai clay from block sample 2 seems to diverge from the linear trend, both test HP and test R show values of k which do not vary much for void ratios above 0.8.

In swelling paths from undisturbed states (OED7 and S), k increases only slightly with increasing void ratio. This result appears to be consistent with the CRS swelling test results shown by Cotecchia (1996), who observed constancy of k before gross yield, applying to both the natural and the reconstituted clay.

Reconstituted Pappadai clay from both block sample 1 and 2 also follows a linear trend post-gross yield, with a lightly higher permeability than the natural clay. The

permeability trend recorded in test EDOR1 appears not in agreement with the other tests.

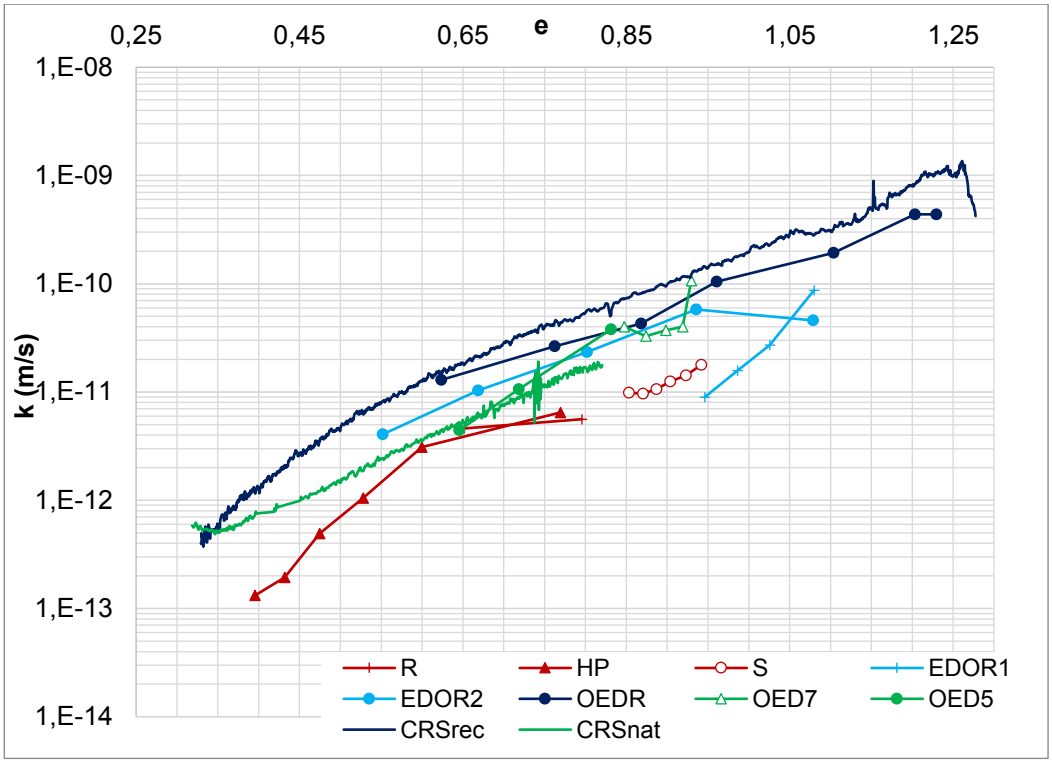

Fig. 6.17 – k values measured from oedometer and CRS tests on natural and reconstituted Pappadai clay. Data from new tests (red for natural and light blue for reconstituted) are compared with data from Cotecchia (1996) (green for natural and blue for reconstituted).

For Lucera clay, a similar trend is observed for the natural clay in the new tests (Fig. 6.18), showing values of permeability approximately constant at the start of compression from the undisturbed state (EDOL1, EDOL2), which then reduce linearly for void ratios below that corresponding to gross-yield, $e_y \approx 0.5$. Test EDHP from Longo (2003) is found not to agree with the logk-e curves exhibited by the new tests on the natural clay. Compression after swelling from the undisturbed state (EDOL6) causes values of permeability reducing with void ratio according to a lower gradient; the logk-e curve superimposes to that of the compression tests from the undisturbed state.

The permeability of the reconstituted clay has a similar linear trend for void ratios below that corresponding to gross yield. The permeability values recorded for the reconstituted clay in this case are closer to those of the natural clay.

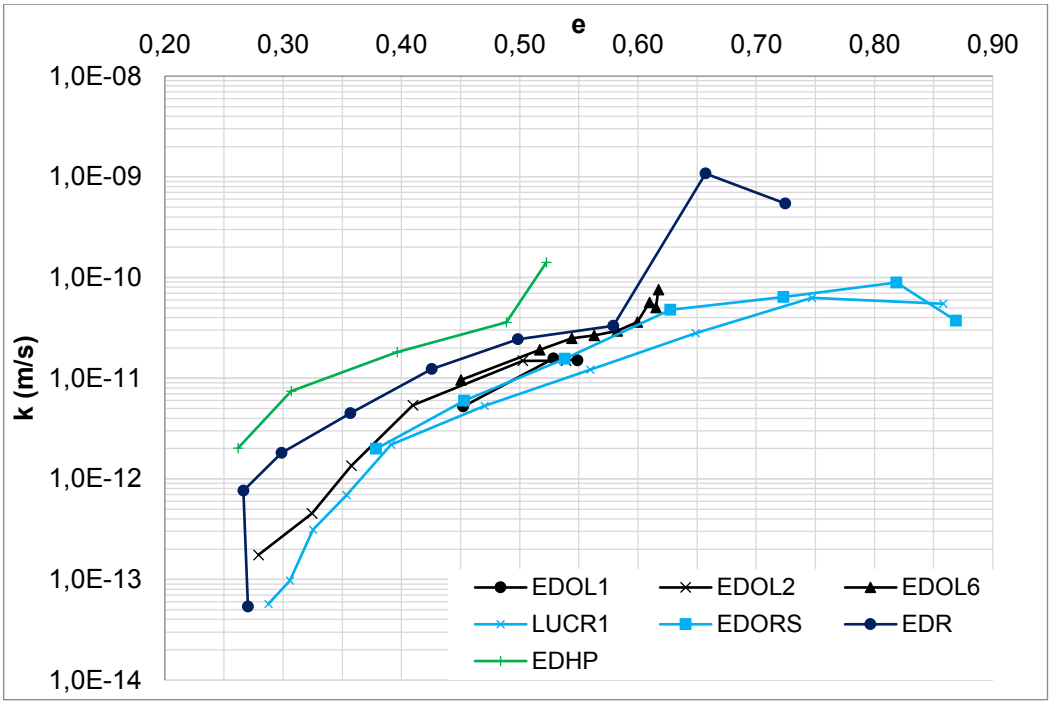

Fig. 6.18 - k values measured from oedometer tests on natural and reconstituted Lucera clay. Data from new tests (black for natural and light blue for reconstituted) are compared with data from Longo (2003) (green for natural and blue for reconstituted).

The permeability values of natural Lucera clay in swelling paths against void ratio are shown in Fig. 6.19, where they are compared with the loading stages of the same tests. The permeability in the stage of swelling from the undisturbed state (EDOL7 and first swelling of EDOL6) is seen to be much lower than that of the clay under compression, differently from what observed for Pappadai clay (Fig. 6.17). Noticeably, in swelling from beyond gross yield (second swelling of EDOL6), the permeability is seen to increase, although remaining lower than that relative to the compression paths. Also, the reconstituted clay in unloading is seen to reduce its permeability with respect to the loading stage.

Lower permeability values in unloading paths have also been observed for the scaly clay of Santa Croce di Magliano (Vitone, 2005; Vitone and Cotecchia, 2011), in oedometer tests on both the natural and the reconstituted clay.

The differences between swelling from the undisturbed state and swelling from beyond gross yield are thought to be associated to the changes in microstructure which develop in the clay in compression post gross-yield.

However, the method of calculation of permeability using the Terzaghi theory (1936) is believed to influence the results, which thus would need to be confirmed using different techniques for the determination of the coefficient of permeability (i.e., direct measurements). The very low permeabilities characterizing these clays are believed not to be compatible with the use of constant head permeameters, available at the geotechnical laboratory of the Technical University of Bari. Hence, specific permeability tests developed on purpose are considered necessary and are among the further developments of the research.

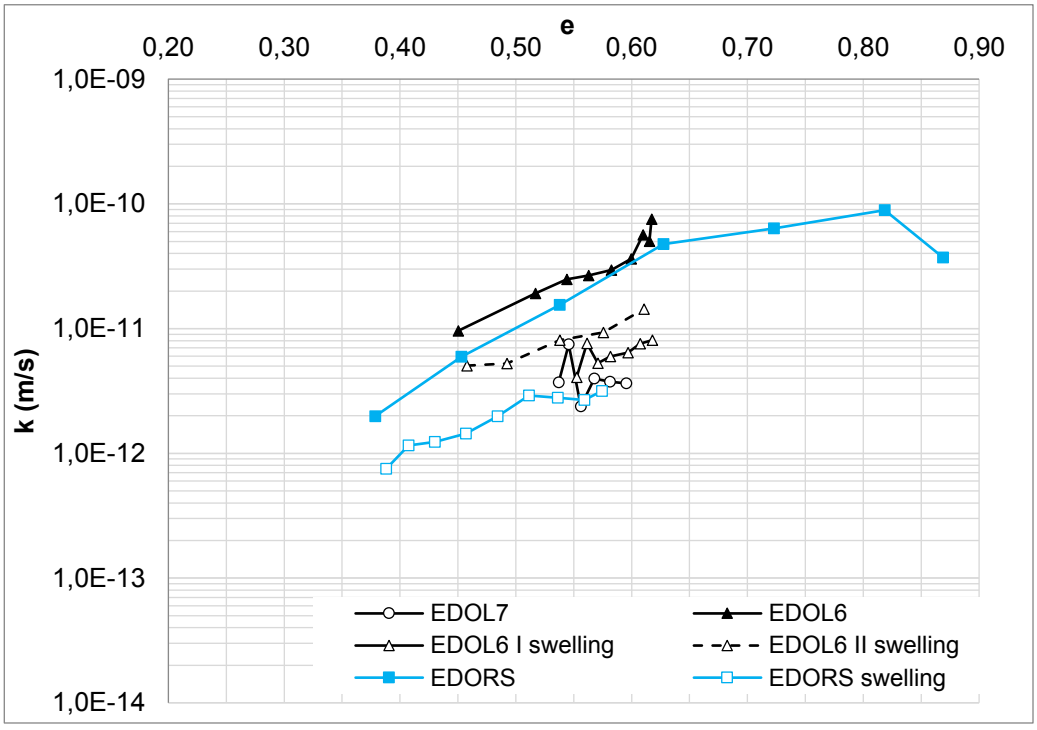

Fig. 6.19 - k values measured in compression and swelling paths on Lucera clay.

In Fig. 6.20, the permeability values for Pappadai and Lucera clay resulting from the oedometer tests included only in this experimental programme are compared.
For a given void ratio, Pappadai clay is seen to have a coefficient of permeability lower than for Lucera clay, both in its natural and reconstituted states.
The difference between the permeabilities of the reconstituted clays is likely to be primarily due to the finer granulometry of Pappadai clay, which has a higher CF than Lucera clay (Section 4.3), but also to the different mineralogy of the two clays, reflected in the higher activity of Pappadai clay. Moreover, as will be shown in Chapter 7, the different permeabilities exhibited by the two reconstituted clays are also significantly influenced by differences in their porosimetry.

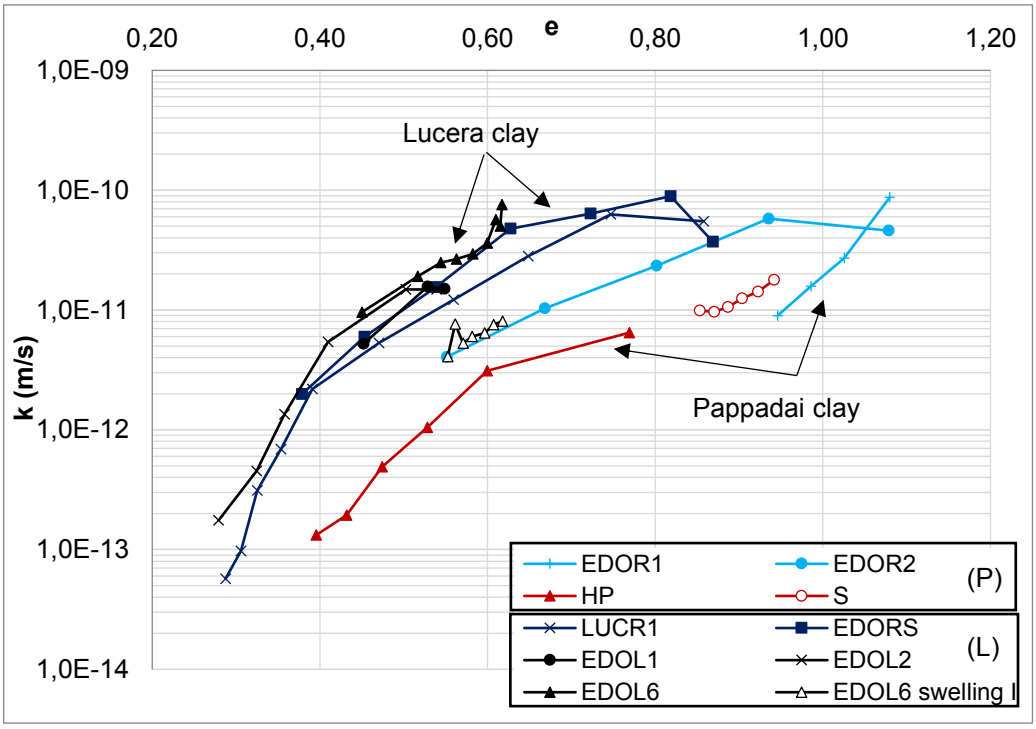

Fig. 6.20 - k values measured from oedometer tests on Lucera and Pappadai clays.

If now for each clay the natural and the reconstituted clay permeabilities are compared, the permeability of the reconstituted clay is seen to be higher than that of the natural

clay at any void ratio for Pappadai, whereas for Lucera clay the natural and the reconstituted clay appear to have very similar values of k up to very high pressures. The differences between the permeability curves of the natural and the reconstituted clay highlight the differences between the porosimetry of the two clays, as will be shown in detail in Chapter 7.

6.3 Isotropic compression tests

In Chapter 5, the isotropic compression tests carried out on Pappadai clay and Lucera clay are reported in Table 5.2; only one new test was carried out on Pappadai clay, i.e., test PRI4 on the reconstituted clay isotropically compressed to 600 kPa.
The test results are compared with the isotropic and swelling test data from Cotecchia (1996) on reconstituted Pappadai clay in Fig. 6.21; also, an isotropic compression test and an isotropic swelling test from the undisturbed state of the natural clay are plotted and both the INCL and INCL* deduced by Cotecchia (1996) from several others are represented.
Although not shown in the graph, the gradient of the natural clay swelling line increases after gross-yield, becoming close to that of the reconstituted clay at a value of p' about twice the yield stress.

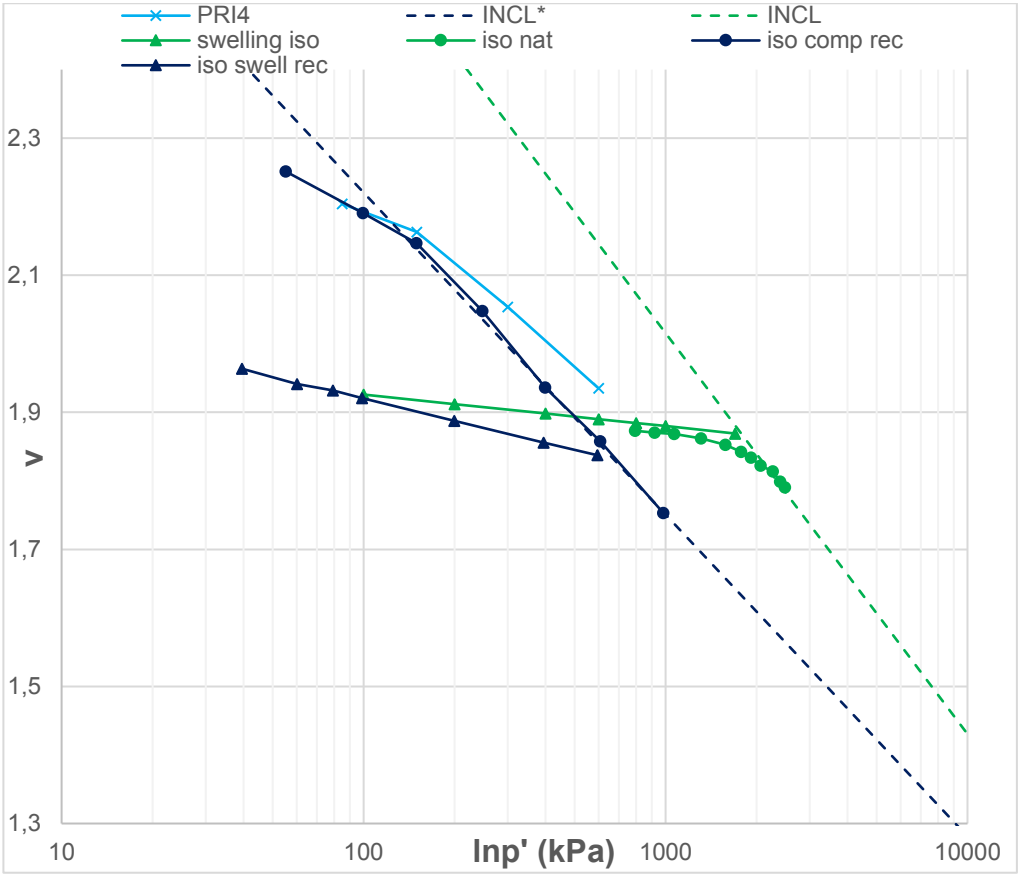

Fig. 6.21 – Isotropic compression and swelling states for Pappadai clay. Data from the new test in light blue are compared with data from Cotecchia (1996) (green for natural and blue for reconstituted).

As for the 1D compression tests (Section 6.2.1), the PRI4 isotropic compression test data are seen to diverge from the other data and from the INCL* defined in 1996. This implies that the manufacturing of the reconstituted clay batch was slightly different. In the following, the isotropic compression behaviour of reconstituted Pappadai clay will then be based on the data from Cotecchia (1996). Also, the equations of the INCL and INCL* identified by Cotecchia (1996) will be considered to apply (Table 6.1).
The compression data for both 1D and isotropic compression of Pappadai clay, natural and reconstituted, are plotted together in Fig. 6.22; the K_0NCL and K_0NCL* defined by Cotecchia (1996) are also shown. One dimensional compression data are reported with

full lines, whereas isotropic compression and swelling data are reported with dashed lines. For clarity, only the data from tests to high pressures have been reported. The values of K_0 and K_0* defined by Cotecchia (1996) in anisotropic compression tests are used to plot the 1D curves in the v-lnp' plane (Table 6.1). According to the discussion in Section 6.2.1, the 1D compression tests on the second block sample are in close agreement with the K_0NCL.

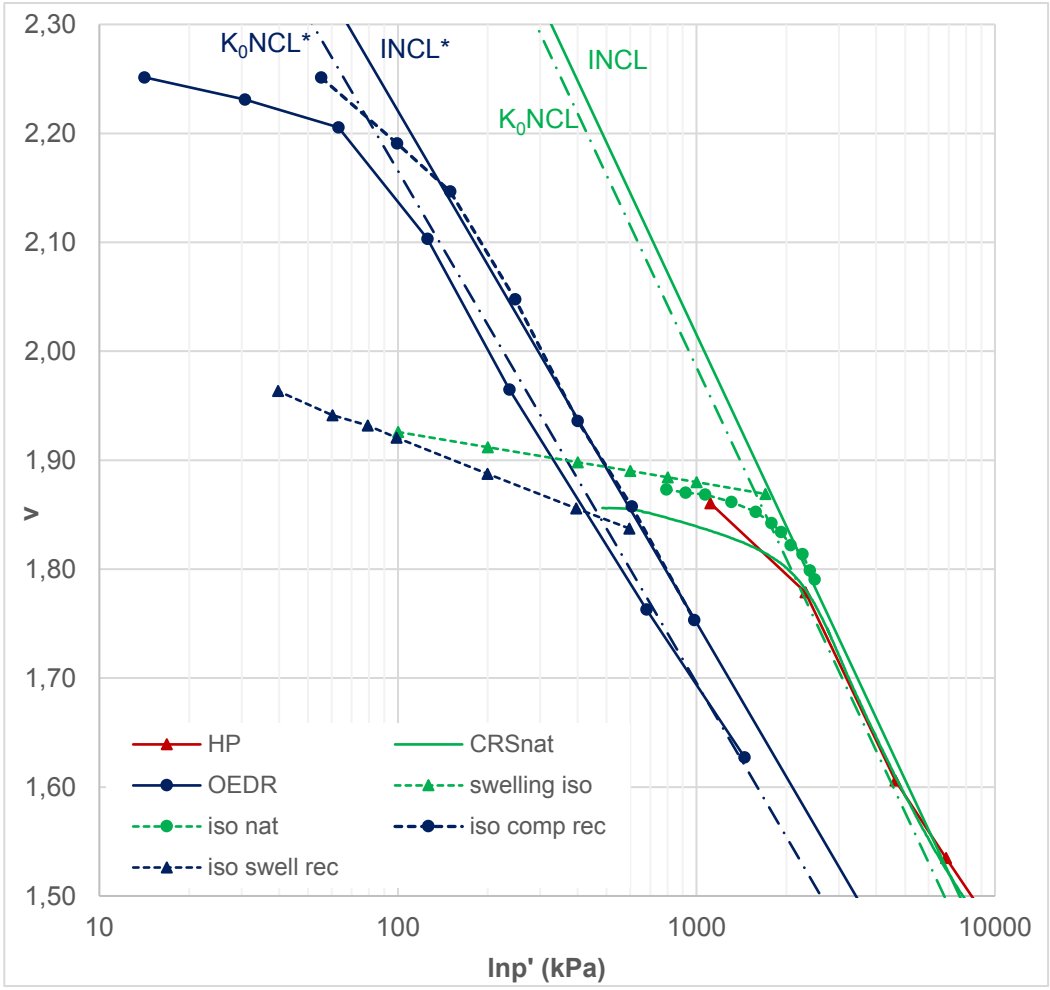

Fig. 6.22 – Isotropic (dashed lines) and 1D (full lines) compression behaviour of Pappadai clay. 1D compression data on the natural clay from the new test in red are compared with data from Cotecchia (1996) (green for natural and blue for reconstituted).

In Fig. 6.22 the values of the isotropic and K_0 gross yield pressures of the natural clay can be identified, corresponding to 2260 and 2000 kPa respectively. The ratio of the isotropic gross yield stress $p'_{y,is}$ to the equivalent pressure taken on the INCL* at the same specific volume is the stress sensitivity in isotropic compression, $S_{\sigma,iso}$, and equals 3.2. The corresponding ratio between $p'_{y,K0}$ and the equivalent pressure taken on the K_0NCL* is the stress sensitivity in oedometric compression, $S_{\sigma,oed}$, and equals 3.5. This ratio is consistent with the stress sensitivity expressed in terms of vertical effective stress measured in oedometer tests. The small difference between the isotropic and oedometric stress sensitivities can be attributed to the different K_0 of the two clays.
The INCL and K_0NCL for Pappadai clay are parallel for both the reconstituted ($\lambda^*=0.204$) and the natural clay ($\lambda=0.254$), in accordance with the Critical State Framework (Chapter 3).

With reference to Lucera clay, two isotropic compression tests were carried out to medium pressures on the natural clay (TNL5 and TNL12) and one isotropic compression test was carried out on the reconstituted clay (LUCRISO). These have been compared with tests carried out by Longo (2003) and Losacco (2004) on the first block sample of Lucera clay (Fig. 6.23).
Losacco (2004) carried out two isotropic compression tests on the natural clay, one to medium pressures (LUCMP) and one to high pressures (LUCHP). Two isotropic compression tests were also performed on the reconstituted clay, TRXA and TRXC. The latter also included a final swelling path to $R=3$.
Longo (2003) developed a stress-path test under controlled loading on a specimen of natural Lucera clay, with the aim to simulate the stress history of a soil element from an excavation wall. The specimen was first taken from an isotropic overconsolidated state to a K_0 state, similar to its in-situ state, by means of a constant p' stress path in which the deviatoric stress q was increased. Then, the undrained lateral unloading was simulated keeping constant the value of q while reducing p'. According to MCC (see Chapter 3), during the constant-q path the specimen is moving on an elastic wall, so the projection of this stress path on the v-lnp' plane is necessarily a swelling line.

Then, this test was used here to get information on the isotropic swelling of natural Lucera clay. This test will also contribute to the definition of the state boundary surface for the natural clay (Section 6.5).

In Fig. 6.23 all the described tests are shown. Remarkably, the curves for both the natural and the reconstituted clay plot very close.

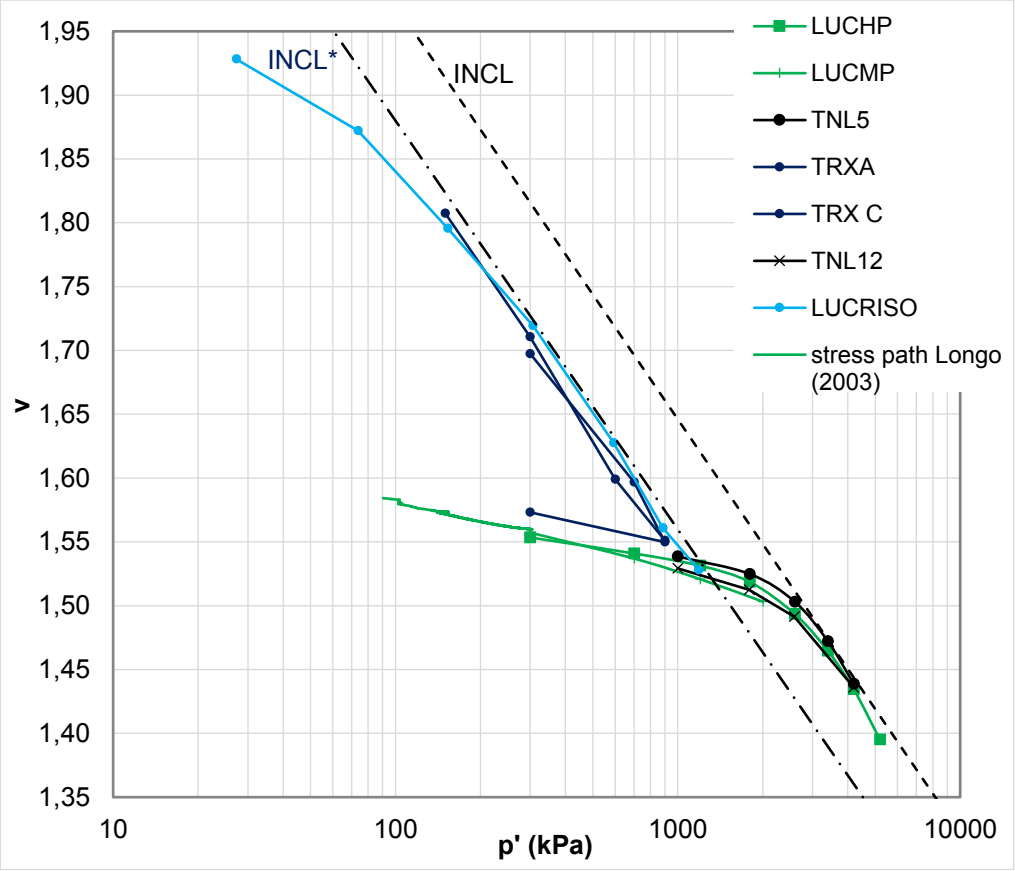

Fig. 6.23 - Isotropic compression curves for natural and reconstituted Lucera clay. Data from new tests (black for natural and light blue for reconstituted) are compared with data from Longo (2003) (green for natural and blue for reconstituted).

The data define for the natural clay the INCL, with a gradient $\lambda = 0.141$ and an intercept $N = 2.62$ at $p' = 1$ kPa. The constant-q stress path and the initial compression before

gross yield of the isotropic compression tests fit a straight line, representing swelling states pre-yield, of gradient $\kappa=0.015$.
For the reconstituted clay, the isotropic compression curves define the INCL*, with a gradient $\lambda*=0.139$ and an intercept $N*=2.52$ at $p'=1$ kPa. The swelling path of test TRX C allows to identify a swelling line of gradient $\kappa*=0.021$.

The compression data for both 1D and isotropic tests are plotted together in Fig. 6.24. The values of K_0 and K_0* used for plotting the 1D curves into the v-lnp' plane are those defined by Mitaritonna (2006) using the empirical formulation proposed by Jaky (1944), corresponding to $K_0=0.60$ and $K_0*=0.56$.
For clarity, only some of the data previously shown and only from tests included in this experimental programme have been reported.
The 1D compression data define for the natural clay the K_0NCL, with a gradient $\lambda=0.141$ and an intercept $N=2.60$ at $p'=1$ kPa. For the reconstituted clay, the 1D compression curves define the K0NCL*, with a gradient $\lambda*=0.139$ and an intercept $N*=2.47$ at $p'=1$ kPa.

In Fig. 6.24 the values of the isotropic and K_0 yield pressures can be identified, corresponding to 2600-2700 and 2000-2100 kPa respectively. The stress sensitivity in isotropic compression, $S_{\sigma,iso}$, equals 1.77. The corresponding ratio between $p'_{y,K0}$ and the equivalent pressure taken on the K_0NCL*, $S_{\sigma,oed}$, is seen to be equal to 1.62. Also for Lucera clay, the oedometric stress sensitivities expressed in terms of p' and in terms of σ'_v are found to be consistent.
As for Pappadai clay, also for Lucera clay the INCL and K_0NCL are parallel for both the reconstituted ($\lambda*=0.139$) and the natural clay ($\lambda=0.141$), so the Critical State Framework is seen to apply to both (Chapter 3). In both cases, the gradient of the NCL for the natural soil is higher than that for the reconstituted, However, both are found to be consistent with the values of C_c measured in the oedometer tests assuming a constant value of K_0.

Basing on evidence from oedometer tests, one main difference between the behaviour of natural and reconstituted clay is that the gradient of the natural clay swelling line increases after yield, becoming closer to that of the reconstituted clay at a value of p' about twice the yield stress. So, the values of κ for swelling from undisturbed state will be defined as $\kappa_{pre\text{-}yield}$, while the $\kappa_{post\text{-}yield}$ will be assumed to equal the κ^* of the reconstituted clay.

In Table 6.1, the soil constants of both the clays are resumed.

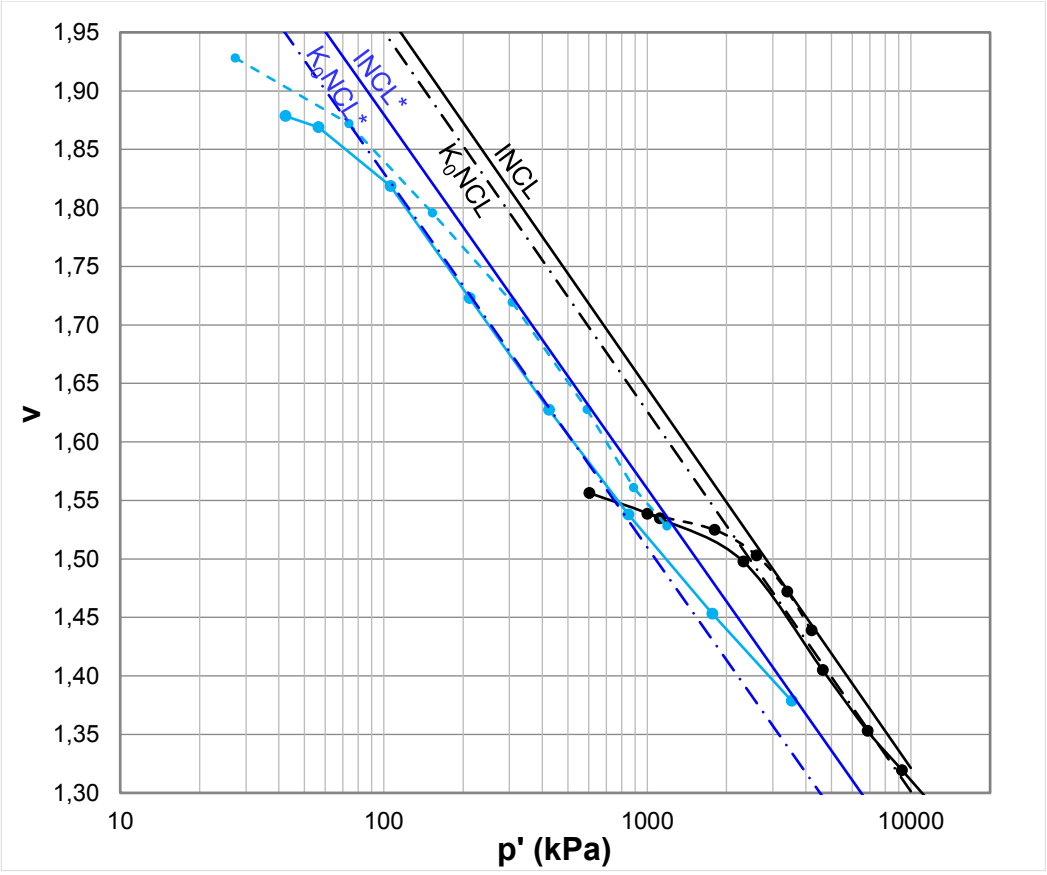

Fig. 6.24 - Isotropic (dashed lines) and 1D (full lines) compression behaviour of Lucera clay (only new test data).

Table 6.1 – Values of soil constants for Pappadai (after Cotecchia, 1996) and Lucera clays.

	λ_{iso}	λ_{oed}	λ^*	N_{iso}	N_{K0}	N^*_{iso}	$\kappa_{pre\text{-}y}$	κ^*	$p'_{y,is}$	$p'_{y,K0}$	K_0	K_0^*
Pappadai	0.254	0.254	*0.204*	3.77	3.74	*3.16*	0.02	*0.046*	2260	2000	0.63	*0.57*
Lucera	0.141	0.141	*0.139*	2.62	2.60	*2.52*	0.015	*0.021*	2700	2100	0.6	*0.56*

6.4 Shear tests

The results of the shear tests on reconstituted (Table 5.3) and natural (Table 5.4) Lucera clay are discussed in the following. All the specimens of the reconstituted clay were trimmed from the batches L1 and L2 of clay consolidated from slurry to 100 kPa vertical stress (Section 5.4.1). The specimens of natural clay were all trimmed from the block sample. All the specimens were consolidated isotropically to states either pre- or post-gross-yield and then sheared, either drained or undrained. As explained in Section 5.1, the investigation on the natural clay was intended to explore the clay behaviour both before and after reaching the current SBS, so two undrained shear tests (TNL10 and TNL11) were stopped half way through the stress path, as will be shown in the following.

Pictures of the specimens at the end of the shear tests are reported in Fig. 5.1. It should be noticed that the size of reconstituted specimen TRL2 is smaller than soon after shear testing, as the photograph has been taken after cutting the extremities of the specimen for the final water content measurement, as explained in Section 5.4.4. Pictures of specimens TNL10 and TNL11 are not reported, as they do not show significative differences in shape and size (except for a small reduction due to isotropic compression for TNL11) with respect to the specimen before testing. Unfortunately, no pictures were taken at specimen TNL12, although it showed an evident failure surface. For specimens in which a failure surface formed (TNL1, TNL4, TNL7, TNL6, TRL2), two portions were taken from inside and outside the shear band and separately subjected to microstructural analyses, as will be further discussed in Chapter 7.

The shear tests on both the natural and the reconstituted clay are compared with the tests on the reconstituted (TRXA, TRXC) and on the natural Lucera clay (TRX1, TRX2, LUCMP, LUCHP) carried out by Longo (2003) and Losacco (2004) in the geotechnical laboratory of the Technical University of Bari on the first block sampled at Lucera; these tests, together with the state parameters of the specimens, are listed in Table 6.2.

With reference to the tests on the natural clay, tests TRX1, TRX2 and LUCMP started from isotropically normally consolidated states pre-gross-yield. In particular, tests TRX1 and TRX2 started with isotropic loading to low consolidation pressures, respectively around 360 and 700 kPa, as the specimens were trimmed from a block sample coming from a lower depth in the deposit (Section 4.2), for which the measured suction was about 300 kPa. On the other hand, test LUCHP was isotropically compressed post-gross-yield prior to shearing. The tests on the reconstituted clay were carried out from an isotropically normally consolidated state (TRXA) and from an overconsolidated state corresponding to $R=3$ (TRXC).

The results of these shear tests will be often compared with those obtained from the new experimental programme, as already done for the compression tests from the new and the previous block samples. In fact, despite the different depth at which they were taken, the two block samples of 2003 and 2016 exhibit very similar macro-behavioural features, due to the noticeable uniformity of the deposit in terms of index properties with depth, as discussed in Section 4.3, especially with reference to the void ratio.

Photographs of the specimens at the end of the tests by Longo (2003) and Losacco (2004) are shown in Fig. 6.26, except for specimen LUCMP for which no photograph was found. The apparatuses used for the tests were TRXA and the HPSPS: the former is similar to apparatus TRXD, described in Chapter 5, but has a lower cell capacity; the latter is the same apparatus used for some tests of the new experimental programme.

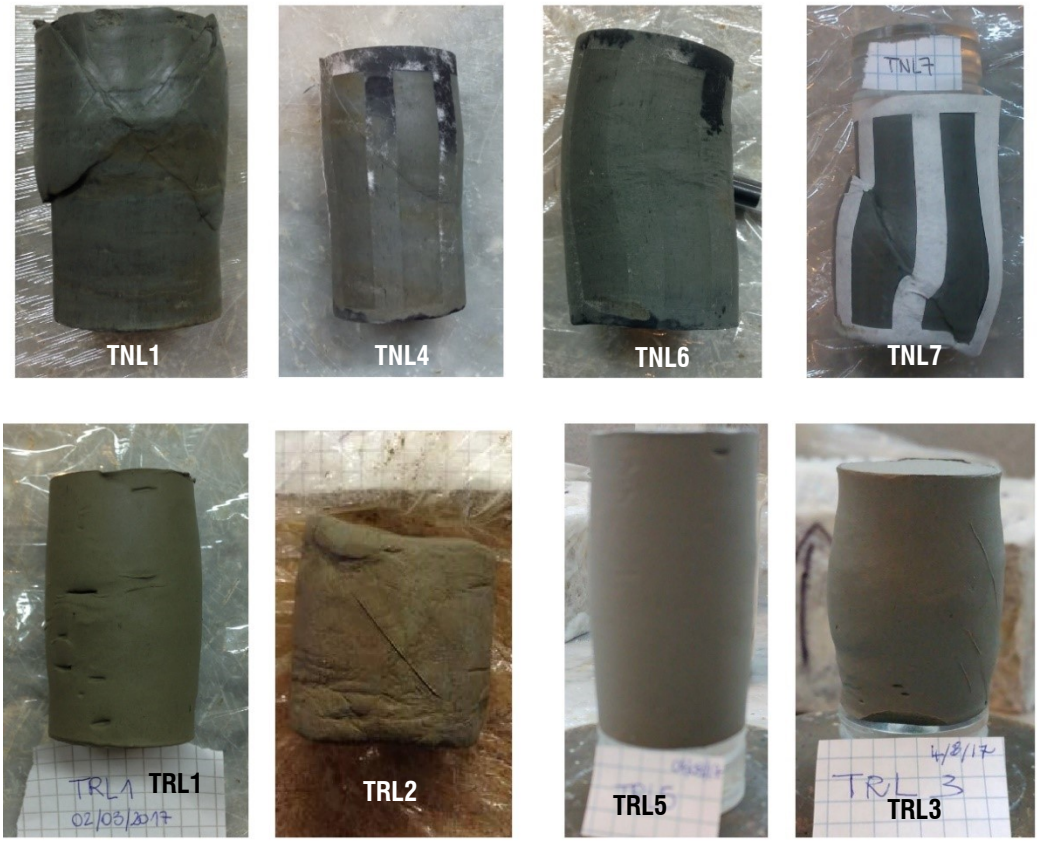

Fig. 6.25 – Pictures of specimens of Lucera clay at the end of shear tests (those of the upper row are natural clay specimens; those of the bottom row are reconstituted clay specimens).

Table 6.2 – Shear tests on natural and reconstituted Lucera clay carried out by Longo (2003) and Losacco (2004).

Test	w_0 (%)	e_0	S_r (%)	p'_p (kPa)	R	e before shearing	shear	ε_a shear (%/min)	Apparatus
TRXA (*)	33	0.910	99	900	1	0.551	U	0.0083	A
TRXC (*)	32.89	0.913	98	296	3	0.573	U	0.0045	A
TRX1	20.68	0.571	99	365	7.4	0.554	U	0.0025	A
TRX2	20.24	0.563	98	704	3.8	0.535	U	0.008	A
LUCMP	18.53	0.557	91	2000	1.3	0.503	U	0.004	HPSPS
LUCHP	18.44	0.553	91	5173	1	0.395	U	0.004	HPSPS

(*) tests on the reconstituted Lucera clay

Fig. 6.26 – Specimens of Lucera clay from Longo (2003) and Losacco (2004) at the end of the tests.

6.4.1 Stress-strain behaviour

The results of the new shear tests on reconstituted Lucera clay (Table 5.3) are discussed first, and then compared with the previous shear tests by Longo (2003) and Losacco (2004). The v-p' state paths of all the shear tests on the reconstituted Lucera clay are shown in Fig. 6.27, in which also the INCL* of the reconstituted clay, the isotropic compression test LUCRISO and the isotropic swelling lines are reported. Initial states in the state paths are indicated with a dot for the new shear tests and with a rhombus for the previous tests.

With reference to the new tests on the reconstituted clay, the variations of the deviatoric stress q, of the stress ratio q/p', of the volumetric strain ε_v in the drained tests (TRL1 and TRL5) and of the excess pore water pressure Δu in the undrained tests (TRL2 and

TRL3) are plotted against axial strain ε_a for reconstituted Lucera clay in Fig. 6.28 to Fig. 6.31.

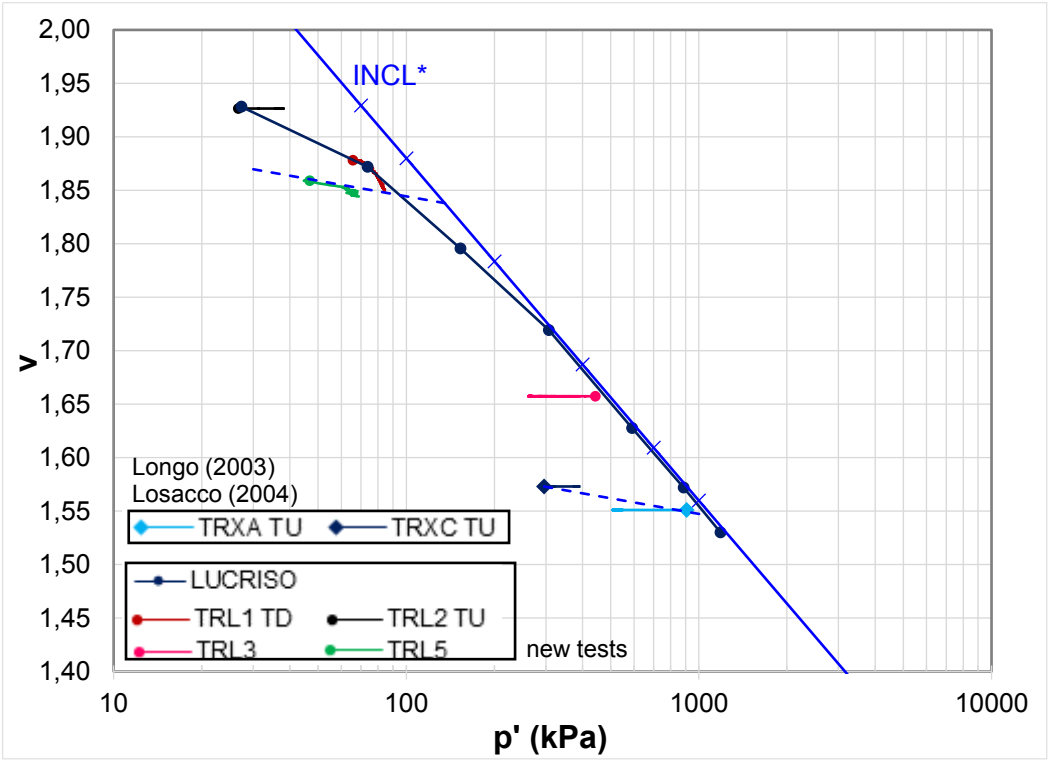

Fig. 6.27 - v-p' states of shear tests on reconstituted Lucera clay: data from both the new experimental programme and from Longo (2003) and Losacco (2004).

In test TRL1 the specimen was consolidated isotropically to 65 kPa, before isotropic gross yield, resulting in a lightly overconsolidated specimen having overconsolidation ratio R=1.8. As expected, the behaviour of the clay was contractant and strain hardening (Fig. 6.28). By the end of the test, the critical state was not reached yet, although the volumetric strain was approaching a constant value and a corresponding q/p' equal to 0.88, which would have been overcome if the test had further proceeded. Hence, the stress ratio at critical state that the specimen would have reached is believed to be higher than 0.88.

The drained shearing of test TRL5 is shown in Fig. 6.29. The clay was just equilibrated in isotropic compression at a mean effective stress equal to its suction (Section 5.4.4),

measured as 43 kPa in the triaxial apparatus by means of an initial undrained loading stage. Hence, the specimen before shearing was overconsolidated and characterized by R=2.8. Due to technical problems, the test had to be stopped at around 11% axial strain. The clay was contractant till the end of testing, since the volumetric strain did not reach a constant value, and exhibited a strain-hardening behaviour. Given the value of R and the test being drained, the specimen is likely to have approached the wet of critical with shearing. By the end of the test, though, the stress ratio approached a constant value of 1.1, higher than the final ratio measured in test TRL1.

Also specimen TRL2 was isotropically consolidated at a mean effective stress equal to its suction, measured in initial undrained loading to be 30 kPa, giving an overconsolidation ratio R of 4. The undrained shear behaviour (Fig. 6.30) of the specimen complied with a decrease in pore pressure and a decrease in deviatoric stress, the latter from the axial strain of 2% onwards. The strain softening developed into the formation of a failure surface, which appeared about the stage when an abrupt decrease in pore pressure was recorded, at 6% axial strain. The stress ratio for test TRL2 was then corrected for localisation using eq. (5.20) and also for membrane effects (Section 5.4.4). At large strains, the corrected stress ratio tends to a constant value of 1.1.

In undrained test TRL3, the specimen was normally consolidated isotropically. As expected, being the specimen isotropically normally consolidated (Table 5.3), its behaviour was contractant and strain-hardening up to 10% axial strain, when a drop in deviatoric stress began (Fig. 6.31). The pore pressure by the end of the test was constant and the ratio q/p' reached and kept a constant value of 0.85 before starting to decrease, at which stage the pore pressure had already become constant. Thereafter, the ratio decreased. However, this value of critical state stress ratio is lower than that determined for the other tests.

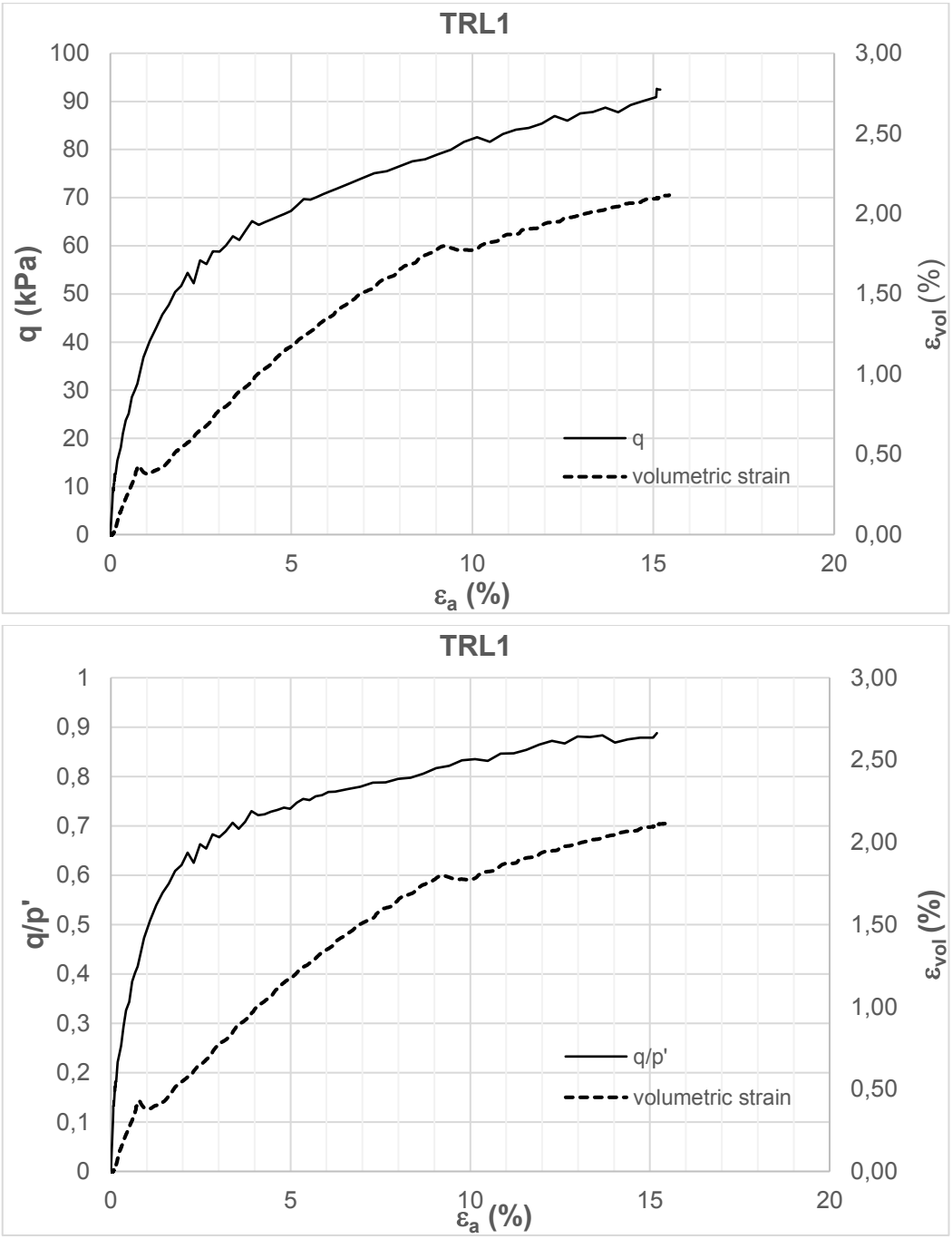

Fig. 6.28 - Reconstituted clay: stress-strain behaviour of isotropically consolidated drained test TRL1 (R=1.8).

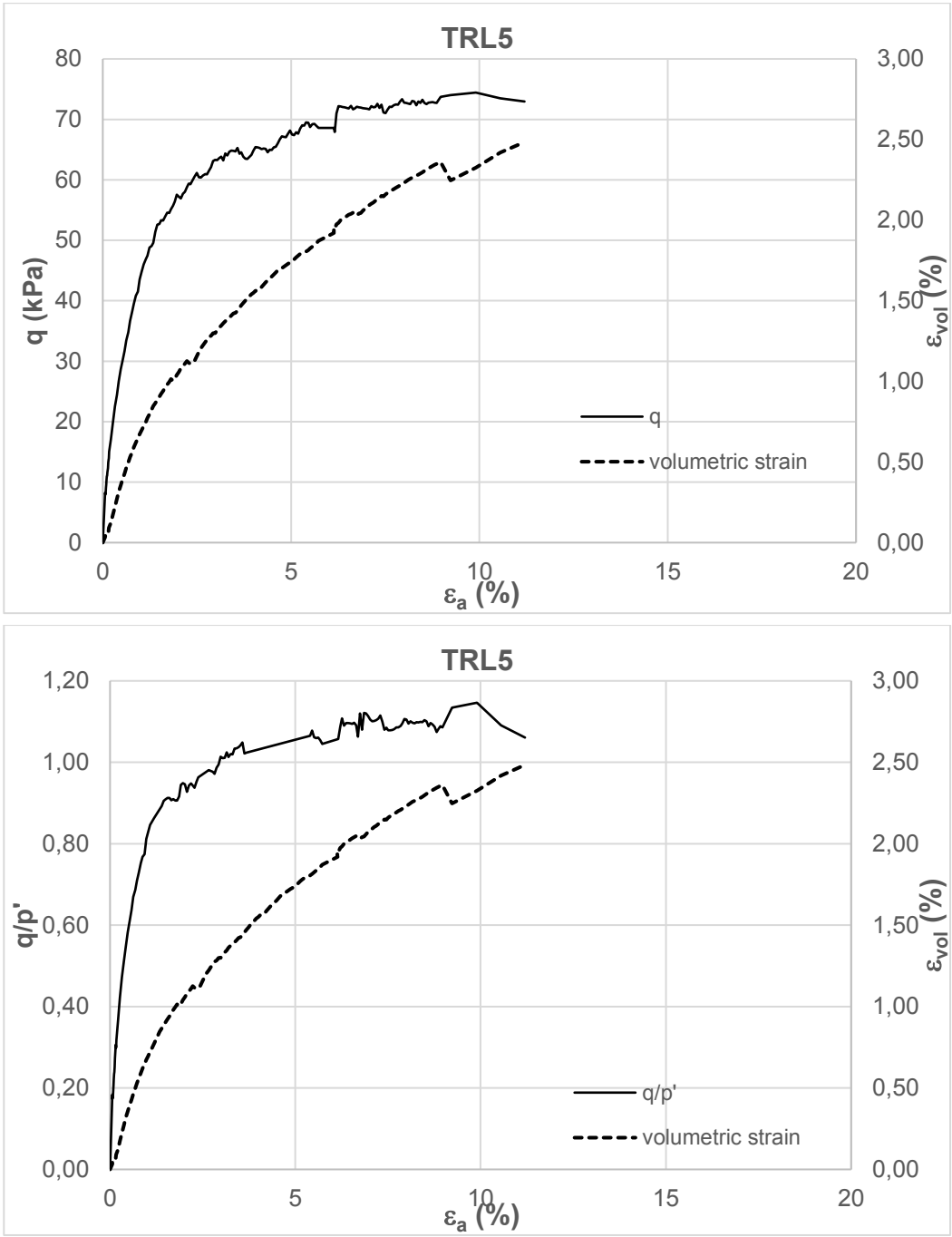

Fig. 6.29 - Reconstituted clay: stress-strain behaviour of isotropically consolidated drained test TRL5 (R=2.8).

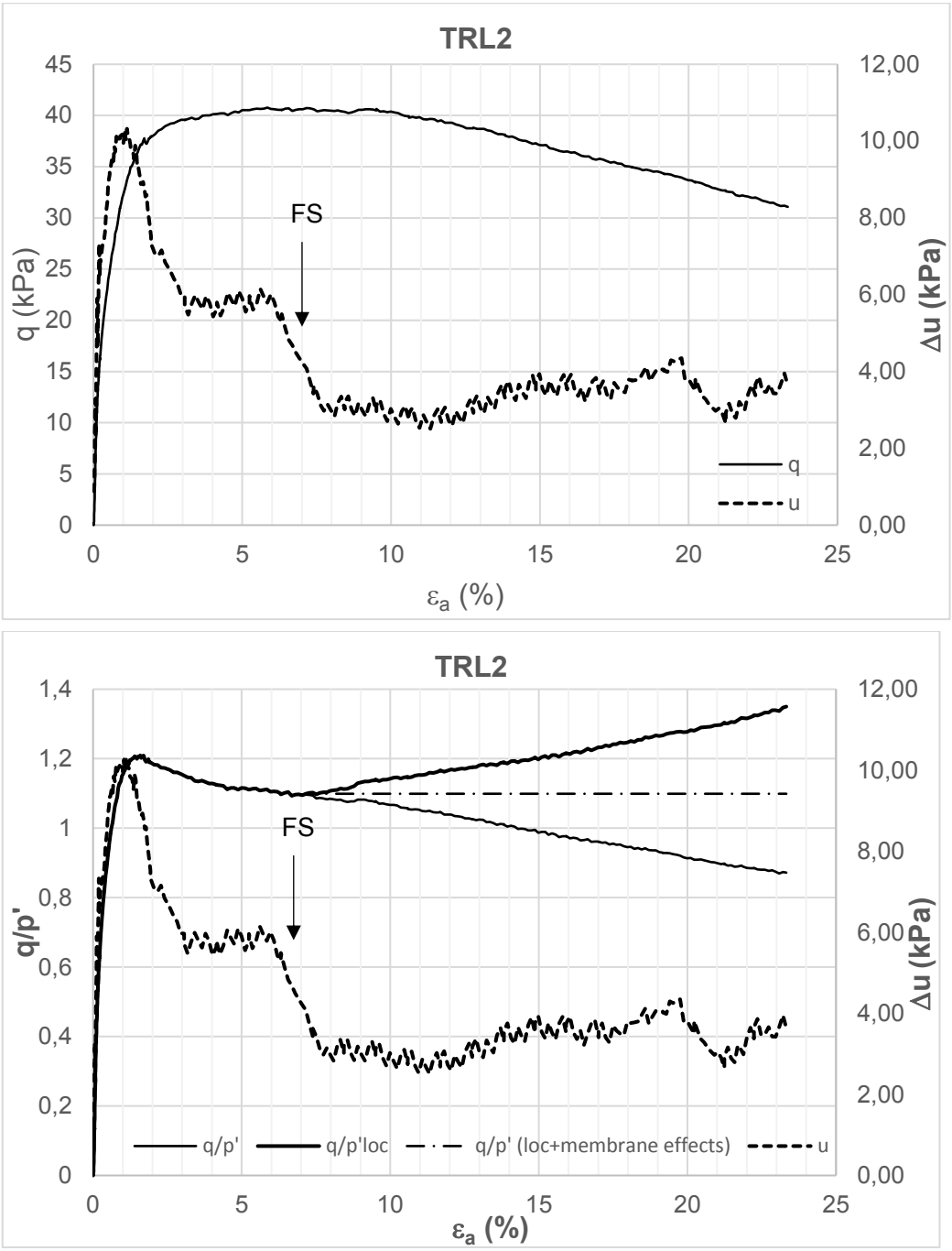

Fig. 6.30 - Reconstituted clay: stress-strain behaviour of isotropically consolidated undrained test TRL2 (R=4).

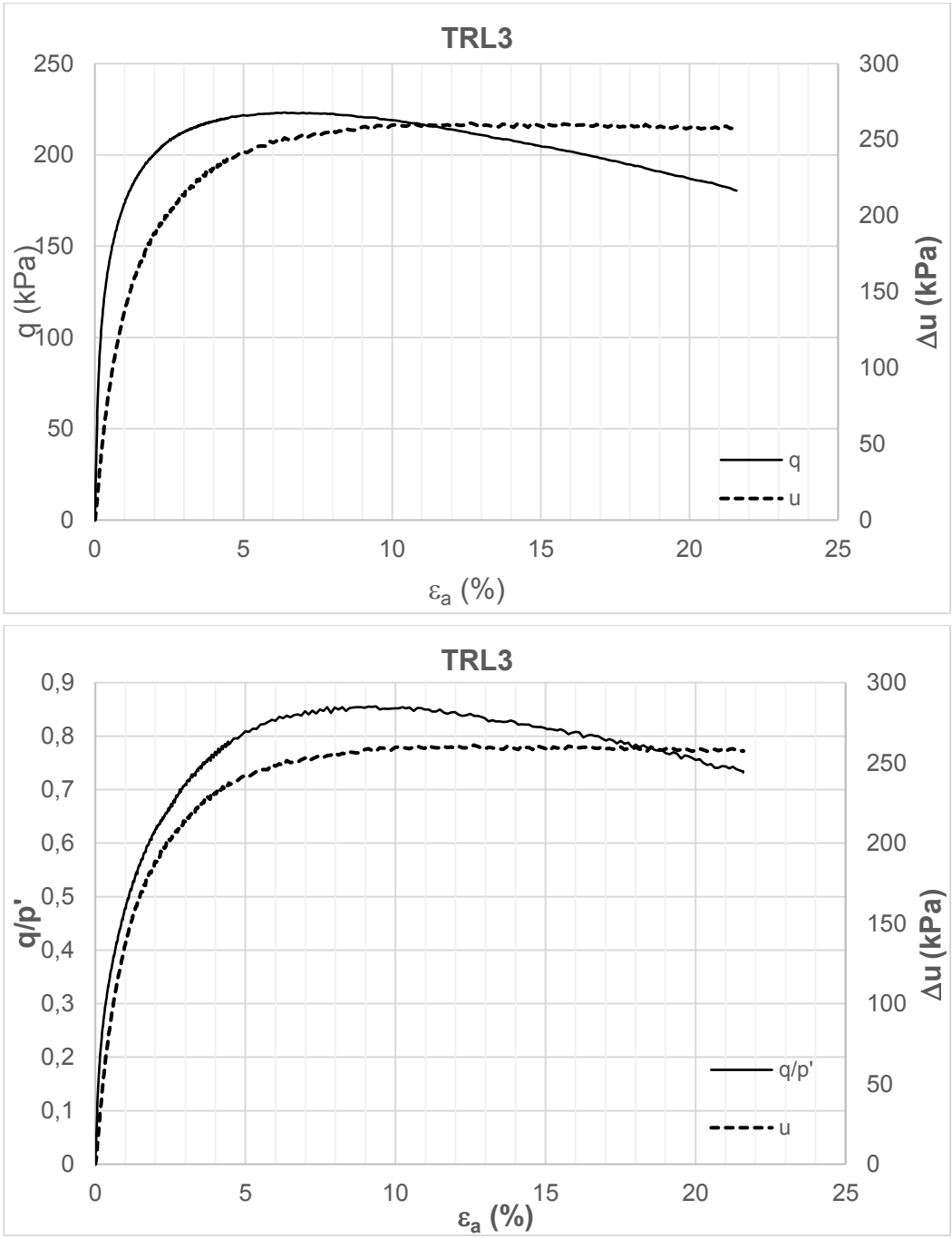

Fig. 6.31 - Reconstituted clay: stress-strain behaviour of isotropically normally consolidated undrained test TRL3.

The results obtained from the described tests are compared with each other and with those of tests TRXA and TRXC on reconstituted Lucera clay of Longo (2003) and Losacco (2004) in terms of trends of deviatoric stress, stress ratio, excess pore water pressure or volumetric strain against axial strain in Fig. 6.32 to Fig. 6.34.

In test TRXA, the specimen was isotropically normally consolidated and then sheared undrained. As expected being R=1 (Table 6.2), the clay exhibited a contractant and strain-hardening behaviour. The stress ratio and pore pressure became constant by the end of the test and the clay reached a critical state with stress ratio 1.06.
The undrained shear of specimen TRXC, isotropically consolidated and then swelled to a value of R=3, is also contractant and strain hardening and reaches critical state at approximately the same stress ratio as TRXA. None of the tests showed strain localisation, as can be seen in Fig. 6.26.

Except for tests TRL1, which should have proceeded further, and for test TRL3, in which an anomalous behaviour was recorded despite the apparent absence of technical problems throughout the shear test, which showed lower values of the final stress ratio (Fig. 6.32b), all the remaining tests appeared to converge to a similar stress ratio at critical state.
All the undrained tests reached a constant final value of the excess pore pressure, whereas the drained tests appeared to approach, but not reach yet, a constant final trend (Fig. 6.33 and Fig. 6.34).

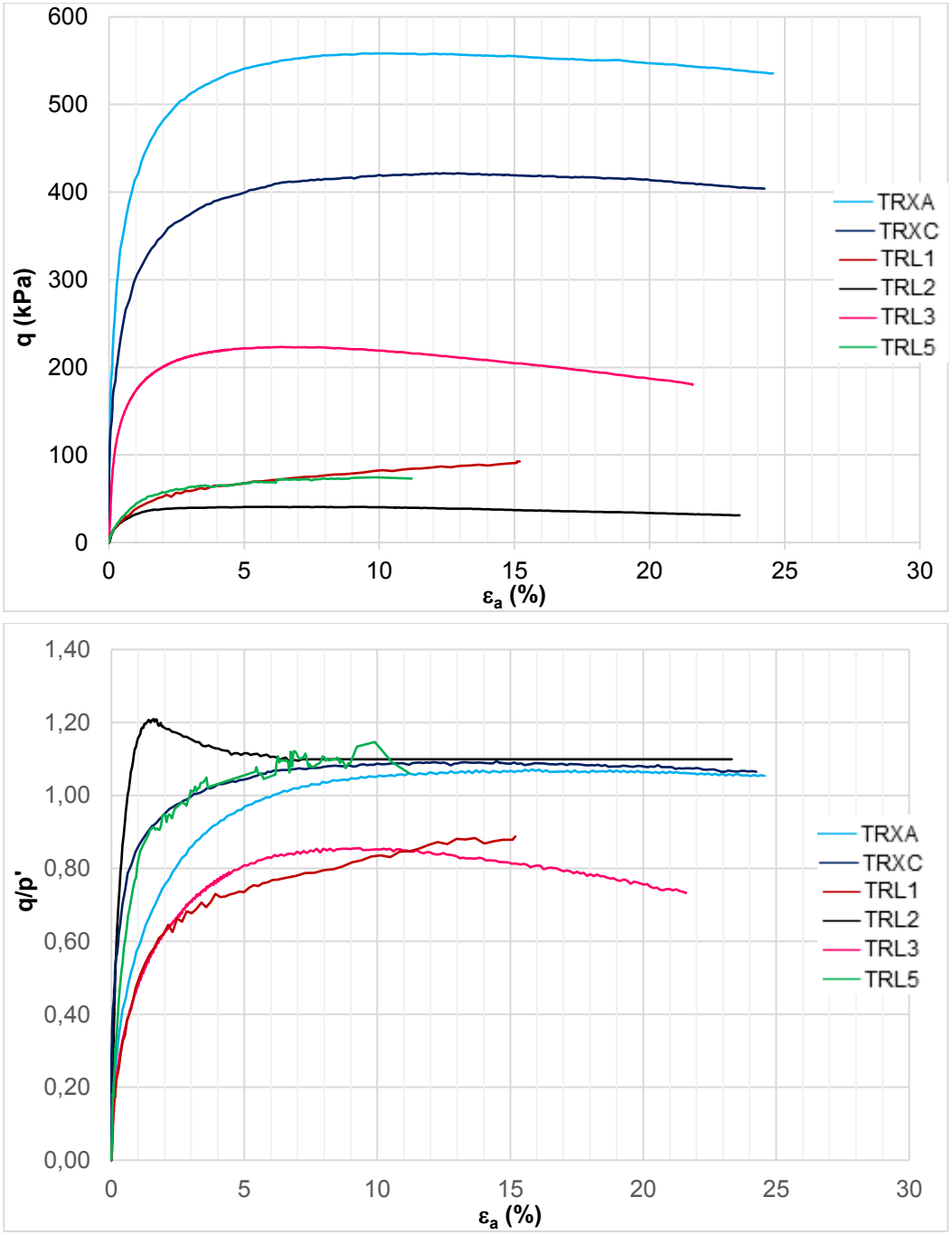

Fig. 6.32 – Comparison of stress- strain behaviour of reconstituted Lucera clay: data from both the new experimental programme and from Longo (2003) and Losacco (2004).

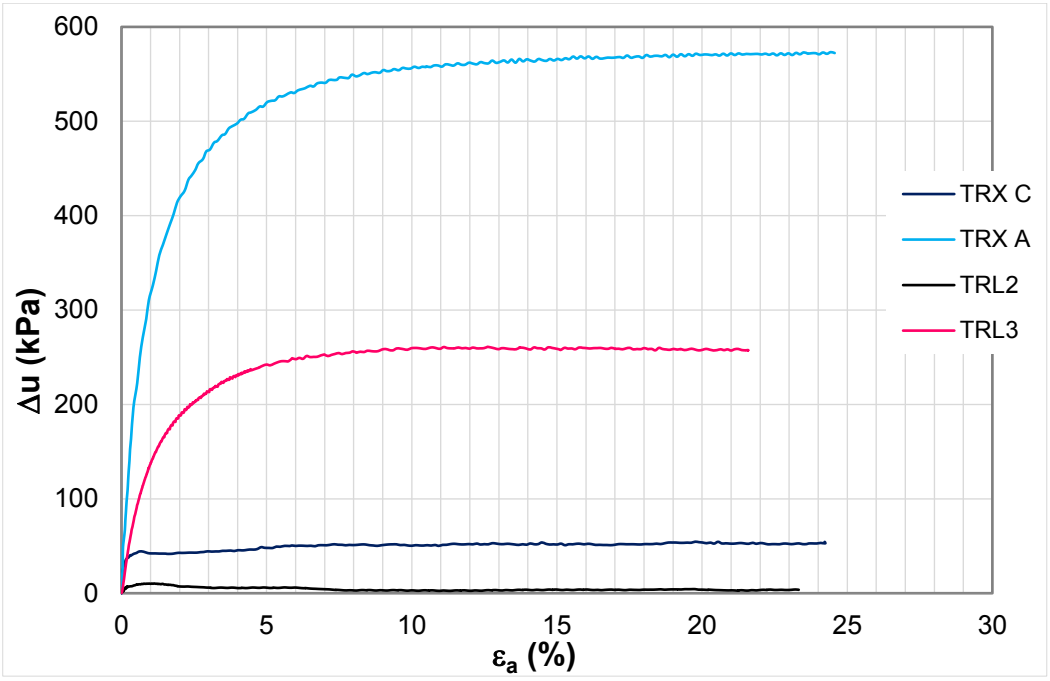

Fig. 6.33 - Comparison of pore pressure increase in undrained tests on reconstituted Lucera clay.

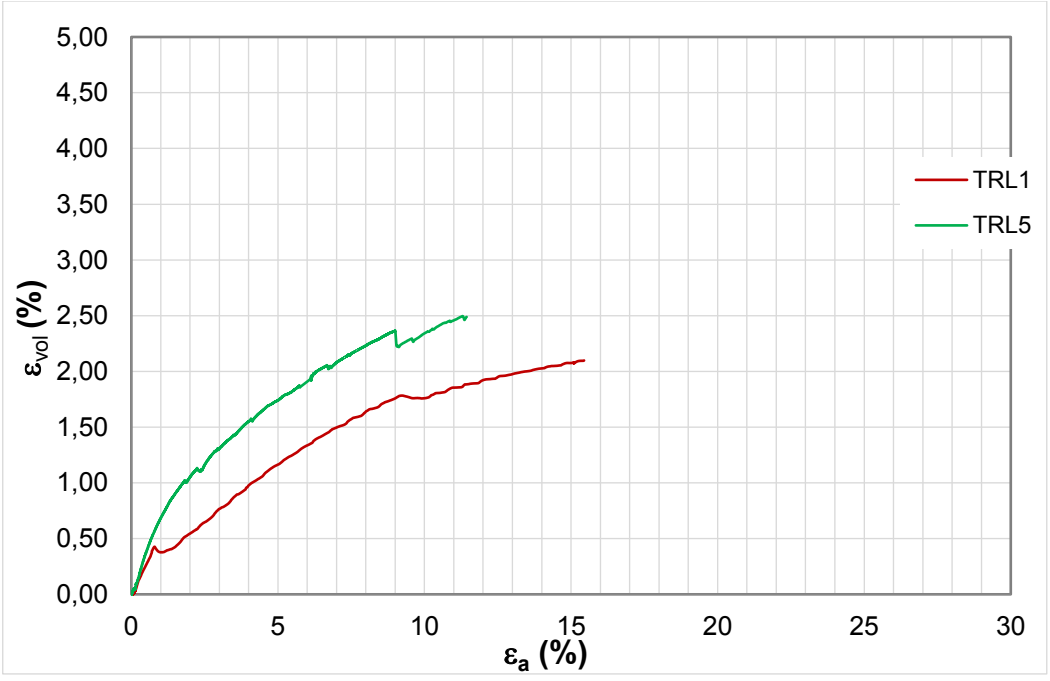

Fig. 6.34 – Comparison of volumetric strain in drained tests on reconstituted Lucera clay.

The shear behaviour of the natural clay is now discussed, first with reference to the new tests. These will be then compared to those of Longo (2003) and Losacco (2004) previously mentioned.
The variation of the clay behaviour with changing isotropic yield stress ratio (YSR) is analysed.
With reference to the shear tests starting from isotropic compression states pre-gross-yield, the isotropic consolidation pressures determining YSR equal to 3 and 1.6 were chosen. The former YSR=3, obtained by means of a re-saturation stage at a mean effective stress approximately equal to the specimen suction (around p'=900 kPa), was chosen as to minimize the effects of strain localization due to negative hardening, which is expected to develop on the dry side of critical. The latter R=1.6 was obtained by compressing the specimen isotropically from undisturbed state to a pre- gross yield state corresponding to around p'=1700 kPa and was intended to bring the clay on the wet side of critical, but keeping at a distance from isotropic gross-yield.
As anticipated, two undrained shear tests, one starting from YSR=3 (TNL10) and the other starting from YSR=1.6 (TNL11) were carried out up to half the peak deviatoric stress recorded in the corresponding tests TNL1 and TNL7, with the aim to explore the clay behaviour before reaching the current SBS.
Only one undrained shear test (TNL12) started from an isotropic compression state post-gross-yield.
The new shear test data are compared with the data from the shear tests of Longo (2003) and Losacco (2004), consisting in tests TRX1 (YSR=7.4), TRX2 (YSR=3.8) and LUCMP (YSR=1.3) compressed isotropically pre-gross-yield, and test LUCHP compressed isotropically post-gross-yield.

The v-p' state paths of all the shear tests on natural Lucera clay from both the new experimental programme and the previous data are reported in Fig. 6.35. Initial states in the state paths are indicated with a dot for the new shear tests and with a rhombus for the previous tests. In the figure, also the INCL and K_0NCL for the natural clay are

reported, together with two isotropic compression tests on the new block sample (TNL5, in red) and on the previous one (LUCHP, in green).

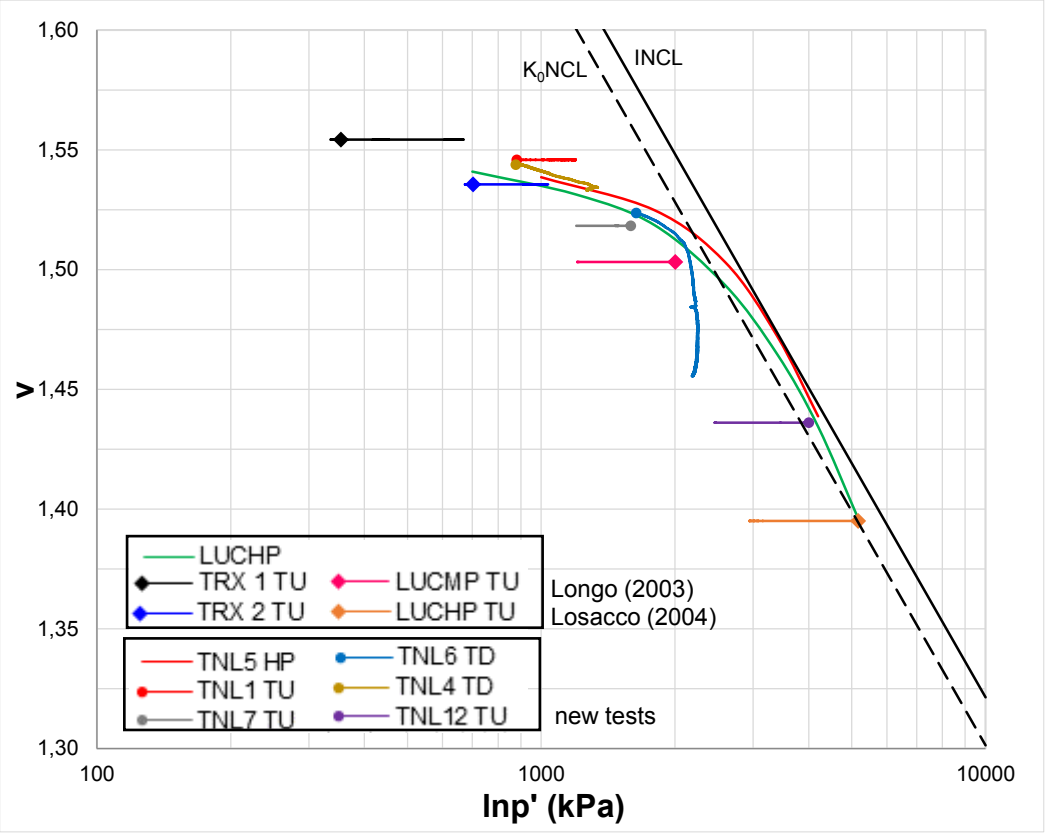

Fig. 6.35 - v-p' states of shear tests on natural Lucera clay: data from both the new experimental programme and from Longo (2003) and Losacco (2004).

The stress-strain behaviour recorded in the new shear tests is analysed in Fig. 6.36 to Fig. 6.40.

For all the tests, the point corresponding to gross-yield in shear is identified from the curve q/p'-ε_a as the point immediately before significant reduction in the gradient of the curve. When a sharp reduction in stress ratio was observed post-peak, the gross-yield point was taken as the peak. The gross yield points are shown on the plots for each test and the values of q/p' at gross yield are reported in Table 6.3.

Tests TNL1 and TNL4 were carried out on specimens having a YSR=3. Under undrained shear in test TNL1 (Fig. 6.36), as can be seen from the trend of excess pore water pressure, the clay exhibited a strongly plastic dilatant behaviour after an initial contraction and a significant strain-softening. Localisation of post-gross yield strains developed into a crossing bands failure surface (Fig. 5.1), at strains beyond the peak deviatoric stress. The formation of the failure surface, indicated with "FS", is seen to correspond to a sharp discontinuity in the Δu-ε_a plot. From the point of formation of the failure surface, the stress invariants were corrected for localisation using eq. (5.20). The stress ratio at gross yield and the final stress ratio are reported in Table 6.3. The results of the undrained shear test TNL10, stopped at half the peak deviatoric stress recognized in test TNL1, have been plotted with those of test TNL1. As expected, test TNL10 follows the same trend in terms of both q, q/p' and u with straining.

Drained specimen TNL4 (Fig. 6.37) exhibited a peak at small strains, after which only a mild strain softening was recorded. Volumetric strains showed a very light contractant behaviour. Since the volumetric strains appeared to have approached a constant value, the test was stopped at this very low axial strain, but actually it should have been carried on further. A clear localisation of strain was visible in the specimen at the end of the test (Fig. 5.1), which though had not yet developed into a failure surface, being rather recognized as an incipient shear band. In both test TNL1 and TNL4, gross yield occurred at the peak stress ratio. This is seen to correspond approximately to the maximum gradient in the decrease of the total excess pore pressure Δu in test TNL1.

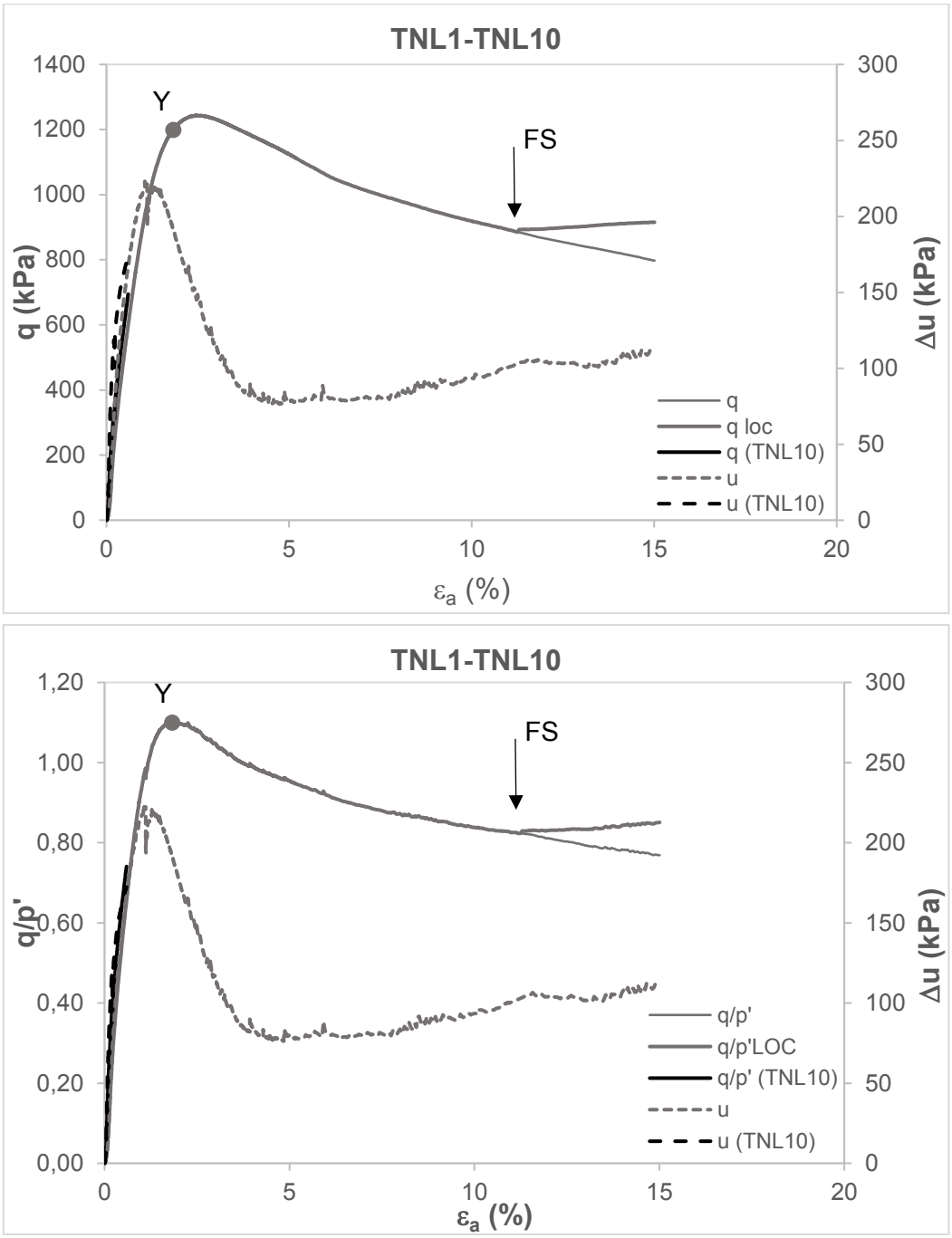

Fig. 6.36 - Natural clay: stress-strain behaviour of isotropically normally consolidated undrained tests TNL1(grey) and TNL10(black) (YSR=3).

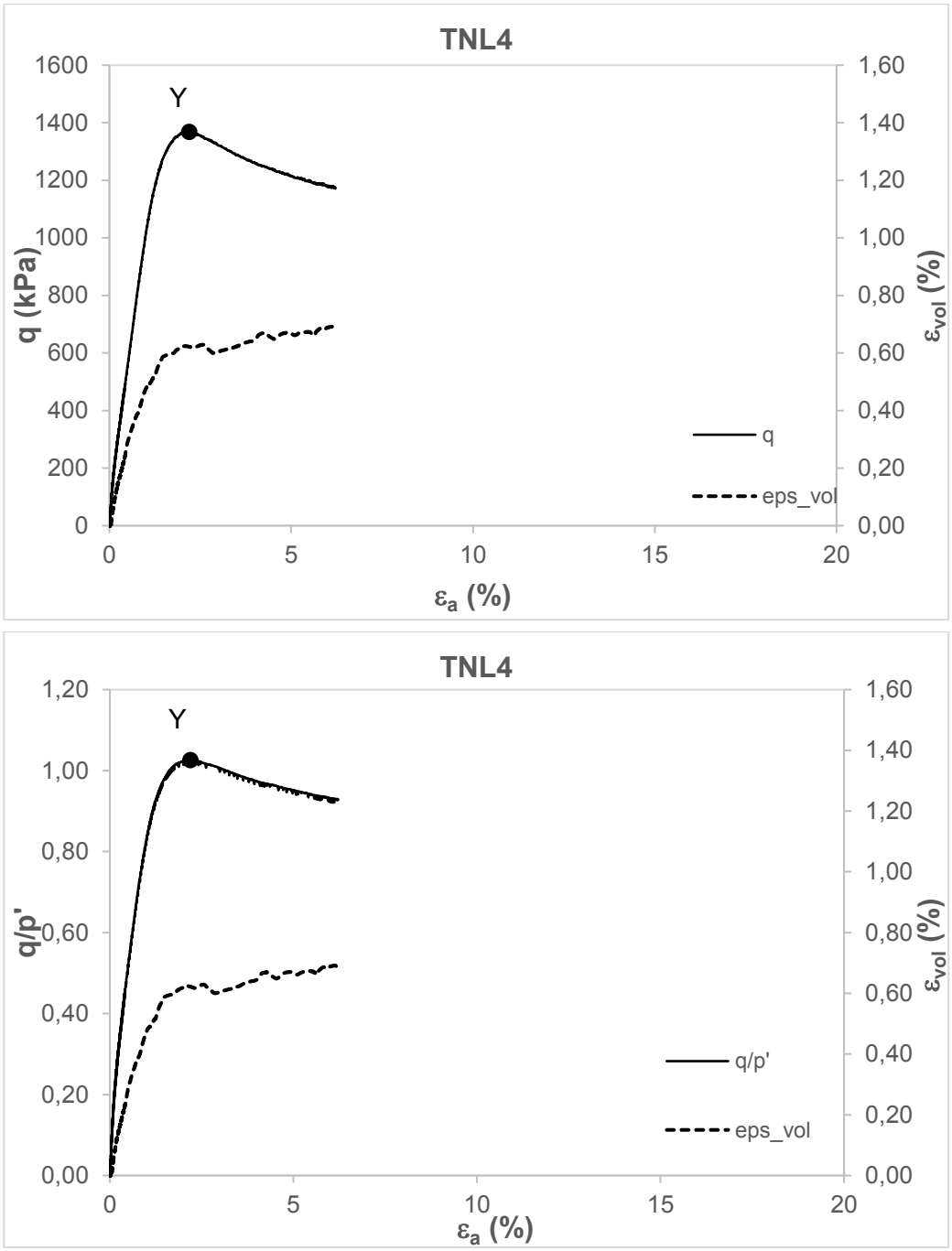

Fig. 6.37 - Natural clay: stress-strain behaviour of isotropically normally consolidated drained tests TNL4 (YSR=3).

As anticipated, in tests TNL7 and TNL6, the clay was compressed isotropically to a pre- gross yield state corresponding to a YSR=1.6.

In the undrained test TNL7 (Fig. 6.38), strain softening occurred, but less pronounced than in test TNL1. The clay behaviour was contractant and the excess pore pressure was seen to reach a constant value, almost an incipient dilation, when the peak stress ratio is reached, showing, thereafter a further light tendency to contraction. Similar results were found in tests on natural Pappadai clay having YSR of about 2 by Cotecchia (1996), who also observed that the incipient dilation became less and less evident as the value of the YSR decreased below 1.5.

At large strains in test TNL7 a failure surface was seen to develop (Fig. 5.1) and, correspondingly, the pore pressure increase appeared to stop and reach a constant value.

The results of test TNL11 have been plotted with those of test TNL7 in Fig. 6.38, to which they noticeably superimpose. Similarly to tests TNL1 and TNL10, test TNL11 follows the same trend as TNL7 in terms of both q, q/p' and Δu.

The specimen TNL6 sheared drained (Fig. 6.39) exhibited a highly contractant volumetric behaviour, compared to that of test TNL4, associated to strain hardening up to around 10% axial strain. Beyond a temporary constancy of stress ratio, strain softening was seen to develop, corresponding in the specimen to a significant strain localisation which appears to have developed more than that of test TNL4, though still being at an incipient stage (Fig. 5.1).

The behaviour of the natural clay at low yield stress ratios is therefore qualitatively different from that of the reconstituted clay, in which contraction is associated to strain-hardening.

In test TNL12 (Fig. 6.40), the clay was compressed beyond isotropic gross yield and during shear it was contractant and exhibited strain-hardening up to gross yield. After that, a temporary constancy of the stress ratio was seen and then the clay started to strain soften, finally developing a failure surface at around 11% axial strain, so the data were corrected for localisation. A small increase in the excess pore pressure was observed related to the failure surface formation.

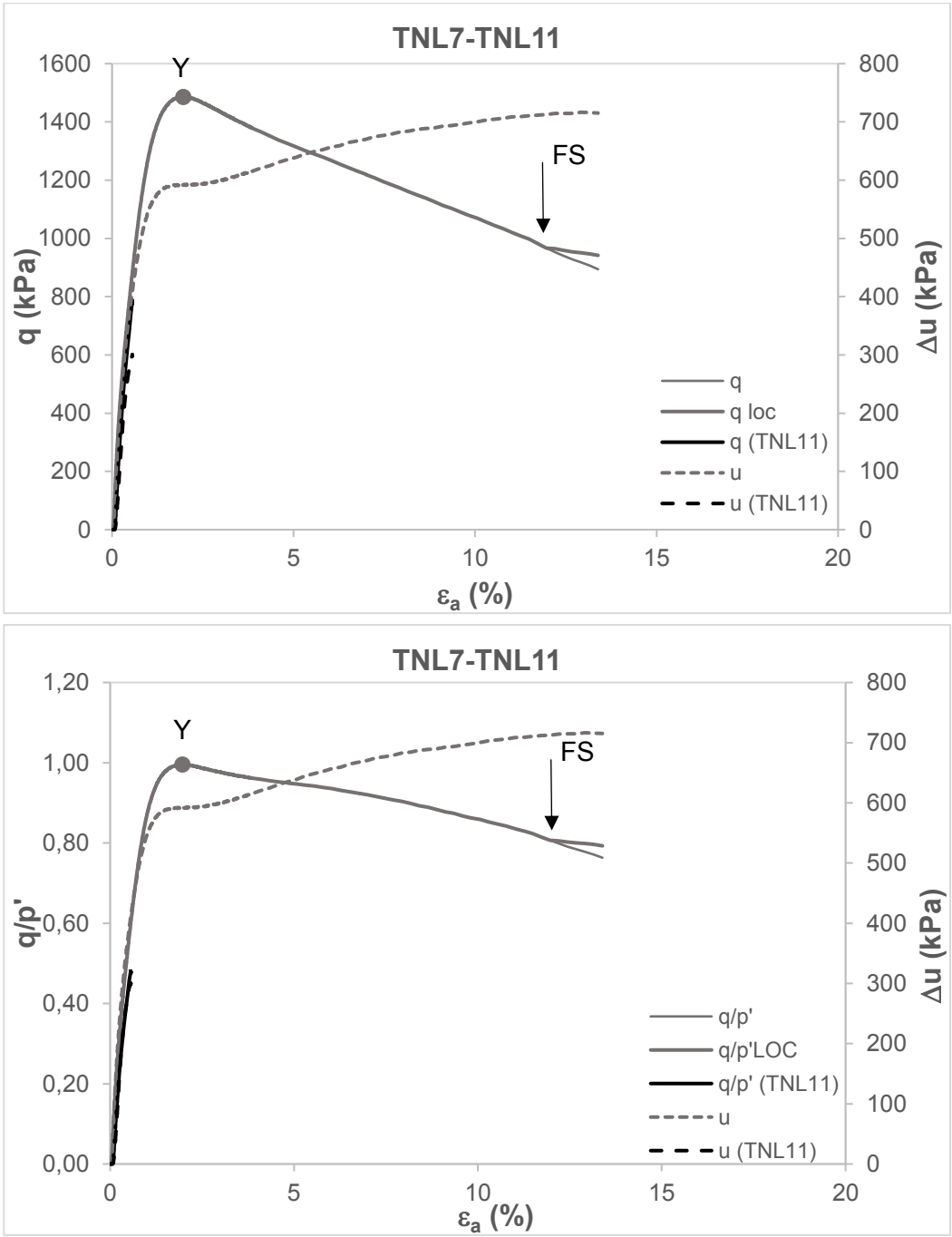

Fig. 6.38 - Natural clay: stress-strain behaviour of isotropically normally consolidated undrained tests TNL7 (grey) and TNL11 (black) (YSR=1.6).

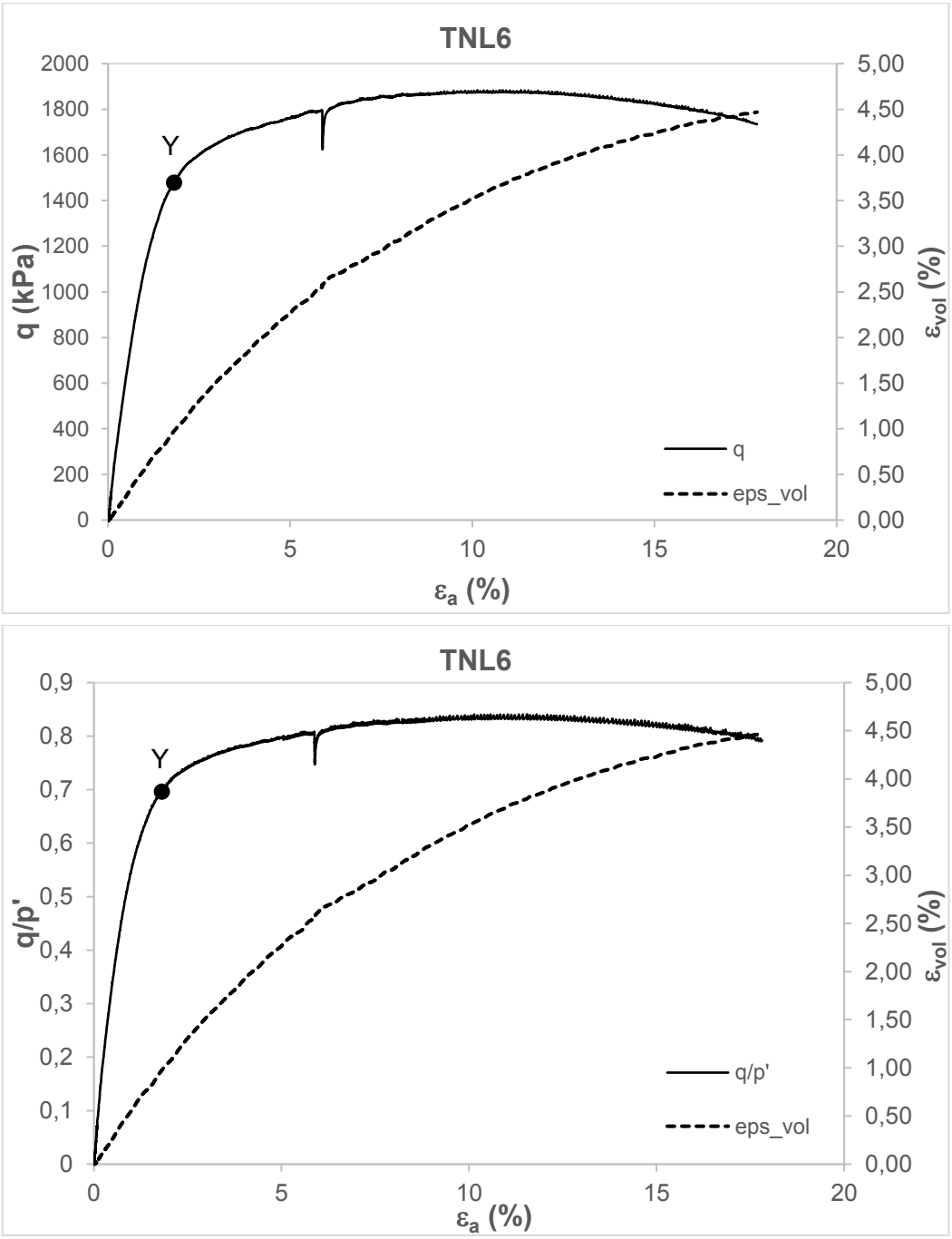

Fig. 6.39 - Natural clay: stress-strain behaviour of isotropically normally consolidated drained tests TNL6 (YSR=1.6).

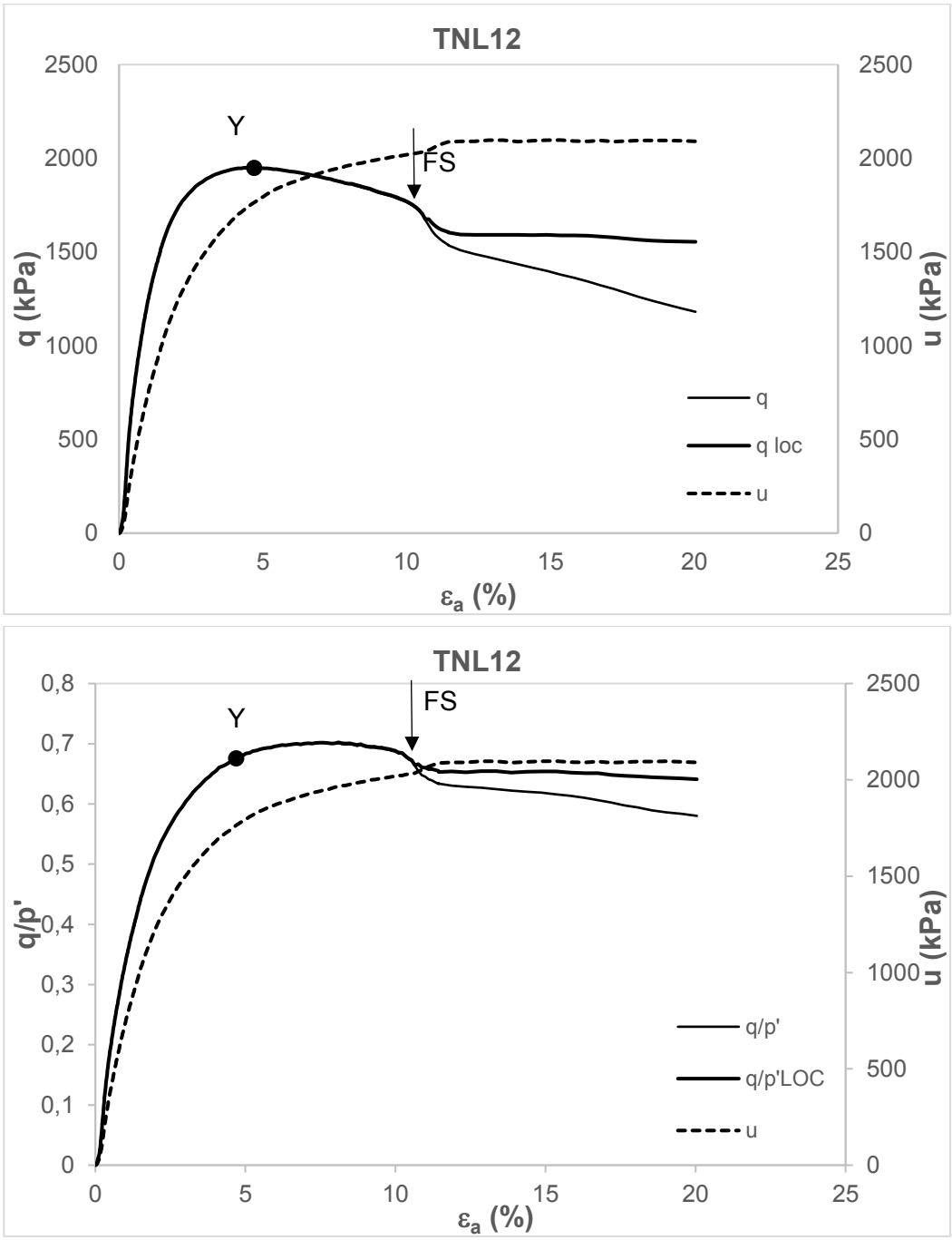

Fig. 6.40 - Natural clay: stress-strain behaviour of isotropically normally consolidated undrained test TNL12.

In Fig. 6.41 to Fig. 6.44, the stress-strain behaviour for the new tests on the natural clay are compared to that recorded in the tests carried out by Longo (2003) and Losacco (2004).
Both undrained tests TRX1 and TRX2 showed the behaviour expected from specimens on the dry of critical, as defined by the CSF, as they were both dilatant after an initial contraction and exhibited a strain softening behaviour. In both the specimens strain localisation developed into a failure surface, which formed at around 3% axial strain in TRX1 and 4.5% axial strain in TRX2 (Fig. 6.41). A significant drop in Δu is seen to correspond to the failure surface formation; this drop is more evident in TRX1, due to the higher YSR. In both the tests, gross yield in shearing could be clearly identified at the peak stress-ratio. The isotropically consolidated specimens of tests LUCMP and LUCHP were brought respectively to medium pressures, still prior to gross isotropic yield, and to high pressures, beyond isotropic gross yield, being properly on the wet of critical. In undrained shear both the specimens exhibited a contractant behaviour, associated to strain softening.

From the comparison of the curves in Fig. 6.41, in which the formation of the failure surfaces is also indicated with an arrow, it can be seen that the difference between the strain at peak deviatoric stress and the formation of the failure surface decreases with increasing YSR, so with decreasing mean effective stress, indicating a more pronounced tendency of the clay to dilate. Cotecchia (1996) observed that at YSR as high as 7 the failure surface developed soon after gross yield, to the point that it was difficult to distinguish the failure surface formation from the brittle drop in deviatoric stress. In any case, the formation of the failure surface seems to have been always consequent to strain softening.
The tests on lightly overconsolidated and normally consolidated specimens of natural clay provide evidence to strain softening of the natural clay concurring with a contractant behaviour, a condition in which a reconstituted clay would have strain hardened.

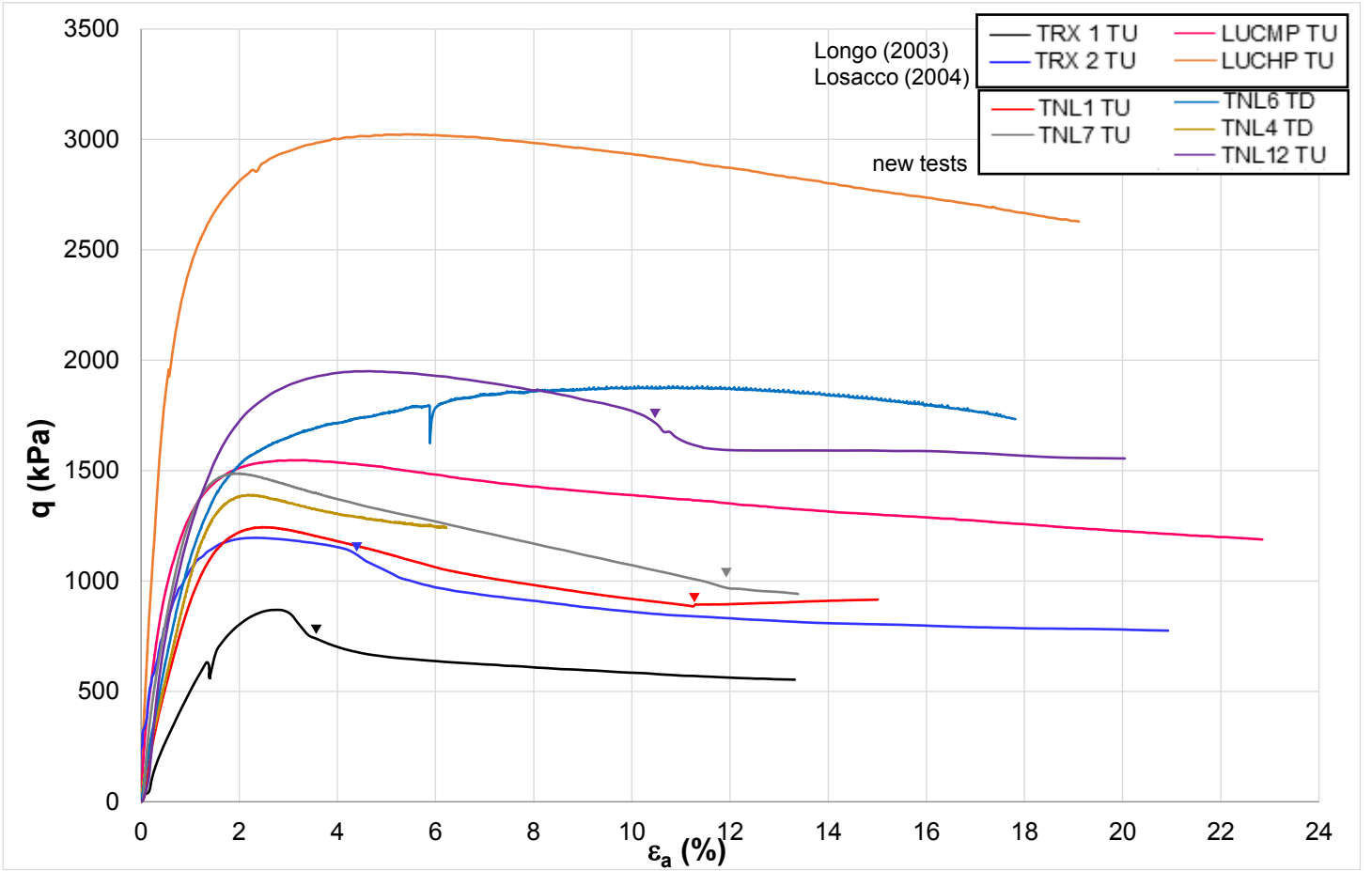

Fig. 6.41 – Comparison of stress-strain behaviour for natural Lucera clay in q-ε_a plane and indication of failure surface formation. Data from the new shear tests and from Longo (2003) and Losacco (2004).

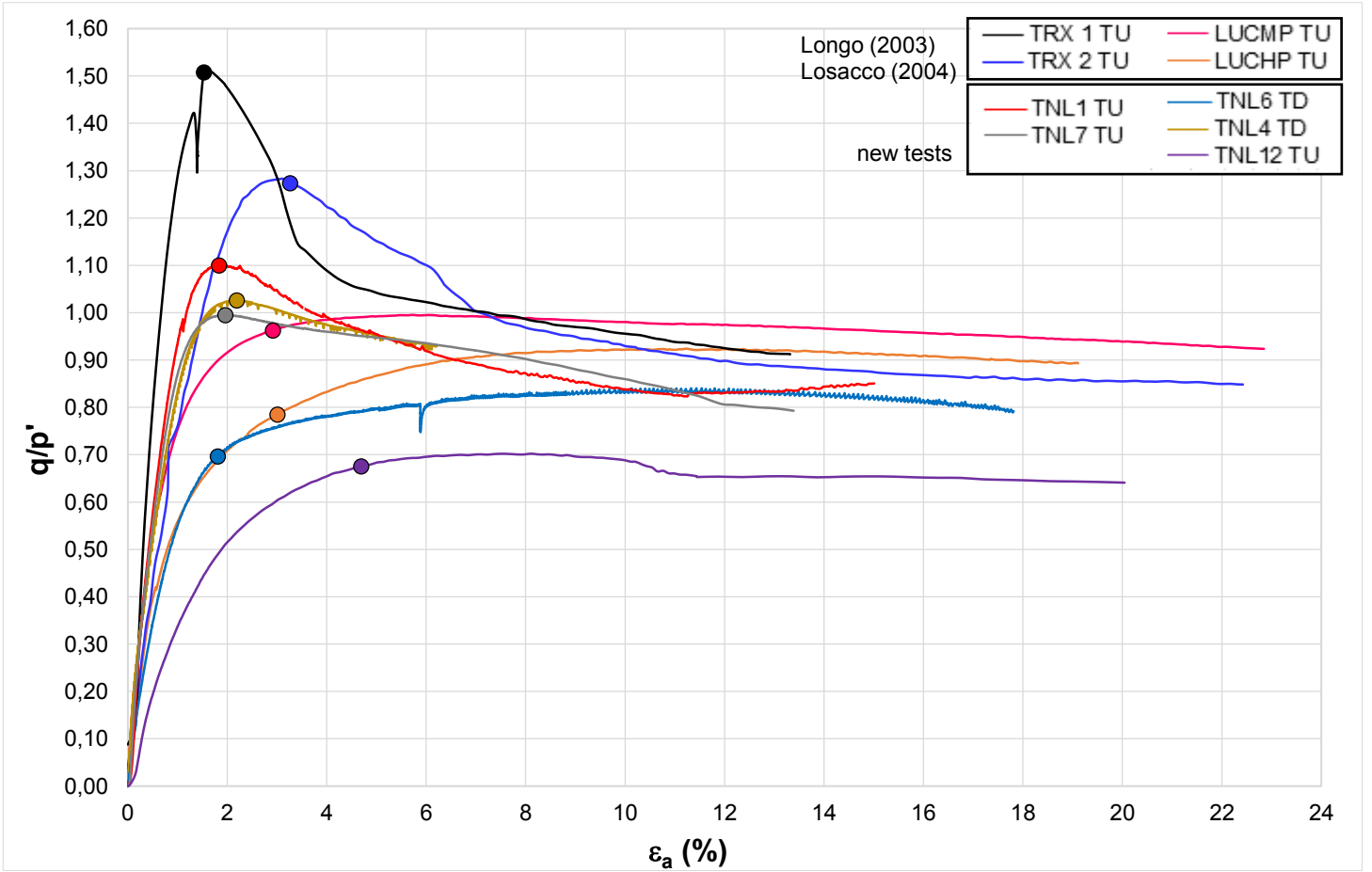

Fig. 6.42 - Comparison of stress- strain behaviour of natural Lucera clay in q/p'-ε_a plane Data from the new shear tests and from Longo (2003) and Losacco (2004)..

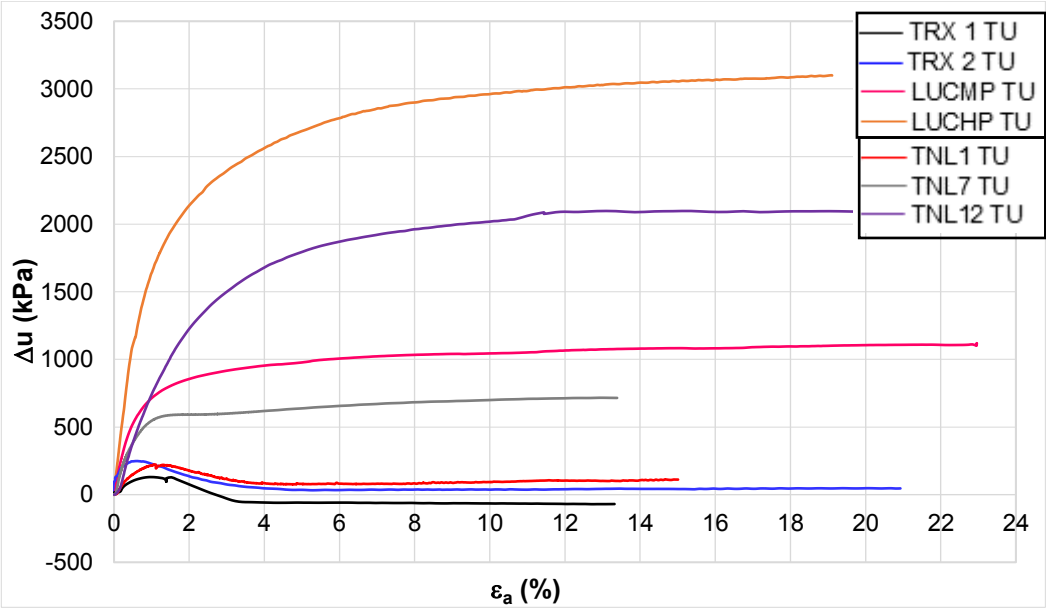

Fig. 6.43 - Comparison of pore pressure increase in undrained tests on natural Lucera clay.

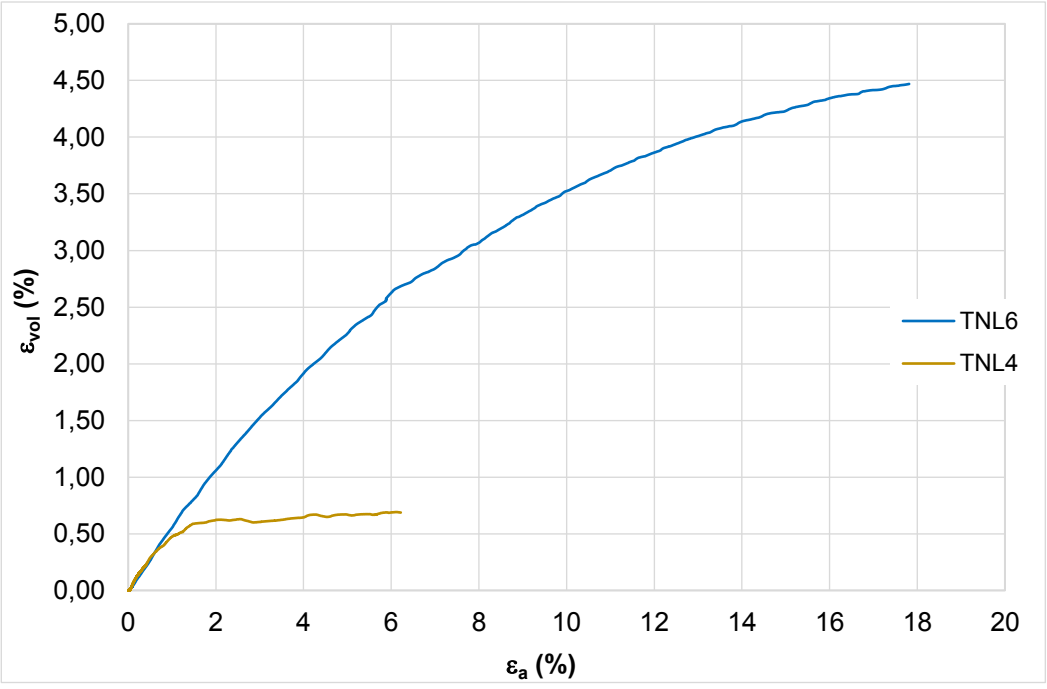

Fig. 6.44 - Comparison of volumetric strain in drained tests on natural Lucera clay.

Table 6.3 – Summary of shear tests results on natural Lucera clay.

	TEST	YSR_{is}	ε_{af} (%)	$(q/p')_y$	$(q/p')_f$	α (°)
UNDRAINED	TNL1	3	15	1.1	0.85	50
	TNL7	1.6	13	0.99	0.79	50
	TNL12	1	20	0.67	0.67	47
	TRX1	7.5	13.2	1.51	0.91	60
	TRX2	3.8	21	1.27	0.84	56
	LUCMP	1.35	23	0.96	0.92	-
	LUCHP	1	19	0.78	0.89	-
DRAINED	TNL4	3	6	1.03	0.92	-
	TNL6	1.6	18	0.69	0.79	50

6.4.2 Flow rules and stress ratios at critical state

To investigate the flow rule of the reconstituted and the natural clay, the plastic strain increment ratios $d\varepsilon_v^p/d\varepsilon_s^p$ during shearing were calculated as discussed in Section 5.4.4.

These ratios are plotted against the stress ratio for the reconstituted clay in Fig. 6.45 and Fig. 6.46. The data from the undrained tests TRXA, TRXC and TRL2 are shown in Fig. 6.45. The data from test TRXA are seen to closely fit a linear trend, which appears to be approximately approached by tests TRXC and TRL2, which however reach zero plastic strain increment ratio joining to test TRXA at a stress ratio of 1.06 from the dilative side of the plot. The linear relation recognized is:

$$\frac{q}{p'} = 1.06 - 2.8\frac{\delta\varepsilon_v^p}{\delta\varepsilon_s^p} \qquad (6.2)$$

which corresponds to eq. (3.29), defining the "basically frictional" behaviour described in Section 3.4.7, with values of the coefficients Q=1.06 and A=2.8.

The drained test TRL1 did not reach zero strain increment ratio (Fig. 6.46), but is seen to approach a straight line in the final part of the curve having Q=1.06, but a higher value of A=3.5 with respect to the tests shown in Fig. 6.45.

For the undrained test TRL3 (Fig. 6.46), the data are seen to approach a linear trend, but with different values of both Q and A with respect to tests TRL1.

In conclusion, a linear flow rule having coefficient Q=1.06 applies to most specimens of reconstituted Lucera clay in the final part of the curve, both for states before and beyond gross-yield. The slope A is seen to be different for drained and undrained tests. A similar behaviour was recognized for reconstituted Pappadai clay by Cotecchia (1996), who found a lower stress ratio at critical state of 0.91. Also the slopes A were found to be lower than those for Lucera, being A=1.47 for undrained and A=0.53 for drained tests.

The gradient of the critical state line for the reconstituted clay is then taken as 1.06, resulting in a friction angle $\phi'_{cs}=26°$. Accordingly, the friction angle found for Pappadai was lower and equal to 23°.

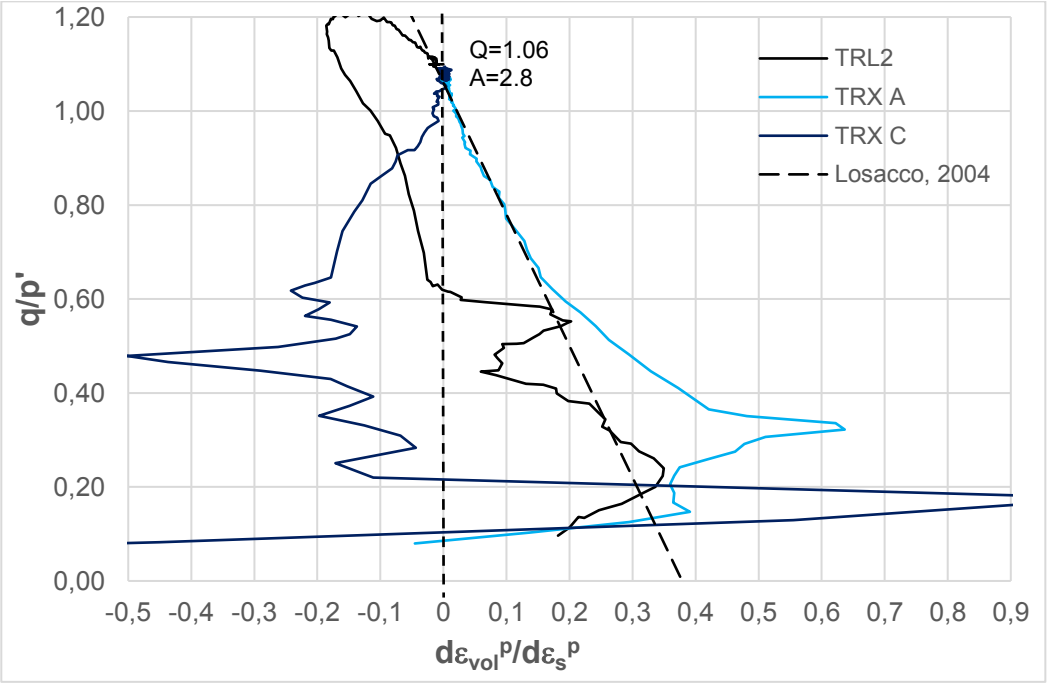

Fig. 6.45 – Reconstituted Lucera clay: flow rules for tests TRXA, TRXC and TRL2.

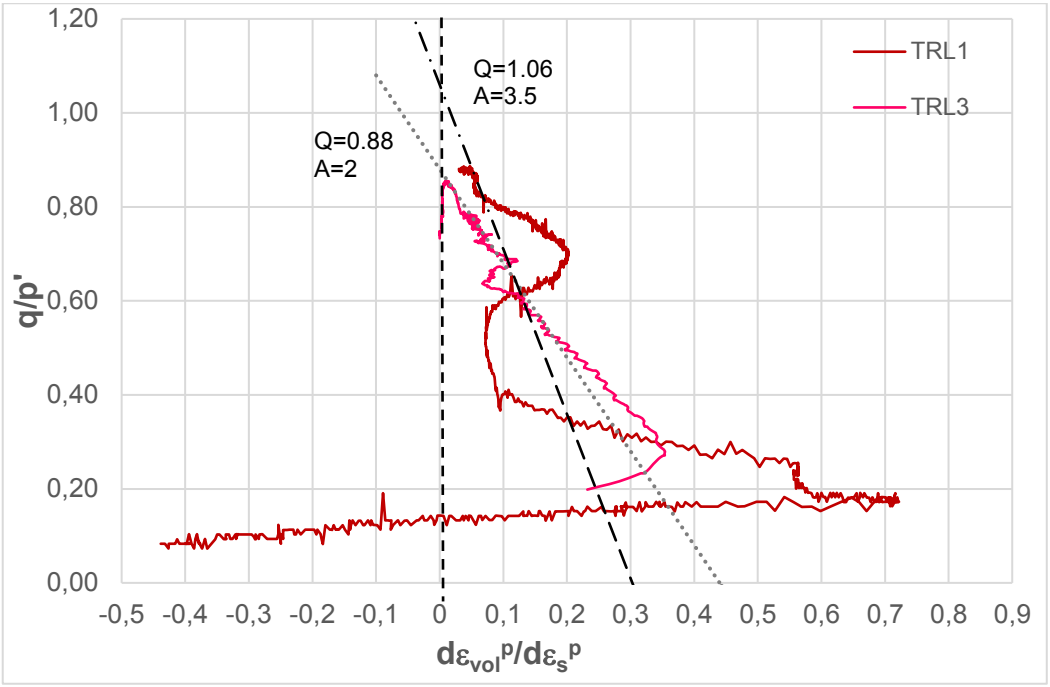

Fig. 6.46 - Reconstituted Lucera clay: flow rules for tests TRL1 and TRL3.

For the natural clay, the plots of the stress ratio against the plastic strain increment ratio are shown in Fig. 6.47 to Fig. 6.49.

According to Losacco (2004), the undrained tests TRX1, TRX2 and LUCMP on specimens consolidated to isotropic states pre-gross yield fit a linear relation with gradient 1.08. For the new tests, both undrained (Fig. 6.47) and drained (Fig. 6.48) from pre-gross yield states, the data are seen to follow a linear trend with gradient 1.03, while the slope is 3.7 for the undrained tests, the same as that identified by Losacco (2004), and 1.8 for the drained tests.

Beyond gross yield (Fig. 6.49), a similar trend can be identified. The slope of the linear relation is unchanged, whereas the value of Q reduces to around 1 for LUCHP and 0.9 for TNL12.

As discussed in Section 3.4.7, the intercept of eq. (3.29) applying to the natural clay is the stress ratio M_{nat}, which divides the behaviour into contractive (wet) and dilative (dry) (Fig. 3.38). Hence, the value of M_{nat}, for natural Lucera clay consolidated pre-gross

yield is found to be 1.03 for the new shear tests, lightly different from that recorded for the previous tests (1.08). However, both values are found to be close to the value of Q determined for the reconstituted Lucera clay, i.e., 1.06. Moreover, the intercept Q reduces for the natural specimens compressed post-yield to 1.

For Pappadai clay, as discussed in Section 3.4.7, M_{nat}, for the natural clay was found to be 1.08 for specimens consolidated both pre- and post-gross-yield; this value was also seen to differ from the Q value identified for the reconstituted Pappadai clay, equal to 0.91.

So for both the natural and the reconstituted clay, the relation between stress and plastic strain increment ratios is linear, having the same intercept for drained and undrained tests, but with different gradients. Moreover, for natural specimens compressed post-yield the intercept is seen to reduce to 1.

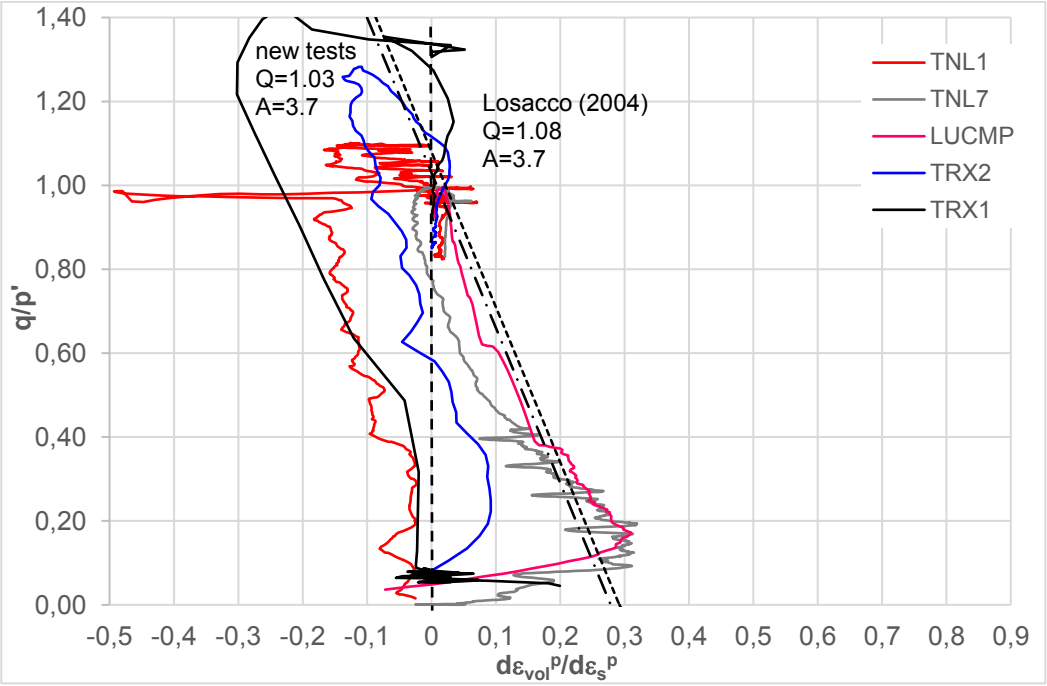

Fig. 6.47 – Natural Lucera clay: flow rules for undrained tests pre-gross-yield.

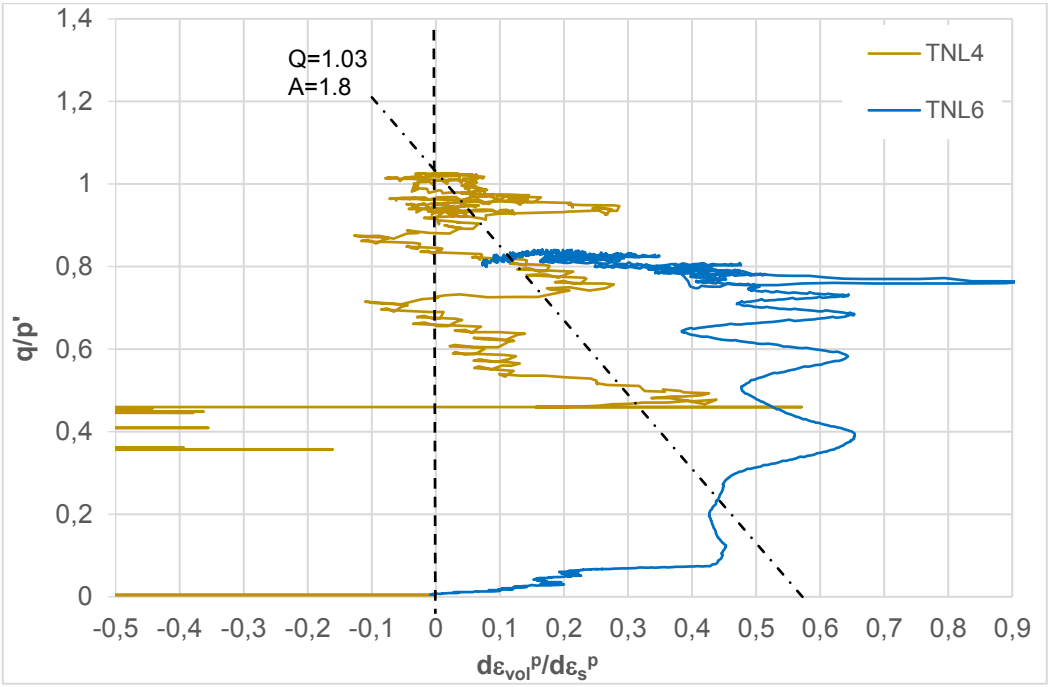

Fig. 6.48 - Natural Lucera clay: flow rules for drained tests pre-gross-yield.

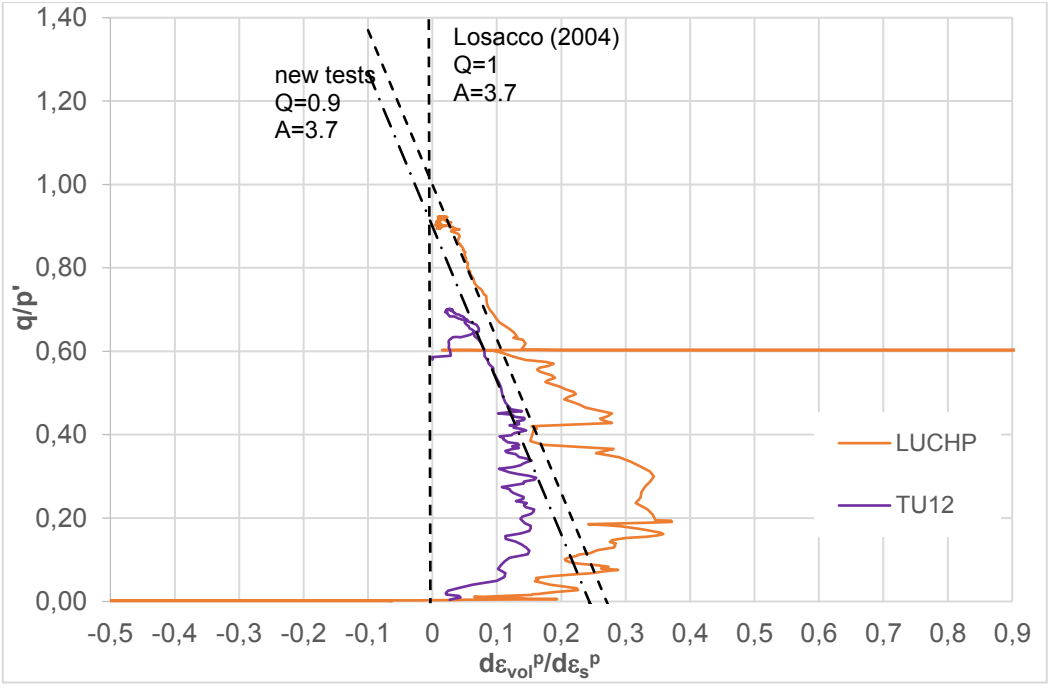

Fig. 6.49 - Natural Lucera clay: flow rules for undrained tests post-gross-yield.

6.4.3 Critical states

The stress paths followed by the reconstituted clay are shown in Fig. 6.50. The lines corresponding to the maximum and minimum critical state stress ratios measured are also plotted, although a gradient 1.06 appears generally applicable.

The v-lnp' state paths during shearing shown earlier are replotted in Fig. 6.51 in which the tentative CSL* is also reported, as will be explained in the following, together with the isotropic and K_0 compression lines are also reported.

Since not all the specimens reached critical state at the end of the tests (test TRL1 was stopped too early and test TRL3 showed an anomalous behaviour) and given the differences observed in the results, a tentative critical state line has been identified on the basis of the final states that the specimens would have reached on a line of gradient 1.06 in plane q-p' (Fig. 6.50). This line is found to be parallel to the compression lines, with a gradient $\lambda^*=0.139$ and an intercept Γ^* of 2.41.

The distance between the isotropic compression and the critical state lines ($N^*- \Gamma^*$), of 0.11, is slightly lower than the difference in the compression and swelling line gradients ($\lambda^*-\kappa^*$) of 0.118, which are equal in Cam Clay.

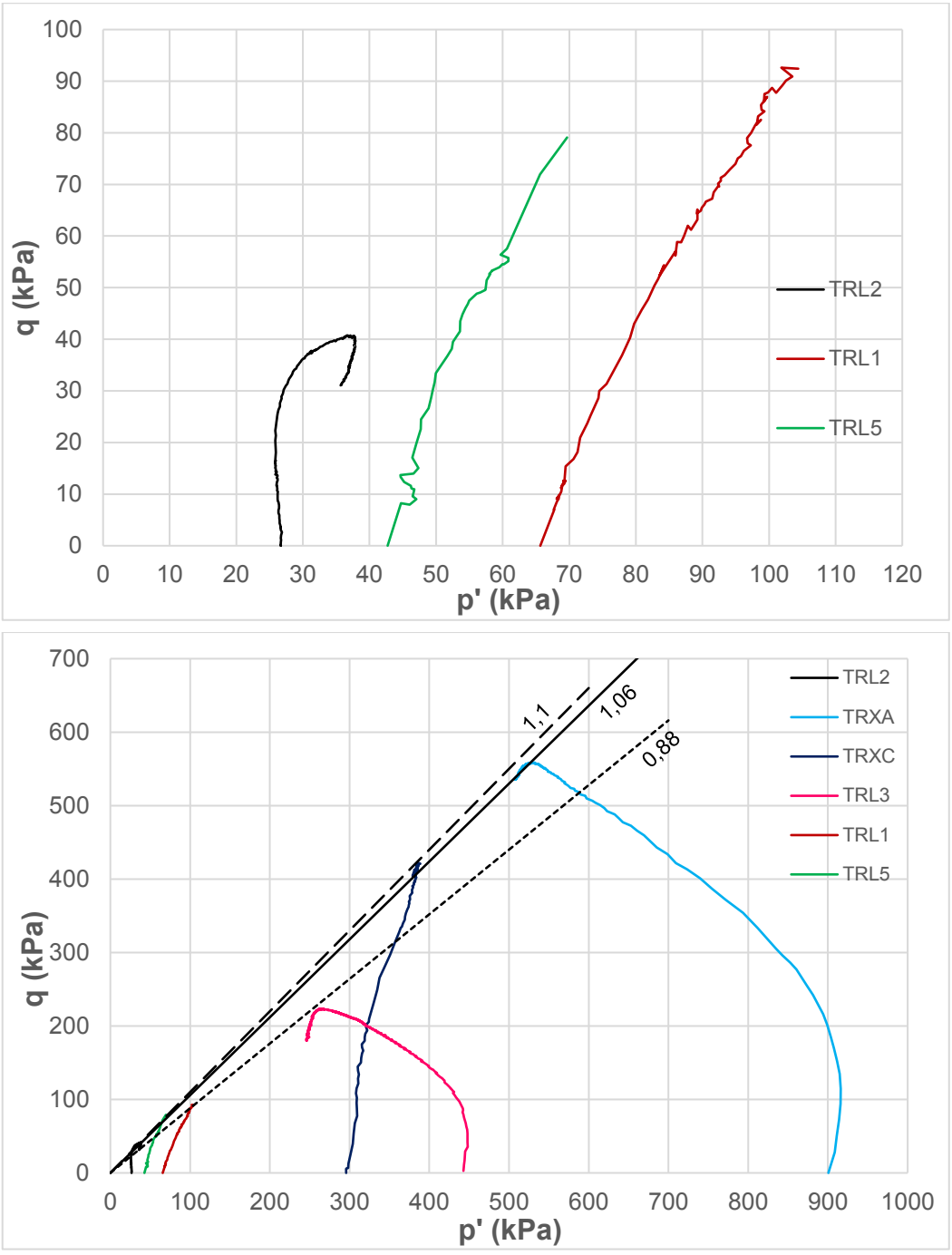

Fig. 6.50 – Reconstituted clay: stress paths (enlarged in the upper graph) and critical state line.

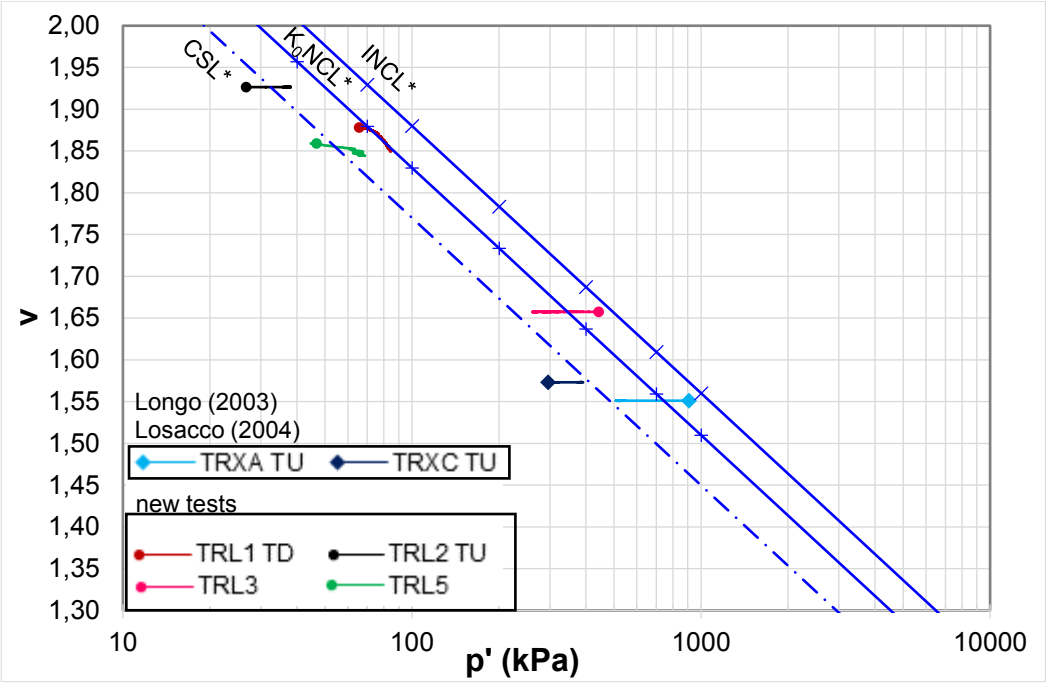

Fig. 6.51 – Reconstituted clay: v-p' state paths and critical state line.

The drained and undrained stress paths for the natural clay are plotted in Fig. 6.52. All the stress paths are seen to fall downwards after peak deviatoric stress. The localisation of deformation, which is often seen to occur in natural specimens, leads to define a pseudo-critical state, rather than a critical state typical of reconstituted clays (see Section 3.4.7), at which strain homogeneity no longer applies. Thus, even after an initial bulging (Fig. 5.1, Fig. 6.26), localisation develops into the formation of a failure surface with single or crossed bands.

The sheared specimens have been assumed to reach a pseudo-critical state when a constant stress ratio and excess pore pressure in undrained tests or volumetric strain in drained tests could be identified with increasing axial strain. For specimens which suffered localisation, the stress path corrected for localisation was considered. The corresponding values of the stress ratios at pseudo-critical states are reported in Table 6.4. These are found to be in good agreement with the value 0.87-0.89 determined by

Losacco (2004). So, in Fig. 6.52 both the critical state lines corresponding to M=0.88 and M=0.81 are plotted.

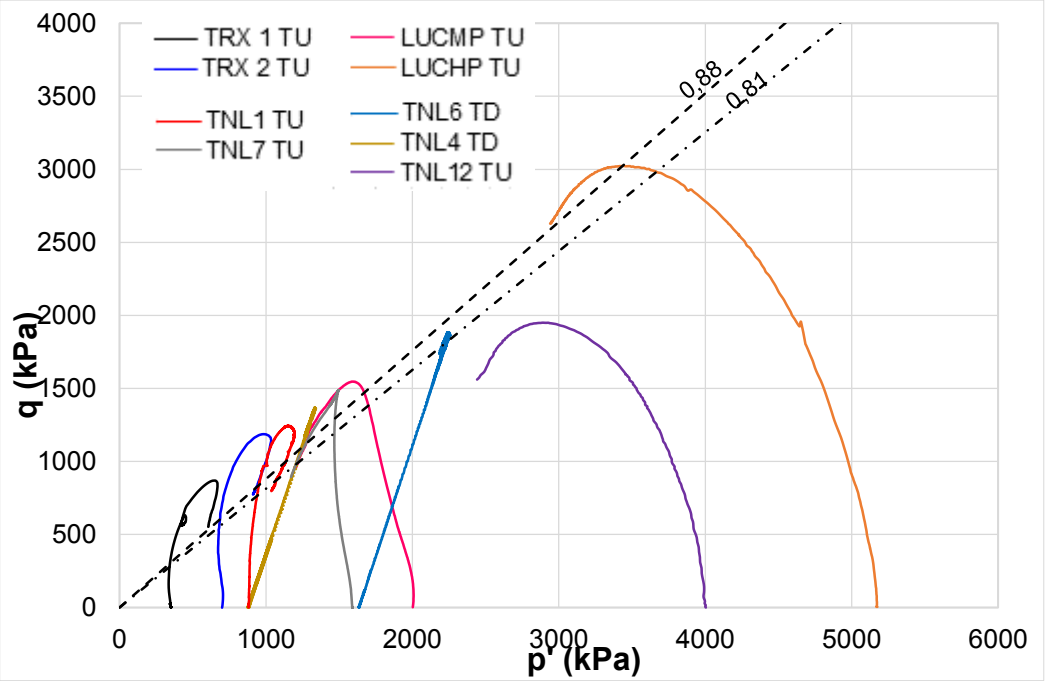

Fig. 6.52 - Natural clay: stress paths and critical state line.

Table 6.4 – Natural clay: pseudo-critical states.

TEST	YSR_{is}	ε_{af} (%)	M
TNL1	3	15	0.85
TNL7	1.6	13	0.79
TNL6	1.6	18	0.8

This value of M is found to be lower than that identified for the reconstituted clay M*=1.06. This difference has been recognized also for other stiff clays and for Pappadai clay, where *M*=0.85 and M*=0.91. The post-rupture friction angle corresponding to M=0.81-0.88 is 21-22°, which is quite lower than the friction angle at critical state for the reconstituted clay (26°).

Evidently, as discussed in Chapter 3 (Fig.3.38, Fig,3.39), the critical state line lies inside the state boundary surface of the soil, as will be shown later, and the stress paths deviate inside the boundary surface when moving towards critical state.
In Fig. 6.53 the drained and undrained stress paths are plotted in the v-lnp' plane together with the isotropic and K_0 normal compression lines. The critical state points are also indicated.

The critical states can be fitted with a straight line, parallel to the isotropic and K_0 normal compression lines, having slope $\lambda = 0.141$ and intercept $\Gamma = 2.51$ at 1 kPa. The state paths which do not arrive to a critical state seem to approach this line.
In conclusion, a critical state line is identified for the natural soil which is consistent with the CSF, being parallel to the compression lines.
The effect of structure on the critical state is evident, given the significant difference in location of the critical state line for the natural clay and the reconstituted clay in v-lnp' plane (Fig. 6.53).

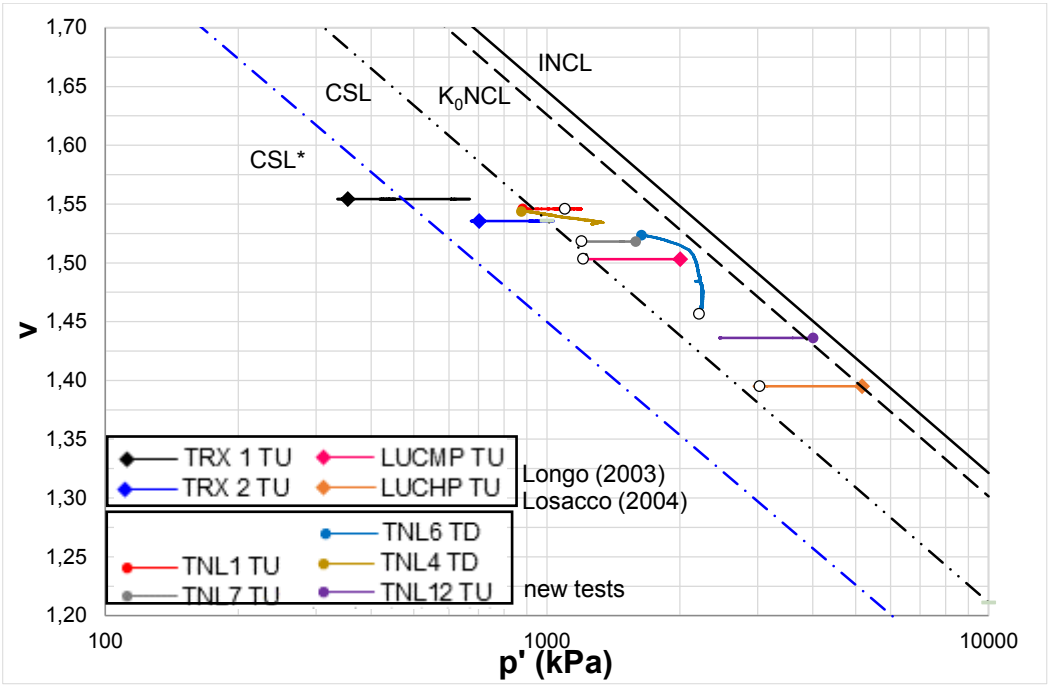

Fig. 6.53 - Natural clay: v-p' state paths and critical states.

6.4.4 Shear stiffness

For each shear test, on either the natural or the reconstituted clay, the tangent shear modulus G (also recalled as shear stiffness hereafter) was calculated by means of a linear regression over a fixed number of data points in the q-ε_s plot. The calculated shear modulus are plotted against the shear strain at the centre of the interval of regression.

Where internal local transducers were used (see Chapter 5), i.e., for test TRL2 for the reconstituted and test TNL7 for the natural clay, the shear stiffness within shear strain increments as low as 0.005% was estimated. The values of the shear stiffness measured by means of external transducers are less accurate than those estimated with local transducers. In fact, the external measurements are generally affected by errors, such as imperfect alignment of the specimen or apparatus compliance, which is not always repeatable. This generally results in lower stiffness values (Cuccovillo and Coop, 1997). By contrast, local internal transducers generally allow to characterize the

initially stress-strain behaviour, up to the yield state corresponding to a significant reduction in shear stiffness. However, even this yield state may be not the initial yield state, as shown by Gasparre (2005) and Gasparre et al. (2007).

This is seen for tests TRL2 and TNL7 (Fig. 6.54, Fig. 6.55), which allow to identify the small strain shear stiffness modulus, G_0, for the reconstituted and the natural clay respectively. This value is found to be of 12.7 MPa for the reconstituted clay at p'=30 kPa and of 350 MPa for the natural clay at p'=1640 kPa.

The shear stiffness curves obtained from the local transducers show, as expected, an initial approximately constant value, which then decreases and tends to converge to the curves derived from external transducer data.

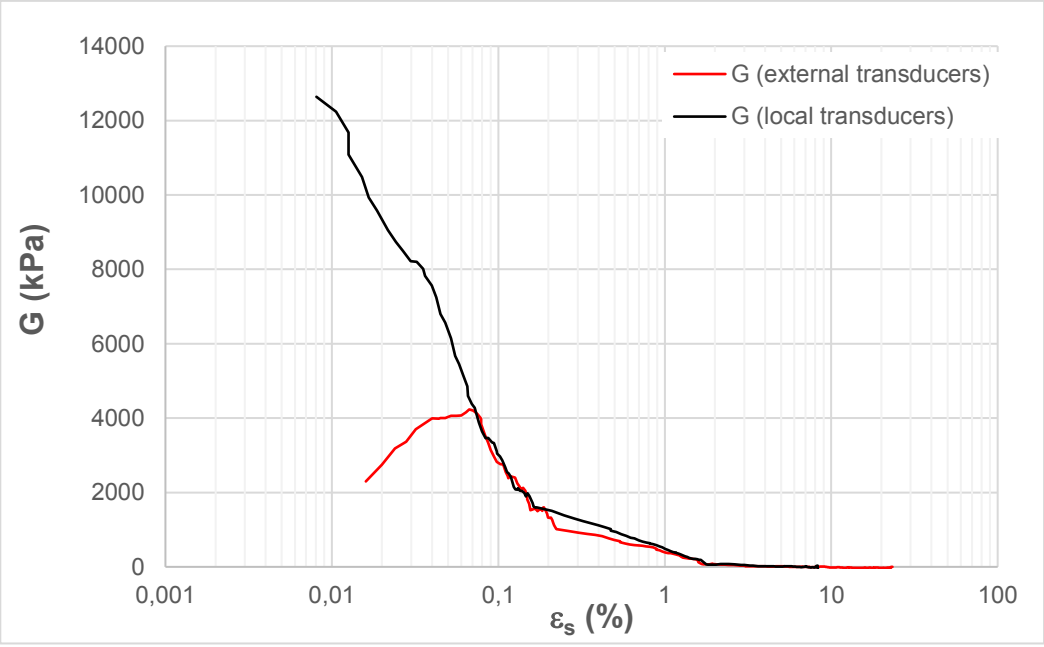

Fig. 6.54 – Comparison of shear stiffness measured by local and external displacement transducers (test TRL2 on reconstituted Lucera clay).

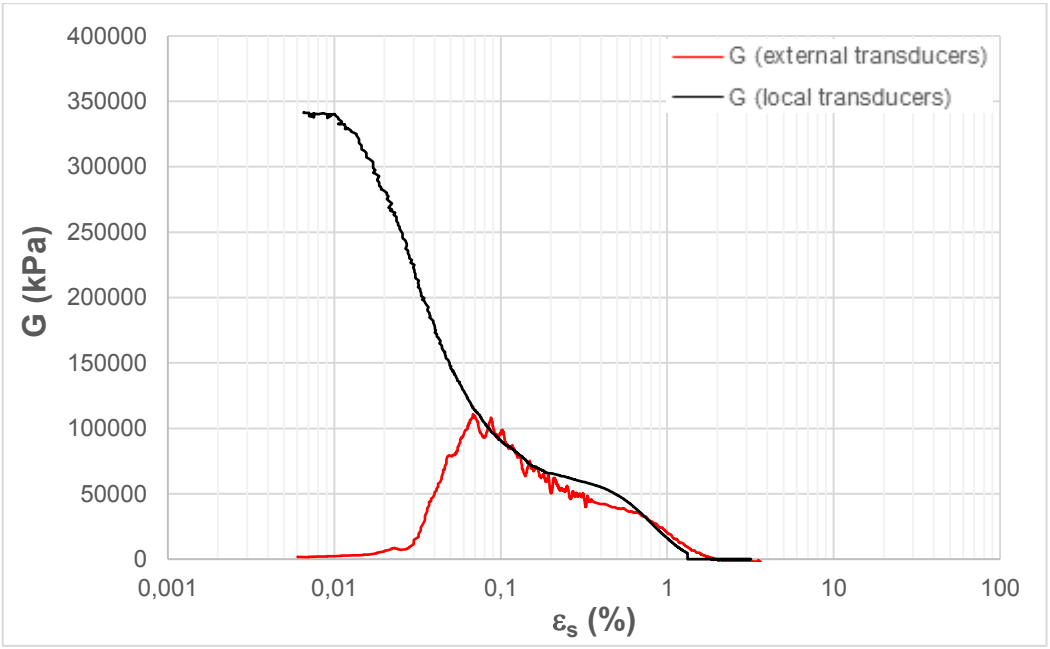

Fig. 6.55 - Comparison of shear stiffness measured by local and external displacement transducers (test TNL7 on natural Lucera clay).

In Fig. 6.56, the tangent shear moduli estimated from external measurements for the reconstituted clay are shown against deviatoric strain; in Fig. 6.56a only the results of the more recent shear tests are plotted. These are compared with those of the previous tests in Fig. 6.56b. As expected, higher stiffnesses correspond to higher confining pressures; for tests starting from similar consolidation states, the curves are seen to be very close and to overlap partially. All the curves finally converge for shear strains higher than 1%. Remarkably, the value of G_0 identified in test TRL2 (Fig. 6.54) is higher than the maximum shear modulus recorded in tests TRL1 and TRL5, which start from higher p'.

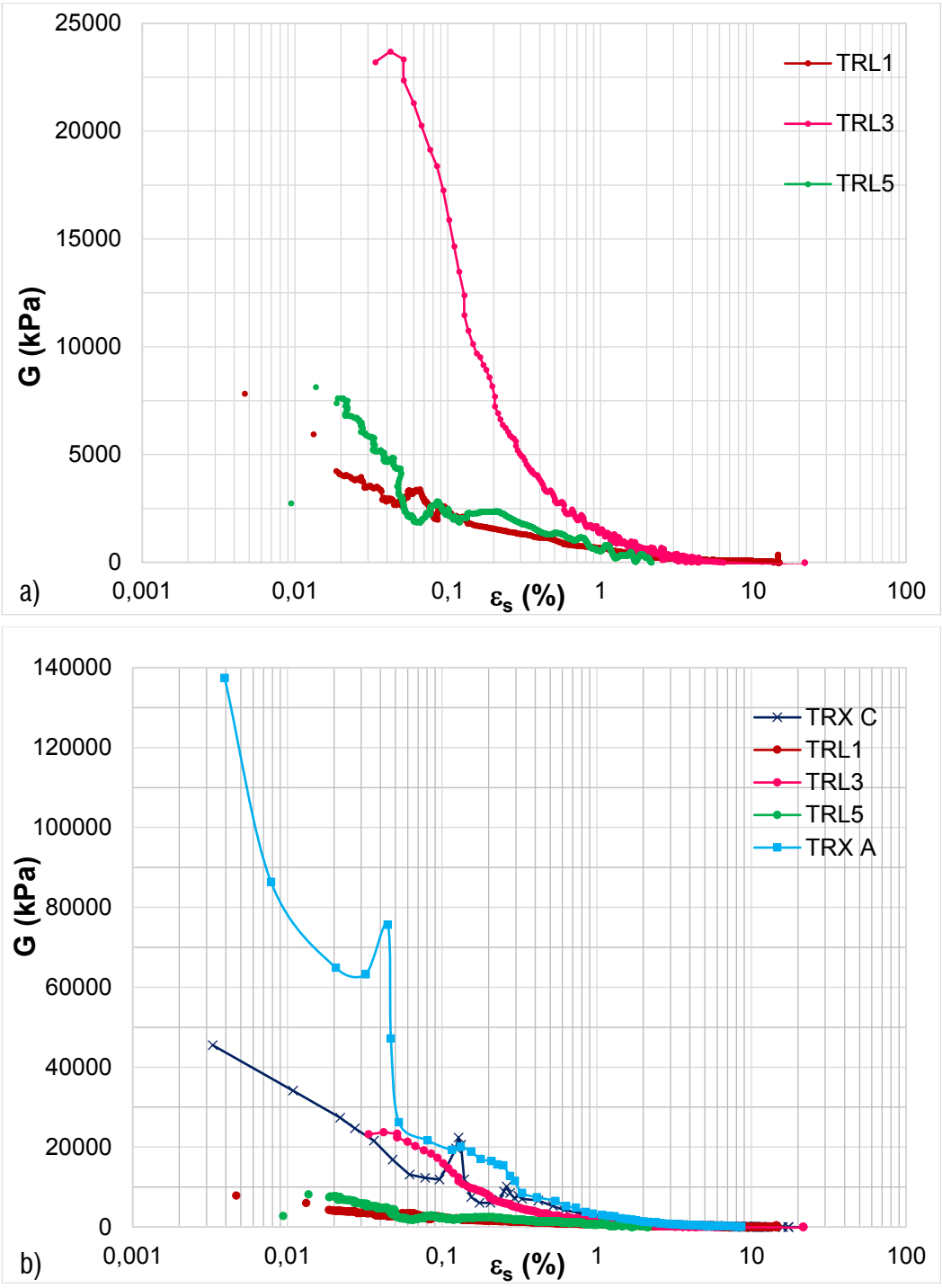

Fig. 6.56 - Shear stiffness of reconstituted Lucera clay.

In Fig. 6.57, the shear stiffnesses estimated from external measurements for all the natural specimens are plotted. Also for the natural clay, the shear stiffness increases with increasing confining pressure, and the curves tend to converge at a deviatoric strain of 1%. Although test TNL7 (Fig. 6.55) was carried out a value of p'=1640 kPa, its small strain stiffness is found to be much higher than that measured in test LUCHP compressed post-gross yield, to a normally consolidated isotropic state.

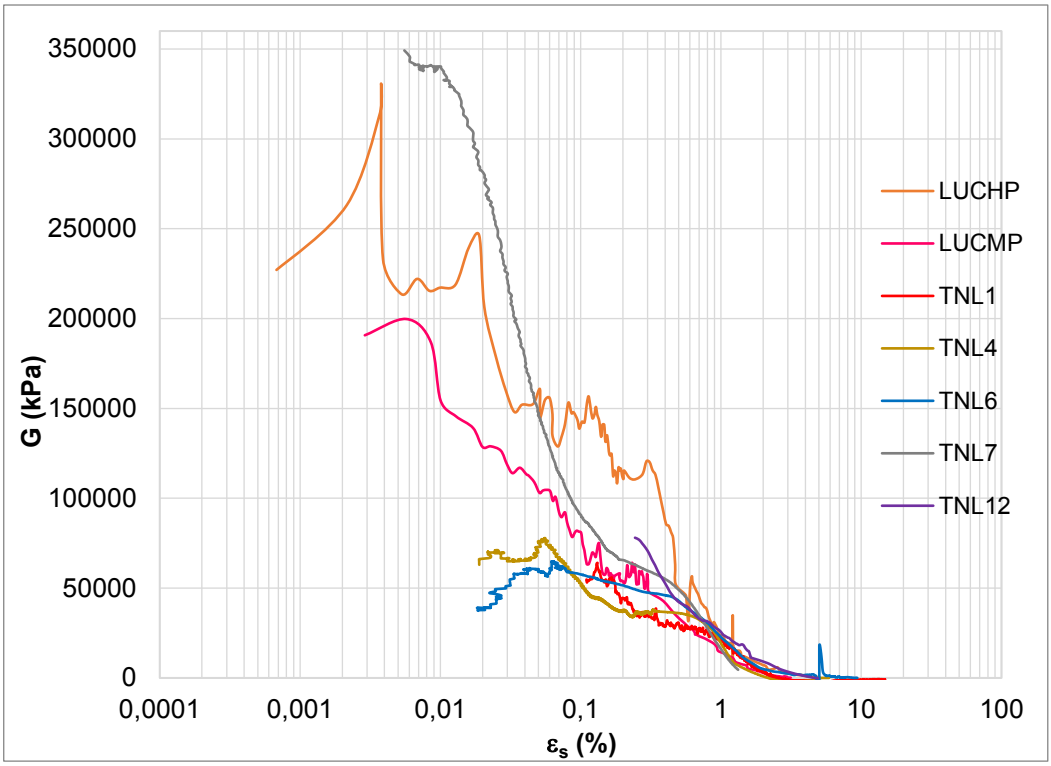

Fig. 6.57 - Shear stiffness of natural Lucera clay.

6.5 State boundary surface

To investigate the shape of the state boundary surface of the reconstituted and of the natural Lucera clay, the stress paths for all the tests discussed so far have been normalized with respect to volume using the equivalent mean effective stress p^*_e, which

corresponds to the current specific volume on the isotropic normal compression line of the reconstituted clay.

The straight INCL* defined earlier has been extended for the normalization purpose, because of the wide range of void ratios covered by the test specimens. Hence, a curvilinear isotropic compression line (Fig. 6.58) has been traced aiming at normalizing all the stress paths, for both the natural and the reconstituted clay. This has been set to follow closely the normally consolidated states followed in isotropic compression in test LUCRISO for 0.55<e<0.7. Thereafter, the same curvature observed in the oedometer test LUCR1 (plotted in v-lnp' plane according to the procedure described in Section 6.3) has been assumed to apply. The curvilinear INCL* so defined is shown in Fig. 6.58.

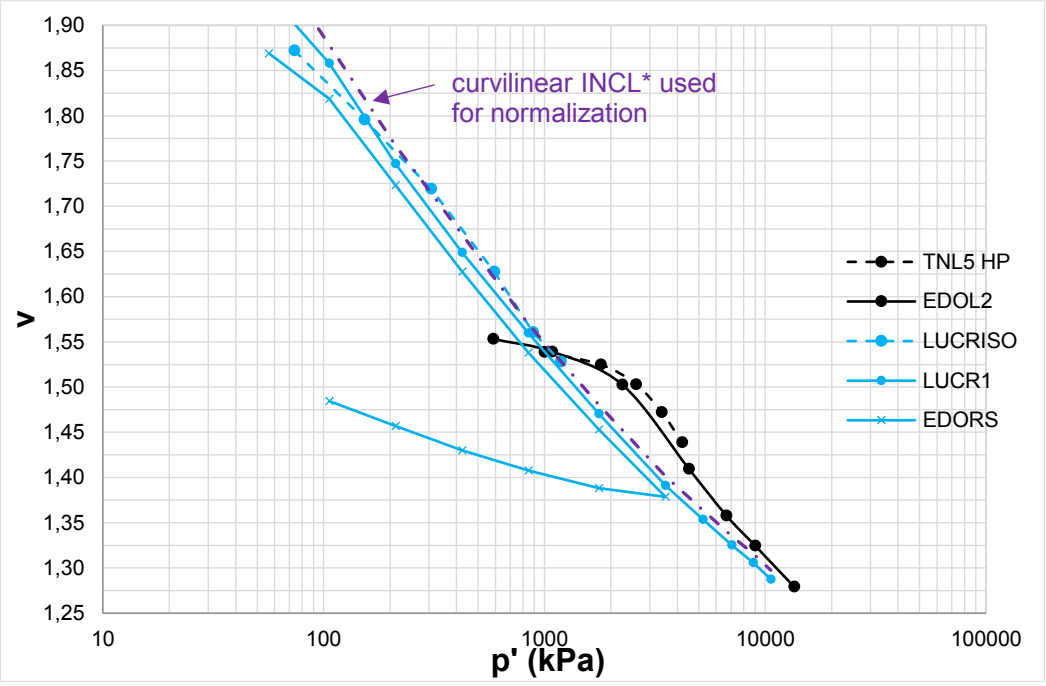

Fig. 6.58 – Definition of a curvilinear isotropic compression line for normalization.

The normalized stress paths followed by the reconstituted clay specimens are plotted in Fig. 6.59. Tests TRX A and TRL3 have initial states on the isotropic normal

compression line. Therefore, according to Rendulic's principle, their normalized stress paths should plot along a single the SBS*, i.e. the SBS* curve in the normalized stress plane. The stress path of test TRL3 is seen to initially follow closely that of test TRXA, and both lightly tend to the right (increasing p'/p_e^*) for low values of normalized deviatoric stress. Thereafter, the states of specimen TRL3 diverge from those of TRX A, as expected given the anomalous behaviour exhibited by the specimen and discussed earlier. Therefore, test TRXA has been considered of reference for the definition of the SBS* on the wet side.

The stress path of the lightly overconsolidated specimen TRL1, which was erroneously stopped too early, rises to the SBS* and then briefly follows it, although not reaching critical state. This is giving further confirmation that the test should have proceeded further.

On the dry side, test TRL2 rises almost vertically and then reaches a tentative Hvoslev surface. Tests TRL5 and TRXC, starting from approximately the same initial normalized state, show an orientation to the right from the very beginning of the test, then rise and approach the same surface, contributing to identify the left side of the SBS*.

The shape of the SBS* identified by the normalized stress paths appears to lightly differ on the wet side from that expected according to the CSF, due to a light bulging towards the right. A similar shape of the SBS* was also recognized for another Italian clay, Montemesola clay (Cafaro and Cotechcia, 2001; Cotecchia et al., 2007). It will be shown in the following that also the SBS of the natural Lucera clay exhibits some peculiarities in shape.

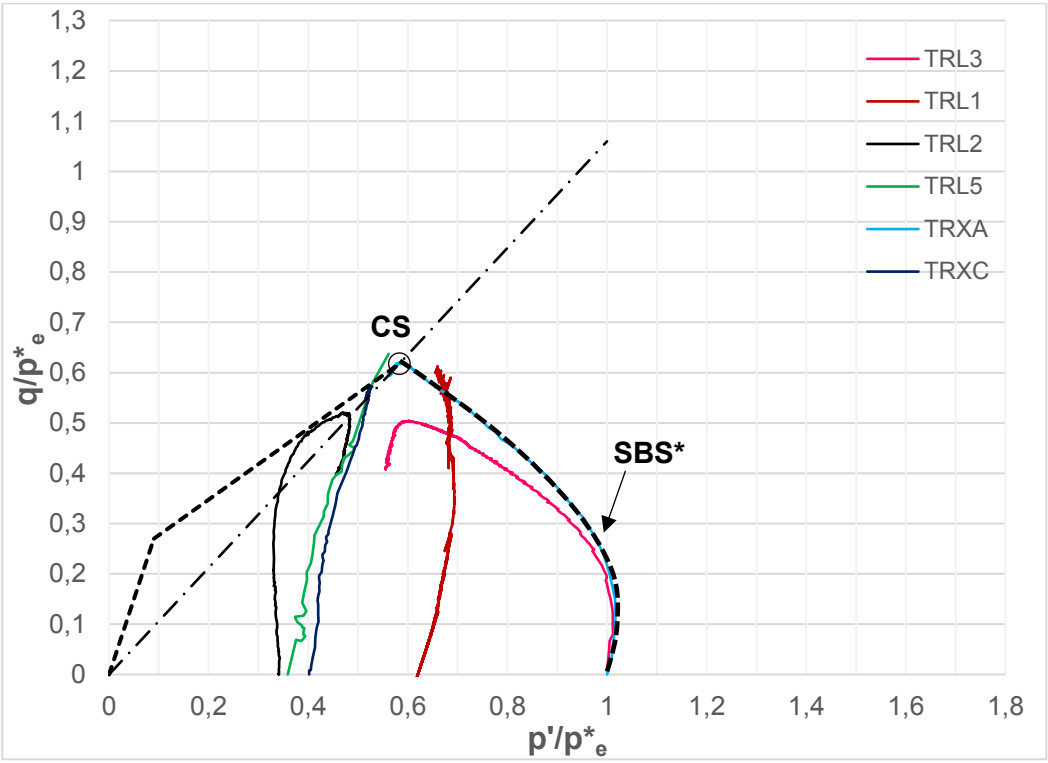

Fig. 6.59 – Reconstituted clay: normalized stress paths and state boundary surface.

Referring now to the natural clay, the normalized shearing stress paths and corresponding gross-yield points for the specimens consolidated to states before isotropic gross yield are plotted in Fig. 6.60a. The gross yield states in isotropic and K_0 compression are also shown. The isotropic gross yield state is plotted along the p'/p^*_e axis, corresponding to $q/p^*_e=0$, at a value equal to the stress sensitivity in isotropic compression, $S_{\sigma,iso}=1.77$ as discussed in Section 6.3. The gross yield state in K_0 compression is plotted on the K_0-line, also reported in Fig. 6.60a. In the figure, also the normalized stress path of the test carried out by Longo (2003) and discussed in Section 6.3 is plotted.

The shearing paths of the clay consolidated beyond isotropic gross yield before shearing are plotted in Fig. 6.60b, where they are compared to the shearing gross yield

states of the specimens consolidated to states before isotropic gross yield and to the normalized stress paths of the reconstituted clay.
In Fig. 6.60a, the current SBS of the natural clay can be clearly identified, based upon the drained and undrained normalized stress paths and on the isotropic and K_0 gross yield states. The drained stress paths have gross yield states on the SBS, differently from those of Pappadai clay which are seen to stop slightly below it, due to a problem of strain rate dependency, as documented by Cotecchia (1996).
A typical arch shape can be identified for the SBS, similar to that observed for Pappadai clay. Remarkably, the undrained stress paths of the dilating specimens rise along the SBS for some distance beyond gross yield. Thereafter, they migrate inside the SBS towards a critical state. The remaining drained and undrained stress paths reach the SBS of the natural clay and then soon leave it. This behaviour is evidently different from that of the reconstituted clay stress paths, which lie on the SBS* post-gross yield in shearing for a while.

In Fig. 6.60b the normalized stress paths for the specimens consolidated to states beyond isotropic gross yield are shown to plot within the current SBS. So, the behaviour of the clay beyond gross yield in compression cannot be normalized solely for volume. These normalized stress paths define the size of the SBS of the natural clay at lower specific volumes. The SBS of the natural clay is also compared with that of the reconstituted clay. The SBS is larger than the SBS*, as expected, confirming the higher strength of the natural clay with respect to that of the reconstituted clay. The size-ratio of the SBS to the corresponding reconstituted SBS*, which represents the strength sensitivity S_t defined in Chapter 3, has been calculated as the ratio of apex values, resulting in $S_t=1.94$. This value is seen to be lightly higher than that of S_σ, resulting in a SBS having a tighter shape on the wet side, as will be further explained in the following.
Moreover, the stress paths for the clay sheared beyond isotropic gross yield, which are seen not to follow isotropic hardening, are representative of the important degradation of structure which occurs post-gross yield in compression as they are no longer on the

SBS, as would be expected for a non-sensitive clay, but lie inside it. Accordingly, from test LUCHP a reduction of the value of S_t to1.33 can be recognized.

The normalized stress paths migrate inside the SBS after gross-yield in shearing, as a consequence of the degradation of structure occurred, and converge to a straight line corresponding to critical state below the SBS. As observed by Cotecchia (1996), they do not join a critical state point in the q/p^*_e-p'/p^*_e plane due to the different gradients of the critical state line of the natural clay and of the isotropic normal compression line for the reconstituted clay in the v-lnp' plane.
Moreover, the straight line of gradient M_{nat}=1.03 intersects the SBS at its apex (Fig. 6.61), which is exactly identified by the gross-yield in shear of the drained test TNL4. This line divides the behavioural framework of the natural clay into a dilative (dry) and a contractant (wet) side.

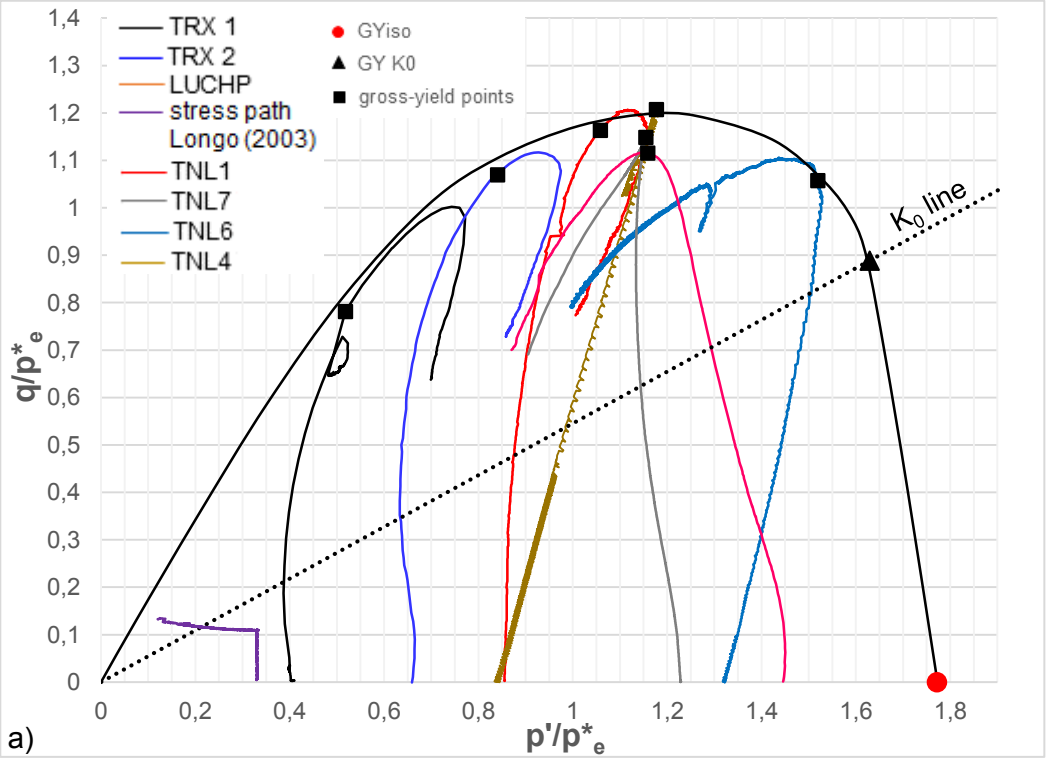

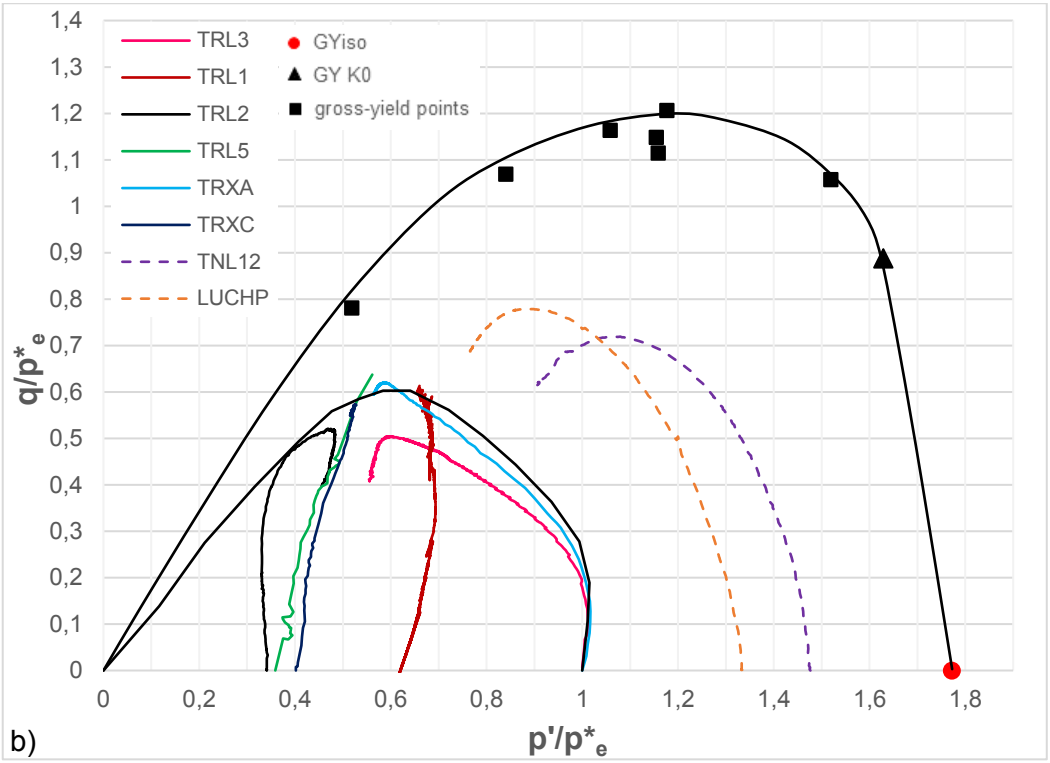

*Fig. 6.60 – Stress paths normalized with respect to the equivalent pressure p*e: (a) natural clay specimens consolidated to states before isotropic yield; (b) natural clay specimens consolidated to states beyond isotropic yield and reconstituted clay specimens.*

The behaviour of Lucera clay follows very closely the behavioural framework defined for Pappadai clay (Fig.3.38).

In Fig. 6.62, the state boundary surfaces identified for the natural and the reconstituted Pappadai and Lucera clays are compared. The SBS* for the reconstituted clays are seen to be very close, although a difference in shape can be observed as discussed earlier. The apices are different, as expected from the different values of M*, which is lower for Pappadai thus causing a smoother apex.

Both the natural clays have an arch-shaped SBS, that is larger than that of the reconstituted clay. For Pappadai, the SBS is larger than for Lucera as a consequence of the higher sensitivity.

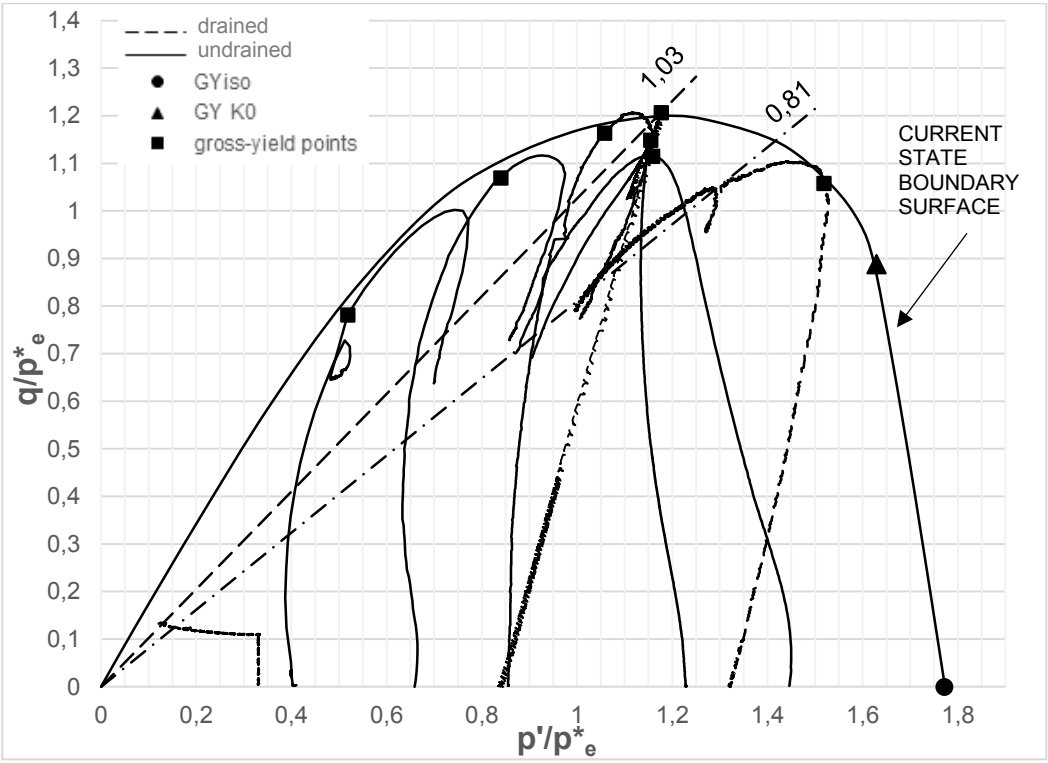

Fig. 6.61 – Normalized stress paths of the natural clay consolidated to states before isotropic yield and dry and wet sides of natural clay framework of behaviour.

Comparing the SBS for the natural Pappadai and Lucera clay, it is clearly seen that although both are arch-shaped, the SBS for Lucera clay is steeper on the wet side and overall tighter than that of Pappadai clay. This difference may be attributed to the different composition of the two clays, since Lucera clay has been found to have a lower CF and a lower activity than Pappadai clay. Similar shapes of the SBS have been in fact recognized for other clays having a silt fraction higher than that of Pappadai, for example for Montemesola clay (Cafaro and Cotecchia, 2001; Cotecchia et al., 2007). In Chapter 8, in the light of the microstructural observations on both Pappadai and Lucera clay, some hypothesis will be formulated which relate this difference in shape to differences recorded in microstructural features.

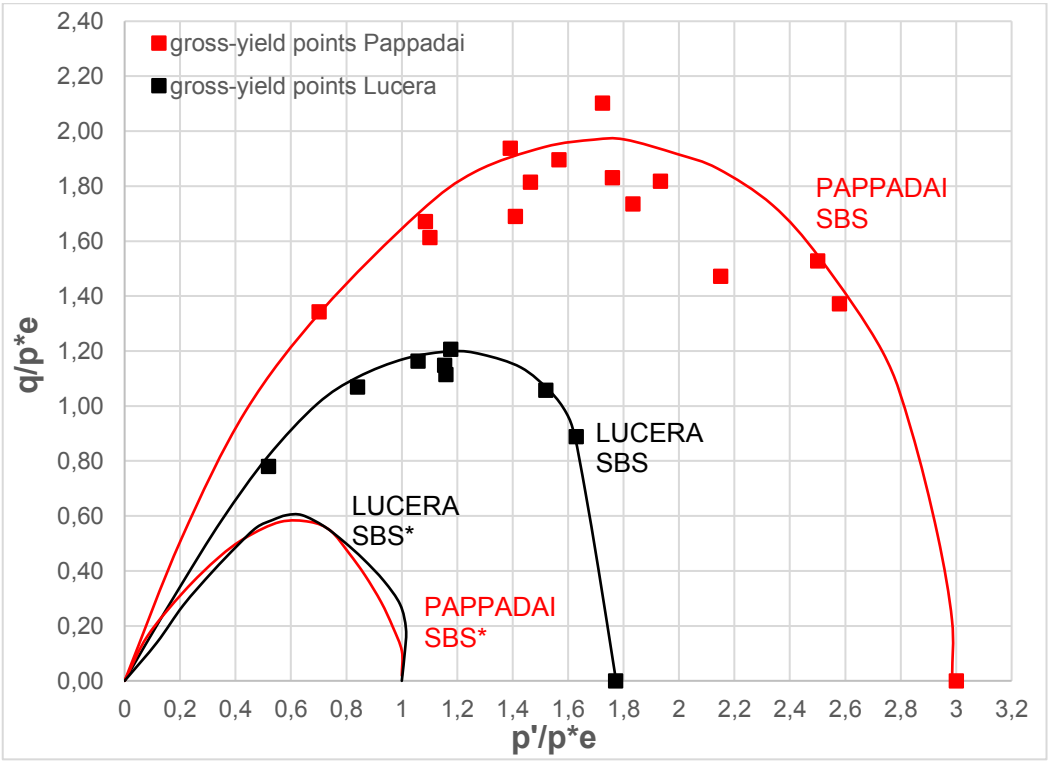

Fig. 6.62 – Comparison of natural and reconstituted state boundary surfaces for Pappadai and Lucera clay (data for Pappadai after Cotecchia, 1996).

7 RESULTS OF THE MICROSTRUCTURAL ANALYSES

7.1 Introduction

The results of the microstructural analyses performed on Pappadai clay and Lucera clay will be presented in this Chapter.

The microstructural investigation is pursued by combining three different techniques, each providing information on some features of the clay microstructure. SEM micrographs and MIP, which conveys a description of the pore distribution, are addressed to the exploration of the clay microfabric and the corresponding degree of orientation, quantified by means of the image processing of the micrographs. Hence, SEM micrographs, image processing results and MIP results will be referred to in the discussion of the features of the clay fabric, together with the cumulative and incremental curves obtained by means of MIP.

In the chapter, the microstructure of the clay is first observed at the initial state, i.e., prior to testing, and then its evolution under different stress-paths is analysed for comparison. This is done for both the natural and the reconstituted clay. After mechanical testing, the specimens to be subjected to microstructural analyses were always unloaded undrained in order to preserve the microstructure acquired during the test, as anticipated in Chapter 5.

In several studies in the literature (e.g., Burland, 1990; Rampello et al., 1993; Coop et al., 1995), the characteristics of the clay microstructure have been speculated, based upon the clay mechanical response at the macro-scale and have been supported by direct observation of the clay at the micro-level. However, the complexity of the chemo-physical processes that develop at the micro-scale (see Chapter 2), during the geological history (e.g., diagenesis, weathering) and, in the recent history, under different loading paths, should be aknowledged in the proposals of interpretation of the micro-phenomena in the background of the clay macro-response, that is seldom the case, not to be over-simplistic in the interpretation of the micro features. Accordingly, in the following the interpretation of the micro-phenomena in the background of different

aspects of the macro-response accounts for a systematic detailed acquisition of data about the features of the clay microstructure at different stages of the clay macro-response (i.e., according to the testing programme discussed in Chapter 5).

7.2 Initial clay microstructure

7.2.1 Microstructure of the undisturbed clay

The microfabric of undisturbed Pappadai clay was first investigated by means of SEM by Cotecchia (1996) for specimens of block sample 1; in this work the microfabric of specimens from Pappadai block sample 2 have been again investigated using a higher resolution FESEM, as explained in Chapter 5. Images from the both the former and the latter study are discussed in the following. On both series of micrographs, image processing has been carried out to measure the degree of orientation of the clay particles. The undisturbed state of Pappadai clay will be synthetically recalled as state P_1 (Fig. 7.41).

Global views of the fabric on a vertical fracture for an undisturbed specimen of Pappadai clay from the block sample 1 are given in Fig.7.1. The fabric appears densely packed and numerous sub-horizontal strata of iso-oriented edges of particles can be seen. As particularly visible in Fig. 7.1b, some strata are more densely packed than others. The degrees of orientation obtained from the image processing of the two images are higher than 0.21, thus being classifying the fabric as well oriented (Martinez-Nistal et al., 1999). An example of the application of the image processing technique described in Section 5.3.3 is reported in Fig. 7.2 for the micrograph of Fig. 7.1b: both the thinned image and the resulting direction histogram are shown. From the direction histogram (Fig. 7.2), the particles appear markedly oriented towards the horizontal direction.

In Fig. 7.3 and Fig. 7.4 three pictures on specimens of Pappadai clay from the block sample 1 (Fig. 7.3) and from the block sample 2 (Fig. 7.4), at a similar magnification, higher than that applying to the micrographs in Fig. 7.1, are compared. In all the images, the clay particles are seen to form domains, in which they are in face to face contact. Both small and large domains can be recognized. Iso-oriented domains densely packed in stacks (Section 2.10), forming strata which lie in sub-horizontal directions, are seen

(Fig. 7.4). However, many of these layers also bend towards sub-vertical directions and some sub-vertical strata truncating the horizontal ones are also observed (Fig. 7.3). Many domains, which are either in edge to face or in edge to edge contact, are visible too.

For both the processed micrographs (Fig. 7.3, Fig. 7.4a), the degrees of orientation are indicating a well-oriented fabric. This is found to be higher than for Fig. 7.4a, as a consequence of the thicker stacks visible in the image. An example of application of the image processing technique on a micrograph on block sample 2 (Fig. 7.4a) is given in Fig. 7.5.

Although a difference in the resolution of the SEM applications is recognized, no substantial differences are observed in the portrayed fabrics. This similarity between the undisturbed fabrics of the two block samples was expected, since the mechanical tests (Chapter 6) had given superimposed results and confirmed the validity of the parameters identified by Cotecchia (1996) for the description of the natural clay behaviour.

Moreover, the application of image processing on the two series of micrographs is seen to give comparable results, as will be further confirmed by other micrographs.

Many Globigerinae and fossil shells were found in the undisturbed Pappadai clay by Cotecchia (1996) and are again seen in the more recent micrographs. In Fig. 7.6a many fossil shells can be recognized, together with crystals of pyrite in bunches. Fig. 7.6b shows a large foraminifera which is found intact and not affected by consolidation. As anticipated in Chapter 2, framboid pyrite crystals were found in the undisturbed clay by Cotecchia (1996), suggesting that sulphide diagenesis occurred in the clay in reducing conditions. Framboid pyrite crystals found in the recently analysed specimen are shown in Fig. 7.7. A large variety of particles is present, among which coarser particles can be identified, such as quartz and calcite grains (Fig. 7.8).

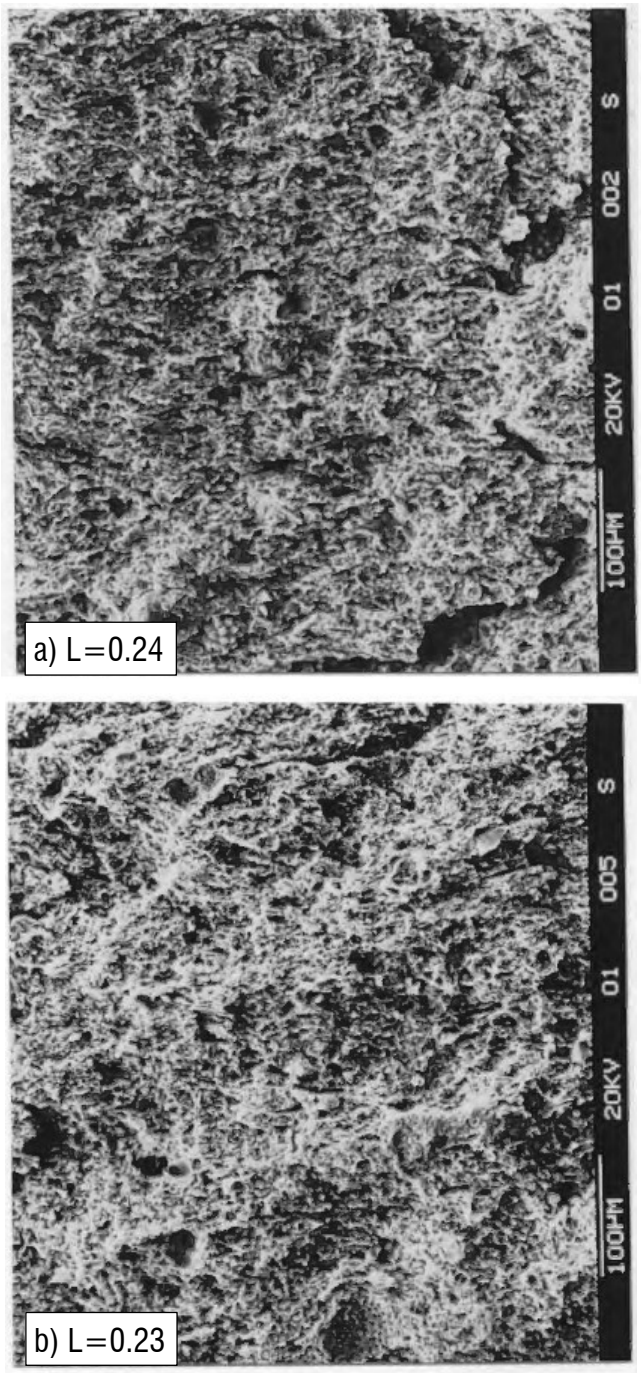

Fig. 7.1 - SEM micrographs along a vertical fracture of undisturbed Pappadai clay at low magnification (after Cotecchia, 1996).

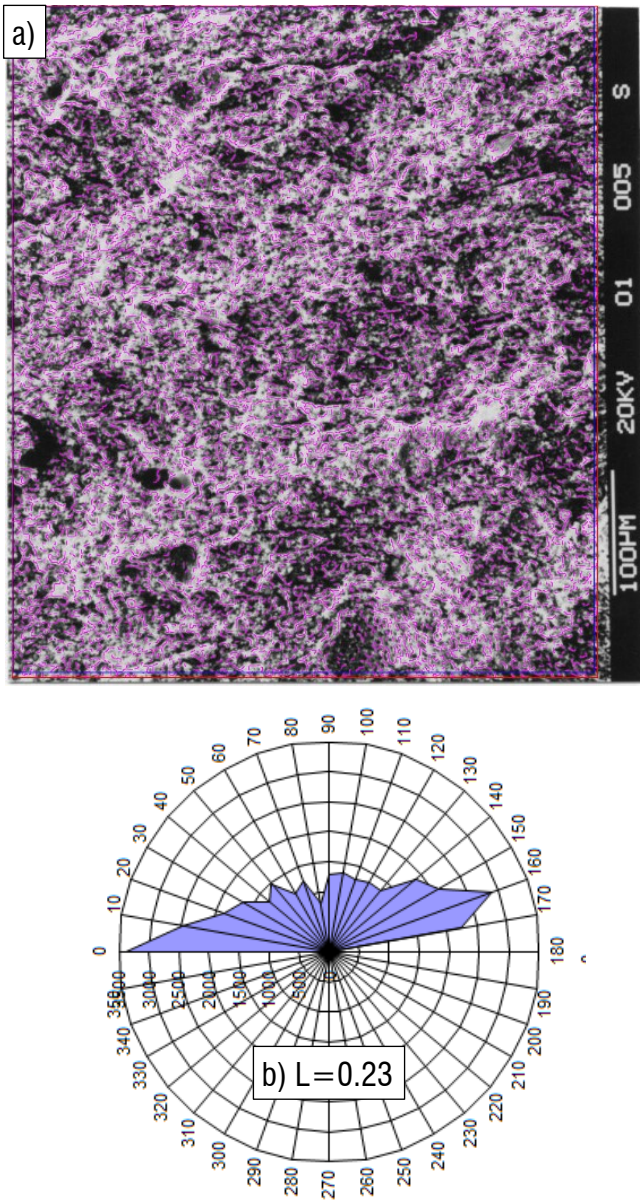

Fig. 7.2 - Image processing of the SEM micrograph in Fig. 7.1b: a) 'thinned' image and b) resulting direction histogram.

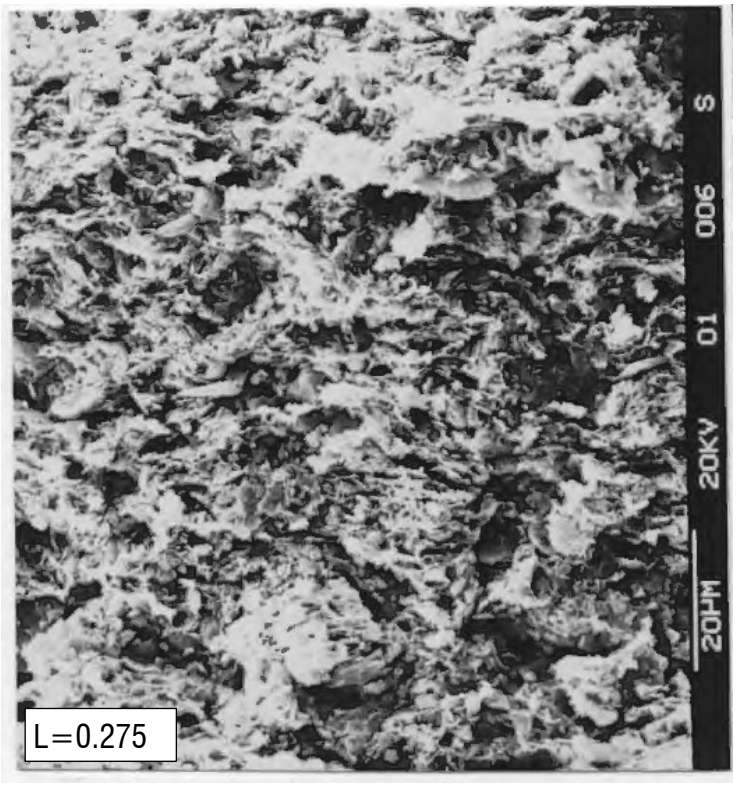

Fig. 7.3 - SEM micrograph along a vertical fracture of undisturbed Pappadai clay at medium magnification (after Cotecchia, 1996).

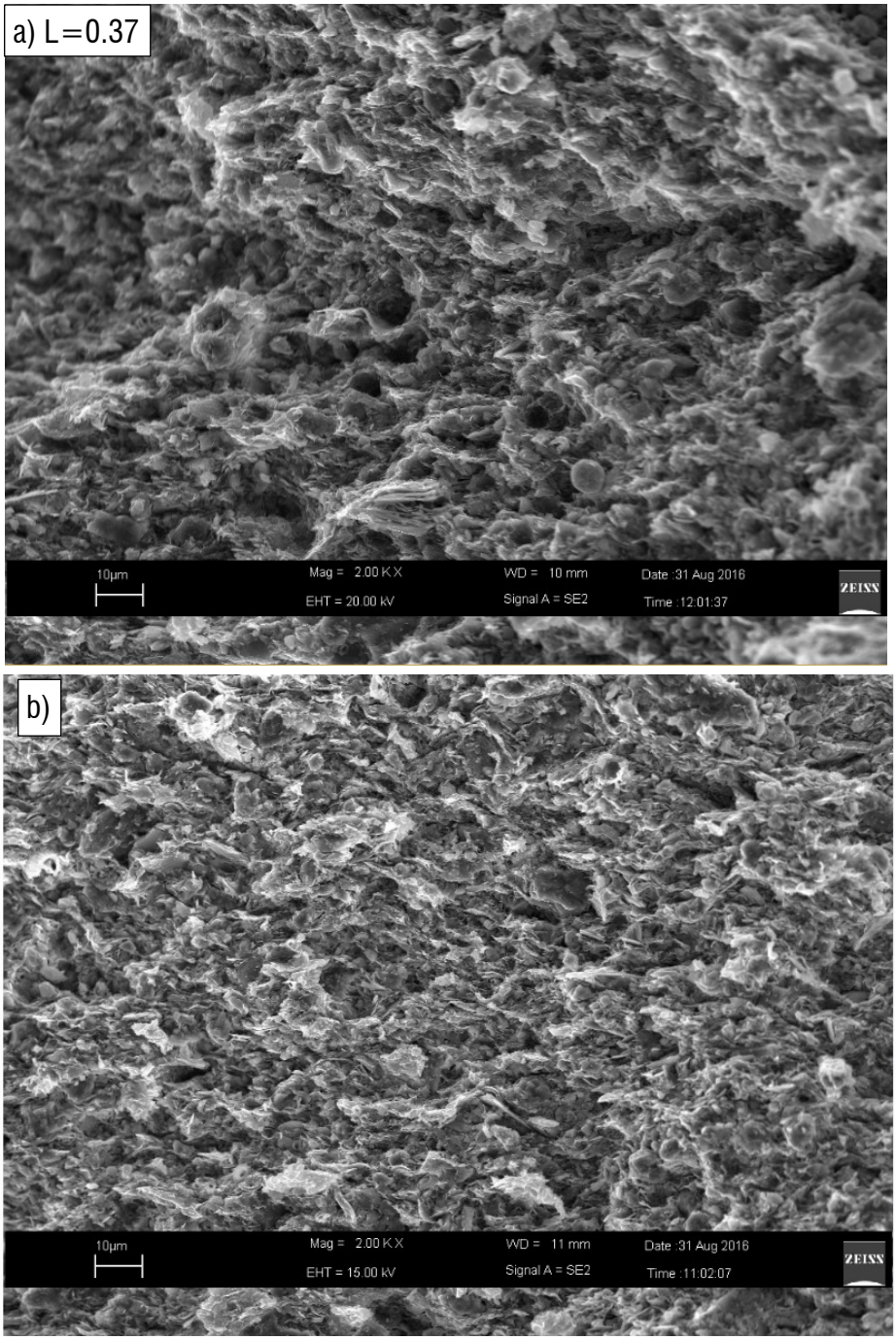

Fig. 7.4 – SEM micrographs along a vertical fracture of undisturbed Pappadai clay at medium magnification.

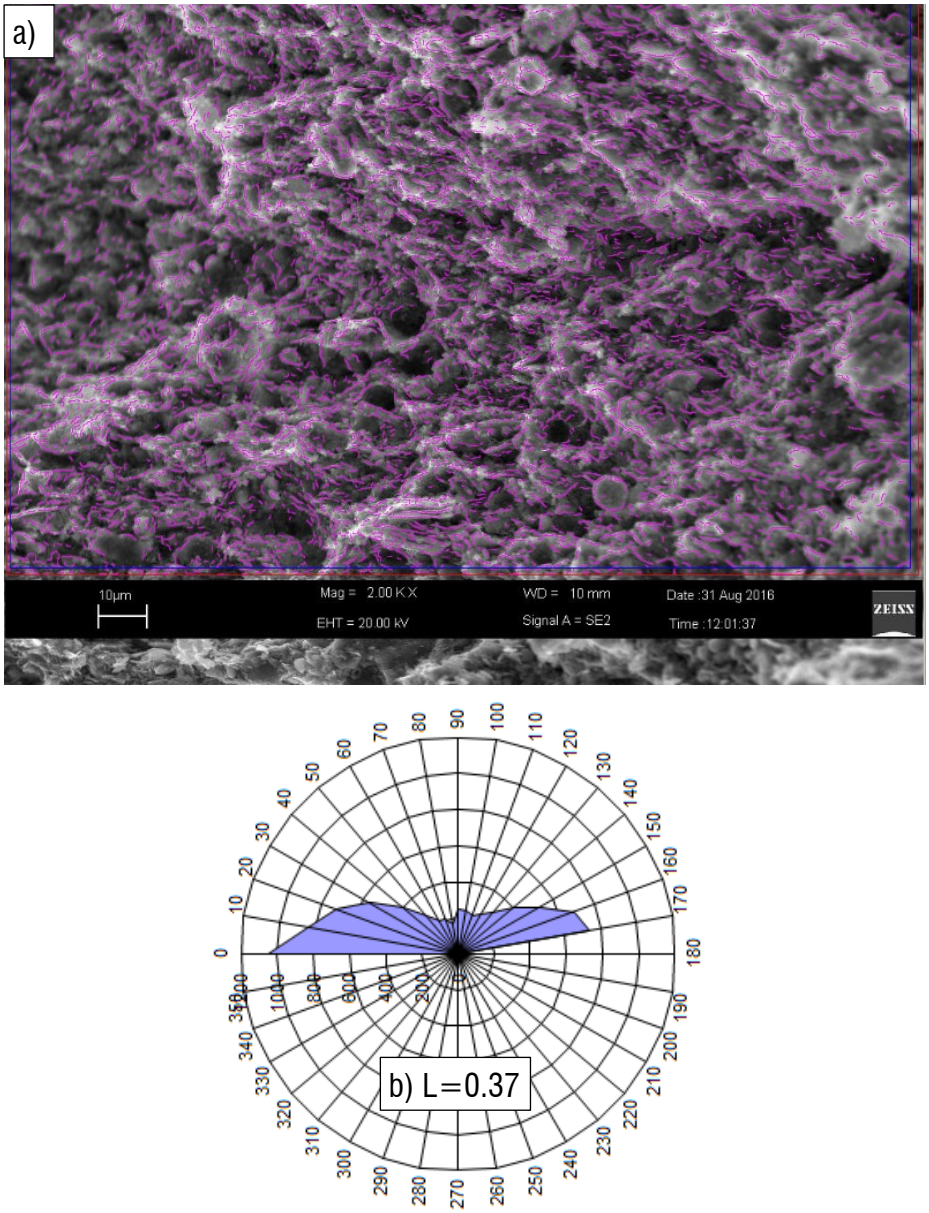

Fig. 7.5 – Image processing of the SEM micrograph in Fig. 7.4a: a) 'thinned' image and b) resulting direction histogram.

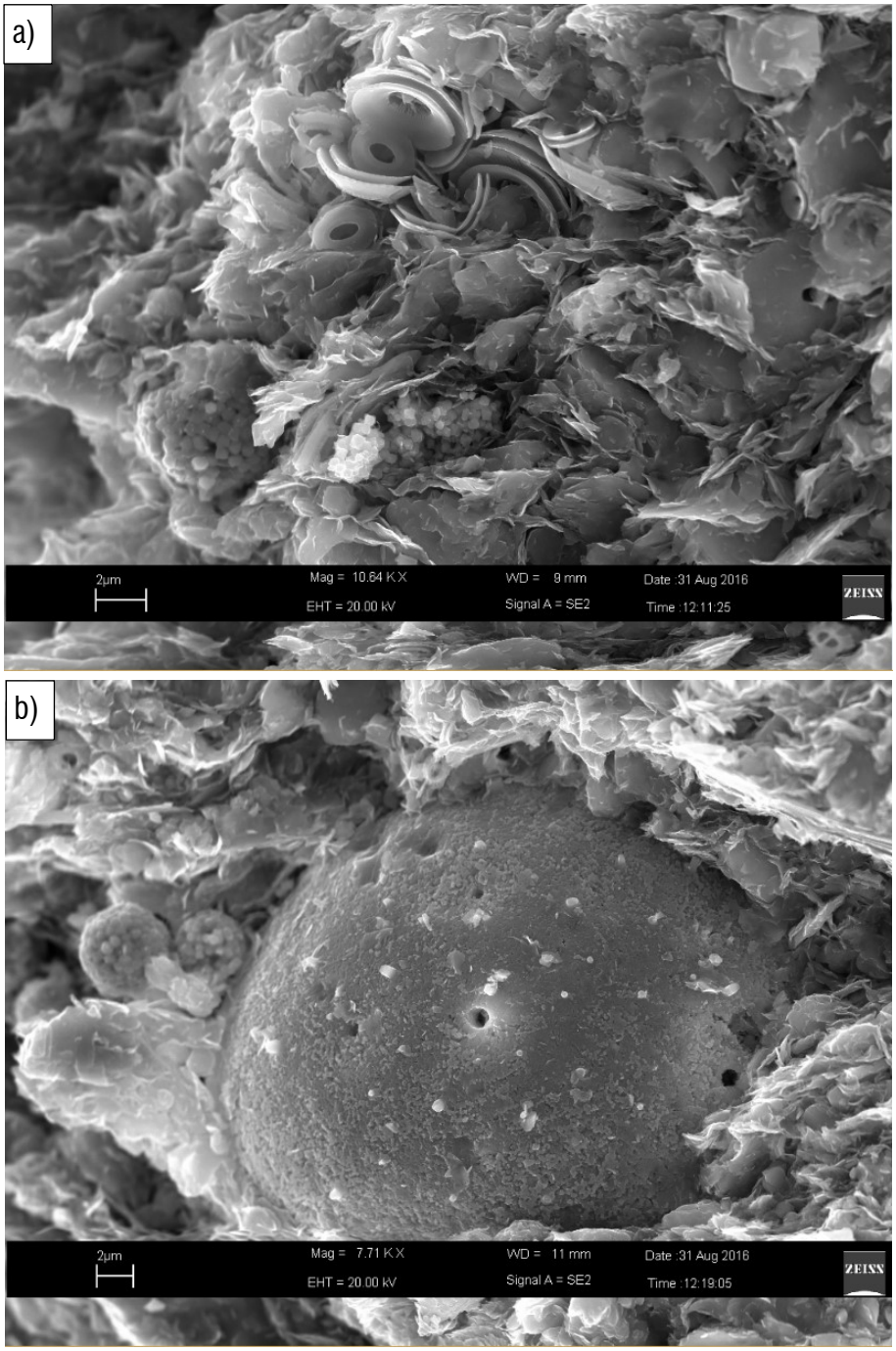

Fig. 7.6 – SEM micrographs along a vertical fracture of undisturbed Pappadai clay. a) Fossil shells and pyrite crystals; b) Foraminifera.

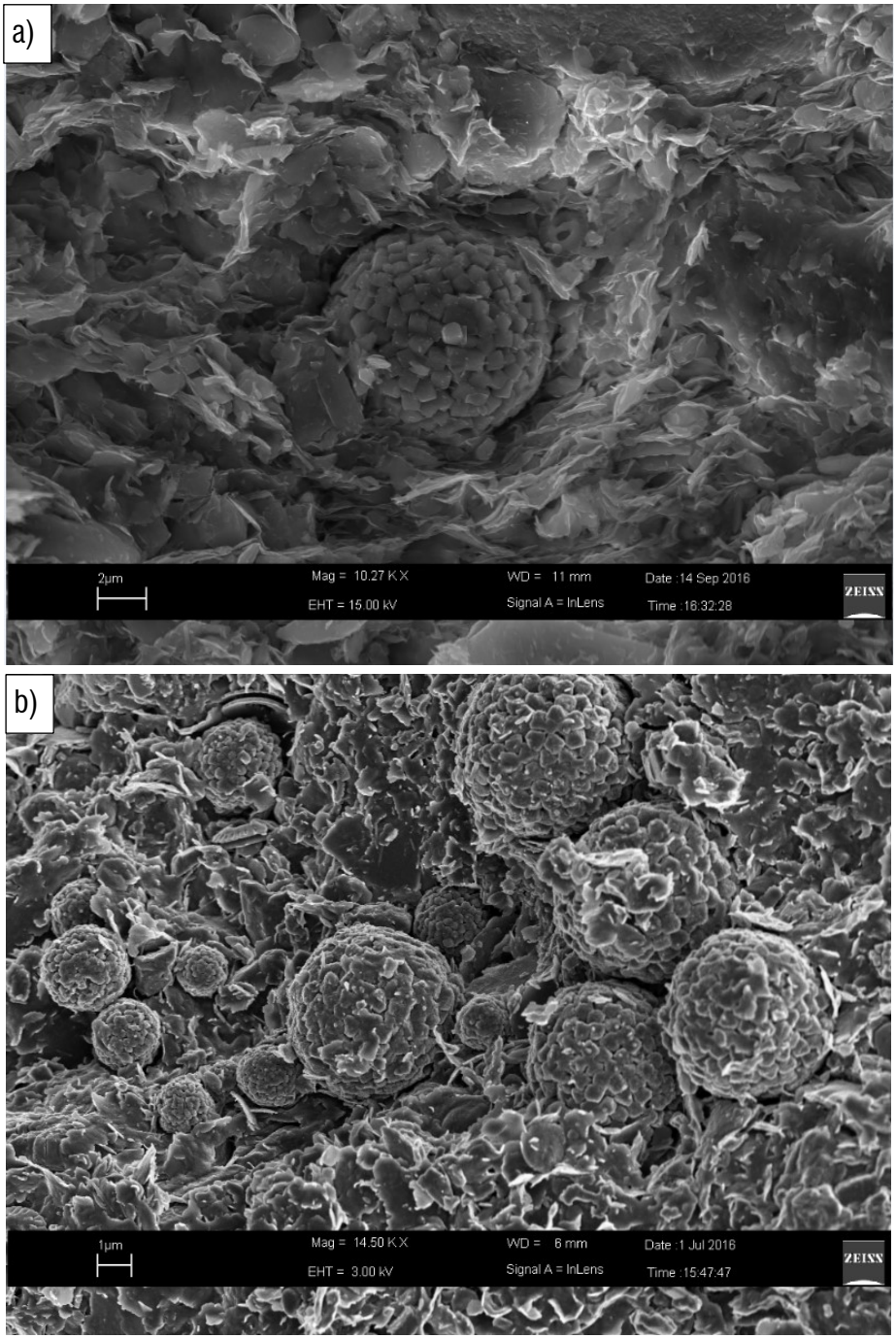

Fig. 7.7 – SEM micrographs along a vertical fracture of undisturbed Pappadai clay: framboid pyrite crystals.

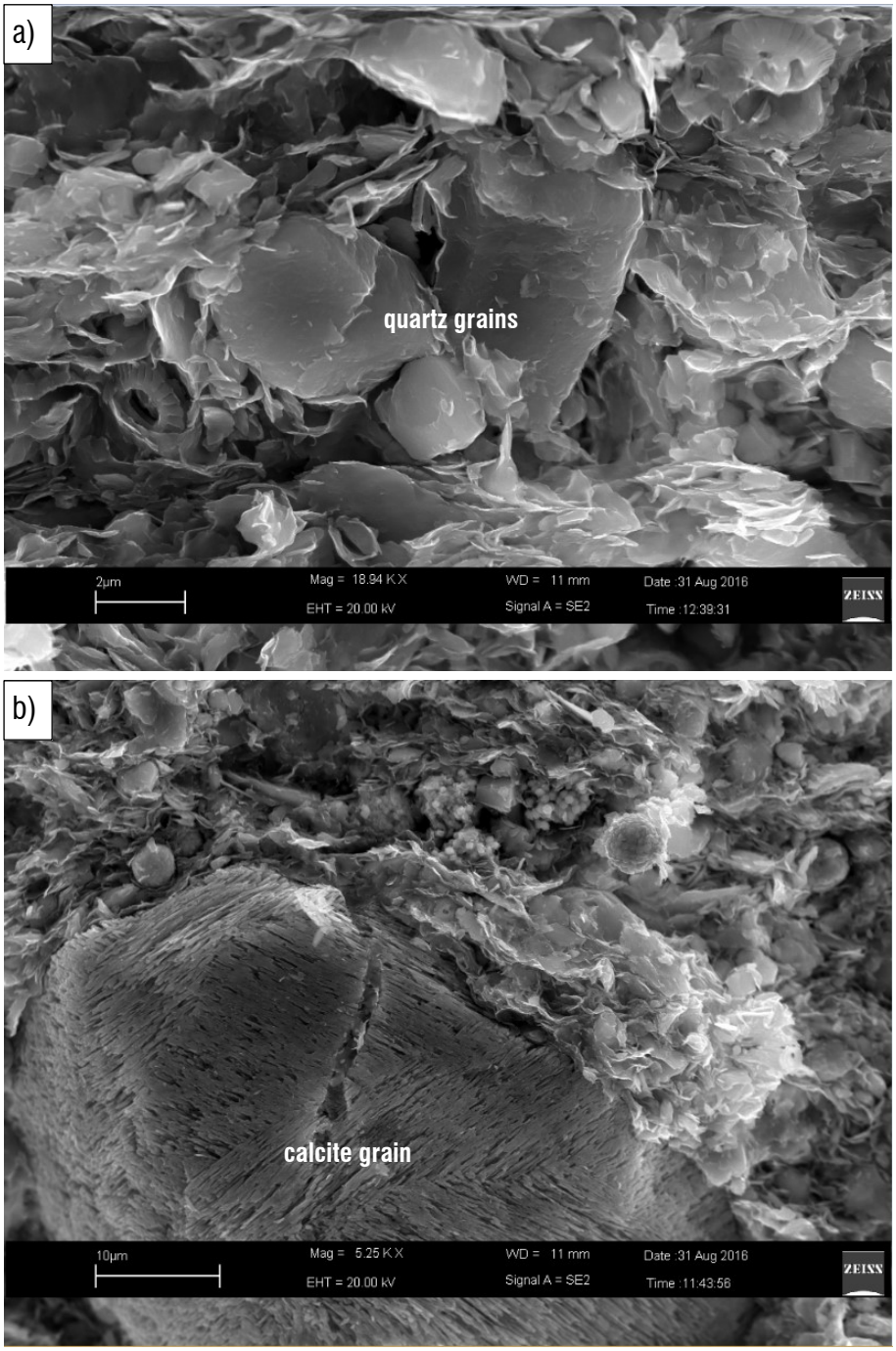

Fig. 7.8 – SEM micrographs along a vertical fracture of undisturbed Pappadai clay: large grains of a) quartz and b) calcite.

On horizontal fractures (Fig. 7.9), particle faces are predominantly seen, supporting the image processing results and confirming that the clay fabric is on average horizontally oriented.

However, the observation of vertical fractures at medium magnification (Fig. 7.3, Fig. 7.4) suggests that there are packed iso-oriented particles forming stacks or "complex laminae" (Sfondrini, 1977) interbedded with zones in which the fabric is more random. To confirm this, higher magnification images were taken by Cotecchia (1996), as those shown in Fig. 7.10, from which the existence of areas of less oriented fabric and confined zones of even chaotic fabric (Fig. 7.10b) can be inferred. The image processing (Fig. 7.11b) reveals in this case a degree of orientation of 0.15, characteristic of a random particle orientation.
Similar photos were taken on the undisturbed specimen from block sample 2 (Fig. 7.12) and show the same fabric feature.
Hence, the clay fabric, which is well packed and well oriented at low magnification (average $L=0.27$), appears at places much less oriented when seen at larger magnification.
Strongly variable particle arrangements can be found adjacent to each other, as flocculated aggregates are interbedded with strata of oriented domains. Stacks of platy particles and domains merge with each other forming large strata (Fig. 7.12b). However, areas where the fabric is chaotic and the particles are mainly in edge-to-face contact are visible.
In Fig. 7.13 a stack of oriented particles is seen to lie above particles in "honeycomb" arrangement. This figure, as others presented, also reveals that the particles are in general in mechanical contact, but does not give any information on the bonding which is known to be present at the contacts.
In the light of the SEM micrographs shown, the hypothesis that crystals, i.e., carbonate crystals, act as bonding between the particles has to be excluded. The SEM shows that a large part of the high calcite content of Pappadai clay is concentrated in fossil shells and detritic crystals. Cotecchia (1996) showed by means of chemical micro-probing

in the SEM, that a carbonate bonding is present in form of a film of amorphous calcite binding the particles and inter-particle contacts of this clay.

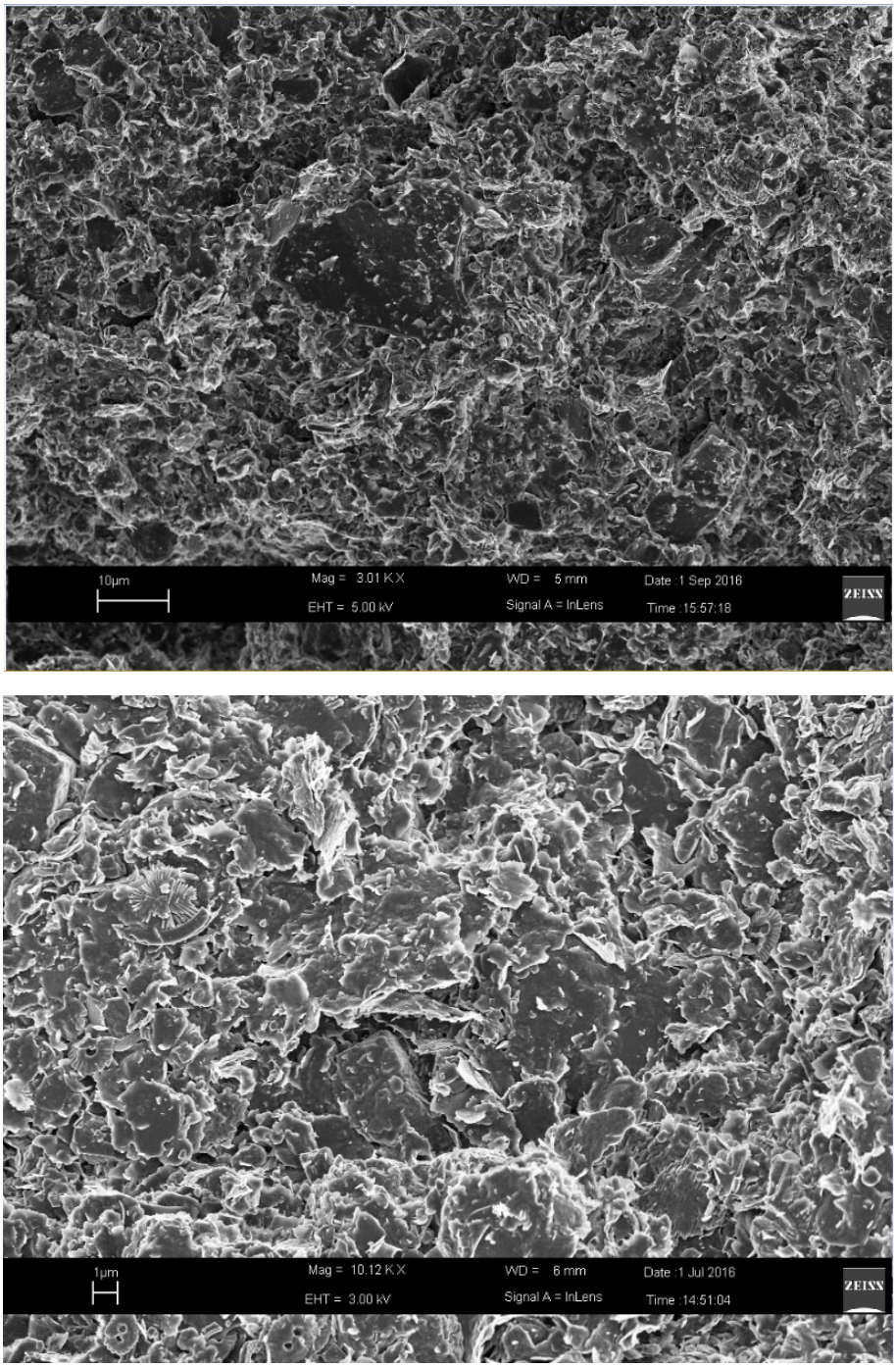

Fig. 7.9 - SEM micrographs along a horizontal fracture of undisturbed Pappadai clay.

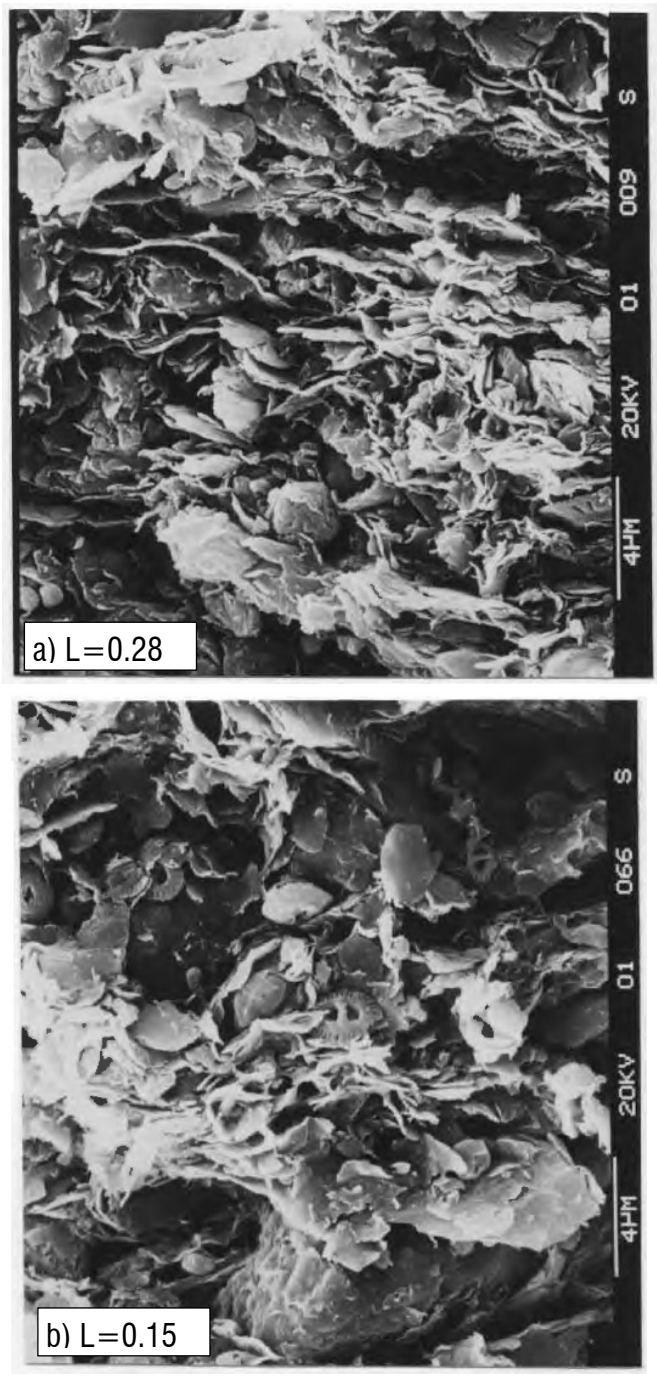

Fig. 7.10 - SEM micrographs along a vertical fracture of undisturbed Pappadai clay at high magnification (after Cotecchia, 1996).

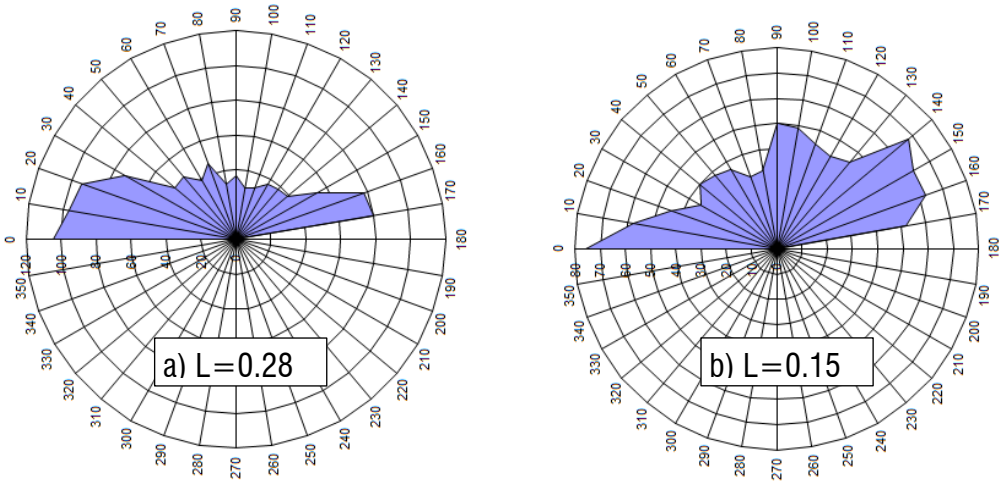

Fig. 7.11 - Direction histograms of the SEM micrographs in Fig. 7.10 on undisturbed Pappadai clay.

In the higher magnifications pictures (e.g., Fig. 7.12, Fig. 7.13), pores between particles and domains can be identified, which have sizes ranging from μm to nm. In some cases, larger pores left by removed fossils or grains are seen, with sizes up to 10-20 μm.

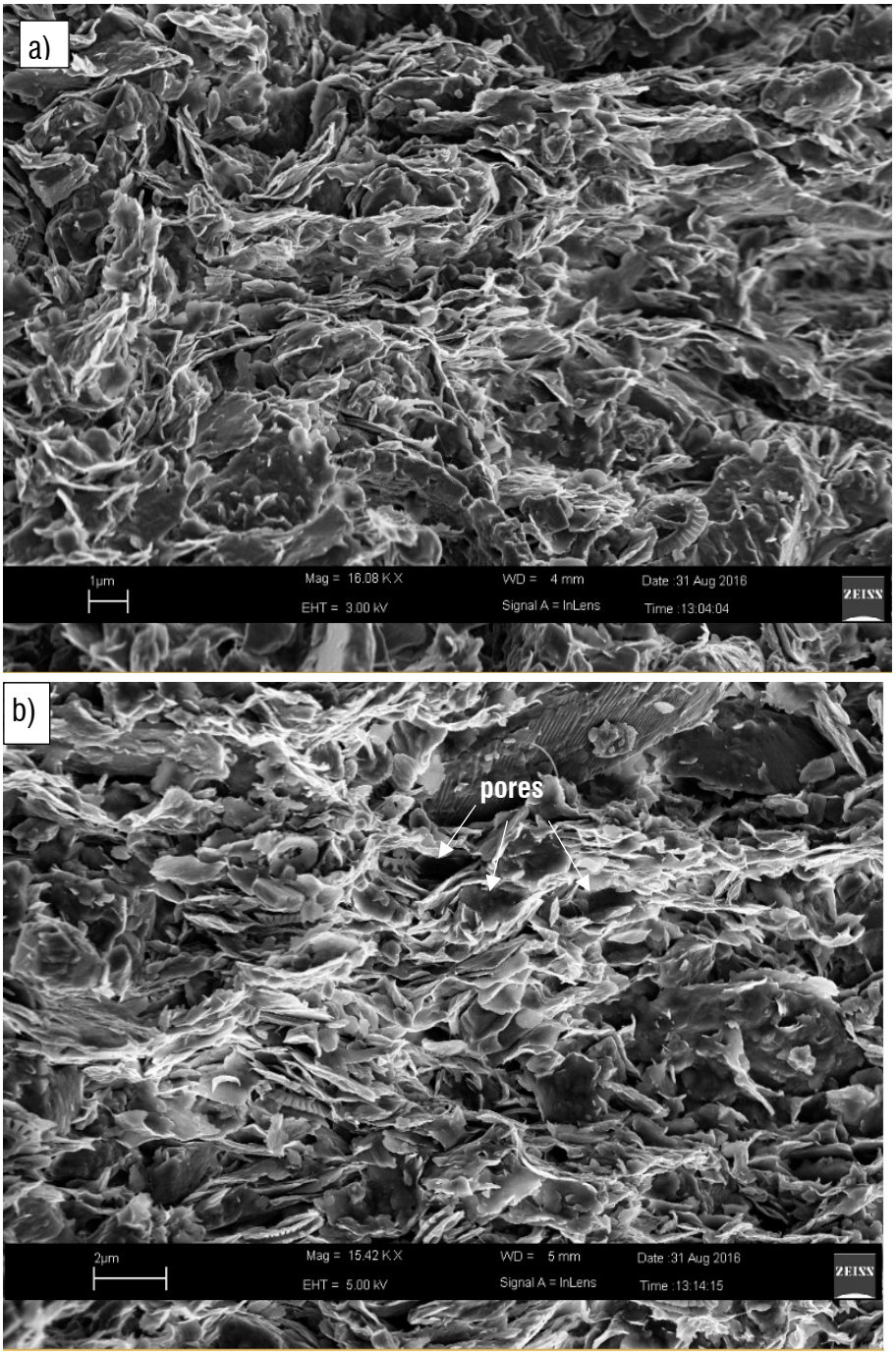

Fig. 7.12 – SEM micrograph along a vertical fracture of undisturbed Pappadai clay at high magnification.

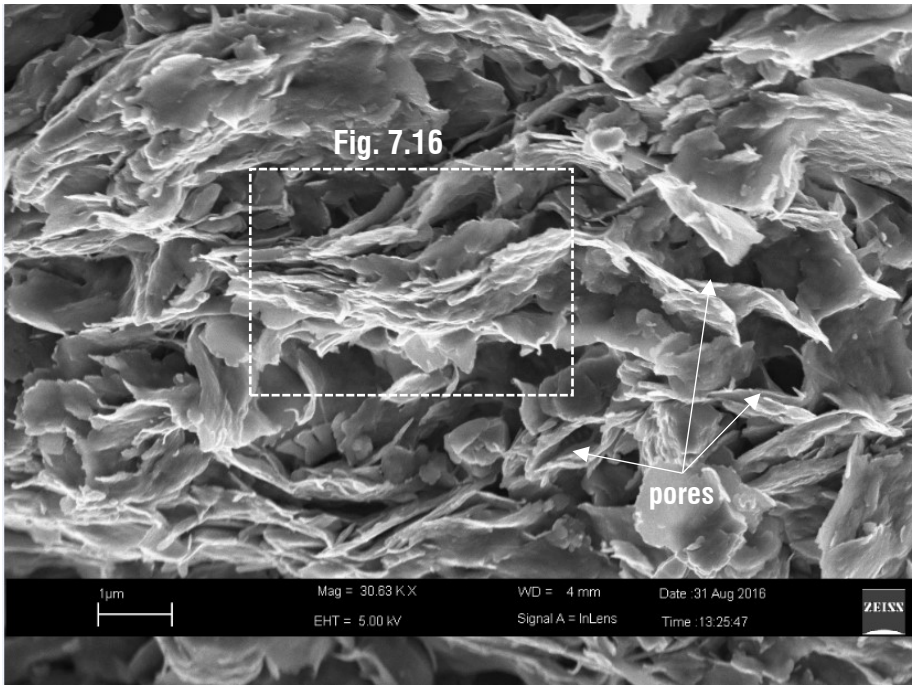

Fig. 7.13 - SEM micrograph along a vertical fracture of undisturbed Pappadai clay at high magnification

The results of MIP on the undisturbed Pappadai clay specimen (block sample 2) are shown in Fig. 7.14 as both cumulative and incremental pore size density functions (PSD). As can be seen in Fig. 7.14a, the volume of mercury intruded in the first stage of the test, that is when the larger "macro" pores (>1 μm) are intruded, is extremely low, then the cumulative curve steeply rises when the smaller "micro" pores are being filled (<1 μm), suggesting that for this specimen they represent the majority of the pore space.

Inheriting a terminology often used in the literature (Chapter 2), the macro-pores will be identified as the inter-aggregate pores and the micro-pores will be assumed to correspond to the intra-aggregate pores. Noticeably, this correspondence is supported by the observation of the SEM micrographs, which show that macro-pores are generally found between aggregates, rather than inside aggregates (e.g., Fig. 7.12, Fig. 7.13).

The PSD of undisturbed Pappadai clay is evidently monomodal (Fig. 7.14b). The abrupt rise in the cumulative intrusion curve corresponds to a sharp peak in the incremental curve, which represents the most frequent pore size, which will be defined “dominant pore size” (abbreviated as DPS). For undisturbed Pappadai clay the DPS is seen to be 220 nm.

A similar markedly monomodal PSD has been observed for other clays in the literature, as for example stiff Boom clay (Lima et al., 2008).

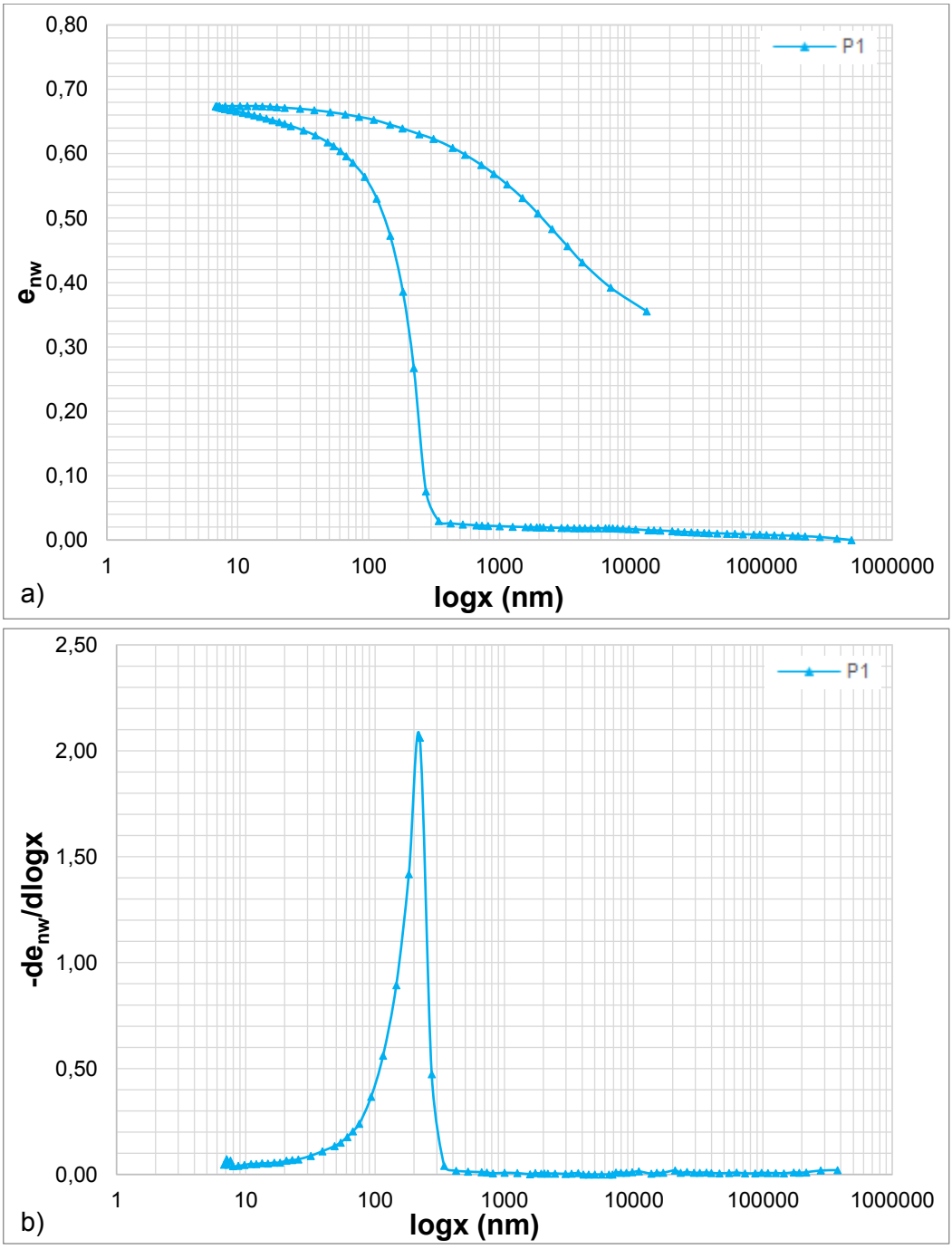

Fig. 7.14 - MIP tests on natural Pappadai clay at undisturbed state (state P_1, e=0.82). a) cumulative and b) derivative curve.

Comparing now the MIP curves in Fig. 7.14 with the SEM images described earlier, the observation can be made that most of the pores observed in the micrographs lie in the range of the macro-porosity. The MIP reveals that the volume occupied by the larger pores represents a very small part of the total pore space in the specimen. Though being small, this volume is detected and appears distributed over a large range of pore diameters (Fig. 7.14a). The variety of sizes of the pores observed in the SEM pictures appears to be in agreement with the measurements.
On the other hand, the recognition of the pores of size equal to the DPS requires the observation of very high magnification pictures, as those shown in Fig. 7.15 and Fig. 7.16. In Fig. 7.15, the pores of size 220 nm are clearly identifiable between particles.
Remarkably, in Fig. 7.16 not only pores of size around 200 nm can be identified, but also smaller pores are seen inside the stack of particles in face-to-face contacts at the centre of the micrograph.
Referring now this observation back to the original lower magnification Fig. 7.13 allows to recognize that the "dominant pores" are found inside the stacks of particles and the densely packed domains.

Referring to the MIP curves, it should be noted that the area subtended by the incremental curve equals the total intruded void ratio, i.e., the total (normalized) pore volume of the specimen. Due to the limitations of MIP examined in Chapter 5, this pore volume does not correspond to the actual specimen pore volume, and in fact the maximum value of e_{nw} in Fig. 7.14a is lightly lower than the void ratio of the specimen.

To conclude the microstructural characterization of the natural Pappadai clay, the interference of bonding with fabric has to be recalled. As outlined in Chapter 6, Pappadai clay has a sensitive bonding, generated in highly calm deposition conditions, which confers higher sensitivity and higher compressibility to Pappadai clay with respect to Lucera clay. This bonding has also been observed to be more disturbed by large swelling paths from undisturbed state, which upon one-dimensional recompression exhibit a light reduction of the gross-yield pressure. In Chapter 8, the difference in

bonding strength observed for the two clays will be seen to reflect also on their different microstructural features.

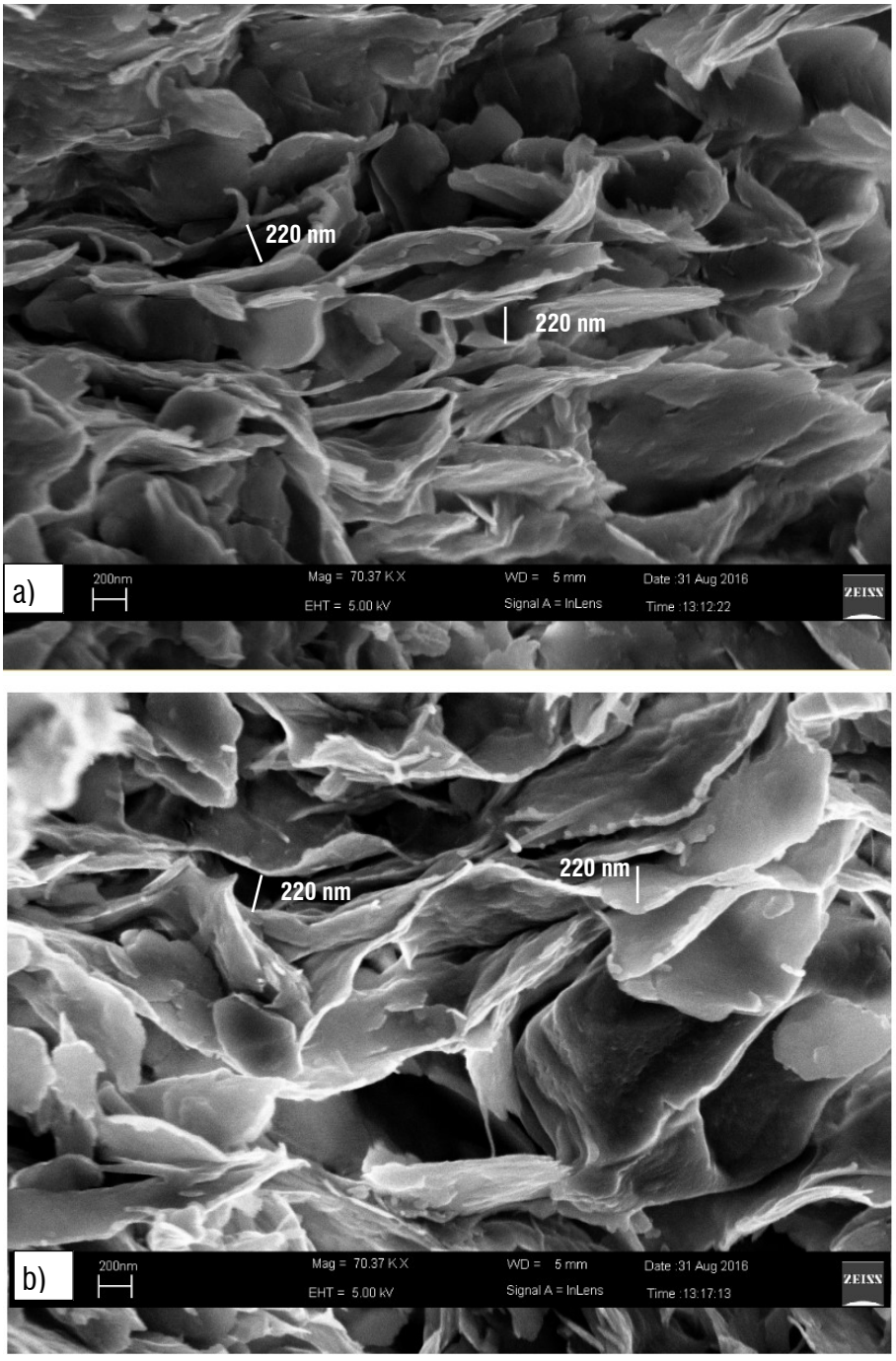

Fig. 7.15 – SEM pictures of undisturbed Pappadai at high magnification: pores having size equal to the DPS can be recognized.

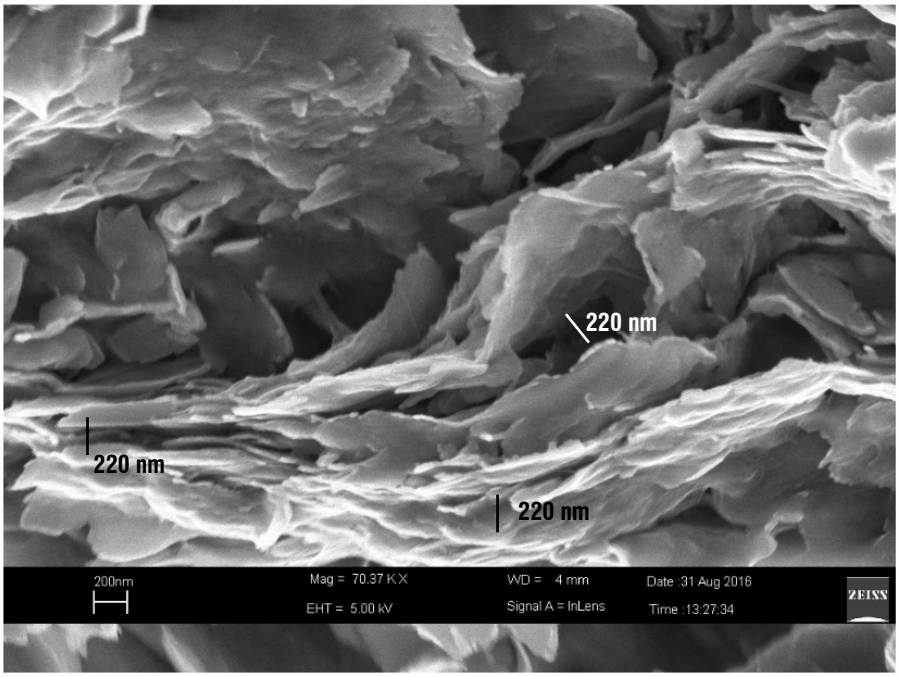

Fig. 7.16 – Enlargement of the micrograph in Fig. 7.13.

The microstructure of undisturbed Lucera clay (also recalled in the following as state L_1) is now analysed. SEM observations carried out by Mitaritonna (2006) on an undisturbed specimen from the first block sampled in 2003 (Table 4.4) will be shown. Due to a failure in the specimen preparation, no FESEM micrographs of the newly sampled undisturbed Lucera clay could be taken. Given the high homogeneity which characterizes the deposit (see Chapter 4) and in the light of the consistent mechanical test results discussed in Chapter 6, the basic features of the clay fabric recognized by Mitaritonna (2006) are believed to describe also the fabric of the more recent undisturbed sample. To further confirm this, the interpretation of the SEM pictures will be compared to the results of the MIP test performed on the undisturbed clay. However, the SEM investigation of the undisturbed clay will be carried out soon, in a continuation of the research.

A general view of the fabric on a quasi-vertical fracture at low magnification (Fig. 7.17) shows the presence of densely packed strata which interbed areas of open fabric including sub-vertical domains. Horizontal complex laminae are systematically interbedded within strata formed by a truss of domains in edge to face contact. The degree of fabric orientation (Fig.7.18), L=0.22, shows that the fabric is about well oriented at this magnification. At a lightly higher magnification (Fig. 7.19a), a similar degree of orientation is obtained. The fabric is thus on average well-oriented, although less oriented than undisturbed Pappadai clay (average L=0.27). Micrographs at medium-low magnification (Fig. 7.19) emphasize the observation that, although being on average well-oriented, the fabric of undisturbed Lucera has more features of "bookhouse" type with respect to Pappadai, resulting in a lower average orientation degree. Flocculated aggregates are diffusely found to alternate with strata of oriented domains, causing a great variability in particle arrangements (Fig. 7.20). Areas where the fabric is chaotic and where the particles are mainly in edge to face or in edge to edge contact are shown in Fig. 7.21.

On a horizontal fracture, shown in Fig. 7.22, the track of an emerging plane in the centre of the picture distinguishes two zones: "zone a" in the right part of the micrograph predominantly shows particle faces, suggesting that part of the clay fabric is oriented; the left-sided "zone b" displays a random fabric. Both small and large domains can be observed. In "zone a" most of the clay particles form domains which are in face to face contact, while in "zone b", strata bending towards sub-vertical directions are seen. Both domains in edge to face and in edge to edge contact may be identified at the bottom of Fig. 7.22.

Hence, the fabric of undisturbed Lucera clay, which appears well packed and on average rather oriented at low magnification, is far less well oriented when seen at larger magnification, similarly to the fabric observed for Pappadai clay but with a lower average degree of orientation. Explanations for this will be discussed in Chapter 8.

Mitaritonna (2006) discussed that the anisotropic stiffness ratio G_{hh}/G_{hv} for undisturbed Lucera clay is ≈ 1 despite the quite significant orientation of the fabric.
Not even in this case the SEM pictures reveal the nature of the bonding between the particles and it might be that this bonding is very homogeneous and gives rise to a degree of elastic shear stiffness isotropy.

Similarly to undisturbed Pappadai clay, fossil shells, globigerinae and detritic crystals are interbedded within the clay particles, as observed by Mitaritonna (2006) and shown in Fig. 7.23. Many fossils have been recently observed also in other specimens of natural Lucera clay (Fig. 7.24). The presence of fossils and crystals changes the surrounding particle arrangements, but it does not affect the general orientation of the clay fabric.

The observation of the undisturbed fabrics of both Pappadai and Lucera clay suggests that these fabrics are the result of the one-dimensional consolidation of a primary bookhouse fabric formed at deposition, under the different deposition conditions discussed in Chapter 4. In Chapter 8 it will be focused the effect of the differences in composition of the two clays on their microfabrics. Indeed, both the edge to face contacts between the domains, as well as the local random fabric, may be considered to be relics of a flocculated fabric formed at deposition.
Both the clay fabrics appear to confirm the scheme proposed by Sfondrini (1977) of the fabric evolution during one-dimensional compression of a flocculated fabric. In fact, as proposed by Sfondrini, during geological history and 1D compression in situ Pappadai clay and Lucera clay appear to have undergone a general reorientation of particles forming the original flocculated fabric, but some zones of the clay experienced more strain than others, so that in some areas packed iso-oriented particles form complex laminae, while in other areas open random fabric is preserved.

This fabric type is recognized also in reconstituted Pappadai and Lucera clays, as is be shown in the following.

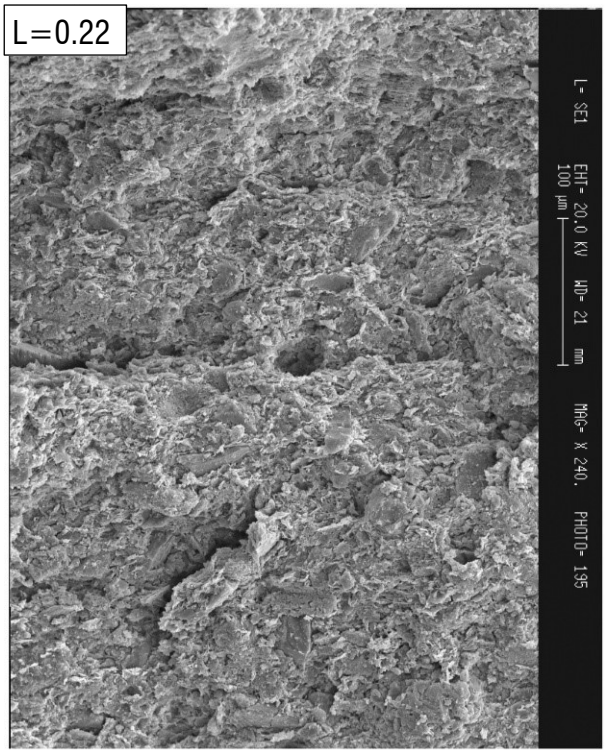

Fig. 7.17 – SEM micrograph of undisturbed Lucera clay along a vertical fracture at low magnification (after Mitaritonna, 2006 on block sample 1).

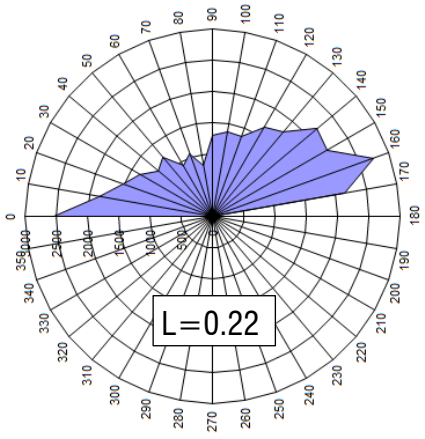

Fig. 7.18 – Direction histogram of the micrograph shown in Fig. 7.17 of undisturbed Lucera clay.

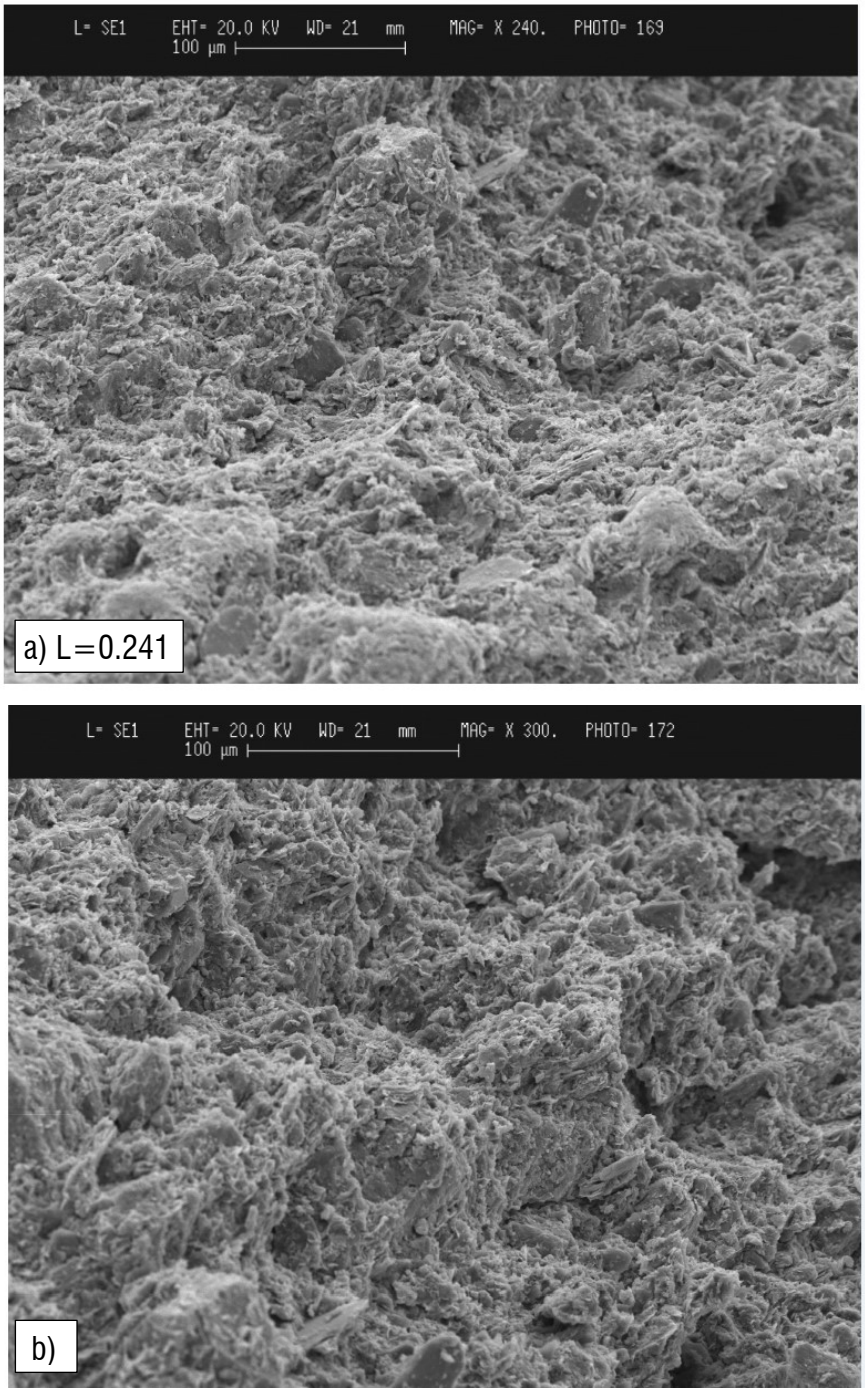

Fig. 7.19 - SEM micrographs along a vertical fracture of undisturbed Lucera clay at medium-low magnification (after Mitaritonna, 2006 on block sample 1).

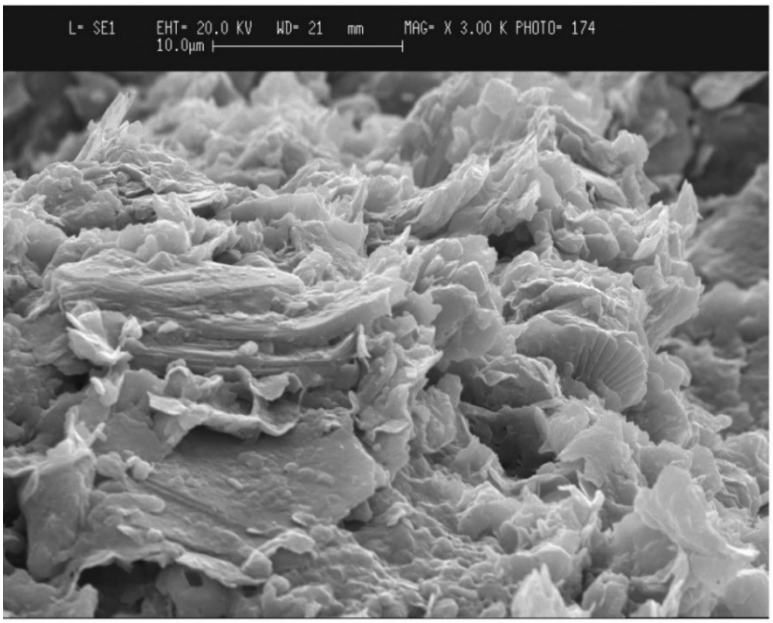

Fig. 7.20 - SEM of undisturbed Lucera clay along a vertical fracture at high magnification (after Mitaritonna, 2006 on block sample 1).

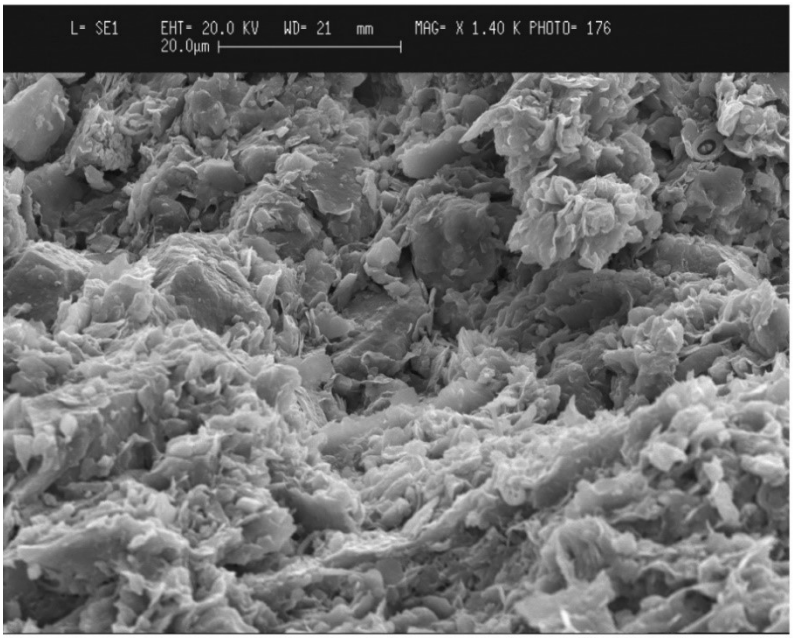

Fig. 7.21 - SEM of undisturbed Lucera clay along a vertical fracture at medium magnification: areas of chaotic fabric with particles mainly in edge-to-face contact (after Mitaritonna, 2006 on block sample 1).

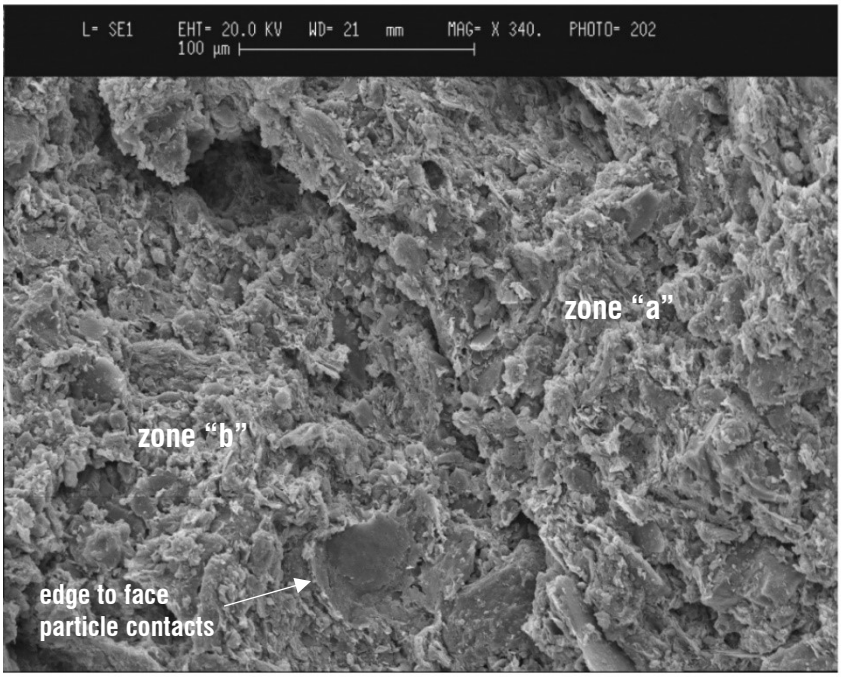

Fig. 7.22 - SEM micrograph of undisturbed Lucera clay along a horizontal fracture (after Mitaritonna, 2006 on block sample 1).

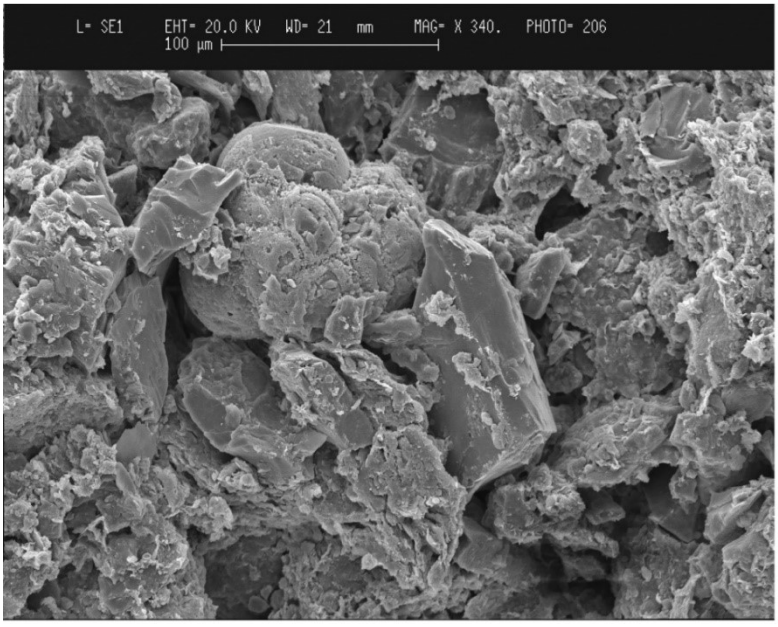

Fig. 7.23 – SEM micrograph of undisturbed Lucera clay: detail of Globigerinae (after Mitaritonna, 2006 on block sample 1).

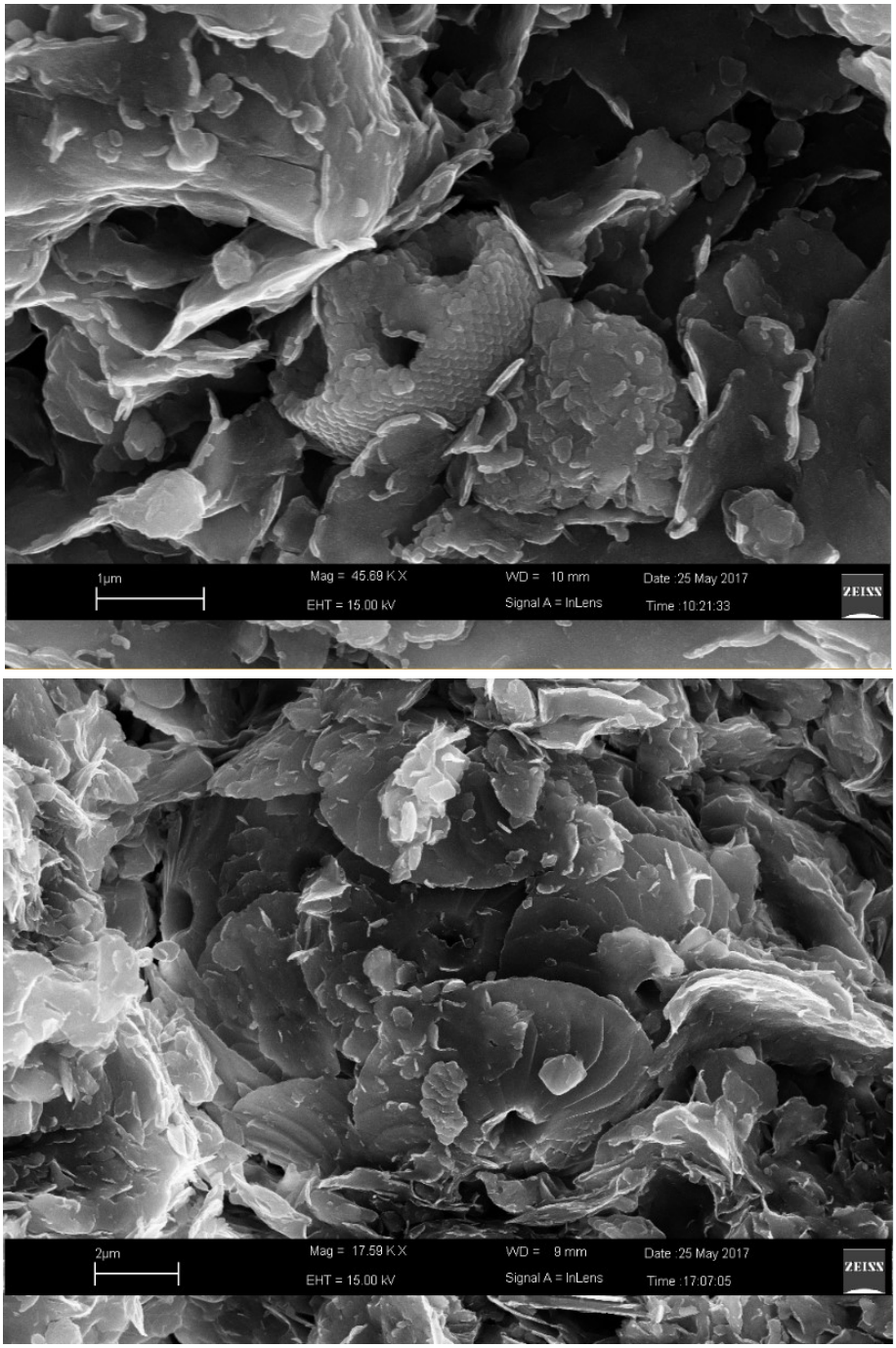

Fig. 7.24 – Fossils in natural Lucera clay.

The distribution of pores within the undisturbed specimen of Lucera clay is shown in Fig. 7.25. The derivative curve also in this case is seen to increase with a slow rate at larger void sizes and then rapidly rise, showing that the pore volume corresponding to the inter-aggregate pores is much smaller than that constituting the micro- or intra-aggregate porosity. This macro-porosity, although being small, is uniformly distributed over a wide range of void sizes ≥ 1 μm (Fig. 7.25a). The incremental curve is monomodal, with an average DPS of 300 nm.

It should be noted that both the derivative and incremental curves of undisturbed Lucera and Pappadai clay have similar shapes. Mono-modality is a common character to the two stiff overconsolidated clays, which however have different DPS, of 220 nm for Pappadai clay and averagely 300 nm for Lucera clay. The frequency of the DPS, i.e., the y-coordinate of the peak value, is much lower for Lucera clay than for Pappadai, because the two clays have different void ratios. Lucera clay specimen has a lower e (0.55) and a larger DPS, which necessarily correspond to a lower frequency at the DPS.

As for Pappadai clay, also for Lucera clay the matching of the MIP results with the SEM pictures reveals that most of the pores seen in the medium and low magnification micrographs is included in the macro-pore volume, which is the smaller part of the total pore space. Being uniformly distributed, this macro-porosity covers a wide range of pore sizes, as confirmed by the SEM images.
Indeed, the dominant pores must be looked for inside the densely packed particles aggregations and stacks.

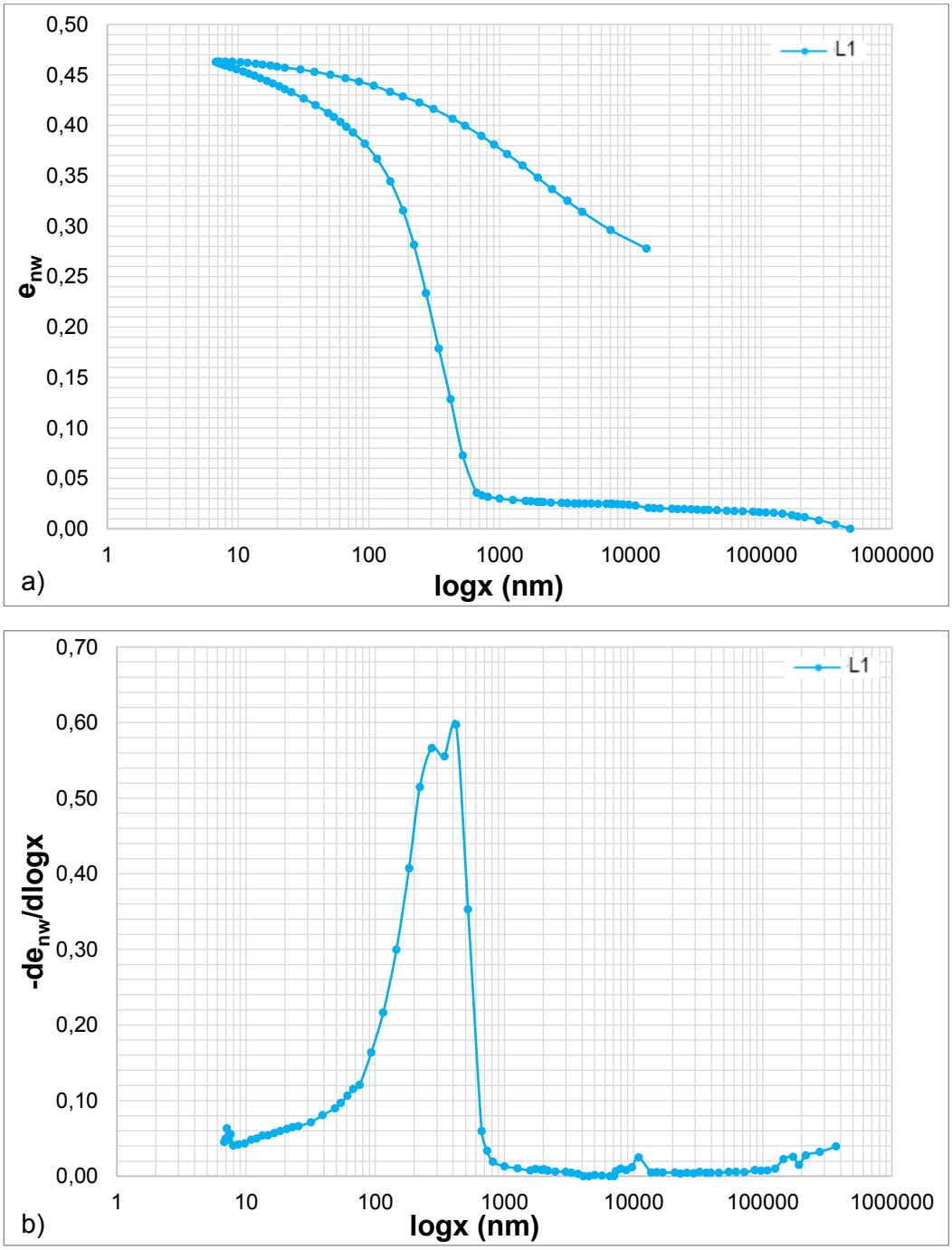

Fig. 7.25 - MIP test on undisturbed Lucera clay (state L_1, e=0.55): a) cumulative and b) derivative curves.

7.2.2 Microstructure of the reconstituted clay after consolidation in the consolidometer

The microstructure of the reconstituted Pappadai clay, one-dimensionally consolidated to σ'_v equal to 200 kPa (state PR), is examined first. The SEM pictures collected by Cotecchia (1996) will be shown, on which image processing has been carried out. Then, the results of a MIP test on a specimen of the recently reconstituted and consolidated Pappadai clay (batch P, Table 5.5) will be shown. The specimen consolidated by Cotecchia has a void ratio of 1.24, which is very close to that analysed by means of MIP (e=1.245).

Fig. 7.26 shows a vertical fracture through the clay. In the top half of the picture the fabric seems oriented since sub-horizontal strata formed by particle edges can be seen. In the lower part of the picture, the fabric is less oriented. Here, both sand grains and clasts of sand-size particles are present and the fabric appears affected by these constituents, as the clay particles cover the sand grains and the surrounding fabric follows their perimeter.

At medium magnification (Fig. 7.27), the reconstituted fabric appears less densely packed than the undisturbed clay fabric, as a consequence of the differences in both vertical pressure and void ratio for the two clays. The open fissure between two sub-horizontal particle domains in the upper part of the image is due to rapid unloading in the consolidometer following compression. Some other fissures are sometimes seen and all develop either at the contact between faces of parallel domains, or at the contact between clay domains and sand grains. Image processing of Fig. 7.27 (Fig. 7.28) reveals a medium-high degree of orientation, similar to that recorded for the undisturbed clay, with particles almost oriented along the horizontal and sub-horizontal directions. Sub-horizontal factures (Fig. 7.29) confirm this result, showing mostly particle faces.

Thin layers formed of well oriented domains are interbedded with large zones of open random fabric (Fig. 7.30), in which differences may exist between the flocculation

modes. The results of image processing (Fig. 7.31) in areas of random fabric confirms the qualitative interpretation, giving low degrees of orientation.
This shows that also in the reconstituted clay, one-dimensional consolidation to a medium pressure, such as σ'_v=200kPa, gives rise to non-uniform fabric changes. Hence, the fabric evolution during one-dimensional consolidation proposed by Sfondrini (1977) seems to apply to both the natural and the reconstituted Pappadai clay.

Although the one-dimensional consolidation of the clay induces a non-uniform fabric, it does induce a progressive increase of the average orientation of the clay particles, as shown by the quite high degrees of orientation seen at medium magnification for both the natural and the reconstituted clay (average L=0.27 for both). The areas of random fabric are more extensive in the reconstituted clay than in the undisturbed one; this is in agreement with the lower compression of the reconstituted clay with respect to the natural one. However, although the undisturbed clay is in general more densely packed than the reconstituted clay, in some areas its fabric is as open as in the reconstituted clay. Indeed, in some zones, the undisturbed fabric is even more chaotic than for the reconstituted clay fabric and, in general, it is more complex, as processes have occurred in the natural clay which do not take place in the reconstituted clay in the laboratory, diagenesis being one of these.

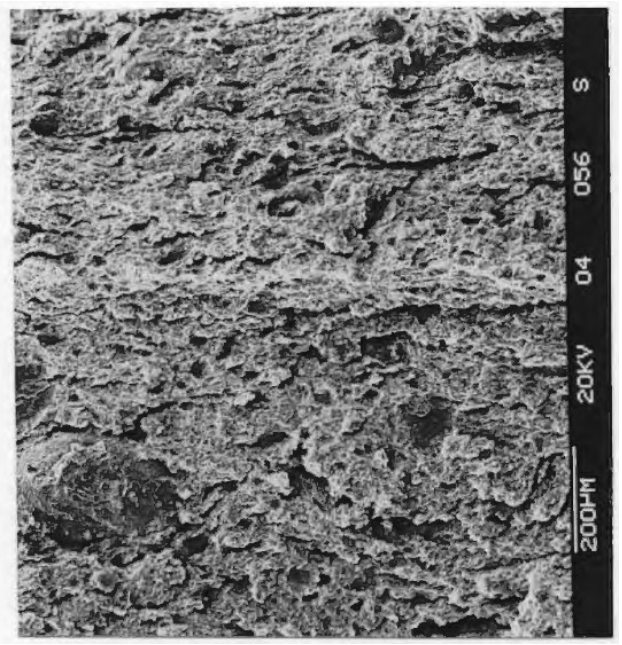

Fig. 7.26 – SEM of reconstituted Pappadai Clay: global view of the fabric on a vertical fracture (after Cotecchia, 1996).

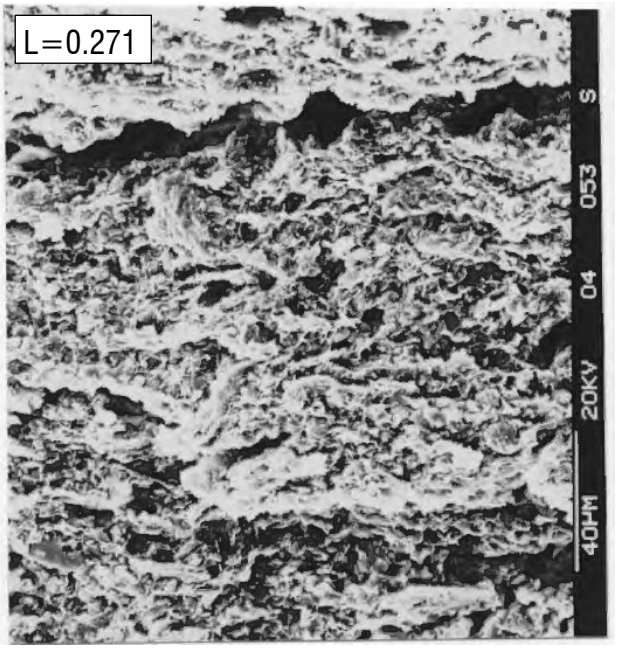

Fig. 7.27 - SEM of reconstituted Pappadai Clay on a vertical fracture at medium magnification (after Cotecchia, 1996).

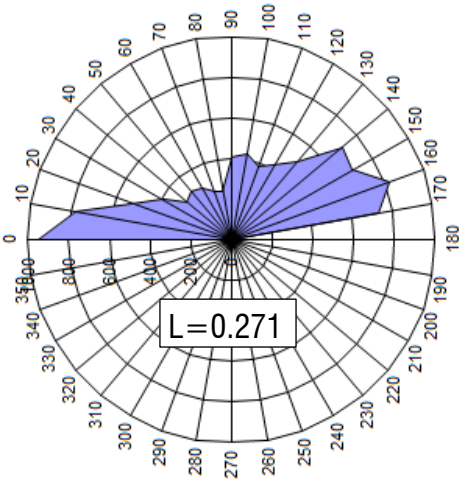

Fig. 7.28 – Direction histogram of the SEM micrograph in Fig. 7.27.

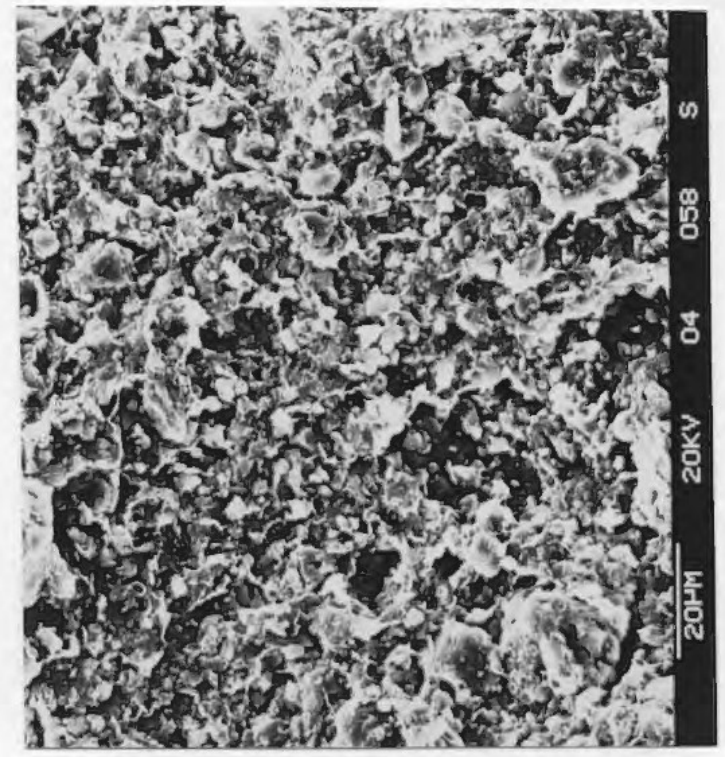

Fig. 7.29 – SEM of reconstituted Pappadai Clay on a sub-horizontal fracture at medium magnification (after Cotecchia, 1996).

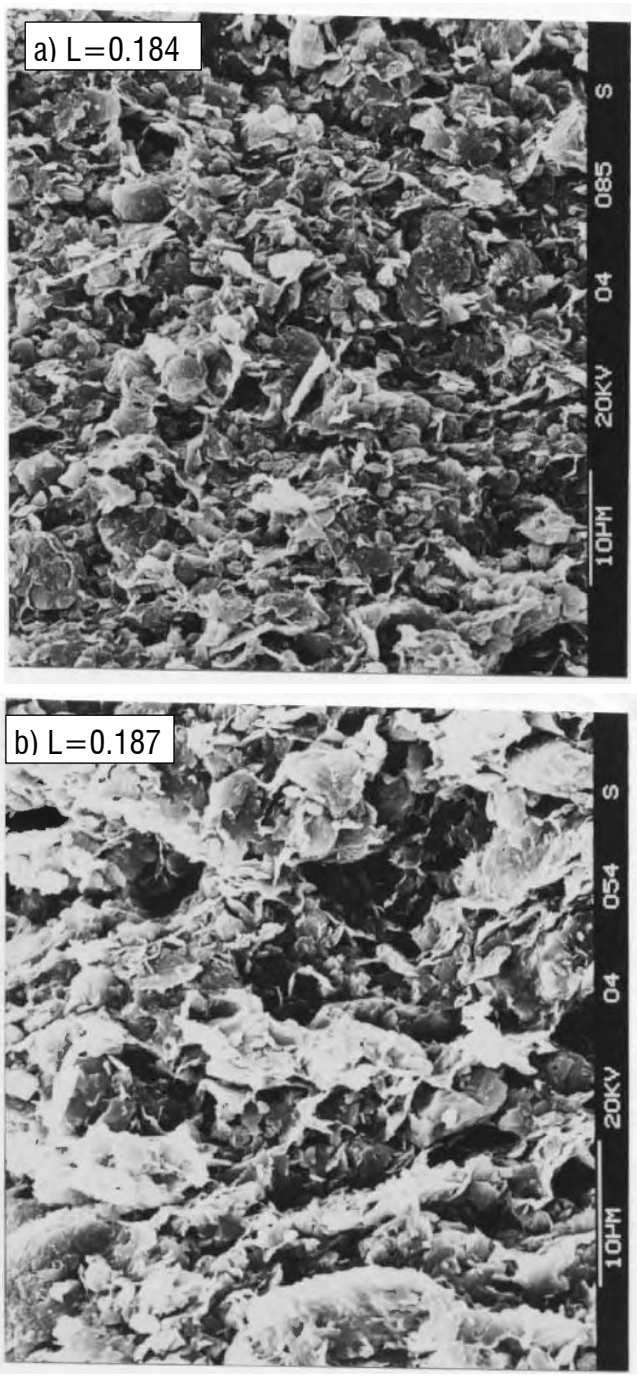

Fig. 7.30 - SEM of reconstituted Pappadai Clay on a vertical fracture at medium magnification (after Cotecchia, 1996).

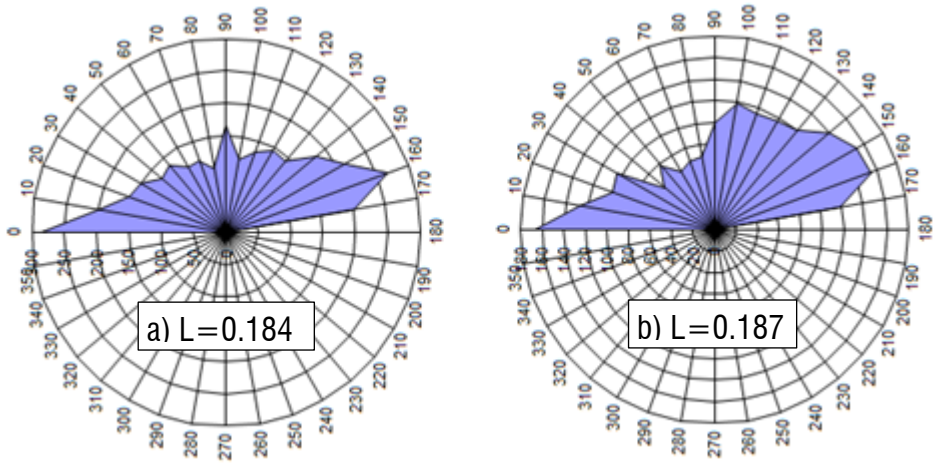

Fig. 7.31 – Direction histograms of the SEM micrographs in Fig. 7.30

The MIP test results for reconstituted Pappadai clay are shown Fig. 7.32, as either cumulative or derivative curve. The step seen in the cumulative curve between 30 and 40 μm is likely to be attributed to the presence of a fissure (as that seen in Fig. 7.27), or a macrovoid due to the previous presence of a sand grain, intruded by mercury in the MIP test. Similarly, the small peaks appearing in the derivative curve at large entrance diameters are presumably related to fissures.

The incremental curve is monomodal, with the DPS at 420 nm, which is about twice the DPS found for the undisturbed clay, but still within the same order of magnitude. So, also for the reconstituted clay, the more frequent pore dimension must be looked for inside the denser particle aggregates. The shape of the incremental curve is less tapered than that of the undisturbed clay, but keeps having a quite high frequency at the DPS.

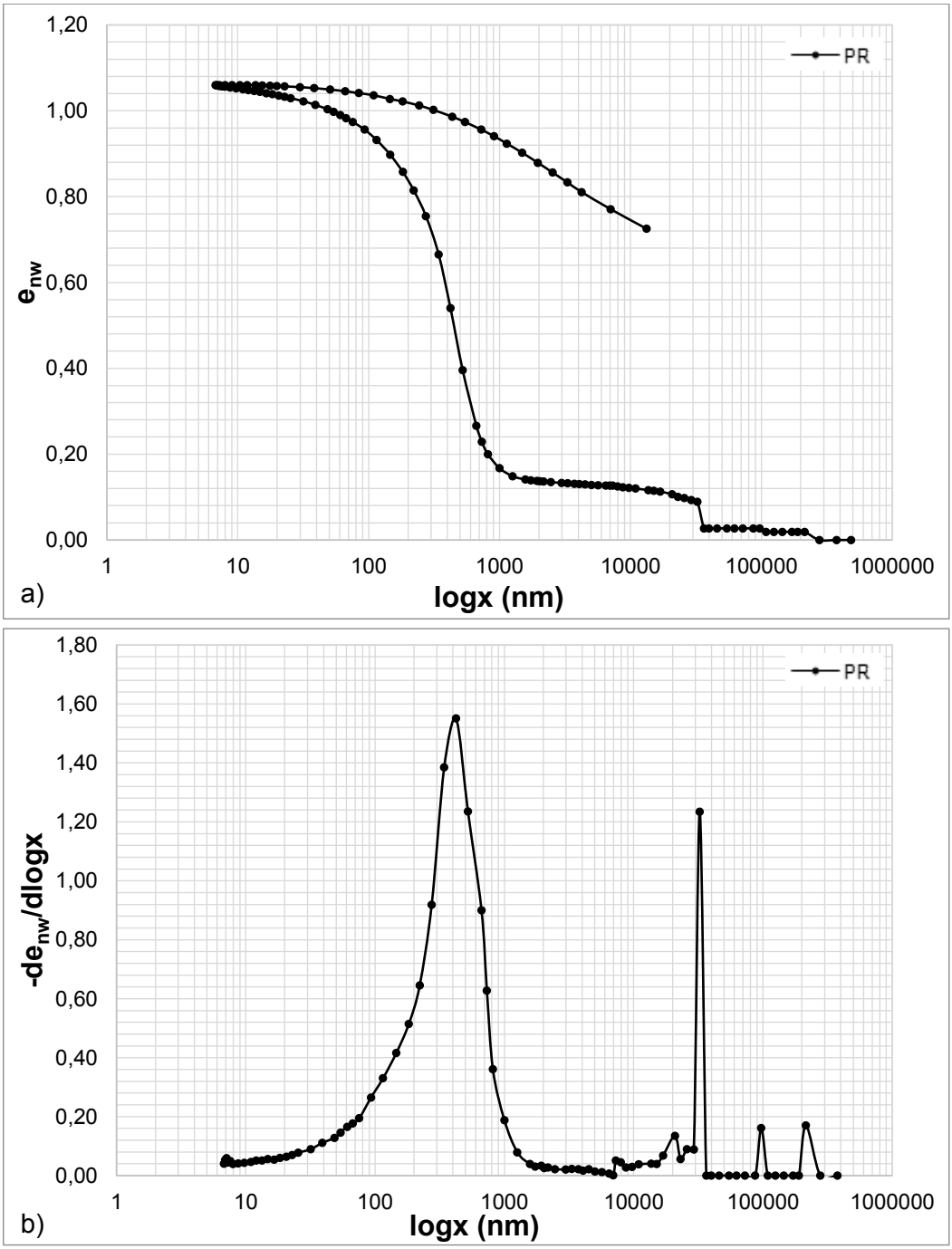

Fig. 7.32 - MIP test on reconstituted Pappadai clay (state PR, e=1.245): a) cumulative and b) derivative curves.

Specimens of reconstituted Lucera clay from batch L1 (Table 5.5) consolidated from slurry to σ'_v=100 kPa (state LR), as discussed in Section 5.4.1, were analysed with both FESEM observations and MIP tests.

A view of the fabric at medium magnification on a vertical fracture is provided by Fig. 7.33. The fabric appears significantly more open and less densely packed than that of the natural clay, a consequence of the much higher void ratio (e=0.92) and of the lower vertical pressure experienced by the reconstituted clay. In Fig. 7.33a, thin stacks of particles are seen to lie in both sub-horizontal and sub-vertical directions, interbedding large areas of more open and flocculated fabric. Overall, the fabric appears even less oriented than that of reconstituted Pappadai clay.
The results of image processing on the micrograph in Fig. 7.33a, shown in Fig. 7.34, confirm the qualitative observation, giving a degree of orientation of 0.192, representative of a low oriented fabric.
Higher magnification pictures (Fig. 7.35 and 7.36) show that the systematic succession of horizontal stacks of domains and strata formed by a truss of domains, recognized in the undisturbed clay, is no longer diffusely recognizable and many features of a typical "book-house" fabric are traceable in the images. Zones of pronounced random fabric with low orientation degree (Fig. 7.35, Fig. 7.36a) are found very close to more oriented particle layers (Fig. 7.36b).
In both cases, the direction histograms (Fig. 7.37) show that several particles are oriented along sub-horizontal and sub-vertical directions, covering the wide range 110°-170° with similar percentages.

Fossil shells can still be recognized (Fig. 7.38), although not as frequently as in the undisturbed clay. Similarly, foraminifera shells and detritic crystal were found at places in reconstituted Pappadai clay (Cotecchia, 1996).

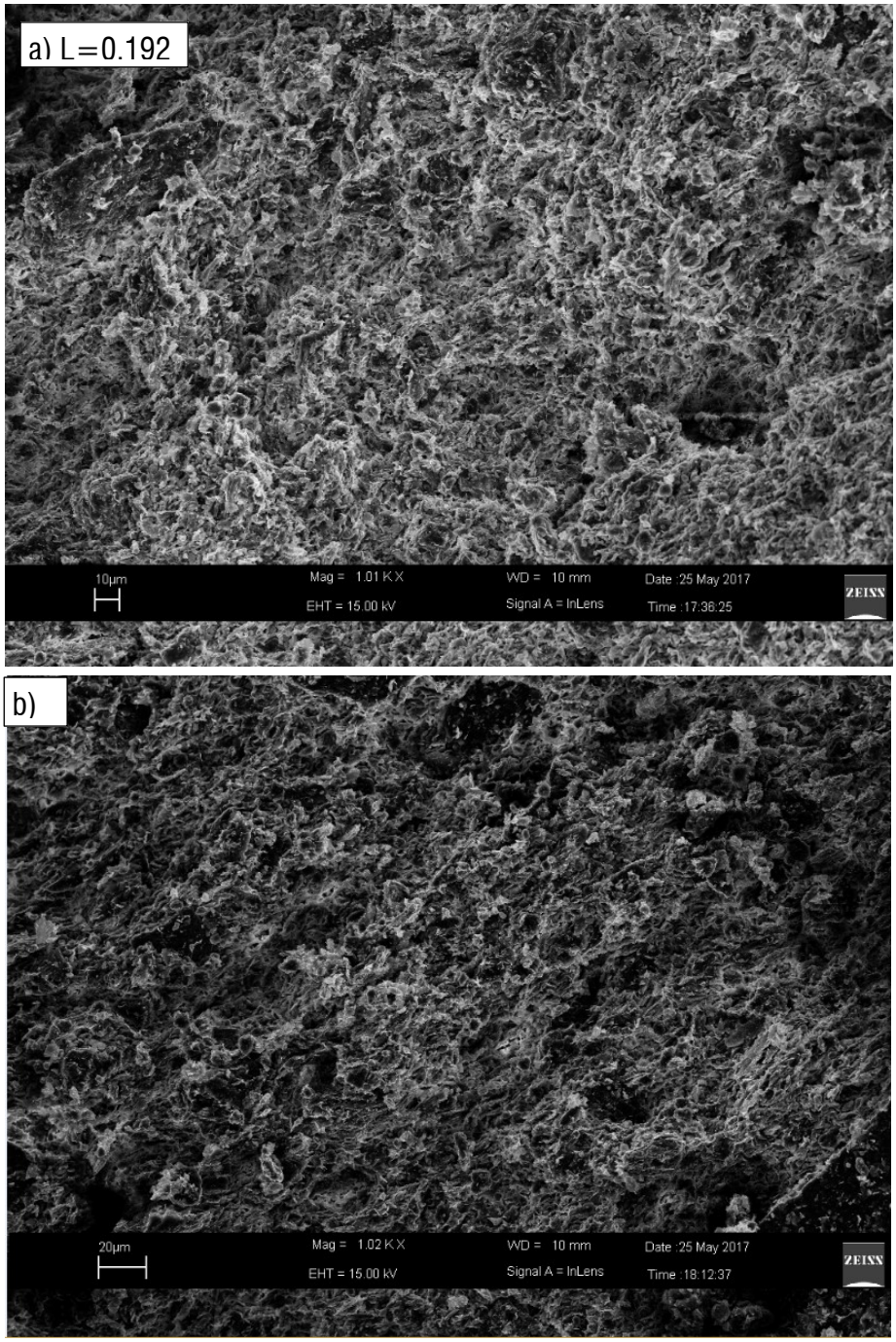

Fig. 7.33 - SEM of reconstituted Lucera clay along a vertical fracture at medium magnification.

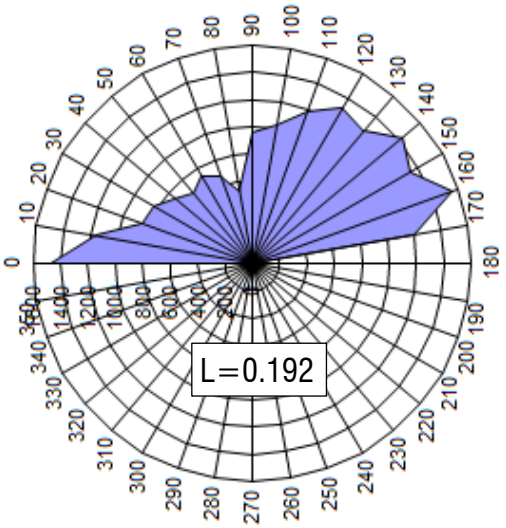

Fig. 7.34 - Direction histogram of reconstituted Lucera clay on the picture in Fig. 7.33a.

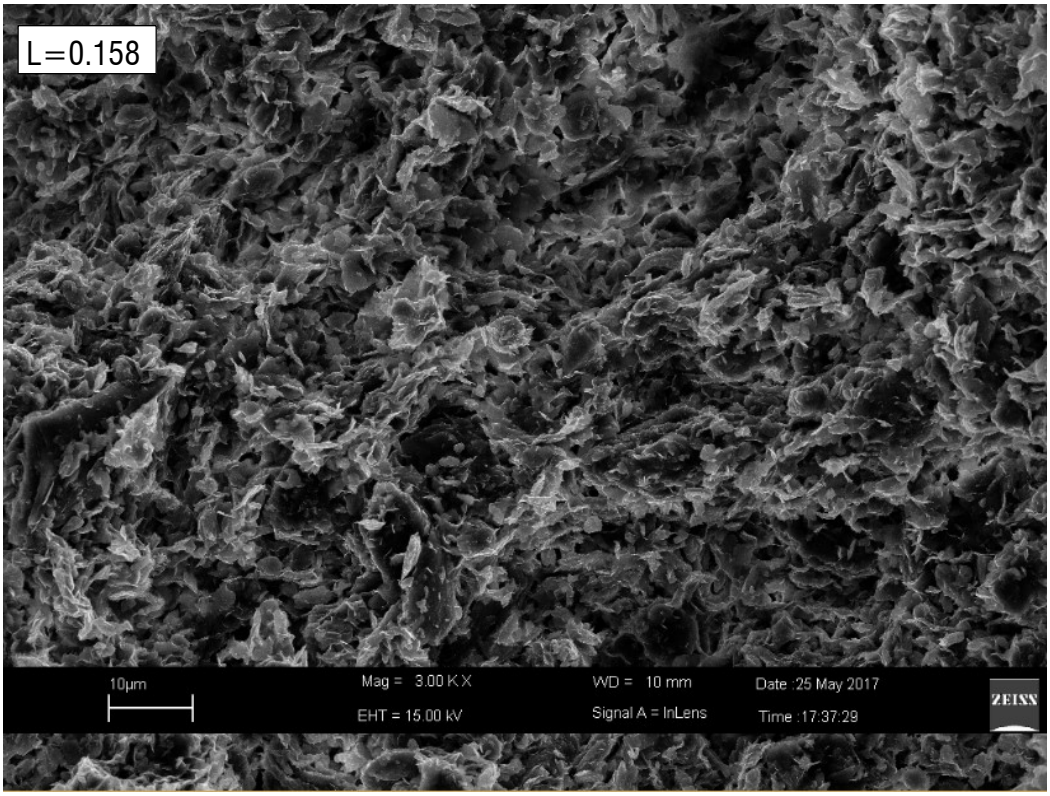

Fig. 7.35 - SEM of undisturbed Lucera clay along a vertical fracture at medium-high magnification.

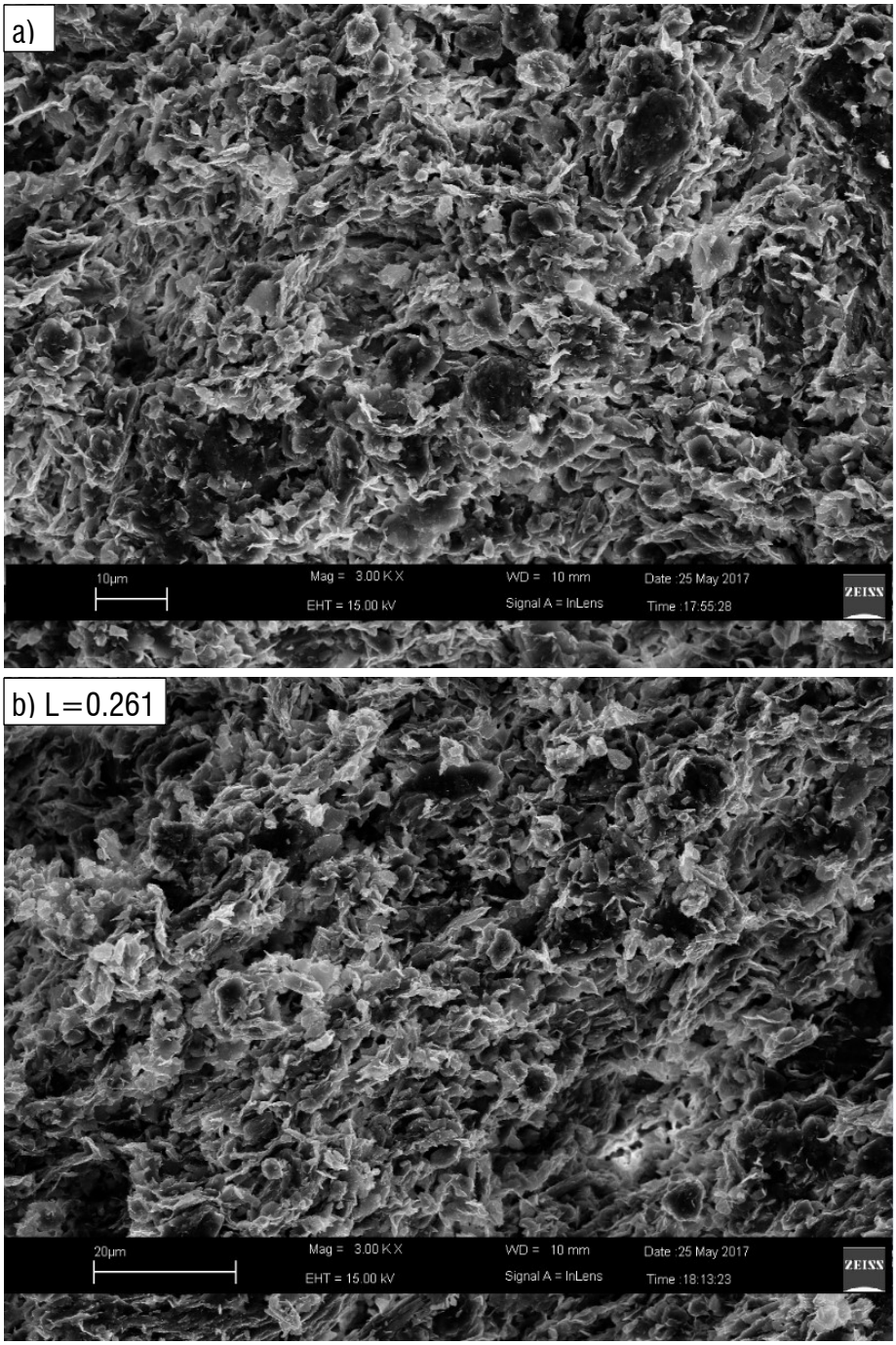

Fig. 7.36 - SEM of undisturbed Lucera clay along a vertical fracture at medium-high magnification.

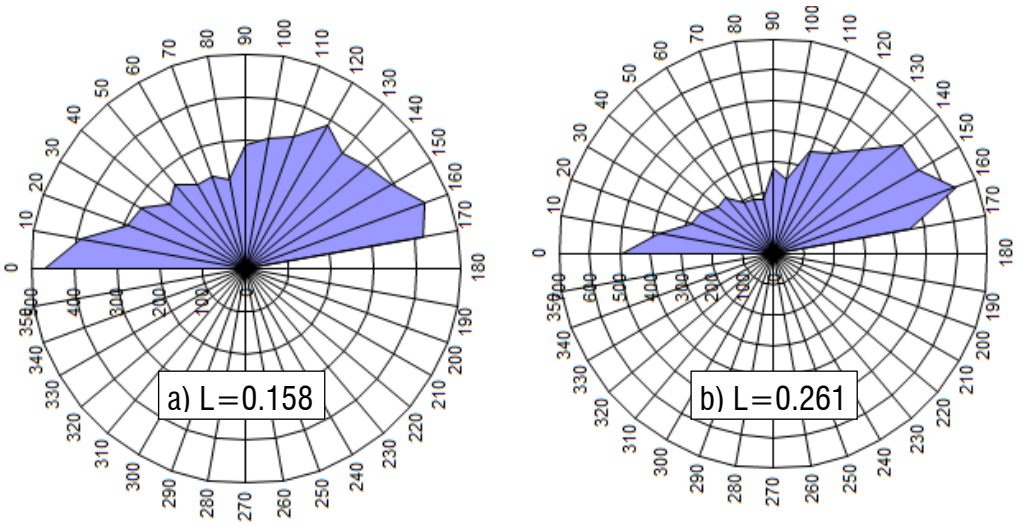

Fig. 7.37 -Direction histograms of the SEM micrographs in (a) Fig. 7.35 and (b) Fig. 7.36b.

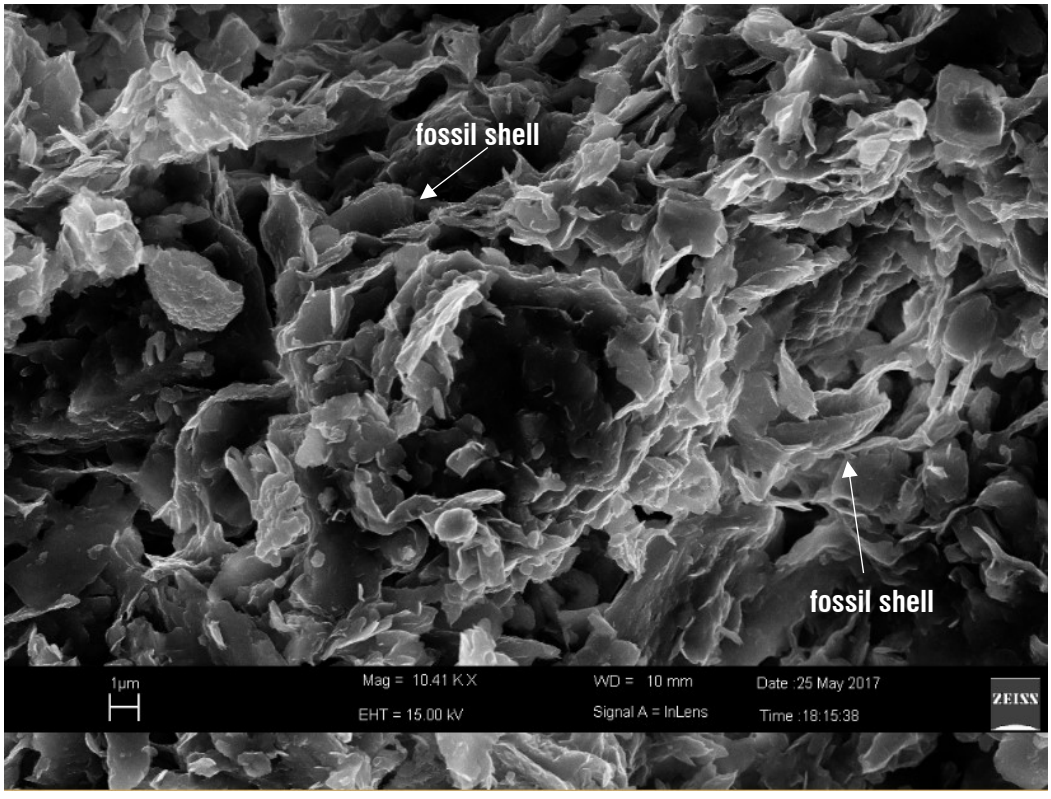

Fig. 7.38 – SEM in reconstituted Lucera clay: fossil shells.

As a confirmation of the differences described, the MIP curves of reconstituted Lucera clay are much different from those presented earlier, although similar basic features can still be recognized.
The cumulative curve shows a less steep increase when passing from the intrusion of the macro-pores to that of the micro-pores and many step increases are seen in the larger entrance diameter range. These correspond to some peaks in the incremental curve at sizes corresponding to fissures (tens of μm) that can open in the specimen, because of the undrained unloading in the consolidometer or during the specimen preparation for microstructural analyses.
The incremental curve exhibits two major peaks, which can be considered as one given their proximity, at around 1 μm entrance diameter and another much smaller peak at around 3 μm. This size appears to be very close to that of the many pores identifiable in Fig. 7.36 and to that of the central pore that is seen in Fig. 7.38.
For sizes below the dominant pore size, the incremental curve gently decreases towards smaller diameters, indicating the presence of a large number of pores in this size range ($\leq$1 μm). As shown in Fig. 7.40, the DPS can be recognized between particles both in edge-to-face contacts and in face-to-face contact, and pores of smaller sizes are present inside the denser particle arrangements.

The lower degree of orientation observed for reconstituted Lucera clay with respect to reconstituted Pappadai clay is believed to be a consequence of the different maximum pressure undergone in the consolidation stage by the two clays, as well as a result of the difference in composition of the two clays (Section 4.3). Apparently, in the reconstituted Lucera clay the consolidation up to of 100 kPa vertical pressure may not have yet re-organized the initial flocculated fabric in the orderly alternation of stacks of domains and honeycomb strata, which instead is seen in the reconstituted Pappadai clay, consolidated to 200 kPa, and in both the undisturbed clays, Pappadai and Lucera. This will be further discussed in Chapter 8.

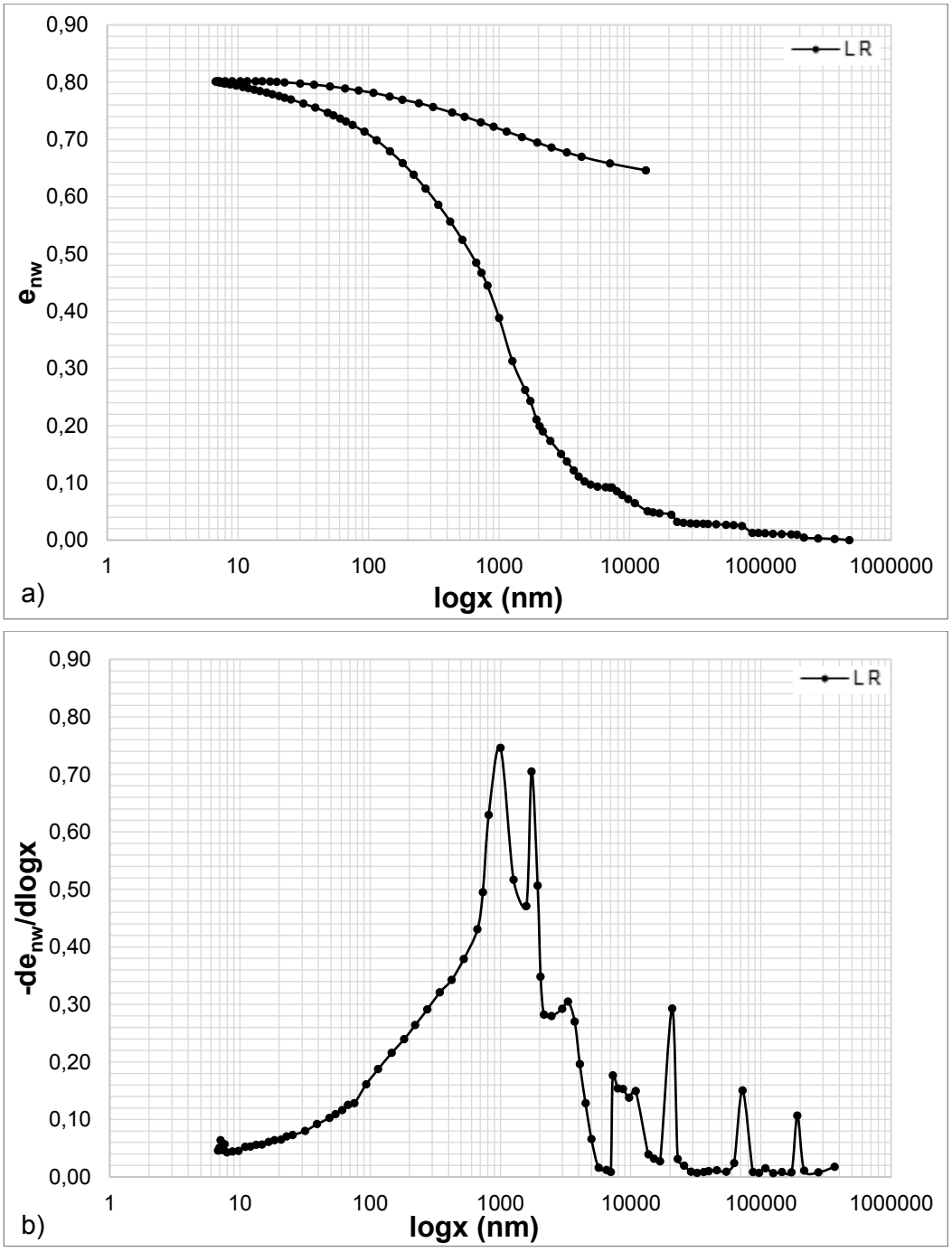

Fig. 7.39 - MIP test on reconstituted Lucera clay (state LR, e=0.92): a) cumulative and b) derivative curves.

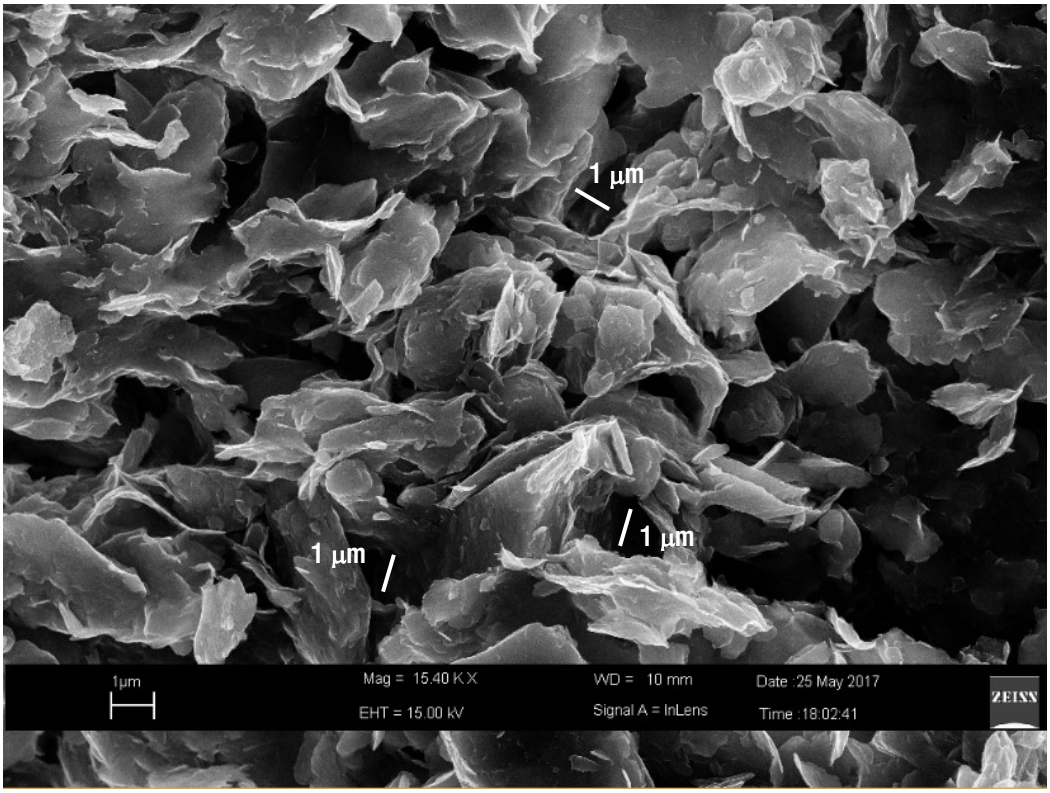

Fig. 7.40 – SEM of reconstituted Lucera clay: identification of the DPS.

7.3 Evolution of microstructure in 1D and isotropic compression

7.3.1 Microstructural changes in 1D compression for the natural clay

In this section, the microstructural changes occurring in the natural Pappadai clay and Lucera clay with one-dimensional compression are discussed.

In Fig. 7.41, the states in both isotropic and oedometric compression at which microstructural analyses were performed (Table 5.1, Table 5.2) are shown in the v-lnp' plane. For clarity, the graph reports only some of the compression tests discussed in Section 6.2.1, and the states at which microstructural analyses were carried out are indicated on these curves. Table 7.1 synthesises the microstructural analyses and the mechanical tests from which the specimens were obtained. The void ratios at the end of testing are reported.

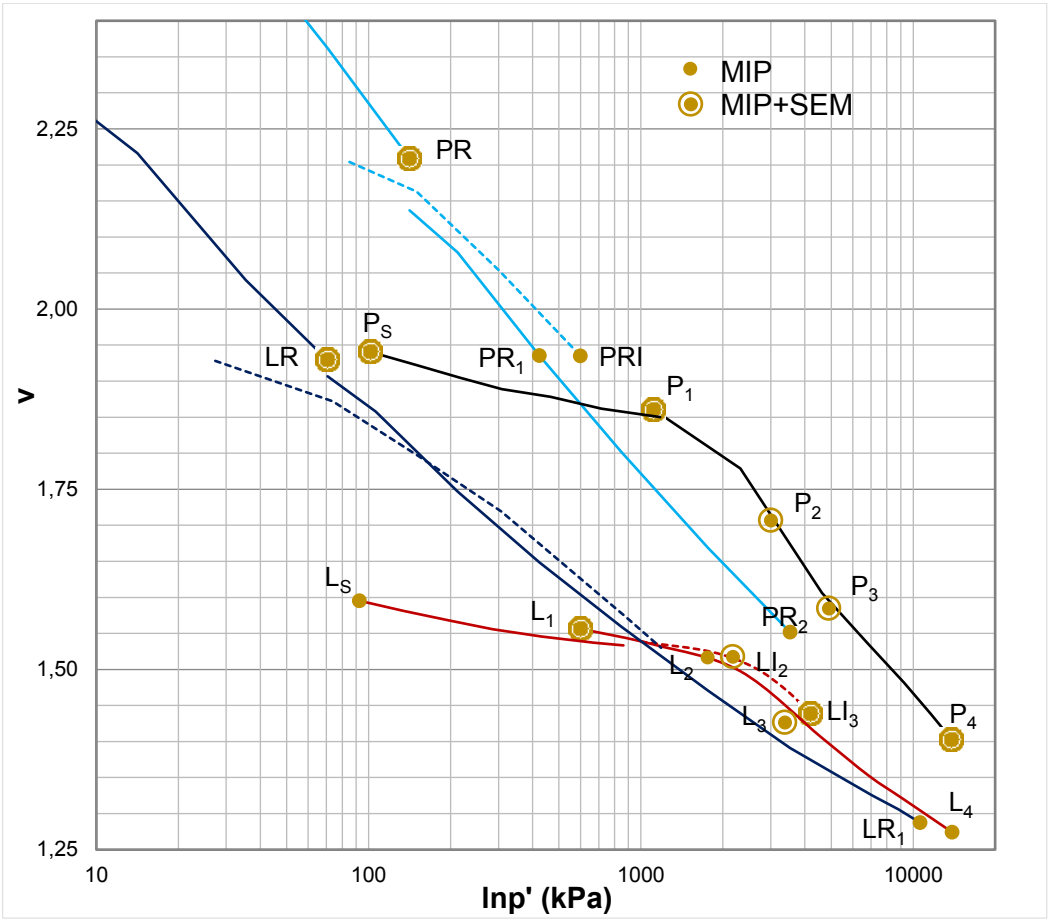

Fig. 7.41 – Microstructural analyses on specimens 1D and isotropically compressed.

It should be noted that the one-dimensional swelling curves are plotted assuming a K_0(OC) calculated according to the formulation of Jaky (1944) which accounts for the OCR. However, their slope appears to be higher than that recorded in of both oedometric swelling (in plane e-σ'_v) and isotropic swelling (in plane v-lnp'). In Fig. 7.41 the spot indicates that a MIP test was carried out on the specimen at the end of the compression test, while the circled spot indicates that both MIP and SEM analyses, including image processing, were carried out on the specimen.

Table 7.1 – Synthesis of microstructural analyses on specimens 1D and isotropically compressed.

MATERIAL	MECHANICAL TEST	v_f	SPECIMEN FOR MICRO-ANALYSES
natural PAPPADAI	-	1.820	P_1
	oed to σ'_v=3 MPa	1.794	P_2
	oed to σ'_v=5 MPa	1.683	P_3
	oed to σ'_v=18.5 MPa	1.480	P_4
	swelled to σ'_v=20 kPa	1.960	P_S
reconstituted PAPPADAI	end of consolidometer	2.245	PR
	oed to σ'_v=600 kPa	1.954	PR_1
	iso to p'=600 kPa	1.935	PRI
	oed to σ'_v=5 MPa	1.552	PR_2
natural LUCERA	-	1.550	L_1
	oed to σ'_v=1.4 MPa	1.534	L_2
	oed to σ'_v=5 MPa	1.462	L_3
	oed to σ'_v=18.5 MPa	1.274	L_4
	swelled to σ'_v=20 kPa	1.595	L_S
	iso to p'=1640 kPa	1.535	LI_2
	iso to p'=4200 kPa	1.439	LI_3
reconstituted LUCERA	end of consolidometer	1.920	LR
	oed to σ'_v=15 MPa	1.289	LR_1

The behaviour in 1D compression for Pappadai clay is examined in this section. On natural Pappadai clay, Cotecchia (1996) carried out SEM observations after 1D compression to two states: immediately post gross-yield (σ'_v=3 MPa) and at large pressures (σ'_v=22 MPa). Also, n the reconstituted clay SEM images were taken by Cotecchia (1996) at high pressures (σ'_v=22 MPa). These SEM images were also subjected to image processing.

The results of the MIP tests on the 1D compressed specimens are shown in Fig. 7.42, together with the MIP results for the undisturbed specimen for comparison.

During compression from P_1 to P_2 (Fig. 7.41), the clay undergoes gross-yielding, so the microstructural analyses allow to observe what happens at gross-yield in the clay. The change in PSD and in fabric due to gross yield could be identified by comparing the MIP and SEM results of specimens P_1 and P_2.
The MIP test on specimen P_2 reveals a very small change in the total intruded pore volume (Fig. 7.42a), while the larger porosity, here called inter-aggregate, increases uniformly, contrarily to what expected. A light shift to the left of the DPS from 220 nm (specimen P_1) to 180 nm is observed, accompanied by a significant reduction in the frequency of the DPS.

With respect to the fabric before gross yield (Fig. 7.3, Fig. 7.4), the fabric after gross yield at medium magnification (Fig. 7.43 to Fig. 7.45) in both the SEM and FESEM applications appears more densely packed. The particle arrangements cannot easily be distinguished and the changes in particle arrangement in the different zones of the clay fabric are not as regular as in the undisturbed clay. The fabric changes thus appear generally chaotic, different particle arrangements merging into each other resulting in ill-defined boundaries. Sub-vertical and sub-horizontal domains may be adjacent to and closely packed with flocculated and honeycomb fabrics. In Fig. 7.45, some massive domains can be seen, which either bend in different directions or merge with areas of densely packed flocculated fabric. Differently from the undisturbed clay, in which sub-horizontal iso-oriented domains could be distinguished from areas of honeycomb fabric, here the two types of arrangement seem to melt in a very dense random fabric. The globigerinae and the crystals observed in the undisturbed specimen appear undamaged by compression (Fig. 7.46, Fig. 7.47) and the clay particles seem to slide along the boundaries of the shells.

Zones with small particle domains densely and chaotically packed are frequent, as those shown in Fig. 7.48 and Fig. 7.49. This significant fabric rearrangement may also be responsible for the unusual increase in the larger porosity observed in the cumulative curve of the specimen compressed beyond gross-yield, with respect to the undisturbed specimen.

The results of image processing on medium magnification micrographs (Fig. 7.43, Fig. 7.44, Fig. 7.45) reveal a degree of orientation which keeps being high (0.24-0.33), but overall does not increase much with respect to the undisturbed clay. Locally, in areas as those shown in Fig. 7.48 and Fig. 7.49, the orientation is seen to increase to values as high as 0.376.

The outlines of the particles in Fig. 7.47 to Fig. 7.49 appear “fringed”. Since fabric changes occurring at gross yield are complex and considerable, it is possible that the state of clay particles is also affected by the yielding process.

The type of fabric observed beyond-gross yield specimen was not recognized in the undisturbed specimen and so may be a peculiar effect of gross yielding, as well as the limited overall increase in the orientation of the fabric.

At the same time, as discussed in Section 6.2.1, the swelling capacity of the clay increases over gross yield to the value exhibited by the reconstituted clay, suggesting a significant degradation of the bonding, which could not be inferred from neither the SEM nor the MIP results. Hence, over gross-yield the clay experiences major bonding degradation with some important changes in fabric, which becomes more chaotic. Even though, the degree of particle orientation overall increases slightly. It may be that the increase in fabric packing at gross yield results in a thickening of the aggregates of oriented particles (thickening of the stacks) and an average orientation of these that is recorded as higher than pre-gross yield by the image processing of the medium magnifications SEM pictures.

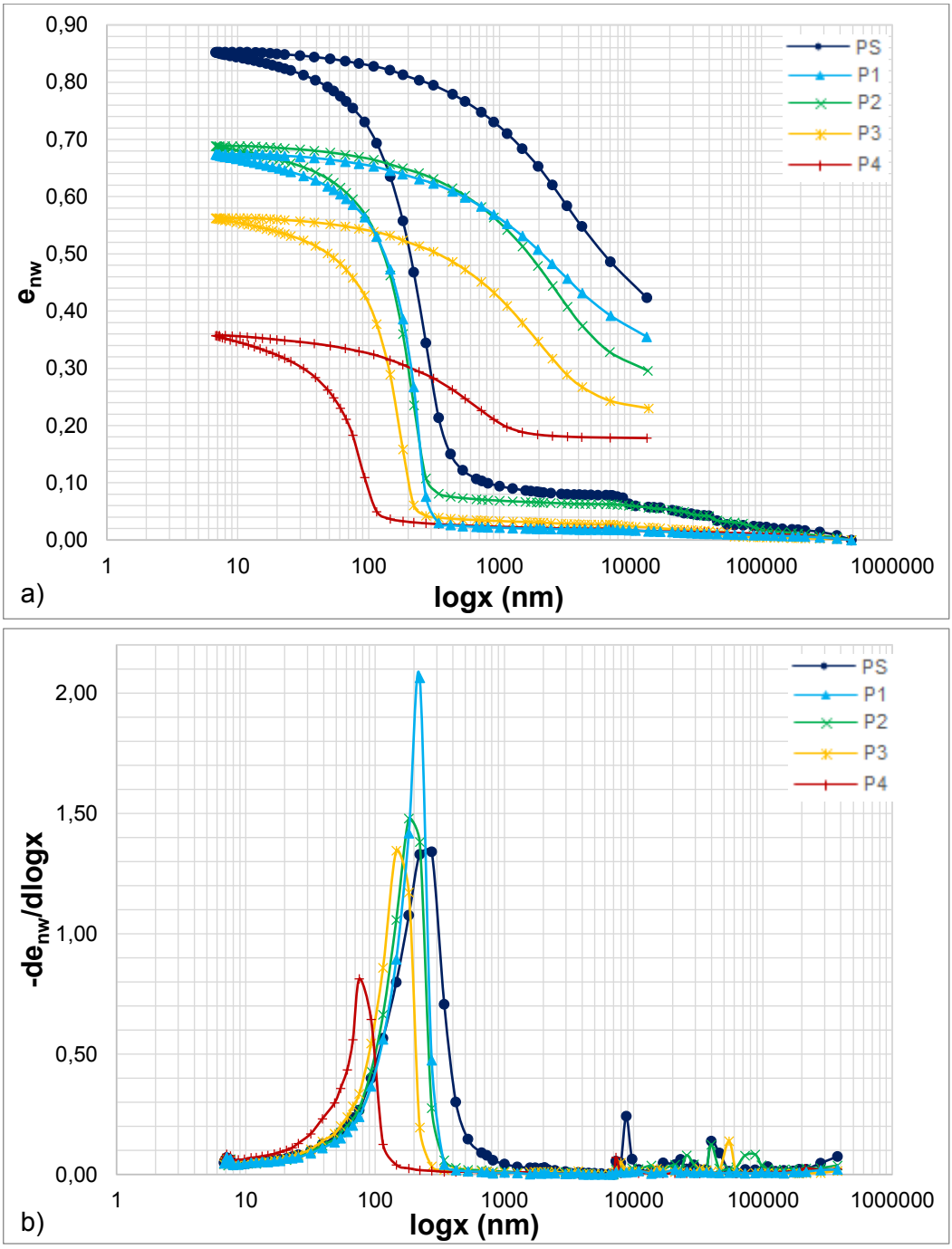

Fig. 7.42 - MIP tests on natural Pappadai clay in 1D compression. a) cumulative and b) derivative curves.

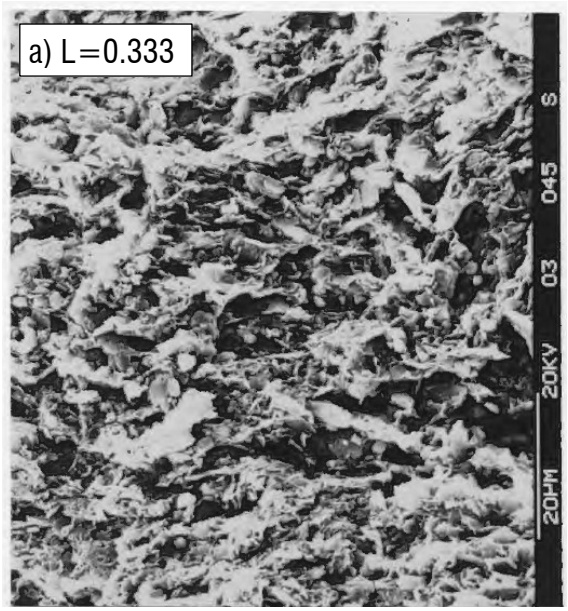

Fig. 7.43 - Natural clay compressed to a σ'_v of 3 MPa: the fabric is more open and flocculated in the centre of the picture; "chaotic masses" of particles are seen in the bottom half and in the top right of the picture.

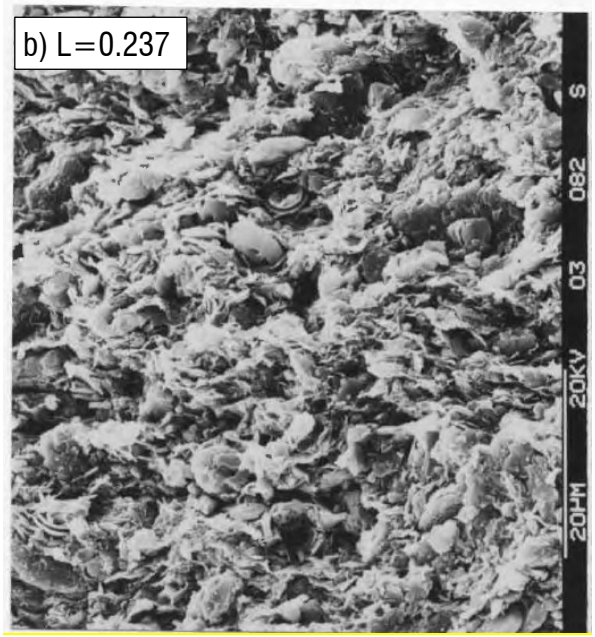

Fig. 7.44 - Natural clay compressed to a σ'_v of 3 MPa: chaotic densely packed fabric (after Cotecchia, 1996).

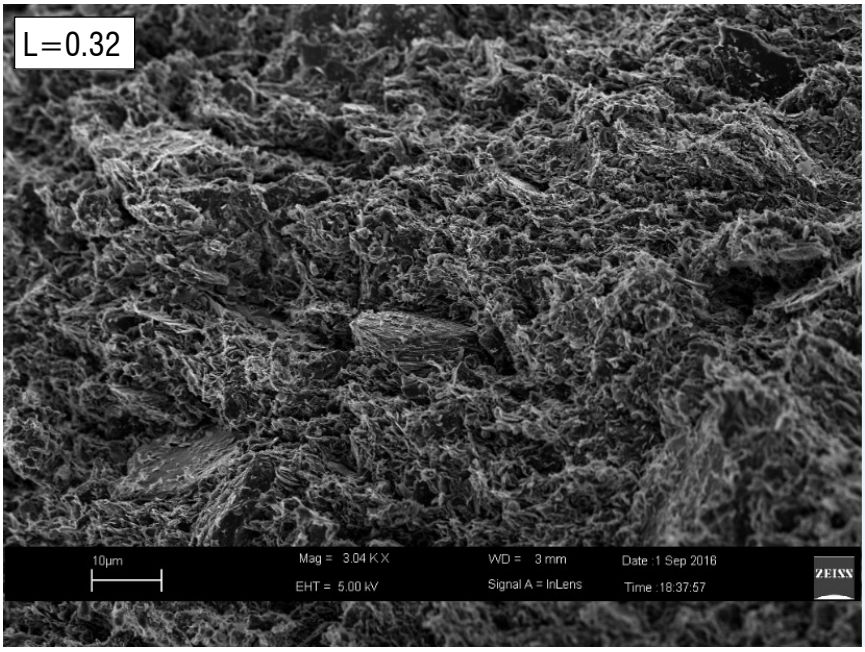

Fig. 7.45 - SEM micrograph along a vertical fracture of Pappadai clay 1D compressed σ'_v=3 MPa at medium magnification.

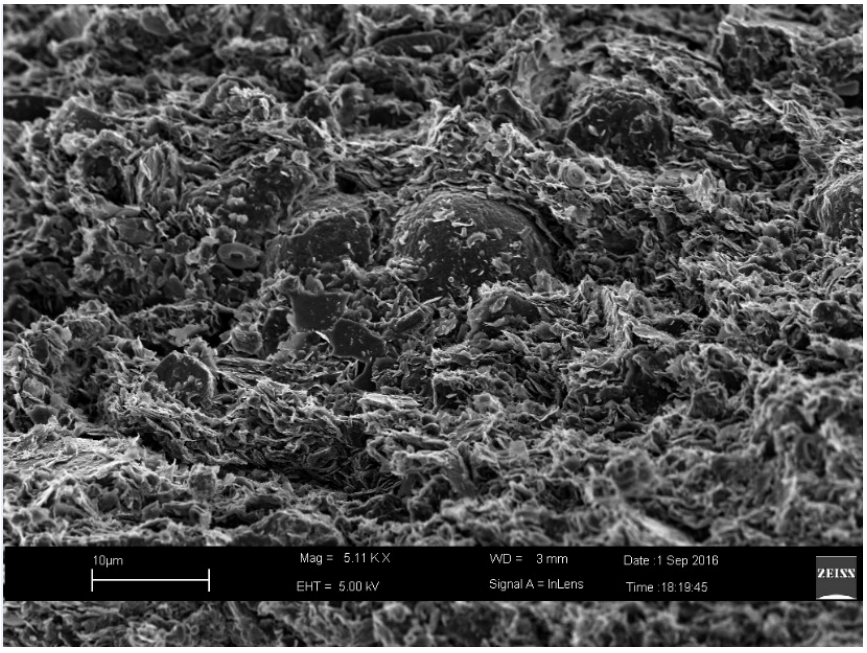

Fig. 7.46 – SEM on natural Pappadai clay compressed to σ'_v=3 MPa: undamaged shells of globigerinae.

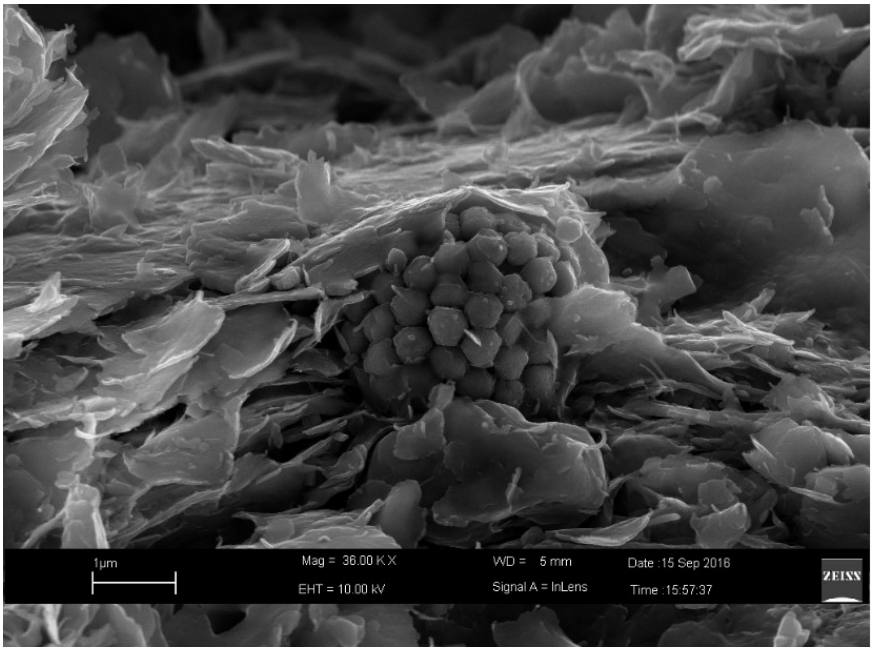

Fig. 7.47 - SEM on natural Pappadai clay compressed to σ'_v=3 MPa: undamaged pyrite crystals.

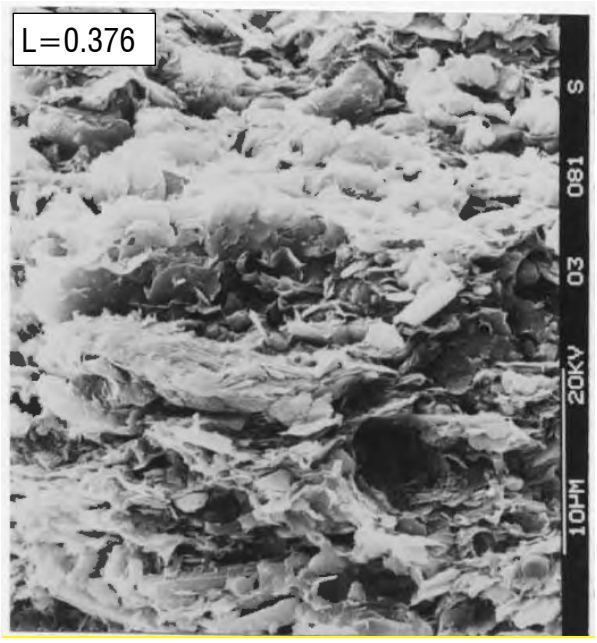

Fig. 7.48 – SEM micrograph along a vertical fracture of natural Pappadai clay compressed σ'_v of 3 MPa; two stacks of iso-orientated particles confine a chaotic mass of particles (after Cotecchia, 1996).

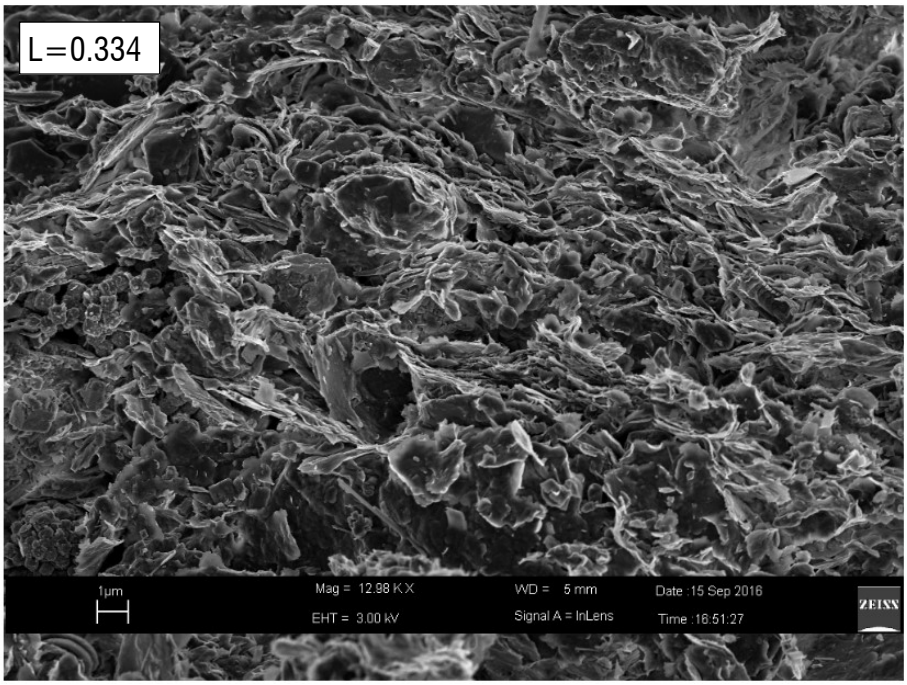

Fig. 7.49 –SEM micrograph along a vertical fracture of Pappadai clay 1D compressed to σ'_v=3 MPa at high magnification.

The compression of the clay to P_3 generates a greater reduction in void ratio, which corresponds to a much lower total intruded volume and a significant loss of macro-porosity (Fig. 7.42a). Despite keeping the same shape, the cumulative curve corresponding to P_3 has the steeper part translated to the left. This change can be more effectively explained by the comparison of the derivative curves, where a translation of the whole curve of specimen P_3 to the left is observed (Fig. 7.42b). The DPS is seen to further decrease to 145 nm and also its frequency is reduced.

The observation of the fabric along a vertical fracture at medium magnification (Fig. 7.50) shows a more densely packed fabric, in which horizontal and sub-horizontal stacks of particles enclosing honeycomb areas can be again recognized (Fig. 7.50a), although at places chaotic masses of particles are still present, as that observed in the upper right corner of Fig. 7.50b. The result of image processing for the micrograph in Fig. 7.50a (Fig. 7.51) denotes a well oriented fabric, which has experienced a slight further increase in fabric orientation with respect to post-gross yield.

The chaotic rearrangement of particles occurred over gross yielding seems to be changed by the further 1D compression, developing a more regular sequence of stacks of particles and flocculated zones, although chaotic masses of particles are still recognizable. It is likely that, at larger pressure, the further advance of this process of reorganization of fabric into a regular structure, more similar to that seen for the undisturbed specimen, may develop.

With compression, crystals of pyrite and calcite (Fig. 7.52, Fig. 7.53), as well as pyrite framboids, are still found unaltered by the loading process, but melting with the clay particles; clay particles are found to adhere to their boundaries in very packed thin strata. The fabric around the crystals is strongly affected by the presence of these silt-size components.

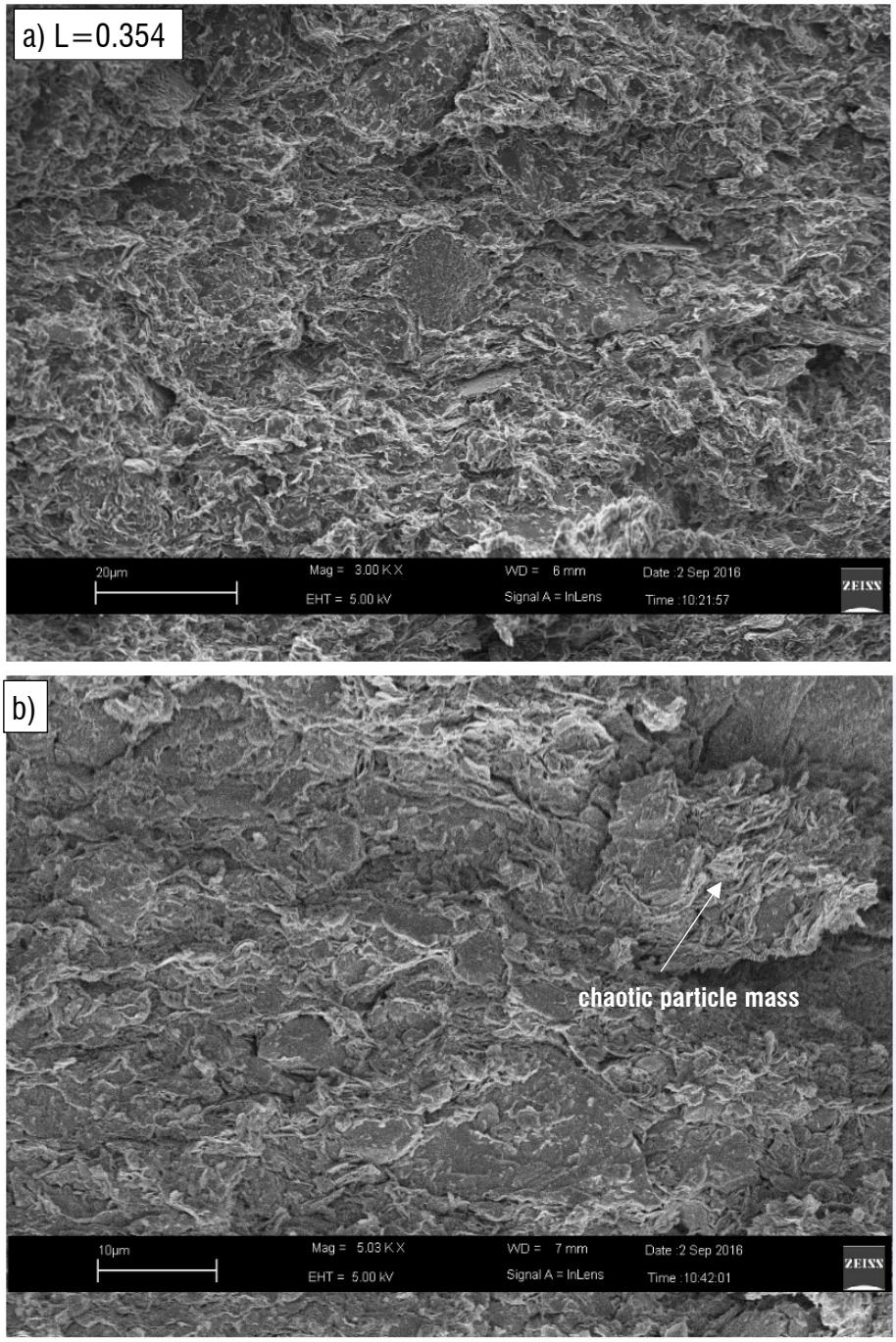

Fig. 7.50 - SEM micrographs along a vertical fracture at medium magnification of Pappadai clay 1D compressed to σ'_v=5 MPa.

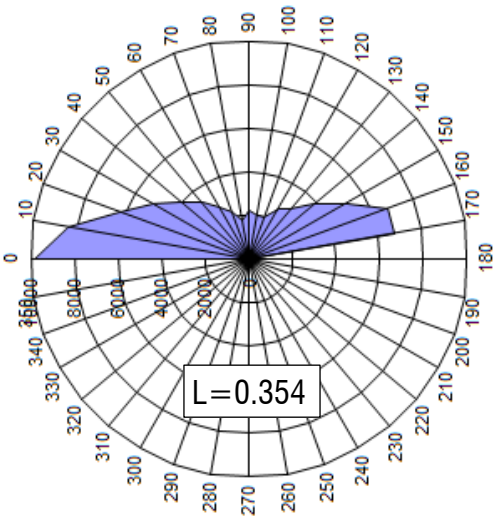

Fig. 7.51 - Direction histograms of the SEM micrographs in Fig. 7.50a.

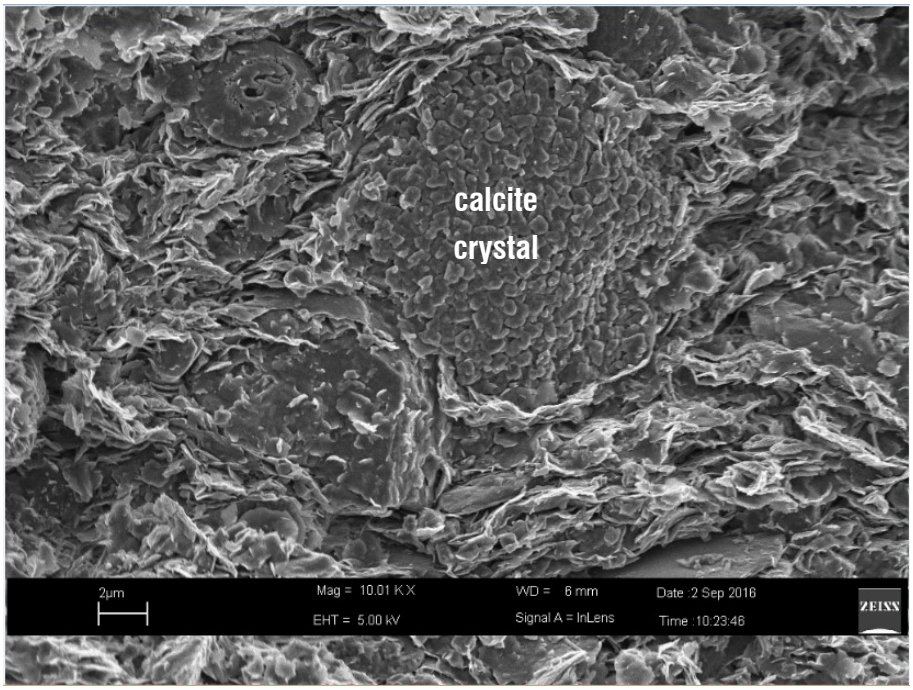

Fig. 7.52 - SEM micrograph along a vertical fracture of Pappadai clay 1D compressed to σ'_v=5 MPa: undamaged calcite crystal.

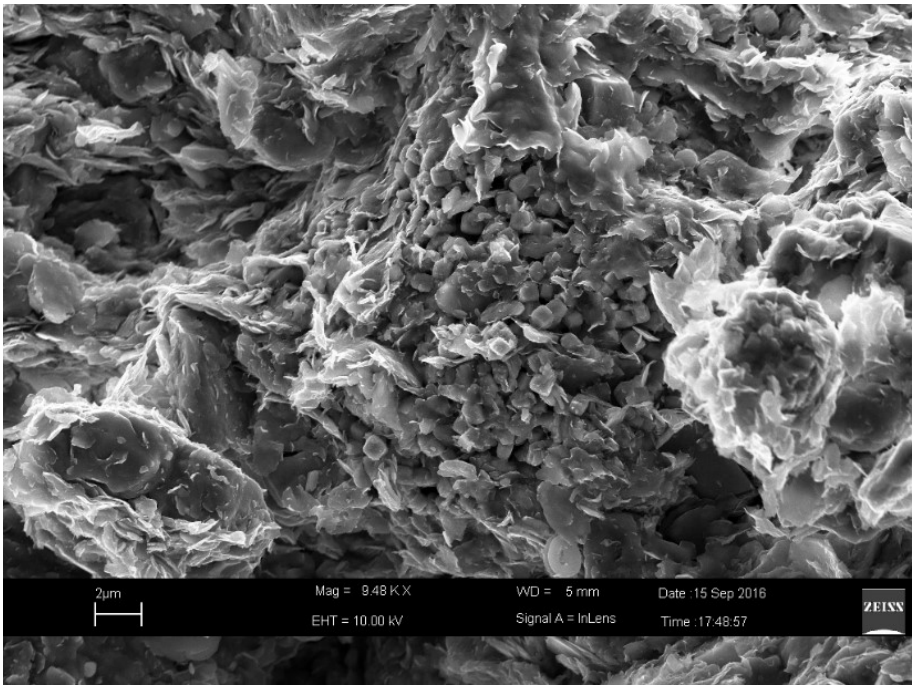

Fig. 7.53 - SEM micrograph along a vertical fracture of Pappadai clay 1D compressed to σ'_v=5 MPa: undamaged pyrite crystal.

With compression to large pressures (point P_4), a major change in the pore size distribution is seen to occur (Fig. 7.42). The significant reduction in void ratio is reflected in the substantial reduction of the total intruded volume, which is accompanied by a further reduction in the macro-pore volume. At these high pressures, inter-aggregate porosity becomes negligible, probably because of a closure of the larger pores induced by both compression and their filling with smaller particles. The incremental curve significantly reduces in terms of frequency of the DPS, and the value of the DPS is further shifted to the left to 75 nm.

Hence, the decrease in void ratio due to 1D compression is firstly reflected in a quick reduction of the volume occupied by the larger pores, accompanied by the shift to the left of PSD, with a decrease of both the size and the frequency of the dominant pore.

The SEM pictures taken by Cotecchia (1996) on natural Pappadai clay compressed to 22 MPa are shown together with those taken at 18.5 MPa at point P_4, as the fabric at the two very high pressures can be reasonably assumed to be the same.
In Fig. 7.54 the fabric on a vertical fracture through the clay is shown at medium-low magnification. Perfectly oriented domains (c.p.o. fabric) form stacks, which are interbedded between piles of mediumly to highly oriented domains. The medium magnification pictures of the fabric on a vertical fracture (Fig. 7.55, Fig. 7.56) indicate a highly oriented fabric, in which thick stacks of particles and domains can be recognized. The qualitative observation is confirmed by the degrees of orientation, which reach values as high as 0.356.
However, areas of flocculated fabric can be recognized in Fig. 7.55 and Fig. 7.56 between the c.p.o. domains and can be seen at higher magnification in Fig. 7.57 and Fig. 7.58. In Fig. 7.59 small interstratified areas of flocculated fabric are also interbedded with the sub-horizontally oriented domains. The areas of flocculated fabric are characterized by degrees of orientation either typical of a low oriented fabric (Fig. 7.57) or lower than the average (Fig. 7.58).

Even after compression to such high pressures, components such as pyrite framboids are found undamaged and completely surrounded by particles of clay compressed in thin stacks around them (Fig. 7.60). At places, these constituents appear totally melted with the clay particle arrangements (Fig. 7.60a). Interestingly, clay particles continue to have fringed borders, and in Fig. 7.57 and Fig. 7.60 small pieces resembling particle edges are seen scattered in the micrograph. Also in this case, the complex structure changes may be affecting the state of the clay particles.

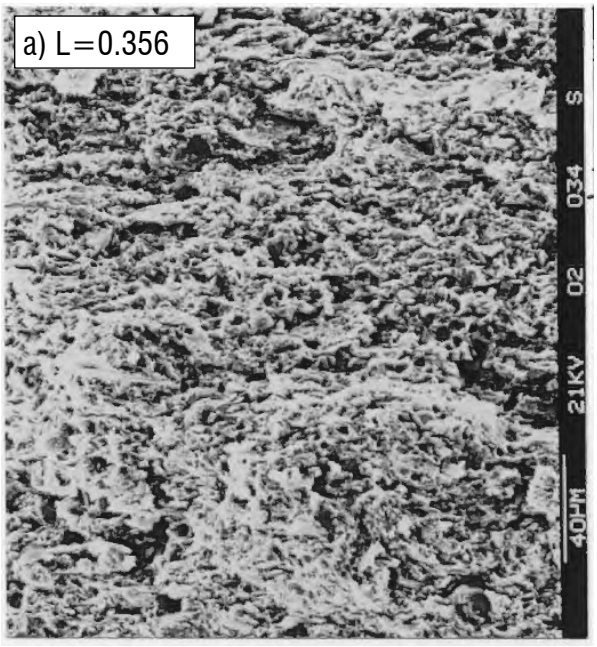

Fig. 7.54 - Natural clay compressed to a σ'_v of 22 MPa: vertical fracture; stacks of c.p.o. fabric within less oriented fabric (after Cotecchia, 1996).

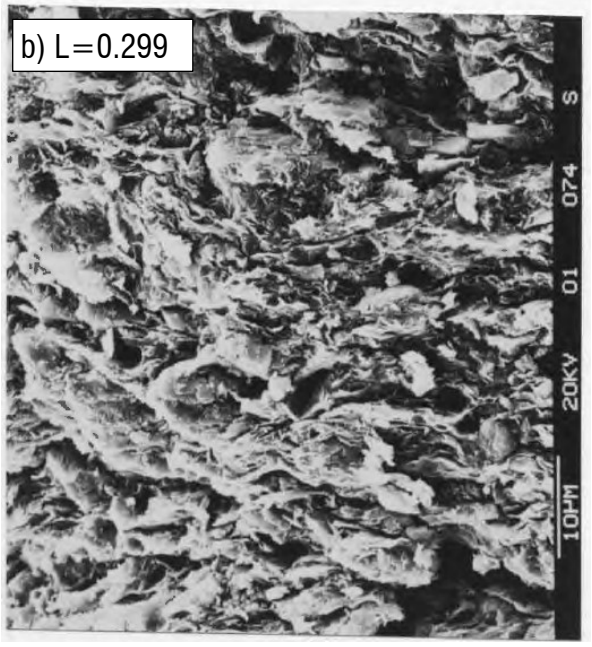

Fig. 7.55 - Natural clay compressed to a σ'_v of 22 MPa: vertical fracture; the fabric is highly oriented, with many stack s of c.p.o. fabric (after Cotecchia, 1996).

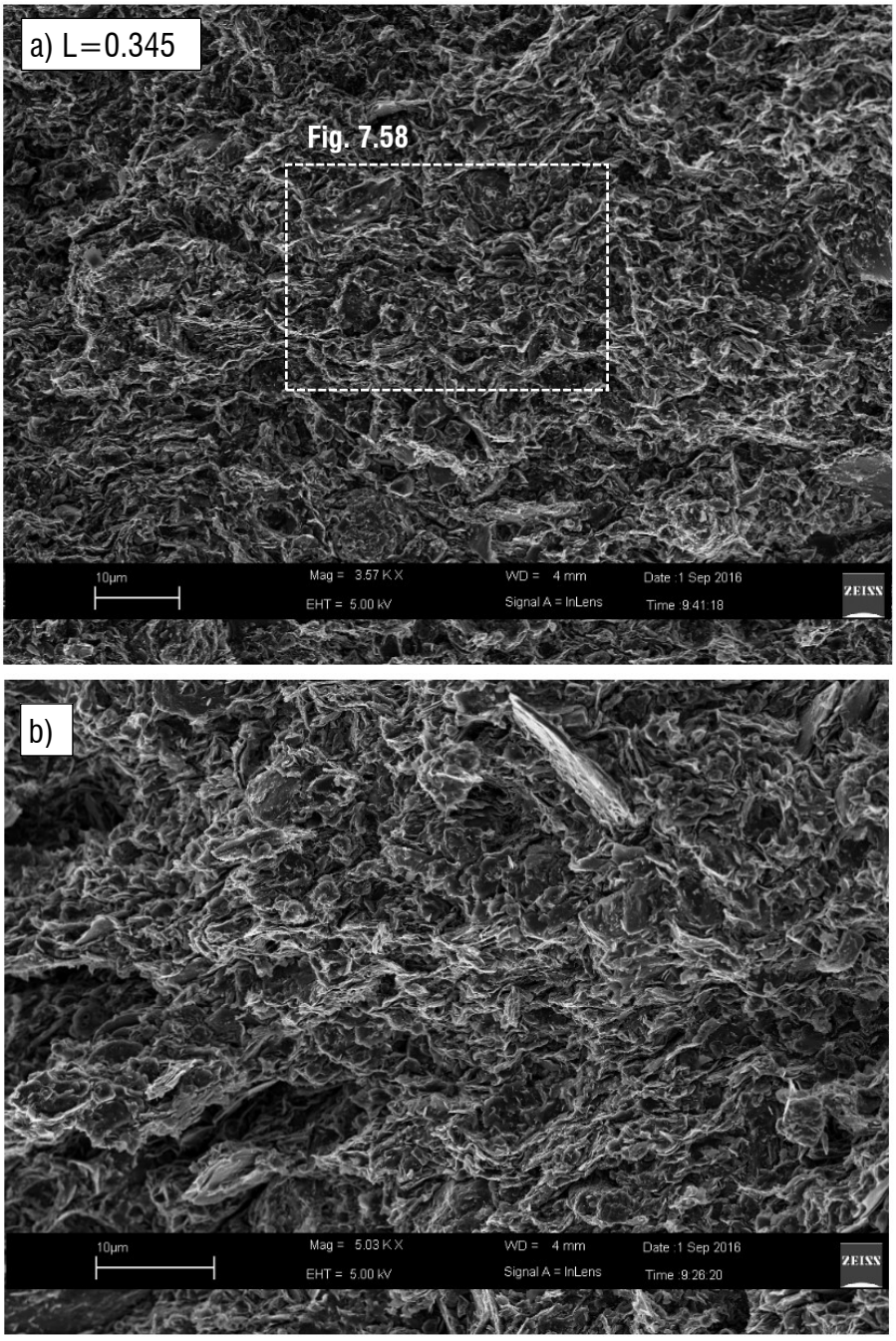

Fig. 7.56 - SEM micrographs along a vertical fracture of Pappadai clay 1D compressed to σ'_v=18.5 MPa at medium magnification.

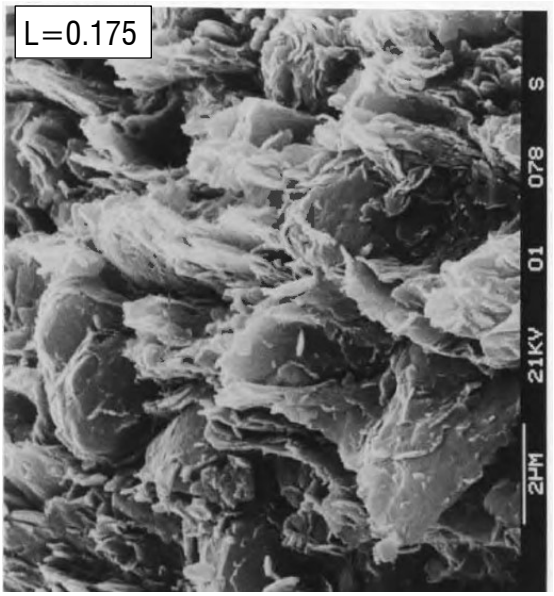

Fig. 7.57 - Natural clay compressed to a σ'_v of 22 MPa: vertical fracture; detail of flocculated fabric (after Cotecchia, 1996).

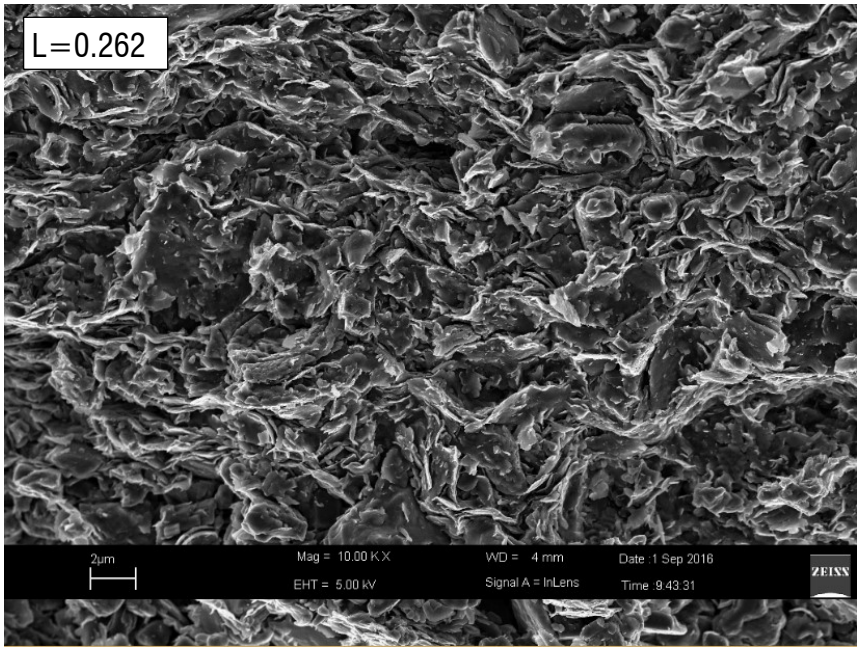

Fig. 7.58 –SEM micrograph along a vertical fracture of Pappadai clay 1D compressed to σ'_v=18.5 MPa at high magnification.

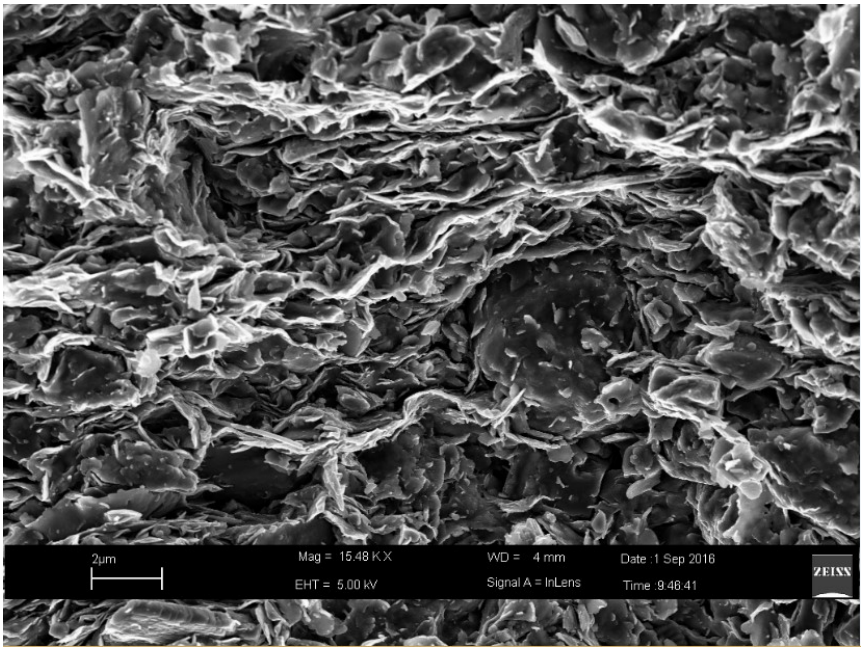

Fig. 7.59 - SEM micrograph along a vertical fracture of Pappadai clay 1D compressed to σ'_v=18.5 MPa at high magnification: evidence of zones of flocculated fabric.

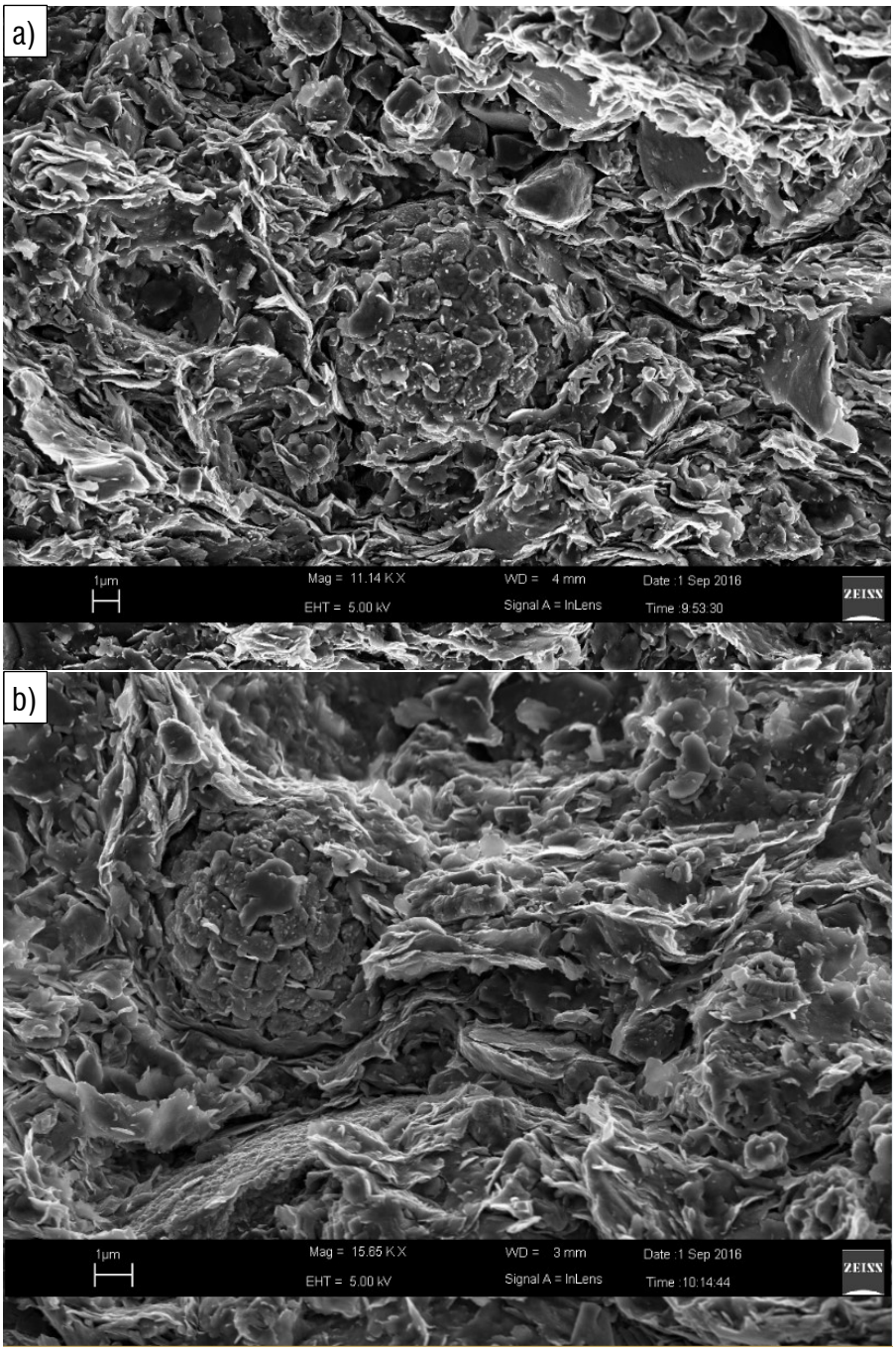

Fig. 7.60 - SEM micrograph along a vertical fracture of Pappadai clay 1D compressed to σ'_v=18.5 MPa: undamaged pyrite framboids.

The behaviour in 1D compression of natural Lucera clay is now examined, with the aim at characterizing the fabric changes and compare them with those observed for natural Pappadai clay.
The microstructure evolution at a pre-gross-yield state, not observed for Pappadai clay, is first observed for Lucera clay, with the aim at investigating the microstructural changes occurring within the clay state boundary surface. In fact, as anticipated in Chapter 3, the assessment of the evolution of the clay microstructure taking place for a natural clay before gross-yield, both in compression and in shearing (which will be discussed later), is crucial for the assessment of the internal causes of the variations in hardening rule that is generally modelled at gross yield, e.g. hardening within the outer bubble and when this is first touched in either bubble models or bounding surface models.

The results of the MIP tests on the 1D compressed specimens are shown in Fig. 7.61, together with the undisturbed specimen for comparison. In Fig. 7.61b, the cumulative curves of Fig. 7.61a are reported with a change of scale for the y-axis, to make the macro-porosity evolution clearer.

When the clay is compressed from the undisturbed state L_1 to the pre-gross-yield state L_2, the soil state moves along the swelling line and small changes in void ratio are recorded. Accordingly, the MIP test on specimen L_2 shows a small reduction in the total intruded volume (Fig. 7.61a), which however corresponds to a more significant decrease in the pore volume of the macro-pores (Fig. 7.61b). The latter is seen to reduce, superimposing to the curves corresponding to states L2 and L3. If the reduction in the macro-porosity is excluded, for the rest very little difference is observed in the derivative curves of specimens L_1 and L_2, the PSD functions being almost identical in both shape and size. The double peak which was seen in specimen L_1, with an average DPS of 300 nm, becomes less pronounced in specimen L_2, with the formation a more evident peak at 270 nm and without modification of the frequency of the dominant pore size. Hence, the reduction in void ratio due to compression to a state pre-gross-yield

appears only reflected in the reduction of the volume of the larger pores, while the small sized porosimetry undergoes minor changes.

When further loaded to L_3, i.e., beyond gross-yield, the clay experiences more relevant microstructural changes. In this case, differently from what observed for Pappadi clay, the decrease in total pore volume is observed to leave almost unchanged the macro-porosity, already compressed by loading pre-gross yield; similarly to what observed for Pappadai clay, instead, at gross yield the micro-porosity is modified. Changes are seen in the incremental curve of L_3 compared to that of L_1; the curve becomes narrower and reaches a slightly higher frequency of the DPS, which becomes 270 nm.
A global view of the fabric at state L_3 is shown in Fig. 7.62 at medium magnification. The fabric appears more densely packed and overall more oriented than the undisturbed fabric. Two horizontal thick stacks of oriented particles can be recognized at the top and bottom of the micrograph; the long one at the bottom is seen to cross a sub-horizontal strata of perfectly oriented fabric to the right side of the picture and bend to a sub-vertical direction on the left side of the picture. Honeycomb particle arrangements are found interbedded between the stacks.
Also at higher magnification (Fig. 7.63) horizontal and sub-horizontal densely packed and highly oriented particle domains are seen, and still local areas of more random fabric appear (Fig. 7.64). Many stacks of perfectly oriented particles are found bended in sub-horizontal directions, as seen in Fig. 7.65, where very thin strata of particle domains in face-to-face contact enclose thin strata of less orderly particles.
The qualitative comparison between the fabric orientation at L_1 and L_3 is confirmed by the results of image processing, which confers degrees of orientation as high as 0.335. Hence, the overall fabric orientation is increasing with respect to the undisturbed state, as was recognized for natural Pappadai clay.

Remarkably, the regular architecture in which c.p.o. strata alternate with flocculated-honeycomb particle arrangements is not ubiquitously found at point L_3, which shows a fabric similar to that observed at point P_3 for natural Pappadai clay. In fact, it may be

reasonably assumed that, in both cases, some effects of the particle re-arrangement occurred at gross yield are still recorded, although the further compression beyond gross yield is contributing to a fabric re-organization towards a repetitive architecture. Then, the gross yield of Lucera clay may be hypothesized to have caused substantial changes to the clay fabric similar to those observed for Pappadai clay. Accordingly, the compression of the natural clay to high stresses beyond yield could be expected to increase the orientation of the fabric, but only to a limited extent.

For both clays, these fabric changes are accompanied by the significant weakening of bonding occurring over gross yield, as discussed in Chapter 6.

At high pressures (L_4), the MIP results show a major change in the PSD (Fig. 7.61). Not much changes appear to take place in the larger pore volume (Fig. 7.61b), which does not reduce with respect to L_3. On the other hand, the incremental curve translates markedly to the left, reaching a DPS of 115 nm, and reduces its height with respect to L_3.

Apparently, the main effect of compression is a translation towards lower pore sizes of the incremental curve, with a concurrent reduction in the frequency of the dominant pore. This is more evident for natural Pappadai clay, which always shows higher frequencies at the DPS than natural Lucera clay. From a physical point of view, this should correspond not only to a compression of the small pores, causing a size reduction, but also to the disappearance of a number of micro-pores, resulting in a decrease of the frequency of the dominant pore. Evidently, the disappeared pores must have been filled by smaller particles.

In conclusion, oedometric compression to a pre-gross-yield state does not induce significant changes in the distribution of the small and dominant pores, and mainly reduces the larger inter-aggregate pores. The corresponding fabric evolution can be reasonably assumed to be very limited (it has still to be investigated). Gross-yield

seems to induce major changes in the clay microstructure, which undergoes a major weakening of bonding, allowing for a chaotic rearrangement of the clay particles and a first more important modification of the porosimetry also for the smaller pore radii. Further compression to high pressures seems to change the chaotic fabric seen post-gross yield into a regular alternation of stacks and areas of flocculated-honeycomb fabric, again similar to the fabric typology recognized in the undisturbed clay, before the gross yielding. Along with these complex post-gross yield fabric re-arrangements, orientation does not increase much. At the same time, after the reduction of the larger porosity upon gross yielding, 1D compression is seen to cause the progressive reduction in size of the DPS and of the number of dominant small pores.

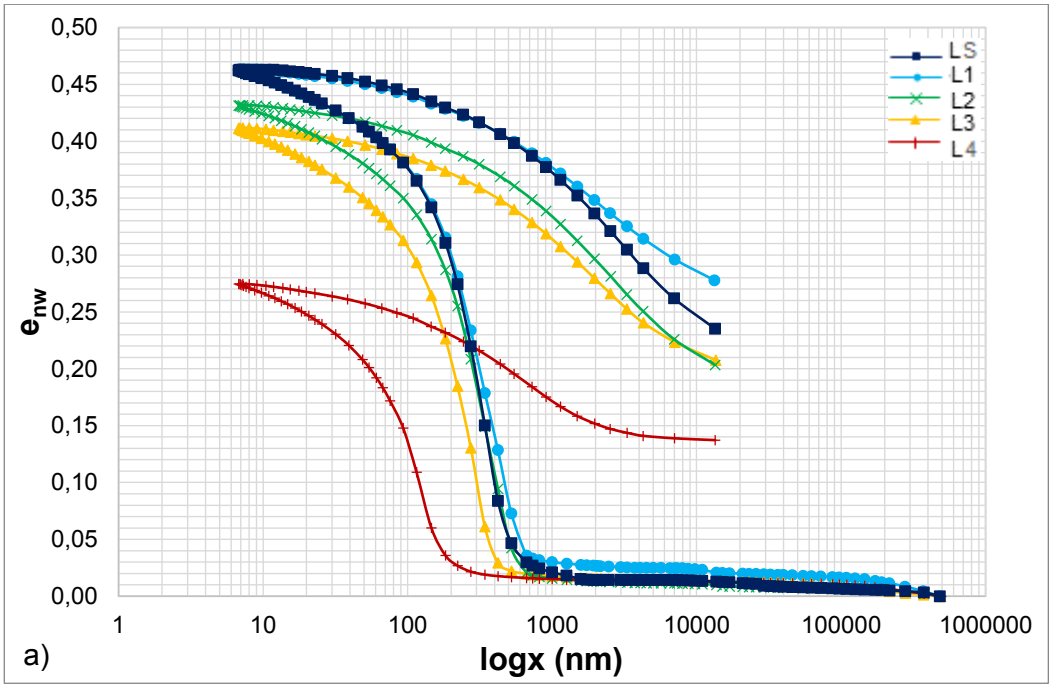
0,50
0,45
0,40
0,35
0,30
0,25
0,20
0,15
0,10
0,05
0,00
e_nw
1
10
100
1000
10000
100000
1000000
logx (nm)
LS
L1
L2
L3
L4
a)

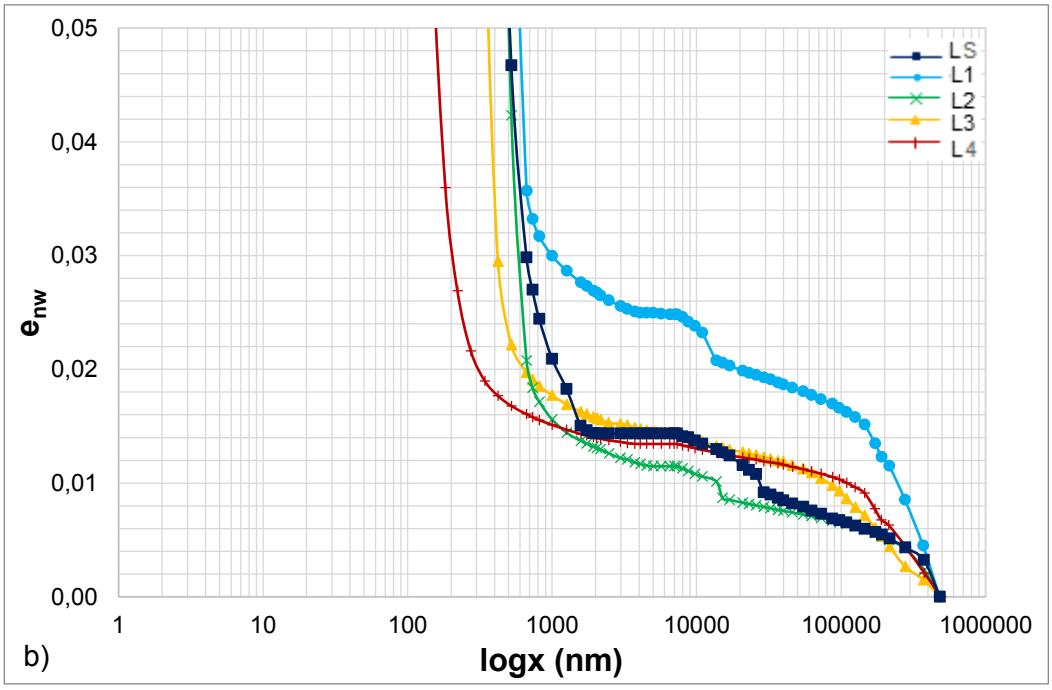
0,05
0,04
0,03
0,02
0,01
0,00
e_nw
1
10
100
1000
10000
100000
1000000
logx (nm)
LS
L1
L2
L3
L4
b)

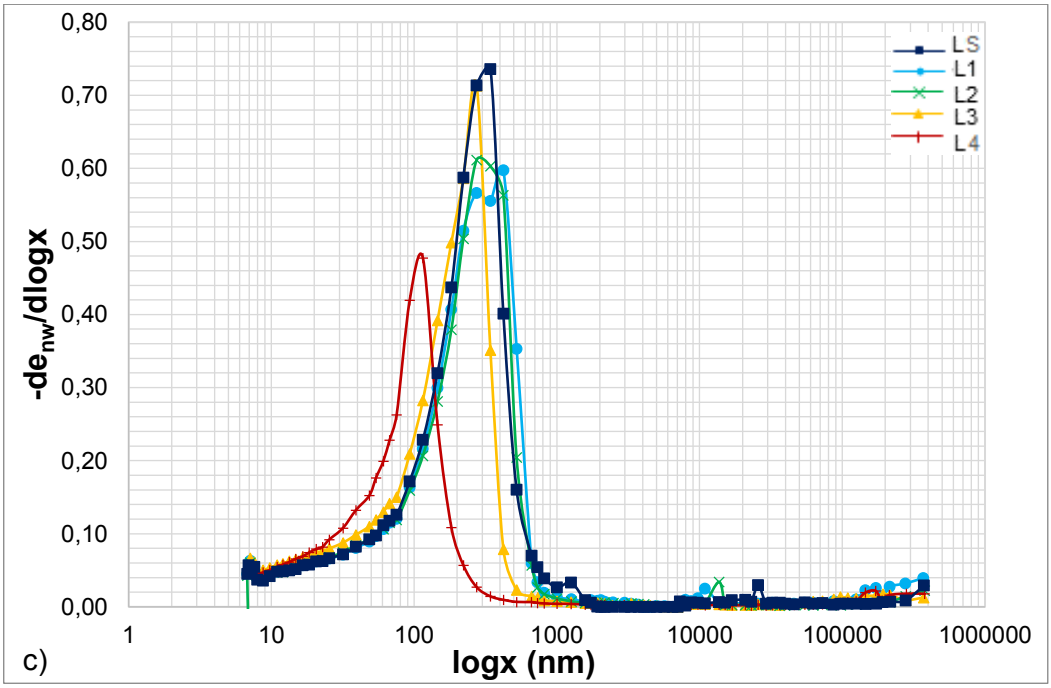

Fig. 7.61 - MIP tests on natural Lucera clay in 1D compression: a) cumulative, b) enlarged cumulative and c) derivative curves.

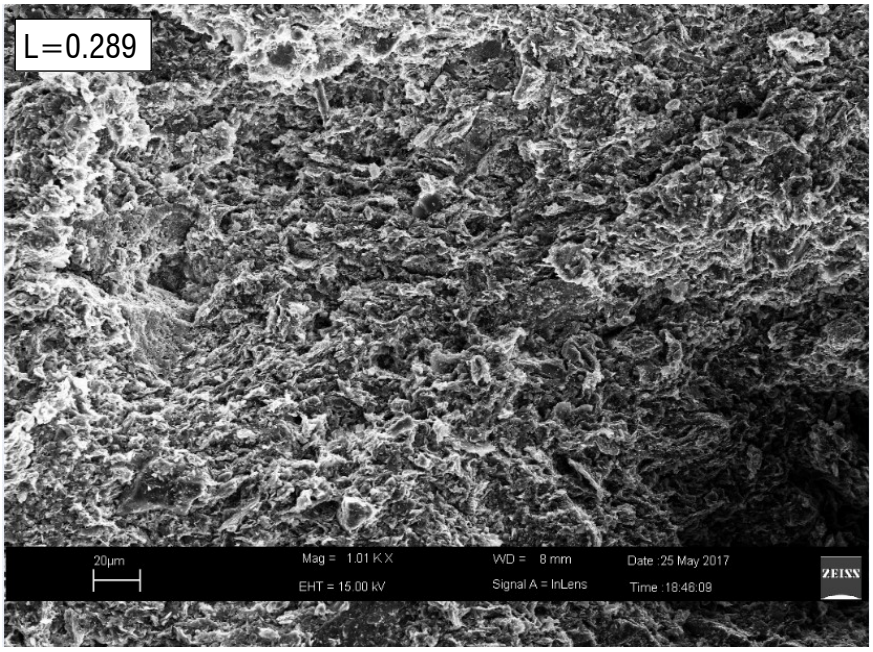

Fig. 7.62 - SEM micrograph along a vertical fracture of Lucera clay 1D compressed to σ'_v=5 MPa at medium magnification.

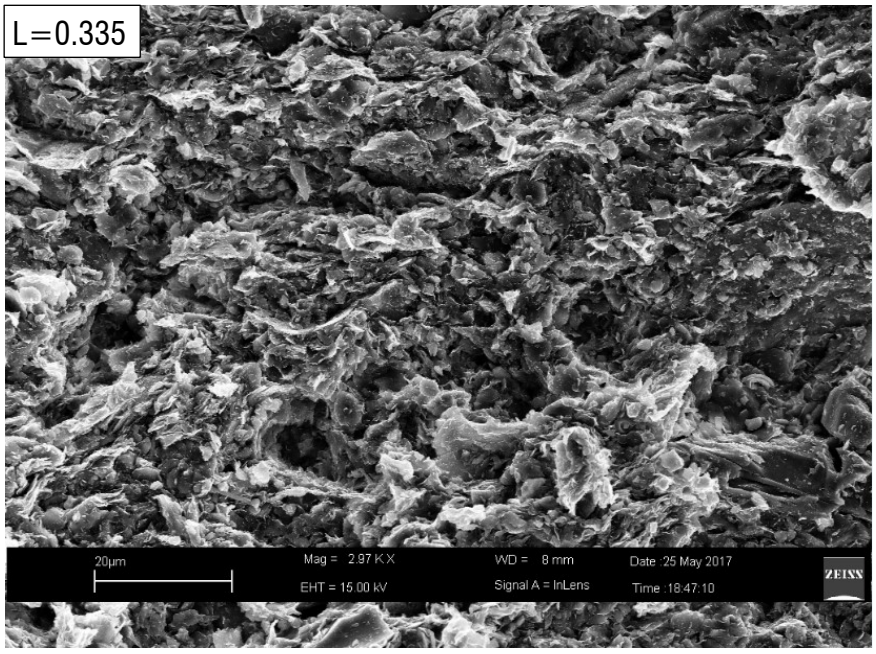

Fig. 7.63 - SEM micrograph along a vertical fracture of Lucera clay 1D compressed to σ'_v=5 MPa at medium-high magnification.

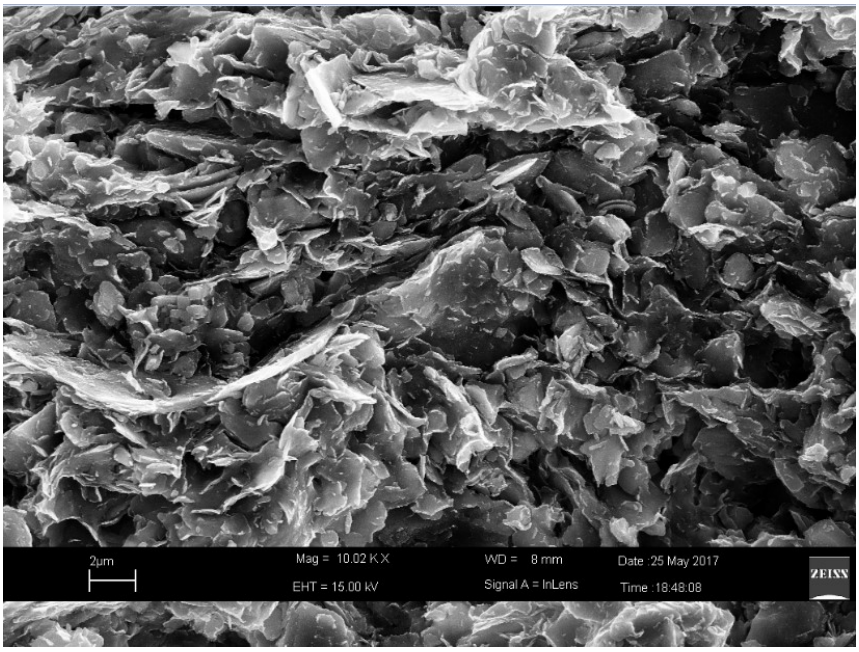

Fig. 7.64 - SEM micrograph along a vertical fracture of natural Lucera clay 1D compressed to σ'_v=5 MPa: areas of flocculated fabric.

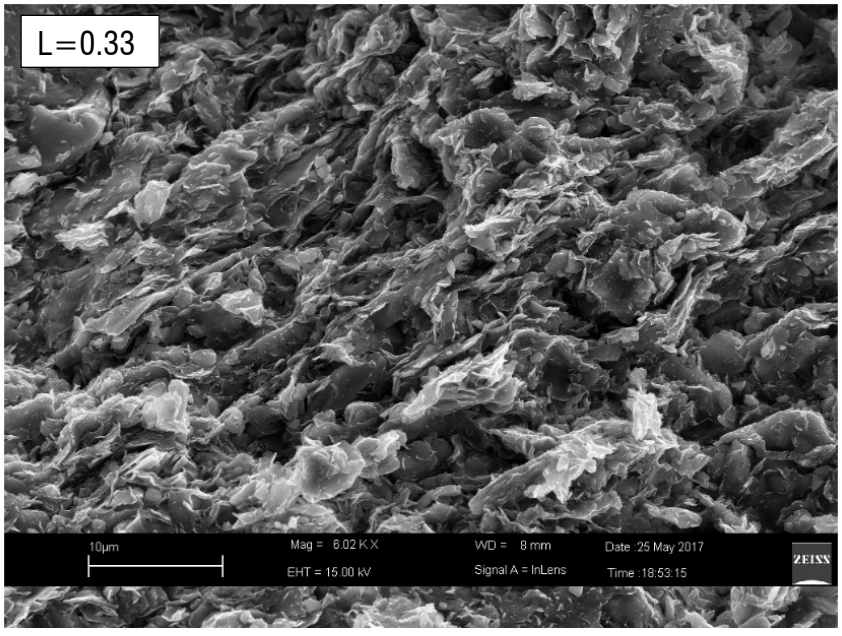

Fig. 7.65 – SEM micrograph along a vertical fracture of natural Lucera clay 1D compressed to σ'_v=5 MPa: view of a c.p.o. domain.

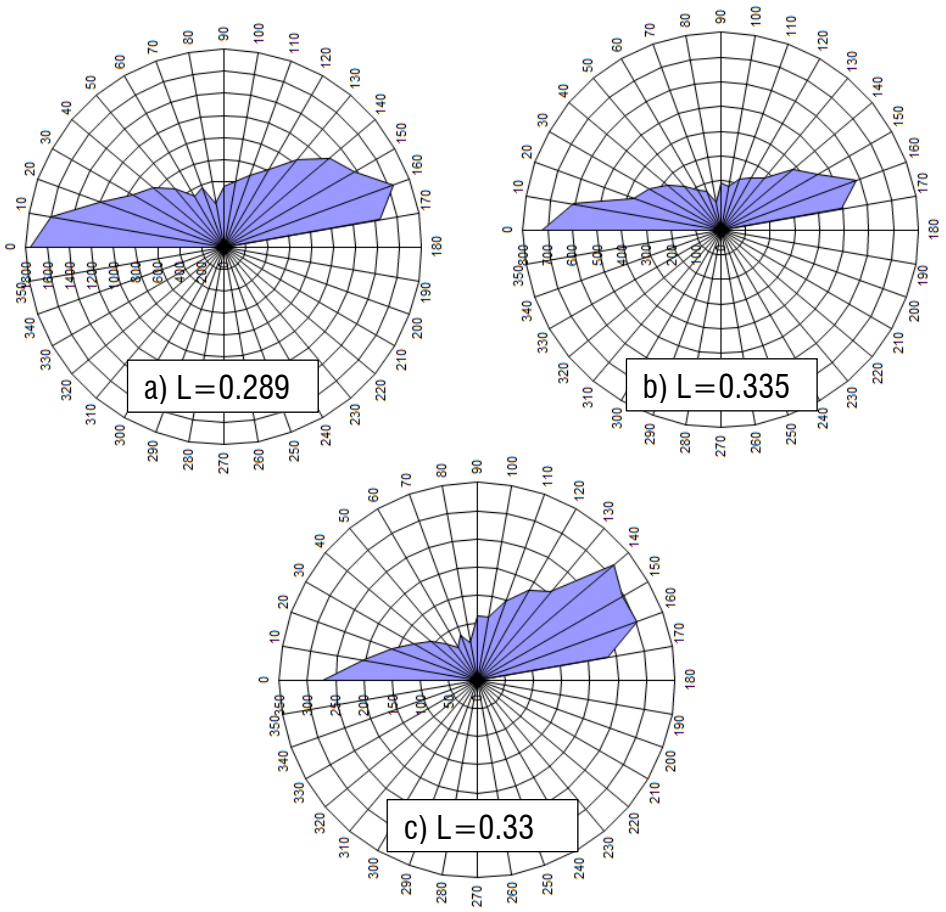

Fig. 7.66 – Direction histograms of natural Lucera clay 1D compressed to σ'_v=5 MPa, referred to a) Fig. 7.62, b) Fig. 7.63 and c) Fig. 7.65.

7.3.2 Microstructural changes in swelling for the natural clay

The changes in microstructure occurring during one-dimensional swelling paths to low pressures are investigated for both Pappadai clay and Lucera clay.

The results of a MIP test on a specimen of natural Pappadai subjected to 1D unloading to 20 kPa from the undisturbed state (point P_S) are shown in Fig. 7.42, together with the curves for the undisturbed specimen and for the specimens subjected to 1D compression. As expected, the cumulative curve (Fig. 7.42a) shows an increase in the total intruded void ratio; the macro-pore volume increases and steps are visible in the curve, which may correspond to fissures opening in the stage of undrained unloading at the end of the test. These appear as small peaks in the derivative curve.
With respect to undisturbed state (P_1), the porosimetry of the swelled specimen (Fig. 7.42b) is still monomodal, but the curve becomes wider and shorter in terms of shape, suggesting that the pore size range has become larger. The DPS is seen to translate slightly to the right, acquiring the value 270 nm, slightly higher than that of the undisturbed specimen (220 nm). On the whole, swelling does not seem to cause a major change in the clay porosimetry.

SEM pictures were taken along a vertical fracture, to observe the changes in fabric after swelling by comparison with the undisturbed state, shown in Section 7.2.1.
An observation at medium magnification (Fig. 7.67) shows quite an open and oriented fabric. Strata of highly oriented particles are recognized to cross the picture at the bottom and at the top along horizontal directions, which at places slightly bend to sub-horizontal directions and generally interbed strata of flocculated particles. A fissure can be observed in the top right corner. The enlargement in Fig. 7.69 shows a thin c.p.o. layer at the bottom, bending to a sub-vertical direction, and a thicker layer of oriented particles in the upper half of the image, along the same sub-vertical direction. The high magnification picture in Fig. 7.70 shows a highly oriented area with many particles in the horizontal direction. Remarkably, particle edges are found to be much less fringed than those seen in the compressed specimens. Small calcite crystals lying between

particles are observed, as were also observed by Cotecchia (1996) in isolated areas of the undisturbed clay.
The degree of orientation is that of a well-oriented fabric (Fig. 7.71), confirming the qualitative interpretation and suggesting that the fabric orientation has not changed much with swelling from the undisturbed state, both at medium and at high magnification. The slight increase in the L values delivered by image processing is mainly attributed to the different quality of the image obtained by means of the FESEM, which, as discussed in Chapter 5, provides higher resolution micrographs than the SEM.

In general, all the microstructural analyses contribute to describe a fabric and pore space which have not evolved much during swelling, despite the large swelling path. As discussed in Section 6.2.1, bonding does not seem to weaken much due to swelling, as on recompression a very close yield state is found.

For all the specimens of Pappadai clay under 1D compression, the orientation curves (Section 5.3.3) plotting the percentages of particles against their orientation for micrographs at the same magnification (3000x) are reported in Fig. 7.72.
The orientation curves clearly show that the fabric orientation undergoes limited changes compared to the very high pressures reached in compression and the very low pressures attained in swelling.

For natural Lucera clay, the MIP test results on the 1D swelled specimen (state L_s) are shown in Fig. 7.61. In this case, the cumulative curve of the swelled specimen (Fig. 7.61a) reaches an unexpectedly low maximum intruded volume with respect to the void ratio calculated from settlements in the swelling test. It is well known that, due to the MIP limitations, the maximum intruded void ratio does not equal the actual void ratio of the specimen and the difference which arises is due to the non-intruded porosity with entrance pore sizes lower than 10 nm and to the non-detectable porosity for pore sizes larger than 400 μm (Section 5.3.2). However, except for specimen at state L_s, for

specimens of both Lucera and Pappadai clay subjected to 1D loading the difference between the void ratio of the specimens and the maximum intruded void ratio had been always found to be repetitive. It may be hypothesised that in this specimen, a higher non- detectable porosity was present, due for example to the widening, during the MIP specimen preparation, of some fissures opened in the undrained unloading stage.
The inter-aggregate intruded volume is found to be lower than that of the undisturbed specimen (Fig. 7.61b), which is quite an unexpected result, probably affected by the anomaly in the difference of the maximum intruded void ratios. The incremental curve is slightly tighter than that of specimen L_1, with a DPS of 340 nm similar to the average 300 nm found for L_1. The frequency of the DPS is lightly higher, differently from what observed for Pappadai clay.

No SEM micrographs were taken for the specimen to support the investigation of the microstructure evolution. However, also in this case the MIP results are suggesting that no significant evolution of pore space has occurred in the specimen unloaded to low pressures. Bonding degradation is considered not be significant because when recompressed after swelling the clay exhibits the same yield stress (Section 6.2.1). In the light of this observations, also the fabric of natural Lucera clay is believed not to undergo dramatic changes under swelling.

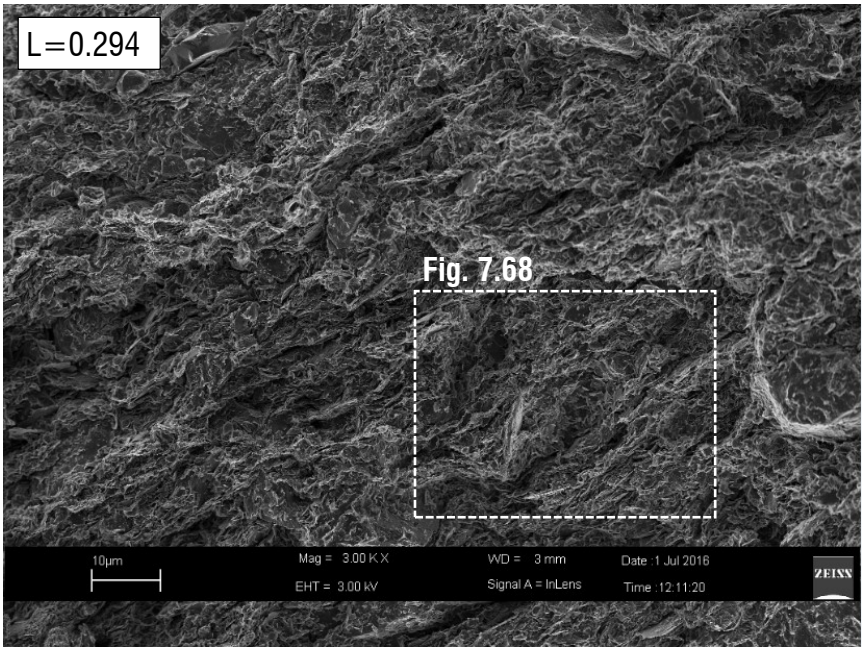

Fig. 7.67 - SEM micrograph along a vertical fracture of natural Pappadai clay 1D swelled to σ'_v=20 kPa at medium magnification.

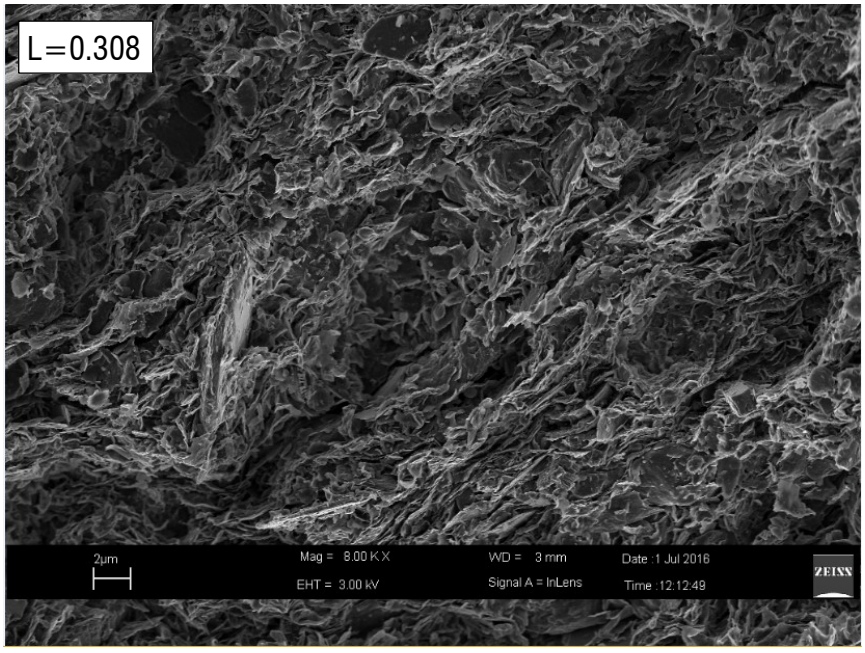

Fig. 7.68 - SEM micrograph along a vertical fracture of natural Pappadai clay 1D swelled to σ'_v=20 kPa: enlargement of Fig. 7.67.

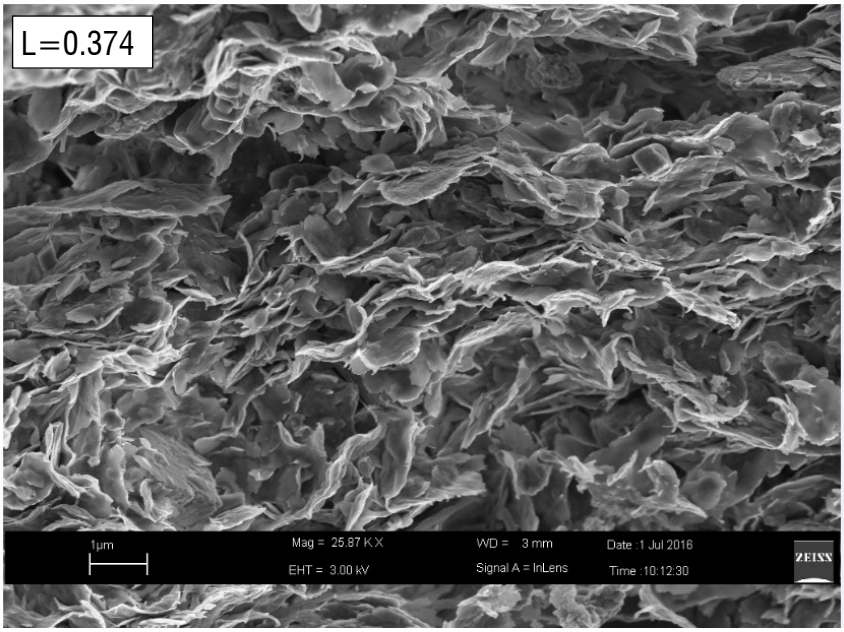

Fig. 7.69 - SEM micrograph along a vertical fracture of Pappadai clay after swelling to σ'_v=20 kPa at high magnification.

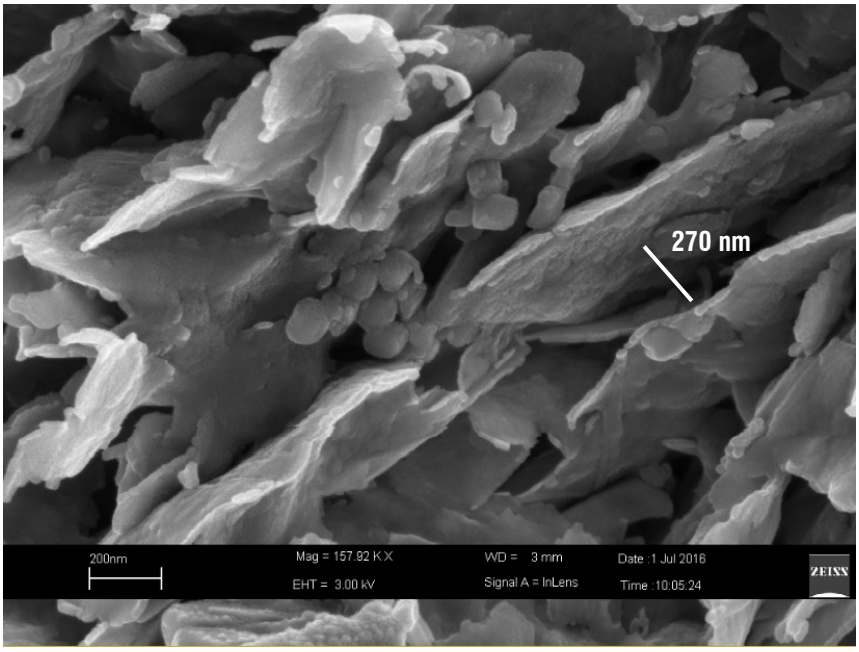

Fig. 7.70 - SEM micrograph along a vertical fracture of Pappadai clay after swelling to σ'_v=20 kPa: pores between particles approaching the DPS.

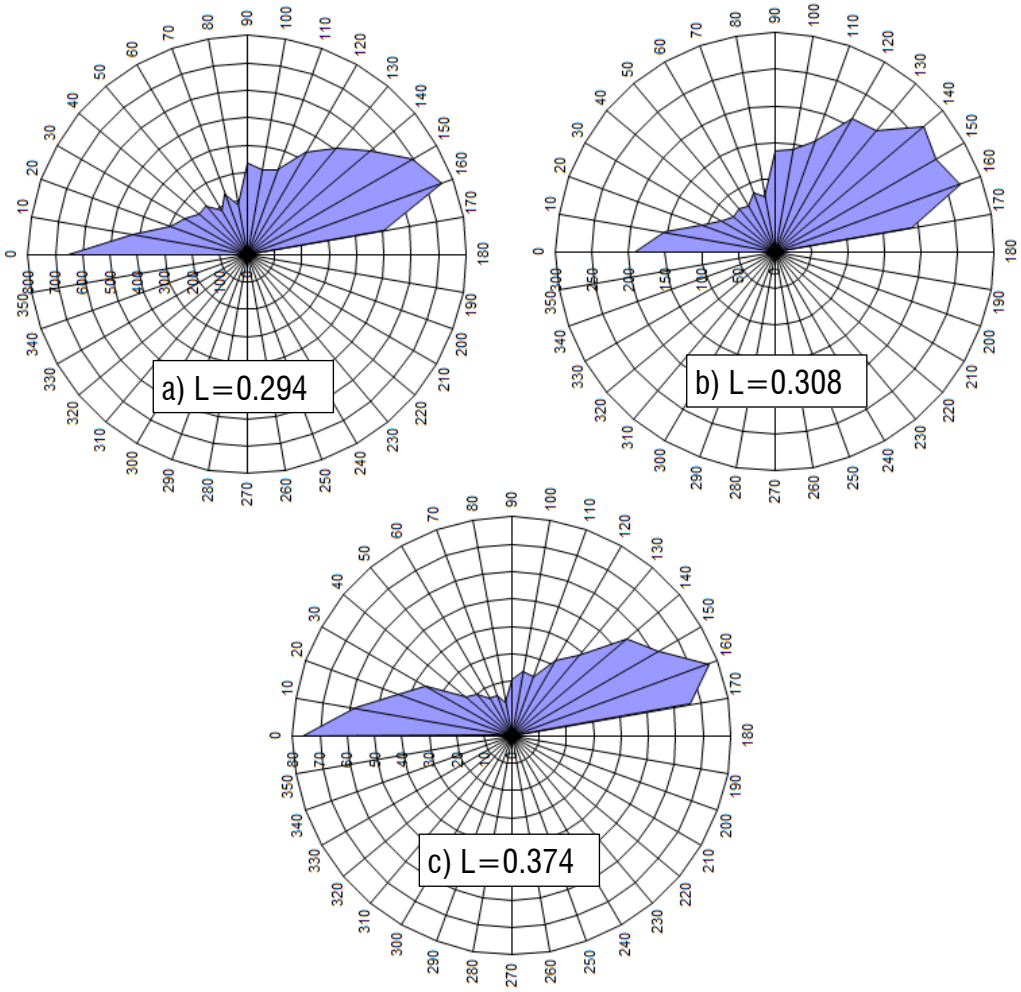

Fig. 7.71 – Direction histograms of Pappadai clay after swelling to σ'_v=20 kPa of the micrographs in a) Fig. 7.67, b) Fig. 7.68 and c) Fig. 7.69

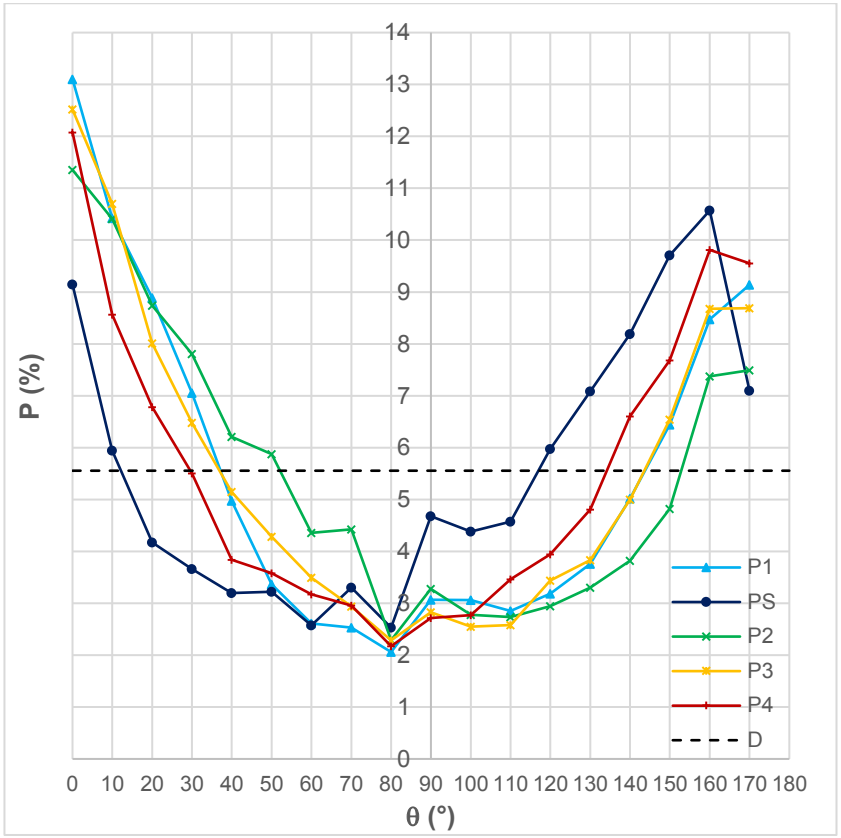

Fig. 7.72 – Orientation curves from SEM micrographs at the same magnification (3000x) for natural Pappadai clay under 1D compression.

7.3.3 Microstructural changes in 1D compression for the reconstituted clay

In this section the microstructure evolution in oedometer compression of the reconstituted Pappadai clay and Lucera clay is analysed.

For reconstitued Pappadai clay, two oedometer tests were performed on the clay consolidated in the consolidometer to σ'_v=200 kPa, to state PR_1 (σ'_v =600 kPa) and to state PR_2 (σ'_v=5000 kPa). The MIP results at these two compression stages are compared with that of the specimen after the consolidation in the consolidometer (Fig. 7.73). The latter microstructure was discussed in Section 7.2.2 and will be considered of reference as initial state.

A progressive reduction in the maximum intruded pore volume is recognized from the cumulative curves, with a concurrent gradual, but significant reduction in the macro-pore volume, which is found to be very low at state PR_2. Similarly to the undisturbed clay under 1D compression, the incremental curves for the reconstituted clay seem to translate towards smaller DPS, becoming narrower with increasing σ'_v. The DPS is seen to shift from an initial value of 420 nm to 270nm at point PR_1 and subsequently around 130 nm at point PR_2. The frequency of the DPS only mildly increases at state PR_1, then falls at state PR_2.

The investigation of the clay fabric by means of SEM applications could not be performed on these two specimens. However, Cotecchia (1996) observed the fabric of the reconstituted clay compressed to a vertical stress of 22 MPa and a void ratio of about 0.3. Some considerations can be done by observing the corresponding SEM micrographs, on which the degree of fabric orientation was measured on purpose.

Global views of the fabric on vertical fractures through the clay are shown in Fig. 7.74. The striking feature of the fabric is its very dense packing. The increase in density of packing is evident in the comparison of these figures with Fig. 7.26, which shows the reconstituted fabric at a void ratio of 1.24.

The fabric at low pressures is rather open and different particle arrangements can be quite easily distinguished. This is much more difficult in the very dense fabric of the clay compressed to high pressures. At low pressures the fabric shows a medium-high

degree of orientation (0.27), whereas in the clay compressed to large pressures a significant fabric orientation is not apparent. In the highly compressed clay shown in Fig. 7.74b, stacks of particles differently oriented and areas of flocculated fabric merge with random or even chaotic particle assemblages. Thus, also for the reconstituted clay the fabric changes are not uniform during compression. The size of the oriented domains increases with compression, but these are also distorted and merge with chaotic aggregates (Fig. 7.75). In areas of more chaotic and less oriented fabric (Fig. 7.76), small particles are often found stuck on the surface of the large particle domains or penetrate into the domains. Chaotic packings of particles similar to the "chaotic masses" seen in the natural clay post-yield can also be recognized in the reconstituted clay at large pressures. Moreover, the surface of clay particles appears to be more damaged than at 200 kPa vertical pressure, suggesting that compression affects also the reconstituted clay particles.

The estimated average degree of fabric orientation is around 0.23 (Fig. 7.77), slightly lower than that found at initial state. Thus, 1D virgin compression to very high stresses appears not to give rise to an increase in orientation, but the fabric keeps being overall well-oriented.
The fabric of the reconstituted Pappadai clay at high stresses is more disordered than expected by Sfondrini (1977) (Fig.2.21). Moreover, it is much less oriented than the kaolin normally consolidated to 4.9 MPa observed by V. Cotecchia et al. (1982) (Fig.2.22) or than the bentonite normally consolidated to 6.3 MPa shown by Hicher et al. (2000) (Fig.2.28). Presumably, the mineralogical composition of the clay influences the fabric changes, so that with increasing compression the fabric orientation of mono-mineralic clay seems greater than the clay formed of different clay minerals.

In the light of this discussion, the orientation of the fabric at intermediate compression states such as PR_1 and PR_2 is not expected to increase with respect to the initial state. In general, 1D compression of the reconstituted Pappadai clay is closing the larger pores and reducing the size of the smaller pores, thus increasing the density of the clay

fabric, without significantly increasing the average orientation. As for the natural clay, the changes in fabric occurring in the reconstituted clay are highly non-uniform.

Reconstituted Lucera clay compressed to state LR_1 at a σ'_v of 15 MPa shows changes in the pore space very similar to those observed for reconstituted Pappadai clay. In Fig. 7.78 the clay compressed to a void ratio of 0.289 has strongly reduced the macro-pores and reduced the overall pore sizes. The incremental curve has not only markedly shifted towards much lower entrance pore diameters, but has also become much thinner and changed its shape to a perfectly monomodal trend. Despite the very small reduction in frequency, the DPS has importantly changed from around 1 μm to 115 nm, i.e. of one order of magnitude.

If the fabric evolution of reconstituted Pappadai clay is assumed to apply also to reconstituted Lucera clay, the latter should have acquired a medium-high orientation of fabric at a pressure not much higher than 100 kPa and then preserved this degree of orientation, without significant changes with 1D compression. The pore space may have consistently reorganized in the initial phase giving a more ordered and regular incremental curve, with DPS progressively reducing with increasing pressures. This hypothesis will be discussed in further detail in Chapter 8.

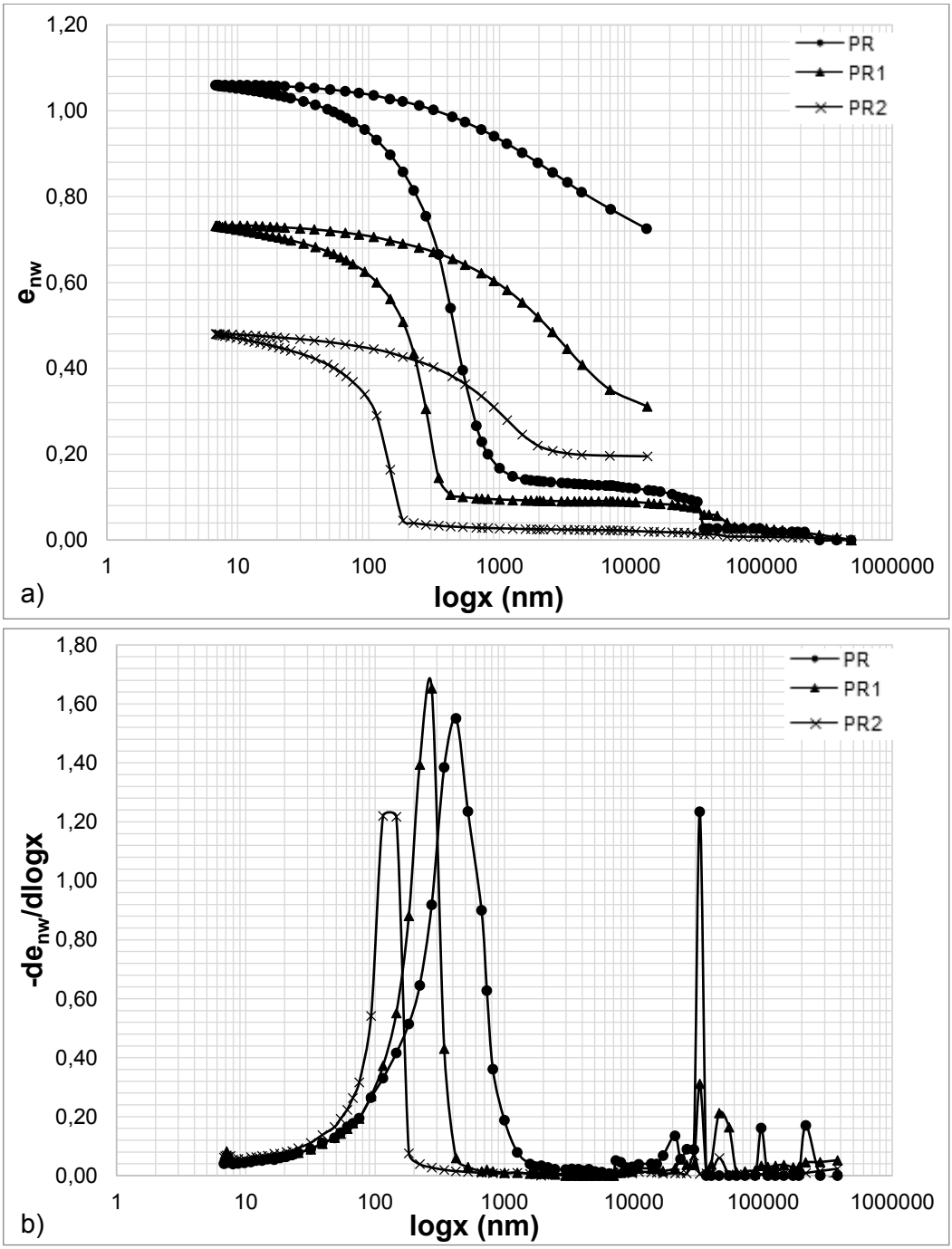

Fig. 7.73 - MIP tests on reconstituted Pappadai in 1D compression. a) cumulative and b) derivative curves.

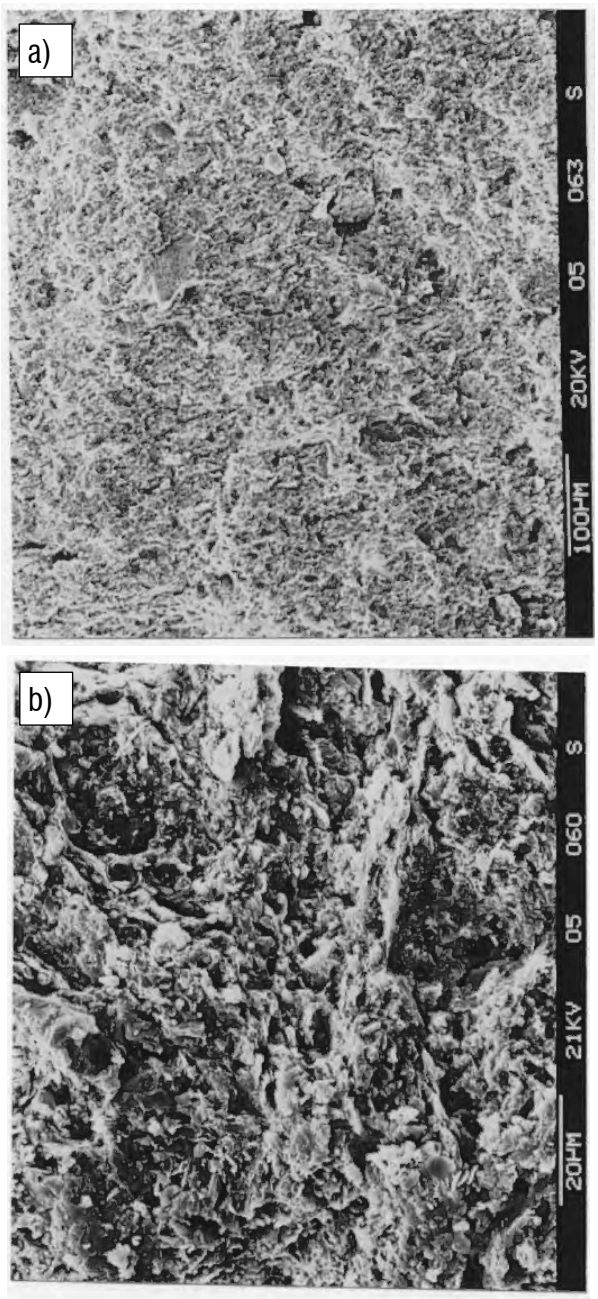

Fig. 7.74 – SEM micrographs of reconstituted Pappadai clay compressed to a σ'_v of 22 MPa: fabric on fractures inclined to the horizontal (after Cotecchia, 1996).

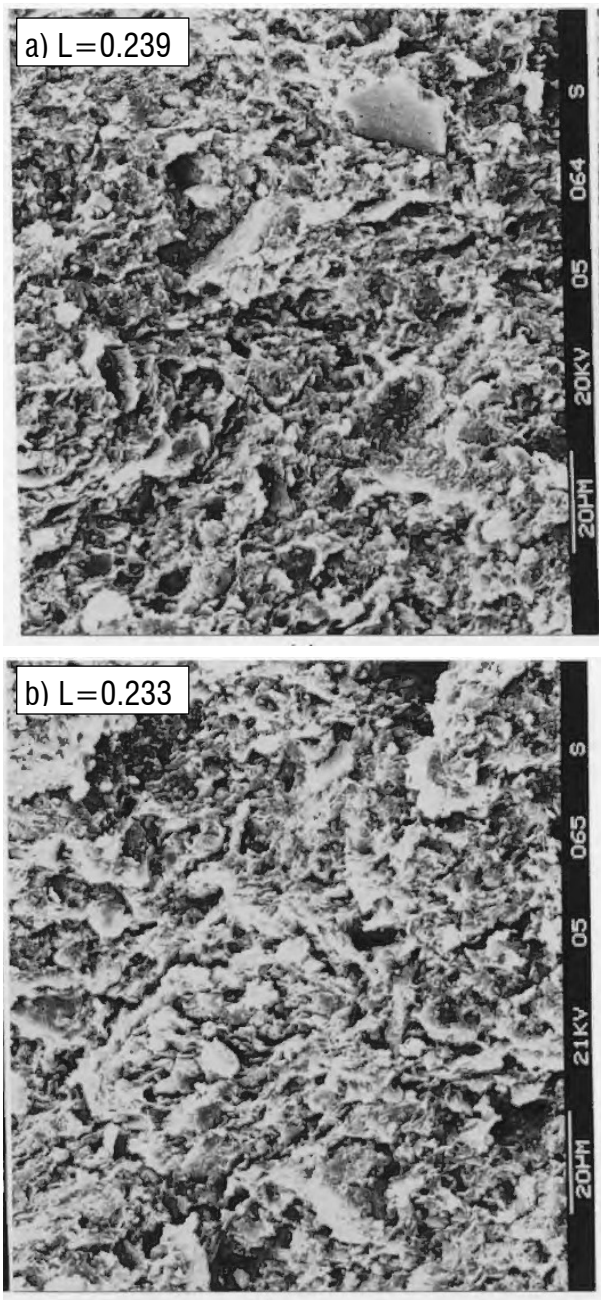

Fig. 7.75 - SEM micrographs of reconstituted Pappadai clay compressed to σ'_v of 22 MPa: fabric on vertical fractures at medium magnification (after Cotecchia, 1996).

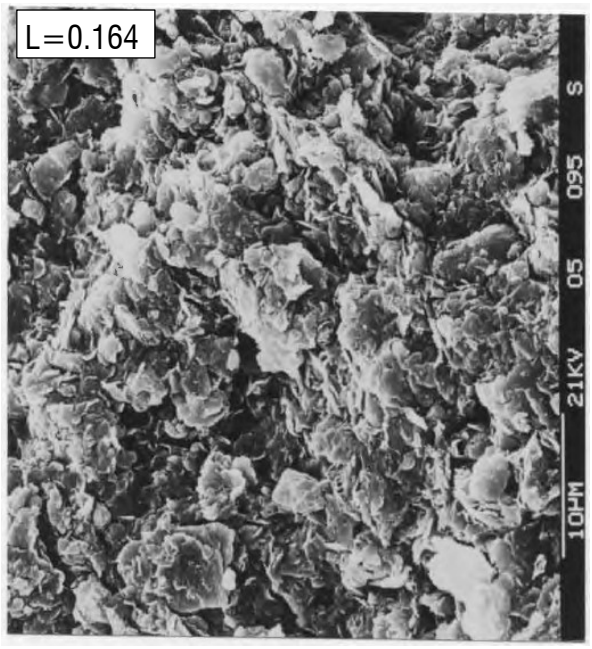

Fig. 7.76 – SEM micrograph on reconstituted Pappadai clay compressed to σ'_v of 22 MPa: areas of chaotic fabric where the small particles are either stuck on the surface of the domains or penetrate into them (after Cotecchia, 1996).

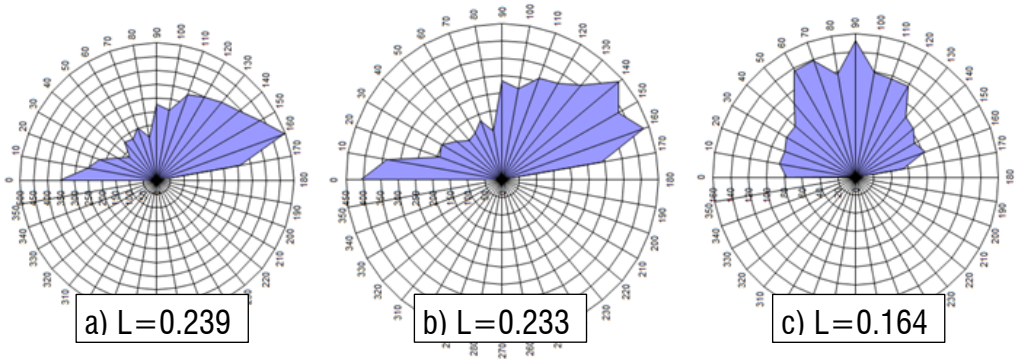

Fig. 7.77 – Direction histograms of reconstituted Pappadai clay compressed to σ'_v of 22 MPa of a) Fig. 7.75a, b)Fig. 7.75b and c) Fig. 7.76.

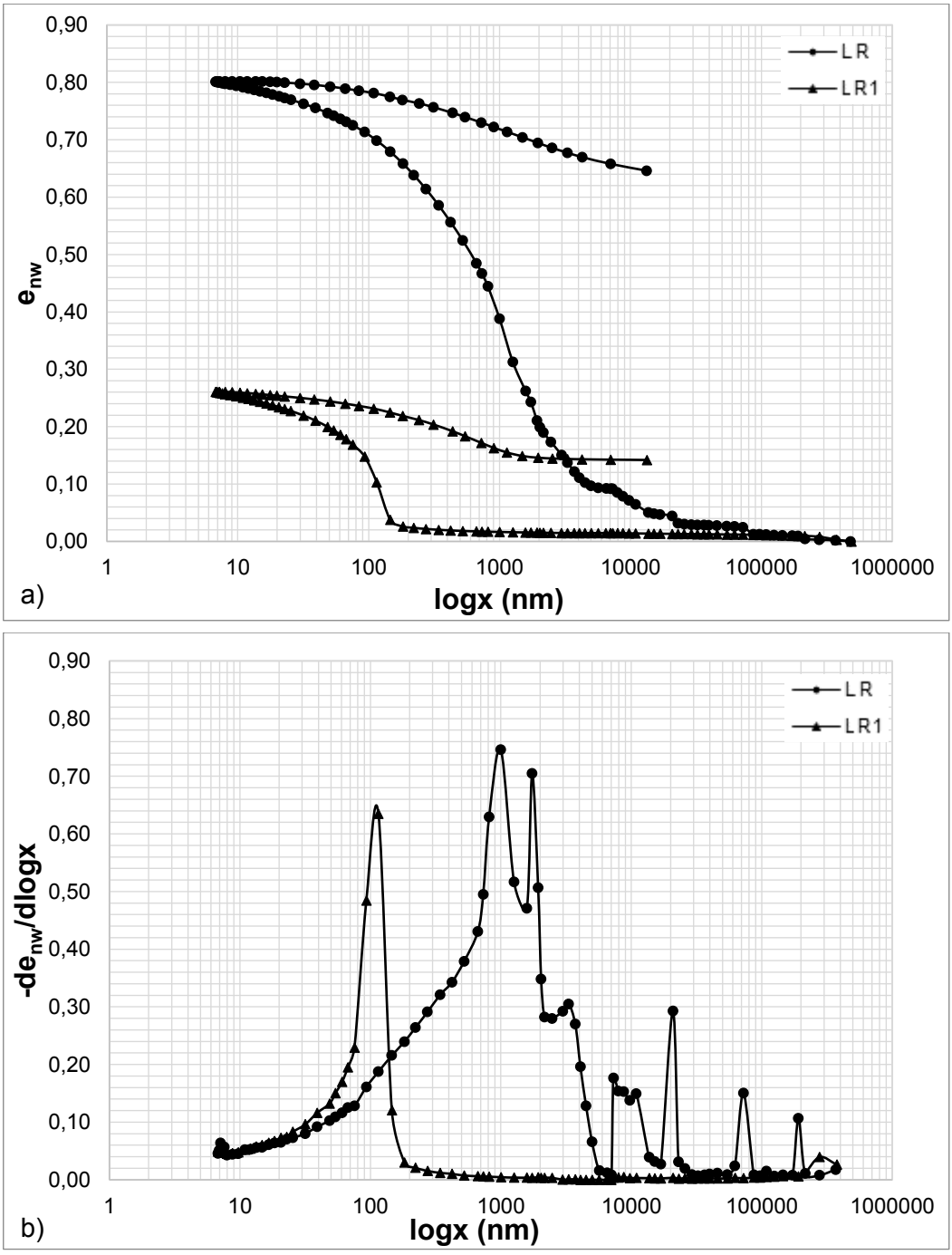

Fig. 7.78 – MIP tests on reconstituted Lucera clay in 1D compression. a) cumulative and b) derivative curves.

7.3.4 Microstructural changes in isotropic compression for the natural clay

The investigation of changes occurring in the microstructure with isotropic compression was made on both natural Lucera clay and reconstituted Pappadai clay specimens. In this section, the changes observed for natural Lucera clay will be discussed.

For natural Lucera clay, the pre-gross yield state LI_2 and the post-gross yield state LI_3 (Fig. 7.41) were analysed by means of both MIP and SEM micrographs. The latter were also subjected to image processing. The isotropic states LI_2 and LI_3 were chosen has to have void ratios similar to those of oedometric states L_2 and L_3, discussed in Section 7.3.1.

The results of MIP tests on states LI_2 and LI_3 are compared with that on the undisturbed specimen L_1 in Fig. 7.79.

Isotropic compression to pre-gross-yield state LI_2 induces a small reduction in void ratio, so the maximum intruded volume of LI_2 and L_1 are very similar. The effects of compression on the cumulative curve is particularly seen in the reduction of the macro pore-volume, which is reduced at all macro-void sizes. Minor differences are observed in the steeper part of the curve, as confirmed by the comparison of incremental curves. The latter are seen to be similar but not identical, indicating that some changes have happened in the pore volume prior to isotropic gross yield, differently from what seen for the case of one-dimensional loading. The curve for the undisturbed specimen is lightly wider on the right side, whereas the two left branches perfectly coincide for entrance pore diameters lower than 200 nm. The dominant pore of the compressed specimen LI_2 is more pronounced and has a higher frequency, but its size is equal to the average DPS for the undisturbed specimen.

If the incremental curves are compared for states L_2 and LI_2 (Fig. 7.80), it is seen that isotropic compression caused more changes, although not dramatic, in the pore size distribution than oedometric compression. However, it should be noted that the state paths followed to compress the clay isotropically from L_1 to LI_2 and one-dimensionally

from L_1 to L_2 (Fig. 7.41) closely approach the gross-yield pressures, respectively in isotropic and K_0 compression. In spite of this, only small changes seem to be caused to the pore volume.

The fabric of the natural clay at state LI_2 is shown in Fig. 7.81 and appears well packed. Strata of oriented domains can be recognized, which interbed flocculated aggregates generating much variable particle arrangements close to each other. Stacks of c.p.o. and domains in which the fabric is more chaotic and particles are mainly in edge to face contact are observed at larger magnification in Fig. 7.82. The degrees of orientation and corresponding direction histograms, reported in Fig. 7.83, show a well-oriented fabric with a medium-high degree of orientation (0.26-0.29), not much changed with respect to the undisturbed fabric.

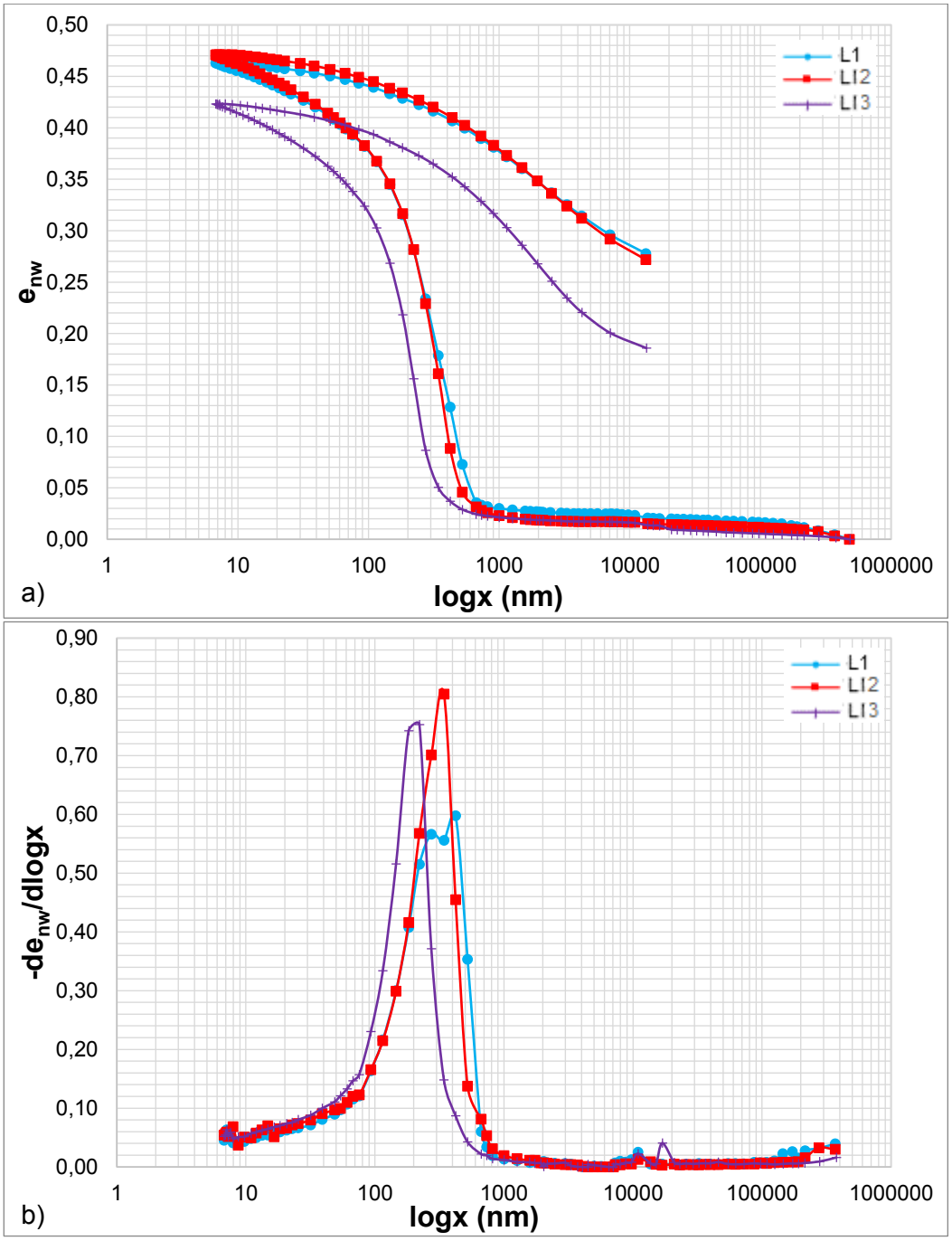

Fig. 7.79 – MIP tests on natural Lucera clay after isotropic compression: a) cumulative and b) derivative curves.

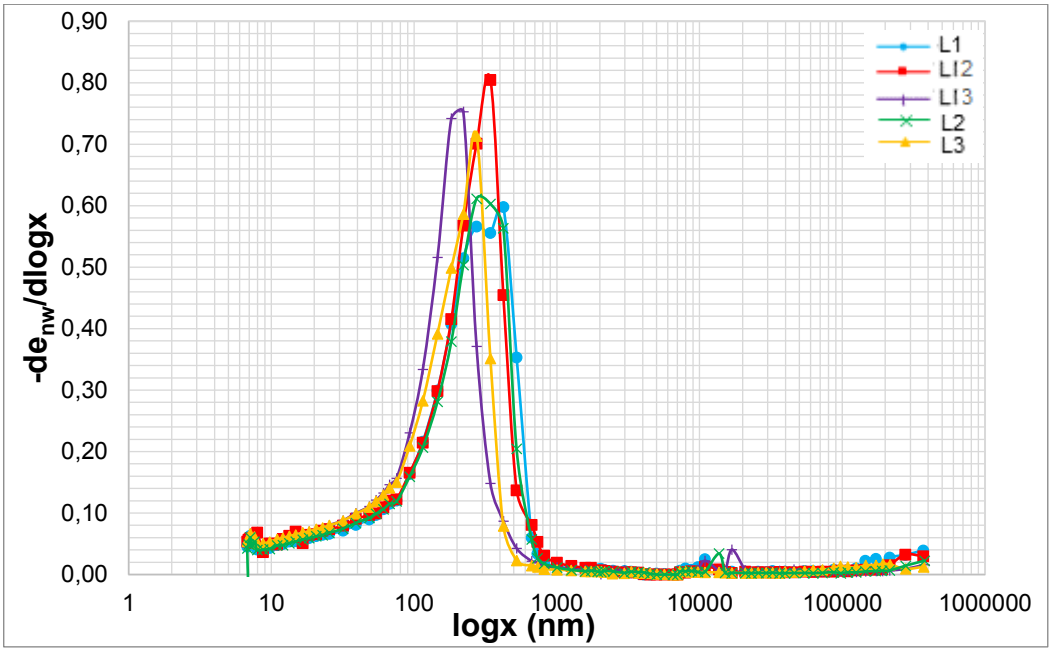

Fig. 7.80 – Comparison of incremental curves for specimens of natural Lucera clay 1D and isotropically compressed to states pre- and post- gross-yield to approximately the same void ratios.

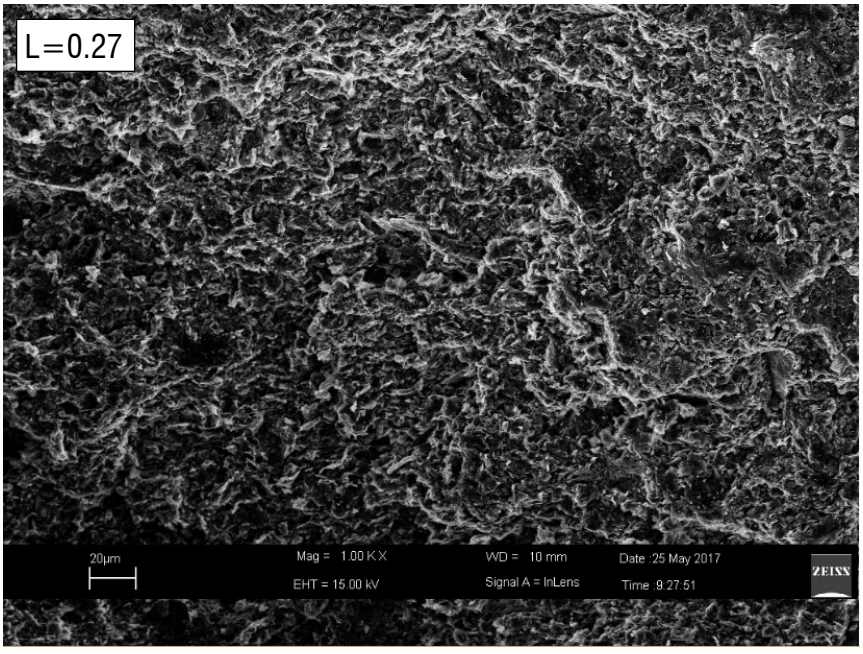

Fig. 7.81 – SEM micrograph of natural Lucera clay isotropically compressed to pre-gross-yield state LI_2 along a vertical fracture at medium magnification.

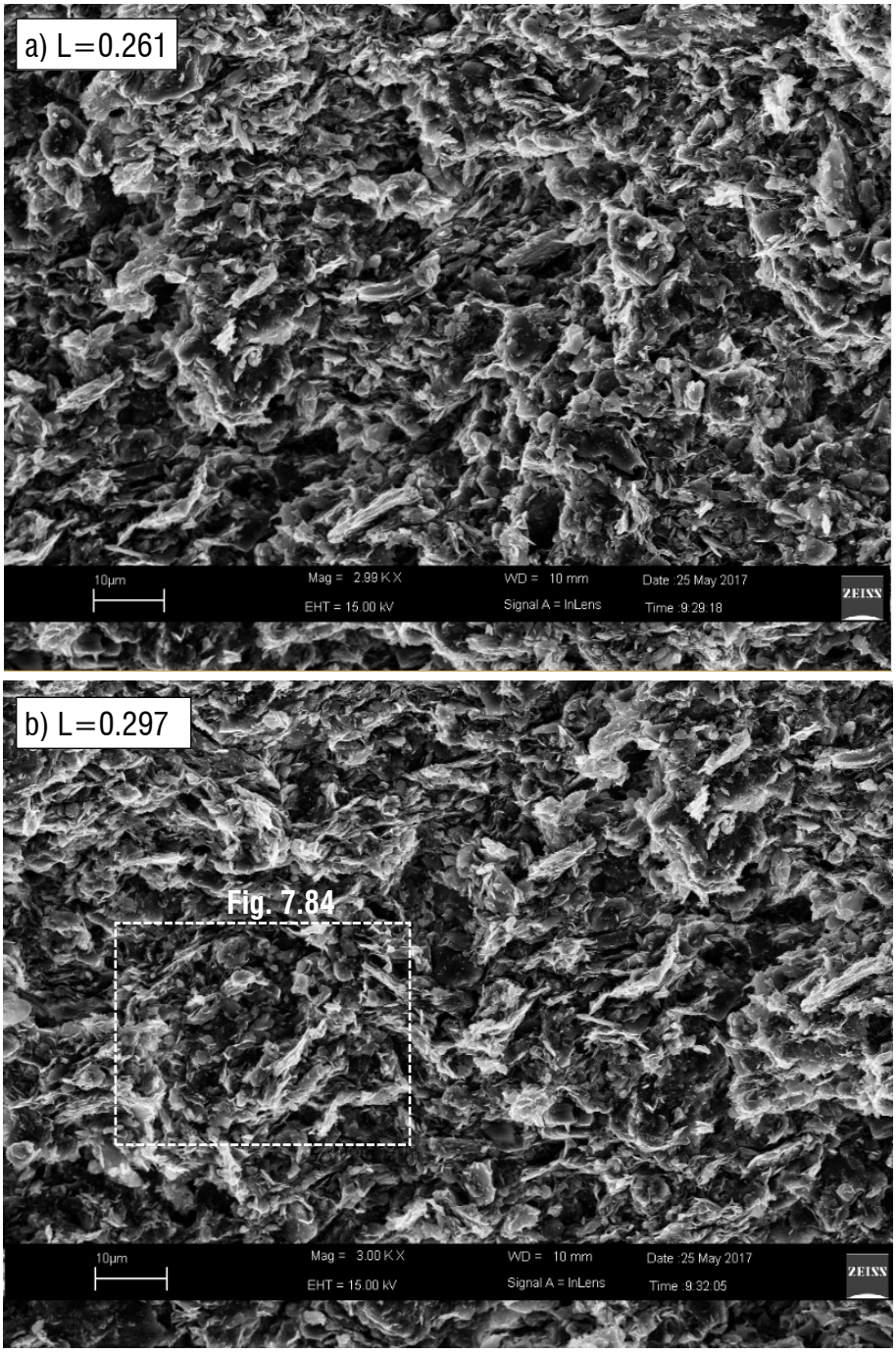

Fig. 7.82 - SEM micrographs of natural Lucera clay isotropically compressed to pre-gross-yield state LI_2 along a vertical fracture at medium-high magnification.

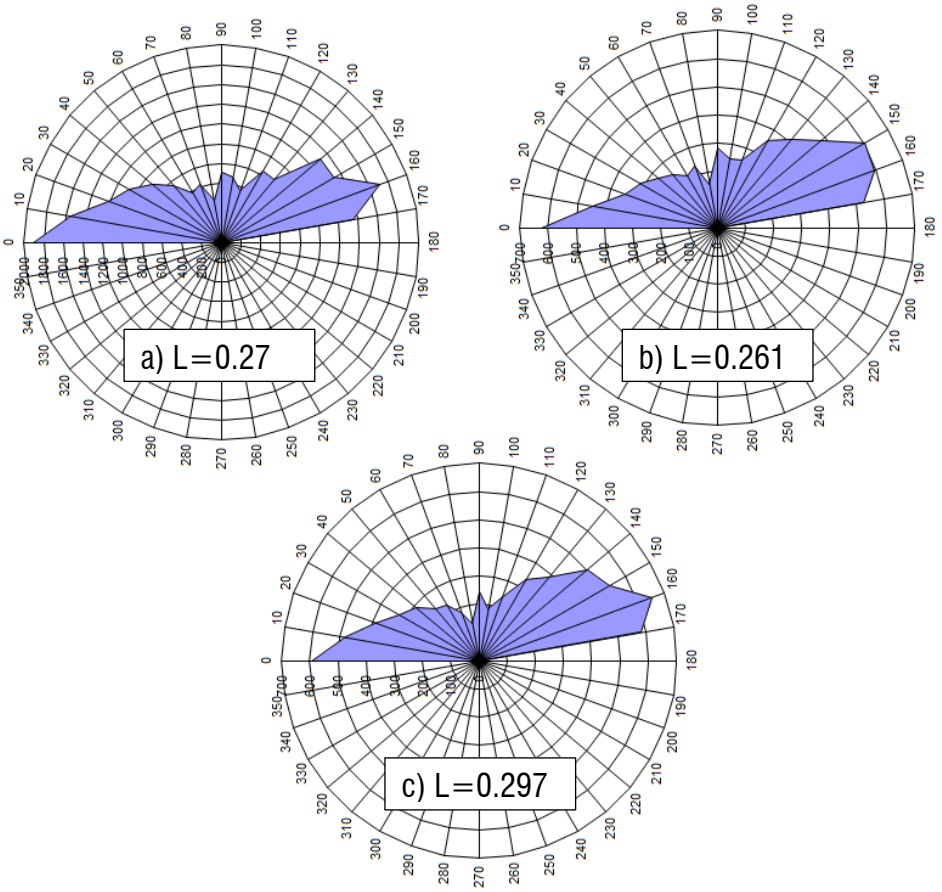

Fig. 7.83 – Direction histograms of natural Lucera clay under isotropic loading to pre-gross-yield state LI_2 of a) Fig. 7.81, b) Fig. 7.82a and c) Fig. 7.82b.

Zooming to very high magnifications (Fig. 7.84), domains can be recognized of thin face-to-face particle strata forming circles which enclose random particles in mainly edge-to-face contacts. These domains, resembling “nuclei” of clay particles, are often seen along vertical fractures (Fig. 7.84, Fig. 7.85); at places, nuclei are found to divide strata of c.p.o. domains (Fig. 7.86).

These particular fabric domains are not observed in the undisturbed or one-dimensionally compressed clay, and are likely to be an effect of isotropic consolidation.

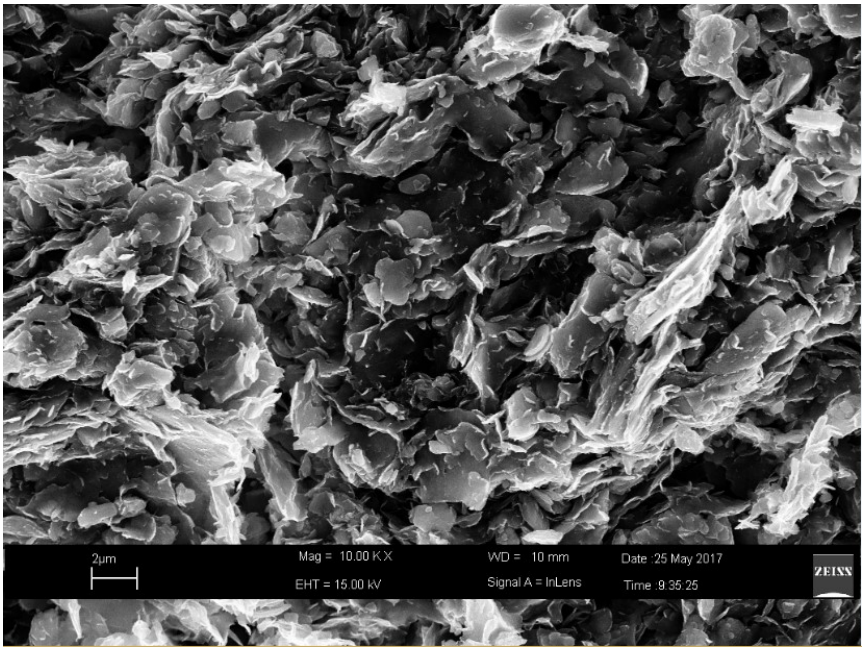

Fig. 7.84 – Enlargement of the micrograph in Fig. 7.82b showing a nucleus formed by clay particles.

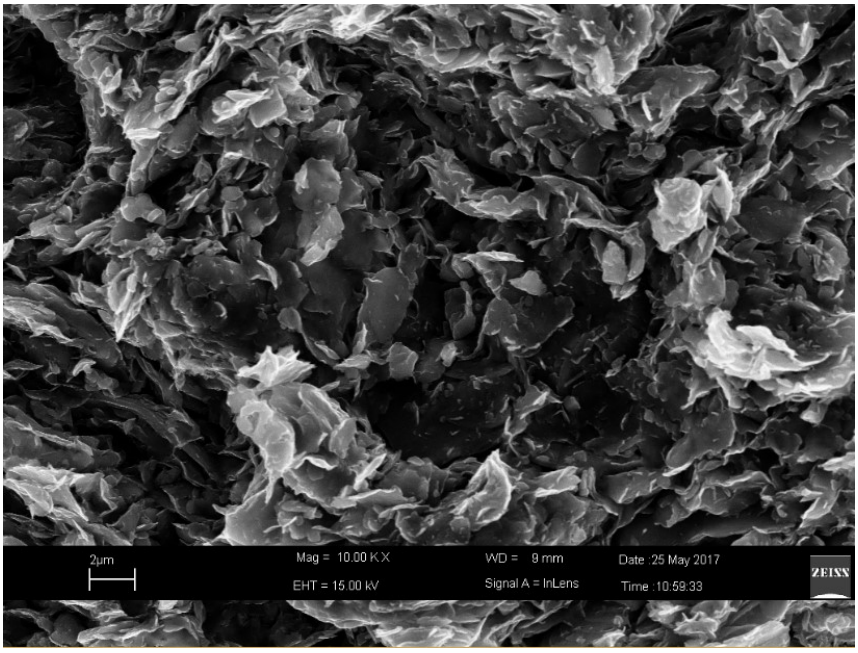

Fig. 7.85 - SEM on natural Lucera clay at state LI_2 along a vertical fracture: example of a particular particle domain.

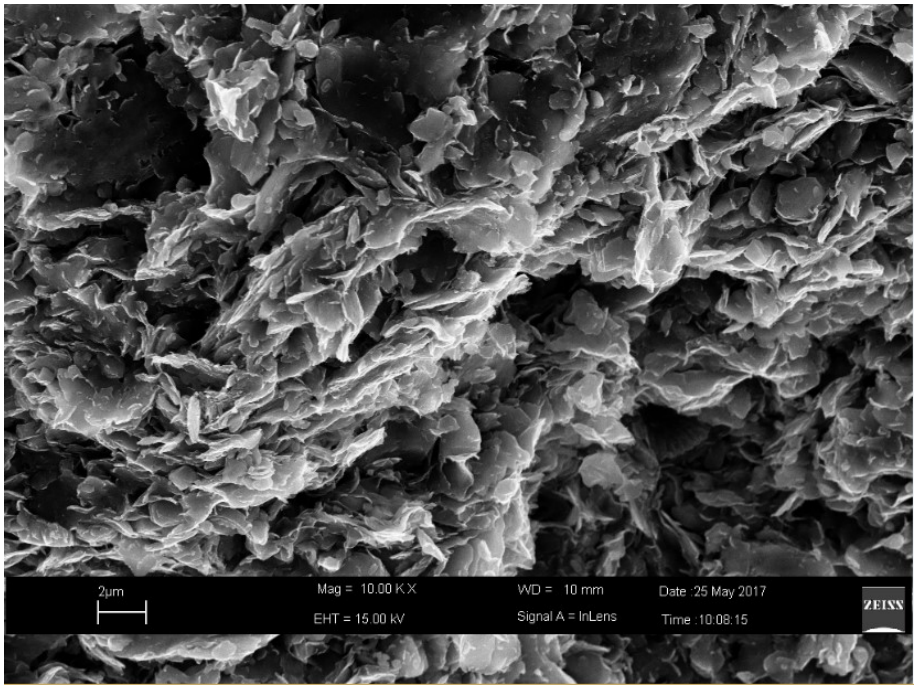

Fig. 7.86 – SEM on natural Lucera clay at state LI_2 showing two nuclei separated by a c.p.o. strata.

When further isotropically compressed to state LI_3, natural Lucera clay mainly experiences a reduction of the DPS to 220 nm, with a small reduction of frequency and a general translation to the left of the incremental curve (Fig. 7.79). This is seen to shift towards lower pore sizes with respect not only to the curve corresponding to state LI_2, which is quite expected, but also with respect to the curve relative to state L_3 (Fig. 7.80). Hence, for natural Lucera clay isotropic compression is seen to alter more than oedometric loading the whole pore size distribution.

The view of specimen LI_3 along a vertical fracture (Fig. 7.87) shows a densely packed fabric in which, other than the long horizontal complex lamina crossing the picture horizontally, many shorter stacks of particles are observed and merge with domains of far less oriented fabric. Overall the fabric appears well oriented, as confirmed by the degree of orientation, corresponding to a well-oriented fabric.

Higher magnification micrographs (Fig. 7.88, Fig. 7.89) again show an almost regular fabric of medium-high orientation in which domains of platy face to face particles interbed more random particle aggregations.
Enlargements (Fig. 7.90, Fig. 7.91) show the presence of small particle aggregations in concentric layouts similar to the those observed in the specimen LI_2, but more compressed and almost completely filled with smaller particles.
Similar particle aggregates defining concentric layouts with distinct nuclei were recognized by Cafaro and Cotecchia (2001) in the weathered yellow Montemesola clay. In that case, the randomly oriented floccules were considered the result of the presence of capillary stresses related to the important drying experienced by the clay. Hence, this type of geometry of particle domains is likely to be associated to the effects of isotropic loading.
The results of image processing on the very enlarged micrographs (Fig. 7.90, Fig. 7.91) show that zones exist in which the fabric orientation is lower.

In general, isotropic compression to medium-high pressures (state LI_3) does not induce significant changes in the fabric orientation recorded at medium magnification, which keeps being well-oriented and at places is found even more oriented than the undisturbed fabric. Accordingly, the pore space does not undergo marked changes and only a small reduction in the DPS is observed.
It is suggested that the pressure reached in isotropic compression to state LI_3, being about 1.5 times the isotropic gross-yield stress, is not capable of changing significantly the fabric architecture developed with one-dimensional loading and is still too low to induce a major microstructure evolution. Hints are found which suggest the alteration of some particle domains, but larger pressures need to be reached to obliterate the fabric architecture produced by one-dimensional loading.

In conclusion, the results of the image processing of micrographs of equal magnification ($\approx$1000x) were used to plot orientation curves for the specimens 1D and isotropically compressed (see Section 5.3.3). The curves are reported in Fig. 7.93 and

confirm that little differences arise with compression in either one-dimensional or isotropic paths to the medium-high pressures reached so far.

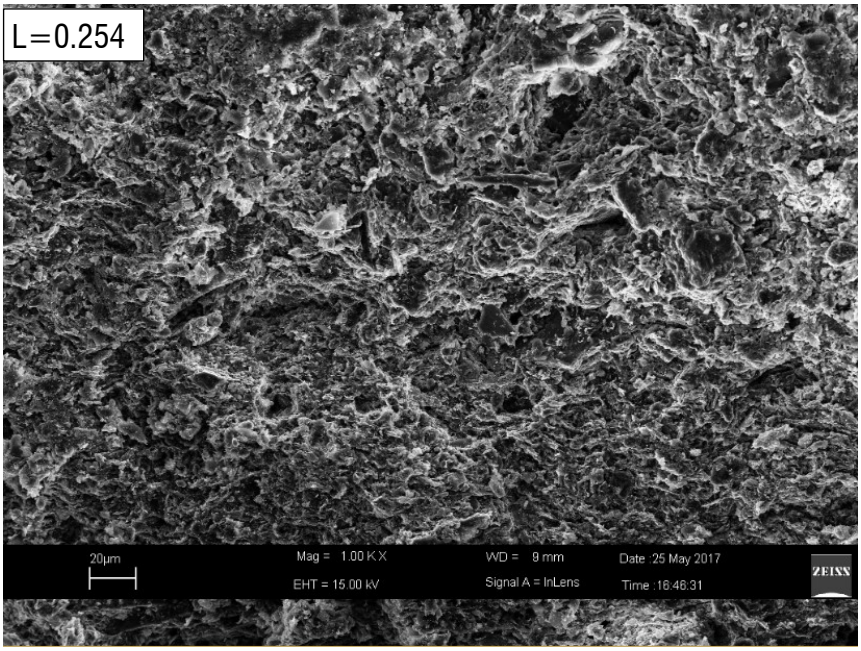

Fig. 7.87 – SEM micrograph along a vertical fracture of natural Lucera clay isotropically compressed to state LI_3 at medium magnification.

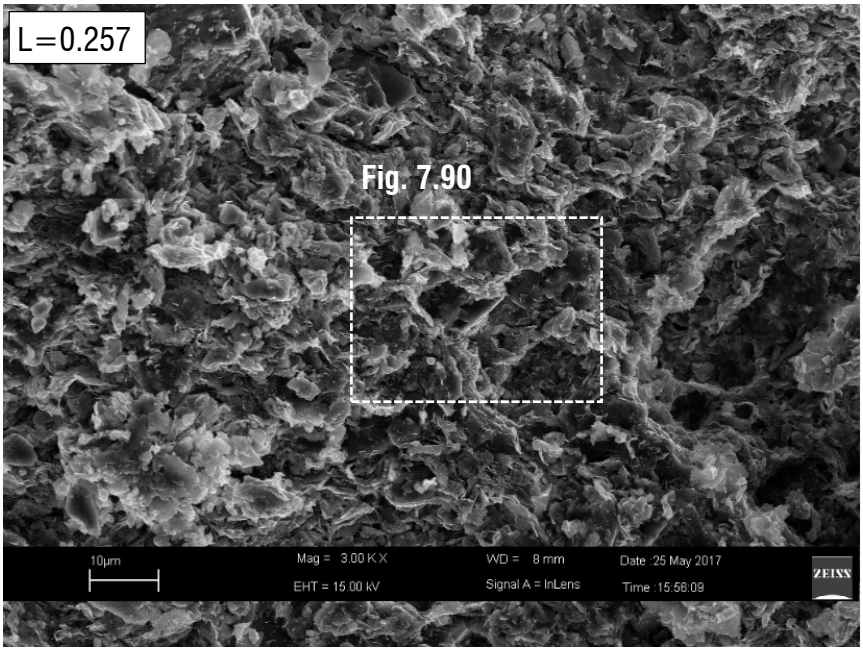

Fig. 7.88 - SEM micrograph along a vertical fracture of natural Lucera clay isotropically compressed to state LI_3 at medium magnification.

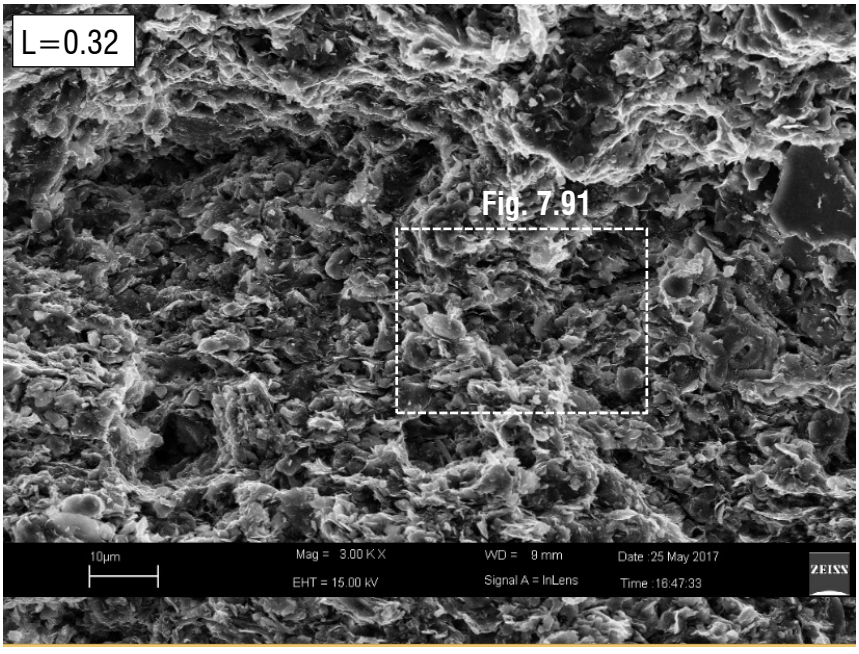

Fig. 7.89 - SEM micrograph along a vertical fracture of natural Lucera clay isotropically compressed to state LI_3 at medium magnification.

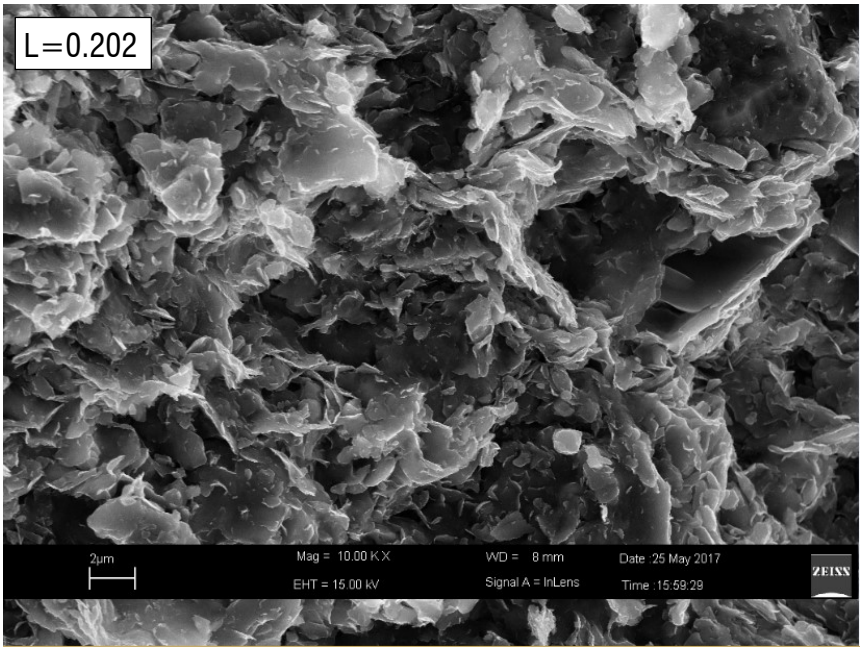

Fig. 7.90 – Enlargement of the micrograph in Fig. 7.88.

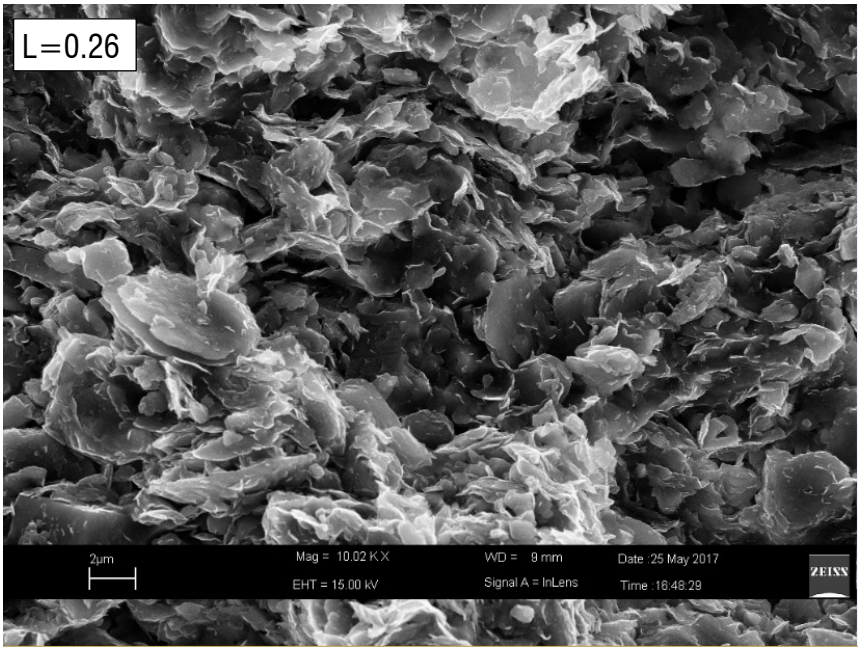

Fig. 7.91 - Enlargement of the micrograph in Fig. 7.89

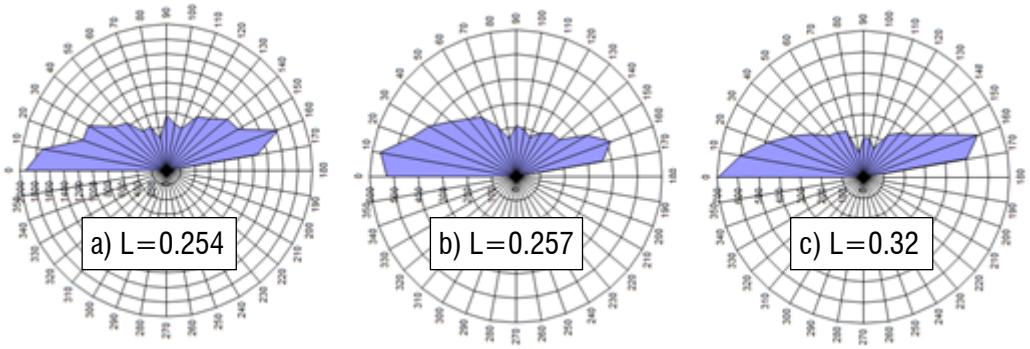

Fig. 7.92 – Direction histograms of the micrographs in a) Fig. 7.87, b) Fig. 7.88 and c) Fig. 7.89.

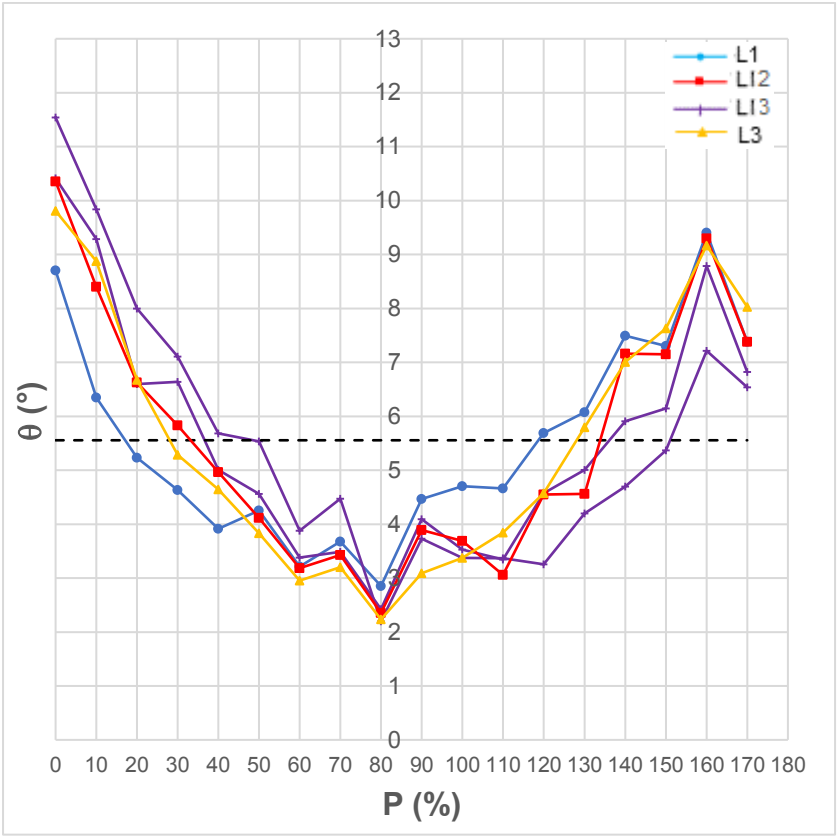

Fig. 7.93 – Orientation curves for natural Lucera clay under 1D and isotropic compression (all curves refer to micrographs of magnification 1000x).

7.3.5 Microstructural changes in isotropic compression for the reconstituted clay

An investigation of the microstructure evolution under isotropic compression was carried out on the Pappadai reconstituted clay comparing state PR_1 and state PRI (Fig. 7.41) at approximately the same void ratio (Table 7.1). MIP tests were carried out on both specimens and the results are compared in Fig. 7.94. The state PR at the end of consolidometer stage is also reported for comparison.

The similarity in the void ratios at states PR_1 and PRI is reflected in the identical value of the maximum intruded void ratio resulting from the cumulative curves (Fig. 7.94a). A difference is observed in the macro-pore volume, which is lower for the isotropic compressed specimen, suggesting that the larger pores are fewer in the isotropic compressed specimen. This difference is reflected in some difference in the small peaks exhibited by the two incremental curves in the inter-aggregate pore size range. Apart from this, the two incremental curves are found perfectly superimposed and with a DPS of 270 nm, lower than that of the undisturbed specimen (420 nm) but with a corresponding slightly higher frequency.

These results indicate that no significant difference seems to exist between the microstructural changes induced by isotropic and by one-dimensional consolidation in the reconstituted clay. Both the loading paths induce in general a translation of the incremental curve towards lower pore diameters and a reduction in the size of the dominant pore.

The effects on fabric and orientation of isotropic and one-dimensional loading could not be explored here, since no SEM micrographs of the corresponding specimens were taken.

However, as discussed in Chapter 2, Mitaritonna et al. (2014) observed that the complete modification of the directional elastic properties of the soil, which go along with the fabric directional character, requires the compression path along a direction different from one-dimensional loading to be extended up to a stress level at least four

times larger than that previously experienced. Accordingly, it may be hypothesised that not even marked fabric and orientation changes would have been recorded in isotropic compression at the investigated pressures, which are around three times larger than the final pressure attained in the consolidometer.

There is no evidence that this behaviour also applies to the natural Lucera clay, but the discussion in Section 7.3.4 indicates that a stress level around 1.5 times larger than that corresponding to the undisturbed state is insufficient to generate significant modification in the fabric directional character, i.e., in its orientation.

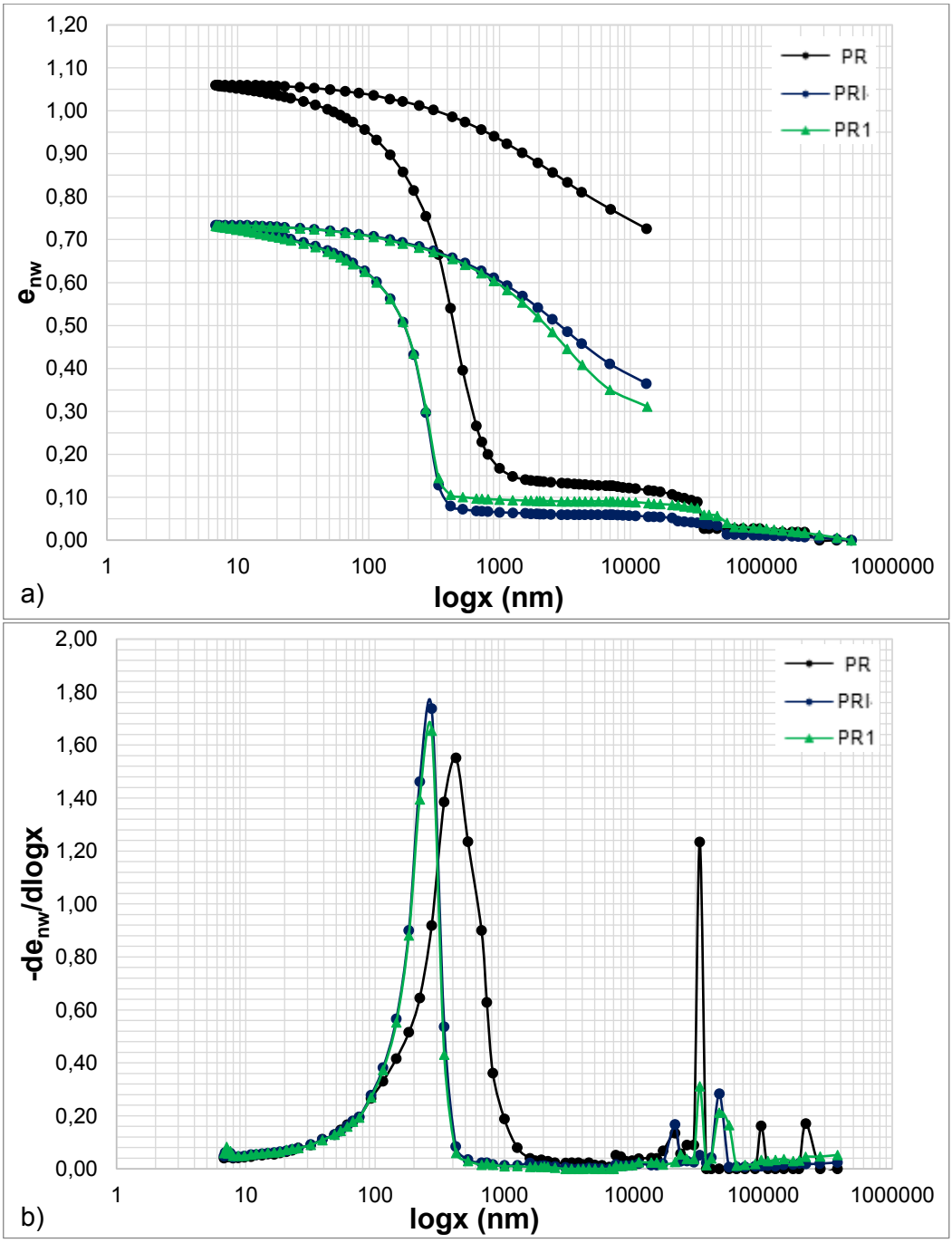

Fig. 7.94 - MIP tests on reconstituted Pappadai clay 1D and isotropically compressed. a) cumulative and b) derivative curves.

7.4 Evolution of microstructure in shear

7.4.1 Microstructural changes for the natural clay under drained shear

The investigation of the microstructural evolution of the clay under shear has been carried out for involved both natural and reconstituted Lucera clay.

As explained in Section 5.1, the investigation on the natural clay was intended to explore the clay behaviour both before and after reaching the current SBS, in both drained and undrained paths. Hence, all the sheared specimens subjected to microstructural analyses started from isotropic consolidation stresses below the isotropic gross-yield. So, as discussed in Chapter 6, the isotropic consolidation pressures determining overconsolidation ratios, R, equal to 3 and 1.6 were chosen, corresponding respectively to the states L_1 and LI_2 described in the previous Section. The former R=3 was chosen as to minimize the effects of strain localization due to negative hardening, which is expected to develop on the dry side of critical, whereas the latter R=1.6 was intended to bring the clay on the wet side of critical, but keeping at a distance from isotropic gross-yield.

The v-p' state paths and the q-p' stress paths for all the shear tests on the natural clay are replotted in Fig. 7.95, in which the states corresponding to microstructural analyses are indicated. For each specimen which underwent microstructural analyses, both MIP and SEM, combined with image processing, were carried out.

In this section, the results of the microstructural analyses on the drained specimens TNL4 (R=3) and TNL6 (R=1.6) are discussed. As seen in Section 6.4.1, the two specimens by the end of the test showed a localization of strain, which however did not develop into a well-defined failure surface. For specimen TNL4, as shown in Fig. 7.96, only one specimen for microstructural analyses was taken from the area of strain localization, which is seen to represent a "incipient" shear band. For specimen TNL6, two specimens for microstructural analyses were taken, from inside and outside the area of strain localization. This was repeated also for other specimens, as will be seen in the following, aiming at investigating both the effects of localization, which as such

developed in an area of confined extension, and the effects induced by shear on the other parts of the specimen not affected by localization, which are thought to be recording the microstructural changes due to shear before the activation of the localization mechanism.

For simplicity, the two specimens will be distinguished as “SB”, abbreviation for (incipient) shear band, and “OB”, abbreviation for outside the shear band (Fig. 7.96).

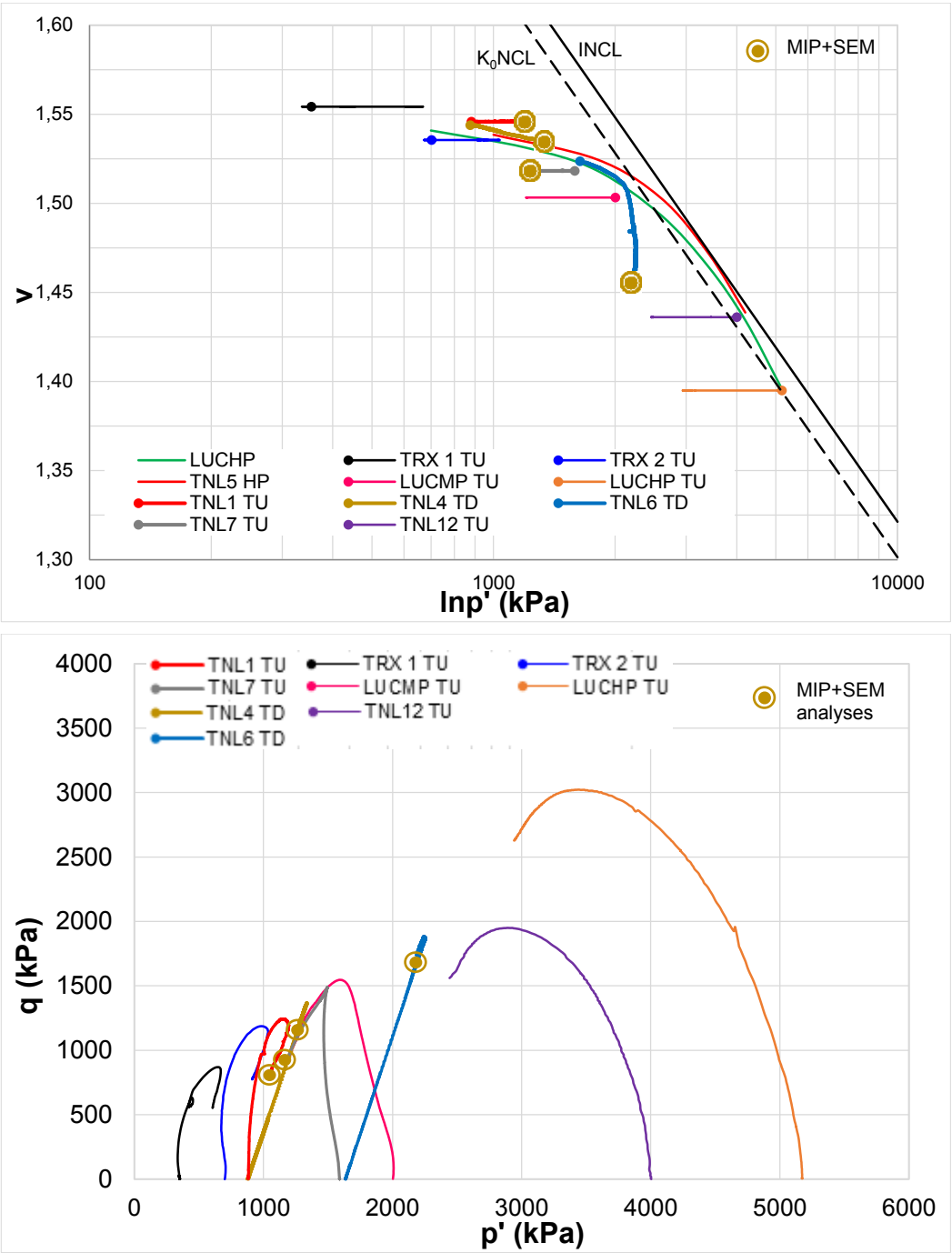

Fig. 7.95 – a) v-p' states and b) stress paths of shear tests on natural Lucera clay: indication of states of microstructural analyses.

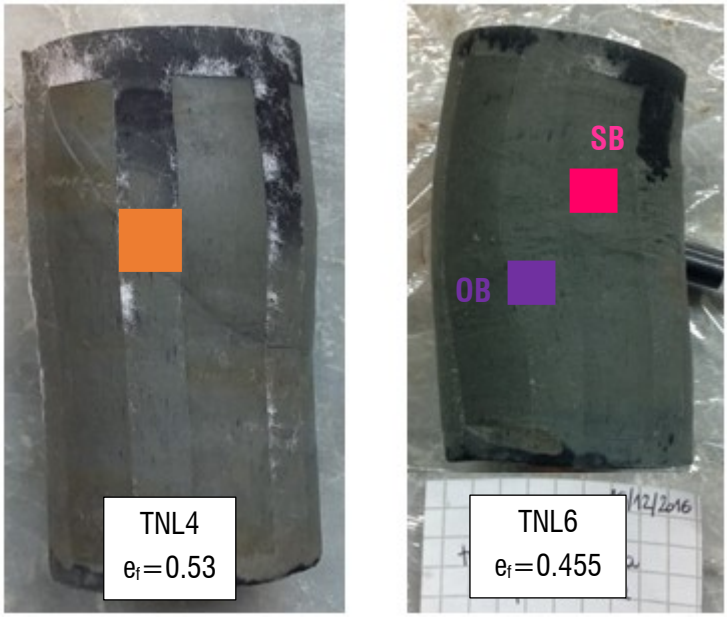

Fig. 7.96 - Specimens TNL4 and TNL6 at the end of the drained shear tests and corresponding final void ratios. The position of the MIP specimens is indicated, inside the band of strain localization for specimen TNL4, inside (pink) and outside (purple) the zone of strain localization for specimen TNL6.

As discussed in Section 6.4.1, in both the shear tests the clay exhibited contractant behaviour. The state paths followed by the two specimens indicate that specimen TNL4 moved along a swelling line, i.e., according to the CSF its stress-path remained on the elastic wall, while specimen TNL6 initially followed a swelling line, then fell towards the CSL.

For each test, the changes in microstructure under shear are studied by comparison with the microstructure at the state prior to shearing, i.e., state L_1 for specimen TNL4 and state LI_2 for specimen TNL6.

The results of the MIP test on specimen TNL4 are compared to those obtained for the undisturbed specimen in Fig. 7.97. The void ratio of specimen TNL4 after the shear test is 0.53.

A small decrease in the maximum intruded void ratio is seen to occur in specimen TNL4, as expected, with a concurrent reduction of the larger pore volume, which uniformly decreases in the range of the inter-aggregate porosity (Fig. 7.97a). The rising part of the cumulative curve is shifted to the left and, accordingly, and the incremental curve exhibits a lightly lower DPS, 270 nm, compared to the average 300 nm of the undisturbed specimen. The frequency of the DPS is seen to increase, indicating that the dominant pores have become not only smaller in size, but also more abundant.

The observation of the fabric of this specimen was made on a vertical fracture crossed by the incipient failure surface (Fig. 7.98). The latter was easily identifiable also at a first observation at the optical microscope.
Micrographs were taken along the incipient shear band (Fig. 7.99, Fig. 7.100).
From these global views, the fabric appears well packed and not much denser than the fabric of the undisturbed specimen (see for example Fig. 7.17). Micrographs at low and medium magnification inside the incipient shear band zone (Fig. 7.101, Fig. 7.102) show degrees of orientation on average higher than those found for the undisturbed state (Fig. 7.17, L=0.22-0.24), which reach values as high as 0.403. The corresponding orientation curve (Fig. 7.112) shows a number of particles oriented along sub-horizontal directions (10°-20°) higher than those in the undisturbed specimen, suggesting that in the shear band zone a re-orientation of particles in the direction of the shear band is taking place.
However, in the same pictures (Fig. 7.101, Fig. 7.102) highly oriented strata of particles crossing the picture in sub-horizontal directions alternate at places domains of more random and flocculated particle arrangements. So, shear may be increasing the overall orientation of particles, but zones which keep a less oriented fabric are still seen.

To investigate the evolution of fabric outside the zone affected by the shear band formation, SEM pictures were also taken along the same vertical fracture of the same specimen in peripheral areas (Fig. 7.104). At some distance from the most strained zone, strata of highly oriented particles interbedded within strata of domains in edge to

face contact are seen, which resemble the architecture characterising the undisturbed specimen. Although zones of more random orientation can still be observed, in these areas an increase in fabric orientation is recorded. Several particles are found to be oriented along sub-horizontal directions (Fig. 7.105).

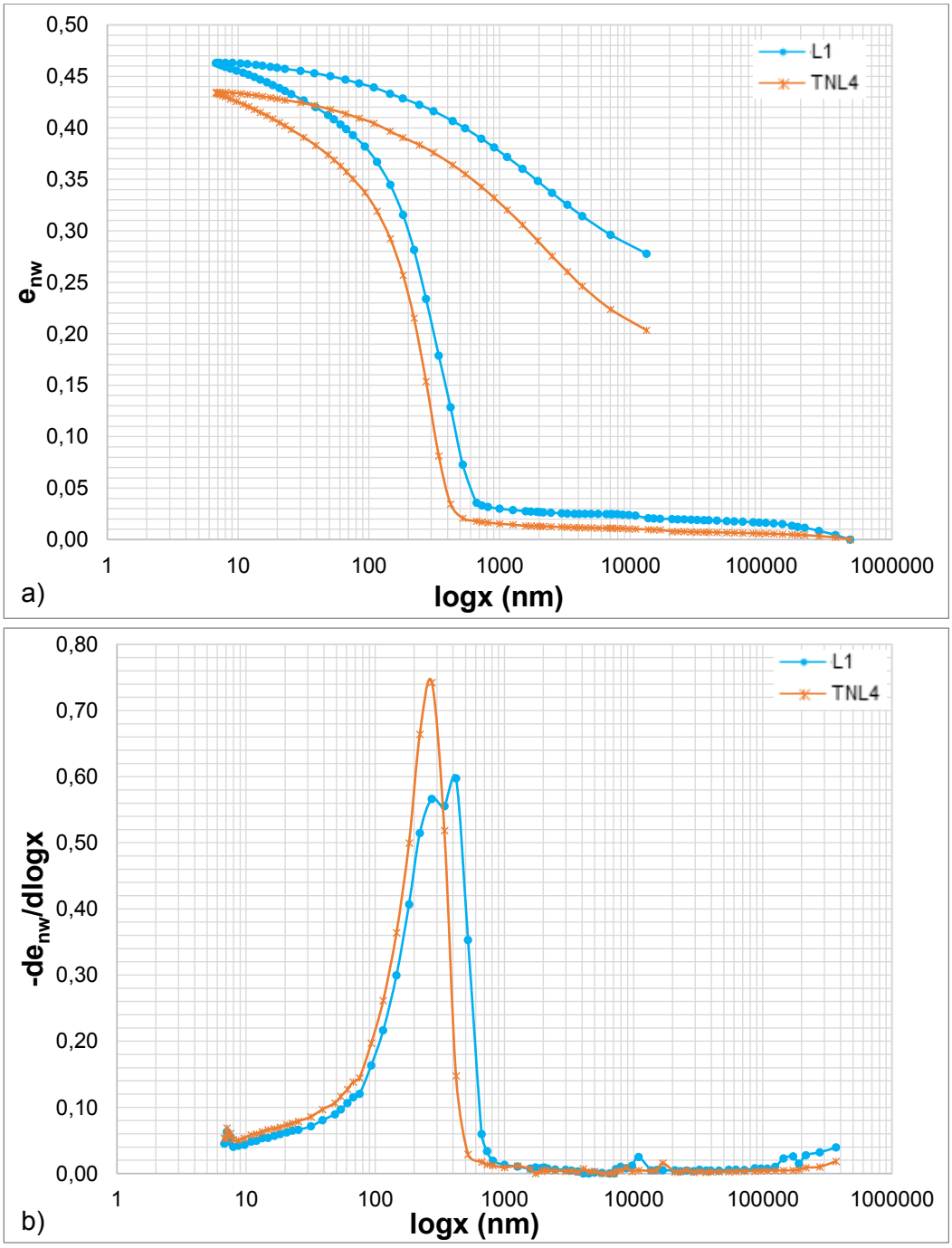

Fig. 7.97 - MIP tests on natural Lucera clay in drained shear TNL4 (R=3, e=0.53) inside the shear band compared to undisturbed state. a) cumulative and b) derivative curves.

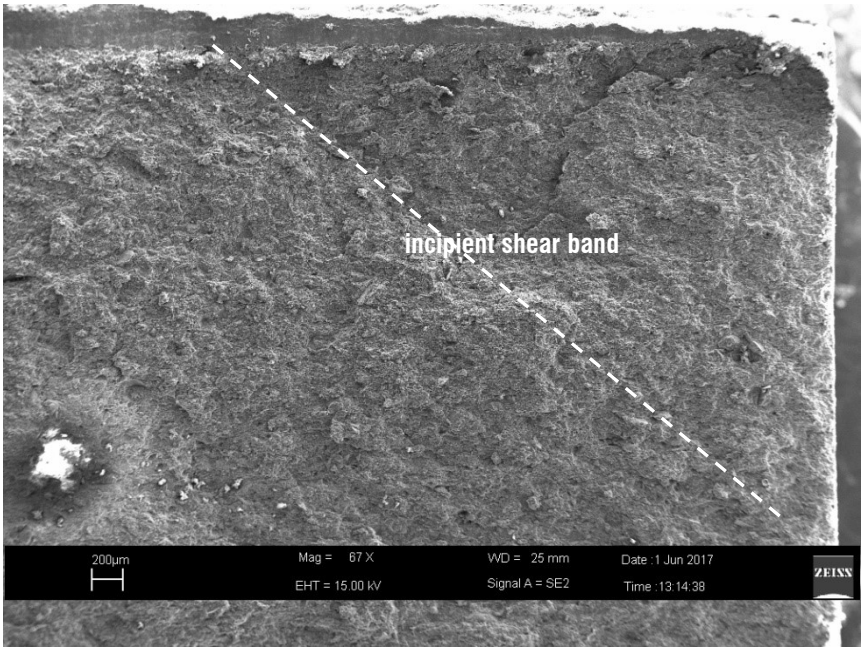

Fig. 7.98 - SEM micrograph of natural Lucera clay specimen TNL4 sheared drained along a vertical fracture: global view and indication of the incipient shear band location.

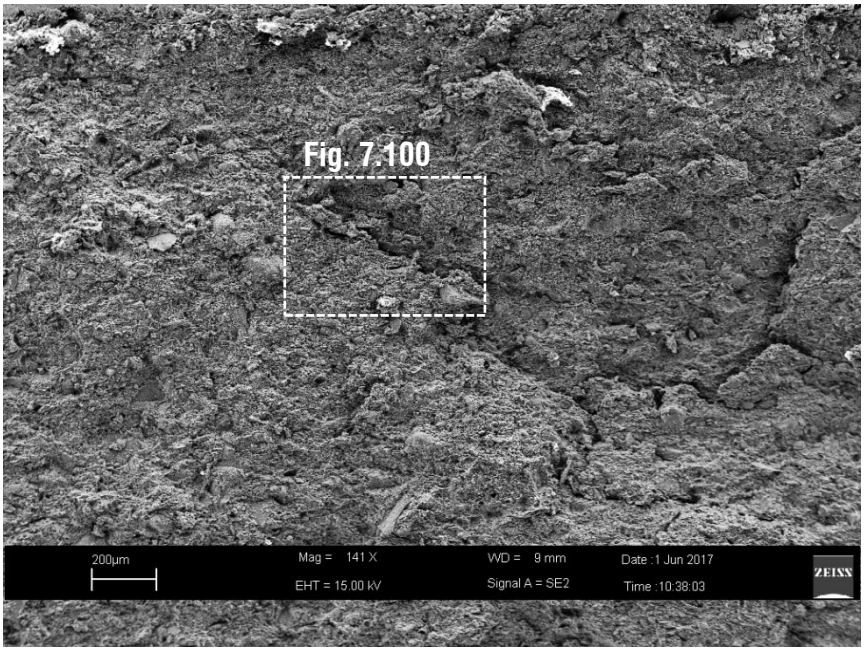

Fig. 7.99 - SEM micrograph of natural Lucera clay specimen TNL4 sheared drained along a vertical fracture at low magnification: enlargement of the incipient shear band.

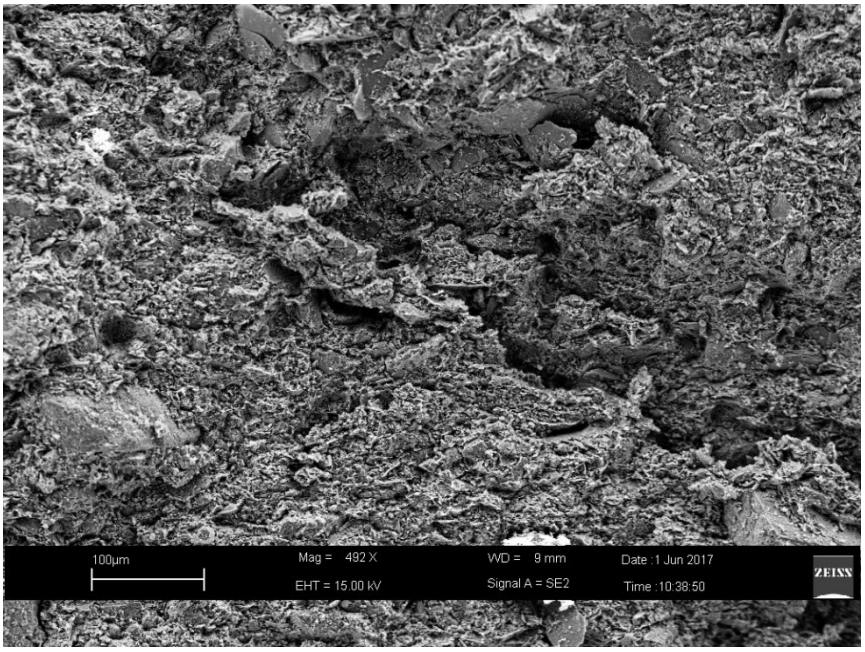

Fig. 7.100 - SEM micrograph of natural Lucera clay specimen TNL4 sheared drained along a vertical fracture at medium- low magnification: enlargement of Fig. 7.99.

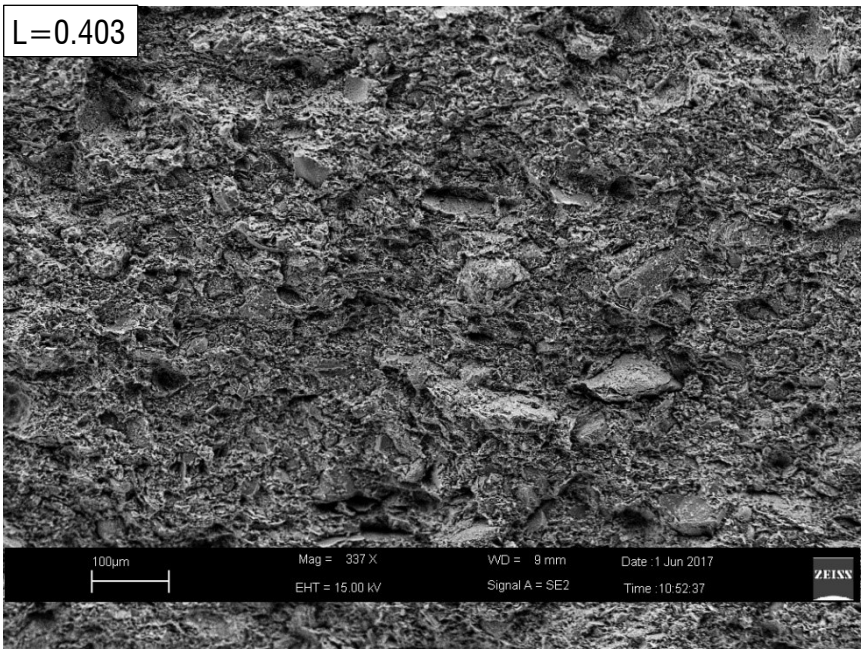

Fig. 7.101 - SEM micrograph of natural Lucera clay specimen TNL4 sheared drained along a vertical fracture at medium-low magnification.

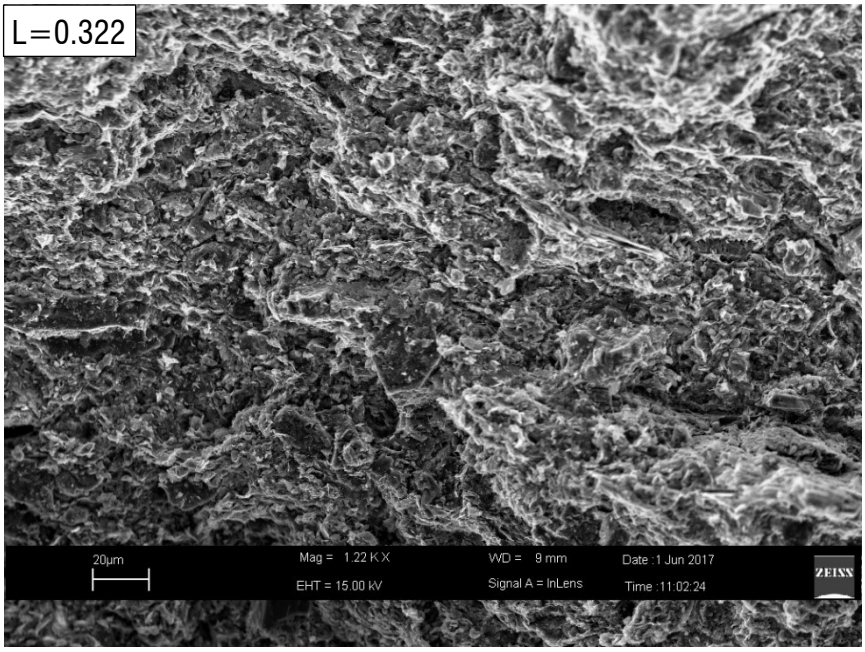

Fig. 7.102 - SEM micrograph of natural Lucera clay specimen TNL4 sheared drained along a vertical fracture at medium-high magnification.

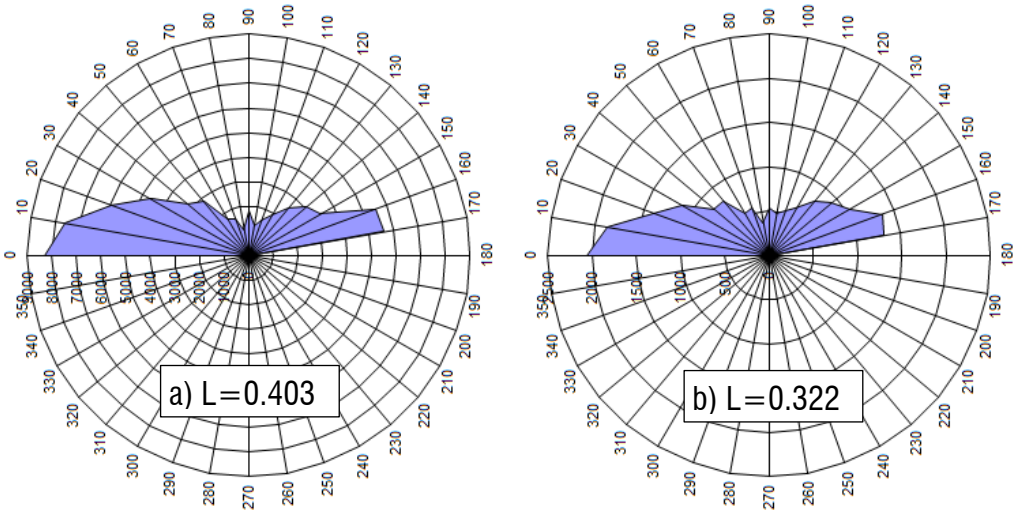

Fig. 7.103 – Direction histograms of specimen TNL4 inside the incipient shear band on micrographs in a) Fig. 7.101 and b) Fig. 7.102.

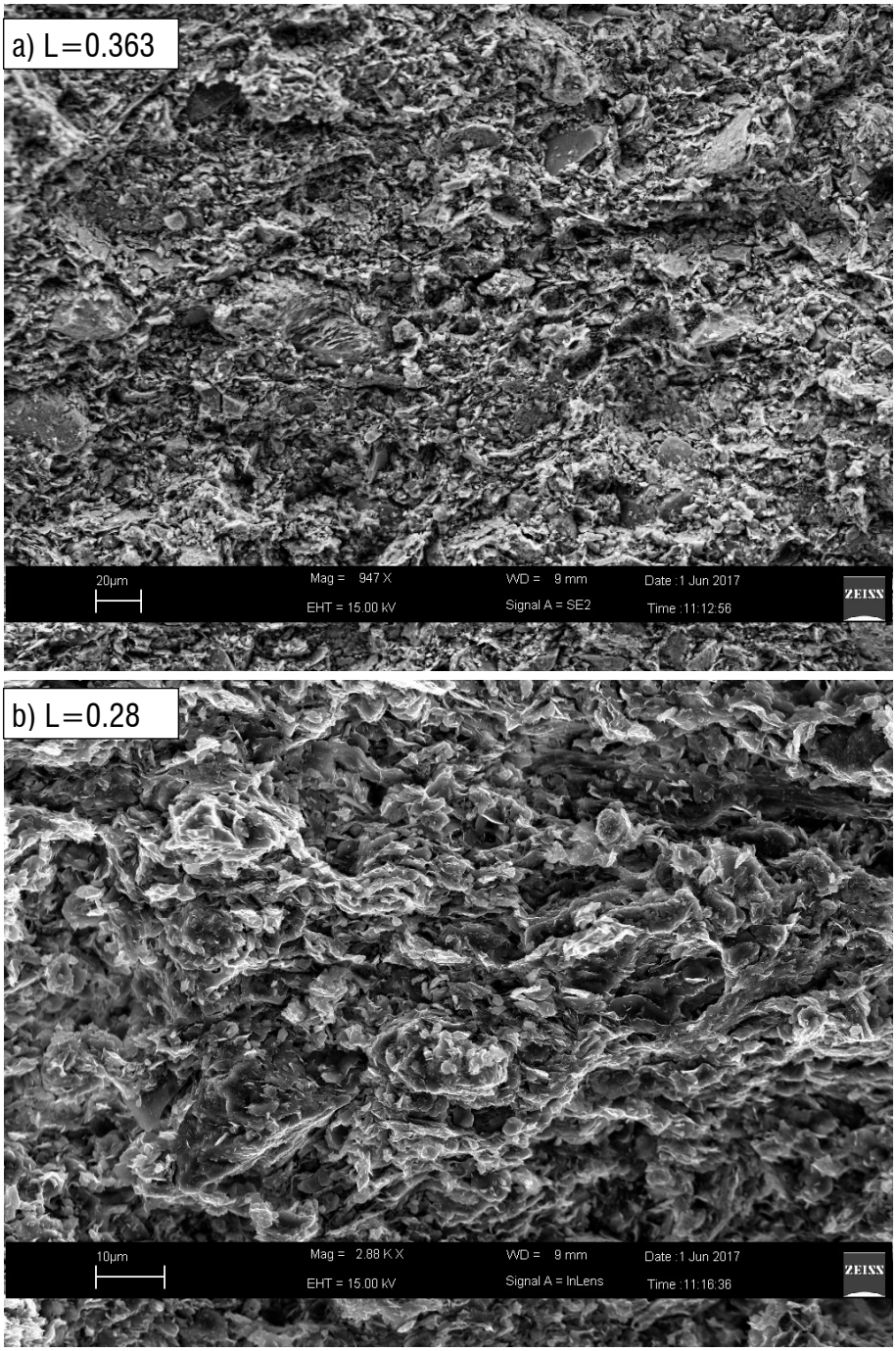

Fig. 7.104 - SEM micrograph of natural Lucera clay specimen TNL4 sheared drained along a vertical fracture outside the shear band zone at a) low and b) medium magnification.

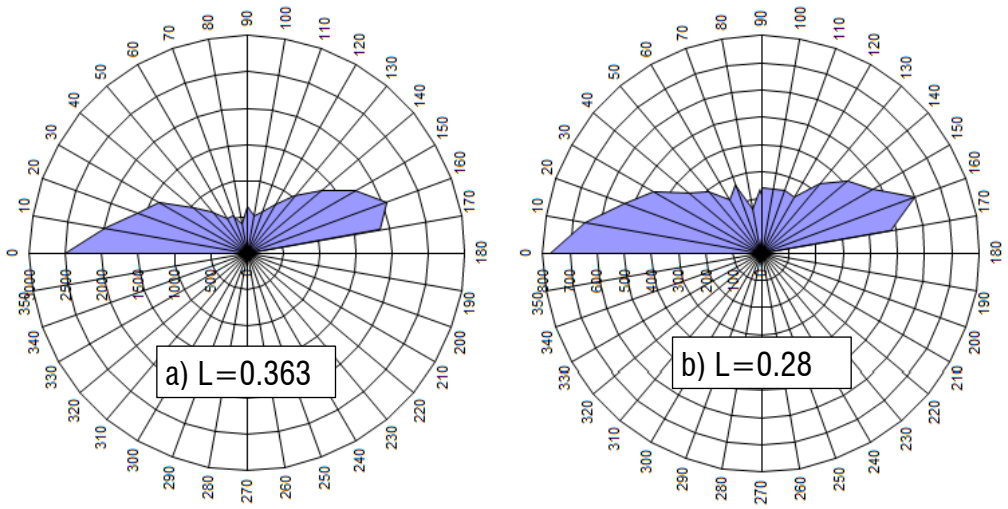

Fig. 7.105 - Direction histograms of specimen TNL4 outside the incipient shear band on micrographs in a) Fig. 7.104a and b) Fig. 7.104b.

Specimen TNL6, sheared drained from an isotropic consolidation state corresponding to state LI_2 (Fig. 7.41), exhibited a strongly contractant behaviour which reduced its initial void ratio to the value 0.455. For this specimen, the highly strained zone observed on the specimen is seen to be larger than that of specimen TNL4.

The MIP curves relative to TNL6 are compared with those of the specimen at point LI_2 in Fig. 7.106. Both the MIP tests on the specimens inside and outside the highly strained zone are shown.

Both SB and OB exhibit maximum intruded void ratios much lower than LI_2, suggesting that both the clay in the proximity and more distant from the shear band are undergoing contraction, consistently with the overall contractant behaviour recorded in the shear test (Fig. 7.106a). Both OB and SB show a reduction in the macro-pore volume, similarly to test TNL4. Hence, the closing of the macro-pore space observed in compression tests also applies to shear tests in which a contractant volumetric behaviour develops.

In Fig. 7.106b, the incremental curves for the three specimens are shown. SB and OB have very similar incremental curves, both in terms of shape, width and DPS. The latter

is for both 220 nm, smaller than that of specimen LI_2 (270 nm). The frequency of the dominant pore is lightly smaller in specimen OB than in specimen SB, but in both cases it is smaller than that of specimen LI_2, indicating that both the size and the amount of the dominant pores have decreased due to shear with respect to the state prior to testing.

Micrographs at low magnification on a vertical fracture across the zone of localization of strain (specimen SB) are shown in Fig. 7.107. A well packed and oriented fabric can be observed, with many sub-horizontally oriented domains. The image processing (Fig. 7.108) confers a high orientation degree up to 0.459, which is higher than the average orientation degree exhibited by specimen LI_2 (0.27-0.29). The orientation degree in this case is even higher than that found for specimen TNL4, probably because of the higher axial strain attained by specimen TNL6.
The orientation curve (Fig. 7.112) shows also here many particles oriented along sub-horizontal directions (140°-160°), which may be gradually reorienting along the direction of shear.

Some discontinuities are found to open between strata of particles in face-to-face contact and follow a direction parallel to that of the evolving shear band, as that indicated in Fig. 7.109. Similar fissures were seen to open in specimens of monomineralic clays (kaolinite and bentonite) under drained shear by Hicher et al. (1994), as discussed in Section 2.13.
At higher magnification (Fig. 7.110, Fig. 7.111), perfectly oriented domains are seen to form stacks interbedded within aggregations of mediumly to highly oriented domains. However, small stratified areas of random fabric still appear between sub-horizontally oriented domains, suggesting a fabric evolution under shear that is highly non- uniform, as that originated by 1D compression. The corresponding orientation degrees confirm an overall increase in fabric orientation, coexisting with less oriented zones.

Given the ill-defined boundaries of the localization zone in specimen TNL6, peripheral areas could not be assumed totally unaffected by localization (as done for specimen TNL4), so no SEM micrographs were taken there. Not even specimen OB has been observed yet by means of SEM, so no information can be gathered on the effects of shear outside the shear band.

However, from the microstructure analyses carried out on specimens TNL4 and TNL6, the conclusion emerges that shear determines an overall increase in the fabric orientation with respect to the fabric prior to testing. Although the two specimens did not develop yet a complete shear surface, the increase in fabric orientation inside the area of strain localization is also due to the reorganization of particles along the direction of the incipient shear surface. Outside the area affected by strain localization, the fabric orientation in specimen TNL4 is seen to increase with respect to the state prior to shearing, but further confirmation will be looked for in the analyses of other sheared specimens.

In any case, the permanence of areas of honeycomb fabric within strata of c.p.o. fabric observed for natural Lucera clay drained specimens appears to confirm the observation, discussed in Section 2.12, that shearing paths generate non-uniform microstructural evolution, similar to that induced by compression (Cotecchia et al., 1982).

In terms of evolution of pore size distribution, drained shear of contractant specimens is seen to determine a reduction in inter-aggregate porosity and a small reduction in the value of the dominant pore size, associated to a change in frequency with respect to the specimen before shearing. Comparing the microstructure evolution inside and outside the shear band, the latter is seen to experience a change in PSD similar to the zone outside the shear band. This is probably an effect of the drained test conditions, which are allowing all the areas of the specimen to experience a quite homogeneous contraction. In undrained sheared specimen, a much more complex microstructural evolution will be seen to take place, especially if the zones inside and outside the shear band are compared.

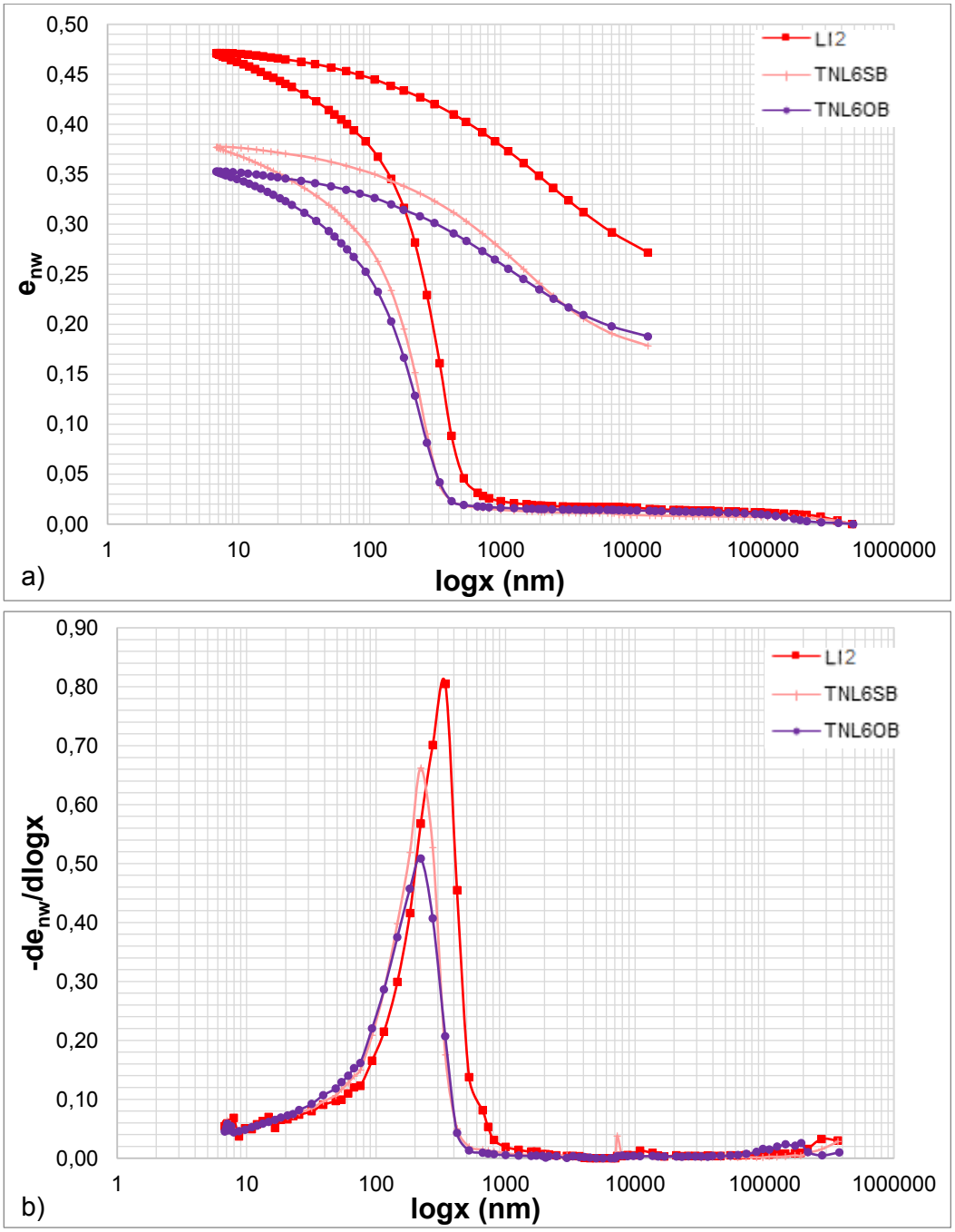

Fig. 7.106 - MIP tests on natural Lucera clay in drained shear TNL6(R=1.6, e=0.455), both inside (SB) and outside (OB) the localization zone, compared to state LI2. a) cumulative and b) derivative curves.

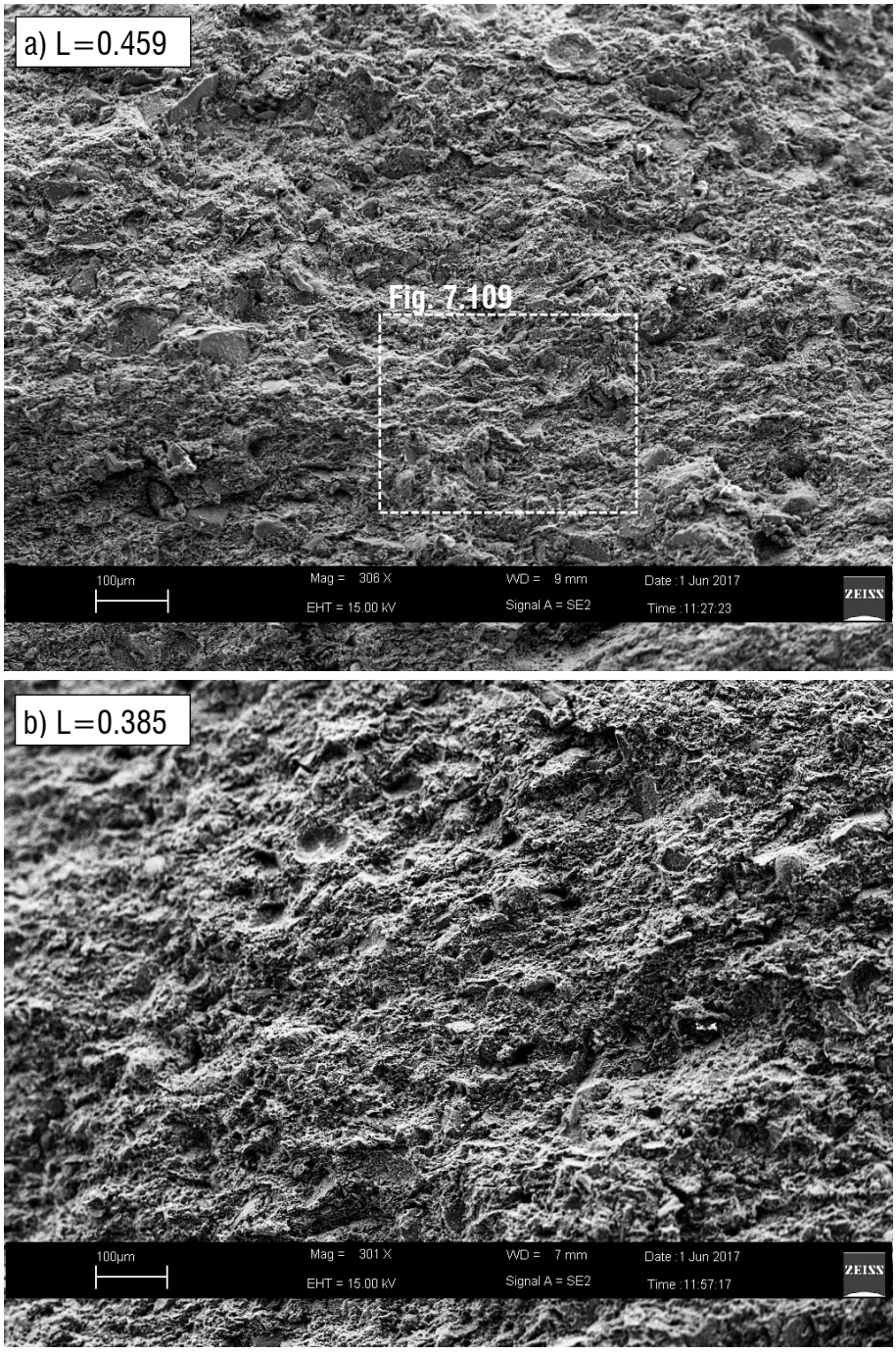

Fig. 7.107 - SEM micrographs of natural Lucera clay specimen TNL6 sheared drained along a vertical fracture at low magnification.

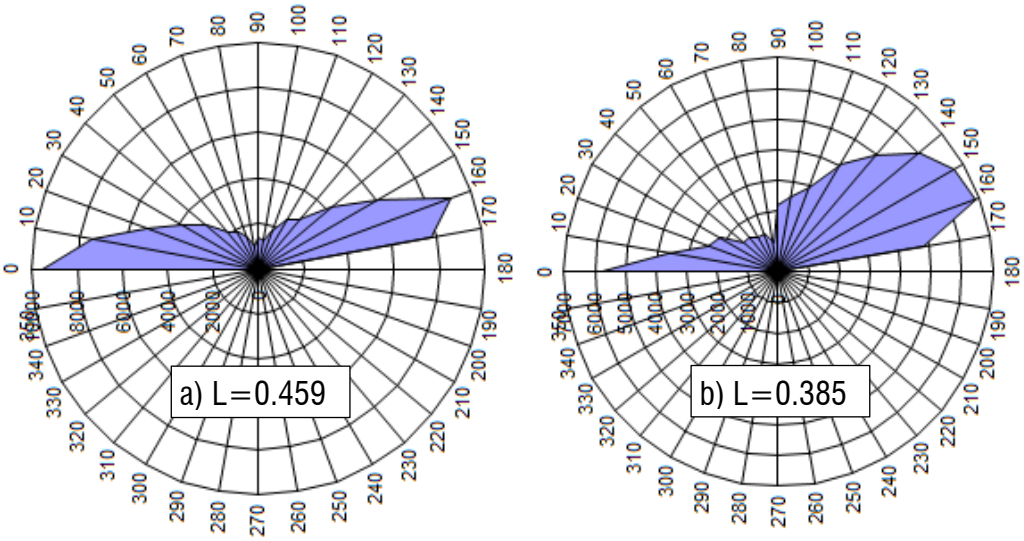

Fig. 7.108 - Direction histograms of specimen TNL6 inside the incipient shear band on micrographs in a) Fig. 7.107a and b) Fig. 7.107b.

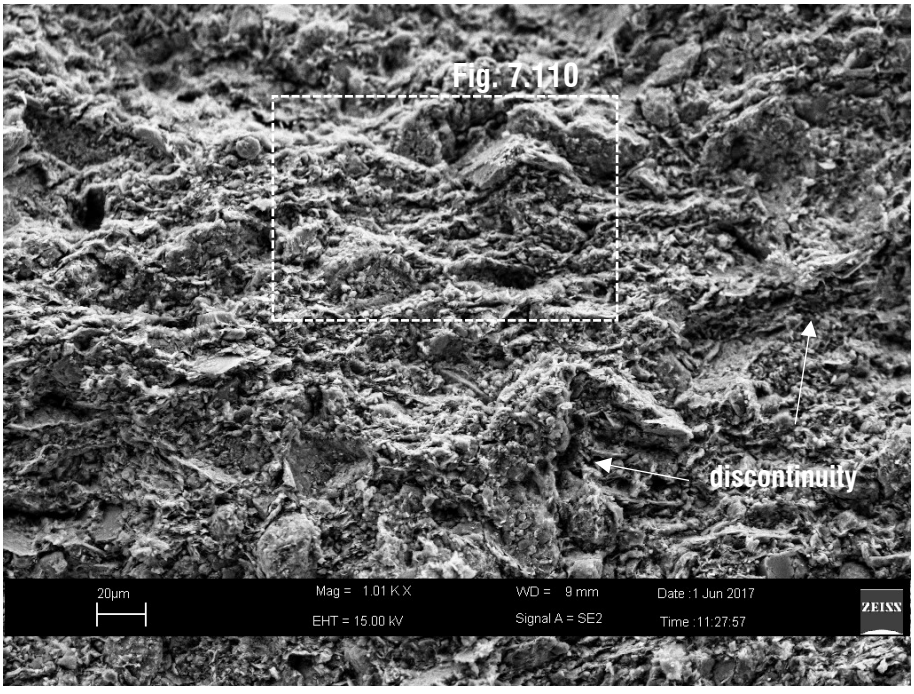

Fig. 7.109 – Enlargement of Fig. 7.107a showing a fissure along the direction of the shear band.

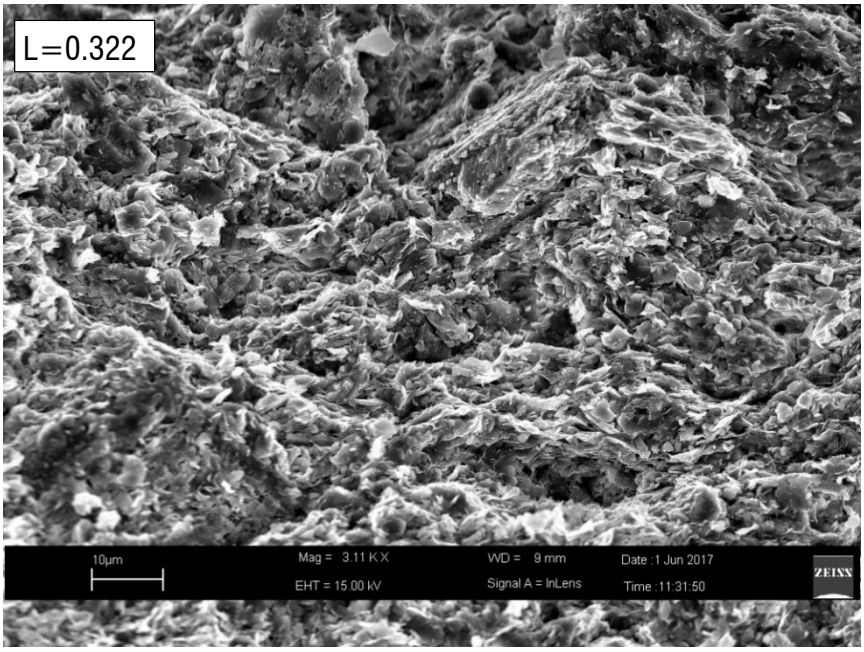

Fig. 7.110 – Enlargement of Fig. 7.109 showing highly oriented strata interbedding areas of random fabric.

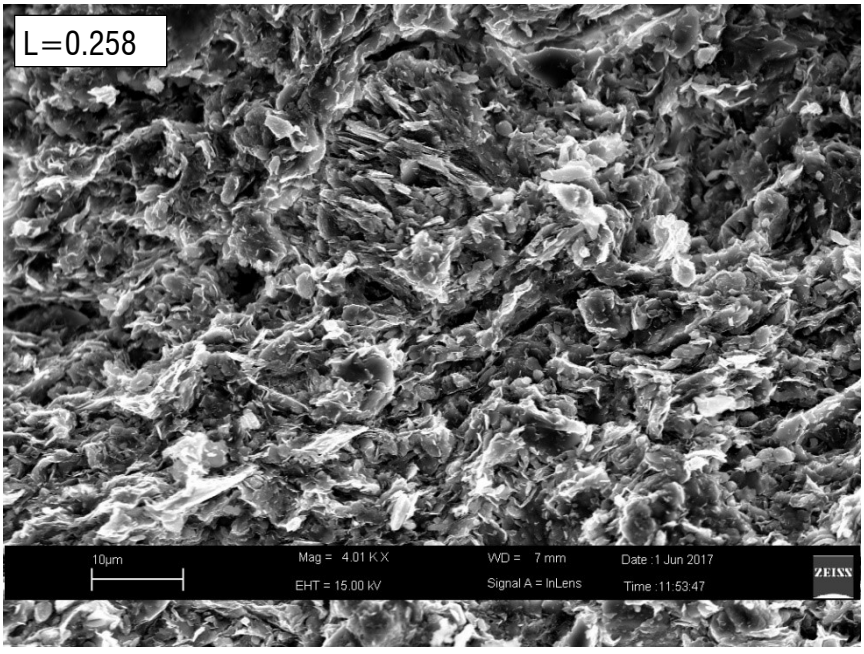

Fig. 7.111 - SEM micrographs of natural Lucera clay specimen TNL6 sheared drained along a vertical fracture at medium magnification.

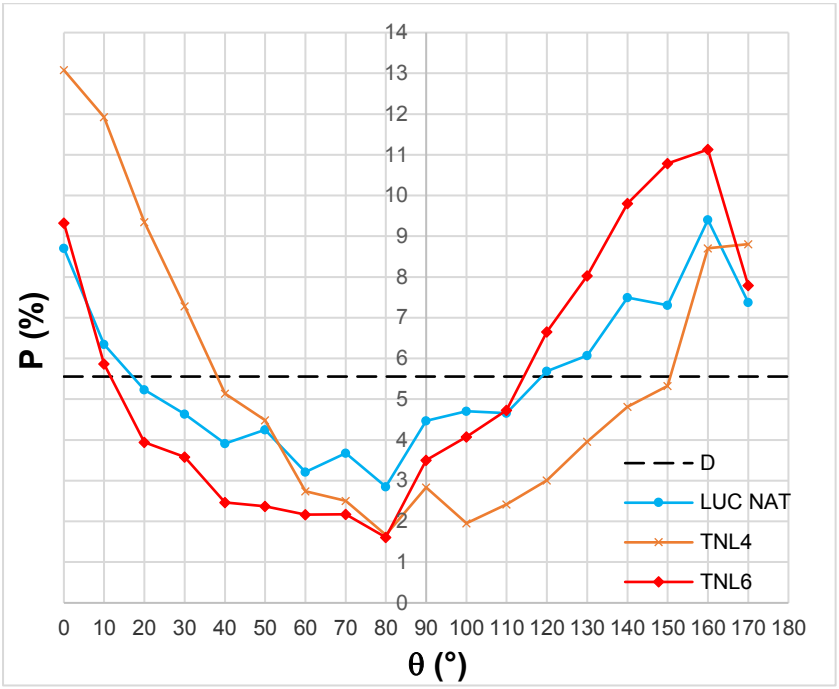

Fig. 7.112 – Orientation curves for natural Lucera clay under drained shear (all curves refer to micrographs of magnification 300x).

7.4.2 Microstructural changes for the natural clay under undrained shear

In this Section, the microstructural analyses on the natural Lucera clay specimens TNL1 (R=3) and TNL7 (R=1.6) sheared undrained will be discussed. The v-p' state paths and q-p' stress paths of the corresponding shear tests are shown in Fig. 7.95.

As discussed in Section 6.4.1, both specimens exhibited marked strain-softening, accompanied, as can be seen from the trend of excess pore water pressure, in specimen TNL1 by a plastic dilative behaviour and in specimen TNL7 by a mainly contractant behaviour. Both the specimens were seen to develop a shear band, so for both microstructural analyses were done both inside and outside the shear band.

The specimens at the end of testing, with indication of the position of the specimens taken from the microstructural analyses both inside and outside the shear bands, are shown in Fig. 7.113. The results of both MIP and SEM analyses, combined with image processing, on the specimens will be discussed here.

As seen in Section 6.4.1, two additional undrained shear tests, TNL10 and TNL11, were carried out, which started from the same isotropic consolidation pressures as specimens TNL1 and TNL7 and were stopped at half the peak deviatoric stress. The MIP test results on these specimens will be also shown and compared with the results obtained on specimens TNL1 and TNL7, with the aim to analyse the changes in microstructure occurred up to this point.

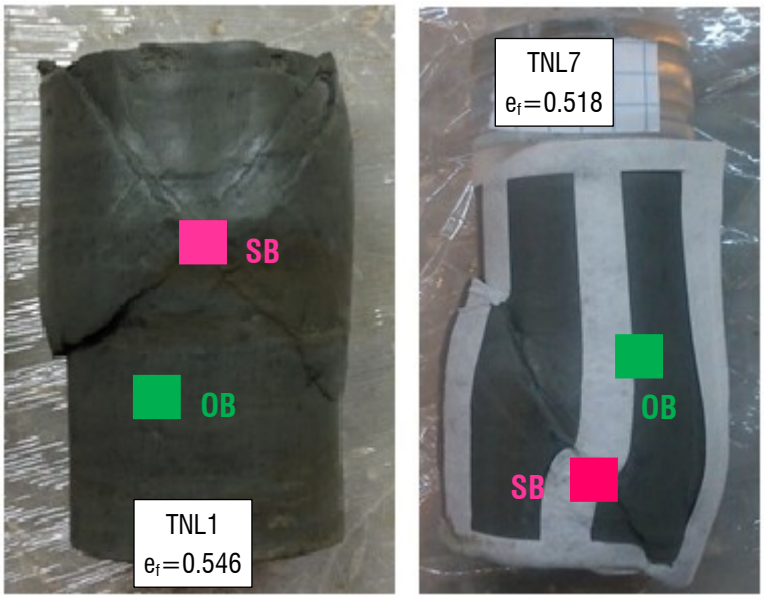

Fig. 7.113 - Specimens TNL1 and TNL7 at the end of the undrained shear tests. The position of the specimens taken for microstructural analyses is indicated, inside the shear bands (SB, pink) and outside the shear bands (OB, green).

The MIP results on specimen TNL1 (e=0.546) both inside (SB) and outside (OB) the shear band are compared with the curves for the undisturbed specimen L_1 and shown in Fig. 7.114.

The specimen SB shows a decrease in the maximum intruded volume with respect to specimen L_1, suggesting a contractant behaviour inside the shear band. By contrast, specimen OB exhibits a maximum intruded volume higher than that of specimen L_1, which is indicative of a dilative behaviour of the clay outside the shear band.

It should be noted that the difference in the maximum intruded volume for SB and OB, which are cut from the same specimen, is certainly related to a difference in the void ratios inside and outside the shear band. Hence, it can be inferred from the MIP results that the clay in the shear band is contracting with respect to the clay outside the shear band.
On the other hand, the relative differences between these values and the maximum intruded void ratio of the undisturbed specimen, being small, may be affected by small differences in the initial void ratios of the specimens before testing. Moreover, the uncertainty related to the instrumental limitations of MIP should be considered, which causes the non-detectability of a part of pore space (Section 5.3.2).
In addition, the analysis of Fig. 7.114b reveals that SB is increasing the large pore volume with respect to the undisturbed specimen, while OB is reducing it. The reduction of the large pore space is consistent with the contractant behaviour exhibited by the specimen before peak stress, which may have closed the larger pores. The increase of larger pore volume shown by SB is believed to be mainly associated with the possible opening of some fissures inside the shear band in the direction parallel to the shear band, similar to the discontinuities seen to develop in the drained shear band of specimen TNL6.

The incremental curves of both SB and OB are translated to the left to the same DPS of 220 nm, lower than that of L_1 (300 nm). The curve of specimen SB appears to have shifted towards a lower pore size range, keeping the frequency of the DPS unchanged, whereas the curve of specimen OB seems to preserve more similarities with that of the undisturbed specimen but with a higher frequency of the DPS.

Analysing specimen SB of TNL1 (Fig. 7.113), SEM micrographs were taken on a vertical fracture crossing the shear band (Fig. 7.115); the large open fissure seen corresponds to the distance between the two edges of the shear band. Strata of perfectly iso-oriented particles along the shear band edge and parallel to it are seen, made of many thinner strata of face to face platy particles, as the enlargements in Fig.

7.116 better show. At higher magnification (Fig. 7.117) some very small domains of particles in edge-to-face contact can be recognized. The degrees of orientation (0.28-0.301) confirm the fabric anisotropy developing in the shear band.
The thickness of the perfectly oriented layer of domains and particles rotated along the shear band direction is believed to be limited. Fig. 7.118 shows a perfectly iso-oriented layer in the right side of the picture, confining with a much less disturbed and oriented area in the left side of the image.
As a confirmation of the high fabric orientation achieved along the shear band, the fabric along the failure surface appears perfectly iso-oriented, with particle faces lying along the shear plane (Fig. 7.119). Observing the fabric along the investigated failure surface, symmetric failure planes corresponding to the other shear band developed in the specimen (Fig. 7.113) are seen to emerge from the failure surface (Fig. 7.120). Enlargements show that these intersecting planes are made of stacks of particles in face to face contact emerging perpendicularly to the main failure plane.

SEM observations were also performed on specimen OB (Fig. 7.113), in order to investigate the fabric changes occurred inside that part of specimen TNL1 not affected by strain localization. A global view along a vertical fracture (Fig. 7.122) shows a densely packed and well oriented fabric, in which numerous sub-horizontal strata of iso-oriented particle edges can be recognized. Fissures oriented along the direction of the shear band are observed. However, on average, the fabric resembles much that observed in the undisturbed specimen. This is confirmed by the view at higher magnification (Fig. 7.123) were the same regular alternation of stacks of c.p.o. interbedded with strata of more random particles found in the undisturbed fabric can be recognized. In Fig. 7.124 an oblique fissure, presumably parallel to the shear band, is seen to cross the micrograph; it appears delimited to the right by a layer of random particle aggregations and to the left intersected by a sub-horizontal stack of particles.
The direction histograms and L values of these micrographs (Fig. 7.125) confirm that a quite high degree of orientation is achieved (up to 0.357) outside the shear band, with particles mainly oriented towards horizontal and sub-horizontal directions.

So, the SEM micrographs both inside and outside the shear band are showing that a higher degree of orientation is achieved under shear. In the shear band, as observed for drained tests, this is related to a re-organization of particles which start rotating along the direction of the shear band. However, also outside the shear band fabric anisotropy is seen to increase, and even higher degrees of orientation are recorded.
In both areas of the specimen, less oriented particle aggregations are still recognized.

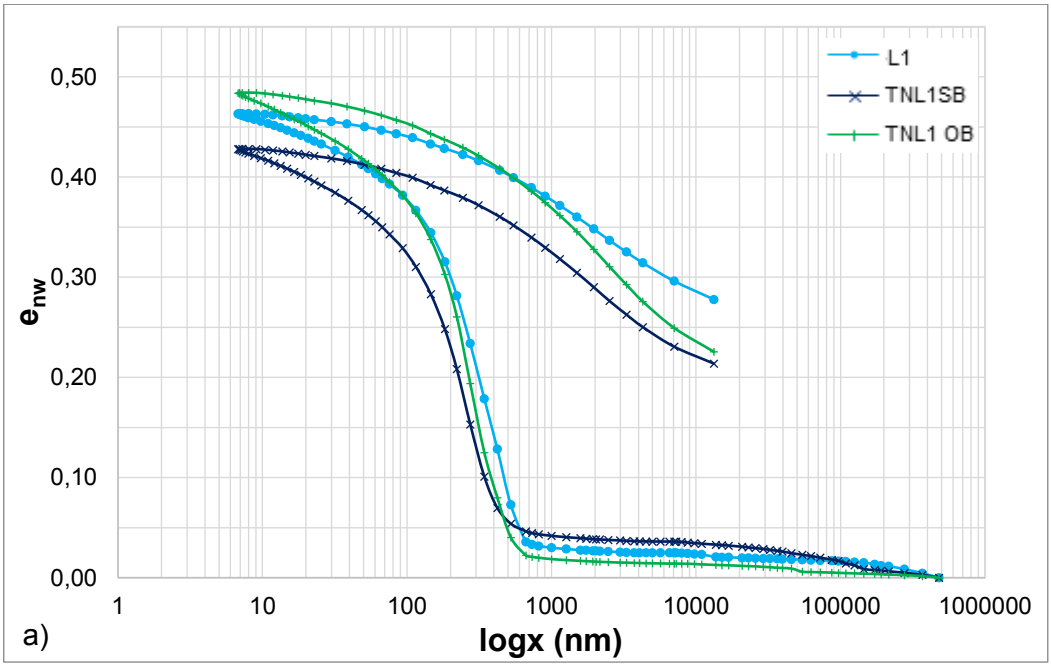
L1
TNL1SB
TNL1 OB
0,50
0,40
0,30
0,20
0,10
0,00
e_{nw}
1
10
100
1000
10000
100000
1000000
logx (nm)
a)

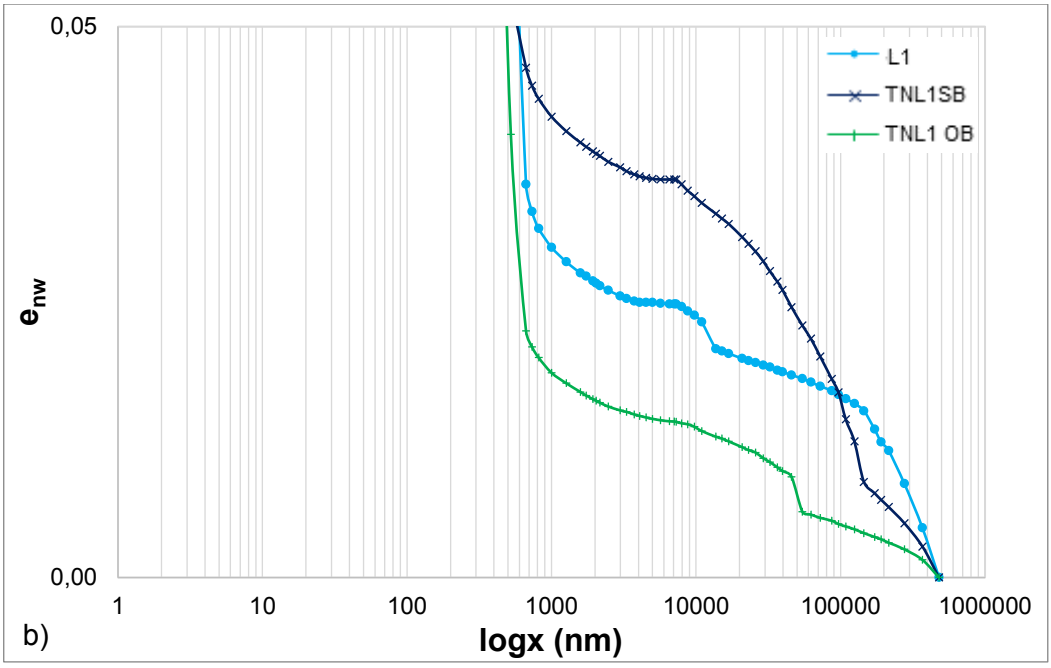
L1
TNL1SB
TNL1 OB
0,05
0,00
e_{nw}
1
10
100
1000
10000
100000
1000000
logx (nm)
b)

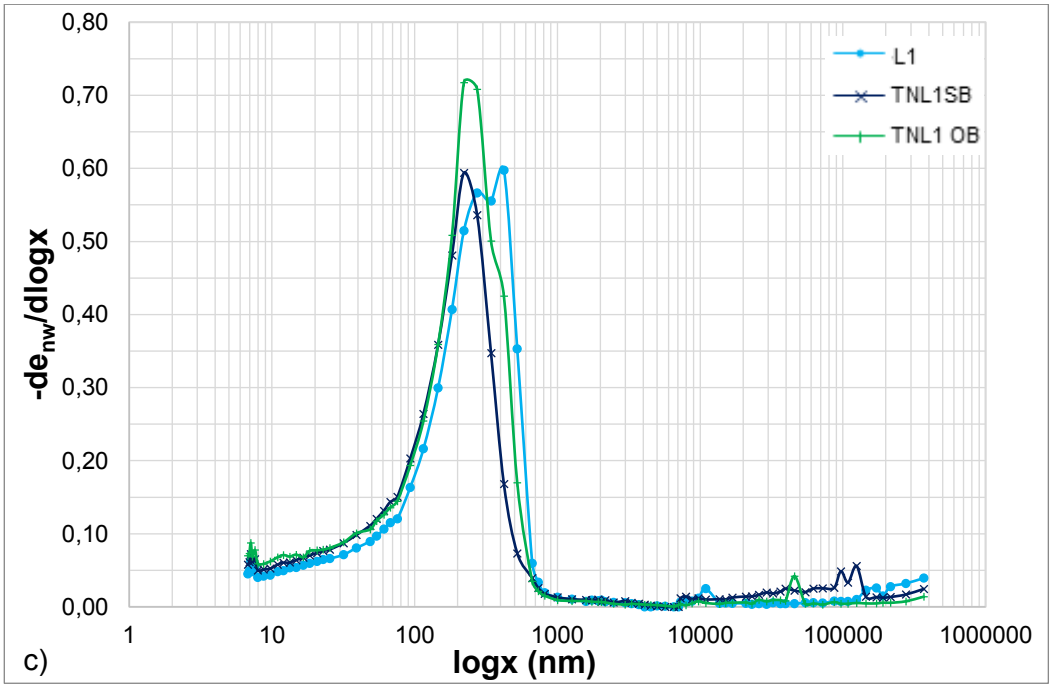

Fig. 7.114 - MIP tests on natural Lucera clay in undrained shear test TNL1 (R=3, e=0.546) inside (SB) and outside (OB) the shear band compared to specimen at undisturbed state. a) cumulative, b) enlarged cumulative and c) derivative curves.

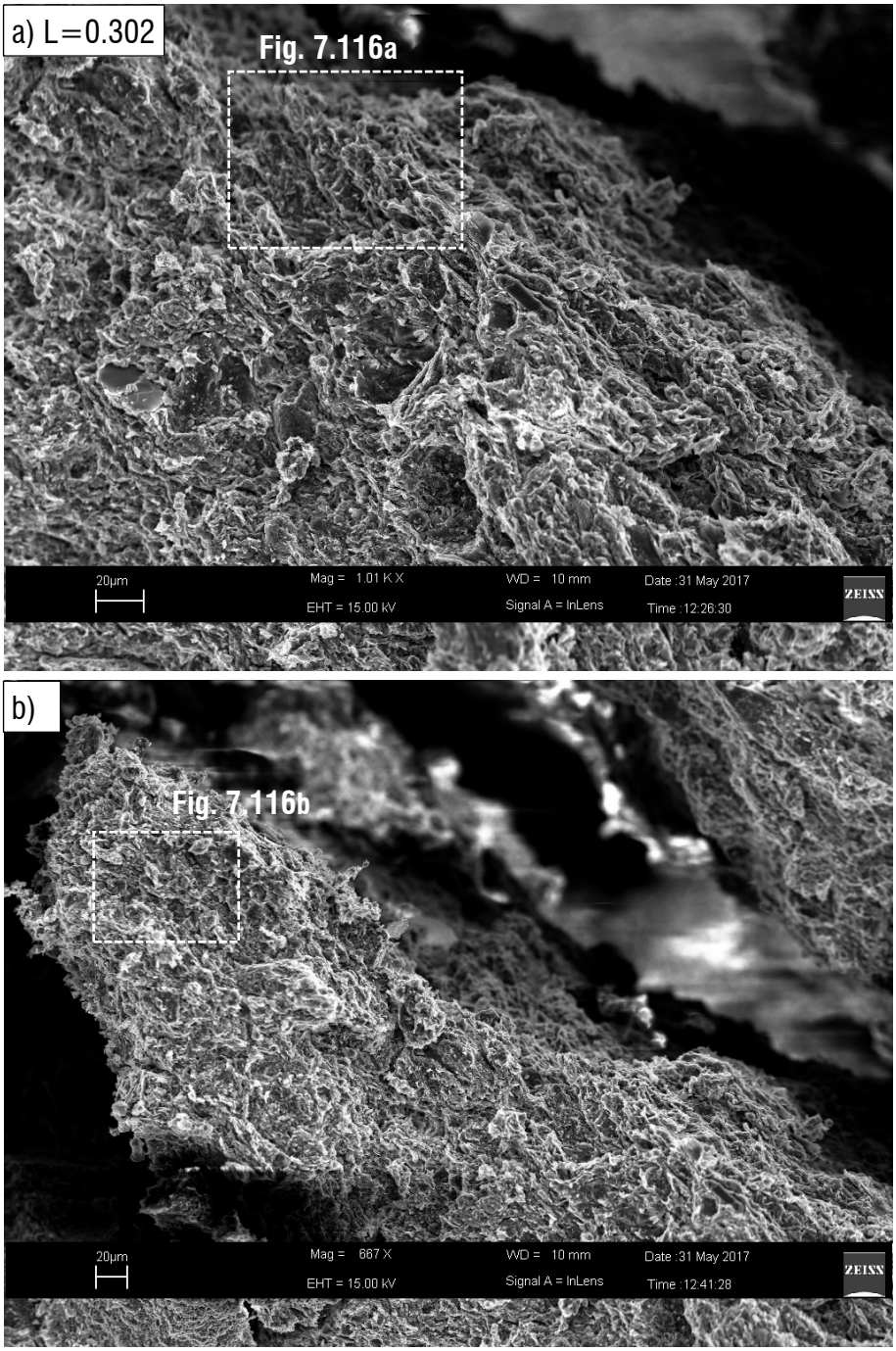

Fig. 7.115 - SEM micrographs of natural Lucera clay specimen TNL1 sheared undrained along a vertical fracture across the shear band at medium magnification.

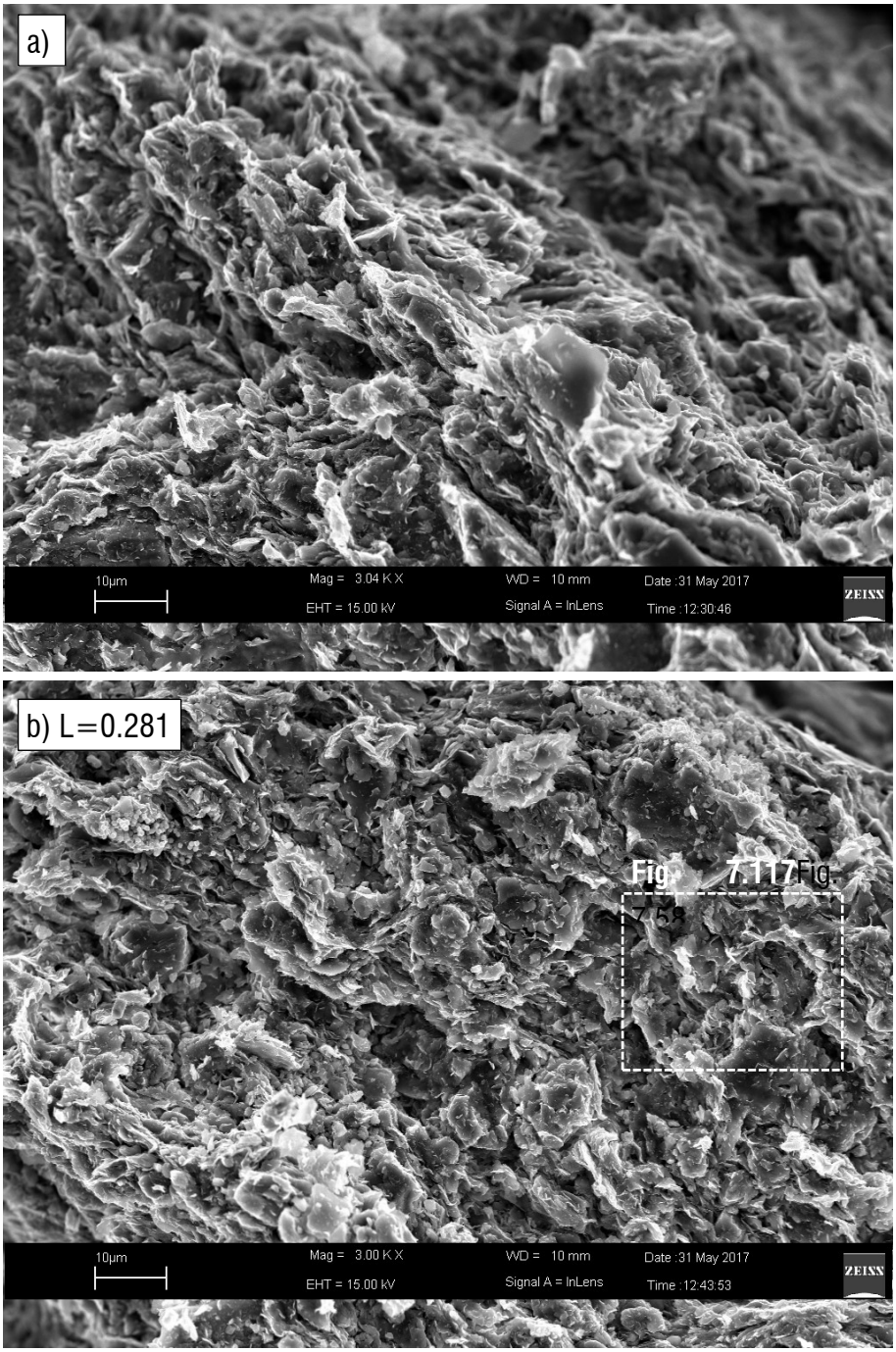

Fig. 7.116 – Enlargements of micrographs in Fig. 7.115.

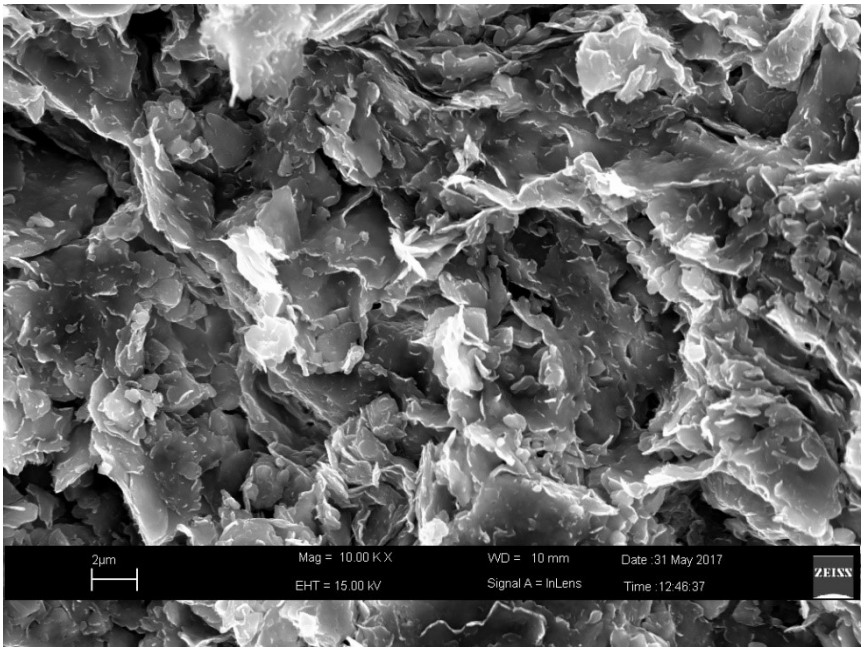

Fig. 7.117 . Enlargement of Fig. 7.116b showing very small domains of edge-to-face particles.

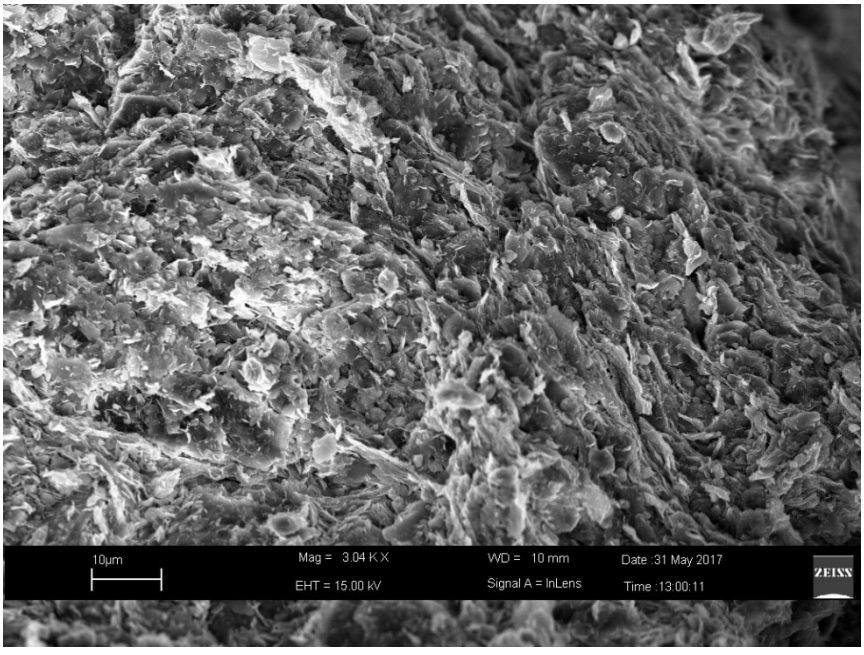

Fig. 7.118 - SEM micrograph of natural Lucera clay specimen TNL1 sheared undrained along a vertical fracture across the shear band at medium-high magnification: highly oriented particles confining with honeycomb arrangements.

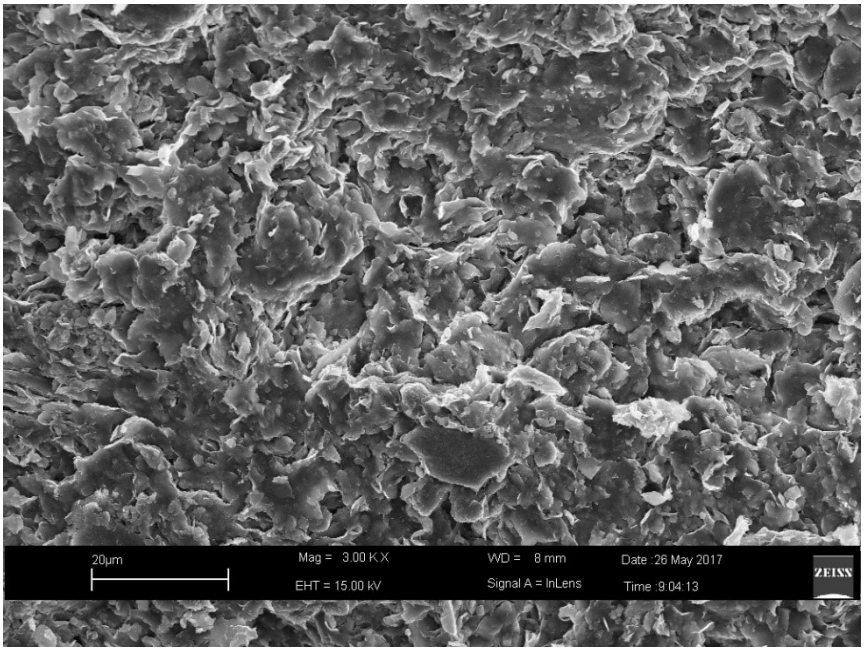

Fig. 7.119 - - SEM micrograph of natural Lucera clay specimen TNL1 sheared undrained along the failure surface.

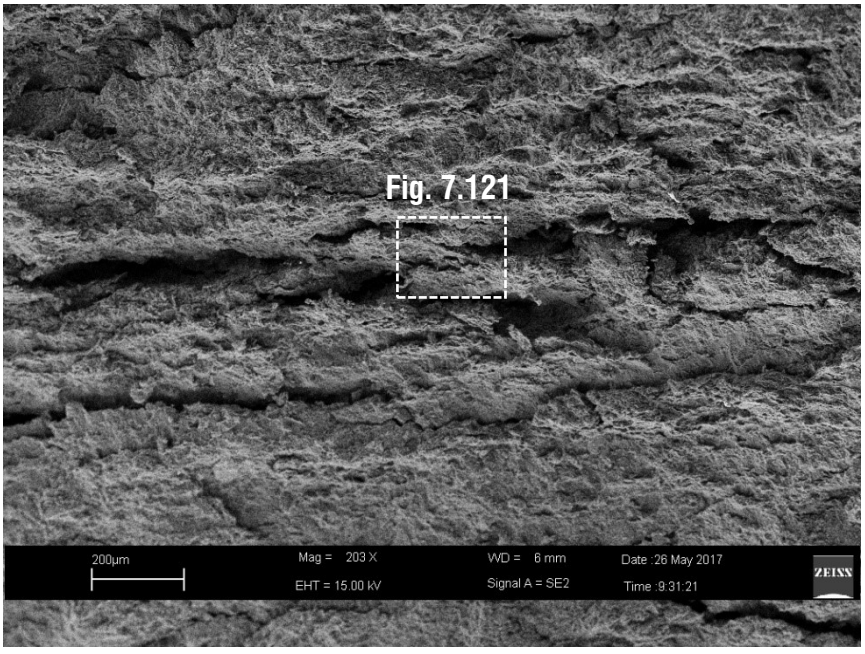

Fig. 7.120 - SEM micrograph of natural Lucera clay specimen TNL1 sheared undrained along the failure surface: intersection with the failure surface of the symmetrical shear band.

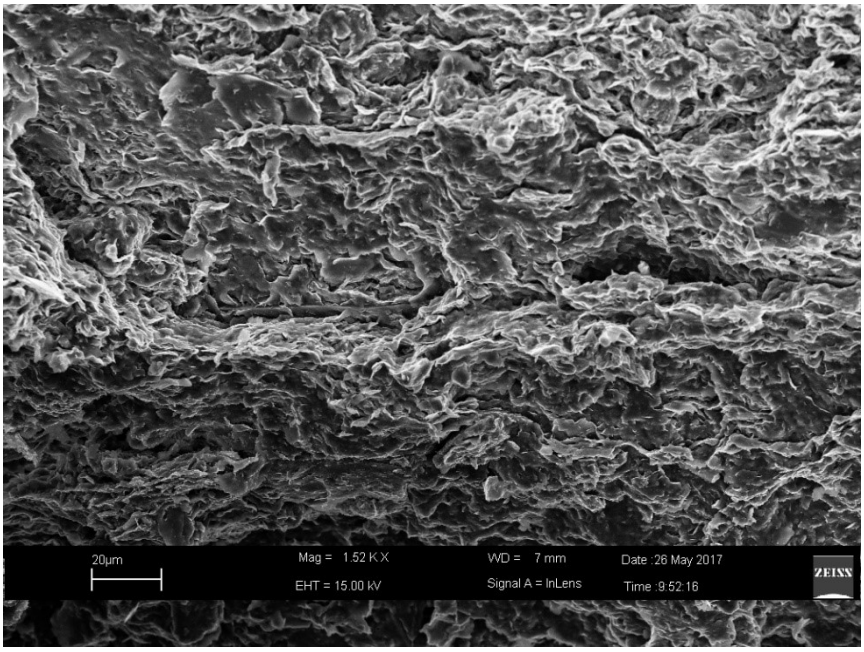

Fig. 7.121 – Enlargement of the micrograph in Fig. 7.120: a perfectly oriented stack of particles emerges from the failure surface of the investigated shear band.

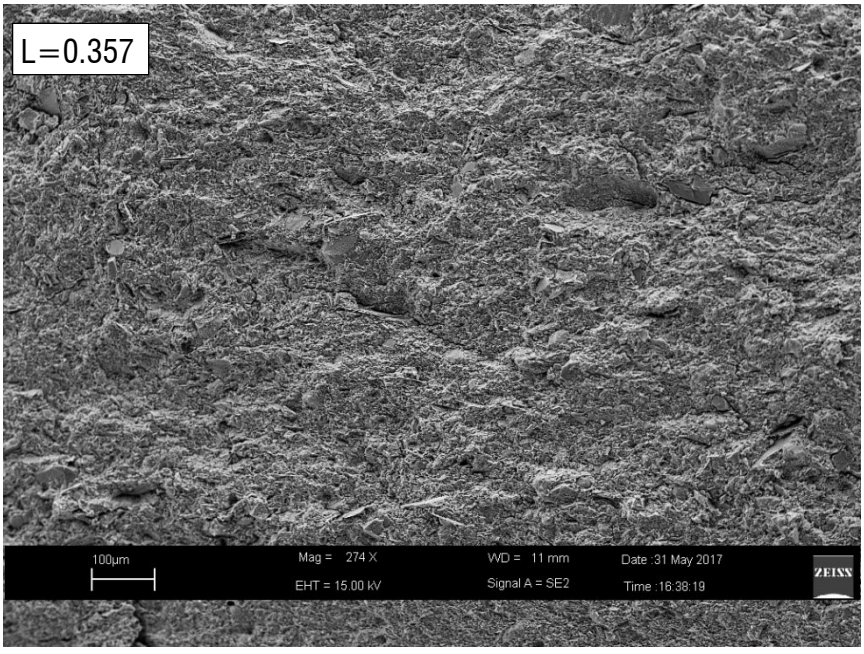

Fig. 7.122 - SEM micrograph of natural Lucera clay specimen TNL1 sheared undrained outside the shear band at low magnification.

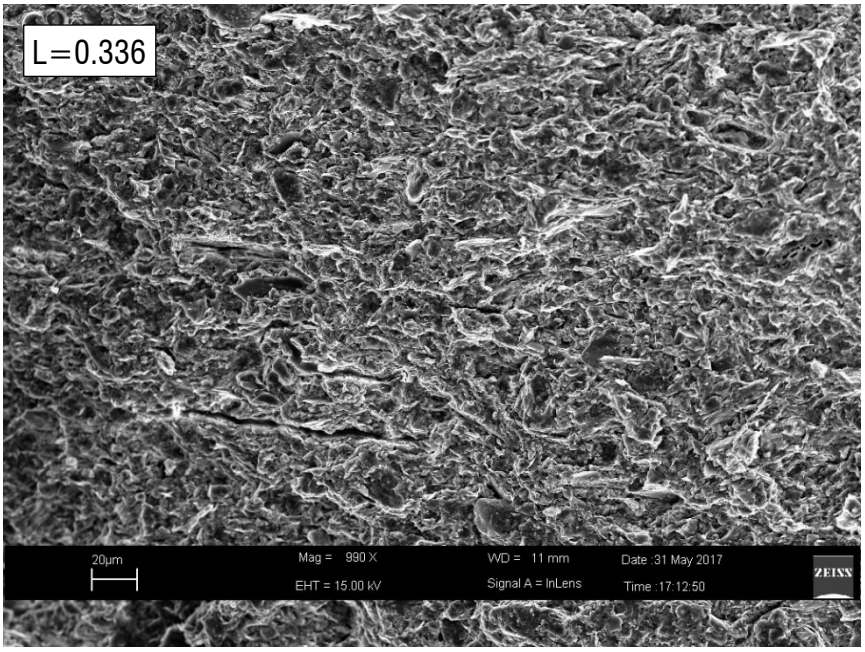

Fig. 7.123 - SEM micrograph of natural Lucera clay specimen TNL1 sheared undrained outside the shear band at medium magnification.

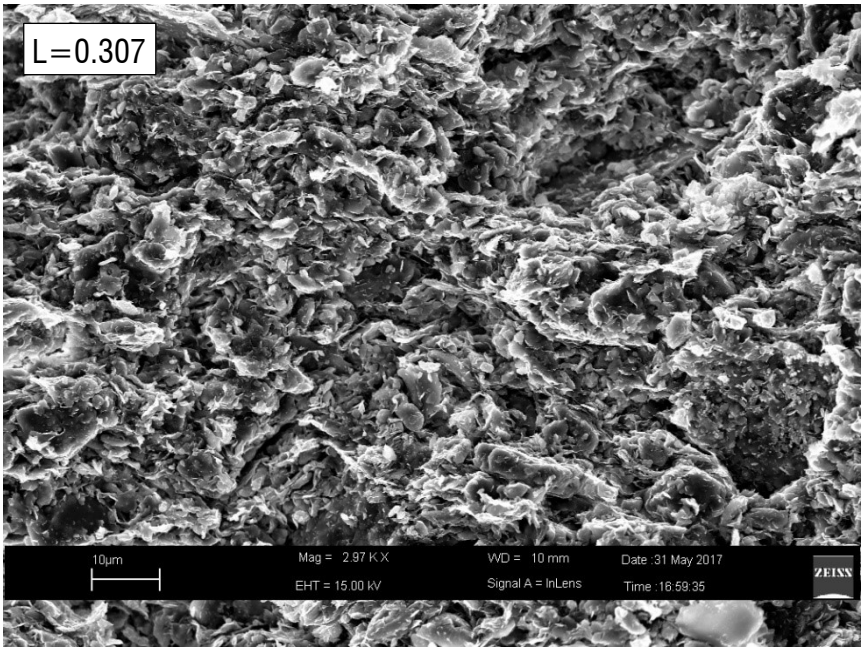

Fig. 7.124 - SEM micrograph of natural Lucera clay specimen TNL1 sheared undrained outside the shear band at medium-high magnification.

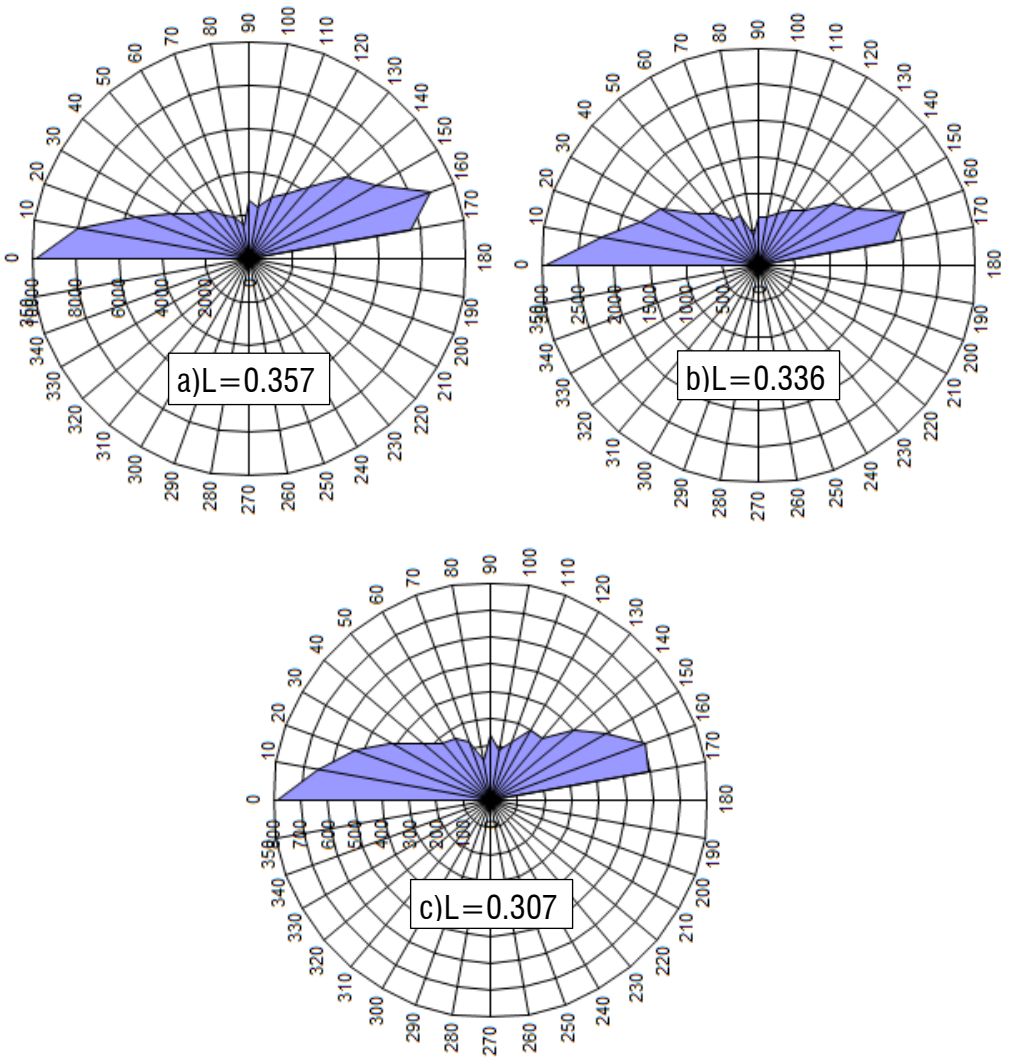

Fig. 7.125 – Direction histograms for the micrographs on specimen TNL1 OB shown in a) Fig. 7.122, b) Fig. 7.123 and c) Fig. 7.124.

The MIP results obtained for specimen TNL1 are compared in Fig. 7.126 to those obtained for specimen TNL10, sheared undrained to half the peak deviatoric stress recorded in test TNL1 (Section 6.4.1).

Apart from a small difference in the maximum intruded void ratios, which is caused by the small difference in void ratios between the undisturbed specimen and the sheared specimen prior to testing, the cumulative curves are completely superimposed.

Accordingly, the incremental curves are almost perfectly identical, the DPS having the same values and frequency and the two branches of the curves being overlapped.

Hence, no pore distribution change is recorded in the clay sheared undrained up to half the peak deviatoric stress, suggesting that the clay is experiencing minor reversible changes up to this point in the stress path.

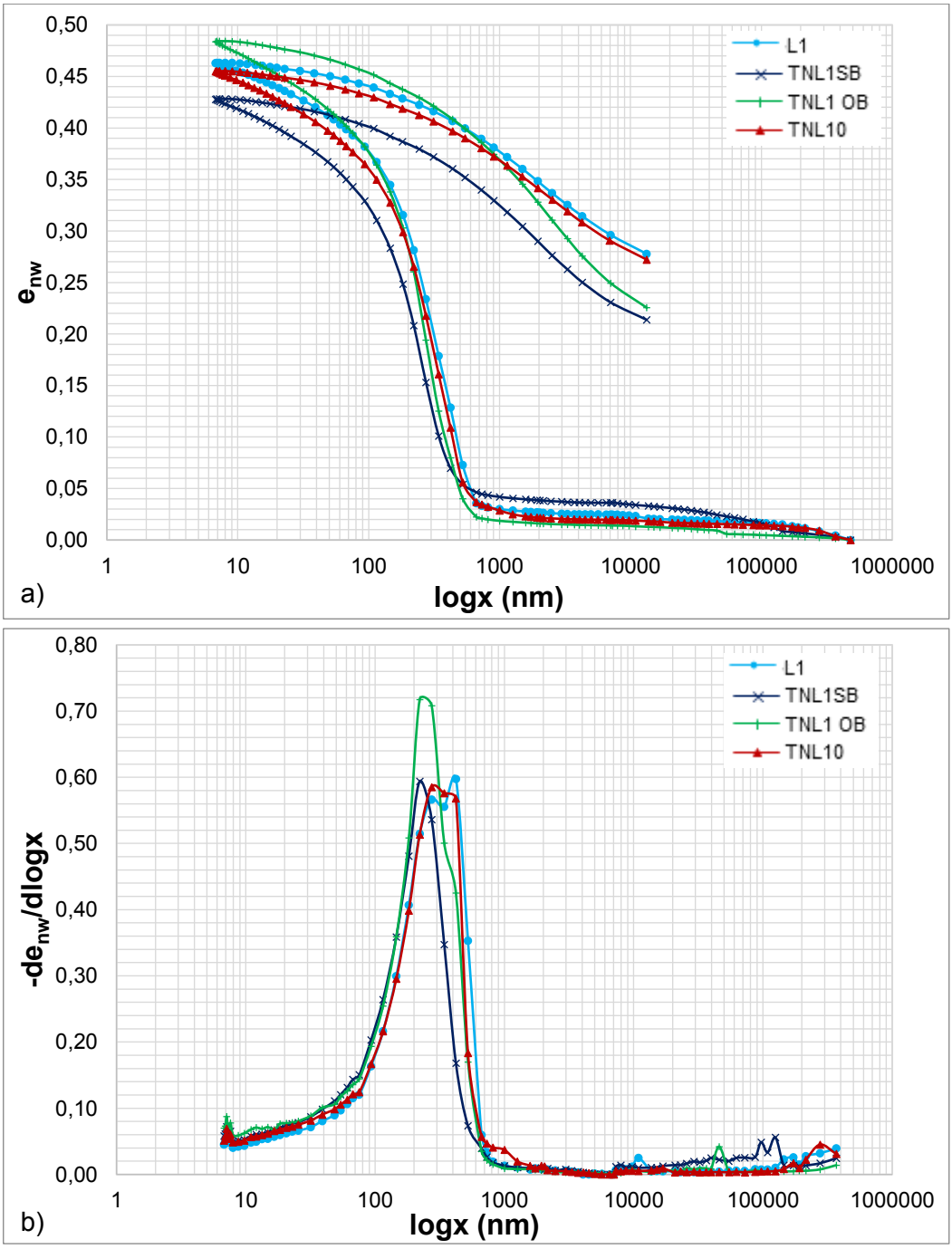

Fig. 7.126 - MIP tests on natural Lucera clay at undisturbed state, in undrained shear TNL1, inside (SB) and outside (OB) the shear band, and at $q_{peak}/2$ (TNL10). a) cumulative and b) derivative curves.

In Fig. 7.127 the MIP test results on specimen TNL7 (e=0.518) both inside (SB) and outside (OB) the shear band are shown, compared to those of specimen LI_2, which represents the state of the specimen prior to shearing.
Both the specimens SB and OB show a maximum intruded void ratio lower than LI_2, suggesting a contraction with respect to the state before shearing both outside and inside the shear band. With respect to the zone outside the shear band, the shear band is again experiencing contraction, as occurred in specimen TNL1.
Specimen OB shows the lowest cumulative intruded volume in the range of the inter-aggregate pore volume with respect to the initial state (Fig. 7.127b), in agreement with the overall contractant behaviour observed in shear, while in specimen SB the macro-pores maintain approximately the same volume they had before shearing.
The incremental curves of both specimens (Fig. 7.127c) show a significant reduction in the height of the PSD, i.e., in the frequency of the dominant pores. This is accompanied by a light reduction in width of the incremental curve of specimen SB, which in fact has the left branch close to that of the undisturbed curve and undergoes a small reduction in the DPS, which becomes 220 nm; outside the shear band, the curve has widened, but the average value of the DPS has not changed.

The changes in pore distribution observed for both the undrained specimens TNL1 and TNL7 are showing higher complexity than those occurring in the drained specimens and are revealing a higher degree of heterogeneity of the changes undergone by the different parts of the specimen. This is mainly attributed to the undrained shear condition, which generates internal drainage between different zones of the specimen that could be causing expulsion of water from the shear band, which thus is seen to contract, and dilation of the zone outside the shear band, in which hence dilation is recorded.
In general, for both drained and undrained tests, shearing paths are seen to translate the position of the incremental curves to the left, suggesting a reduction in the dominant pore dimension and in the overall pore sizes.

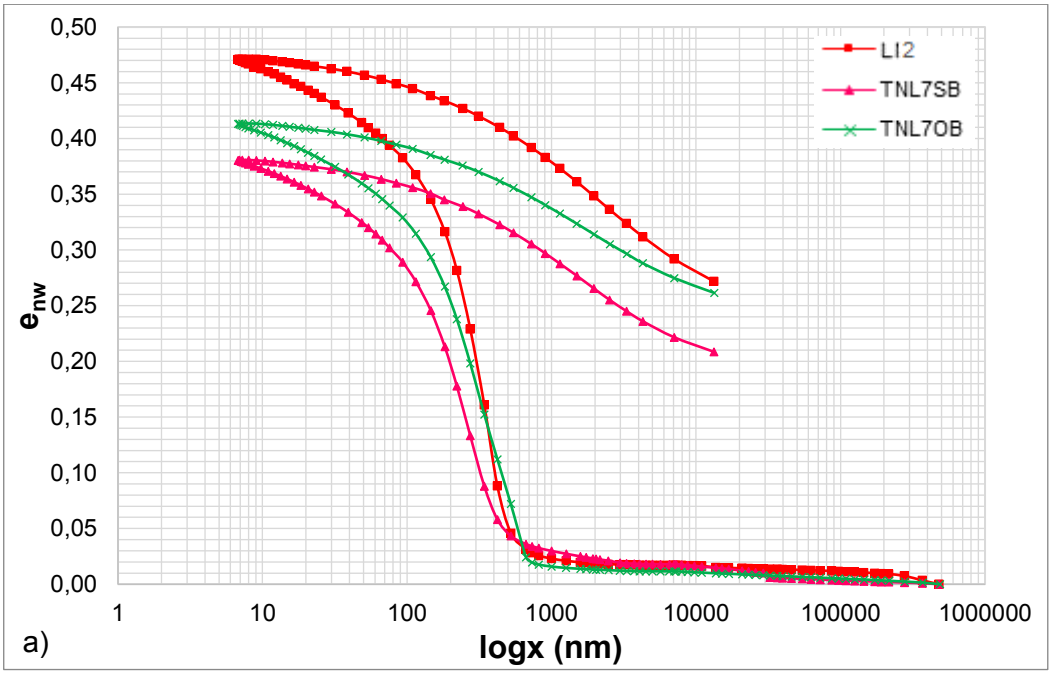
0,50
0,45
0,40
0,35
0,30
0,25
0,20
0,15
0,10
0,05
0,00
e_{nw}
1
10
100
1000
10000
100000
1000000
logx (nm)
LI2
TNL7SB
TNL7OB
a)

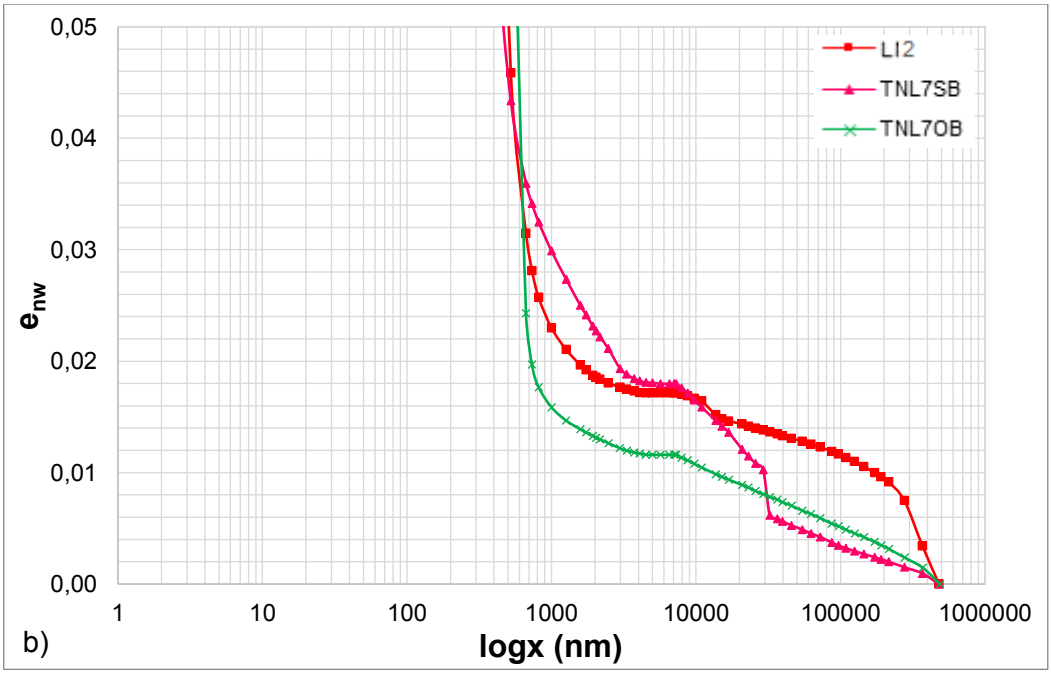
0,05
0,04
0,03
0,02
0,01
0,00
e_{nw}
1
10
100
1000
10000
100000
1000000
logx (nm)
LI2
TNL7SB
TNL7OB
b)

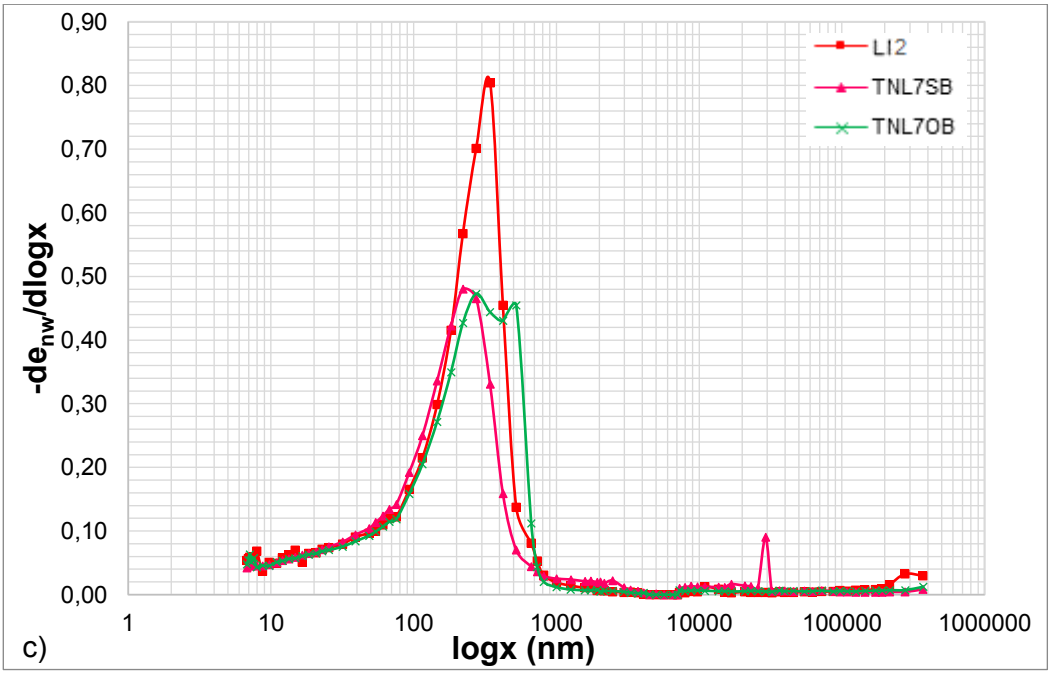

Fig. 7.127 - MIP tests on natural Lucera clay in undrained shear test TNL7 (R=1.6, e=0.518) inside (SB) and outside (OB) the shear band compared to specimen at state LI2. a) cumulative, b) enlarged cumulative and c) derivative curves.

The SEM observation of specimen SB (Fig. 7.128) allows to recognize the main shear band, but also bands of high particle orientation are seen to cross the specimen in a direction parallel to the shear band (Fig. 7.129). A marked anisotropy is induced in the clay by the formation and development of the shear band, in agreement with what seen for specimen TNL1.

Enlargements inside the most deformed zones (Fig. 7.130) show that very dense stacks of face to face perfectly oriented particles generate, in which, at places, very compressed random aggregations are found merged with the c.p.o. strata, as for example that zoomed in Fig. 7.132. Other medium-high magnification pictures (Fig. 7.131) show that very oriented particle domains are found adjacent to more random aggregations of particles. Accordingly, the image processing and resulting direction histogram (Fig. 7.134a) of the micrograph in Fig. 7.131 reveals a well-oriented fabric, but with a degree of orientation affected by the random area, with several particles

oriented along sub-vertical directions. A higher degree of orientation is conveyed by Fig. 7.133.

So, the SEM micrographs both inside and outside the shear band are showing that a higher degree of orientation is achieved under shear. In the shear band, as observed for drained tests, this is related to a re-organization of particles which start rotating along the direction of the shear band. Relating this fabric evolution to the changes observed in pore distributions, it may be hypothesised that the re-orientation of particles along the shear band direction is causing a concurrent contraction of the whole zone crossed by the shear band.
However, also outside the shear band fabric anisotropy is seen to increase, and even higher degrees of orientation are recorded.
In both areas of the specimen, less oriented particle aggregations are still recognized

In Fig. 7.135, the MIP results on specimen TNL11 sheared undrained to half the peak deviatoric stress of test TNL7 are shown, compared to the results of test TNL7 (SB and OB) and with the state LI_2 prior to shearing.
Also in this case, the maximum intruded void ratio for specimen TNL11 is lightly higher than that of specimen LI_2, since a small difference existed in the void ratios of the two specimens at undisturbed state (Table 5.2, Table 5.4). Except for this, both the cumulative and incremental curves are superimposed, the latter only presenting small differences in the frequency of the DPS.

So, in agreement with the previous discussion on specimen TNL10, also for specimen TNL11 no significant changes in the pore distribution occurs up to half the peak deviatoric stress, suggesting that the structure changes that are taking place in the specimen are minor when sheared undrained before gross-yield in shear, i.e., before reaching the SBS. These results suggest that the CSF applies to the behaviour of the clay under undrained shear and that the elastic behaviour predicted by the MCC inside

the SBS may well simulate the effects of minor microstructural evolution up to half the peak deviatoric stress.

A similar observation was also seen to apply to the compression behaviour: limited changes were seen to occur when compressing the clay to states pre-gross-yield. This was found to be particularly true for the oedometric compression of natural Lucera clay, while the specimen isotropically compressed pre-gross-yield exhibited more evident, although not dramatic, modifications of microstructure. But it should be noticed that the pre-gross-yield compression states tested were much closer to isotropic and K_0 gross-yield than the pre-gross-yield states attained in shear paths.

Certainly, the analysis of microstructure on a specimen sheared up to a deviatoric stress immediately pre-gross-yield in shear would be of help in understanding the evolution of microstructural changes and would show the extent to which plastic hardening inside the SBS represents microstructural changes pre- gross yield in shear.

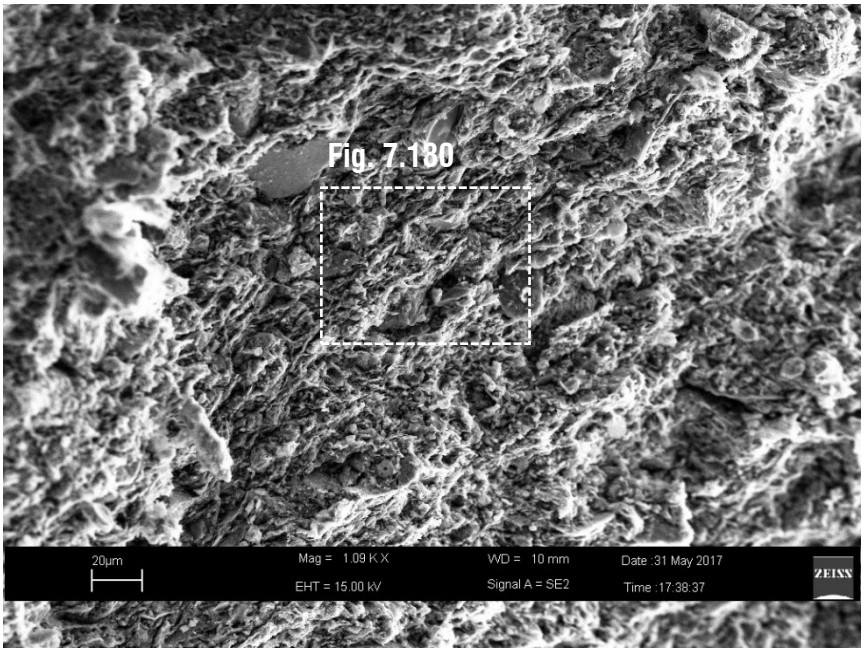

Fig. 7.128 - SEM micrograph of natural Lucera clay specimen TNL7 sheared undrained inside the shear band: detail of the shear band observed on a vertical fracture.

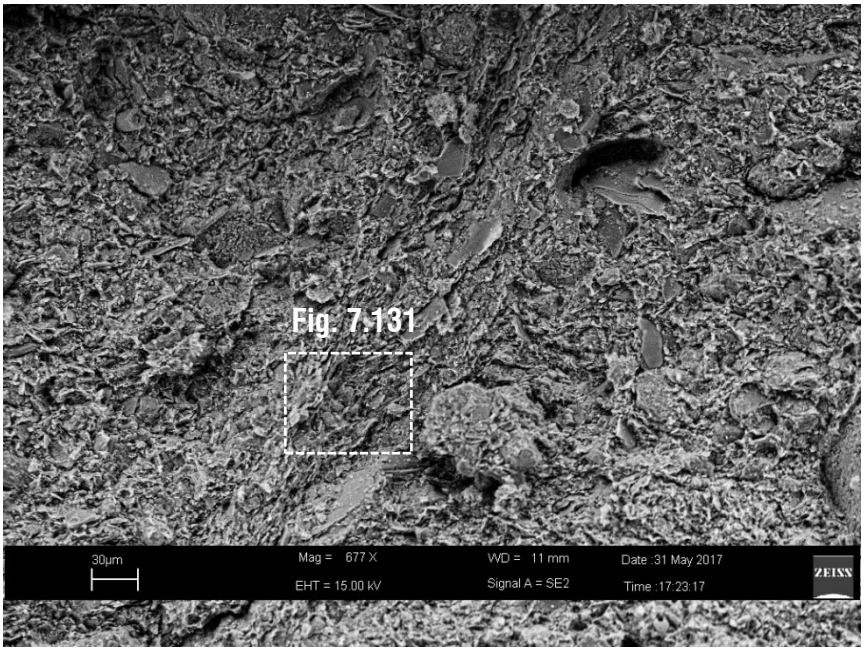

Fig. 7.129 - SEM micrograph of natural Lucera clay specimen TNL7 sheared undrained inside the shear band: detail of a highly oriented band parallel to the shear band.

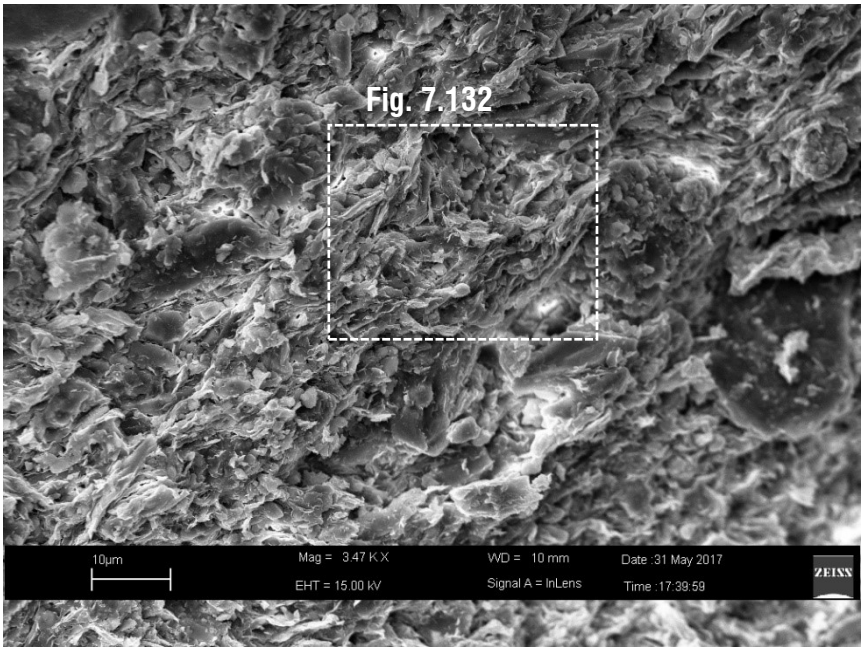

Fig. 7.130 – Enlargement of the micrograph in Fig. 7.128.

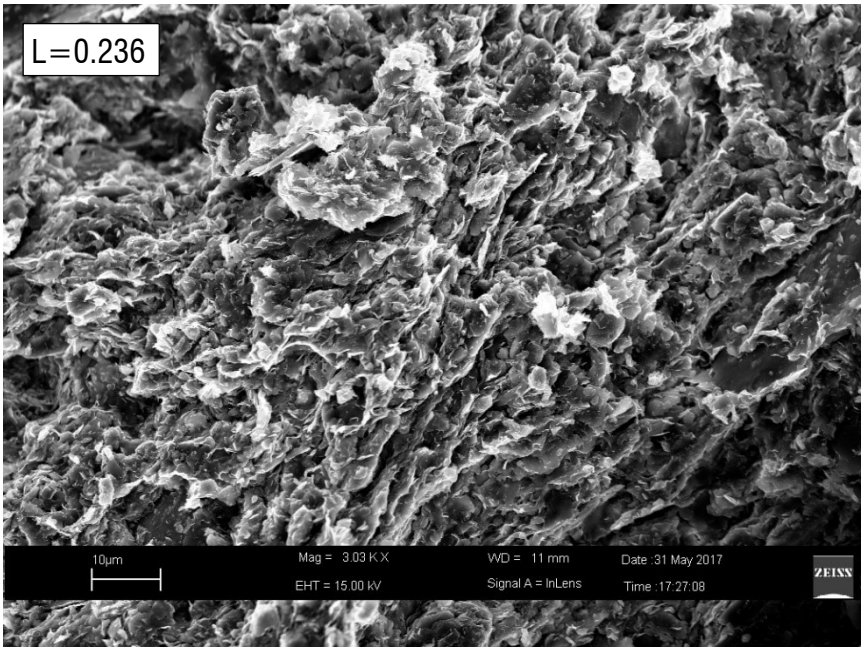

Fig. 7.131 – Enlargement of the micrograph in Fig. 7.129.

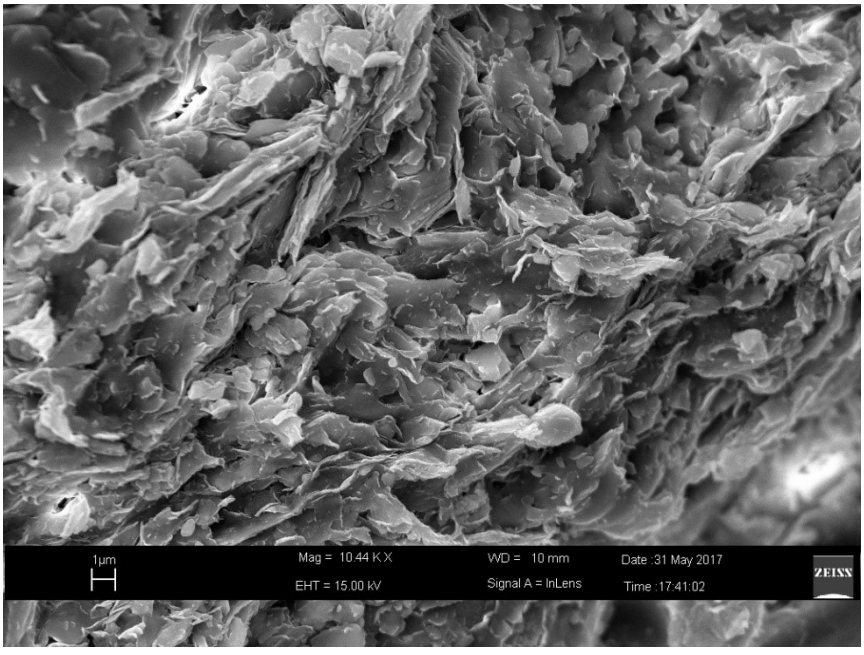

Fig. 7.132 – Enlargement of the micrograph in Fig. 7.130.

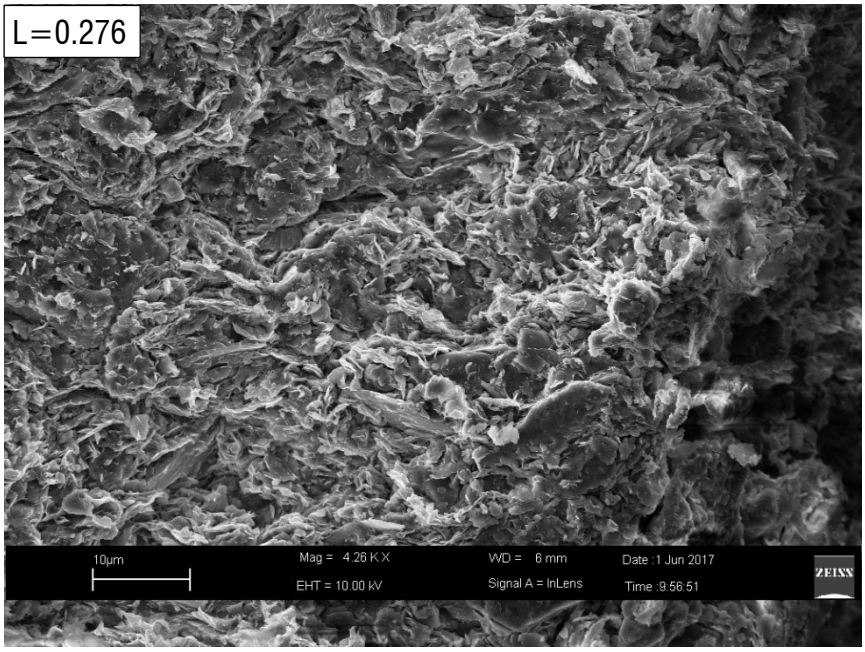

Fig. 7.133 - SEM micrograph of natural Lucera clay specimen TNL7 sheared undrained inside the shear band at medium-high magnification.

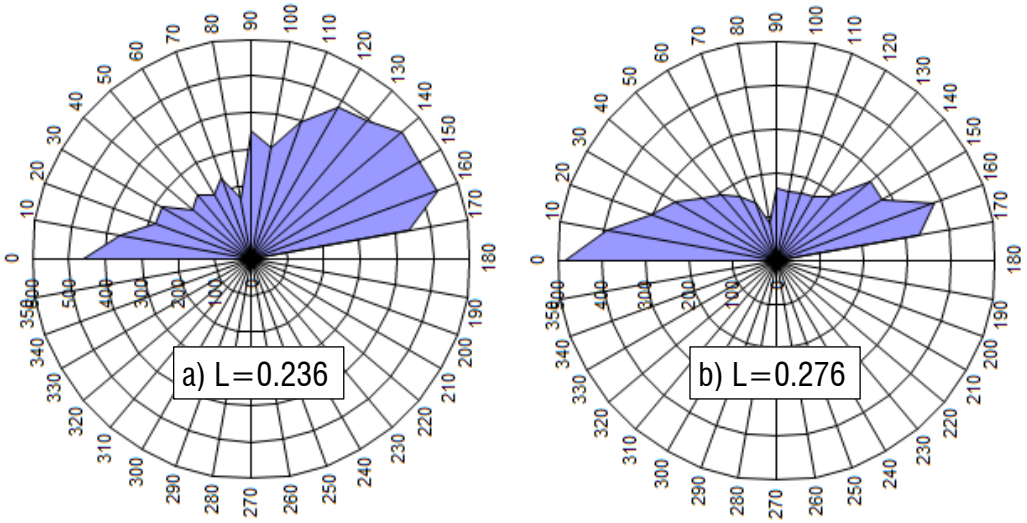

Fig. 7.134 – Direction histograms of the SEM micrographs in (a) Fig. 7.131 and (b) Fig. 7.133 .

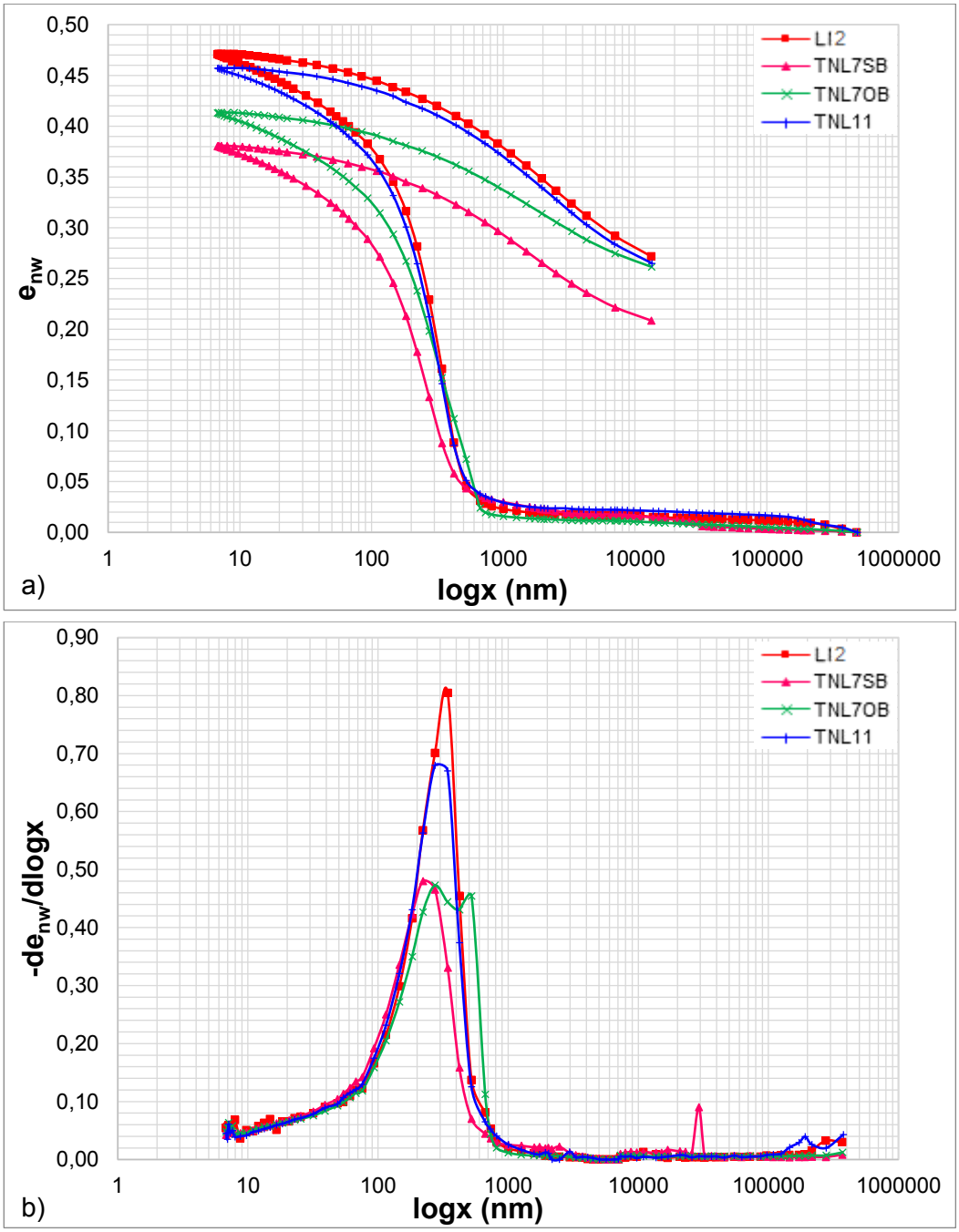

Fig. 7.135 - MIP tests on natural Lucera clay at state LI2, in undrained shear TNL7 (R=1.6, e=0.518) inside (SB) and outside (OB) the shear band, and at $q_{peak}/2$ (TNL11). a) cumulative and b) derivative curves.

7.4.3 Microstructural changes for the reconstituted clay under shear

The microstructural analyses on sheared specimens of reconstituted Lucera clay were carried out on two specimens: TRL2, sheared undrained from an overconsolidation ratio R=4 and TRL1, sheared drained from R=1.8. The v-p' state paths and the q-p' stress paths are reported for all the shear tests on reconstituted Lucera clay in Fig. 7.136; the location of the specimens subjected to the microstructural analyses are reported.

The behaviour exhibited by the clay in the two tests was discussed in detail in Section 6.4.1. Specimen TRL2 was dilatant and exhibited strain-softening, which developed into a shear band; by contrast, specimen TRL1 was contractant and strain-hardening, but the test was stopped too soon and the specimen did not reach the critical state.

The two specimens at the end of shearing are shown in Fig. 7.137, in which the position of the specimens prepared for microstructural analyses is also indicated. For TRL1 the specimen for MIP and SEM, combined with image processing was taken at the core of the specimen, where it is supposed to be less affected by boundary conditions. For specimen TRL2, only MIP tests were carried out on two portions, inside (SB) and outside (OB) the shear band.

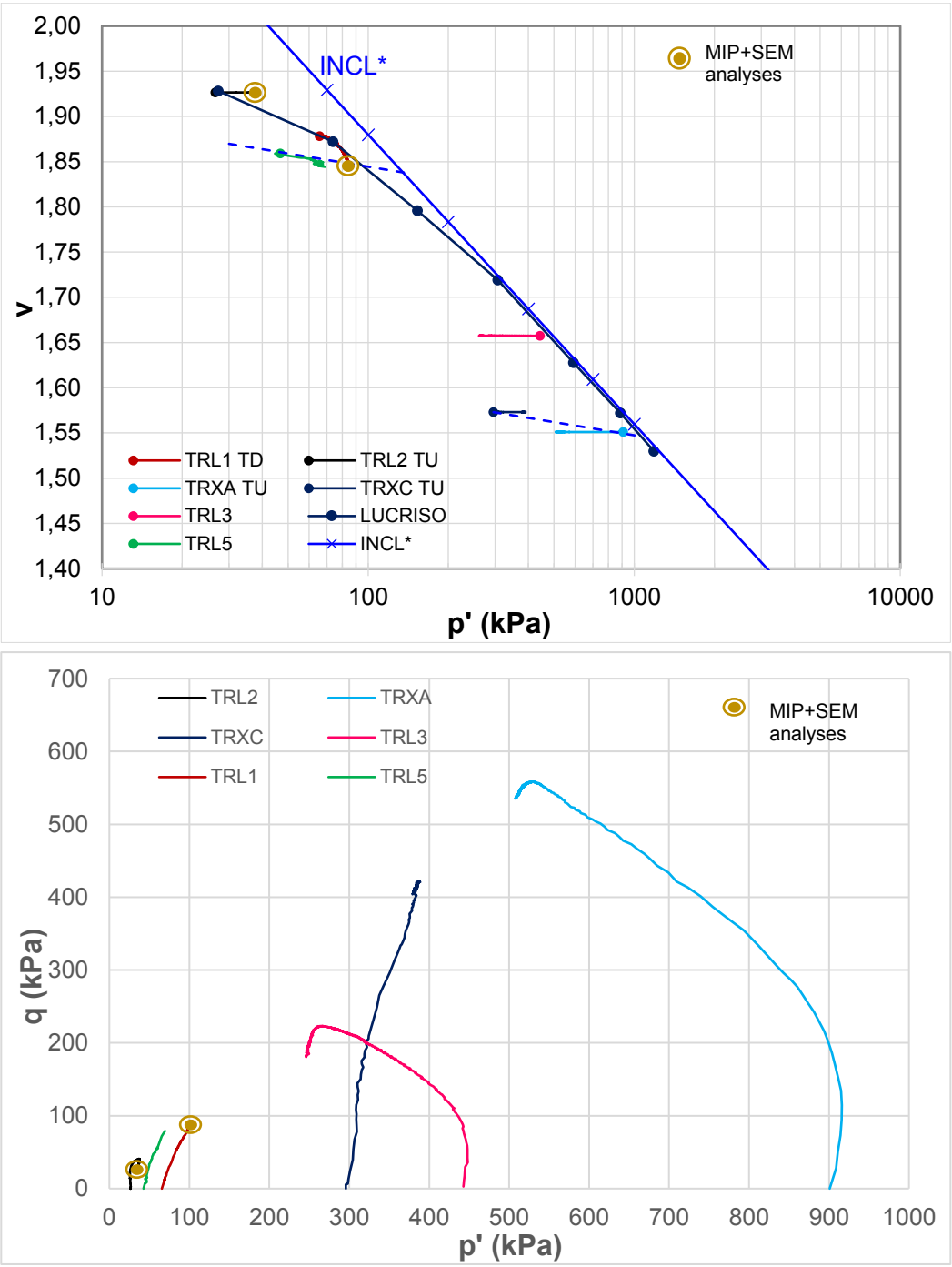

Fig. 7.136 – a) v-p' states and b) stress paths of shear tests on reconstituted Lucera clay: indication of states of microstructural analyses.

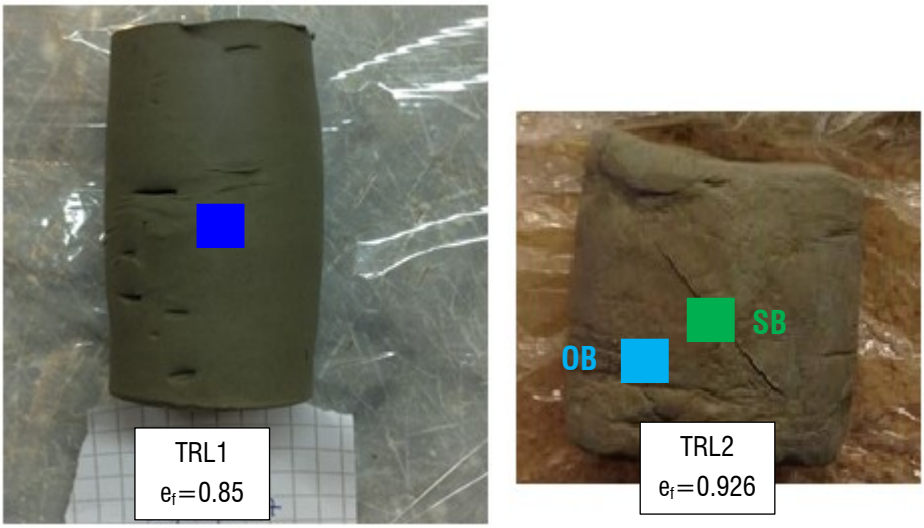

Fig. 7.137 – Specimens TRL1 and TRL2 (from which the extremities were cut for measurements of w) at the end of the drained and undrained shear tests respectively. Position of MIP specimens is indicated.

The results of the MIP tests on specimen TRL2 (e=0.926) are shown in Fig. 7.138, compared with the curves for the specimen at state LR (Fig. 7.41), i.e., after consolidometer stage. The cumulative curves show that specimen SB has the highest maximum intruded void ratio, indicating a dilative behaviour both with respect to the specimen OB and with respect to the state prior to shearing. The macro-pore volume of SB is undergoing an overall decrease, although the step in the cumulative curve at around 50 μm, which may be related to the presence of a fissure, can be misleading. On the other hand, the specimen OB displays a reduction of maximum intruded void ratio and undergoes a complex change in the macro pore volume. The abrupt change in slope shown by the cumulative curve of specimen OB at around 7 μm (circled for clarity in Fig. 7.138a), and corresponding to a discontinuity in the incremental curves, is sometimes seen in MIP tests results as it is due to the transfer of the specimen during the MIP test from the low to the high-pressure port (Section 5.3.2). Thus, it is not considered as a true description of the intrusion mode around these pore sizes.
Also in this case, the maximum void ratios reached by the two portions taken from specimen TRL2 can be assumed to have the same void ratio at the beginning of the

tests, so the difference observed is only caused by non-uniform modifications of the pore volume induced by shear. As for natural undrained shear, a role is played by internal drainage occurring inside the specimen during testing. In this case, pore water seems to be recalled by the shear zone, which dilates, from the more peripheral parts of the specimen, which instead contract.

Incremental curves (Fig. 7.138b) confirm that in specimen SB the macro-porosity seen at state LR is lost almost completely and simultaneously lower pore sizes concentrated in a more restricted range of sizes are acquired, with a DPS slightly reduced to around 800 nm and with a higher frequency. Instead specimen OB exhibits a much more disordered PSD, which keeps being more similar to that of specimen LR: the larger peak entrance diameter at around 3 μm is unchanged, while the dominant pore is shifted to the left to around 300 nm. However, the irregularities shown by specimen OB are likely to be attributed not only to a complex pore volume change, but also to some degree of disturbance in the specimen subjected to the MIP test.

For TRL2, no SEM micrographs were taken, but the MIP results are believed to suggest an overall fabric organization similar to that of specimen LR, with an increase in orientation along the shear band.

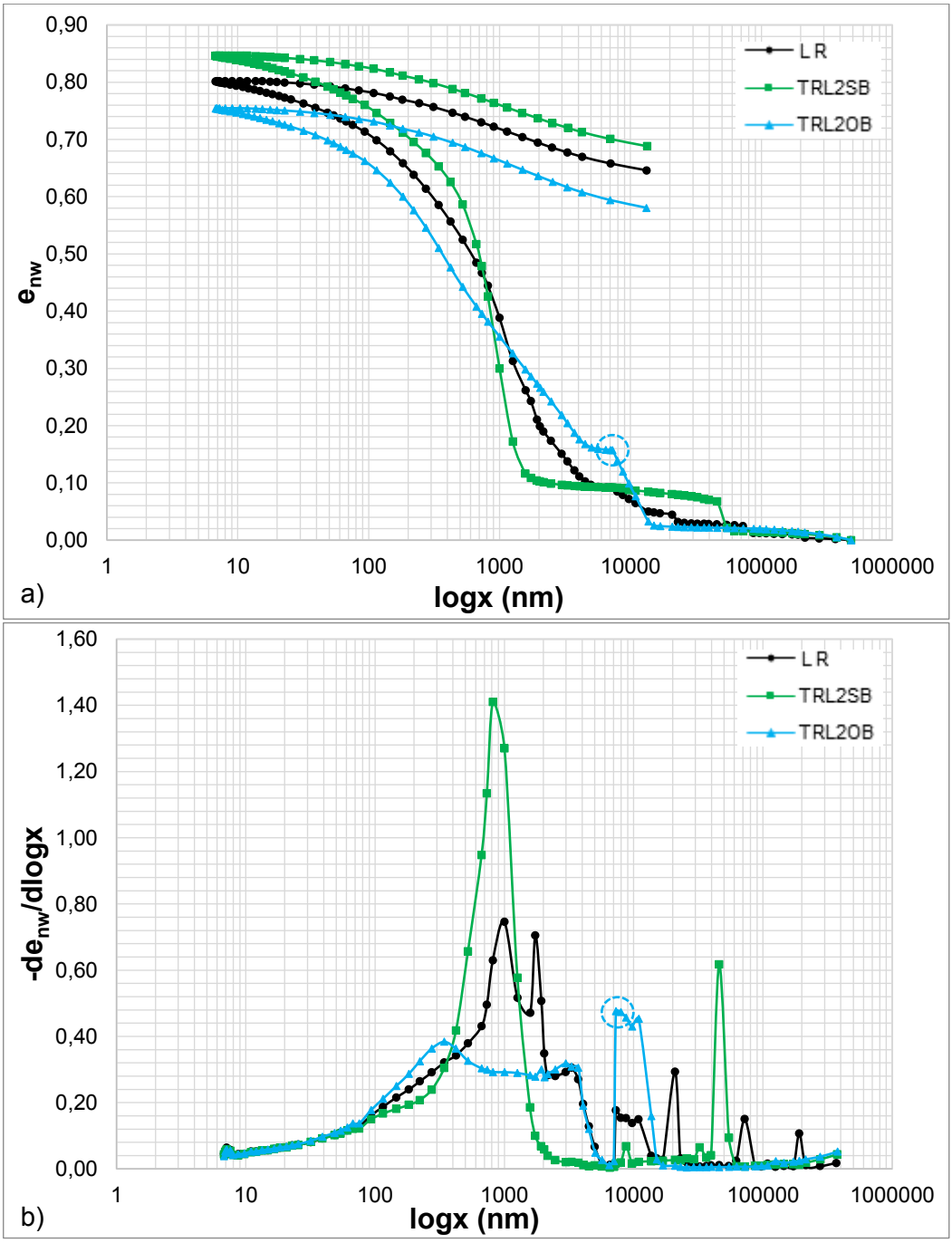

Fig. 7.138 – MIP tests on reconstituted Lucera clay at state LR and in undrained shear TRL2 (R=4, e=0.926), both inside (SB) and outside (OB) the shear band. a) cumulative and b) derivative curves.

The results of the MIP test on TRL1 subjected to drained shear are now discussed. In Fig. 7.139, these results are compared with those of specimen LR, as done for specimen TRL2. To be rigorous, the comparison should have been made with a specimen of reconstituted clay isotropically compressed to 65 kPa, which would have represented the state of the specimen TRL1 prior to shear testing. However, very small changes in microstructure are expected to occur under isotropic compression from 30 kPa (which is approximately the pressure p' corresponding to state LR) to 65 kPa, so specimen LR is used for comparison.

A first consideration has to be made about the difference between the maximum intruded void ratios for the specimens TRL1 and LR, which is lower than expected. This is believed to be related to a difference between the non-detected void ratio in the two specimens, as occurred for the specimen of natural Lucera clay 1D swelled (L_S). In this case, it is suspected that the specimen tested from TRL1 had locally a higher void ratio than that the final void ratio determined from the shear test.

However, the remaining part of the cumulative curve testifies the effects of shear, which are recognized to be similar to those manifested in the other specimens investigated so far. A significant decrease in the macro-pore volume is observed, with an important shift of the incremental curve towards smaller and more concentrated pore sizes. In this case the DPS is almost unchanged, but the pore space must have undergone a total reorganization towards smaller and more numerous pores.

A SEM micrograph giving a global view of the fabric on a vertical fracture (Fig. 7.140) shows a quite packed and oriented fabric, in which many elements recognized in the specimen after consolidometer stage can be found. In fact, horizontal and sub-horizontal complex laminae are visible, delimiting at places lower orientation layers. The degree of orientation is much higher than that measured in the specimen after consolidometer stage (average 0.192), suggesting that an overall increase in fabric anisotropy has occurred. Remarkably, the absence of a failure surface in this specimen

is indicative that shear is inducing fabric orientation also when particles are not re-orienting along the shear band.
At higher magnification (Fig. 7.141), thin layers of highly oriented compressed particles in face to face contact cross the micrograph along sub-horizontal directions. Also here a marked degree of fabric orientation arises, despite zones of low orientation being present at places. An enlargement (Fig. 7.142) taken between two stacks allows to observe close the less oriented particle aggregations, as confirmed by the lower degree of orientation.

Hence, the MIP tests on reconstituted Lucera clay are confirming that the evolution of microstructure experienced in undrained shear is far more complex and heterogenous than that induced by drained shears, due to the drainage occurring inside the specimen. Both the drained test and the undrained test inside the shear band on the reconstituted Lucera clay are achieving of a lower DPS. For the drained specimen, the fabric is found to have a similar architecture to that of the specimen prior to shearing, but with a higher degree of orientation.
The increase in orientation occurring in specimen TRL1, which did not develop a shear band, is confirming that shear is inducing an overall increase in fabric orientation also when the mechanism of particle orientation along the direction of the shear band is not activated. Furthermore, as observed for the natural sheared specimens, the average increase in fabric anisotropy occurs with random areas of far lower orientation still preserved.

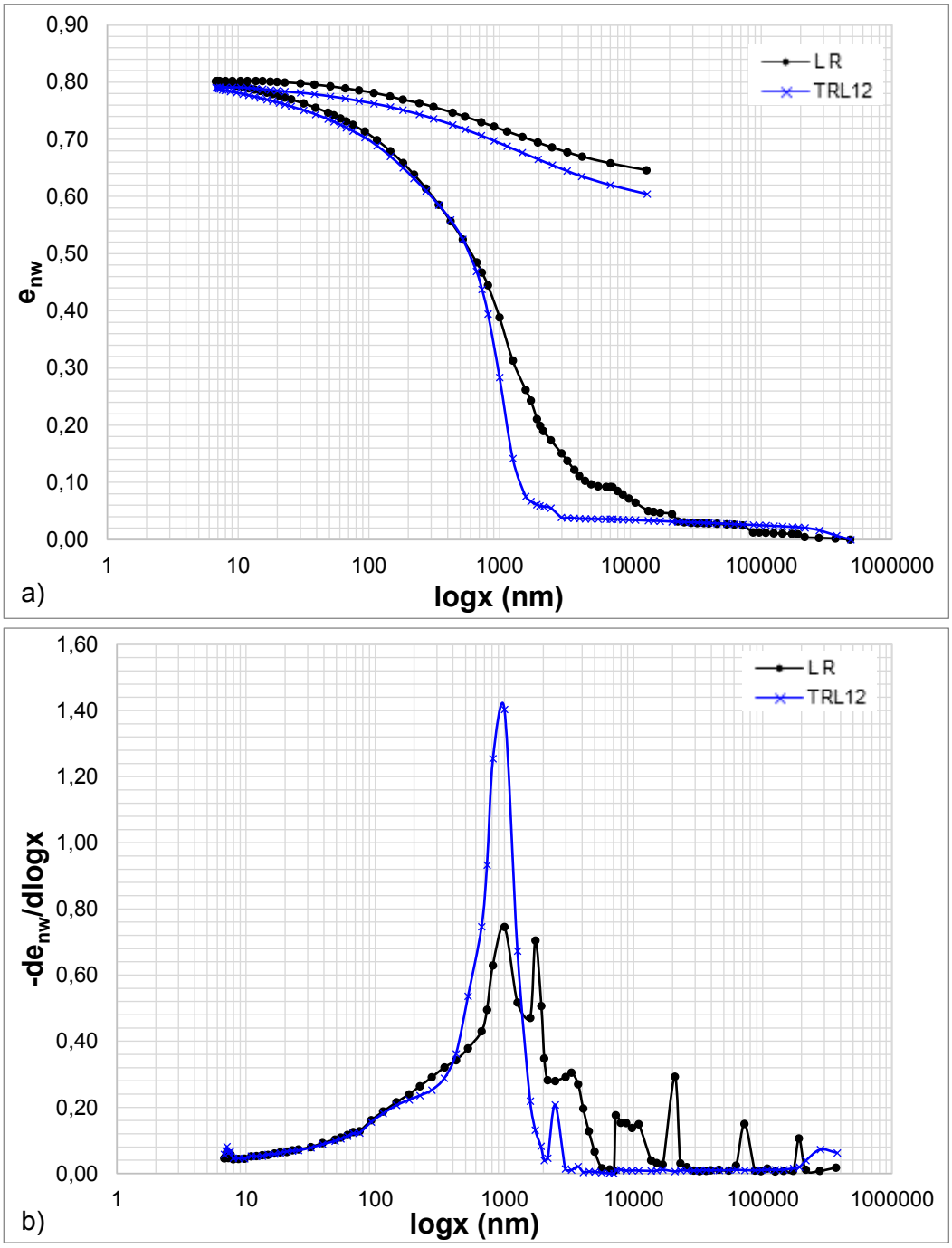

Fig. 7.139 - MIP tests on reconstituted Lucera clay at state LR and in drained shear TRL1 (R=1.8, e=0.85), both inside (SB) and outside (OB) the shear band. a) cumulative and b) derivative curves.

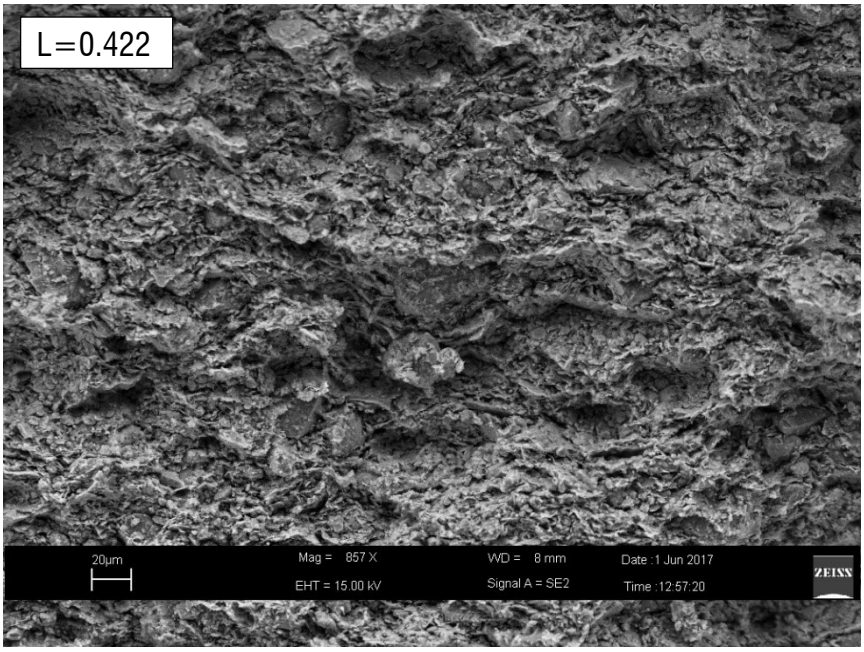

Fig. 7.140 - SEM micrograph of reconstituted Lucera clay specimen TRL1 sheared drained at low magnification.

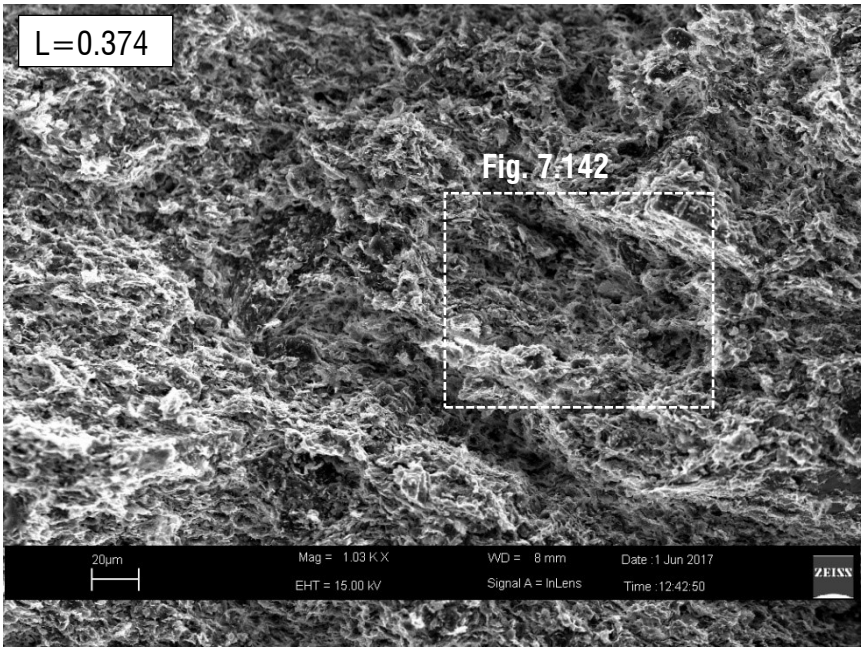

Fig. 7.141 - SEM micrograph of reconstituted Lucera clay specimen TRL1 sheared drained at medium magnification.

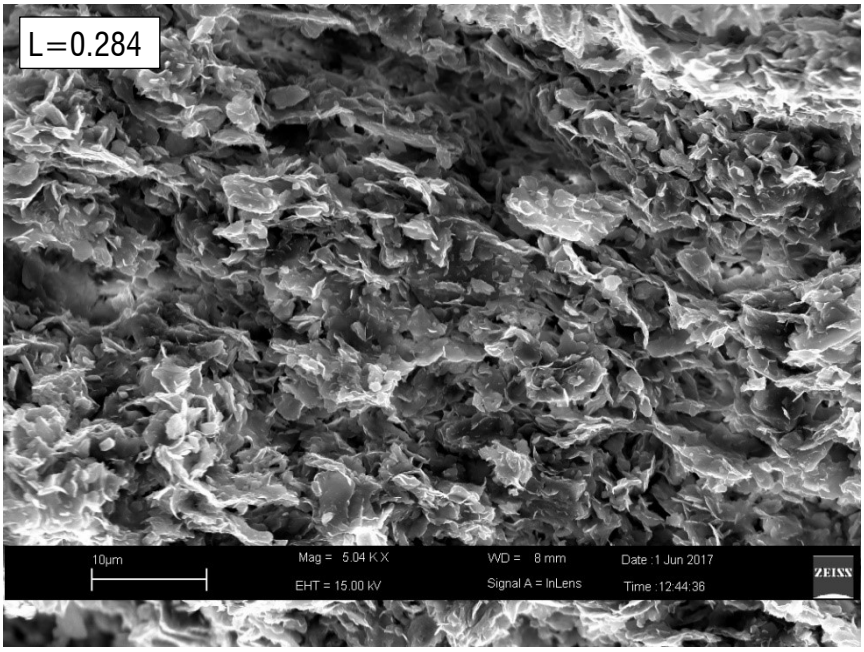

Fig. 7.142 – Enlargement of the micrograph in Fig. 7.141, showing the fabric generated by drained shear at high magnification.

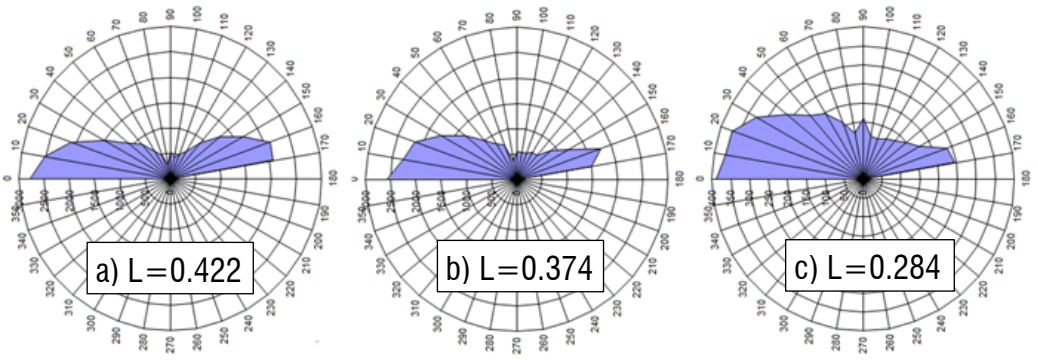

Fig. 7.143 – Direction histograms of specimen TRL1 on the micrographs in a) Fig. 7.140, b)Fig. 7.141 and c) Fig. 7.142.

8 DISCUSSION OF THE RESULTS

8.1 Introduction

In Chapter 2, the effects of deposition conditions and of subsequent changes, occurring under burial, of the fabric of clays of different composition were discussed and the conclusion was drawn that, for a given composition, a number of chemo-physical processes can develop and cause substantial changes of both the bonding, the fabric and the poresimetry of the clay with time.
The analysis of the microstructural evolution experienced by the clay under compression and shearing has shown that complex fabric and pore distribution changes occur within both the natural and the reconstituted clay, according to similar patterns of evolution, which will be assessed in the present chapter through a synthesis of the results of the analyses presented in the previous chapters.
Given the complexity of the chemo-physical processes that, at the micro-scale, control the clay state and structural features, and so, indirectly, the clay macro-response, an enhancement of the strategy to predict the clay macro-behaviour accounting for the processes at the micro-scale which control it can be pursued through a rational association of the different aspects of the clay macro-response to the clay microstructural features and their variations in the background of the macroresponse.

In the present Chapter, the microstructural features of the two studied clays, Pappadai and Lucera clay, and of other clays for which microstructural studies have been published in the literature, will be compared and interpreted, associating the micro-features and processes to factors such as: the soil composition, the microstructural features developed with consolidation and burial, the clay loading history and the loading paths during which given microstructural changes take place.
Table 8.1 summarises the properties of the different soils analysed in this Chapter, which go from stiff clays to soft sensitive clays. The mineralogy is reported as percentages of the clay minerals within the clay fraction, , except for Pappadai, London and St Marcel clay, for which it is bulk mineralogical composition (Section 4.3);

percentages of clay minerals are shown, when available, otherwise the minerals are listed in descending order of dominance.

The evolution in microstructure, in compression and shearing, analysed for Pappadai and Lucera clay will be compared to that observed for the other clays.
Examples will be given of the need for both micro and macro studies to define the classes of clays represented by a given type of modelling, since the clay micro-features, especially for natural clays in which bonding interferes significantly with fabric, cannot be inferred from macro-analyses.

Table 8.1 – Summary of the properties of the analysed clays.

Clay	z (m)	w_0 (%)	e_0	σ'_{v0} (kPa)	CF	LL	IP	A	mineralogy	YSR	S_t
Pappadai *Cotecchia (1996), this work**	25	30 *(29)*	0.88 *(0.82)*	414 *(1000-1200)*	58	65	35	0.6	I (20%) Ch (14%) S (12%) K (12%) I/S (10%)	6	3.5
Lucera *this work, Mitaritonna (2006)*	40	18	0.55	≈800	48	48	24	0.5	I/S 77 (40-45%) K (9%) I (8%) Ch (6%)	3.7	2
Boom *Belanteur et al. (1997), Delage et al. (2007), Lima et al. (2008), Della vecchia et al. (2011)*	223	22.6-24	0.58-0.61	2250	50-60	67	38	0.7	I (50%) S (30%) I/S+K (10%)	2.4	2 (?)
London *Gasparre (2005)* *Gasparre et al. (2007)* *Bishop et al. (1965)* *Burland et al. (1990)* brown weathered rec London *Skempton (1944), Monroy et al. (2006)*	1-45 30-140 4-6	21-29 22-26 -	0.6-0.8 1.175		41-63 42-60 58	59-78 60-71 83	33-62 36-43 29	0.7-0.8 0.5	I (21-38%) K (11-15%) Ch, S, M -	3-20 16-40 -	1.3-2.9 2.1 -
Gulf of Guinea *Hattab and Fleureau (2013)*	10	130-170	3.28	36.5	40-60	110-160	70-80	1.5	K (50%) S (15-25%)	1.3-1.4	6-8
St Marcel *Delage and Lefebvre (1984)*	5.2	80	2.3	<10	80	60	35	0.4	Ch (4-16%) I (2-10%) V (2-9%)		19
Bothkennar *Hight (1992), Smith (1992), Tanaka (2003)*	17	70	1.61	>100	28-40	55-86	40-50	1.3	I K	1.4-1.6	4-7

**changes due to drying in block sample 2 are reported in parenthesis*

8.2 Factors controlling the current clay microstructure

As first, the the microstructure of the different clays, of different geological history, listed in Table 8.1 will be compared, starting with the stiff clays. The current microstructure, i.e., the microstructure at undisturbed state, of both Pappadai and Lucera clay has been discussed in Section 7.2.1 and is here compared with that of undisturbed Boom clay.

Boom clay is a high plasticity marine clay, retrieved at a depth of 223 m below ground level at Mol, in Belgium. The clay is a Tertiary clay, highly consolidated and only lightly overconsolidated but, because of the great depth from which the samples were taken, the clay is very stiff and, most probably, diagenized (Horseman et al., 1987; Burland, 1990). Accordingly, as found for Pappadai and Lucera clays, Horseman et al. (1987) report for Boom clay a YSR exceeding the OCR, giving evidence to a strengthening of the clay microstructure under burial as a result of diagenesis. Also Boom clay is thus found to have a post-sedimentation structure, as shown in Fig.3.22.

The plasticity index of Boom clay is lightly higher than that of Pappadai clay, the two clays having approximately the same clay fraction, probably due to the higher smectite content (Table 8.1) resulting in the slightly higher activity of Boom clay. Among the three clays, Lucera clay is the least plastic and the one with the coarsest composition, having the lowest CF.

The comparison of the pore distributions of the two clays investigated in this research with Boom clay (MIP results reported by Lima et al., 2008), is shown in Fig. 8.1. For each clay, some properties are briefly recalled in the graph (void ratio and vertical effective stress at undisturbed state, CF and activity) and the dominant pore size is indicated next to the peak. For Boom and Pappadai clay the preconsolidation pressure σ'_p experienced by the clay during its geological history is also reported, as it is considered to be responsible for the current clay microfabric. For Boom clay, Delage et al. (2007) report a maximum vertical effective stress at the end of the deposition process, before unloading, diagenesis and creep, of 5.2 MPa. For Lucera clay, as explained in Chapter 4, the estimation of σ'_p is quite complex, but it is assumed that

Lucera clay has experienced a lower preconsolidation pressure than that undergone by Pappadai clay, the latter given by Cotecchia (1996).
Accordingly, the highest preconsolidation pressure is that of Boom clay, which is causing the much smaller DPS.
As anticipated in Chapter 7, natural Boom clay has a typical monomodal PSD, similar to those observed for Pappadai clay and Lucera clay. For Boom and Pappadai clay, lower dominant pore sizes are identified, respectively 65 nm and 220 nm, with respect to Lucera clay, for which the DPS is around 300 nm, in agreement with the values of the preconsolidation pressures of the clays.
The CF and activity of Lucera clay, being the lowest, are apparently causing its DPS to be larger than for both Pappadai and Boom clay, although the latter has approximately the same void ratio of Lucera. The similar void ratio of Lucera clay and Boom clay despite the latter having experienced a higher preconsolidation pressure, is due to the higher activity of Boom clay. Pappadai clay, having intermediate CF and A with respect to the other two clays and intermediate preconsolidation pressure, is placed between the curves for Boom and Lucera, as the DPS is evidently going along with both the clay composition and mechanical loading history. The higher void ratio of Pappadai clay is causing its DPS to have a higher frequency than the remaining clays.
It should be noted that deposition conditions, in addition to composition, are influencing the pore size distribution of the clay. The still water basin in which Pappadai clay deposited, combined with the finer composition, has allowed for higher void ratios and smaller pores than those of Lucera clay, which in fact generated in a more turbulent and chaotic environment (Chapter 4). The latter, as discussed in Chapter 6, also contributed to the creation of a less sensitive bonding than that of Pappadai clay, which in fact undergoes a more rapid degradation.

Hence, the analysis of the PSD curves for the three stiff clays is showing that the clay fraction and activity have a role in determining the position of the curve, i.e., the range of pore sizes mainly present in the clay pore structure. Consistently, higher clay fractions correspond to a lower DPS pore dimension range. Higher activities, which are

generally associated to the presence of smaller active particles, also induce lower pore sizes. Also, the differences in deposition conditions and mechanical loading history have been seen to influence the pore size distribution and the value of the DPS shown by the clay.

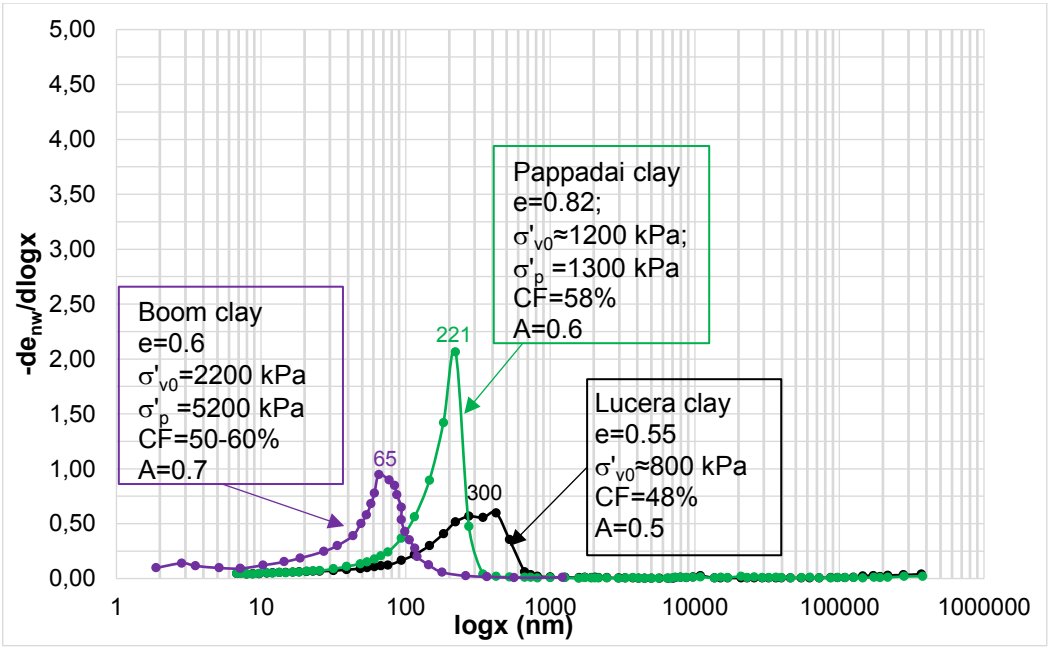

Fig. 8.1 – Comparison of PSD curves for stiff Pappadai, Lucera and Boom clay at undisturbed state (data on Boom clay after Lima et al., 2008).

Both undisturbed Pappadai clay and Lucera clay, shown in Section 7.2.1 (see for example Fig.7.4 for Pappadai and Fig.7.18 for Lucera), are seen to have a complex fabric, characterized by areas of packed iso-oriented particles forming "complex laminae", alternating areas of open random fabric, which are considered to be the memory of a flocculated fabric formed at deposition. For both the clays, the scheme proposed by Sfondrini (1975) of the fabric evolution during one-dimensional compression of a flocculated fabric applies (Fig. 2.21).

The two clays at current state display a well-oriented fabric, which however appears less oriented for Lucera (average L=0.22) than for Pappadai (average L=0.27).

This difference in fabric orientation is reflected in the different shapes of their incremental curves (Fig. 8.1). For Lucera clay, a wider and shorter incremental curve is identified, which can be reasonably thought to denote a less orderly fabric, in which a larger variety of pore sizes, less concentrated around the dominant pore size, is recognized.

As discussed in Section 7.2.1, the dominant pore size identified by the MIP curves is found inside the stacks of particles. An example is reported in the very high magnification micrograph (70000x) in Fig. 8.2a for Pappadai clay at undisturbed state, in which pores having the dimension of the dominant pore size are indicated. For Lucera clay, such high magnification micrographs were not available for the undisturbed specimen, so the micrograph in Fig. 8.2b refers to state LI_2 (Section 7.3.4), isotropically consolidated from undisturbed state to pre-gross-yield. This specimen is undergoing some microstructural changes, although limited, as it is closely approaching the isotropic gross-yield (see Section 7.3.4 and 8.4.2); its dominant pore size, which is identified in Fig. 8.2b, maintains the same average value of the undisturbed specimen. Hence, also for undisturbed Lucera clay the DPS is found inside the stacks of particles and these small intra-aggregate pores represent the more frequent pore size inside the specimen.

For Boom clay, SEM micrographs after Lima et al. (2008) are shown in Fig. 8.3. The pictures show the high density of the specimen. The micrograph in Fig. 8.3a is thought to represent a horizontal fracture on which particle faces are mainly visible, indicating a fabric anisotropy. For Fig. 8.3b, the orientation of the fracture plane is not clear. The pictures do not allow to make further considerations on fabric orientation, but, if the conclusions drawn for Pappadai and Lucera clay apply, the monomodal PSD curve of Boom clay associated to a composition as fine as that of Pappadai clay are suggesting a quite high degree of orientation.

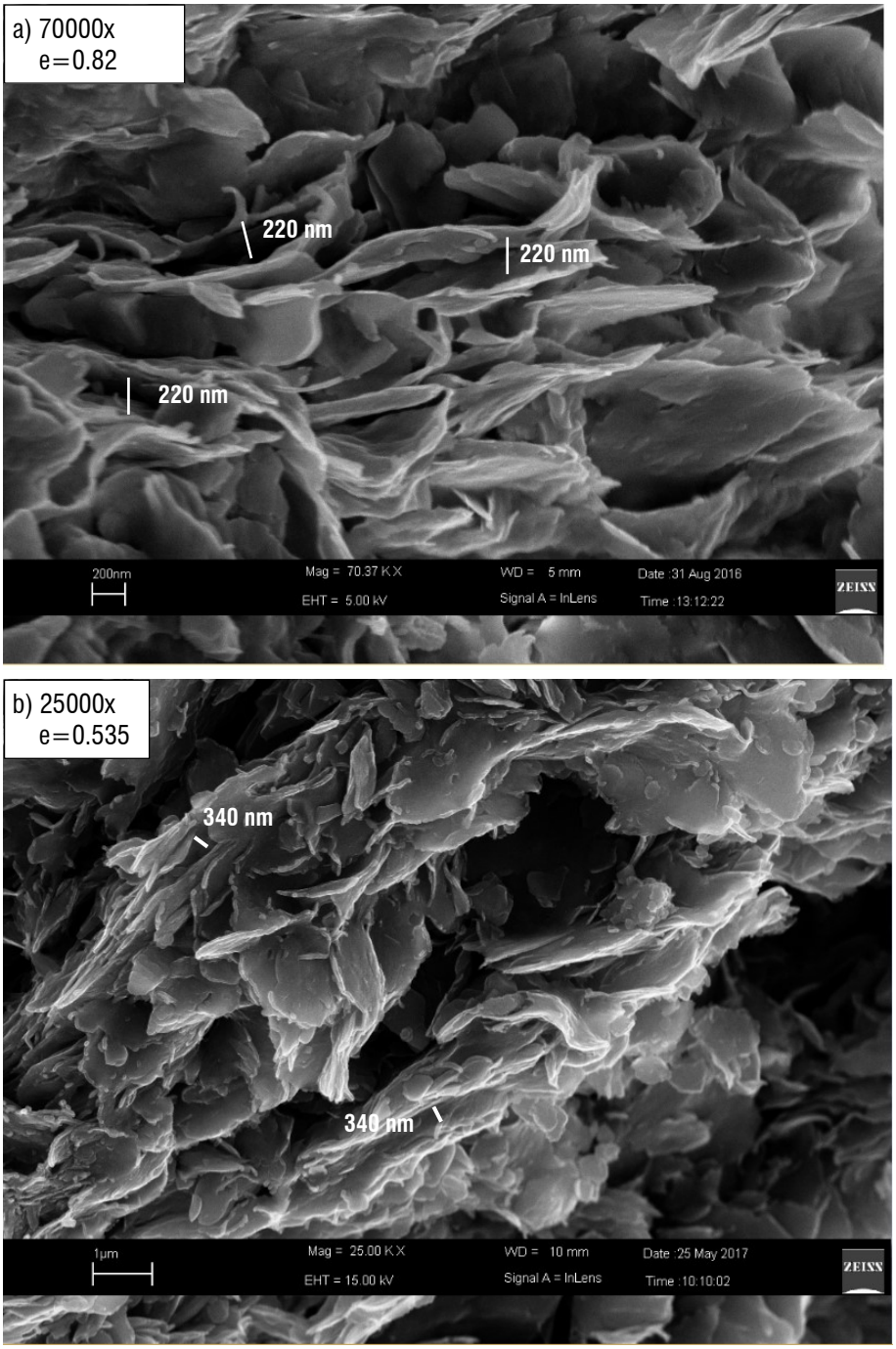

Fig. 8.2 –High magnification SEM micrographs of a) undisturbed Pappadai clay and b) natural Lucera clay at state LI_2, in which pores having the size of the DPS are recognized.

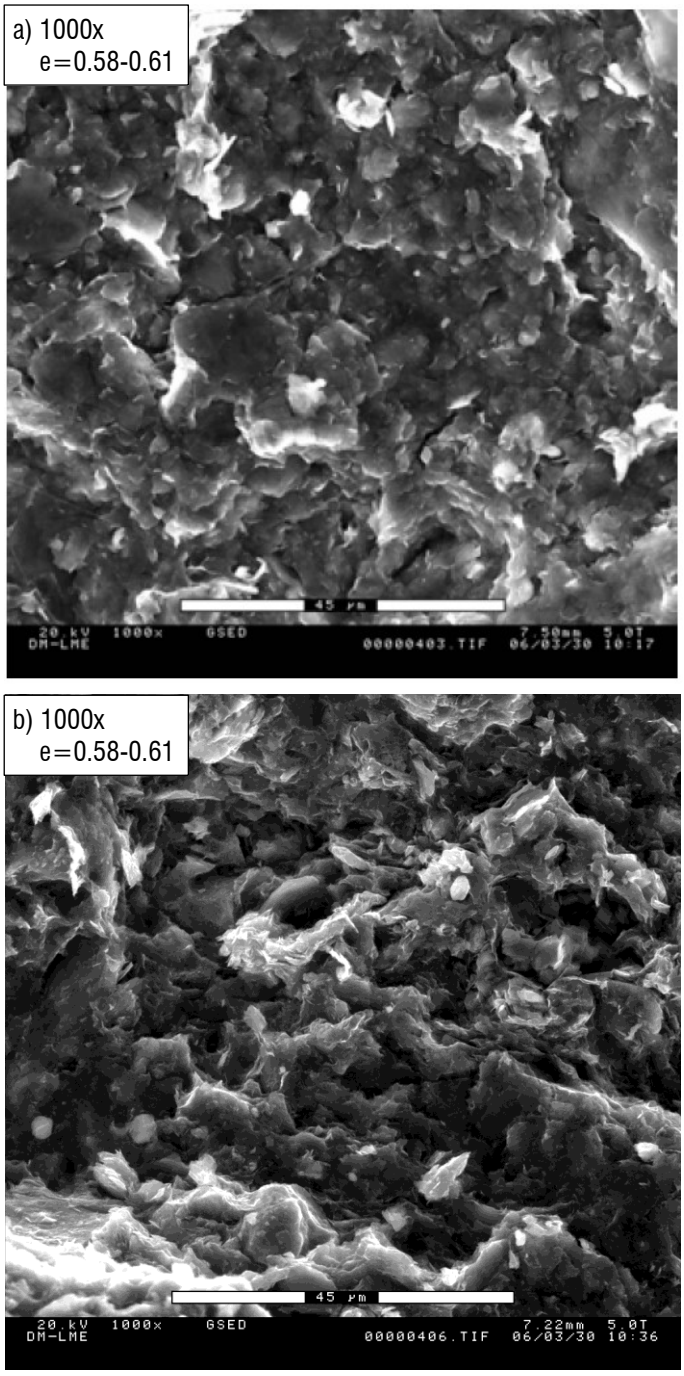

Fig. 8.3 - SEM micrographs of undisturbed Boom clay (after Lima et al., 2008).

A similar investigation of the factors intervening in the determination of the current clay microstructure is here carried out for three soft clays, St. Marcel clay, Gulf of Guinea clay and Bothkennar clay. The three clays have already been presented in both Chapter 2 and Chapter 3. Given the role of the processes occurred in the clays under burial, some information about the clay geological and loading history is briefly recalled in the following.

In general, natural soft clays tend to be normally or lightly overconsolidated and their structure may be stronger than that of the corresponding reconstituted clay, but less stable. Generally, these clays have an in situ vertical effective stress lying close to their SCC and a YSR very close to the OCR. Their sensitivity is a "sedimentation sensitivity" (Cotecchia, 1996), which defines the higher strength of the natural sedimentation structure with respect to the strength of the reconstituted clay.

Being one of the so-called Champlain Sea clays (Delage and Lefebvre, 1984), St Marcel clay is an example of the very highly sensitive Eastern Canadian clays, which are largely the product of sedimentation in preglacial and post-glacial water bodies (Quigley, 1980). Around 10000 years ago, the saline waters of the Champlain Sea were gradually replaced by brackish waters and then by freshwater as a consequence of the retreat of ice fronts to the North. As discussed in Chapter 2, the high sensitivities were induced by leaching, a process in which the salt concentration in the pore water is reduced by the leaching action of fresh water (Skempton and Northey, 1952).
Mineralogical analyses have shown that in these clays a high proportion of the clay fraction may not be made of clay minerals, rather it may be formed by primary minerals ground down to very small sizes by glaciers and forming a rock-flour.
For St Marcel clay, Delage and Lefebvre (1984) and Delage (2010) only plot MIP cumulative curves, as those shown in Fig.2.14. To compare the clay microstructure to that of the other cited clays, for most of which MIP results are reported in the literature as incremental curves, the cumulative curves have been replotted here as incremental curves. For this reason, the resulting incremental curves are less densely defined than

those reported for the other clays, especially for pore diameters lower than 100 nm and larger than 20 μm (Fig. 8.4), corresponding to those parts of the cumulative curve which are flatter and more difficult to replot. The specimens of St Marcel clay tested by Delage and Lefebvre (1984) come from 5.2 m depth in a site located on the South shore of the St. Lawrence river, to the northeast of Montreal.

Gulf of Guinea clay is a deep water marine sediment from an oil-producing area in the Gulf of Guinea. The soil is a normally consolidated structured clay which underwent, throughout the sedimentation and consolidation process in the seabed, a mild physical-chemical cementation (De Gennaro et al., 2005; Hattab and Favre, 2010; Hattab et al., 2013). The Authors report that after sedimentation, some processes occur to GoG sediments, which act in terms of overall structural effect, giving rise to an increase in strength, although the clay is geologically normally consolidated. This is particularly true for the sediments near the seabed (3 m depth), where yield stress ratios were found close to 2, whereas for depths above 10 meters, additional strength seems to stabilize with YSR of about 1.3–1.4 (De Gennaro et al., 2005). The specimens analysed here, discussed by Hattab et al. (2013), come from below 10 m depth down a core taken at sea water depth of 700 m in the GoG. The clay was analysed in both its natural and reconstituted state; the Authors carried out compression and triaxial tests, as will be shown in the following sections.

Bothkennar clay is a soft clay from the site of Bothkennar, in Scotland, having medium to high strength sensitivity and being lightly overconsolidated (Hight et al., 1992; Smith et al., 1992). In fact, it is geologically recent and has a low YSR, so it can be assumed to have a sedimentation structure (Fig.3.22; Cotecchia and Chandler, 2000). It originated in a sheltered depositional environment in brackish water in which a flocculated fabric originated. Post-depositional bonding, ageing and leaching have determined structural effects in the clay (Hight et al., 1992).

The incremental MIP curves for the three soft clays are shown in Fig. 8.4. All the three clays are characterized by pore size distribution curves having markedly higher peaks and being wider than those of the stiff clays in Fig. 8.1.

The PSD of St Marcel clay, that has the highest CF, shows the lowest DPS (380 nm), followed by GoG clay (1000 nm) and Bothkennar clay (1700 nm), which correspondingly has the lowest CF. The higher void ratios are reflected in higher frequencies of the dominant pore sizes.

Considering the effect of activity, A, on the curves of GoG and Bothkennar clays, the higher activity of GoG, combined with the higher CF, is seen to induce a lower dominant pore size than that of Bothkennar clay. By contrast, St Marcel clay has the lowest activity but also the highest CF, which is believed to cause the smallest DPS. So, the effect of CF in determining the size of the most frequent pores in the clay, i.e., the DPS, seems to dominate over the role played by A.

Comparing Fig. 8.1 and Fig. 8.4, in general a difference of one logarithmic cycle is found between the dominant pore sizes of undisturbed soft and stiff clays.

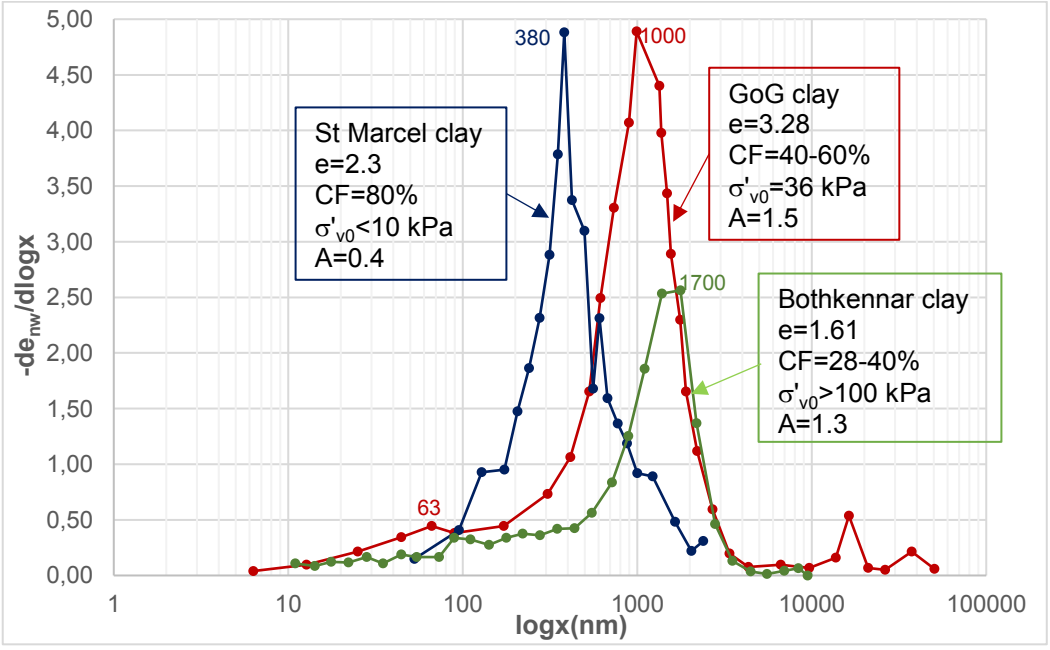

Fig. 8.4 - Comparison of PSD curves for soft St Marcel, Gulf of Guinea and Bothkennar clay at undisturbed state (after Delage and Lefevbre, 1984; Hattab et al., 2013; Tanaka, 2003 respectively).

As observed by Hattab et al. (2013), undisturbed Gulf of Guinea clay is actually characterized by the presence of two pore families which give rise to two peaks in the MIP incremental curve shown in Fig. 8.4. The dominant peak, referred to earlier as the DPS (1000 nm), refers to the inter-aggregate pore family, while the much smaller peak observed at 63 nm is related to the intra-aggregate porosity.
One SEM micrograph of undisturbed GoG clay is shown in Fig. 8.5. Despite this picture not being very descriptive, the Authors state that many images of the undisturbed clay indicate a poorly oriented fabric and an irregular network of pores crossing the material (Hattab et al., 2013), which agrees with the wide and bimodal MIP curve for GoG clay shown in Fig. 8.4.

Some SEM micrographs for the undisturbed St Marcel clay reported by Delage and Lefebvre (1984) were shown in Section 2.10. As seen in Fig.2.12, the microstructure of St Marcel clay is aggregated, and aggregates and clay bridges crossing interaggregate pores can be identified (Fig. 8.6).
A similar fabric type was recognized in a high-water content reconstituted kaolin (Fig. 2.10) by V. Cotecchia et al. (1982). Both the latter and the soft sensitive St Marcel clay are thus seen to resemble much the scheme of Griffiths and Joshi (1990), shown in Fig.2.9, proposed for a reconstituted clay. Hence, the SEM micrographs in Fig.2.10, Fig.2.12 and Fig. 8.6 seem to suggest that the scheme from Griffiths and Joshy applies in general to a high-water content clay under initial loading from slurry (early virgin compression), either in situ or in the laboratory, but for compression stresses below a given threshold, which generates a quasi-permanent particle orientation for 1D compression conditions, as suggested by Sfondrini (1975).
Given the high void ratio and the very low overburden pressures, the fabric of St Marcel clay is very open and possesses a large inter-aggregate porosity, as denounced by both the SEM pictures and the MIP curve in Fig. 8.4. The clay particles are often found not to be in contact, which is possible for the presence of bonding. Although the presence of amorphous oxides has been suspected to play a bonding role in some soft

clays, in general their bonding has developed, in the field of electrostatic and electro-magnetic forces, during the clay deposition and Quaternary history and has not allowed one-dimensional compression in situ to generate an oriented fabric.
However, the clay bonding is suspected to be very unstable, since soft clays lose a large proportion of strength upon straining, with a consequent significant collapse in sensitivity.
The type of clay fabric recognized in undisturbed soft clays is the same found locally preserved in the fabric of stiff clays, which incorporates the relics of the fabric at deposition. Hence, the current fabric of undisturbed stiff clays is suggested to represent a further evolution stage in compression of the flocculated fabric characterizing soft clays, similar to that present at their early deposition stage.

Despite the major difference in geological history, the microstructures of the stiff clays and that of the sensitive soft clays have both been shown to embody fabrics of high complexity and the interference of bonding with fabric.
The analysis of the microstructure of soft clays is outlining a specific microstructural behaviour, applying to high-water content clays under initial loading from slurry, i.e., during early virgin compression.
At this stage, the fabric is made of aggregates and pores in a flocculated arrangement, in which clay bridges crossing inter-aggregate pores can be identified, as described by Griffiths and Joshy (1990), Fig.2.9.
This fabric architecture is also recognized in reconstituted illite at liquid limit by Griffiths and Joshy (1990) and in reconstituted kaolin at high-water content by V. Cotecchia et al. (1982).
At these low pressures, the pore structure generally has a large dominant pore size with a very high frequency in the range of the inter-aggregate pore sizes, and a much lower peak corresponding to the intra-aggregate pore family. This bi-modal character is clearly recognized for GoG clay, while it is less evident for St Marcel clay (Fig. 8.4). For the latter clay, the MIP curve shows the presence of a large number of pores between

200 nm and 100 nm, suggesting a significant intra-aggregate porosity, although the distribution of pores smaller than 100 nm is unknown.
The same bi-modal pore structure is identified by Yu et al. (2016) for a kaolin slurry reconstituted at twice the liquid limit and then consolidated to 50 kPa, as shown in Fig. 8.7. The incremental curve is evidently showing two dominant modes, corresponding to two dominant pore sizes: the main one is in the range of the inter- aggregate porosity, the other one is in the range of the intra-aggregate pores. With further compression to 100 kPa, the curve keeps being bimodal, with a small reduction of the size of the dominant inter-aggregate pore.

Hence, the analysis of the data is showing that at low pressures and high-water contents, both natural soft clays and reconstituted clays, such as kaolinite and illite, have a fabric architecture analogous to the scheme proposed by Griffiths and Joshy (1990), with aggregates and clay bridges between aggregates and a porosimetry, often bimodal, presenting a large inter-aggregate pore volume, with a dominant pore size in the range of the large inter-aggregate pores.
The value of the dominant pore size has been shown to be influenced by the clay composition.

Reconstituted GoG clay, prepared by Hattab et al. (2013) according to the procedure suggested by Burland (1990) and 1D consolidated to 80 kPa, and remoulded St Marcel clay (Delage and Lefebvre, 1984) are found to adhere to this pattern of behaviour. The incremental curves, shown for the two clays in Fig.8.8, indicate in both cases the presence of a large inter-aggregate porosity with a dominant pore size in the range of the inter-aggregate pore sizes. Reconstituted GoG clay shows a markedly bimodal porosity, similar to that observed for the undisturbed clay, and noticeably the two clays have identical values of the smaller dominant intra-aggregate pore (63 nm), which is a consequence of the clay composition, as will be discussed later in further detail.

The SEM micrographs of both reconstituted GoG (Fig. 8.9) and remoulded St Marcel (Fig.2.13) are portraying a fabric very similar to that of the scheme of Griffiths and Joshi (1990) with a low degree of orientation.

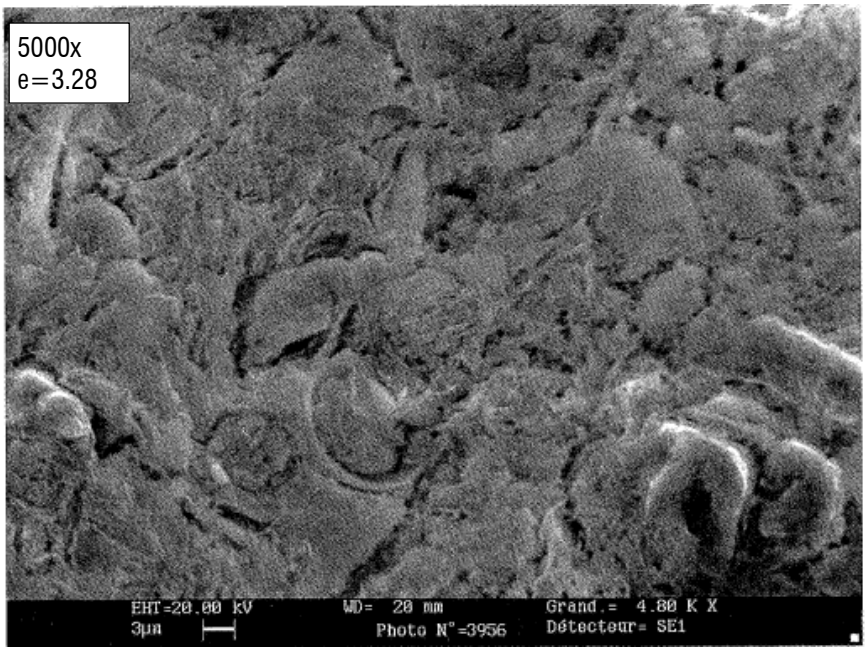

Fig. 8.5 - SEM micrograph of undisturbed Gulf of Guinea clay on a vertical plane (after Hattab et al., 2013).

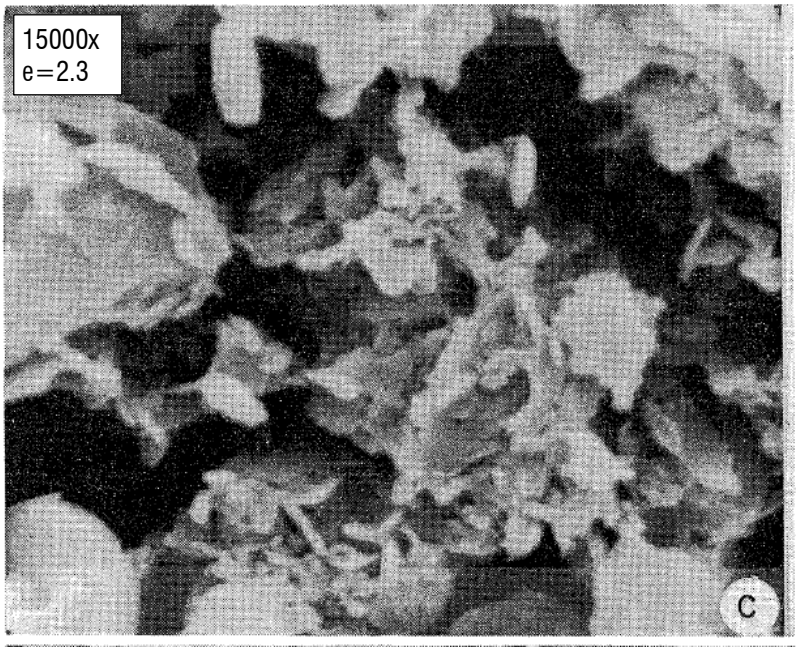

Fig. 8.6 - SEM micrograph of undisturbed St Marcel clay on a vertical plane at high magnification (after Delage and Lefebvre, 1984).

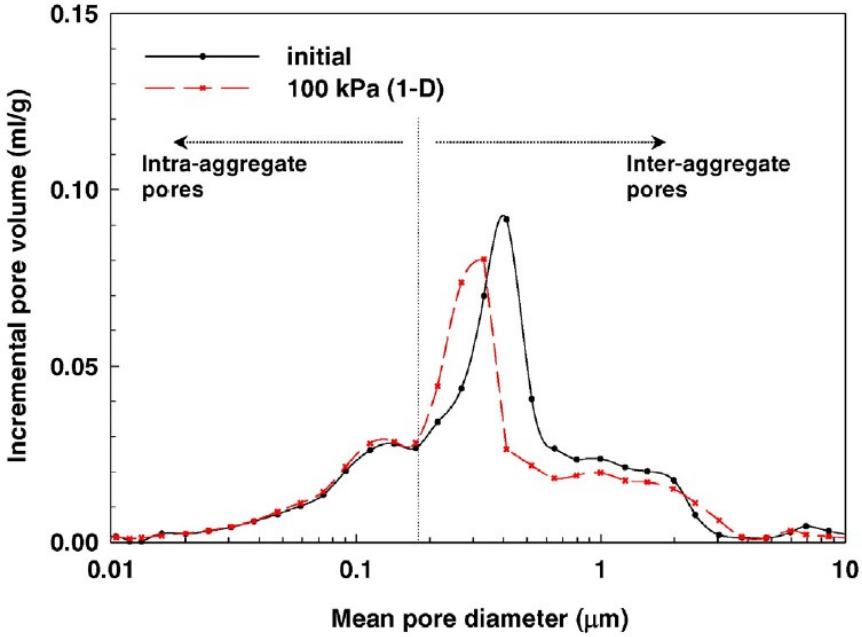

Fig. 8.7 – Pore-size changes of a kaolin slurry, prepared at twice the LL, after 1D consolidation to 50 and 100 kPa (after Yu et al., 2016).

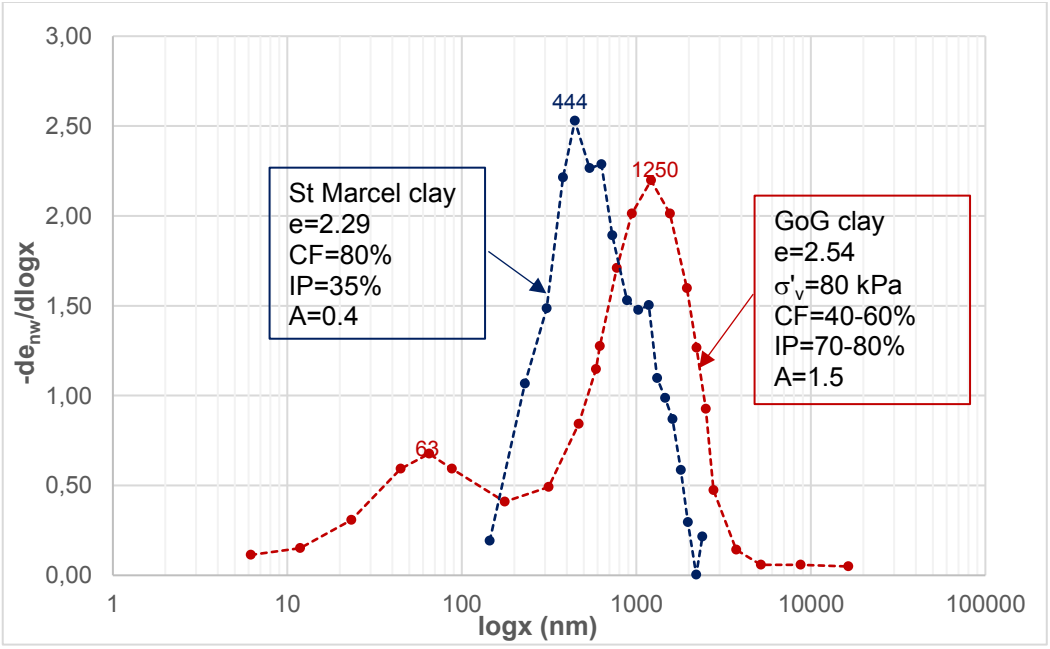

Fig. 8.8 - Comparison of PSD curves for remoulded St Marcel clay and reconstituted Gulf of Guinea clay (after Delage and Lefebvre, 1984 and Hattab et al., 2013).

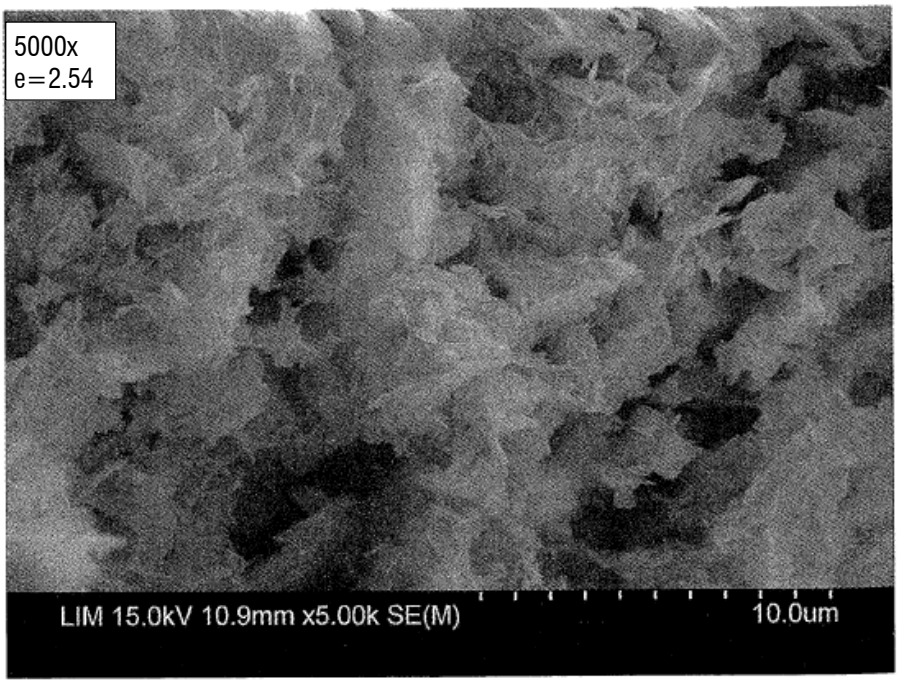

Fig. 8.9 - SEM micrograph of reconstituted GoG clay consolidated at σ'_v=80 kPa (after Hattab et al., 2013).

If now the microstructures of reconstituted Pappadai clay and Lucera clay are analysed in the light of these findings, further behavioural elements can be defined. In addition, the microstructure of brown weathered reconstituted London clay, prepared according to Burland (1990) and 1D consolidated to 108 kPa, is considered. This final pressure is very close to that attained in the consolidometer for reconstituted Lucera clay (100 kPa) and lower than that reached for Pappadai clay (200 kPa).
These pressures are higher than the low pressures which the either natural or reconstituted clays discussed above, which possess a fabric of the type depicted by Griffiths and Joshi. Therefore, the fabrics of the clay specimens considered in the following represent the effects of a further virgin compression stage.

The incremental MIP results for reconstituted Pappadai, Lucera and London clay are shown in Fig. 8.10. Reconstituted London clay, having the same CF as reconstituted

Pappadai clay and a slightly lower activity, is found to the right of the curve for Pappadai clay. Certainly, this is also an effect of the lower pressure to which London clay has been consolidated. Pappadai clay shows a markedly monomodal PSD; London clay has a mainly monomodal trend, but for pore sizes smaller than 100 nm the incremental curve is seen to mildly rise, suggesting that probably, at a lower consolidation pressure, a more pronounced bi-modal trend would have been visible.
For reconstituted Lucera clay, a more irregular incremental curve is measured with a large dominant pore size in the inter-aggregate pore range. This MIP curve suggests that a combined effect of the coarser composition and of the lower consolidation pressure attained for reconstituted Lucera clay is causing a less regular pore distribution and a much larger dominant pore size.
The careful analysis of the SEM micrographs of both reconstituted Pappadai and Lucera clay, combined with the examination of the MIP test results for the two clays, carried out in Section 7.2.2, revealed a lower degree of orientation for reconstituted Lucera clay. In fact, it was concluded that the consolidation up to 100 kPa vertical pressure had not allowed the full re-organization of the initial flocculated fabric, generated at very low pressures, into the alternation of stacks of domains and honeycomb strata, which instead is seen in the reconstituted Pappadai clay.
For reconstituted London clay, Monroy et al. (2006) report two SEM micrographs, shown in Fig. 8.11, which appear to have been taken on a horizontal fracture. Only particle faces are seen, indicating a certain orientation towards the horizontal direction.

Hence, the microstructures of the analysed clays seem to suggest the existence, for both natural and reconstituted clays, of a threshold pressure beyond which a reduction of the inter-aggregate porosity and the loss of the potential bi-modal distribution occurs, with the conversion into a monomodal pore size distribution with one dominant pore size, gradually shifting towards the intra-aggregate pore dimension. Correspondingly, the fabric develops a coalescence of the iso-oriented particle aggregations, which thus become thicker, causing the increase in frequency of the dominant pore size, which in

fact is found inside the stacks of particles (Fig. 8.2). Accordingly, the clay fabric acquires an anisotropic structure.
Evidently, the fabric is gradually abandoning the scheme of Griffiths and Joshi (1990) and changing its architecture towards that proposed by Sfondrini (1975), characterized by an alternation of stacks or "complex laminae" and areas of honeycomb fabric interbedded within the stacks.

The threshold pressure activating the microstructural re-organization process depends on both the composition and the bonding strength of the clay, but in general the process applies to all clays, both natural and reconstituted.
This evolution in microfabric of the clay goes along with an increase of the fabric anisotropy, due to the development of average medium-high degrees of orientation, applying beyond a given threshold pressure.
As observed in Section 7.3 for Pappadai clay and Lucera clay, the average medium-high fabric orientation acquired at the threshold pressure does not change significantly with further 1D loading, either for the natural or for the reconstituted clay. In the following, this finding will be seen to be valid also for other clays.

The microstructural data discussed so far appear to identify the value of this threshold pressure between 100 and 200 kPa. Indeed, at 200 kPa reconstituted Pappadai clay already shows the features described for the fabric changed by the re-organization process. On the other hand, these features are not fully recognized in reconstituted Lucera clay, which evidently would have needed to attain a pressure in the consolidometer higher than 100 kPa. The data for reconstituted London clay also seem to suggest a threshold pressure included in this range. Reconstituted GoG clay, consolidated to 80 kPa, is seen to be still in the pre-re-organization stage, confirming that a pressure higher than 80 kPa is necessary. A further confirmation derives from Hattab and Fleureau (2010), who observed that reconstituted kaolin, prepared according to Burland (1990) and consolidated to 120 kPa, shows an oriented fabric (Fig.2.23).

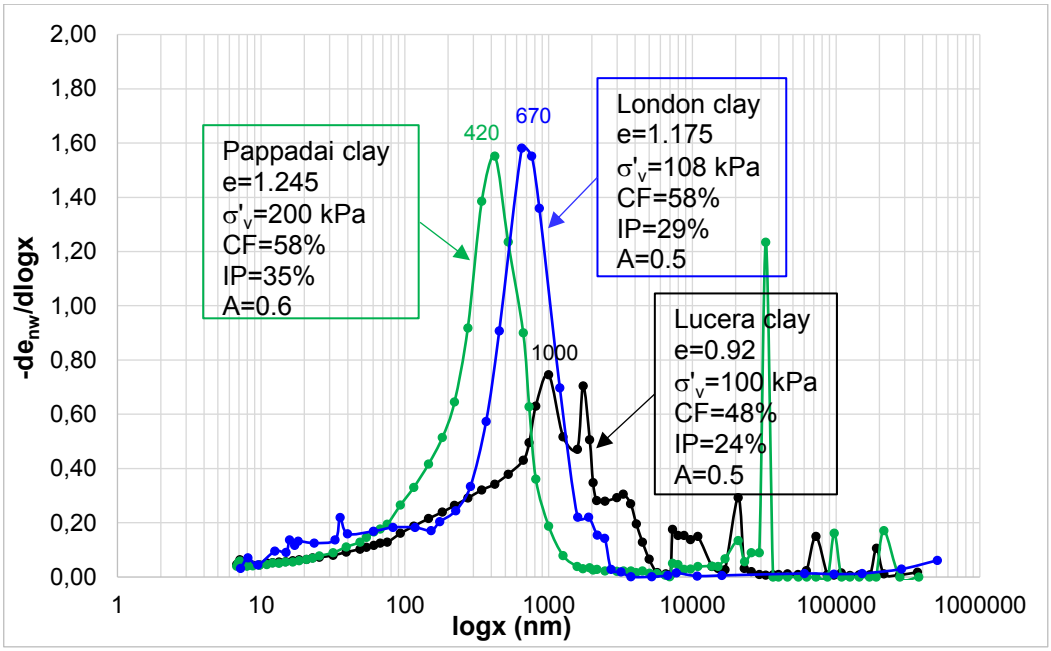

Fig. 8.10 – Comparison of PSD curves for reconstituted stiff Pappadai, Lucera and London clay after compression in consolidometer (data for London clay after Monroy et al., 2006).

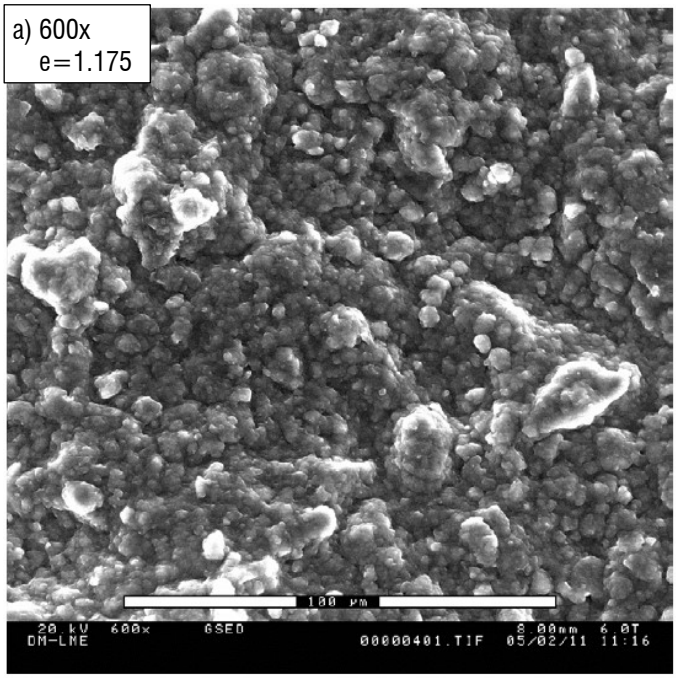

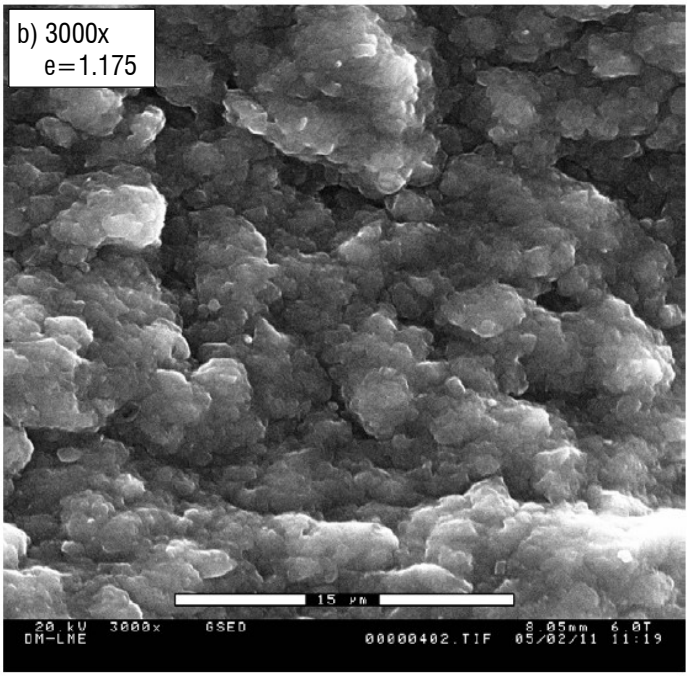

Fig. 8.11 - SEM micrographs of reconstituted London clay consolidated to σ'_v=108 kPa at a) 1000x and b) 3000x magnification (after Monroy et al., 2006).

8.3 A novel microstructural interpretation of sensitivity

According to the Sensitivity Framework (Cotecchia and Chandler, 2000), extensively discussed in Chapter 3, the role of sensitivity is that of a scalar parameter representing the overall effect of the various structural elements on the gross yielding of the clay. Accordingly, this parameter allows to define the effects of the differences in microstructure between the natural and the reconstituted clay on the size of the SBS of the clay (Cotecchia and Chandler, 2000). When clays from different classes are considered, the different sensitivities describe the differences in effect on gross yielding of differences in microstructure.
Through the analysis of the microstructure of clays part of different classes, characterized by different sensitivities, the microstructural features corresponding to different clay sensitivities have been addressed and some relations between the variations of some microstructural features and the variations in clay sensitivity have been deduced.

Soft clays are characterized by high sensitivities and are found, in their undisturbed state, at very high-water contents and very low pressures. Natural GoG clay, for example, is found in situ at a σ'_v=36 kPa and a void ratio of 3.28. Reconstituted GoG clay, consolidated to a vertical effective pressure of 80 kPa, has a much lower void ratio of 2.54 (Hattab et al., 2013).
If the pore size distribution of the two clays are compared, as shown in Fig. 8.12, the two curves are seen to be very similar, in both shape and dominant pore diameters. In agreement with the conclusion drawn in the previous Section, both the PSD curves are bimodal, with a dominant pore in the range of the inter-aggregate porosity and the other, much smaller, in the range of the intra-aggregate pores. The natural clay PSD, however, is exhibiting a significantly higher frequency of the inter-aggregate pore, which is related to the noticeable difference in the void ratios of the two clays. Being the clays at similar pressures, the remarkable difference in void ratio is related to the high sensitivity of the clay. The latter is thus reflecting the difference between the the frequencies of the dominant inter-aggregate pore between the natural and the reconstituted clay. Thus, in

the natural clay microstructure the prevailing pores are those between the aggregates and the pores having the size of the large dominant pore (1 μm) are much more than in the reconstituted clay.
Given the fabric scheme applying to these clays at very low pressures, the presence of such a number of inter-aggregate pores of size 1 μm is likely to be due to the presence of stronger clay bridges between the aggregates.
Similar considerations can be drawn from the comparison of natural and remoulded St Marcel clay, also shown in Fig. 8.12. If the microstructure of the reconstituted clay is considered to be "stable", so as to have sensitivity 1, then the difference between the pore distributions should be only related to the natural clay sensitivity. So, in line with the behaviour of GoG clay, the natural and the remoulded St Marcel clay, despite having very similar void ratios, have incremental MIP curves showing very similar dominant porosity with a much higher frequency of the dominant pore for the natural clay.
Pusch (1970) interpreted remoulding as a destruction of initial interaggregate links, which constitute the points of weakness of the initial structure. Accordingly, Delage and Lefebvre (1984) attribute the difference recognized in the fabric of the natural and the remoulded St Marcel clay to the different distribution of the inter-aggregate porosity due to a difference in the inter-aggregate links, which according to the Authors are allowing larger inter-aggregate pores in the natural clay. Indeed, the comparison of the MIP results in terms of incremental curves is showing that inter-aggregate pores are more numerous, rather than larger in size, in the natural clay.

Hence, in undisturbed soft clays the high sensitivity is related to inter-aggregate bridges, or links, stronger than those present in the reconstituted clays. Their presence is allowing for a higher amount of large inter-aggregate pores having the size of the large dominant pore. The latter is found to have a higher frequency, as a reflection in terms of pore size distribution of the high sensitivity. Upon remoulding, or reconstitution, many large interaggregate pores are lost, probably filled in by particles.

If now natural and reconstituted stiff clays are considered for both the case of Pappadai clay and Lucera clay (Fig. 8.13), the incremental curves are seen again to be of the same typology (similar shapes), but the coincidence of the dominant pore size does not apply any more, as a consequence of the larger difference between the pressures to which the reconstituted and the natural clay being considered. However, if the natural and the reconstituted incremental curves for specimens brought to approximately the same pressure in 1D compression are compared, as will be seen in the following, the similarity in DPS is again recognized and so is the difference in frequency, the latter being higher for the natural clay. Indeed, this difference is expected to be much less pronounced than for soft clays, due to the much lower sensitivity values characterizing the stiff clays.

In the previous Section, the influence of the clay composition was recognized in determining the position of the DPS, hence the range of sizes of the pores mainly characterizing the clay pore structure. Given the identity of this dominant pore in both the natural and the reconstituted clay, this pore size can be considered as an intrinsic pore size, being the expression of an intrinsic aggregative behaviour, which is mainly driven by the clay composition.

To conclude, the difference in void ratio between the natural clay and the reconstituted clay at the same pressure, which is related to the sensitivity of the natural clay, is due to the presence in the reconstituted clay of a lower number of pores having the same size as those present in the natural clay, rather than being generated by a smaller dominant pore size in the reconstituted clay. So, the difference between the natural and the reconstituted clay is linked to a different distribution of pores having the same range of sizes, rather than by a compression of the pore structure. The compression, in fact, generates a translation to the left of the PSD and of the whole incremental curve. This will be shown to be the mechanism of evolution of microstructure under compression.

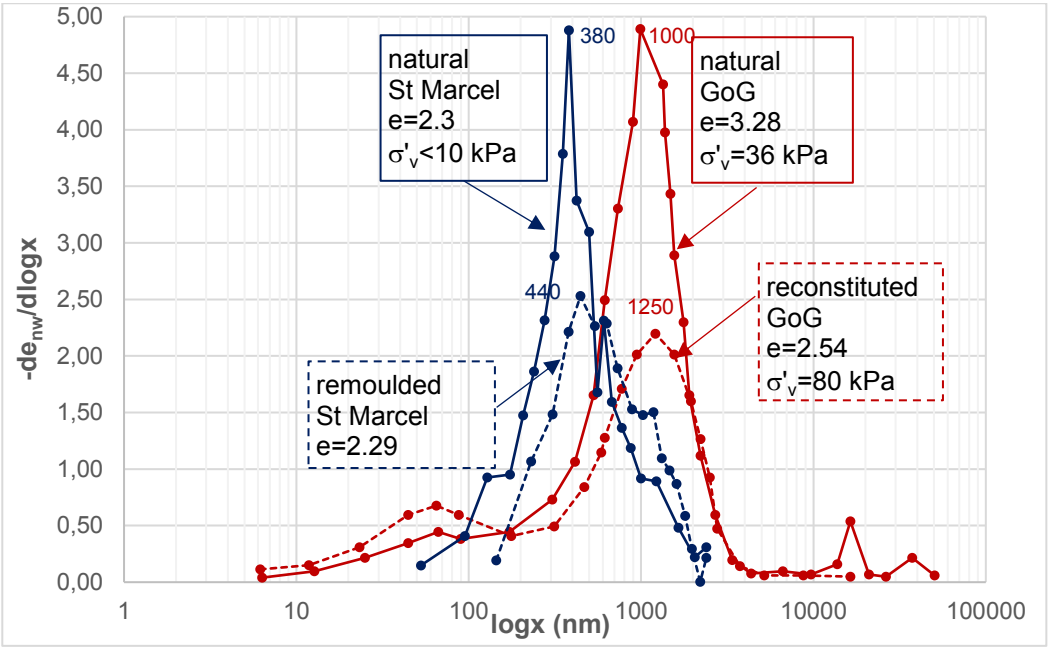

Fig. 8.12 - Comparison of PSD curves for the undisturbed and reconstituted soft clays of St Marcel and GoG (after Delage and Lefebvre, 1984 and Hattab et al., 2013).

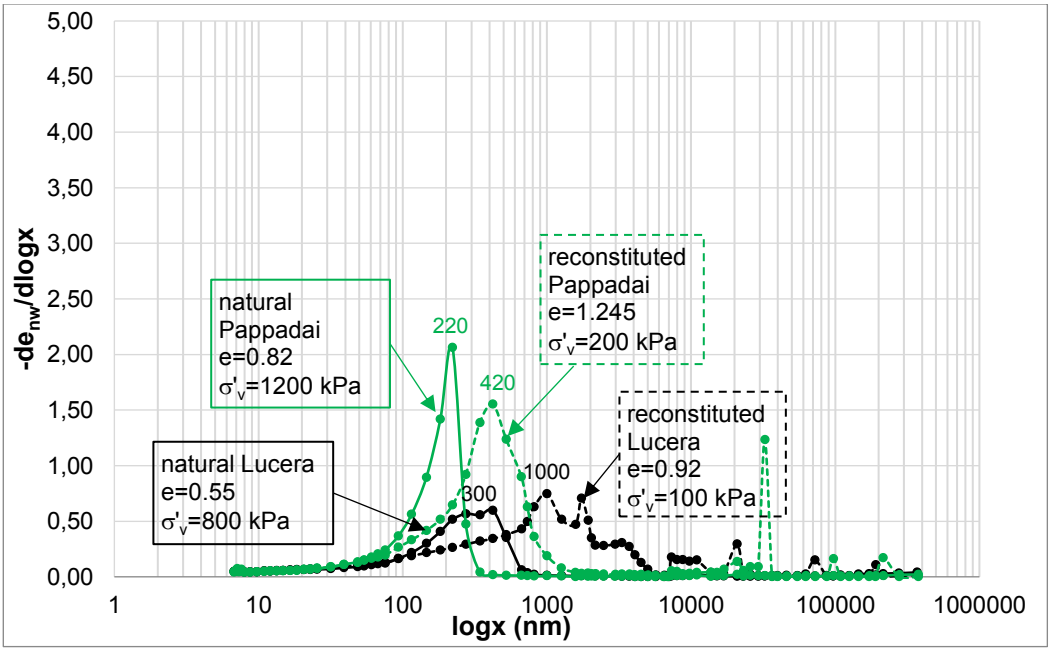

Fig. 8.13 – Comparison of PSD curves for the undisturbed and reconstituted stiff clays of Pappadai and Lucera.

8.4 Micro to macro compression behaviour

8.4.1 One-dimensional compression

In Section 8.2, the mechanism of evolution of the clay microstructure under 1D compression from low pressures and high-water contents up to a threshold pressure of re-organization of both the fabric and the pore structure has been formulated, starting from the analysis of data from the literature and from this work. This mechanism was seen to apply both to natural and reconstituted clays. In this Section, the evolution of microstructure when the clay is further compressed beyond the threshold pressure will be discussed.

The microstructural changes occurring under 1D compression and swelling for natural and reconstituted Pappadai and Lucera clay have been discussed in detail in Chapter 7. To define the microstructural evolution, both changes in pore structure, fabric architecture and degree of fabric orientation have been investigated and will be recalled. The behaviour exhibited by stiff clays in 1D compression will be then compared with that observed for soft clays.

For the natural stiff clay, oedometric compression is primarily seen to close the larger inter-aggregate pores as a consequence of the reduction in void ratio. Pre-gross-yield, very small changes occur in the pore distribution, with corresponding very limited modifications of the fabric.

Gross-yield induces a significant degradation of bonding and major changes in the clay microstructure, which undergoes a chaotic rearrangement of fabric and a first more important modification of the pore structure and distribution. Beyond gross-yield, the main effect of 1D compression is found to be a translation towards lower pore sizes of the incremental curve, with a concurrent reduction in the frequency of the dominant pore size. This necessarily implies not only a compression of the small pores, causing the reduction of the DPS, but also the disappearance of a number of micro-pores, manifesting in a decrease in the frequency of the dominant pore. The loss of pores is reasonably related to the presence of small particles filling pre-existing pores. With compression post-gross-yield, the chaotic fabric created at yield evolves into a

succession of horizontal stacks of domains and strata formed by a truss of domains, that is the same fabric organization recognized in the undisturbed clay (Sfondrini, 1975).
Along with these complex post-gross yield fabric re-arrangements, orientation does not increase much.

In Fig. 8.14, the MIP curves corresponding to the different states in 1D compression analysed for the natural stiff Pappadai and Lucera clay are compared. The state of Lucera clay pre-gross yield compression is not reported.
The reduction of both size and frequency of the dominant pore is more evident for natural Pappadai clay, which always shows higher frequencies than natural Lucera clay. This is due to the higher void ratios of Pappadai clay, combined with its higher compressibility, which is determining a more pronounced structure degradation with compression. In fact, as discussed in Section 8.1, Pappadai clay and Lucera clay, have different bonding nature and strength, as a consequence of the different deposition conditions.
The higher sensitivity of the bonding of Pappadai clay is also reflected, as shown in Section 6.2, in the more evident, although not dramatic, impact of large swelling from the undisturbed state on the gross-yield pressure in recompression (Fig.6.6). The specimens of both Pappadai and Lucera clay subjected to large swelling from undisturbed state are also shown in Fig. 8.14. In both cases, limited changes are recorded in the swelled specimen with respect to the undisturbed state, but if for swelled Pappadai clay the DPS, as well as its frequency, are seen to change, for swelled Lucera clay the DPS is left almost unchanged, with a light increase in frequency, as a result of the lower disturbance occurred to bonding.
However, the limited extent of the microstructural changes experienced under swelling is confirmed by the almost unchanged fabric and degree of orientation.

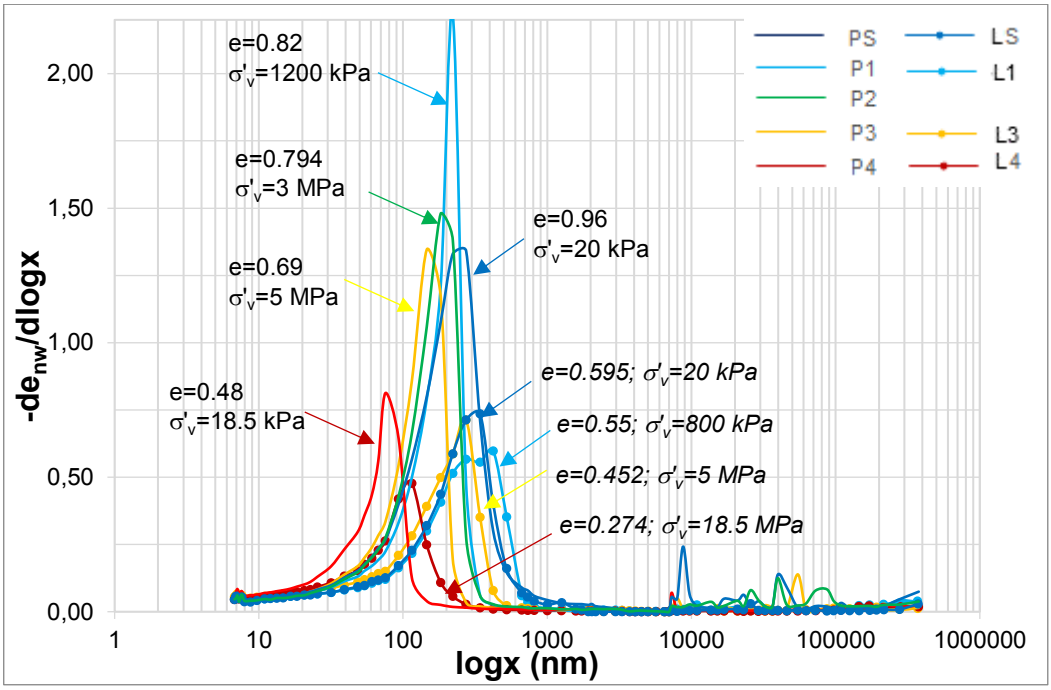

Fig. 8.14 - Evolution in 1D compression of PSD curves of natural stiff Pappadai clay (e and σ'_v in standard character) and Lucera clay (e and σ'_v in italics).

With reference to Fig. 8.14, it should be noted that for either clays, the lowest pore entrance diameters, i.e., below 20 nm for Pappadai clay and below 30 nm for Lucera clay, do not vary up to compression to high pressures. This suggests that the smallest micro-porosity (1 order of magnitude smaller than the DPS) is not affected by compression, despite the very high pressures attained. The size and quantity of pores not affected by compression is believed to depend on the clay mineralogy; further confirmation of this will be given in the following.

For the reconstituted Pappadai clay and Lucera clay, the effects of 1D compression on the clay microstructure, discussed in Section 7.3.3, are found to be very similar to those occurring for the natural clay. Compression closes the larger pores and reduces the size of the dominant pore, thus increasing the density of the clay fabric, without

significantly increasing the average orientation. As for the natural clay, the changes in fabric occurring in the reconstituted clay are highly non-uniform.
The evolution in 1D compression is compared for the natural and the reconstituted clays, for Pappadai clay in Fig. 8.15 and for Lucera clay in Fig. 8.16. For natural Lucera clay, the pre-gross-yield state in compression has been omitted. Despite the differences in pressures, the natural and the reconstituted clay show a very similar trend of evolution.
Remarkably, natural and reconstituted specimens of the same clay have PSD of similar shape and natural and reconstituted specimens tested at similar pressures exhibit very similar dominant pore size (see, for example, for Pappadai clay specimen P_3 and specimen PR_2, both compressed to σ'_v=5 MPa), confirming the microstructural interpretation of sensitivity formulated earlier.

The evolution of microstructure in 1D compression for the soft St Marcel clay and GoG clay studied by Delage and Lefebvre (1984) and Hattab et al. (2013) is reported here.
As explained in Section 2.10, specimens of natural St Marcel clay were 1D compressed to 23, 124, 421 and 1452 kPa and MIP tests were carried out on each specimen after unloading in several stages to 4 kPa. The results of the MIP tests presented by Delage and Lefebvre (1984) as reverse cumulative curves are plotted as incremental curves, compared to the undisturbed state, in Fig. 8.17.
With advancing compression, the incremental curves are rapidly converging towards a curve of much lower dominant pore size, width and height, i.e., frequency of the DPS, as a consequence of the abrupt collapse of the large inter-aggregate porosity, reflected in the high compressibility of the clay. No significant changes are observed in the curve corresponding to 23 kPa loading, since it is a pre-gross-yield compression state, being σ'_{vy}=54 kPa for St Marcel clay (Delage and Lefebvre, 1984). Beyond gross-yield, major contraction of the inter-aggregate pore volume occurs, corresponding to a progressive flattening of the right branch of the curves. The latter, by contrast, keep being overlapped for pore entrance diameters lower than 200 nm, which hence are not altered by compression and constitute the intra-aggregate unchanged porosity

recognized by Delage and Lefebvre (1984) and Delage (2010). The conclusion follows that the dominant inter-aggregate pore, characterizing the pore structure at very low pressures, is progressively collapsing to a small intra-aggregate dominant pore. These data are providing further confirmation to the mechanism of evolution of microstructure occurring over the threshold pressure of fabric re-organization and giving evidence to the transition from a pore structure dominated by large interaggregate porosity, which is allowed for by the high clay sensitivity, to a pore structure of prevailing small intra-aggregate pores.
Accordingly, the clay fabric at the undisturbed state, in which macro inter-aggregate pores are formed by bridges between the aggregates, is found still preserved at 23 kPa; also in the specimen consolidated to 124 kPa many intact macro pores can still be observed. With further compression, the fabric becomes denser and some induced anisotropy is recognized.

Similar porosimetry changes are observed for natural GoG clay, compressed from the undisturbed state to 200 and 1000 kPa, as shown in Fig. 8.18. An abrupt collapse of the inter-aggregate pores is the main effect of 1D compression, which is seen to develop over the range of pressures defining the threshold pressure of the microstructure re-organization ($\approx$200 kPa). With further compression, translation of the DPS towards lower diameters is recognized. The presence of a marked intra-aggregate dominant pore in the undisturbed specimen at 63 nm makes even clearer the progressive reduction in size of the large inter-aggregate dominant pore and its convergence towards the dominant intra-aggregate pore size. According to Hattab et al., the SEM analysis on compressed reconstituted GoG clay reveals a structural reorganization of the particles, which become more oriented towards the horizontal direction, whereas the same type of structure is not uniformly recognized in the natural compressed specimen.

Hence, 1D compression tests on both St Marcel and GoG clays are confirming that beyond the threshold pressure of microstructural reorganization, a transition occurs

from a dominant inter-aggregate porosity to a much smaller dominant intra-aggregate porosity, with a consequent loss of bimodality. The fabric of the clay achieves an overall degree of anisotropy that does not evolve significantly with further compression.

The pressures attained in 1D compression for St Marcel clay and GoG clay seem to be large enough to compress almost completely the inter-aggregate porosity, so as to render the pore volume almost made of intra-aggregate pores. The analysis of compressed specimens of stiff Pappadai and Lucera clay is suggesting that with further compression the dominant intra-aggregate pore could further reduce in size.

The PSD in 1D compression of the natural and the reconstituted GoG clay are compared in Fig. 8.19. From the initial state, representing the state after consolidometer stage (σ'_v=80 kPa), the reconstituted clay is further compressed to the same pressures of the natural clay.
The dominant intra-aggregate pore at 63 nm is common to all curves, which in fact are found superimposed for pore diameters below this value. This dominant pore size is considered to be representative of the influence of composition on the clay pore structure. Since Pappadai, Lucera and GoG clay have similar CF, but neither Lucera nor Pappadai exhibit the intra-aggregate porosimetry recorded for GoG clay,, the pore size distribution of GoG clay is believed to be mainly controlled by the clay activity, i.e. by its mineralogy, which is characterized by a significant smectite content, responsible for a significantly higher A than that of Pappadai and Lucera clay.
It should be noted (Fig. 8.19) that after compression to σ'_v=200 kPa, the MIP tests on the reconstituted and the natural specimen of GoG clay show the same maximum intruded volume. The actual void ratio of the two specimens is not reported by Hattab et al. (2013). Although not commented by the Authors, the 1D compression curves for the natural and the reconstituted clay start converging at pressures higher than 200 kPa and it is likely than the void ratios of the two specimens are close, the void ratio of the natural clay being higher than that of the natural clay. Probably, the coincidence of the maximum intruded void ratio has to be attributed to an anomaly in one of the MIP tests.

This anomaly might also have affected to some extent the frequency of the dominant inter-aggregate pore of the natural specimen compressed to 200 kPa, which appears lower than that of the reconstituted clay compressed to the same void ratio, contrasting with the identity in void ratios and with the natural clay having a lower DPS.

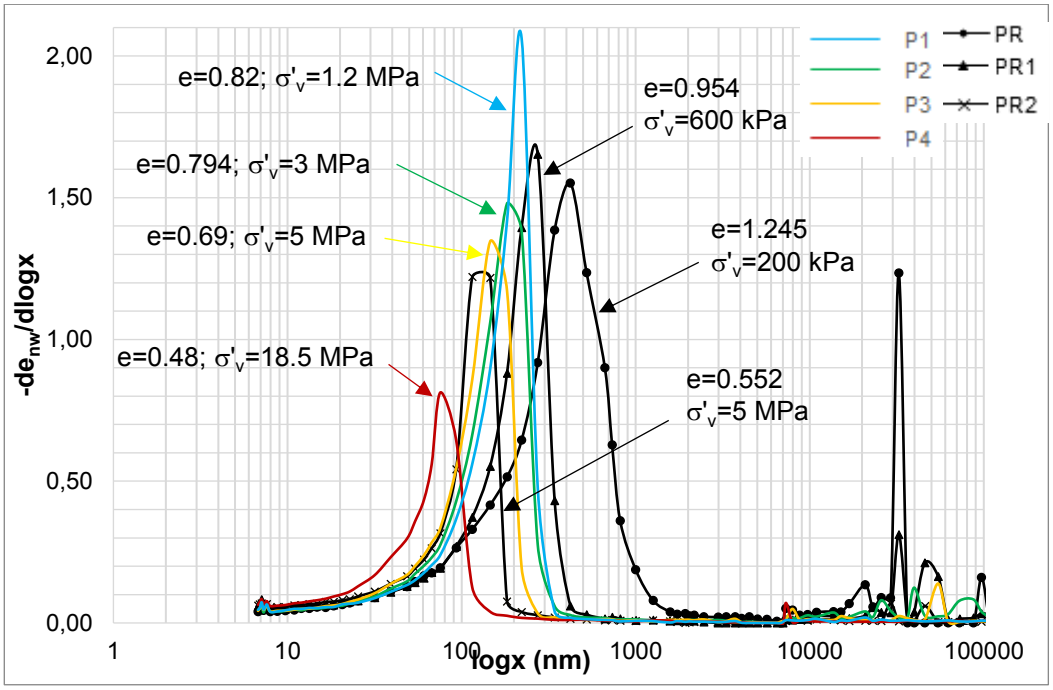

Fig. 8.15 - Evolution in 1D compression of PSD curves of natural and reconstituted Pappadai clay.

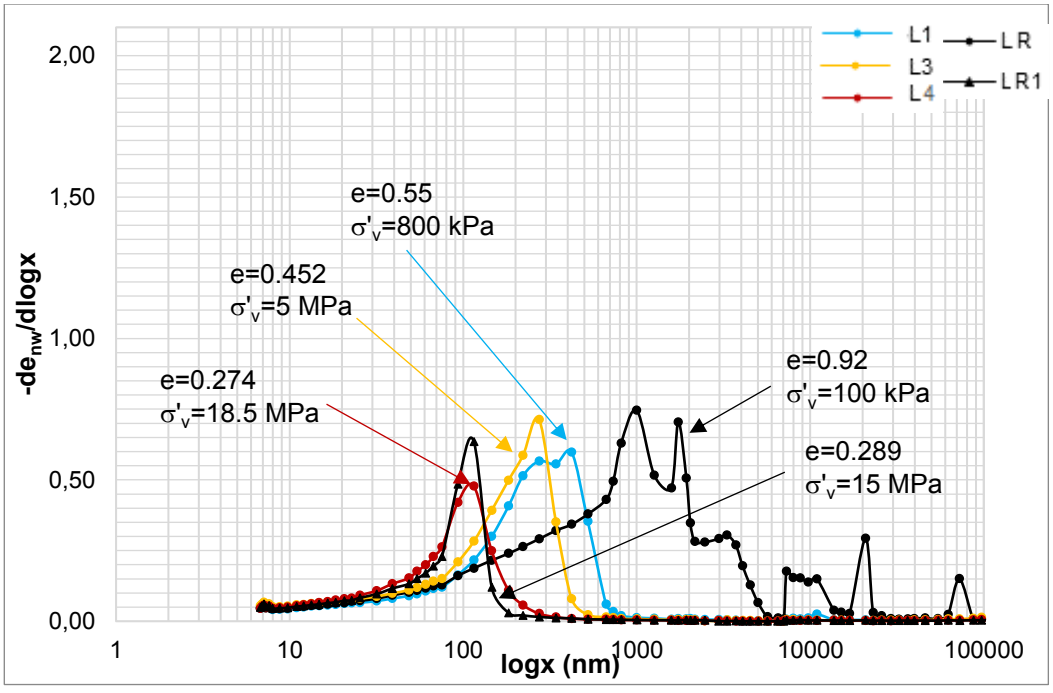

Fig. 8.16 - Evolution in 1D compression of PSD curves of natural and reconstituted Lucera clay.

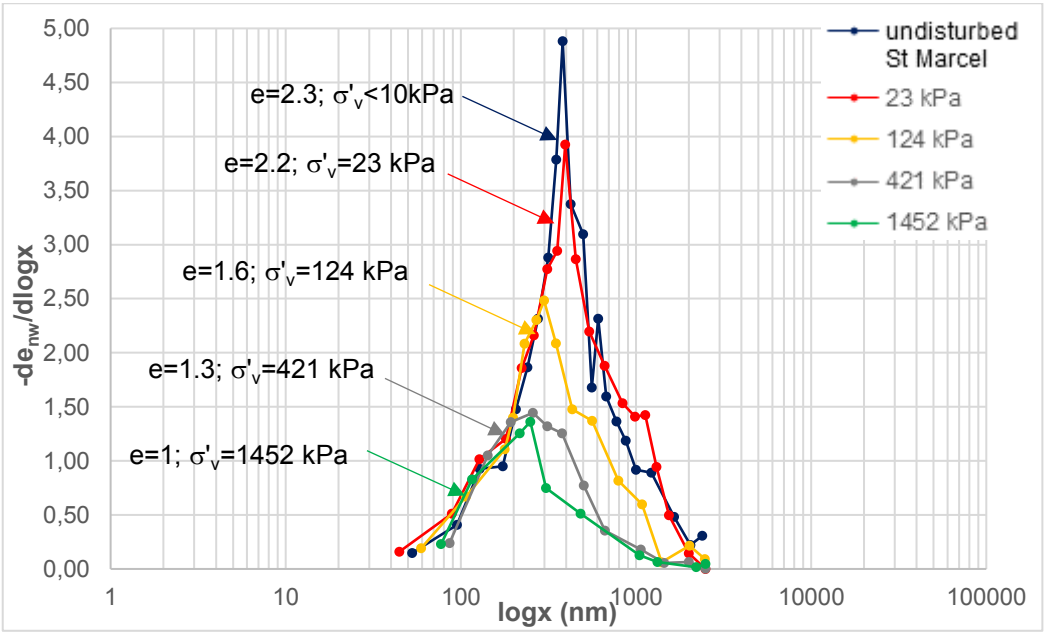

Fig. 8.17 - Evolution in 1D compression of PSD curves of natural soft St Marcel clay (replotted after Delage and Lefebvre, 1984).

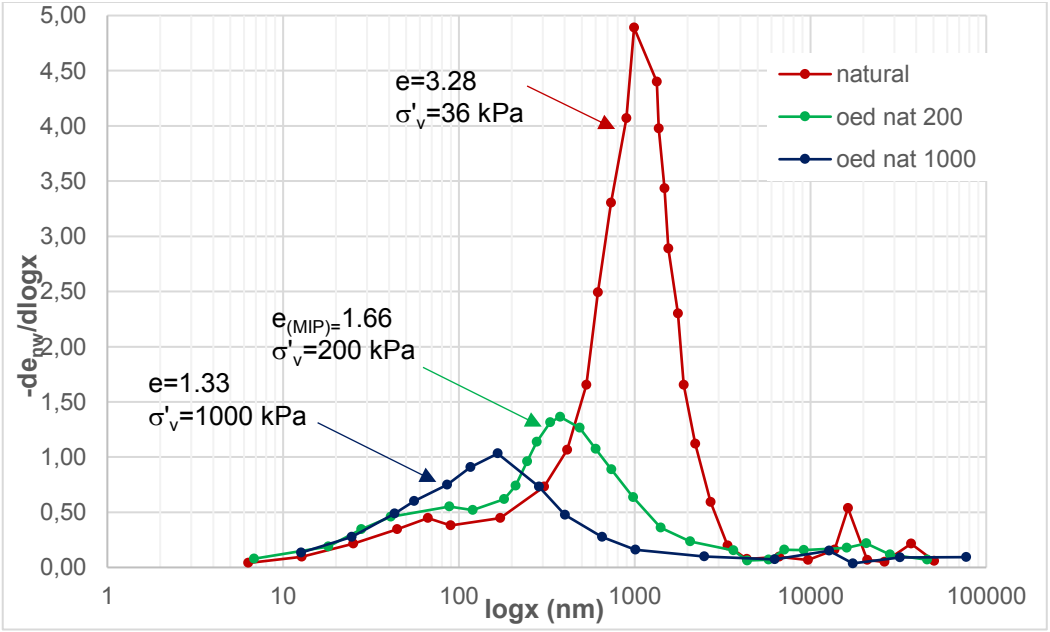

Fig. 8.18 - Evolution in 1D compression of PSD curves of natural soft GoG clay (after Hattab et al., 2013). Note that $e_{(MIP)}$ is the maximum void ratio measured in the MIP test, reported in case the actual void ratio is unknown.

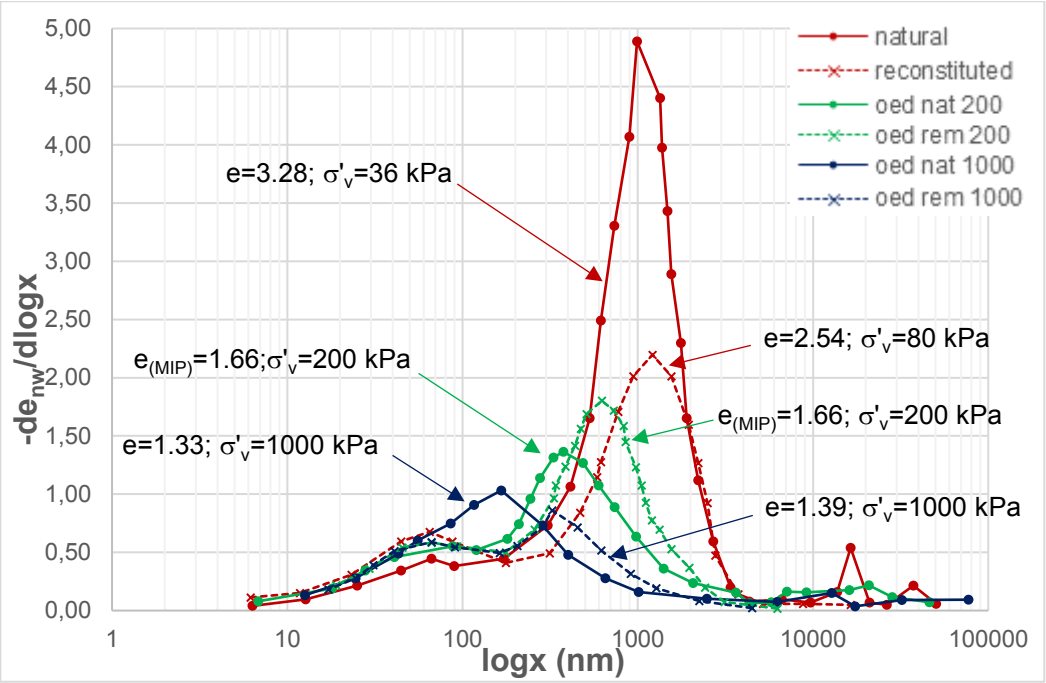

Fig. 8.19 – Evolution in 1D compression of PSD curves of natural and reconstituted GoG clay (after Hattab et al., 2013). Note that $e_{(MIP)}$ is the maximum void ratio measured in the MIP test, reported in case the actual void ratio is unknown.

The qualitative analysis of the data for both stiff and soft clays carried out so far can be enriched with quantitative assessments of the relations between macro-parameters and micro-parameters; the latter may be those describing the shape of the pore size distribution curve and its evolution under 1D loading.

As first, the evolution of the DPS with increasing vertical effective stress will be discussed (Fig. 8.20). The reported data refer to Lucera and Pappadai clay, both natural and reconstituted, and to natural St Marcel clay and GoG clay, the latter both natural and reconstituted. For all the clays, the dominant pore size reported in the graph has been chosen as the one showing the higher frequency in the pore size distribution (Fig. 8.17, Fig. 8.18, Fig. 8.19). For St Marcel clay, the data point corresponding to the undisturbed state has not been reported, as the corresponding pressure is not well defined. However, since the DPS of the curve at 23 kPa (pre-gross-yield) is almost

identical to that of the undisturbed state (Fig. 8.17), this will be considered for all the plots shown subsequently.
For each clay, as often outlined earlier, a reduction in the DPS is occurring with increasing σ'_v. The same linear trend of reduction of DPS can be recognized for natural and reconstituted Pappadai clay and for natural Lucera clay, although for the latter the DPS at 5 MPa appears not to be adhering to the trend identified by the other specimens. For reconstituted Lucera clay, the DPS at large pressures is found to agree with the trend, whereas the DPS at 100 kPa, i.e., that of the specimen after the consolidometer stage, is found at values of DPS as high as those of natural and reconstituted GoG at similar pressures. Hence, a confirmation is given that below the threshold pressure of microstructural re-organization (indicated with an arrow in Fig. 8.20), the pore size distribution is governed by the inter-aggregate porosity, which is also causing low fabric orientation. Beyond the threshold, the inter-aggregate porosity collapses and the dominating porosity is changed into the intra-aggregate porosity, with a corresponding achievement of fabric anisotropy. With further loading, the dominant intra-aggregate pore size continues to reduce. Remarkably, this trend of reduction of the dominant intra-aggregate pore size with increasing pressure is about linear and is common to all the clays analysed, despite their different compositions.
The influence of composition is instead apparent when St Marcel clay is considered: at very low pressures, the clay is exhibiting small inter-aggregate dominant pores, as a result of its CF being much higher (80%) and less active than for the other clays in the plot (40-60%). At the same time, the similarity in the DPS of reconstituted Lucera and natural and reconstituted GoG is likely to be due to the very similar CF of the two clays.

The variation of the frequency of the DPS with increasing vertical effective stress is shown in Fig. 8.22. As qualitatively observed, the rate of reduction of the frequency of the DPS mainly depends on the clay sensitivity, being higher for highly sensitive clays, which possess a more unstable bonding and exhibit higher compressibility. Pappadai clay experiences a lower rate of reduction of frequency, being a medium-low sensitivity clay. Lucera clay, having sensitivity $\approx$2, is found almost not to modify at all the

frequency of its DPS. In agreement with the microstructural interpretation of sensitivity discussed in Section 8.3, which is considering the undisturbed clay sensitivity reflected in the difference in the frequency of the incremental curves for the undisturbed and the reconstituted specimen at the same pressure, a very similar linear trend is identified for both reconstituted clays (S_σ=1) and clays of low sensitivity, as Lucera clay.

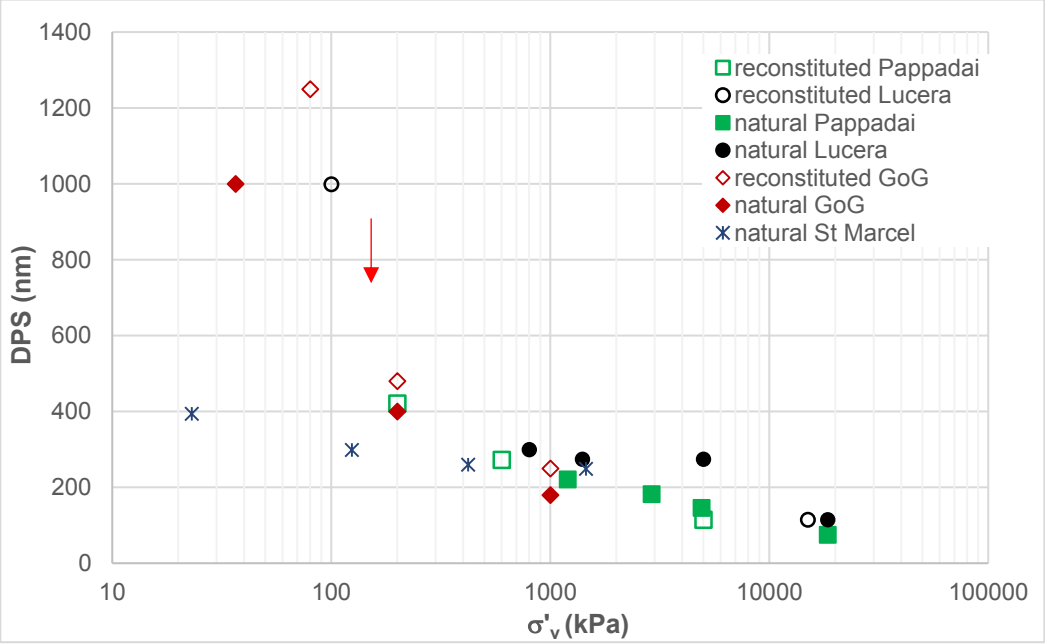

Fig. 8.20 – Dominant pore size against vertical effective stress in 1D compression for Pappadai, Lucera, GoG and St Marcel clay. The threshold pressure for microstructural re-organization is indicated with an arrow.

In the attempt of describing the evolving shape of the pore size distribution curve, the parameter "width" has been identified, which describes the average width of the curve. It is calculated as the ratio of the total area subtended by the incremental curve to the frequency of the DPS, i.e., the height of the curve. Thus, this parameter is representing the width of a rectangle equivalent to the PSD curve and with height equal to the frequency of the dominant pore. The plot in Fig. 8.22 reports the change in width of the pore size distribution with increasing pressure for the examined clays. The prevailing

influence on the width seems to be exerted by the clay activity: GoG clay, both natural and reconstituted and both before and after the threshold pressure of 100-200 kPa, has higher widths than the other clays, as an effect of its higher activity. Lucera and Pappadai clay, having similar CF as GoG but much lower activity, are showing much lower width. St Marcel clay, having low activity, aligns with Pappadai and Lucera clay.

In Fig. 8.23, the evolution of the DPS with sensitivity in 1D compression is shown for those clays for which data of 1D compression for both the natural and the reconstituted clay were known, thus allowing the calculation of evolving sensitivity, i.e., for Pappadai, Lucera and GoG clay (for the latter, the data from the 1D compression curves given by Hattab et al., 2013 have been considered). For each clay a trend is identified with an arrow directed towards $S_\sigma=1$. For Pappadai and Lucera clay, also the data corresponding to the swelled specimen are reported, allowing to define an initial vertical part of the trend which includes the undisturbed and the swelled specimens, plus possible pre-gross yield states, at the same sensitivity and with very similar DPS values. Analogously, the sensitivity of GoG clay is assumed to be constant up to gross-yield. The graph shows that the reduction in DPS occurs at a rate depending on the clay sensitivity, so that the higher is the sensitivity, the higher rate of reduction of DPS is recorded. When approaching $S_\sigma=1$, i.e., at very large pressures for the stiff clays, the trends of Pappadai and Lucera clay are seen to converge towards a very similar value of DPS. At very large pressures, it is possible either that the pore size distribution achieves a minimum DPS value and, with increasing pressures, this remains constant, or that the frequency of the DPS reaches a constant value and, with further loading, only the DPS continues to reduce. If the first mechanism applies, the two trends gathered for Pappadai and Lucera clay are converging towards a similar DPS, which is likely to be a “critical dominant pore size”, which does not compress with further loading. In this case, the critical DPS would indicate the achievement of a condition of stability for the clay microstructure.

The graph in Fig. 8.23 discussed so far is relating a macro-parameter, the clay sensitivity, which embodies the effects of microstructure on the macro-behaviour, to the evolution of the microstructure actually recorded in two clays from different classes (soft and stiff), in terms of modification of pore size distribution. Hence, the graph is describing a trend of microstructure degradation with the evolution of a parameter of macro-behaviour. In Chapter 3 advanced constitutive models for natural soils were described and some of them, such as the model of Rouainia and Wood (2000) and that of Baudet and Stallebrass (2004), were seen to incorporate a "structure degradation law" relating the size of the structure surface (r for Rouainia and Wood; s, corresponding to the clay sensitivity, for Baudet and Stallebrass) to both volumetric and deviatoric plastic strains by means of a parameter k, defining the rate of destructuration, which is a scalar parameter chosen by means of a calibration procedure.

It is here shown that the rate of degradation of the clay microstructure can be indeed related to the real evolution of porosimetry experienced by the clay, either soft or stiff, in this case under a 1D compression path. The re-formulation of the parameter k as an algorithm accounting for the variations of the micro-structural parameters with loading , of the type presented above, could be a strategy to incorporate the micro-behaviour in the formulation of the constitutive model.

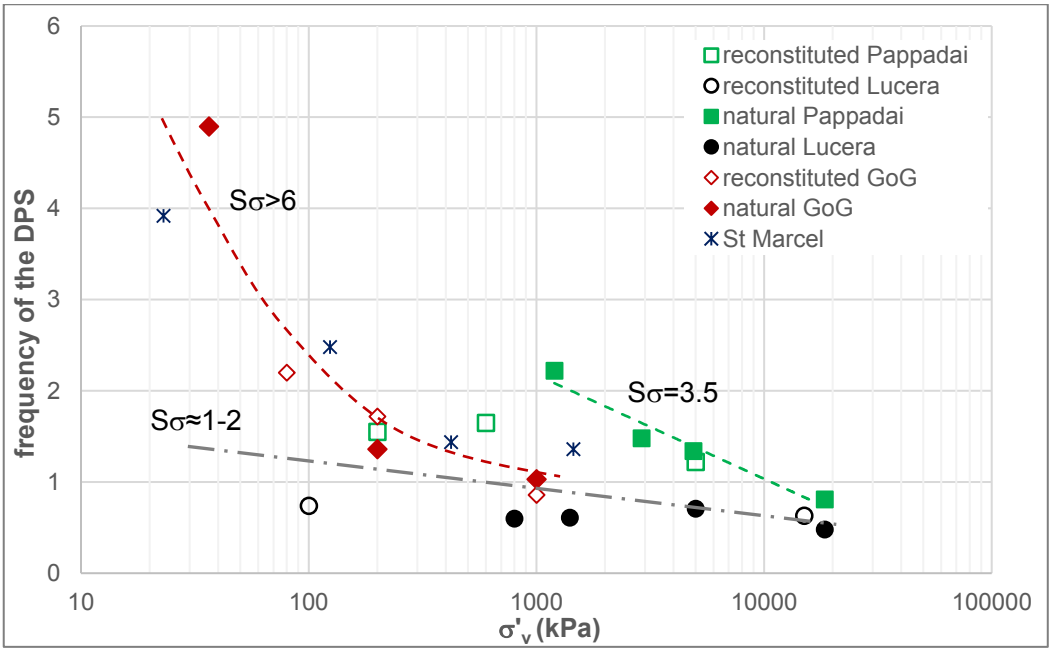

Fig. 8.21 – Frequency of the DPS against vertical effective stress in 1D compression for Pappadai, Lucera, GoG and St Marcel clay.

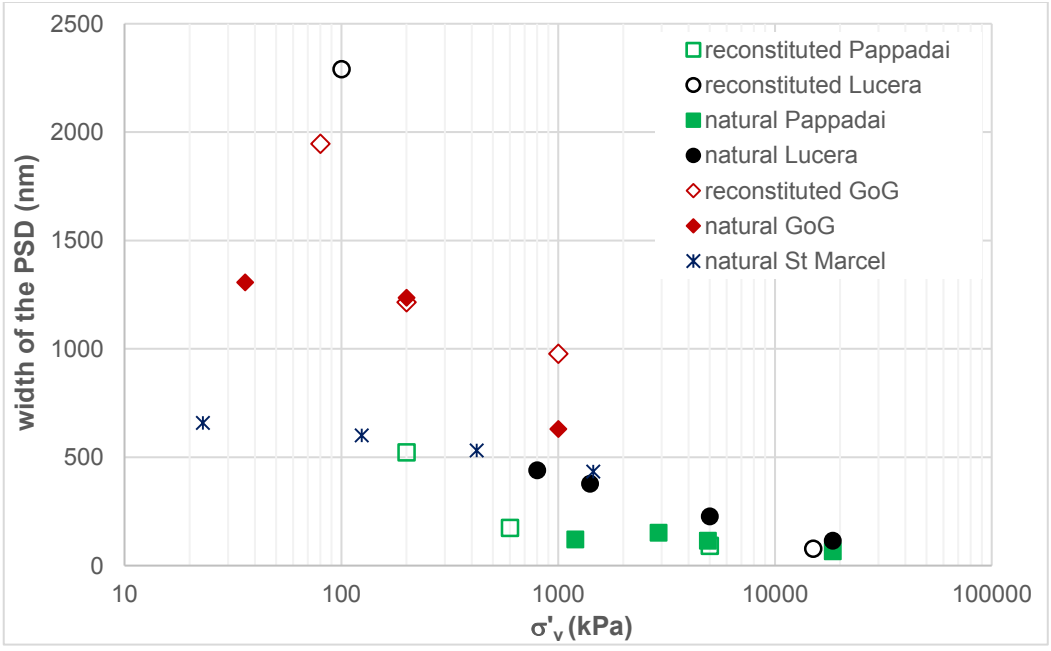

Fig. 8.22 – Width of the pore size distribution curve against vertical effective stress in 1D compression for Pappadai, Lucera, GoG and St Marcel clay.

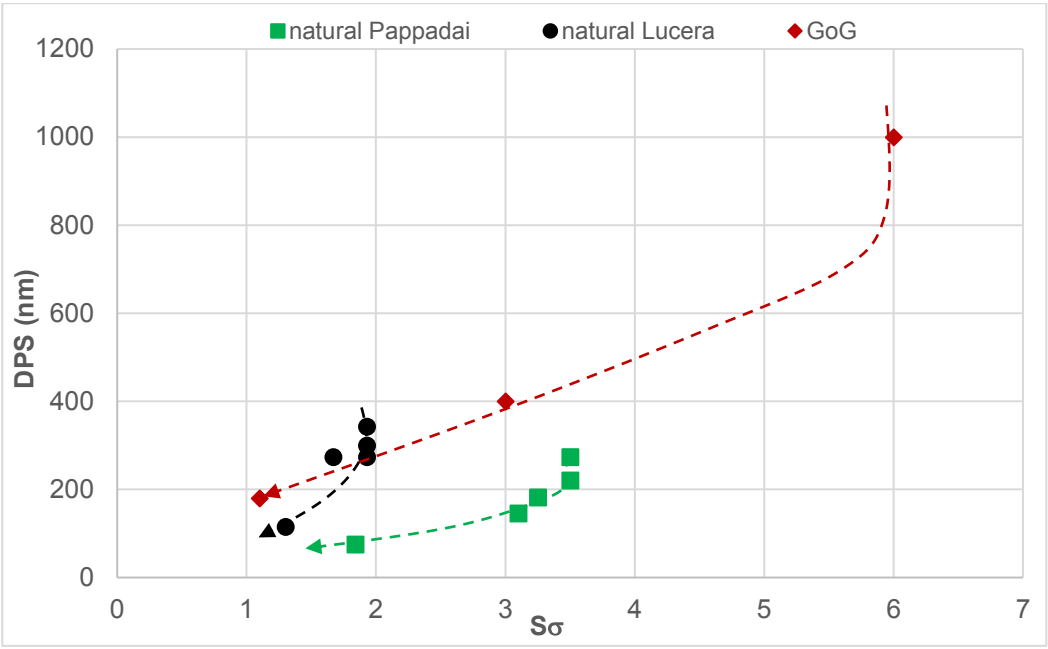

Fig. 8.23 – Dominant pore size against sensitivity in 1D compression for Pappadai, Lucera and GoG clay.

8.4.2 Isotropic compression

The microstructural evolution recorded under isotropic compression has been discussed in Chapter 7 for both the natural clay (Section 7.3.4) and the reconstituted clay (Section 7.3.5).

For the natural clay, the investigation has involved both a pre- and a post-gross yield state, respectively natural Lucera clay states LI_2 and LI_3.

The micro-analysis of the specimen at state LI_2, approaching the isotropic gross-yield (Fig.7.41), conveyed interesting information about the changes in microstructure in the vicinity of gross-yield. In fact, differently from the corresponding state (at the same void ratio) in oedometric compression pre-gross-yield L_2 (for which almost no change of pore size distribution with respect to the undisturbed state was recorded), specimen LI_2 represents the first stages of fabric and PSD reorganization induced by the progressive isotropic gross-yielding, that evolves across the whole range of states within the highest curvature portion of the v-lnp' compression curve.

Where the pore size distribution is seen to maintain unchanged the value of the PSD recorded for the undisturbed state, a higher frequency is recorded for the PSD (Fig.7.80). This variation is considered as representative of the porosimetry modifications preliminary to those occurring with post-gross yield compression, in which the frequency of the DPS decreases with increasing pressure (Fig. 8.21). At the same time, by state LI2 the clay fabric orientation is not experiencing much changes, keeping its degree of orientation almost unaltered, except for the local development of some concentric layouts of particles which seem to be characteristic of isotropic loading (Cafaro and Cotecchia, 2001).
When isotropically compressed post-gross-yield to a pressure 1.5 times larger than the isotropic gross-yield stress, the natural clay does not undergo significant further changes in fabric orientation, or in porosimetry, except for a small reduction in the DPS value and in its frequency.

For the reconstituted clay isotropically compressed to a pressure 3 times larger than the mean effective stress attained in the consolidometer, the microstructural changes induced by isotropic loading are similar to those recorded in one-dimensional compression to the same void ratio. Both the loading paths are seen to induce a translation of the incremental curve towards lower pore diameters and a reduction in the size of the dominant pore (Fig. 7.94). In isotropic compression, the frequencies are seen to increase slightly with respect to state PR (end of consolidometer stage), but it is likely that an intermediate stage, not investigated here, in which the frequency increases soon after state PR exists, and that the frequency starts to decrease thereafter.

These results are in agreement with Mitaritonna et al. (2014), who observed that, for reconstituted Lucera clay the fabric directional properties change for compressions different from the one-dimensional compression, if the compression path is extended up to a stress level at least four times larger than that previously experienced. As discussed in Section 2.11, Mitaritonna et al. (2014) recognized that the application of

an isotropic stress path from around 70 kPa to reconstituted Lucera clay up to 1350 kPa causes a reduction in stiffness anisotropy ratio G_{hh}/G_{hv} with respect to the value measured in K_0 compression. Accordingly, the initially well oriented fabric (shown in Fig. 2.27a) undergoes a severe rearrangement into a far less oriented fabric. As a confirmation, the SEM images (shown in Fig. 2.33) of a specimen subjected to a stress ratio $\eta=0.3$, being very close to an isotropic stress path, do not show a preferred orientation and are characterized by a much lower degree of fabric orientation L, corresponding to random orientation (Martinez-Nistal, 1999; see Chapter 5).
It should be noted that the degree of fabric orientation delivered by the image processing of the micrograph of Mitaritonna et al. (2014) of reconstituted Lucera clay after consolidation in the consolidometer (Fig. 2.27a) appears excessively high and is found not to be in agreement with the maximum pressure attained in the consolidometer (100 kPa) by Mitaritonna (2006), which has been shown to be lower than the threshold pressure of fabric re-organization for Lucera clay.
This is thought to be due to the lower quality of the micrographs analysed by Mitaritonna et al. (2014) with respect to those obtained through the FESEM in this research work, which convey much lower degrees of fabric orientation for reconstituted Lucera clay at 100 kPa. However, a significant reduction in the value of L is recorded from the micrograph portraying, with the same low resolution, the specimen of reconstituted Lucera clay subjected to the stress ratio $\eta=0.3$ with respect to that of the specimen after the consolidometer stage. Remarkably, the reduction in the fabric orientation is further confirmed by the correspondent reduction in the elastic stiffness anisotropy ratio.

Despite being formulated for reconstituted clays, the finding that to change the fabric directional properties along a compression path different from the one-dimensional compression, a pressure at least four times larger than that previously experienced is required (Mitaritonna et al., 2014) could also justify the limited microstructure evolution undergone by the natural clay, since the pressure reached in isotropic compression

was not large enough to change the fabric setup developed with one-dimensional loading and to induce a major microstructure evolution.
Hence, isotropic compression tests to larger pressures on the natural clay, at least four times larger than the isotropic gross-yield stress, need to be carried out in the future to investigate the modification of microstructure induced by isotropic compression.

Hattab et al. (2013) subjected both natural and reconstituted GoG clay to isotropic compression to pressures more than 10 times the isotropic gross-yield. They observed that isotropic compression strongly reduces both the dominant pore size and its frequency.
A comparison is made, not discussed by the Authors, between the evolution of the pore size distribution in either one-dimensional and isotropic compression for the natural GoG clay (Fig. 8.24). The void ratios and pressures reached by the end of the tests are reported next to each incremental curve; since the K_0(NC) for GoG is not given by Hattab et al. (2013), the value of K_0(NC)=0.55-0.6 (average 0.57) measured by Le (2008) in a K_0-stress path test on the natural sediment of GoG is used. So, in (Fig. 8.24) the vertical effective pressures are reported as p'.
It is seen that the specimen compressed isotropically to p'=900 kPa has experienced a change in pore size distribution comparable to that experienced by the specimen one-dimensionally compressed to p'=720 kPa. The latter has a lower frequency for the PSD due to its lower void ratio. Hence, the rate of change in microstructure is comparable for the different compression ratio, although slightly higher in isotropic compression, especially if the rate is calculated with respect to the void ratio variation.

This is seen more clearly in the graph in Fig. 8.25, in which the evolution of the DPS is plotted against the volumetric strain ε_{vol} in either 1D compression or isotropic compression. The graph reports the plot for natural Pappadai, Lucera and GoG clay; the points (DPS; ε_{vol}) in 1D compression are connected with a full line, while the "+" symbols represent the points corresponding to the isotropic compression from undisturbed state. The corresponding PSD curves for natural GoG clay are those in Fig.

8.24. The plot shows that the collapse of the DPS in 1D compression is more rapid for the soft GoG clay, as already remarked, as a result of the higher initial void ratio and compressibility. For natural Lucera clay (Fig. 8.25), isotropic compression induces the same DPS modification as that induced by 1D compression to similar volumetric strain. By contrast, for natural GoG clay, isotropic compression is confirmed to induce a major reduction in DPS, i.e., a major modification of the pore structure, than the 1D compression path at the same volumetric strain.

This finding is giving a strong microstructural confirmation to the hypothesis, formulated by Cotecchia and Chandler (2000) and Cotecchia et al. (2011) and earlier recalled in Section 3.4.6, that the difference between the shape of the SBS and the corresponding gross yield curves for soft natural clays differs from that of reconstituted clays and stiff natural clays one-dimensionally consolidated in early virgin compression (arch shaped), due to the circumstance that soft natural clays, which are the most sensitive, possess a structure which is disturbed by the application of isotropic loads much more than by oedometric loading.
Consequently, soft clays experience higher structure degradation under isotropic loading than under 1D compression paths; this cuases, for the same volumetric strain increment, major structure degradation in isotropic compression than in one-dimensional compression, resulting in an inclined gross-yield surfaces, with $p'_{y,is} < p'_{y,K0}$, as those exhibited by the soft sensitive Bothkennar clay (Fig.3.24) and St Alban clay (Fig.3.25). The SBS obtained by Le (2008) for the soft sediment of Gulf of Guinea is of the same type, as shown in Fig. 8.26.

Moreover, the microstructural analysis and interpretation carried out throughout the present Chapter for soft clays, among which particular attention has been devoted to GoG clay, is showing that, despite having the peculiar shape of SBS explained above, the undisturbed soft clays do not possess an oriented fabric. In fact, at the very low pressures and high water contents, characterizing the clay early stages of compression, the fabric scheme proposed by Griffiths and Joshi (1990) is applicable,

with a non-oriented flocculated fabric. Therefore, fabric orientation (anisotropy) is not an internal factor necessarily determining $p'_{y,is} < p'_{y,K0}$ and associated to a SBS symmetrical about the K_0 line (Fig. 8.26).
On the contrary, the soft clay fabric is seen to acquire a fabric orientation once a threshold pressure of microstructural reorganization has been overcome, which generally occurs between 100 and 200 kPa (Section 8.2). This value of pressure, being the clay soft, is often found to be higher than the clay one dimensional gross-yield pressure (e.g., $\sigma'_{vy} = 63$ kPa for natural GoG, $\sigma'_{vy} = 54$ kPa for natural St Marcel). This means that, if a constitutive model such as that of Koskinen et al. (2002), developed for soft "structured" clays, is chosen to simulate the soft clay behaviour, when the soft clay starts re-organizing its fabric towards an oriented fabric, the yield surface has already been touched and the rotational hardening has already been activated, causing a progressive rotation of the yield curve towards a target value implying a lower inclination of the yield surface.

Conversely, the study carried out for Pappadai clay and Lucera clay is providing the microstructural evidence that clays of oriented fabric may exhibit $p'_{y,is} > p'_{y,K0}$, supporting the belief that the modelling of inclined gross-yield surfaces is not applicable to all one-dimensional consolidated clays (Cotecchia and Chandler, 2011).

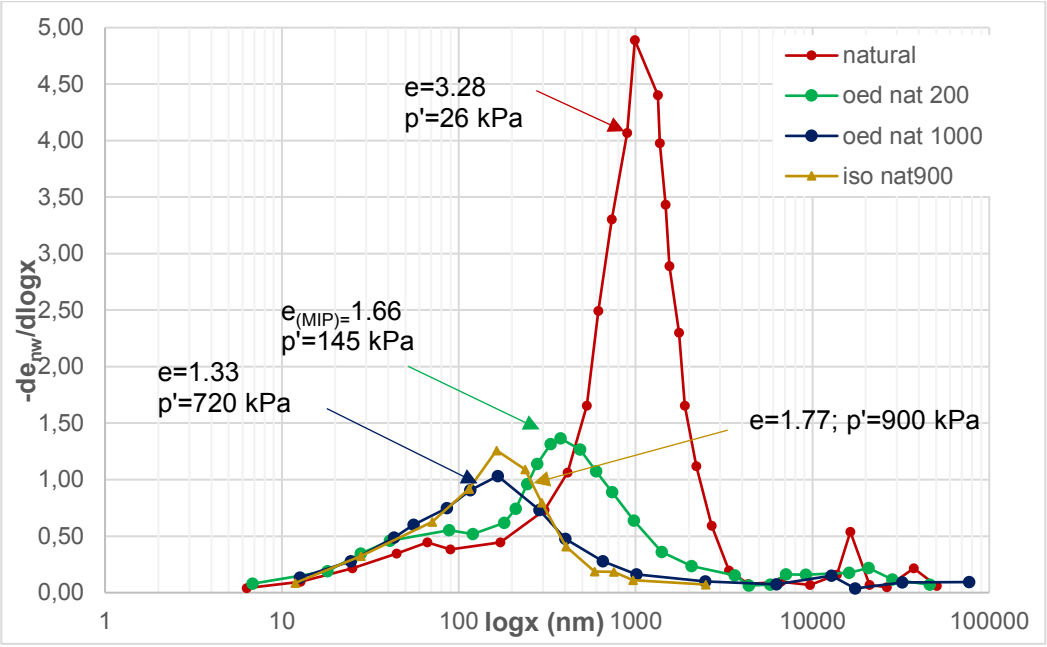

Fig. 8.24 - Comparison of natural GoG specimens 1D and isotropically compressed (after Hattab et al., 2013).

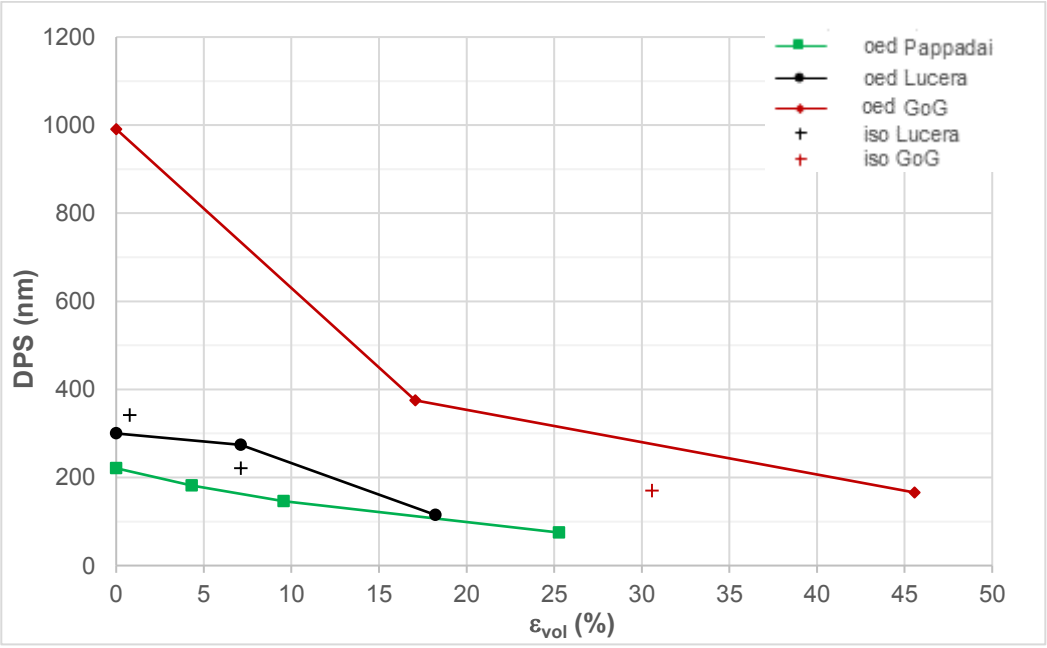

Fig. 8.25 – Evolution of DPS with volumetric strain for natural GoG clay in 1D and isotropic compression.

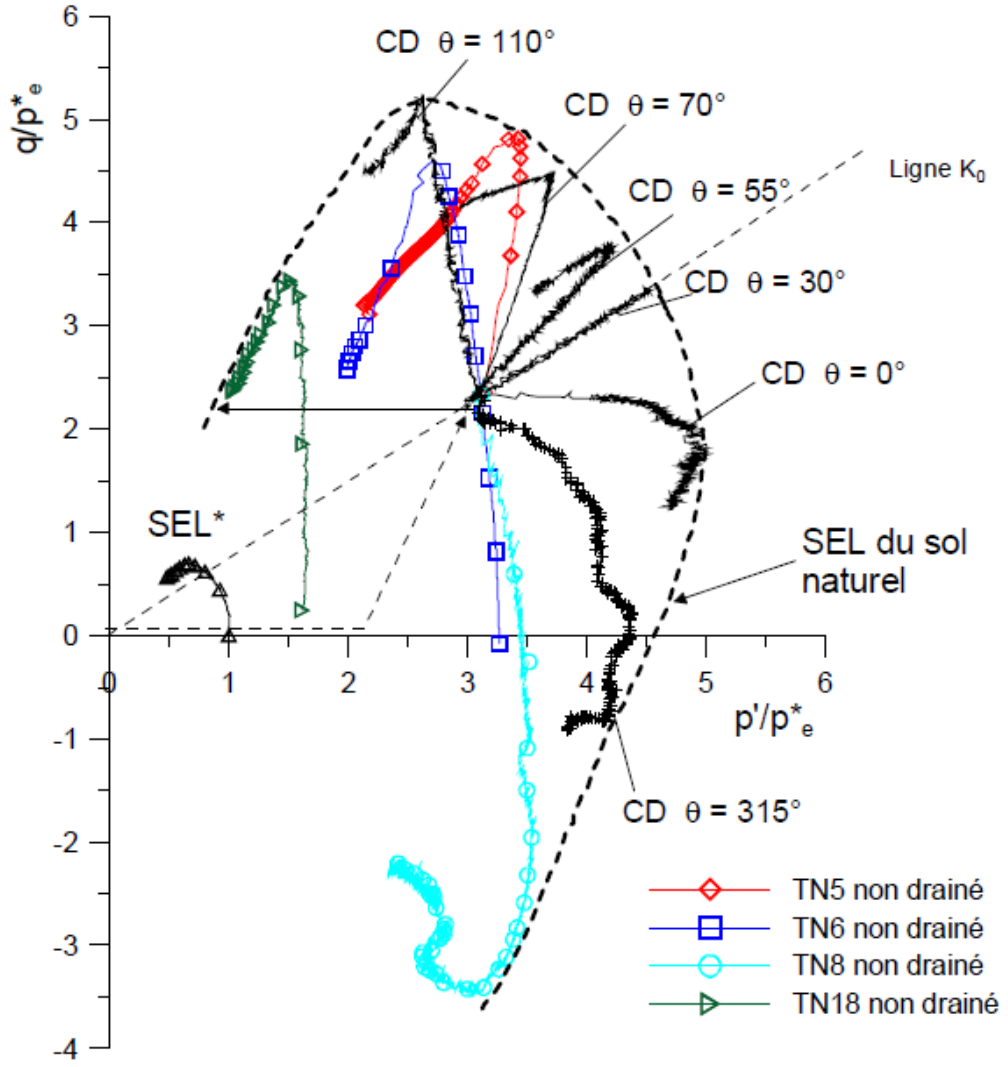

Fig. 8.26 – State boundary surfaces of the natural and reconstituted sediments of Gulf of Guinea (after Le, 2008).

8.5 Micro to macro shear behaviour

The study of the microstructural evolution in shear has been discussed in Section 7.4 for both natural and reconstituted Lucera clay.

The macro-behaviour of the natural clay was explored both before and after reaching the SBS, by means of shear tests, both drained and undrained, consolidated to isotropic consolidation stresses below the isotropic gross-yield stress. All the sheared natural specimens that underwent further shear straining after reaching the SBS experienced, to some extent, a strain localization, although a failure surface did not always develop. Hence, the microstructural analyses were carried out both inside the strain localization area, or shear band, to investigate the effects of strain localization on the microstructure, and on peripheral parts, aside the shear band and not affected by localization, in which the microstructural changes due to shear before the activation of the localization mechanism are being recorded.
As discussed in Section 7.4.2, to explore the microstructural changes suffered by the clay under shear half way through the path to reach the shearing gross-yield (i.e. the SBS), two undrained shear tests were stopped at half the peak deviatoric stress attained in the tests carried out up to large strains, starting from the same isotropic consolidation stress.
For the reconstituted clay, microstructural analyses were carried out on two specimens, one sheared drained from a lightly overconsolidated state, which did not reach the critical state, the other sheared undrained from the dry side of critical, which developed a shear band. For the latter the microstructure was analysed both inside and outside the shear band.

The microstructure analyses on the natural specimens subjected to drained shearing allowed to investigate the microstructural changes due to contractancy in shear, as both the specimens were contractant and, in both cases, also the microstructural changes occurring inside the shear band were representative of an overall continuum strain field, since the shear band was incipient (i.e., before the complete development of strain localization) and in neither of the specimens a complete failure surface deveoped.
An overall increase in the fabric orientation with respect to the fabric prior to shearing was recognized. Inside the area of strain localization, the increase in fabric orientation

is also due to the reorganization of particles along the direction of the incipient shear band, as confirmed by both the direction histograms and the orientation curves resulting from image processing, in which a number of particles re-orienting in the direction of the shear band is observed (Fig.7.112). Outside the area affected by strain localization, the fabric orientation is seen to increase with respect to the state prior to shearing.
In terms of evolution of the pore size distribution, drained shear of contractant specimens is seen to determine a reduction in inter-aggregate porosity, both inside and outside the shear band, hence the specimens are experiencing the closure of the macro-pores, also observed in compression tests. A small reduction in the value of the dominant pore size, combined with a small change in frequency with respect to the specimen before shearing, is also recorded both inside and outside the shear band, suggesting that all the areas of the specimen experience contraction, allowed for by the drained test condition.

The microstructural analyses on the undrained shear specimens allowed to study the microstructural changes occurred both inside the shear band, present and completely developed in both the specimens, and outside the shear band. Both the zones were seen to achieve a higher degree of orientation than that recorded for the clay before shearing, similarly to what observed in the drained tests. In the shear band, as for the drained tests, this is related to a re-organization of particles, which start rotating along the direction of the shear band. However, also outside the shear band the fabric anisotropy increases, and even higher degrees of orientation are recorded.
Remarkably, in both drained and undrained specimens, areas of honeycomb fabric are found preserved in bewteen strata of c.p.o. fabric, confirming that shearing generates a non-uniform microstructural evolution, similar to that induced by compression (V. Cotecchia et al., 1982; F. Cotecchia & Chandler 1998; F. Cotecchia et al. 2011).

In terms of changes in pore size distribution, also for the undrained tests shearing in general translates the incremental curve to the left with respect to that prior to shearing,

with a reduction in the dominant pore dimension and of all the pore sizes overall, irrespective of the specimen plastic dilatancy or contractancy. However, complex and heterogenous changes in fabric are recorded in the different parts of the specimen, also due to internal drainage between the different portions of the specimen.

For the specimens sheared up to half the peak deviatoric stress, no significant changes in the pore distribution are observed, suggesting that the microstructural changes taking place half way through the shear path inside the SBS are minor, or negligible (Fig.7.126, Fig.7.135). Similarly, limited changes were seen to occur when compressing the clay to states pre-gross-yield.

Hence, the conclusion follows that the elastic behaviour assumed by the MCC inside the SBS, as well as by models for "structured" soils predicting elastic behaviour inside the structure yield surface (e.g., S-CLAY1S of Koskinen et al., 2002), may fit the clay behaviour under monotonic loading because the microstructural changes occurring inside the SBS are minor, or negligible, hence deformation is close to reversible along large part of the loading path, but for the portion approaching gross yielding (e.g., specimen LI_2 compressed isotropically to a pre-gross-yield state, Fig.7.79). However, Massaro (2004) showed that for Pappadai clay cyclic shear loading from about $1/3q_{peak}$ up to about $2/3q_{peak}$ causes some degradation of structure, since it causes a reduction of the gross yield deviatoric stress in shearing and a reduction of the structure surface. Hence, the extent to which microstructural changes pre- gross yield in shear become more significant, requiring the use of constitutive models enabling plastic hardening inside the SBS, is to be studied by means of microstructural analyses on specimens either sheared up to deviatoric stresses closer to gross-yield state in shear, or on specimens subjected to important cyclic shearing (several cycles). These tests and the corresponding microstructural analyses are planned as future work, as well as microstructural analyses at states post-gross-yield in shear, before strain localization. For monotonic shear paths and for swelling-recompression paths up to states prior to the pressure range representing gross yielding (knee of the compression curve in the v-lnp' plane, or knee in the q-ε_s curve), the clay bonding and fabric are not found to

suffer significant degradation based upon the new direct experimental evidences discussed so far for the natural clay.

The microstructure analyses on the sheared specimens of reconstituted Lucera clay confirm that the evolution of microstructure experienced in undrained shear is far more complex and heterogenous than that induced by drained shear, due to the internal drainage occurring inside the specimen. Both the drained specimen, which did not experience strain localization, and the undrained specimen inside the shear band of reconstituted Lucera clay are achieving of a lower DPS.
For the drained specimen, the fabric post-gross yield in shearing confirms that shearing induces an overall increase in fabric orientation, also where shear strained is not localizing. In any case, the average increase in fabric anisotropy complies with the occurrence of preserved local areas of far lower orientation.

The microstructural changes induced by shearing of either natural or reconstituted Lucera clay agree with those found in the literature for sheared monomineralic clay specimens, discussed in Section 2.12. For these, drained shearing has been seen to induce a progressive increase in fabric orientation, even when no shear plane is observed in the specimen (Hattab and Fleureau, 2010), with a concurrent reduction in the inter-aggregate porosity. The features observed for Lucera clay inside the shear band confirm some features recognized also inside the shear band of either kaolinite or bentonite specimens by Hicher et al. (1994).
In general, the microstructural changes recorded in one-dimensional and isotropic compression and in shear for both stiff clays and soft clays beyond the threshold pressure of fabric re-organization are outlining a general mechanism of microstructural evolution over gross-yield and post-gross-yield, applying to both compression and shear loading paths.
Over gross-yield a progressive bonding degradation is recorded over the range of pressures including the gross-yield pressure, combined with the onset of major fabric re-organization. Post-gross-yield, bonding is completely weakened and fabric

undergoes a further reorganization from the chaotic architecture arisen over yield to a more orderly architecture, in which stacks of domains increase and become thicker, still alternating areas in which a honeycomb fabric is preserved. Concurrently, the inter-aggregate porosity is collapsed and the dominant pore size reduces to the range of the intra-aggregate pore sizes, which are mainly found inside the stacks.
The average orientation recorded on medium magnification micrographs is not seen to evolve much along the one-dimensional compression path, whereas along shear paths the average orientation increases, both outside the strain localisation areas and, particularly, inside the shear band. Along isotropic compression paths, the average degree of orientation does not change, unless very large pressures are attained and, in this case, it decreases.
Therefore, rather than one-dimensional compression paths, the major increase in orientation is induced by shear paths.

As discussed in Section 6.5, the normalized shear stress paths for all the shear tests carried out on the specimens of Lucera clay, together with the gross-yield states in isotropic and K_0 compression, allow to identify a typical arch shape for the clay state boundary surface (Fig. 6.33), which is similar to that observed for Pappadai clay and for the other one-dimensionally consolidated clays discussed in Section 3.4.6, although slightly steeper on the right side. In Chapter 6, the hypothesis was formulated that this difference may be related to the different composition of the two clays, since Lucera clay has been found to have a lower CF and a lower activity than Pappadai clay. Indeed, a similar shape of the SBS had been recognized for Montemesola clay (Cotecchia et al., 2007), also being more silty than Pappadai clay. The microstructural observations have also shown that the undisturbed Lucera clay is characterized by a degree of orientation lower than that recognized for undisturbed Pappadai clay, which is related to both the coarser composition of Lucera clay and to the different deposition conditions in which the two clays originated. This microstructural feature could possibly be responsible for the gross-yield states in isotropic and K_0 compression being closer than for Pappadai clay, resulting in a tighter SBS.

Similarly to what observed by Cotecchia (1996) for Pappadai clay, Lucera clay specimens are seen to join post-gross-yield in shear a single locus of post-rupture states, inside the SBS, defining a pseudo-critical state (Cotecchia and Chandler, 1997) characterized by a stress ratio M ($<M_{nat}$). These states are aligned along a straight line to the left of the INCL in the v-lnp' plane. As this pseudo-critical state locus differs from the critical state of the same clay when reconstituted, the natural clay does not get to the same state of the reconstituted even after large shearing. Similarly, when compressed to large pressures, the natural clay keeps being different from the reconstituted clay, despite the similar shape induced in the pore size distribution, which is mainly an effect of the same clay composition (Fig. 8.15, Fig. 8.16).

Moreover, similarly to what observed for Pappadai clay, the normalized stress paths of the specimens sheared beyond isotropic yield plot within the current SBS, as a result of the important degradation of bonding and evolution in fabric occurring post-gross yield in compression. No microstructural analyses could be carried out in this work on sheared specimens consolidated beyond gross-yield, which are among the priorities of the future developments of the research.

will be formulated which relate this difference in shape to differences recorded in microstructural features.

On both natural and reconstituted GoG clay, Hattab et al. (2013) carried out microstructural analyses on specimens sheared drained from different isotropic normally consolidated states.
In Fig. 8.27, the MIP result for a natural specimen isotropically compressed from undisturbed state to p'=40 kPa (pre-gross-yield) and sheared drained is compared with the PSD curve of the undisturbed specimen (p'=26 kPa), where no significant structural modifications have been found to occur in the isotropic compression stage. As observed for drained tests on natural Lucera clay, the contractant behaviour in shear

is reflected in a reduction of the inter-aggregate porosity, corresponding to an inter-aggregate dominant pore size almost unchanged but with a much lower frequency. Noticeably, the intra-aggregate dominant pore size only undergoes a small increase in frequency.

The incremental PSD of the undisturbed specimen of GoG clay and that of the reconstituted specimen after consolidation in the consolidometer are compared with the MIP results for the specimens of both the natural and the reconstituted GoG clay sheared drained from different isotropic normally consolidated states (Fig. 8.28).
In general, if the effects of the contractancy due to shearing and to the previous isotropic compression are considered, it is seen that significant changes occur to the inter-aggregate pores, while the intra-aggregate pore distribution remains almost unchanged. The natural and reconstituted specimens sheared from the same isotropic compression state (especially the specimens sheared from p'=200 kPa in Fig. 8.28) keep showing pore size distributions of similar shape and of the same DPS; only the DPS frequency differ between the natural and the reconstituted clay, here considered to be effect of the natural clay sensitivity, as discussed for the specimens subjected to compression.
For the sake of comparison, the incremental curves recorded in the drained shear tests on natural Lucera clay (TNL4 and TNL6, Section 7.4.1) are reported in Fig. 8.29, together with the corresponding states prior to shearing (L1 and LI2, Fig.7.41).
The trend of microstructural evolution under drained shear depicted for the stiff Lucera clay differs from that applying to soft GoG clay only for the role that bimodality plays in the soft clay microstructure, as extensively discussed in the previous Sections. Hence, for both stiff and soft clays, the drained shear path (in which contractant behaviour is recorded) and the isotropic compression path prior to shearing are determining a reduction in the dominant pore size, being in the range of either the intra-aggregate (stiff clays and soft clays beyond threshold pressure) or the inter-aggregate (soft clays below threshold pressure) pore sizes, and a decrease in the frequency of the DPS.

Furthermore, Hattab et al. observe that at critical state reconstituted and natural specimens plot on different lines in plane v-lnp', which they interpret as a confirmation that the natural and the reconstituted clay do not reach the same state, but keep showing different behaviour also at large shear strain.

Hence, the conclusion that can be gathered from the analysis of the microstructure evolution, in compression and shear, for both stiff and soft clays, is that the natural and the reconstituted clay do not achieve the same microstructure after large straining, either in compression or in shear, even if many processes of microstructure modification are common to both natural and reconstituted clay (e.g., the non-uniform fabric developing upon straining, or the increase in orientation induced by shear paths).

Regardless of this basic feature of behaviour, some advanced constitutive models for structured soils (e.g., Rouainia and Wood, 2000) assume that destructuration contributes to the hardening rule with a negative component bringing the structure surface at large strains to coincide to the reference surface defined for the reconstituted soil; this is not the case for the model from Baudet & Stallerbrass (2004).

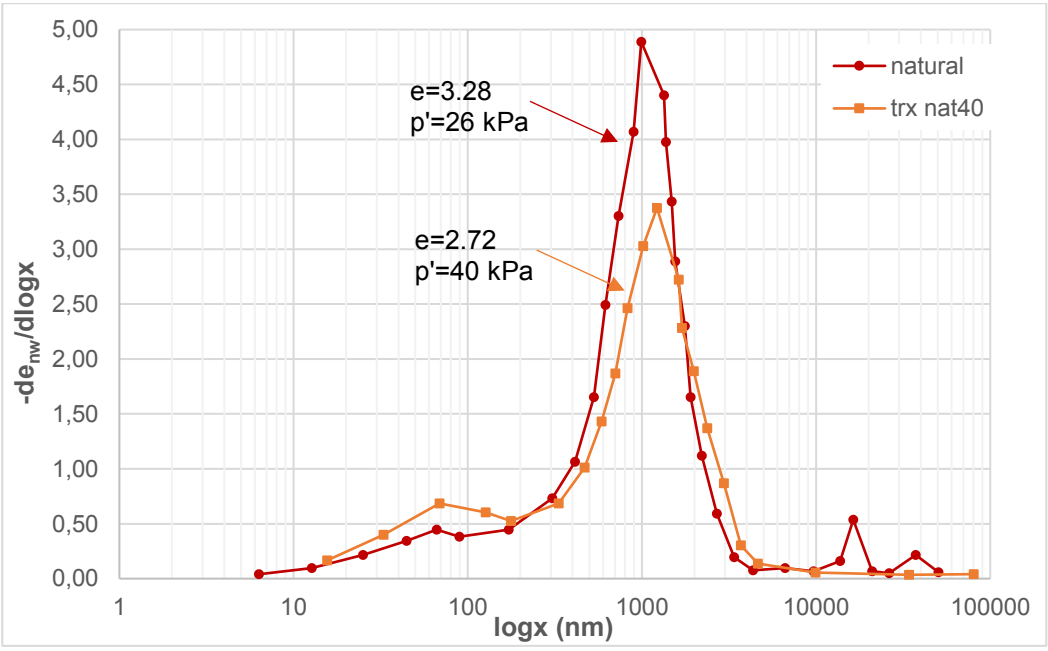

Fig. 8.27 – Comparison of the undisturbed specimen of Gulf of Guinea clay and the specimen sheared drained from a lightly over-consolidated state (after Hattab et al., 2013).

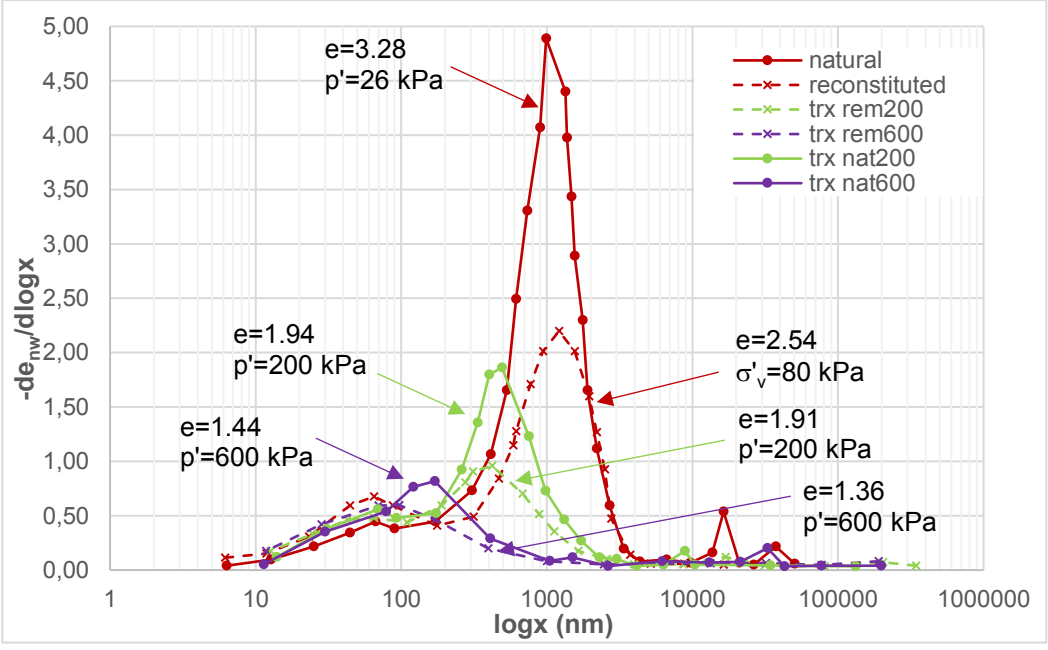

Fig. 8.28 – Evolution in drained shear of natural and reconstituted Gulf of Guinea clay compressed isotropically beyond gross-yield (after Hattab et al., 2013).

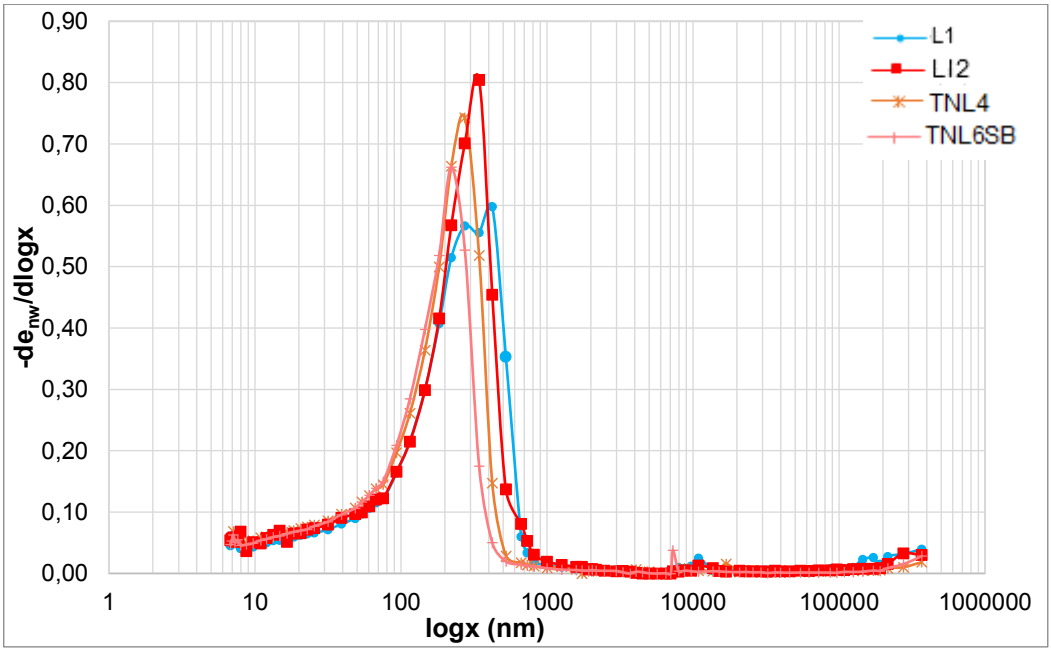

Fig. 8.29 - Evolution in drained shear of natural Lucera clay in drained shears TNL4 and TNL6, compared to isotropic pre-yield compression states prior to shearing, respectively L1 and LI2 (Fig. 7.41).

8.6 Possible further advancements of clay constitutive modelling

8.6.1 Role and shape of the gross yield surface for the natural soil

Kinematic hardening models have been developed to improve the simulation of the soil behaviour below the SBS, which Cam Clay simulated assuming isotropic elastic behaviour, in particular to improve the prediction of the cyclic soil response (e.g., Al-Tabbaa and Wood, 1989).

When conceived for either the reconstituted or for the natural "structured" soils, kinematic hardening models assume three stages of soil behaviour. The following discussion will be referred to the modelling of a natural soil.

The first stage develops inside the inner yield surface (i.e., the "bubble" for the models of Al-Tabbaa and Wood, 1989, and Rouainia and Wood, 2000, or the "plastic yield envelope" for the model of Kavvadas and Amorosi, 2000), which encloses the soil elastic domain. The dimension of this elastic domain was measured by Gasparre et al.

(2007) for natural London clay to have size, in the q-p' plane, of approximately 3 kPa (bubble diameter).

Inside the elastic domain only reversible volumetric and deviatoric strain increments are assumed to arise as a consequence of small stress increments. In general, the elastic stress-strain response depends on the bulk modulus K' and on the shear modulus G' (see for example eq. (3.3) and (3.4)), being correlated by ν', and hence both depending on the mean effective stress p' and on the soil specific volume according to the relation:

$$K' = \frac{vp'}{\kappa *} \qquad (8.1)$$

where $\kappa*$ is the slope of the swelling line in the plane v-lnp' for the reconstituted soil.

Some constitutive models, e.g., that of Rouainia and Wood, can incorporate the well-known law of Viggiani and Atkinson (1995) for G_0 of a reconstituted soil; however, also in the latter case, the behaviour inside the inner yield surface is fully elastic and only related to the soil specific volume (i.e., its porosity), to the mean effective stress p' and to the overconsolidation ratio, R_0.

In terms of micro-response, the soil microstructure in this first stage of loading has been seen to undergo negligible changes with loading, and so the new measurements seem to support the assumptions of these models for monotonic loading.

Correlations have been proposed in the literature which allow to account for some features of the clay microstructure at very small strains.

Cafaro and Cotecchia (2001) proposed that the very small strain shear stiffness G_0 for a natural clay should be not only related to the mean effective stress, p', and to the overconsolidation ratio R_0, but also to the clay sensitivity, thus representing the effects of the microstructural strength on the clay stiffness. Consequently, they expressed G_0 as:

$$G_0 = aS_\sigma^b p'^n R_0^m \qquad (8.2)$$

where a and b are constants, m depends on structure and n is that of Viggiani and Atkinson (1995) and does not depend on structure, but only on clay composition (e.g., PI). For models implementing anisotropic elastic stiffness, hence more advanced than Cam Clay type models in this respect, the work from Mitaritonna et al. (2014) would

be particularly useful and grounded on micro to macro experimental evidence. Mitaritonna et al. (2014) correlated the elastic stiffness anisotropy G_{hh}/G_{hv} to the evolution of fabric orientation for reconstituted Lucera clay, intended as evolution of the degree of orientation L, as defined by Martinez-Nistal et al. (1999) and also used in this work, as discussed in Chapter 5.

When the soil state, moving inside the elastic domain, reaches the boundary of the inner yield surface, plastic strain increments arise, the amount of which depends on the location of the soil state with respect to the outer structure yield surface by means of an interpolation rule for the calculation of the plastic modulus. Meanwhile, from this point onwards, the inner yield surface is dragged by the current state inside the outer yield locus. The translation of the inner yield locus is controlled by a kinematic hardening translation law, which accounts for both the relative position of the inner bubble with respect to the outer yield locus, and the change in size of the yield loci that has been activated by the newly arisen plastic strains.
Hence, as soon as the inner yield locus is reached, plastic strain increments are generated, which activate the hardening rule, which is generally isotropic (Rouainia and Wood, 2000; Kavvadas and Amorosi, 2000; Baudet and Stallebrass, 2004).
The hardening rule generally calculates the variation in size of all the yield loci generated by the plastic volumetric strain increment, adopting the same formulation of the Cam Clay isotropic hardening rule. It actually acts on all the yield loci because their sizes are generally related by scalar factors. For example, in the model of Rouainia and Wood, the isotropic hardening law controls the size of the reference surface p_c (Fig.3.40), but also of the inner bubble and of the structure surface, the sizes of which are related to p_c by scalar parameters (R and r, respectively).
In addition, in general, the size of the structure surface is also made to depend on another isotropic hardening contribution, effect of structure degradation, which relates the size of the structure surface to the plastic volumetric and deviatoric strains by means of parameters such as the rate of destructuration (in the models of Rouainia and

Wood and Baudet and Stallebrass) or structure degradation parameters (ζ_v, η_v, ζ_q, η_q in the model of Kavvadas and Amorosi).

So, kinematic hardening models conceive an outer yield surface, representative of the clay structure, whose size starts evolving (isotropic hardening depending on both volumetric and deviatoric plastic strain increments) when the inner yield locus is reached by the current state, i.e., when the current state is still inside the structure yield surface.

This 'structure surface', adopted by kinematic hardening models to embody the effects of the natural clay structure on the macro-response, does not conceptually coincide with the current state boundary surface of the clay, which instead is the surface including the "structure permitted" space (Leroueil and Vaughan, 1990) as result of the initial microstructural features of the clay and of their evolution with straining. As recalled in Chapter 3, the effects of the difference between the strength of the structure of the natural clay and that of the reconstituted clay are reflected in the different size of their SBS. In agreement with this, the Sensitivity Framework (Cotecchia and Chandler, 2000) conceives sensitivity as a scalar parameter allowing to define the effects on the size of the material response of the differences in microstructure between natural and reconstituted clays. The only model implementing to date this experimental evidence, by means of a "sensitivity" surface and a structure degradation law accounting for the change in size of the sensitivity surface due to the reduction in the clay sensitivity, is the model of Baudet and Stallebrass (2004), discussed in Section 3.5.3.

It should be noted that in the kinematic hardening models, the plastic modulus, which controls the amount of plastic deformation, has a formulation that provides small plastic strain increments inside the structure surface and major plastic strains once the structure yield locus is reached. This allows to produce small isotropic re-sizing of the structure surface as long as the current state is inside it, also allowing the structure surface itself to adjust with respect to its initial size (established by means of the

assigned initial state and parameter values), and be touched by the stress path on which the current state is moving at the gross-yield point.
Whether the experimentally determined gross-yield stress is correctly predicted by the model depends particularly on the choice of the model parameters controlling the interpolation rule which defines the value of the plastic modulus before the current state reaches the structure surface (e.g., B and ψ for the model of Rouainia and Wood).
If an isotropic compression path from an overconsolidated to a normally consolidated state is simulated, for example, in the v-lnp' plane, the current state starts moving inside the inner bubble, hence along a swelling line of slope κ^*. Then, once outside the elastic domain, the current state continues moving along the swelling path, the slope of which is controlled by the amount of the plastic strains that are developing, the latter depending on the above-mentioned parameters of the interpolation rule for the plastic modulus. It follows that for a natural clay, these parameters should be correlated to the clay bonding, which is known to affect the slope of the swelling line before gross-yield. This procedure has been adopted in the calibration of the parameters B and ψ of Rouainia and Wood (2000) model for Pappadai clay, as will be shown in the following. On the other hand, microstructural observations have shown that minor microstructural changes occur both in compression and shear (at least up to half the peak deviatoric stress) inside the SBS, corresponding to stress paths which project on a unique swelling line in the v-lnp' plane.

The third stage of soil behaviour starts when the current state is on the structure surface and major plastic strains occur. At this point, major structure degradation occurs, reflected in a significant increase of the negative component of isotropic hardening, which reduces the size of the structure surface. This reduction (active both before and after gross-yield) depends, as discussed earlier, on some structure parameters and on the volumetric and the deviatoric plastic strain increments. The latter in some models are found multiplied by a scalar parameter (e.g., $A<1$ in Rouainia and Wood, eqs. 3.34 and 3.35), which allows to reduce or neglect the role played in the destructuration

process by the deviatoric component of strains. On the contrary, the model of Baudet and Stallebrass (2004) does not introduce any reducing parameter.
Cotecchia et al. (2011) assume that the microstructure controls in a similar way the gross-yield stresses along any stress path, except for very soft sensitive clays, which experience a higher rate of microstructural degradation under low η compression paths. The Authors claim that when compressing a natural clay up to post-gross-yield pressures, either along an isotropic path, or along a K_0 stress path, the natural clay is seen to reach gross yielding in isotropic compression at an earlier stage than for anisotropic compression. This is likely to be due to the stability of the clay microstructure, that is lost more upon the increase of the minor principal stress (the radial stress), than due to the increase of the maximum principal stress.
In shearing paths, experimental results for natural soils, as those discussed by Cotecchia (1996) and in this work among many others, have shown that the negative component of hardening caused by structure degradation, which adds to either the hardening complying with Taylor's dilatancy rule, is mainly induced by plastic deviatoric strains. With respect to that, the choice of the above-mentioned parameter A of Rouainia and Wood model is quite a difficult task, if the microstructural processes occurring in the clay are considered, as the same parameter has to be uniquely defined both in compression and shear. For this reason, the value of A is often chosen as 0.5, so that the same influence is attributed to both the components of strain that however, at the same time, see their effects halved.

With regard to the SBS of the clay, predicted by a kinematic hardening model by calibrating the model by simulating probing stress paths, may benefit by the knowledge of the shape to be expected depending on the clay microstructural features. For example, for either one-dimensionally reconstituted clays and firm to stiff natural clays, this has been found to be arch-shaped. Hence, the model adopted to simulate a clay belonging to these classes, if correctly calibrated, is expected to portray a gross yield surface of arch-shaped type.

The SBS identified for Pappadai clay by Cotecchia (1996) and for Lucera clay in this work have been shown and compared in Fig. 6.35. Both the SBS are arch-shaped and, as expected, the SBS of Pappadai clay is larger as a consequence of its higher sensitivity. For Lucera clay, the SBS appears steeper on the wet side, as the stress sensitivity in oedometric compression $S_{\sigma,oed}=1.93$ is lightly higher than the stress sensitivity recognized in isotropic compression $S_{\sigma,iso}=1.77$, as discussed in Chapter 6. As a result, the strength sensitivity $S_t=1.94$ lightly differs from the isotropic stress sensitivity, conveying a lightly tighter curve with respect to that of Pappadai clay, for which the stress and strength sensitivities are found to be much closer.

Moreover, as anticipated in Section 8.4.2, being for both the clays the fabric well-oriented at the undisturbed state, with average degree of orientation L of 0.22-0.24 for Lucera clay and 0.27 for Pappadai clay, Lucera clay and Pappadai clay are providing the microstructural evidence that the inherent anisotropy of natural and K_0 consolidated clays is the dominant factor giving rise to an arch-shaped gross-yield curve and that the modelling of inclined gross-yield surfaces is not applicable to all one-dimensional consolidated clays (Cotecchia and Chandler, 2011).

On the other hand, the soft Gulf of Guinea clay has confirmed, through microstructural evidence, the hypothesis that soft clays undergo major structure degradation under isotropic paths than under 1D compression paths, thus explaining the experimentally observed difference in shape of the SBS of soft clays with respect to reconstituted and stiff clays.
Hence, the effectiveness of adopting rotated yield surfaces to model soft clays (e.g., Wheeler et al., 2003 and Koskinen et al., 2002) is confirmed for the peculiar microstructure of this class of clays, but it is found not to be connected to anisotropic fabric properties of the clay.

8.6.2 Modelling of Pappadai clay

The model of Rouainia and Wood (2000) was used to simulate some of the experimental test results of Cotecchia (1996) on natural Pappadai clay, during a visiting period at the University of Newcastle under the supervision of Dr. G. Elia and Prof. M. Rouainia. The calibration was primarily aimed at achieving a deeper knowledge of the model and of the role of its parameters, especially of those concerned with the effects of structure and the degradation of structure.

The calibration of the model for Pappadai clay started with the definition of a first tentative set of model parameters by comparison with the INCL and K_0NCL defined for the clay, with two oedometer tests on the natural clay (OED5 and CRSnat; Fig.6.3) and two oedometer tests on the reconstituted clay (OEDR and CRSrec; Fig.6.3). Reference parameter values or ranges of values were considered at this stage, as suggested by the supervisors or adopted in previous model parameter calibrations of other natural clays (e.g., the low sensitivity Norrköping clay on which the model was tested by Rouainia and Wood, 2000).

Then, with the input of these parameters in the model, a set of shear tests was simulated and an iterative calibration procedure was followed, with subsequent adjustments of the parameter values, to improve the fitting of the experimental data.

Drained and undrained shear tests were chosen, consolidated isotropically both before and after gross-yield, which were considered to be representative of the mechanical behaviour in shear of the clay and of the structure degradation processes affecting Pappadai clay during the consolidation and shearing stages.

Fig. 8.30 shows the stress paths of the tests: the undrained shear test TN11 and the drained shear test TN18 consolidated pre-gross-yield were considered, while the undrained test TN12 and the drained TN17 both consolidated post-gross-yield were chosen. In Fig. 8.31 the state paths of the shear tests are also shown. It should be noticed that test TN17 was lightly overconsolidated before the shear test started.

All the numerical tests were performed reproducing the same sequence of stages as that imposed in the real tests carried out in the laboratory on the natural clay. For all the shear test computations, a stage of isotropic compression to the same isotropic consolidation pressure as that reached in the shear test before shearing was applied, prior to the simulation of the shearing stage, whether drained or undrained. The light overconsolidation undergone by specimen TN17 was not accounted for in the simulations.

For all the tests, the same initial state was imposed, in order to allow for the simulation of the same initial yield surfaces in all the tests, keeping unchanged the value of p_c (Fig. 3.40), taken as half the equivalent pressure at the initial void ratio on the isotropic compression line for the reconstituted clay.

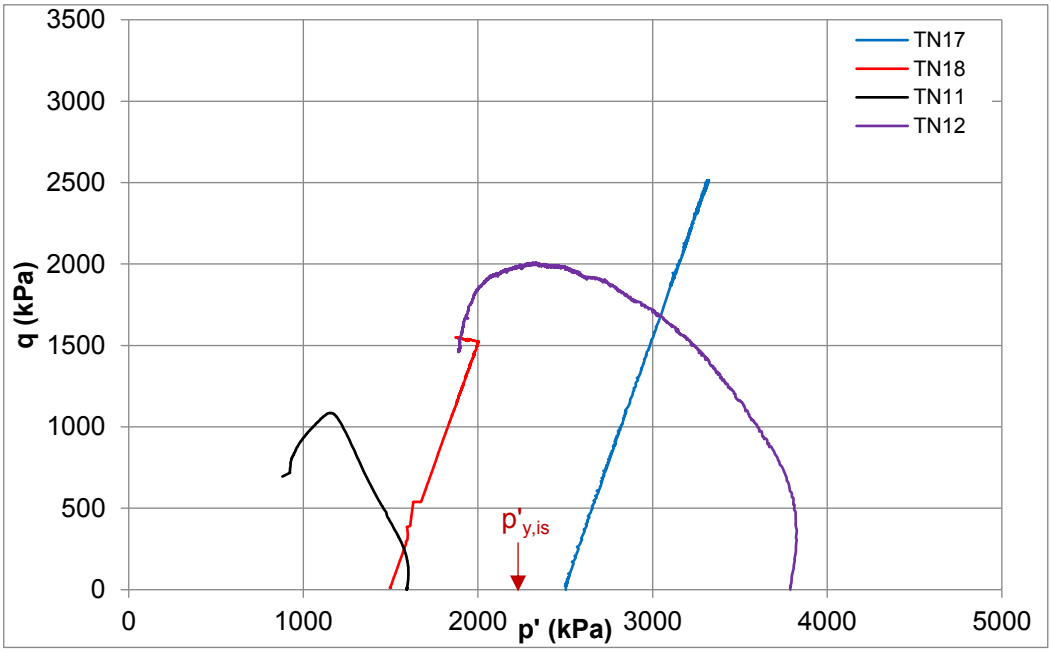

Fig. 8.30 – Stress paths of the drained and undrained shear tests on natural Pappadai clay used for the calibration of the model of Rouainia and Wood (2000) (test data after Cotecchia, 1996).

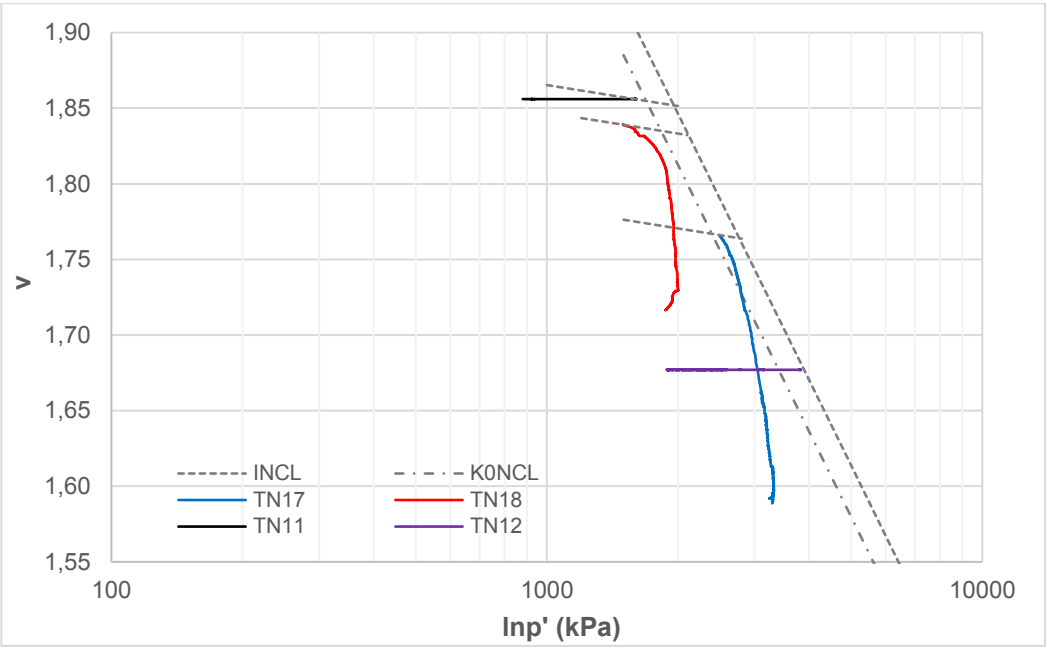

Fig. 8.31 – v-lnp' state paths of the drained and undrained shear tests on natural Pappadai clay used for the calibration of the model of Rouainia and Wood (2000) (test data after Cotecchia, 1996).

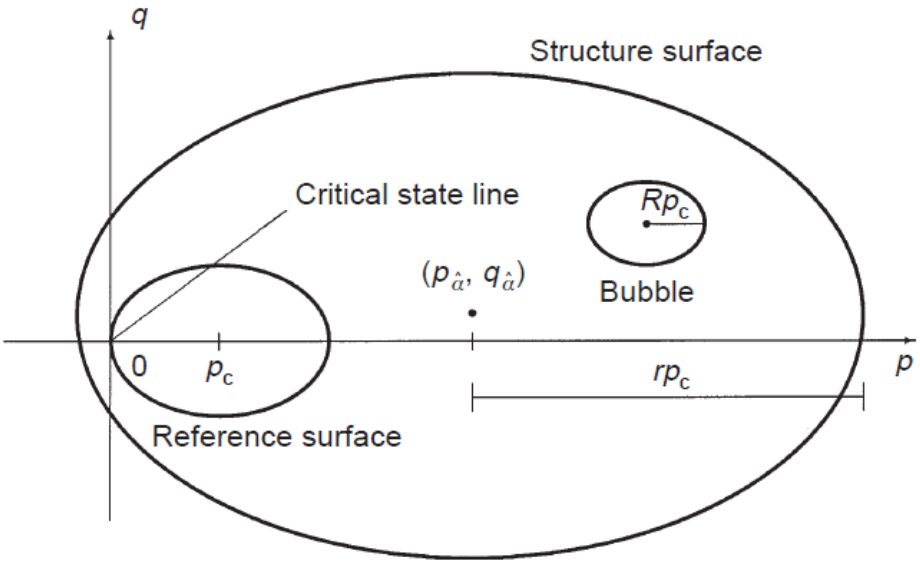

Fig. 8.32 – Bubble surface, structure surface and reference surface in the model of Rouainia and Wood (2000).

The final set of parameters chosen is reported in Table 8.2 and explained in the following.

The parameters κ^* and λ^* of the model are defined as those relative to the reconstituted clay in the plane lnv-lnp' (Butterfield, 1979). Hence, for the model calibration, these parameters were defined converting in the plane lnv-lnp' the values of the parameters defined in plane v-lnp', which were given in Table 6.1. The parameter M* was assumed equal to the critical state stress ratio defined for the reconstituted Pappadai clay (Cotecchia, 1996).

The initial size of the structure surface, r_0, was assumed to be equal to the oedometric stress sensitivity $S_{\sigma,oed}=3.5$ of natural Pappadai clay, rather than equal to the isotropic stress sensitivity $S_{\sigma,iso}=3.2$, which is lightly lower. In fact, despite the conceptual difference between the structure surface and the SBS discussed in the previous Section, the model suggests the analogy between the isotropic gross-yield stress $p'_{y,is}$ and the length $r_0 p_c$ of the horizontal axis of the ellipse defining the structure yield surface for the natural clay at initial state (Fig. 3.40). However, as often suggested when calibrating multiple yield surface constitutive models (Puzrin and Houlsby, 2001), the initial length of the horizontal axis of the structure surface has been assumed to be slightly larger than the observed $p'_{y,is.}$ This is mainly done with the aim to avoid the intersection of the inner yield surface with the structure yield surface when the shearing path starts from an isotropically normally consolidated state.

The initial material anisotropy, η_0, was assumed to be 0, with the aim to neglect it in the simulation.

The choice of the model parameters R, size of the inner yield surface, B and ψ, parameters of the interpolation rule for the calculation of the plastic modulus inside the structure surface (eq. 3.39), was done carefully, being these parameters responsible for the resulting slope of the swelling line of the natural clay, as anticipated in the previous Section. In addition, B and ψ influence the location of both the isotropic and K_0 compression gross-yield states, as they act on the plastic strain increments arising before the current state reaches the structure yield surface.

Hence, the parameters were calibrated in order to obtain a slope of the swelling line before gross-yield which could properly simulate that of natural Pappadai clay, thus reflecting the effect of the clay bonding in determining a low swelling capacity for the natural clay, as discussed in Chapter 6. The size R of the bubble was assumed to be 0.25, which is higher than the suggested reference values 0.05-0.1 (Rouainia and Wood, 2000). The values chosen for the parameters B and ψ were aimed at increasing the value of the plastic modulus, thus reducing the predicted plastic strain increments along the swelling path. So, given the interpolation rule in eq. 3.39, a high value of B and a low value of ψ were intended to be used.
Despite the reference value of $\approx$2 for B (Rouainia and Wood, 2000), for Pappadai clay the value B=5 was used; ψ was assumed equal to 1.5, i.e., the lower value in the suggested reference range 1.5-2.5.
The parameter A was taken equal to 0,5, in order not to alter the proportion of distortional and volumetric plastic strain contributing to the degradation of structure (eq.3.35-3.36).
The parameter k, rate of destructuration (eq.3.35), was seen to have the main influence on the evolution of the structure parameter r with loading. A low value of 0.3 was chosen with respect to the reference range (1-4), since it will be shown to improve the simulation of the trend of reduction of the structure parameter r in one-dimensional compression.

Fig. 8.33 shows the comparison between the experimental oedometer compression tests (OED5 and CRSnat for the natural clay, OEDR and CRSrec for the reconstituted clay) and the corresponding numerical predictions, for both the natural and the reconstituted clay. Remarkably, the gross-yield stress in one-dimensional compression and the slope of the swelling line are satisfactorily reproduced by the model.
In Fig. 8.34, Fig. 8.35 and Fig. 8.36 the experimental stress-strain behaviour is compared with that predicted by the numerical tests. It should be noted that in some cases the numerical tests stop at lower deviatoric strains then that reached in the tests on the natural clay; this was generally due to the attainment of the maximum assigned

number of iterations. In all these cases, the simulations should have been repeated changing the size of the increment interval.

The q-ε_s curves (Fig. 8.34) show that, although the model tends to underestimate the deviatoric stresses, it is able to reproduce the post-peak strain softening observed in the undrained tests and the monotonic strain hardening exhibited by the drained tests.

Comparing the trend of excess pore water pressure in the undrained tests (Fig. 8.35) and of the volumetric strains in the drained tests (Fig. 8.36) against the shear strains, it is seen that the general patterns are satisfactorily reproduced by the model, except for test TN11, for which the simulation underestimates the excess pore water pressures, and for test TN17, for which the model predicts larger volumetric strains.

The comparison of the experimental and numerical stress paths (Fig. 8.37) also appears satisfactory, but less accurate than the predictions of excess pore water pressure and of the volumetric strains; the peak deviatoric stress for the undrained tests is underestimated, as recognized from the q-ε_s curves.

In Fig. 8.38 the simulated state paths are compared with the experimental ones. A good agreement with the specific volume predicted at the end of the isotropic compression stage is obtained only for test TN18, as the numerical isotropic compression test brought the current state along the same swelling line on which the initial state for test TN18 is seen to lie. As the initial state is assumed to be the same in all the numerical tests and the isotropic compression pressure before shearing is very similar for test TN11 and test TN18, the specific volume for test TN11 is lower than the experimental value. For the tests isotropically consolidated post-gross-yield, the void ratio at the end of the compression stage is in both cases overestimated.

However, the model seems to fit the general state path trends.

Table 8.2 – Rouainia and Wood (2000) model parameters for Pappadai clay.

Parameter	value
κ^*	0.018
ν	0.25
λ^*	0.126
M*	0.91
R	0.25
r_0	3.5
B	5
ψ	1.5
k	0.3
A	0.5
η_0	0

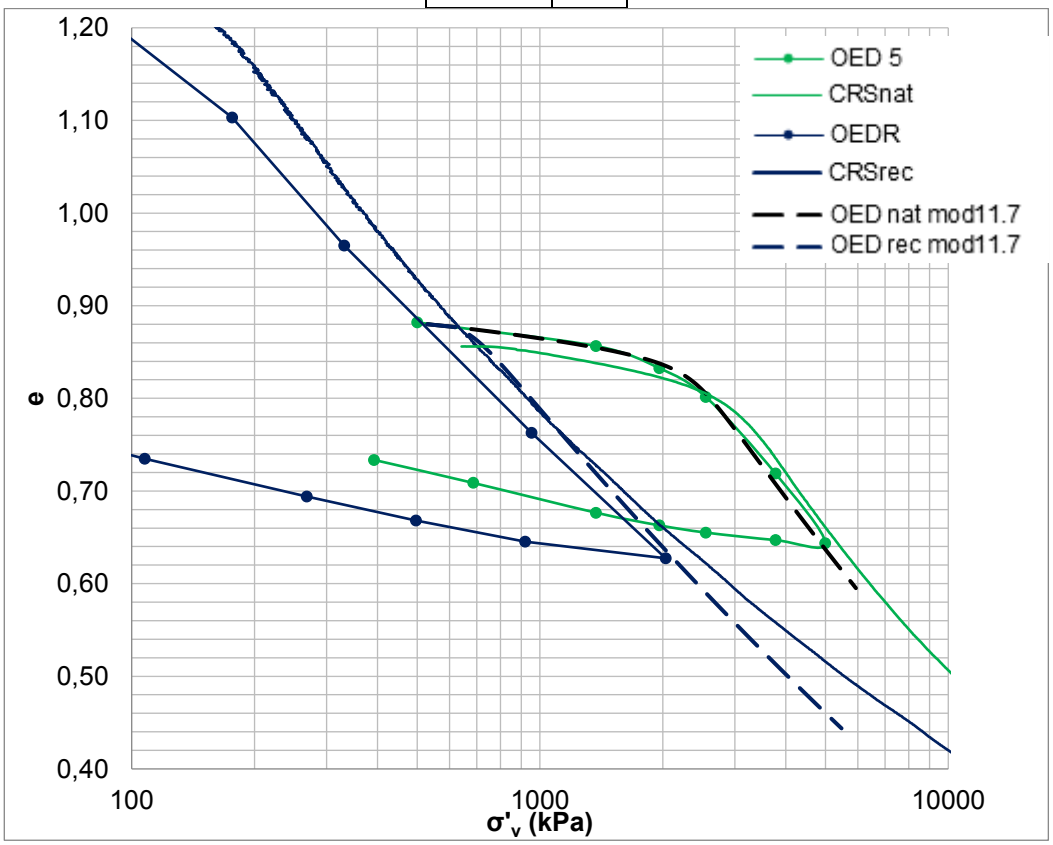

Fig. 8.33 – One dimensional compression curves for natural Pappadai clay: experimental data in full lines (after Cotecchia, 1996) and numerical results in dashed lines.

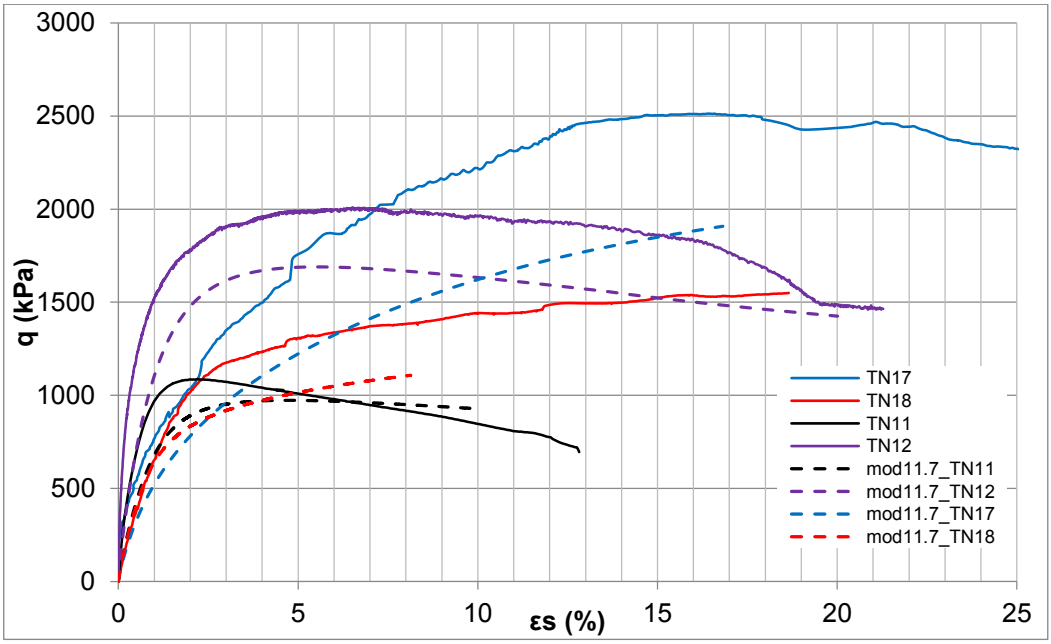

Fig. 8.34 - Stress-strain curves for the shear tests on natural Pappadai clay: experimental data in full lines (after Cotecchia, 1996) and numerical results in dashed lines.

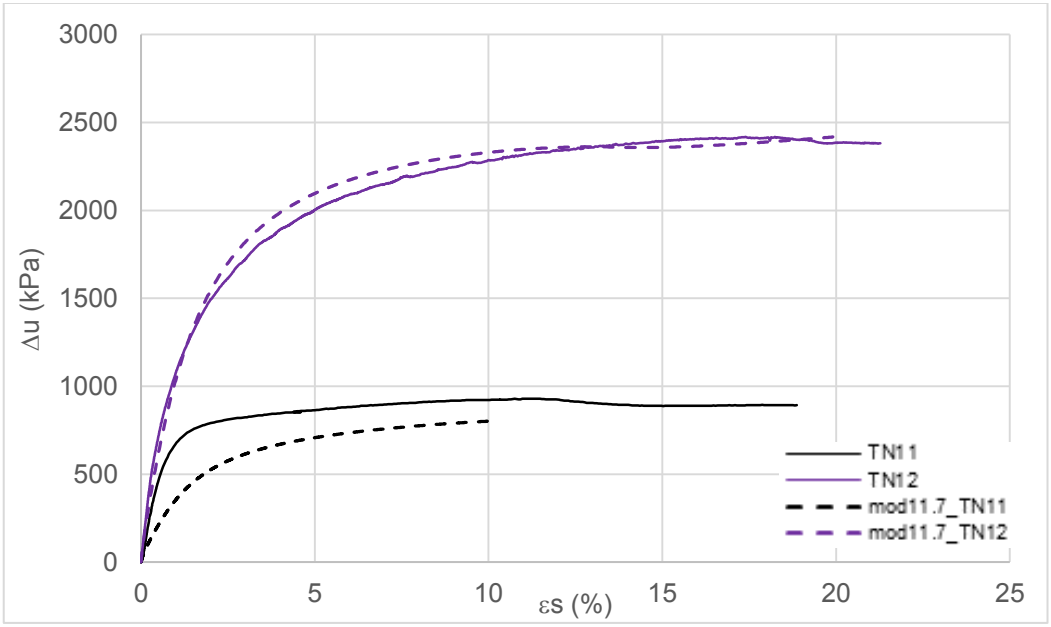

Fig. 8.35 – Excess pore water pressure against deviatoric strain for the shear tests on natural Pappadai clay: experimental data in full lines (after Cotecchia, 1996) and numerical results in dashed lines.

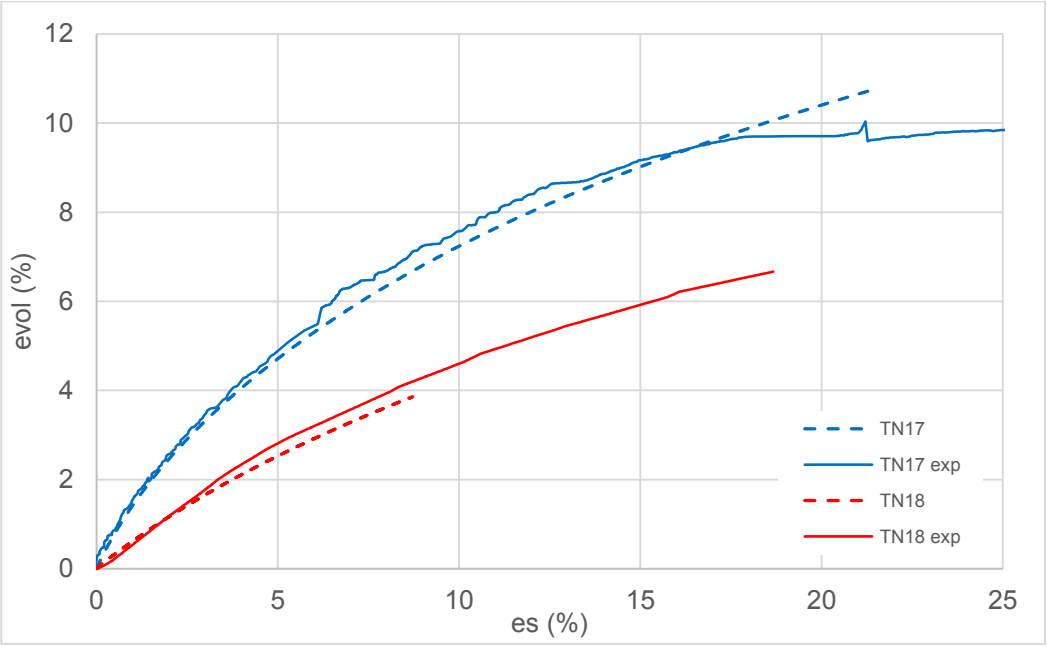

Fig. 8.36 – Volumetric strains against deviatoric strains for the shear tests on natural Pappadai clay: experimental data in full lines (after Cotecchia, 1996) and numerical results in dashed lines.

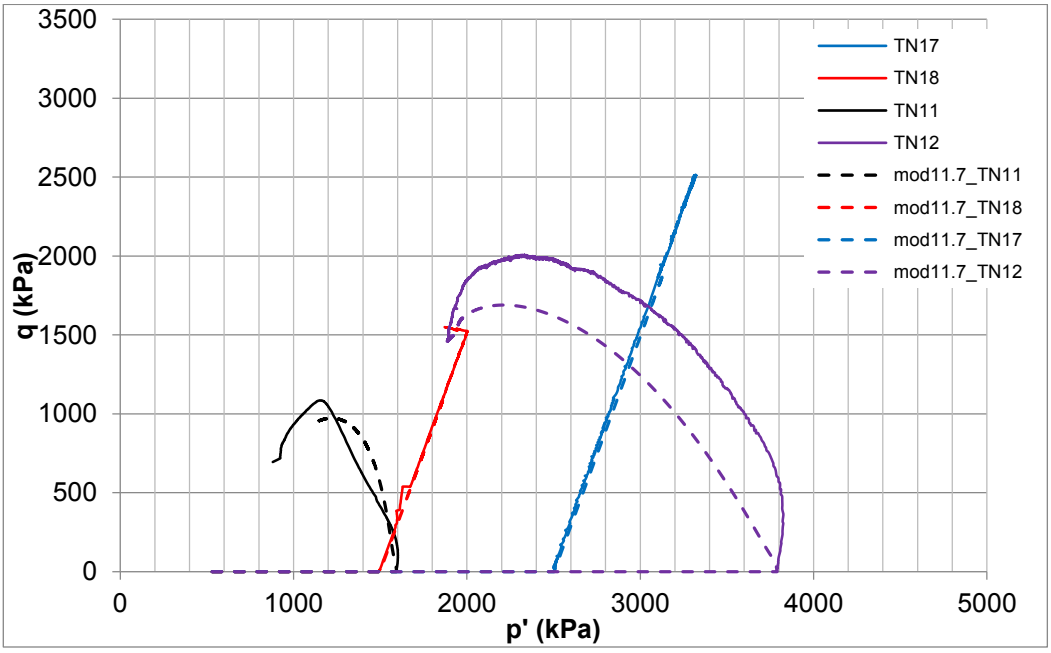

Fig. 8.37 - Stress paths for the shear tests on natural Pappadai clay: experimental data in full lines (after Cotecchia, 1996) and numerical results in dashed lines.

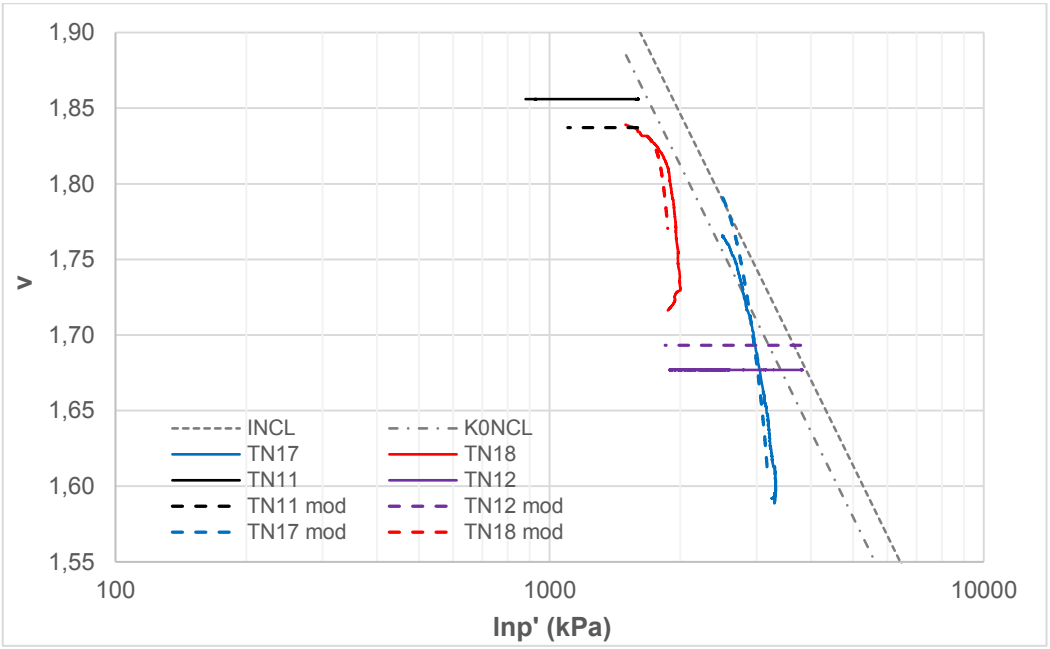

Fig. 8.38 – State paths for the shear tests on natural Pappadai clay: experimental data in full lines (after Cotecchia, 1996) and numerical results in dashed lines.

The combination of the parameters for the model calibration was evaluated also with respect to the predicted trend of evolution of the structure parameter r, which conceptually should represent the effects of the natural clay microstructure and of the changes it is undergoing.

The evolution of r with σ'_v is plotted for a one-dimensional compression test simulation in Fig. 8.39. A reduction of r is seen to occur before gross-yield, contrary to the definition of stress sensitivity formulated by Cotecchia and Chandler (2000), hence confirming the different meaning of the two structure parameters and the difference between the structure surface of the model and the clay SBS. However, the use of a very low rate of destructuration k, combined with the other parameter values, allows to obtain a low decrease of r before gross-yield. By contrast, the simulated one-dimensional compression post-gross-yield is giving a value of $r=2.75$ at $\sigma'_v=6$ MPa, which is higher than the sensitivity resulting from the experimental data, which is around 2 at $\sigma'_v=6$ MPa (Fig. 6.3).

Following this, it is believed that different values for the rate of destructuration k should be adopted pre- and post- gross-yield, as suggested by the sensitivity framework and confirmed by the whole microstructural analyses discussed in the previous chapters. These in fact, suggest that the microstructural changes occurring pre-gross-yield, in both compression and shear, are smaller than those recorded post-gross-yield.

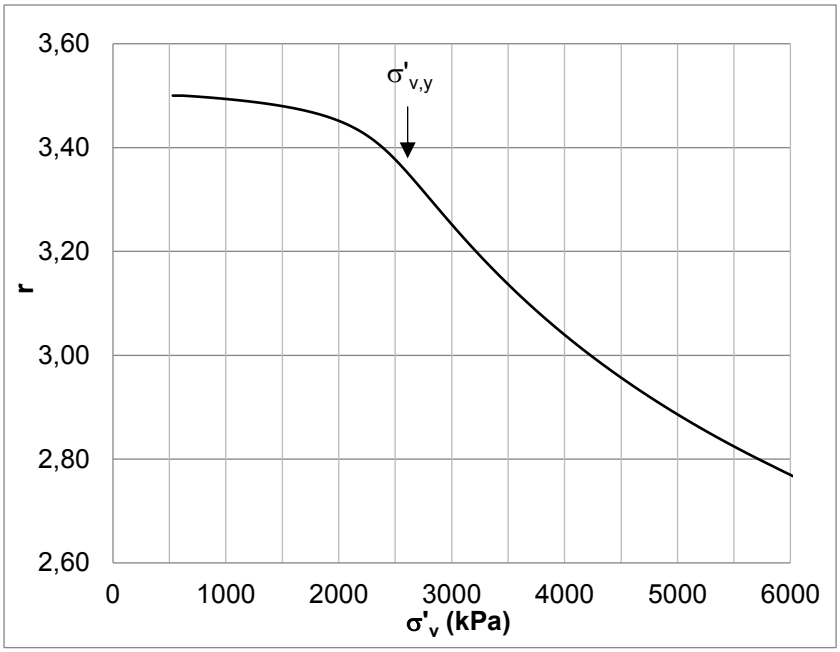

Fig. 8.39 – Evolution of the parameter r in a one-dimensional compression test simulation.

Moreover, in the light of the previous discussion on the different impact of volumetric and deviatoric strains on structure degradation in different loading paths (Section 8.6.1), it is believed that differentiating both the rate of destructuration and the parameter A when simulating compression and shearing stages would improve the simulation of the experimental data.

It should be noticed that the model was not evaluated with respect to experimental shear data referring to the dry side of critical. This is among the future developments of the research work.

For the sake of comparison, the calibration of the model of Kavvadas and Amorosi (2000) carried out by Amorosi et al. (2001) for natural Pappadai clay is briefly recalled. The Authors used the same experimental test results from Cotecchia (1996) and adopted a similar iterative calibration procedure starting from isotropic compression tests and from the undrained shear test TN11. It should be noted that, differently from the model of Rouainia and Wood (2000), this model does not require a reference surface for the reconstituted soil. However, some model parameters are assumed equal to those of the reconstituted soil (e.g., $\kappa^*$and $\lambda*$, slopes of the swelling line and of the INCL* for the reconstituted clay in the plane v-lnp') and subsequently adjusted to fit the experimental data of the natural soil.
The isotropic compression tests allowed to define the initial length of the horizontal axis of the Bond Stength Envelope (BSE, Fig.3.41), which also in this case was assumed slightly larger than the $p'_{y,is}$; the pre-gross-yield part of the test was used to calibrate the parameters κ^* and α^* (parameter for the hyper-elastic behaviour), both influencing the response inside the Plastic Yield Envelope (the elastic domain, PYE), and γ, parameter of the interpolation law for the plastic modulus, influencing the response inside the BSE.
$\lambda*$ and the volumetric structure degradation parameters, ζ_v and η_v, were evaluated on the basis of the post-gross-yield part of the isotropic compression curve.
The shear test TN11 from a pre-gross-yield compression state was used to evaluate the parameter c, the axes size ratio of the BSE, which was chosen very close to value $M_{nat}=1.08$ for Pappadai clay, and the deviatoric structure degradation parameters, ζ_q, η_q. The ratio between the size of the BSE and that of the PYE, ξ, was assumed equal to 0.001. Hence, a much smaller elastic domain with respect to that adopted in the simulation with Rouainia and Wood model was adopted.
The complete set of parameter values used for the calibration is listed in Table 8.3.

Table 8.3 – Kavvadas and Amorosi (2000) model parameters for Pappadai clay.

Parameter	value
κ^*	0.013
α^*	103
λ^*	0.22
c	1.1
ζ_v	3.0
η_v	9.5
ζ_q	3
η_q	0.1
γ	3.5

The comparison between the isotropic compression tests and the corresponding numerical predictions obtained from the chosen set of parameters are shown in Fig. 8.40. The Authors comment that the values of the volumetric hardening parameters (ζ_v and η_v) are such that a significant structure degradation still takes place at high pressures; this is believed to be a consequence of calibrating the volumetric structure degradation parameters on the isotropic normal compression line for the natural clay. However, this choice seems to affect neither the location of the gross-yield in compression, nor the slope of the swelling line for the natural clay, probably for the influence of a value of κ^* much lower than that observed experimentally for the reconstituted clay.

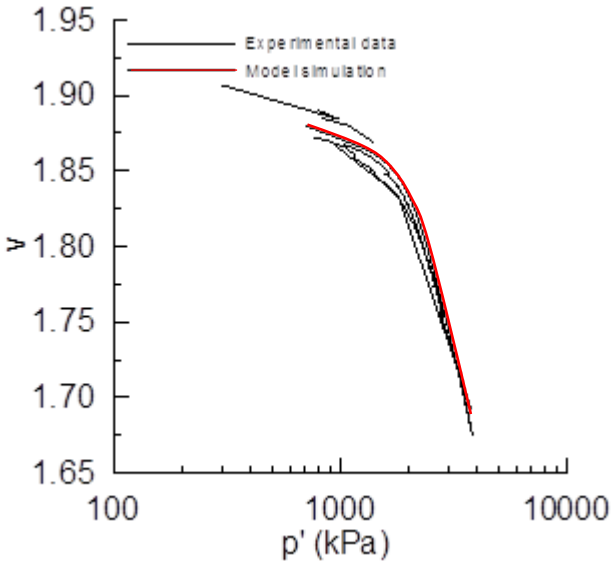

Fig. 8.40 – Comparison between isotropic compression curves from experimental and numerical data (after Amorosi et al., 2001)

The comparison between the observed and predicted stress-strain behaviour of the clay in the shear tests TN11, TN12, TN17 and TN18 is shown in Fig. 8.41 and Fig. 8.42. The numerical results are reported as continuous lines for undrained tests and dashed lines for the drained tests; the experimental data are reported with symbols. Each curve is indicated with the corresponding test code: standard characters indicate the experimental curve, italics is used for the numerical simulations.

The q-ε_a curves show that the model can properly simulate the strain hardening observed in the drained tests (TN17, TN18) and also the strain softening exhibited by the undrained test compressed post-gross-yield (TN12), while it gives a worst prediction for the undrained test consolidated pre-gross-yield (TN11). If compared with those obtained with the model of Rouainia and Wood (Fig. 8.34), these curves are in general seen to give a better prediction of natural Pappadai clay behaviour. By contrast, the excess pore pressures and volumetric strains against deviatoric strains are quite satisfactorily reproduced for the shear tests consolidated pre-gross-yield, but poorly reproduced for the tests consolidated post-gross-yield. Hence, the previous calibration appears to give better predictions. Moreover, both the models still need to be evaluated on the dry side of critical.

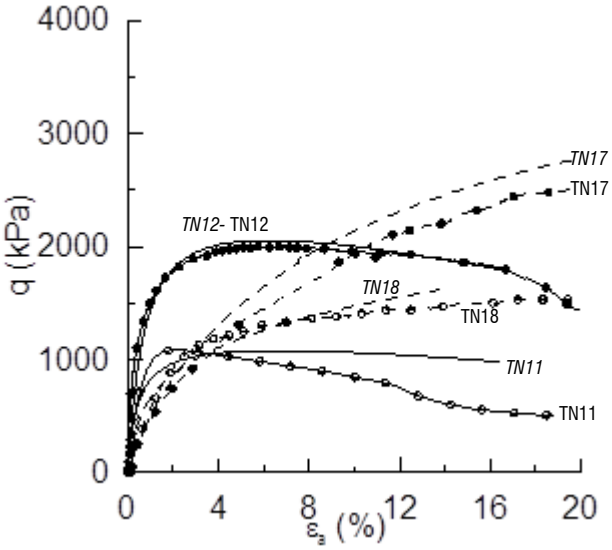

Fig. 8.41 – Comparison between stress-strain curves from experimental and numerical data (after Amorosi et al., 2001).

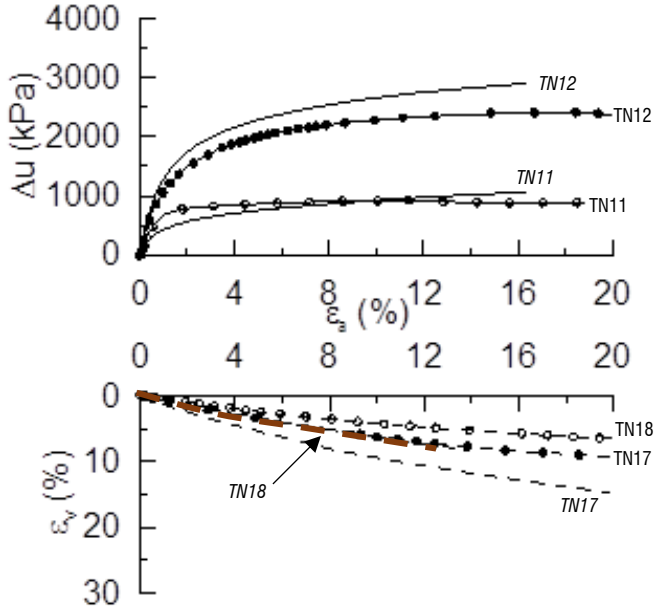

Fig. 8.42 - Comparison between excess pore water pressure and volumetric strains against axial strain from experimental and numerical data (after Amorosi et al., 2001).

To conclude, both the models used to simulate natural Pappadai clay behaviour give overall satisfactorily results if the parameters describing the behaviour inside the structure surface and the structure degradation parameters are chosen in the light of the observed effects of structure on the clay macro-response.

However, the use of the same set of parameters both in compression and shear, as well as the use of the same parameters to simulate both the pre- and post- yield behaviour appears to contradict both the experimental macro-behaviour and the microstructural evidence.

The definition of ranges for the parameter values or the introduction of algorithms to describe the evolution of the parameters of structure degradation, based on the microstructural observation of the processes underlying the observed macro-response, could provide a support for the correct choice of the parameter values, which often reduces to a simple fitting procedure. This advancement could improve the correlation between the modelling strategies and the parameter values with the different specific classes of soils and microstructural features.

9 CONCLUSIONS

This chapter summarises the main findings of the research and provides some ideas on future developments of the research work.

To start with, it is worth recalling how the analysis of the microstructure of Pappadai clay and of Lucera clay has provided evidence of the extent to which the clay microstructural features strongly depend on several factors, such as the clay composition, the deposition conditions, the loading history that the clay has experienced, which are just the most important.

Before this research, it was already known that the deposition conditions in which Pappadai clay deposited (Cotecchia, 1996), which were highly still, combined with its fine granulometry and high plasticity, have allowed for a relatively sensitive macro-behaviour, which has been found, inthis research, to be more sensitive than for Lucera clay, as given evidence by the stress sensitivity values of the two clays. Accordingly, Pappadai clay has a higher void ratio at gross yield than Lucera clay, despite the quite close values of the gross yield stresses. It may be speculated that this has been allowed for by bonding features developing in Pappadai clay, seemingly since deposition and, thereafter, during diagenesis, allowing for a higher porosity fabric. Where all these considerations are based on observations of the clay macro-behaviour, the present research work has provided evidence to the fact that the higher porosity of the more sensitive clay, i.e., Pappadai clay, is monomodal and distributed, overall, in pores which are smaller than for the slightly coarser and less plastic Lucera clay. A smaller dominant pore size, also characterized by a remarkably high frequency, applies to Pappadai clay, by comparison with the larger DPS, of lower frequency, of Lucera clay. So, among highly consolidated clays, such as Pappadai clay and Lucera clay, the higher void ratio of the more sensitive clay is not guaranteed by the presence of larger pores, but by the much larger amount of smaller pores. This is a first finding which may be considered quite unexpected, which shows how, being several the factors controlling the clay microstructural features, these cannot be deduced solely through speculative phenomenological interpretations and need a thorough investigation at the micro-scale.

Only systematic investigations at the micro-scale may bring about the assessment of how the different factors influencing the clay micro to macro behaviour combine to determine the clay micro-structure and macro-response. In this respect, the methodology adopted in this research, complies with this requirement and has provided some evidences which may represent a start for the derivation of a general framework of relations between clay micro -features and facets of macro-behaviour.

With this aim, the findings concerning reconstituted clays will be recalled first, in order to compare, thereafter, the differences in micro to macro behaviour of the natural clay with respect to the reconstituted clay.
Comparing the pore size distributions of reconstituted Paddai clay and Lucera clay, a significant difference has been recognized: reconstituted Pappadai clay, consolidated in consolidometer to 200 kPa, exhibits a regular monomodal pore size distribution and a small dominant pore size, combined with a high frequency, i.e., a tipology of porosimetry similar to the natural Pappadai clay; in the same way, also reconstituted Lucera clay, consolidated to 100 kPa, shows a noticeably less orderly porosimetry with respect to reconstituted Pappadai clay, confirming that at least in part, the two clays differ in porosimetry in both the reconstituted and the natural condition. In particular, reconstituted Lucera clay involves a larger range of pore sizes, overall larger than those present in the reconstituted Pappadai clay. As a result, a much larger dominant pore size is found, characterized by a much lower frequency. The fabrics of the two reconstituted clays are also found to differ. In fact, if both the reconstituted clays overall adhere to the complex fabric scheme, described by Sfondrini (1975), applying to one-dimensional compression of a flocculated fabric (Fig.2.21), reconstituted Pappadai clay appears much more orderly than reconstituted Lucera clay, the latter being characterized by more open and diffuse areas of random fabric. This difference is confirmed by a quite low degree of fabric orientation for Lucera clay, contrarily to reconstituted Pappadai clay for which instead a well-oriented fabric results from image processing. Hence, the difference in porosimetry between Pappadai clay and Lucera clay is, at least in part, due to their differences in composition. However, it must be

recalled also that the two reconstituted clays subjected to micro-analyses had been consolidated to different vertical stresses, the one for Pappadai clay (200kPa) being twice that applied to the reconstituted Lucera clay (100kPa). It is hence reckoned that, other than the differences in composition between the clays, a role is played in determining the clay fabric features also by the pressure to which the clay has been consolidated.

It is then worth investigating first the influence of composition, i.e. granulometry and mineralogy, on the reconstituted and natural clay micro-fabric, and to examine the influence of the vertical pressure in 1D compression afterwards. As anticipated earlier, the pore size distributions, differ for both natural Lucera (Fig.7.25) and Pappadai clay (Fig.7.14) and for the same clays when reconstituted (Figs.7.32, 7.39). Both natural and reconstituted Pappadai clay have a strictly monomodal porosimetry, with a DPS in the range of the 'micro-pores', considered to be intra-aggregate, whereas the Lucera clay pores vary in a larger range for both the natural and the reconstituted clay fabric. Comparing the two studied stiff clays with another stiff clay from the literature, Boom clay (Fig.8.1), and with the highly sensitive soft St Marcel clay, GoG clay and Bothkennar clay (Fig.8.4), the impact of composition has been characterized. It is found that the dominant pore size becomes smaller with the increase in clay fraction and activity index, CF and A. This result is quite expected, as high clay fractions correspond to very fine granulometries and high activities are generally associated to the presence of smaller active particles.

The influence of the vertical pressure on the fabric orientation and porosimetry has been studied comparing the data for reconstituted Pappadai and Lucera clay with those for other soft sensitive clays, in their natural state (at very small vertical pressures), or, otherwise, in the reconstituted conditions.

Through the analysis of the microstructural features of the natural soft clays of St Marcel, Gulf of Guinea and Bothkennar, which are found in situ at very low pressures (lower than 100 kPa), and high-water contents, a completely different fabric arrangement could be recognized with respect to either reconstituted Pappadai clay at 200kPa vertical pressure, or natural Pappadai clay (preconsolidated to 1300kPa vertical

pressure). In the soft clays, particles are often found flocculated and not in contact and aggregates are linked by clay bridges, resembling the fabric scheme suggested by Griffiths and Joshi (1990), observed also for monomineralic reconstituted clays at the state of slurry (V. Cotecchia et al., 1982). Associated to this fabric architecture, which is clearly randomly oriented, bimodal porosimetries were observed, with large dominant pore size in the range of the inter-aggregate porosity (around 1 order of magnitude larger than the dominant pore sizes found in stiff clays).

Since both the reconstituted and the natural stiff clays are analysed under pressures much higher than those to which the soft clays are subjected (about tens of kPa per the soft clays, 100kPa for the reconstituted clays, and 1000kPa for the stiff clays), their microstructural features have been examined as result of progressive one-dimensional compression from early stages of compression to high pressures. With compression it appears that a major fabric evolution occurs when passing from the very early stages, at low pressures, to medium pressures. A flocculated random fabric of the type depicted by Griffiths and Joshi (1990), combined with a bimodal porosimetry in which large pores dominate, characterizes both the reconstituted and the natural clay at low pressures and high water contents. When subjected to one-dimensional compression to a threshold pressure, such fabric experiences a complex re-organization, which involves the collapse of the inter-aggregate porosity and the conversion of the bi-modal pore size distribution into a monomodal distribution, with a consequent important loss of large pores. Concurrently, a coalescence of domains into a more oriented fabric takes place, with the thickening of stacks, which though still interbed areas in which a random fabric is preserved, as memory of the original flocculated fabric that has collapsed. The resulting fabric resembles the fabric architecture recognized by Sfondrini (1975) (Fig.2.21). At this point, the dominant pores have become much smaller, in the range of the micro-pores, and are mainly located inside the strata of oriented stacks. Correspondingly, fabric achieves a degree of anisotropy corresponding to a particle orientation in the range from medium to high degree.

The threshold vertical pressure activating the fabric re-organization mechanism has been found in the range from slightly below 100 to about 200 kPa for the examined clays (from the literature and tested in the research); the clay composition seems to influence this threshold value. So, for example, reconstituted Lucera clay and reconstituted London clay, consolidated to the same vertical pressure, around 100 kPa, are found to be at different stages of the re-organization process, which appears almost complete for London clay and, conversely, not achieved yet by Lucera clay, which is characterized by a much larger dominant pore size and a much less oriented fabric, likely because of its coarser granulometry.
Beyond the threshold pressure, the clay porosimetry generally becomes monomodal, with the DPS being in the range of the micro-pores.
One-dimensional compression beyond the threshold pressure, of either reconstituted Lucera, Pappadai, or GoG clay, is seen to cause the further reduction in size of the dominant pore and an overall translation of the incremental MIP curve towards a lower pore size range, with a concurrent reduction in the frequency of the dominant pore size, which must necessarily correspond to the presence of small particles filling pre-existing pores. The fabric scheme predicted by Sfondrini (1975) applies to the fabric of reconstituted Lucera clay and Pappadai clay and, remarkably, it is recognized up to very large pressures, in combination with a degree of fabric orientation which, once the threshold pressure has been overcome, does not increase much with further compression.

The recognition of the effects of one-dimensional compression on fabric according to the scheme of Sfondrini (1975), applying to both the natural undisturbed clay and the reconstituted clay compressed beyond the threshold, prompts the conclusion that fabric changes are highly non uniform. Indeed, areas of random fabric are found preserved even at very high pressures. Therefore, the technique of fabric observation must necessarily take into account the fundamental finding. The fabric scheme as that above-mentioned, is nonetheless found to be characterized by a medium-high fabric orientation index, L, when the image processing is carried out at medium magnification;

but it varies significantly when higher magnifications are explored. As outlined in Chapter 5, different image processing techniques exist and not all of them are operator-independent as that proposed by Martinez-Nistal et al. (1999), adopted in this research. Some authors, e.g., Hattab and Fleureau (2010) and Hicher et al. (2000), have in fact developed techniques to quantify the fabric orientation which are based on the visual recognition of the clay particles, hence being operator-dependent and applicable only to specific types of clays, for example reconstituted kaolinite (Hattab and Fleureau, 2010), in which particles can be quite easily recognized. The immediate consequence of this is the difficulty of analysing large fabric areas and the need to analyse micrographs, portraying areas of limited extension, which are considered as the reference picture. The technique then requires the extraction from the reference picture of a number of higher magnification pictures of assigned size, which are manually "quantified" by the operator, who draws oriented segments along the direction of the particle orientation, superimposed to the particle itself. In the end, the direction histogram referred to the original picture is obtained by superimposing the direction histograms deriving from the zoomed micrographs.

This technique is quite time-consuming and is not applicable to clay fabrics of high complexity; furthermore, it does not allow to deliver information at a medium magnification, conveying knowledge of the average fabric features. As demonstrated by Mitaritonna et al. (2014), the clay mechanical anisotropy has to be related to the medium magnification scale.

Among the future developments of this research, the enhancement of the image processing technique is considered one of the priorities, with the aim to obtain an automatic recognition of the features of different areas of fabric in the micrographs (e.g., recognition of the difference between stacks and random particle aggregations), which should then be followed by an effective averaging of the partial results derived from the different areas. Furthermore, the improvement of the technique could consist in adding functionalities, such as the calculation of the area occupied by voids, or the calculation of the average size ratio of the particle, to cite some. These developments

are believed to be possible only through the help of experts in research fields such as physics and computer science.

Other interesting considerations have concerned the source of sensitivity at the micro-scale. When analysing the difference between natural highly sensitive clays, such as GoG and St Marcel clay, either reconstituted/remoulded (St Marcel) or natural, which are characterized by similar pressures and much different void ratios as a consequence of their different compositions and sensitivities, a remarkable similarity in the dominant pore size for the natural and the corresponding reconstituted/remoulded clay is observed, the reconstituted/remoulded clay having a significantly lower frequency than the natural clay. This observation has brought forward the recognition of a microstructural interpretation of the clay sensitivity, which is identified in the different frequency exhibited by the incremental curves of the natural and the reconstituted clay at the same dominant pore size. The clay sensitivity is hence reflected in the presence in the reconstituted clay of a lower number of pores having the same size as those present in the natural clay, rather than being generated by a smaller dominant pore size in the reconstituted clay. The same interpretation of sensitivity applies to the natural stiff clays, which, however, possess much lower sensitivities. When comparing the natural and reconstituted clay at similar pressure in 1D compression, the higher frequency corresponding to the same dominant pore size for the natural clay, with respect to the reconstituted clay, is again recognized.
In addition, in the undisturbed soft clays, the high sensitivity is related to the presence of the inter-aggregate bridges, or links (Delage and Lefebvre, 1984; Pusch, 1970), stronger than those present in the corresponding reconstituted or remoulded clay. These collapse with compression beyond the threshold pressure discussed earlier, with the consequent loss of sensitivity.

With natural stiff clay, also other phenomena take place with compression and swelling. For both the clays, limited changes of both microstructure and fabric orientation are recorded in the 1D swelled specimens with respect to the undisturbed state, which are

even less pronounced for swelled Lucera clay, as a result of the lower disturbance occurred to bonding. Hence, pre-gross-yield very small changes occur to the pore distribution. This peculiar aspect of behaviour, also recognized in isotropic compression and shear, will be recalled in the following.

Gross-yield induces a significant bonding degradation. In particular, over gross yield, the degradation of the diagenetic bonding occurs, which had formed in the clay under burial at pressures larger than the threshold pressure cited earlier. Together with the bonding degradation, a chaotic rearrangement of fabric and a first more important modification of the pore structure and distribution takes place. Beyond gross-yield, a translation towards lower pore sizes of the incremental curve occurs, with a concurrent reduction in the frequency of the dominant pore size, which must necessarily correspond to the presence of small particles filling pre-existing pores. The chaotic fabric created at yield re-arranges with compression post-gross-yield, restoring the same orderly succession of horizontal stacks and truss of domains recognized in the undisturbed clay (Sfondrini, 1975). Correspondingly, over gross-yield and post-gross-yield, the orientation of fabric is changed only to a limited extent, similarly to what recorded in both the Lucera and Pappadai reconstituted clays.
The different bonding nature and strength of Pappadai clay and Lucera clay, which is causing the higher compressibility of Pappadai clay, is further reflected in the higher rate of structure degradation recorded in compression.

It may be concluded that, for both soft and stiff clays, 1D compression beyond the threshold pressure causes, after the collapse of the dominant inter-aggregate pores, a loss of bimodality and transition to monomodality, which continues to evolve, reaching smaller and smaller dominant pore sizes with increasing pressure. This finding contradicts with much literature on soft clays (Delage and Lefebvre,1984; Delage, 2010; Hattab et al., 2013) and on reconstituted clays (Hattab and Fleureau, 2010; Yu et al., 2016) which claims that one-dimensional compression only causes changes to inter-aggregate pores, leaving unaltered the intra-aggregate porosity. Evidently, if

sufficiently large pressures are attained, the inter-aggregate porosity, which is the first to collapse, progressively disappears and the intra-aggregate porosity dominates the pore size distribution, further reducing with increasing pressures.
Concurrently, the anisotropy of fabric acquired over the threshold does not change much with further compression; hence, a remarkably non uniform fabric evolution occurs with further 1D loading up to pressures much larger than the initial ones, similarly to what observed for stiff clays.

The data of microstructural evolution under one-dimensional compression for the clays from the two different classes, soft and stiff, have allowed quantitative assessments of the relations between macro-parameters and micro-parameters describing the shape of the pore size distribution curve and its evolution under 1D loading.
The plot of the dominant pore size against vertical effective stress for both soft and stiff clays, natural and reconstituted, has given further confirmation of the effect induced on the clay microstructure by compression beyond the threshold pressure, which is identifying two stages of micro, and correspondingly macro, behaviour: a first stage, below the threshold, dominated by the inter-aggregate porosity, which is characterized by low fabric orientation, and a second stage, beyond the threshold, in which the inter-aggregate porosity collapses and the dominating porosity is changed into the intra-aggregate porosity, with a corresponding achievement of fabric anisotropy. The further achievement is that beyond the threshold, this trend of reduction of the dominant intra-aggregate pore size with increasing pressure is about linear in a DPS-σ'_v plot and is common to all the clays analysed, despite their different compositions. Also, the trend of evolution of the frequency of the dominant pore size and of the width of the pore size distribution against vertical effective stress have been plotted, providing an example of the possibility of describing the real evolution of microstructural features, in this case under a 1D compression path. All these microstructural changes are generally simulated, in advanced constitutive models for natural soils, by means of theoretical laws of structure degradation whose parameters are calibrated to fit the material macro-behaviour. The wish is that the scalar parameters being proposed here, which represent

the different facets of the clay micro-structure and their evolution with loading, may be useful, within the constitutive models, to relate the macro-response to the features of the clay micro-structure.

Also, some microstructural processes underlying the clay response to isotropic compression have been recognized, both for the natural Pappadai clay and for the reconstituted Lucera clay.
When compressed isotropically to post-gross-yield states, both reconstituted Pappadai clay (compressed to a pressure 3 times larger than that attained in the consolidometer) and natural Lucera clay (loaded to a pressure 1.5 times larger than the isotropic gross-yield stress), are seen to undergo microstructural changes similar to those induced by one-dimensional compression to the same void ratio. A similar reduction in the size of the dominant pore is recorded in isotropic and one-dimensional compression, without significant changes in fabric orientation. It is hence suspected that for both the clays the stress level reached in isotropic compression is too low to induce major microstructural changes. This hypothesis is consistent with what found by Mitaritonna et al. (2014) for reconstituted Lucera clay, who found that, for compressions along paths different from the one-dimensional path, a stress level at least four times larger than that previously experienced is required to change the fabric directional properties. Mitaritonna et al. recognized a significant reduction in the degree of fabric orientation for reconstituted Lucera clay compressed beyond four times the gross-yield pressure along a stress path $\eta=0.3$ and, accordingly, a noticeable reduction in elastic stiffness anisotropy, which they demonstrate to go along with fabric anisotropy, up to the same pressure value along an isotropic stress path.
However, the incomplete microstructural data and the lack of evidence that this finding also applies to the natural clay lead to planning future isotropic compression tests up to much larger pressures, on both the natural and the reconstituted clay, to investigate the modification of microstructure induced by isotropic compression.

On the other hand, the assessment of the microstructural changes induced by isotropic compression for natural soft clays has provided the evidence that higher structure degradation is caused for the same volumetric strain increment by isotropic compression with respect to that induced by one-dimensional compression. Isotropic compression generates a more pronounced collapse of the pore size distribution than the further one-dimensional compression. This finding represents the microstructural confirmation of the interpretation, formulated by Cotecchia and Chandler (2000) and Cotecchia et al. (2011), that the difference between in the shape of the SBS and the corresponding gross yield curves of soft natural clays (shape elongated with the K_0 compression line) and of stiff clays (arch shape) is due to the fact that the highly sensitive soft clay possesses a structure which is disturbed by the application of isotropic loads much more than by oedometric loading. For this microstructural feature, soft clays show a gross-yield pressure in isotropic compression lower than that exhibited in one-dimensional compression, and consequently a gross-yield surface which seems symmetrical about the K_0 line.

Moreover, being the soft clays flocculated at undisturbed state, the condition of $p'_{y,is} < p'_{y,K0}$ and the associated SBS symmetrical about the K_0 line is shown not to be associated to fabric orientation, as assumed by many constitutive models for soft clays (e.g., Wheeler et al., 2003; Koskinen et al., 2002).

Accordingly, the study carried out for Pappadai clay and Lucera clay is providing the microstructural evidence that clays of oriented fabric may exhibit $p'_{y,is} > p'_{y,K0}$, confirming from a microstructural point of view the belief that the modelling of inclined gross-yield surfaces is not applicable to all one-dimensional consolidated clays (Cotecchia and Chandler, 2011).

Moreover, being both well-oriented at the undisturbed state, the microstructures of natural Pappadai and Lucera clay are confirming that the inherent anisotropy of natural and K_0 consolidated clays is the dominant factor giving rise to an arch-shaped gross-yield curve (Cotecchia and Chandler, 2000). The values of average degree of orientation L to which their arch shaped SBS are specifically associated are 0.22-0.24 for Lucera

clay and 0.27 for Pappadai clay. The lower degree of orientation of Lucera clay, which is an effect of the coarser composition of the clay, is reflected in an overall tighter and steeper SBS on the wet side, conveying closer gross-yield states in isotropic and K_0 compression.
Indeed, a similar shape was observed for the SBS of another Italian clay, Montemesola clay (Cafaro, 1998; Cafaro and Cotecchia, 2001; Cotecchia et al., 2007), more silty than Pappadai clay.
The microstructural differences between the natural and the reconstituted clay, for both Pappadai and Lucera clay, which are associated to the clay sensitivity, are also reflected in the different size of the two SBS with respect to their SBS*, the SBS being larger for Pappadai clay.

As previously anticipated, it has been noticeably recognized that in both oedometric and isotropic compression, the specimens compressed or recompressed after swelling up to states prior to the pressure range representing gross yielding show limited microstructural changes. Some microstructure change is recorded only in paths approaching gross-yielding (in the range of states within the highest curvature portion of the v-lnp' compression curve). A further confirmation of the limited microstructural evolution inside the SBS was also obtained through shear tests up to half the peak deviatoric stress, which highlighted that that the microstructural changes taking place half way through the shear path inside the SBS are minor, or negligible.
The conclusion has been drawn that, if loading does not approach gross-yielding and is kept monotonic, the clay experiences microstructural changes close to reversible, or negligible. This finding justifies the applicability of Cam Clay like models to the monotonic loading response of clays (e.g., Cam Clay; Wheeler et al., 2003; Koskinen et al., 2002). Future shear tests up to deviatoric stresses closer to gross-yield state in shear, or on specimens subjected to several shear cycles, are planned with the aim to realize to which extent microstructural changes pre- gross yield can be still considered exiguous.

From the shear tests carried out up to the SBS, on the natural and the reconstituted Lucera clay (from isotropic consolidation states pre-gross-yield), both drained and undrained, the microstructural evidence has been gathered of the changes induced by shearing, both inside the shear band (incipient in some specimens and completely developed in others) and outside. In both drained and undrained shear tests, on either the natural or the reconstituted clay, shearing is found to induce a higher degree of particle orientation than that recorded in compression. Such high degree of orientation is found both inside and outside the shear band. In the shear band, this is quite expected, being related to a re-organization of particles: both the qualitative observation of the SEM pictures, in agreement with previous works in the literature, and the image processing, show that particles start rotating along the direction of the shear band and give rise to very high degrees of fabric orientation.
Noticeably, though, also outside the shear band the fabric anisotropy increases, and degrees of fabric orientation higher than those recorded in the specimen before shearing are recorded. This occurs in combination with a non-uniform fabric evolution, in which areas of honeycomb fabric are found preserved in between strata of c.p.o. fabric, similar to that induced by compression (V. Cotecchia et al., 1982; F. Cotecchia & Chandler 1998; F. Cotecchia et al. 2011).

In terms of changes in pore size distribution, drained and undrained shearing of the stiff clay is found to reduce the dominant pore dimension and, overall, all the pore sizes. The specimens sheared undrained undergo greatly heterogenous changes than the specimens sheared drained, as a result of the internal drainage between the different portions of the specimen.
Moreover, if specimens sheared from different isotropic compression states are compared, both for stiff Lucera clay and for soft clays from the literature (Hattab et al., 2013), shearing on the wet side is seen to determine a significant reduction of the dominant pore size.

Microstructural analyses on sheared specimens of Lucera clay consolidated beyond gross-yield, for which the normalized stress paths have been shown to plot within the current SBS, are among the priorities of the future developments of the research, as well as drained shear tests consolidated to higher overconsolidation ratios, to explore the microstructural changes occurring with dilation upon shearing.

In general, it may be concluded that both in compression and shear, both for stiff and soft clays, the analysis of the microstructure evolution is outlining that the natural and the reconstituted clay do not achieve the same microstructure after large straining, though many similar trends of microstructural modification are recognized, as described so far. This finding is often contradicted by the models (e.g., Rouainia and Wood, 2000), which assume that the natural clay destructuration induced by large straining brings the structure surface to finally coincide with the reference surface. On the other hand, some models correctly account for this microstructural finding, e.g., the model of Baudet and Stallebrass (2004).

Finally, some further considerations prompting advancements in constitutive modelling of natural clay behaviour are formulated.
The current SBS of the clay predicted by a kinematic hardening model, by calibrating the model by means of simulation of probing stress paths, may benefit from the knowledge of the shape to be expected, which has been shown to strictly depend on the clay microstructural features.
For example, it has been shown that for either one-dimensionally reconstituted clays and firm to stiff natural clays, the SBS is arch-shaped. Hence, the model adopted to simulate a clay belonging to these classes, if correctly calibrated, is expected to portray a gross yield surface of arch-shaped type.
Concerning the behaviour inside the elastic domain, correlations proposed in the literature to account for some features of the clay microstructure at very small strains have been recalled (e.g., Cafaro and Cotecchia, 2001; Mitaritonna et al., 2014).

The calibration of the models of Rouainia and Wood (2000) and of Kavvadas and Amorosi (2000) (Amorosi et al. 2001), has shown that, although the final prediction of the natural Pappadai clay behaviour on the wet side is satisfactory with both the models (the model application to the dry sie has still to be done), the predictions required the calibration of several parameters, many of which of no physical meaning. Furthermore, some trial and error steps were necessary to define the size of the initial structure surface of the clay, which is assumed to reduce with the evolving yielding inside the SBS, due to structure degradation assumed to develop with this yielding. As shown by the present work, such 'destructuring' is not important along large part of the clay straining within the SBS, but this destructuring is part of the design of both models, due to a speculative assumption, which results in quite a costly calibration effort. This assumption is important for both the models because it leads to algorithms which may allow (with given calibration) for hardening considered to represent the effects of evolving anisotropy of the material under compression. So, such algorithms may result in a great flexibility of the models to predict variable behaviours, but always after onerous calibrations of the model based upon on purpose designed experimental tests. It is wished that results of the type gathered in the present research may help to connect further the modelling strategy to the real material features at the micro-scale, as for example connecting the model algorithms and their predictions to the effects of more realistic changes in the structural features of the material, than those invoked so far. Also, it is hoped that the new findings may allow for a simplification of the models, through their more guided application to the different classes of clays (e.g., soft clays pre-threshold pressure in compression, soft clays post-threshold pressure, stiff diagenized clays, reconstituted clays at high pressures etc.), also by benefiting from the relations between micro features and macrobehaviour of the type pioneered in this thesis.

10 ACKNOWLEDGEMENTS

First of all, I wish to thank with my most sincere gratitude Prof. Federica Cotecchia, who encouraged me all along this arduous journey and constantly inspired me with her distinctive strength and passion. I need to thank her for guiding me through this research and for believing in me when I myself was unhopeful.

I express all my gratitude to Dr. Francesco Cafaro, who gave me precious suggestions throughout these three years and initiated me to the geotechnical laboratory, of which I knew (and managed to do) very little at the beginning of my PhD. I thank him for his patience with me and with my tests, especially during my months in Barcelona.

I need to express special thanks to Prof. Antonio Gens, whose support was fundamental for this research. I thank him for hosting me at UPC during my several visits, for introducing me to constitutive modelling and for allowing me to make such a large number of tests, but also for his sincere and critical approach to each result and analysis and for the enduring trust in this work.

I am also particularly grateful to Prof. Enrique Romero, who welcomed me in the geotechnical laboratory of UPC, for arranging and making possible all the MIP tests in this research and for patiently analysing and commenting the results with me. I need to particularly thank Rodrigo, who not only was essential in carrying out the tests but also made me feel home and enjoy my stay at UPC.

Among the people who made this research possible, I wish to thank Dr. Vito Summa of the CNR-IMAA of Tito Scalo (PZ) who gave me the possibility of analysing a large number of SEM specimens and enthusiastically spent hours with me to get through them, without ever losing interest in my work. I address special thanks to Antonio Lettino, who patiently guided me through all the SEM observations and dedicated days to my clay specimens with passion and curiosity.

I also would like to thank Dr. Martinez-Nistal from the University of Oviedo for processing a very large number of SEM images in a very short time.

I need to address sincere thanks to Dr. Gaetano Elia for hosting me at the University of Newcastle and giving me the opportunity to get familiar with constitutive modelling. In

particular, I am grateful for the hospitality that he and his family showed me. I also thank Prof. Rouainia for the interest in my work and for his interesting suggestions.
I address my sincere thanks to Salvatore Schiavone, who taught me a number of secrets and patiently sustained and corrected me in my first steps in the geotechnical laboratory. Without him my wide testing programme would not have been possible.
I also need to thank Angelo Miccoli from the geotechnical laboratory of Taranto, that I also invaded to carry out some tests at the very beginning of my PhD, and Mimmo Carpanese from GEO, whose presence and help in the block sampling of Lucera clay was fundamental.

My deepest thanks go to all the people who were beside me all along these three years at the Section of Geotechnics at the Polytechnic of Bari.
I need to particularly thank Dr. Osvaldo Bottiglieri for being always supportive and curious about my research and for helping me in all the moments (many moments) of despair in the laboratory. I am also grateful to Prof. Claudia Vitone, who helped me move my first steps in the laboratory and in the world of research.
I will never be able to express my gratitude and affection to Francesca, my travelling companion, Dario and Vito, for sharing with me every day of these three hard and challenging years. Their way of being encouraging and optimistic was reassuring and vital in all the moments in which I felt too weak to go on.
My sincere gratitude goes to Mauricio, Clara, Tere and Josbel at UPC and to Salvatore at CNR-IMAA. I will take with me their warmth and kindness.

My deepest and most intimate thanks are addressed to my family, for being always beside me with patience and love, and to Tommaso, for enjoying together the times of success and facing together the times of failure.

11 REFERENCES

Ackerley S.K., Hellings J.E. and Jardine R.J. (1987), *Discussion on: A new device for measuring local axial strains on triaxial specimens*, Géotechnique 37 (3), pp.413-417.

Al Tabbaa A. and Muir Wood D. (1989), *An experimentally based `bubble' model for clay, in: Numerical models in geomechanics*, S. Pietruszczak and G. N. Pande (Eds.), Proc. 3rd Int. Conf. on Numerical Methods in Geomechanics, pp. 91-99.

Allmann M.A. and Atkinson J.H. (1992), *Mechanical properties of reconstituted Bothkennar Clay*, Géotechnique 42, pp. 289-302.

Amorosi A., Cotecchia F. and Kavvadas M. (2001), *The mechanical behaviour of a natural clay: experimental results and constitutive modelling*, Proceedings 15th International Conference on Soil Mechanics and Geotechnical Engineering, Istanbul, Turkey (1), pp.13-16.

Anagnostopoulos A.G., Kalteziotis N., Tsiambaos G.K. and Kavvadas M. (1991), *Geotechnical properties of the Corinth Canal marls*, Geotechnical and Geological Engineering, pp. 1-26.

Atkinson J.H. and Bransby P.L. (1978), *The Mechanics of Soils. An introduction to Critical State Soil Mechanics*, Mc Graw-Hill Book Co., London.

Atkinson J.H. and Richardson O. (1987), *The effects of locai drainage in shear zones on the undrained strength of the overconsolidated clay*, Géotechnique 37 (3), pp. 393-403.

Atkinson J.H., Richardson D. and Stallerbrass S.E. (1990), *Effects of recent stress history on the stiffness of overconsolidated soils*, Géotechnique 40 (4), pp. 531-540.

Aversa S., Evangelista A., Leroueil S. and Picarelli L. (1993), *Some aspects of the rnechanical behaviour of structured soils and soft rocks*, Proc. Conf. on Geotechnical Engn. of Hard soils Soft rocks, Athens, Balkema, pp. 359-366.

Balasubramaniam A.S. (1969), *Some factors influencing the stress-strain behaviour of clay*, PhD Thesis, University of Cambridge.

Baldi G., Hight D.W. and Thomas G.E. (1988), *A revaluation of conventional triaxial test methods*, Advanced Triaxial of Soil and Rock, ASTM STP 977, R.T. Donaghe, R.C. Chaney and M.L. Silver, Eds., ASTM, Philadelphia, pp. 219-263.

Baudet B.A., Stallebrass S.E. (2004), *A constitutive model for structured clays*, Géotechnique 54, pp. 269-278.

Belanteur N., Tacherifet S., Pakzad M. (2007), *Étude des comportements mécanique, thermo-mécanique et hydro-mécanique des argiles gonflantes et non gonflantes fortement compactées*, Rev. Fr. Géotech., 78, pp. 31-50.

Bishop A.W. and Henkel O.J. (1962), *The measurement of soil properties in the triaxial test*, Edward Arno Id L TD (London).

Bishop A.W., Webb 0.L. and Lewin P.I. (1965), *Undisturbed samples of London Clay from the Ashford Common Shaft: strength-effective stress relationships*, Géotechnique 15, pp. 1-31.

Bishop A. W.and Wesley L.D. (1975), *A hydraulic triaxial apparatus for controlled stress path testing*, Géotechnique 25 (4), pp. 657-670.

Bjerrum L. (1967), *Engineering geology of Norwegian normally-consolidated marine clays as related to settlements of buildings*, Géotechnique 17 (2), pp. 81-118.

Blith F.G.H. and de Freitas M.H. (1984), *A geology for engineers*, 7th Edition 1984, Eduard Arnold LTD, London.

Bolt G.H. (1956), *Physico-chemical analysis of the compressibility of pure clays*, Géotechnique 6 (1), pp. 86-93.

Bottiglieri O. (2009), *Caratterizzazione idraulica di un terreno a grana media parzialmente saturo*, PhD thesis, Technical University of Bari.

Bressani L.A. (1990), *Experimental properties of bonded soils*, PhD thesis, University of London.

Brooker E. W. and Ireland H.O. (1965), *Earth pressure at rest related to stress history*, Canadian Geotechnical Journal, 1 (1), pp. 1-15.

BS 1377 - *Methods of testing for soils* (1975), British Standards Institutions, London.

Burghignoli A. (1979), *An experimental study of the structural viscosity of soft clays by means of continuos consolidation tests*, Proc. of the 7th ECSMFE, Vol.2, pp. 23-28.

Burland J.B. (1990), *On the compressibility and shear strength of natural clays*, Géotechnique 40 (3), pp. 329-378.

Burland J.B., Rampello S., Georgiannou V.N. and Calabresi G. (1996), *A laboratory study of the strength of four stiff clays,* Geotechnique 46 (3), pp. 491-514.

Cafaro F. (1998), *Influenza dell'alterazione di origine climatica sulle proprietà geotecniche di un'argilla grigio-azzurra pleistocenica*, PhD thesis, Technical University of Bari.

Cafaro F. and Cotecchia F. (2001), *Structure degradation and changes in the mechanical behaviour of a stiff clay due to weathering*, Géotechnique 51 (5), pp. 441–453.

Campanella R.G. and Vaid Y.P. (1972), *A simple K_0-triaxial cell*, Canadian Geotechnical Journal, 9 (3), pp. 249-260.

Canestrari F. and Scarpelli G. (1993), *Stress-dilatancy and strength of Ancona Clay*, Proc. of the Conf. on Geotechnical Engn. of Hard soils-Soft rocks, Athens, Balkema, pp. 417-424.

Casagrande A. (1936-a), *Characteristics of cohesionless soils affecting the stability of slopes and earth fills*, Journal of the Boston Soc. Civ. Eng., pp. 257-276.

Casagrande A. (1936-b), *The determination of the preconsolidation load and its practical significance*, Proc. 1st ICSMFE, Harvard University Cambridge, Mass., Vol.3, pp. 61-64.

Chandler R.J. (1966), *The measurement of residual strength in triaxial compression*, Géotechnique 16 (3), pp. 181-186.

Chandler R.J. (1968), *A note on the measurement of strength m the undrained triaxial compression test*, Géotechnique 18, pp. 261-266.

Chandler R.J. (1972), *Lias clay: Weathering processes and their effect on shear strength*, Géotechnique 22, pp.403-431.

Chandler R.J. and Gutierrez C.I. (1986), *The filter-paper method of suction measurement*, Géotechnique 36 (2), Technical note, pp. 235-238.

Chandler R.J. and Apted J.P. (1988), *The effects of weathering on the strength of London Clay*, Quarterly Journal of Engineering Geology, London, 21, pp. 59-68.

Chandler R.J., Crilly M.S. and Montgomery-Smith G. (1992), *A low-cost method of assessing clay desiccation for low-rise buildings*, Proc. Instn. Civ. Engng. 2, pp. 82-89.

Ciaranfi N., Nuovo G. and Ricchetti G. (1971), *Le argille di Taranto e di Montemesola* (Studio Geologico, Geochimico e Paleontologico), Boll. Soc. Geol. Tt., pp. 293-314.

Ciaranfi N., Pieri P. and Ricchetti G. (1988*), Note alla carta geologica delle Murge e del Salento (Puglia Centromeridionale)*, Mem. Soc. Geol. Italia, 41, pp. 449-460.

Clayton C.R.I. and Khatrush S.A. (1986), *A new device for measuring local rudal strains on triaxial specimens*, Géotechnique 36 (4), pp. 593-597.

Coop M.R. (1990), *The mechanics of uncemented carbonate soils*, Géotechnique 40 (4), pp. 607-626.

Coop M. R. and Atkinson J.H. (1993), T*he mechanics of cemented carbonate sands*, Géotechnique 43 (1), pp. 53-67.

Coop M.R., Atkinson J.H. and Taylor R.N. (1995), *Strength, yielding and stiffness of structured and unstructured soils*, Proc. 11th ECSMFE, Copenhagen, 1, pp. 55-62.

Coop M.R. and Cotecchia F. (1995), *The compression of sediments at the archaeological site of Sibari*, Proc. 11th ECSMFE, Copenhagen, 8, pp. 19-26.

Cotecchia F. (1990), *Study of the relationships between the undrained shear strength of clay and its overconsolidation ratio. Analysis of the application of these relationships to the undrained shear strength values of six soft clays and two highly overconsolidated natural clays*, Msc Dissertation, Imperial College, University of London.

Cotecchia F. (1996), *The effects of structure on the properties of an Italian Pleistocene clay*, PhD thesis, Imperial College, University of London.

Cotecchia F., Chandler R.J. (1995), *The geotechnical properties of the Pleistocene clays of the Pappadai valley*, Q. J. Engng. Geol. 28, pp. 5-22.

Cotecchia F., Chandler R.J. (1997), *The influence of structure on the pre-failure behaviour of a natural clay*, Géotechnique 47 (3), pp. 523-544.

Cotecchia F., Chandler R.J. (1998), *One-dimensional compression of a natural clay: structural changes and mechanical effects*, in: Proc., 2nd Int. Symp. Hard Soils Soft Rocks, Naples, pp. 103-114.

Cotecchia F., Chandler R.J. (2000), *A general framework for the mechanical behaviour of clays*, Géotechnique 50 (4), pp. 431-447.

Cotecchia F., Cafaro F., Aresta B. (2007), *Structure and mechanical response of sub-apennine blue clays in relation to their geological and recent loading history*, Géotechnique 57 (2), pp. 167-180.

Cotecchia F., Mitaritonna G. and Vitone C. (2011), *Investigating the influence of microstructure, loading history and fissuring on the clay response*. Keynote lecture. International Symposium on Deformation Characteristics of Geomaterials, September 1-3, 2011, Seoul, Korea, pp. 35-85.

Cotecchia F. and Vitone C. (2011), *On the model requirements to predict the behaviour of fissured clays*, XV ECSMGE, Atene, Grecia, 11-15 Settembre 2011, pp. 525-530.

Cotecchia F., Cafaro F. and Guglielmi S. (2016), *Microstructural changes in clays generated by compression explored by means of SEM and Image Processing*, VI Italian Conference of researcher in geotechnical engineering "Geotechnical Engineering in Multisciplinary Research: from Microscale to Regional Scale", CNRIG2016 – Procedia Engineering 158, pp. 57-62.

Cotecchia V., Federico A. and Trizzino R. (1982-a), *Microtessiture di sedimenti argillosi*. *Analisi delle tipologie e terminologie, ed applicazione nel campo della geotecnica*, Geologia Applicata e Idrogeologia, Vol. 17, pp. 1-34.

Cotecchia V., Federico A. and Trizzino R. (1982-b), *Microtessiture di sedimenti argillosi. Esperimenti su Kaolinite e Bentonite ed esempi di sedimenti argillosi dell'Italia Meridionale*, Geologia Applicata e idrogeologia, Vol.17, pp. 53-78.

Cotecchia V., Melidoro G., Romanazzi L. and Spilotro G. (1977), *Osservazioni sul comportamento geotecnico delle Argille di Taranto determinato da alcuni caratteri geologici*, Geologia Applicata e Idrogeologia, Vol.12, pp. 311-323.

Cotecchia V., Monterisi L., Sembenelli P. and Claps G.A. (1993*), La costruzione dell'invaso Pappadai in Puglia*, Quarry and Construction, N.10, October, pp. 87-97.

Crawford C.B. (1965), *The resistance of soil structure to consolidation*, Canadian Geotechnical Journal 11 (2), pp. 90-97.

Cuccovillo T. and Coop.M.R. (1996), *The measurement of local axial strains in triaxial tests using LVDT's*, Géotechnique 47 (1), pp. 167-171.

Cundall P.A. and Strack O.D.L. (1979), *A discrete numerical model for granular assemblies*, Géotechnique 29 (1), pp. 47–65.

Davis E.H. and Raymond G.P. (1965), *A non-linear theory of consolidation*, Géotechnique 15 (2), pp. 161-173.

Davison L.R. and Atkinson J.H. (1990), *Continuous loading oedometer testing of soils*, Quarterly Journal of Engineering Geology, London, Vol.23, pp. 347-355.

Delage P. (2010), *Microstructure approach to the sensitivity and compressibility of some Eastern Canada sensitive clays*, Géotechnique, 60 (5), pp. 53-368.

Delage P., Lefebvre G. (1984), *Study of the structure of a sensitive Champlain clay and of its evolution during consolidation*, Can. Geotech.J. 21 (1), pp. 21-35.

Delage P., Le T.-T., Tang A.-M., Cui Y: J., Li X.-L. (2007), *Suction effects in deep Boom Clay block samples*. Technical Note. Géotechnique, 57 (1), pp. 239-244.

Dell'Anna L. and Laviano R. (1991), *Mineralogical and Chemical classification of Pleistocene clays from the Lucanian Basin (Southern Italy) for the use in the Italian tile industry*, Applied Clay Science, 6, pp. 233-243.

Del Prete M. and Valentini G. (1991*), Le caratteristiche Geotecniche delle Argille Azzurre dell'Italia Sud-Orientale in relazione alle differenti situazioni stratigrafiche e tettoniche*, Geologia Applicata e Idrogeologia, Vol.6, pp. 197-215.

De Marco A, Moresi M. and Nuovo G. (1981), *Le argille dei bacini di Taranto e di Grottaglie Montemesola: caratteri granulometrici, mineralogici e chimici*, Società Italiana di Mineralogia e Petrografia, 37, pp. 24 1-266.

Desrues J. (1992), *Strain localisation in geomaterials: experimental basis*, Programma di Istruzione Permanente, Politecnico di Milano.

Diamond S. (1970), *Pore Size Distribution in Clays*, Clays and Clay Minerals 18, pp. 7-23

di Prisco C., Nova R. (1995), *Effect of induced anisotropy on the behaviour of sands and their modelling via strain hardening plasticity*, Proc., V Int. Symp. Plast., pp. 515-518.

Elia G., Cotecchia F., Pedone G., Vaunat J., Vardon Philip J., Pereira C., Springman S., Rouainia R., Esch John V., Koda E., Josifovski J., Nocilla A., Askarinejad A., Stirling R., Helm P., Lollino P., Osinski P. (2017), *Numerical modelling of slope–vegetation–atmosphere interaction: an overview*, Quarterly Journal of Engineering Geology and Hydrogeology 50 (2).

Gasparre A. (2005), *Advanced laboratory characterisation of London clay*, PhD thesis, Imperial College, University of London.

Gasparre A., Nishimura S., Coop M.R., Jardine R.J. (2007), *The influence of structure on the behaviour of London Clay*, Géotechnique 57 (1), pp. 19-31

Gens A. (1982), *Stress-strain and strength characteristics of a low plasticity clay*, PhD Thesis, London University.

Gens A. and Potts D.M. (1982), *Application of critical state models to the prediction of the behaviour o f a normally consolidated low plasticity clay*, Proc. Int. Symp. of Numerical Models in Geomechanics, Zurich, 13-17, pp. 312-323.

Gens A. and Potts D.M. (1982), *A theoretical model for describing the behaviour of soils not obeying Rendulic's principle*, Proc. Int. Syrnp. of Numerical Models in Geomechanics, Zurich, pp. 24-32.

Georgiannou V.N., Burland J.B. and Hight D. W. (1990), *The undrained behaviour of clayey sands in triaxial compression and extension*, Géotechnique 40 (3), pp. 431-449.

Gibson R.E. and Henkel D.J. (1954), *Influence of duration of tests at constant rate of strain on measured drained strength*, Géotechnique 1 (4), pp. 6-32.

Gibson R.E. and Lo K.Y. (1961), *A theory of consolidation for soil exhibiting secondary compressions*, Report No.41, Norwegian Geotechnical Institute, pp. 3-16.

Gillott J. E. (1973), *Methods of sample preparation for microstructurel analysis of soil, Soil Microscopy*, Proc. 4th Int. Working Meeting Soil Micromorphology, Kingston (ed. G. K Rutherford) 1, pp. 143–164

González Molano N.A. (2011), *Development of a family of constitutive models for geotechnical applications*, PhD thesis, Universitat Politècnica de Catalunya, Barcelona.

Graham J. and Houlsby G. T. (1983), *Elastic anisotropy of a natural clay*, Géotechnique 33 (2), pp. 165-180.

Graham J., Crooks J.H.A. and Beli A.L. (1983), *Time effects on the stress-strain behaviour of natural clays*, Géotechnique 33 (2), pp.327-340.

Graham J., Crooks J.H.A. and Lau S.L.K. (1988), *Yield envelopes: identification and geometric properties*, Géotechnique 38 (1), pp.125-134.

Griffiths F.J. and Joshi R.C. (1989), *Change in pore size distribution due to consolidation of clays*, Géotechnique 39 (1), pp. 159–167.

Griffiths F.J. and Joshy R.C. (1990), *Clay fabric response to consolidation*, Applied Clay Science, 5, pp. 37-66.

Hashiguchi K. (1985), *Two- and three-surface models of plasticity*, Proc. 5th Int. Conf. Numerical Methods Geomechanics, Nagoya, pp. 125-134.

Hashiguchi K. (2009), *Elastoplasticity theory*, Springer, 432 pp.

Hattab M. and Fleureau J-M. (2010), *Experimental study of kaolin particle orientation mechanism*, Géotechnique 60 (5), pp. 323–331.

Hattab M., Hammad T., Fleureau J.-M., Hicher P.-Y. (2013), *Behaviour of a sensitive marine sediment: microstructural investigation*, Géotechnique 63 (1), pp. 71-84.

Hattab M., Hammad T. and Fleureau J.-M. (2015), *Internal friction angle variation in a kaolin/montmorillonite clay mix and microstructural identification*, Géotechnique 65 (1), pp. 1-11.

Hawkins A.B. and Mc Donald C. (1992), *Decalcification and residual shear strength reduction in Fuller's Earth Clay*, Géotechnique 42 (3), pp. 453-464.

Head K.H. (1980), *Manual of soil laboratory testing*, 3 Vols., London, Plymouth, Pentek.

Henkel D.J. (1956), *The effects of overconsolidation on the behaviour of clays during shearing*, Géotechnique 6, pp.139-150.

Henkel D.J. (1960), *The relationships between the effective stresses and water content in saturated clays*, Géotechnique 10, pp.41-54.

Hicher P.-Y. and Wahyudi H. (1994), *Microstructural analysis of strain-localisation in clays*, Computers and Geotechnics 16, pp. 205-222.

Hicher P.-Y., Wahyudi H. and Tessier D. (2000), *Microstructural analysis of inherent and induced anisotropy in clay*, Mech. Cohes.-Frict. Mater. 5, pp. 341-371.

Hight D. W. (1982*), A sirnple piezometer probe for the routine measurement of pore pressure in triaxial tests on saturated soils*, Technical Note, Géotechnique 32 (4), pp. 396-401.

Hight D. W., Bond A. J., Legge J. D. (1992) – *Characterization of the Bothkennar clay: an overview*. Géotechnique 42, pp. 303-347.

Horseman S.T., Winter M.G. and Entwistle D.C. (1987), *Geotechnical characterization of Boom Clay in relation to disposal of radioactive waste*, Luxembourg: Office for Official Publications of the European Community.

Hvorslev M.J. (1937), *Uber die Festigkeitseigenschaften Gestorter Bindiger Boden (On the strength properties of remoulded cohesive soils)*. Thesis, 159 pp., Copenhagen.

Jaky J. (1944), *The coefficient of earth pressure*, J.Soc. Hungarian Archit. Engrs.

Janbu N. and Senneset K. (1979), *Interpretation procedures for obtaining soil deformation parameters*, Proc. of the 7th ESMFE, 1, pp. 185-188.

Jardine R.J. (1992), *Some observations on the kinematic nature of soil stiffness*, Soils and Foundations, Vol.32 (2), pp. 111-124.

Kavvadas M. and Amorosi A. (2000), *A constitutive model for structured soils*, Géotechnique 50 (3), pp. 263–273.

Knabe T., Datcheva M., Lahmer T., Cotecchia F. and Schanz T. (2013), *Identification of constitutive parameters of soil using an optimization strategy and statistical analysis*, Computers and Geotechnics 49, pp. 143–157.

Koskinen M., Karstunen M. and Wheeler S.J. (2002), *Modelling destructuration and anisotropy of a natural soft clay*, Numerical Methods in Geotechnical Engineering, Mestat ed., Presses de l'ENPC/LCPC, Paris, pp. 11-19.

Lacasse S., Berre T. and Lefebvre G. (1985), *Block sampling of sensitive clays*, Proc.11th SMFE, San Francisco, Vol.2, pp. 887-892.

Ladde C.C. and Lambe T.W. (1963), *The strength of undisturbed clay determined from undrained tests*, ASTM, STP 361, pp. 342-371.

Ladde C.C., Foot R., Scholosser F. and Poulos H.G. (1977*), Stress deformation and strength characteristics: State of the Airport*", Proc. 9th leSMFE, Tokio, pp. 421-494.

Lagioia R. and Nova R. (1993), *A constitutive model for soft rocks*, Proc. eonf. on Geotechnical Engn. of Hard soils - Soft rocks, Athens, Balkema, pp. 625-632.

Lambe T.W. (1953), *The structure of inorganic soils*, Proc. ASCE, 79, Separate n.315.

Lambe T.W. and Withmann R.V. (1969), *Soil Mechanics*, John Wiley & Sons fnc., New York.

Le M.H. (2008), *Caractérisation physique et mécanique des sols marins d'offshore profond*, PhD Thesis, ENPC, Paris.

Leonards O.A. and Ramiah B.K. (1959), *Time effects in the consolidation of clay*, ASTM Special technical publication No.254, pp. 116-130.

Leroueil S., Tavenas F., Brucy F., La Rochelle P., Roy M. (1979), *Behaviour of destructured natural clays*, Proc. A.S.C.E. 105, GT6, pp. 759-778.

Leroueil S., Sanson L. and Bozozuk M. (1983), *Laboratory and field determination of preconsolidation pressure at Gloucester*, Canadian Geotechnical Journal 20 (3), pp. 477-490.

Leroueil S., Tavenas F. and Locat J. (1984), *Discussion on: Correlations between index tests and the properties of remoulded clays* Géotechnique 35 (2), pp. 223-226.

Leroueil S., Kabbaj M., Tavenas F. and Bouchard R. (1985), *Stress-strain rate relation for the compressibility of sensitive natural clays*, Géotechnique 35 (2), pp. 159-180.

Leroueil S. and Vaughan P.R. (1990), *The important and congruent effects of structure in natural soils and weak rocks*, Géotechnique 40 (3), pp.467-488.

Leroux A. (1975), *Les differentes textures. Leur influence sur le comportment des sols argileux et marneux*, Geologia Applicata e Idrogeologia (10), pp. 67-85.

Li X., Li X.-S. (2009), *Micro-macro quantification of the internal structure of granular materials,* Journal of engineering mechanics 135 (7).

Lima A., Romero E., Pineda J.A and Gens A. (2008), *Low-strain shear modulus dependence on water content of a natural stiff clay*, Conference Paper.

Locat J., Lefebvre G. and Ballivy G. (1984), *Mineralogy, chemistry and physical properties interrelationships of some sensitive clays of Eastern Canada*, Can. Geotech. J. 21 (3), pp. 530–540.

Locat J. and Lefebvre G. (1985), *The compressibility and sensitivity of an artificially sedimented clay soil: the Grande Baleine marine clay*, Mar. Geores. Geotechnol. 6 (1), pp. 1–27.

Loudon P.A. (1967), *Some deformation characteristics of Kaolin*, PhD Thesis, University of Cambridge.

Lowe J., Jonas E. and Obrician V. (1969), *Controlled gradient consolidation test*, Jour. Soil Mechanics and Found. Div. ASCE, 95, SMl Jan. 1969, pp. 77-97.

Lupini J.F., Hight D.W. and Cavounidis S. (1980), *Some observations of microfabric and their role in understanding soil behaviour*, Rivista Italiana di geotecnica (2), pp. 112-123.

Maccarini M. (1987*), Laboratory studies of weakly bonded artificial soil*, PhD Thesis, University of London.

Marhinho F.A.M. (1994), *Shrinkage behaviour of some plastic soils*, PhD thesis, University of London.

Martinez-Nistal A., Vinale F., Setti M., Cotecchia F. (1999), *A scanning electron microscopy image processing method for quantifying fabric orientation of clay geomaterials*, Applied Clay Science 14, pp. 235-243.

Mayne P.W. and Kulhaway F.H. (1982), *K_0-OCR relationships in soil*, Proc.ASCE, 108, GT6, pp. 851-872.

Menkiti C.O. (1995), *Behaviour of clay and clayey-sand with particular reference to principal stress rotation*, PhD thesis, University of London.

Mesri G. and Rokhsar A. (1974), *Theory of consolidation for clays*. Proc. ASCE, 100, GT8, pp. 889-904.

Mesri G. and Godlewsky P.M. (1977). *Time and stress-compressibility interrelationship*, Proc. ASCE, 103, GT5, pp. 417-430.

Mesri G. and Godlewsky P.M. (1979), *Time and stress-compressibility interrelationship*, Discussion, Proc.ASCE (May), GT1, pp. 106-113.

Mesri G. and Choi Y.K. (1985), *The uniqueness of the End of Primary (EOP) void ratio - effective stress relationships.* Proc. 9th ICSMEF, San Francisco, pp. 587-590.

Mitaritonna G. (2006), *An experimental investigation on the very small strain stiffness anisotropy of fine grained soils*, PhD thesis, Technical University of Bari.

Mitaritonna G., Amorosi A. and Cotecchia F. (2014), *Experimental investigation of the evolution of elastic stiffness anisotropy in a clayey soil*, Géotecnique 64 (6), pp. 463-475.

Mitchell J.K. and Houston W.N. (1969), *Causes of clay sensitivity*, Proc. ASCE, SM3, pp. 845- 871.

Mitchell J.K. (1976), *Fundamentals of soil behaviour*, New York, Wiley.

Mitchell J. K. and Soga K. (2005), *Fundamentals of Soil Behavior (third ed.)*, John Wiley & Sons Inc., Hoboken, NJ, 577 pp.

Mokni M. (1992), *Relations entre le comportement en masse et la localisation de la deformation dans le materiaux granulaires*, These de doctorat, UJF-INPG.

Monroy R., Zdravkovic L., Ridley A. (2010), *Evolution of microstructure in compacted London Clay during wetting and loading*, Géotechnique 60 (2), pp. 105-119.

Morgenstern N.R. and Tchalenko J.S. (1967a), *Microscopic structures in kaolin subjected to direct shear*, Géotechnique 17, pp. 309-328.

Morgenstern N.R. and Tchalenko J.S. (1967b), *The optical determination of preferred orientation in clays and its application to the study of microstructure in consolidated kaolin, I*, Proc. R. Soc., A 300, pp. 218-234.

Mroz Z. (1967), *On the description of anisotropic workhardening*, J. Mech. Phys. Solids. 1967, Vol. 15, pp. 163-175.

Mroz Z., Norris V.A. and Zienkiewicz O.C. (1979), *Application of an anisotropic hardening model in the analysis of elasto-plastic deformation of soils*, Géotechnique 29 (1), pp. 1-34.

Nova R. and Wood D.M. (1979), *A constitutive model far sand in triaxial compression*, Int. Journal far Numerical Methods in Geomechanics, 3, pp.255-278.

O'Brien N.R. and Slatt R.M. (1990), *Argillaceous Rock atlas*, SpringerVelag.

Oda M. (1993), *Inherent and induced anisotropy in plasticity theory of granular soils*, Mech. Mater. 16 (1–2).

Ogniben L. (1969), *Schema introduttivo alla geologia del confine calabro-lucano*, Memorie della Società Geologica Italiana, 8.

Parry R.H.G. (1960), *Triaxial compression and extension tests on remoulded saturated clay*, Géotechnique 10, pp.166-180.

Pender M.J. (1978), *A model for the behaviour of overconsolidated soil*, Géotechnique 28 (1), pp. 1-25.

Pickles A.R. (1989), *The application of critical state soil mechanics to predict ground deformations below an embankment constructed on soft alluvium*, PhD Thesis, City University, London.

Push R. (1966), *Quick clay microstructure*, Engineering Geology, Vol.1 (6), pp. 433-443.

Pusch R. (1970), *Microstructural changes in soft quick clay at failure*, Can. Geotech. J. 7 (1), pp. 1–7.

Quigley R.M. (1980), *Geology, mineralogy, and geochemistry of Canadian soft soils: a geotechnical perspective*, Can. Geotech. J. 17, pp. 261-285.

Rampello S. (1993), *Compressibilità di campioni indisturbati e ricostituiti di alcune argille consistenti*, Gruppo Nazionale di Coordinamento per gli studi di Ingegneria Geotecnica, CNR, Attività di Ricerca anno 1992-93.

Rampello S., Viggiani G. and Georgiannou V.N. (1993), *Strength and dilatancy of natural and reconstituted Vallericca Clay*, Proc. Conf. on Geotechnical Engn. of Hard Soils-Soft rocks, Athens, Balkema, pp. 761-768.

Rampello S. and Silvestri F. (1993), *The stress-strain behaviour of natural and reconstituted samples of two overconsolidated clays*, Proc. Conf. on Geotechnical Engn. of Hard Soils-Soft rocks, Athens, Balkema, pp. 769-778.

Rendulic L. (1936), *Pore-index and Pare-water Pressure*, Baningeenieur 17, pp. 559.

Ricchetti G. (1967), *Osservazioni preliminari sulla geologia e morfologia dei depositi quaternari nei dintorni del Mar Piccolo (Taranto)*, Atti Acc.Gioenia in Catania, S.6, 18, pp. 123-130.

Ridley A.M. (1993), *The measurement of soil moisture suction*, PhD thesis, London University.

Romero E., Gens A., Lloret A. (1999) - *Water permeability, water retention and microstructure of unsaturated Boom clay*. Engineering Geology, n. 54, pp. 117-127.

Romero E., Della vecchia G., Jommi C. (2011) – *An insight into the water retention properties of compacted clayey soils*. Géotechnique 61 (4), pp. 313-328.

Roscoe K.H., Schofield A.N. and Wroth C.P. (1958), *On the yielding of soils*, Géotechnique 8, pp. 22-53.

Roscoe K.H. and Poorooshabs H.B. (1963), *A theoretical and experimental study of strain in triaxial compression tests on normally consolidated soils*, Géotechnique 13 (1), pp. 12-38.

Roscoe K.H. and Burland J.B. (1968), *On the generalized stress-strain behaviour of wet clay*, In Engineering Plasticity (J. Heymann and F.A. Leckie, eds), Cambridge University Press, Cambridge, pp. 535-609.

Rosenqvist I.T. (1963), *The influence of physico-chemical factors upon the mechanical properties of clays*, Norwegian Geotechnical Institution, Publ. n.54, pp. 1-19.

Rossato G., Ninis N.L. and Jardine R.J. (1992), *Properties of some kaolin-based model clay soils*, Geotechnical Testing Journal, GTJODJ, Vol.15 (2), pp. 166-179.

Rouainia M. and Muir Wood D. (2000), *A kinematic hardening constitutive model for natural clays with loss of structure*, Géotechnique 50 (2), pp. 315-321.

Rowe P.W. (1962), *The stress-dilatancy relation for static equilibrium of an assembly of particles in contact*, proc. R. Soc. A., 264, pp. 500-527.

Rowe P.W. and Barden L. (1966), *A new consolidation cell*, Geotechnique 16, pp. 162-170.

Samuels S.G. (1975), *Some properties of the Gault Clay from Ely-Ouse Essex water tunnel*, Géotechnique 25 (2), pp. 239-264.

Sandroni S. (1977), *The strength of London Clay in total and effective stress terms*, PhD Thesis, London University.

Santamarina J.C., Klein K.A., Palomino A., Guimaraes M.S. (2002), *Micro-scale aspects of chemical-mechanical coupling: Interparticle forces and fabric*, in Chemo-mechanical coupling in clays: from nano-scale to engineering applications, C.D. Maio, T. Hueckel and B. Loret (Eds).

Sasanian S., Newson T.A. (2013), *Use of mercury intrusion porosimetry for microstructural investigation of reconstituted clays at high water contents*, Engineering Geology 158, pp. 15–22.

Schmertmann J.H. (1969), *Swell sensitivity*, Géotechnique 19 (41), pp. 530-533.

Schmidt B. (1966), *Discussion on: Earth pressure at rest related to stress history*, Canadian Geotechnical Journal, Vol.3 (4), pp. 237-242.

Schofield A.N. and Wroth C.P. (1968), *Critical State Soil Mechanics*, Mc Graw-Hill Book Co., London.

Schreiner H.D. (1988), *Volume change of compacted highly plastic clays*, PhD thesis, London University.

Sfondrini G. (1975), *Caratteri microtessiturali e microstrutturali di alcuni sedimenti argillosi connessi con la natura e il tipo delle sollecitazioni subite*, Geologia Applicata ed Idrogeologia, 10, parte 2, pp. 87-124.

Sides G. and Barden L. (1970), *The microstructure of dispersed and flocculated samples of kaolinite, illite and montmorillonite*, Canadian Geotechnical Journal 8, pp. 391-399.

Skempton A.W. and Bishop A.W. (1950), *Measurement of shear strength of soils*, Discussion by A.W. Bishop, Géotechnique 2 (2), pp. 113-120.

Skempton A.W. and Northey R.D. (1952), *The sensitivity of clays*, Géotechnique 3 (1), pp. 30-53.

Skempton A. W. (1953), *The colloidal activity of clays*, Proc. 3rd ICSMFE, Zurich, 1, pp. 57-61.

Skempton A. W. (1954), *The structure of inorganic soil*, Proc.ASCE, SMJ, Vol.80, pp. 19-22.

Skempton A. W. (1954-a), *The pore-pressure coefficients A and B*, Géotechnique 4, pp. 143-147.

Skempton A. W. (1961) *Horizontal stresses in an overconsolidated Eocene clay*, Proc. 5th ICSMFE, Paris 1, pp. 351-357.

Skempton A.W. and Sowa V.A. (1963), *The behaviour of saturated clays during sampling and testing*, Géotechnique 13 (4), pp. 269-290.

Skempton A.W. (1970), *The consolidation of clays by gravitational compaction,* Q.J. Geological Soc. No.125, pp. 373-411.

Smart P. and Tovey N.K. (1981), *Electron microscopy of soils and sediments: examples*, Oxford University Press, pp. 178.

Smart P. and Tovey N.K. (1982), *Electron microscopy of soils and sediments: techniques*, Oxford University Press, pp. 264.

Smith P.R. (1992), *The behaviour of natural high compressibility clays with special reference to consolidation on soft ground*, PhD Thesis, London University.

Srnith P.R., Jardine R.J. and Hight D.W. (1992), *On the yielding of Bothkennar clay*, Géotechnique 42, pp. 257-274.

Stallebrass S.E. and Taylor R.N. (1997), *The development and evaluation of a constitutive model for the prediction of ground movements in overconsolidated clay*, Géotechnique 47 (2), pp. 235–253.

Suklje L. (1969), *Rheological aspects of soil mechanics*, London, Wiley-Interscience.

Tanaka H. and Locat J. (1999), *A microstructural investigation of Osaka Bay clay: the impact of microfossils on its mechanical behaviour*, Can. Geotech. J. 36, pp. 493–508.

Tanaka H. (2003), Pore size distribution and hydraulic conductivity characteristics of marine clays, 2nd International Symposium on Contaminated Sediments, pp. 151-157.

Tavenas F. and Lerouil S. (1985), *Discussion*, Proc. 11th CCSMFE, San Francisco 5, pp. 2693- 2694.

Taylor D.W. (1948), *Fundamentals of soil mechanics*, John Wiley and Sons, New York.

Tchalenko J.S. (1967), *The influence of shear and consolidation on the microscopic structure of some clays*, PhD thesis, London University.

Terzaghi K. (1925), *Erdbaumechanik auf Bodenphysikalischer Grundlage*, Leipzig, Deuticke, 399 pp.

Terzaghi K. (1944), *Ends and means in Soil Mechanics*, Engineering Journal (Canada), Vol.27, pp. 608.

Terzaghi K. and Peck R.B. (1967), *Soil Mechanics in Engineering Practice*, John Wiley and Sons, New York.

Tillard-Ngan D., Desrues J., Raynaud S. and Mazerolla F. (1992), *Strain localisation in the Beaucaire marl*, Structure and Mechanical Behaviour of Geomaterials, pp. 1-16.

Torrance J.K. (1975), *On the Role of Chemistry in the Development and Behavior of the Sensitive Marine Clays of Canada and Scandinavia*, Can. Geotech. J. 12, pp. 326-335.

van Eekelen H. and Potts D.M. (1978), *The behaviour of Drammen Clay under cyclic loading*, Géotechnique 28 (2), pp. 173-196.

Veniale F. (1983), *Consolidamento e stabilizzazione dei terreni argillosi mediante diffusione di sali (KCI)*, Ingegneria Ferroviaria, Vol.6, pp. 1-9.

Veniale F. (1985), *The role of microfabric in clay soil stability*, Miner. Petrogr. Acta, Vol.29-A, pp. 101-119.

Viggiani G., Rampello S. and Georgiannou V.N. (1993), *Experimental analysis of localization phenomena in triaxial tests on stiff clays*, Proc. Conf. on Geotechnical Engn. of Hard Soils-Soft rocks, Athens, Balkema, pp. 849-856.

Viggiani G. and Atkinson J.H. (1995), *Stiffness of fine-grained soil at very small strains*, Géotechnique 45 (2), pp. 249-265.

Vitone C. (2005), *Comportamento meccanico di argille da intensamente a mediamente fessurate*, PhD Thesis, Technical University of Bari.

Vitone C., Cotecchia F., Desrues J. and Viggiani G. (2009), *An approach to the interpretation of the mechanical behaviour of intensely fissured clays*, Soils & Foudation Journal, Vol. 49 (3), pp. 355-368.

Vitone C. and Cotecchia F. (2011), *The influence of intense fissuring on the mechanical behaviour of clays*, Géotechnique 61 (12), pp. 1003-1018.

Webb D.L. (1964), *The mechanical properties of undisturbed samples of London Clay and Pierre shale*, PhD thesis, London University.

Wenk H.R. (1976), *Electron-Microscopy in Mineralogy*, Springer Velag, Berlin Heidelberg New York.

Wheeler S.J., Näätänen A., Karstunen M. and Lojander M. (2003), *An anisotropic elastoplastic model for soft clays*, Can. Geotech. J. 40, pp. 403–418.

Whittle A. J. and Kavvadas M. (1994), *Formulation of the MIT-E3 constitutive model for overconsolidated clays*, Journal Geotech. Eng. division, ASCE 120 (1), pp. 173-198.

Wood D.M. (1974), *Some aspect of the mechanical behaviour of kaolin under truly triaxial conditions of stress and strain*, PhD thesis, Cambridge University.

Wood D.M. (1990), *Soil behaviour and critical state mechanics*, Cambridge University Press.

Wiewiora A., Sanchez-Soto P.J., Aviles M.A., Justo A. and Perez-Rodriguez J.L. (1993), *Effect of grinding and leaching on polytypic structure of pyrophyllite*, Applied Clay Science, 8, pp. 261-282.

Wissa A.E.Z., Christian J.T., Davis E.H. and Heiberg S. (1971), *Consolidation at constant rate of strain*, Proc. ASCE, 97, SMIO, pp. 1393-1413.

Wroth C.P. (1958), *Shear behaviour of soils*, PhD Thesis, Cambridge University.

Wroth C.P. (1984), *The interplay of in situ soil tests*, Géotechnique 34 (4), pp. 449-489.

Yu C.Y., Chow J.K. and Wang Y.-H. (2016), *Pore-size changes and responses of kaolinite with different structures subject to consolidation and shearing*, Engineering Geology 202, pp. 122–131.

12 CURRICULUM

SIMONA GUGLIELMI

PERSONAL INFORMATION	
Address	Via G. Pascoli, 25 – Andria (BAT)
E-mail	simona.guglielmi@poliba.it simona.guglielmi90@gmail.com
Date of birth	07/01/1990
EDUCATION	
Nov 2014- now	*Ph. D. Student Environmental and Building Risk and Development* *XXX cycle* Technical University of Bari - DICATECh Supervisors: Prof. Federica Cotecchia [(1)], Prof. Francesco Cafaro[(1)], Prof. Antonio Gens Solè[(2)] [(1)] Technical University of Bari [(2)] Universitat Politècnica de Catalunya
Jan 2016 - now	*Collaboration in a National Research Project (Prin 2015): "Innovative monitoring and design strategies for sustainable landslide risk mitigation".* Coordinator: Prof.ssa Federica Cotecchia.
April 2014- Dec 2015	*Collaboration in a National Research Project (Prin 2013): "Landslide risk mitigation by means of sustainable intervention strategies".* Coordinator: Prof. Leonardo Cascini. Technical University of Bari - DICATECh Collaboration with University of Salerno, Fisciano (SA)

Sept 2011 – March 2014	*Second Level Degree* *Master of Science in Civil Engineering* Curriculum Geotechnical Engineering Technical University of Bari Thesis in Slope Stability and Soil Dynamics Title: “Environmental engineering operations for mitigation of landsliding” in collaboration with Prati Armati S.r.l. Thesis supervisor: Prof. Federica Cotecchia Co-supervisor: Dr. Giuseppe Pedone Final degree mark: 110/110 with honours
Dec 2013 – Jan 2014	Traineeship at Prati Armati S.r.l.
Sept 2008 – Nov 2011	*First Level Degree* *Bachelor of Science in Civil Engineering* Technical University of Bari Thesis in Applied Geology Title: “Evaluation of saltwater-freshwater equilibrium in the coastal aquifer of Salento (Puglia)” Thesis supervisor: Prof. Maria Dolores Fidelibus Final degree mark: 110/110 with honours
Sept 2003 – July 2008	*Scientific certificate* *Italian secondary school diploma* Liceo scientifico statale R. Nuzzi – Via Cinzio Violante, 18 - 76123 Andria (BT) School-leaving examination mark: 100/100 with honours

RESEARCH PROJECTS

2013-2015	*PRIN 2013, Progetto di Ricerca di Interesse Nazionale, entitled “Landslide risk mitigation by means of sustainable intervention strategies”.* Coordinator: Prof.ssa Federica Cotecchia
2012-2016	*COST, European Cooperation in Science and Technology, Action TU1202 "Impact of climate change on engineered slopes for infrastuctures",* Working Group 1 on Numerical Modelling;

2015-now | *PRIN 2015, Progetto di Ricerca di Interesse Nazionale, entitled "Innovative monitoring and design strategies for sustainable landslide risk mitigation".* Coordinator: Prof.ssa Federica Cotecchia.

SEMINARS

Oral presentations:

2017 | *"Investigation of the microstructural evolution in compression and shear of a stiff clay".* IARG 2017, 5th-7th July 2017, Matera.

2016 | *"Investigation of microstructural analysis in clays with compression and desaturation, explored by means of SEM, Image Processing e MIP",* I Ciclo di Seminari Geotecnici, Technical University of Bari, 1st April 2016.

2015 | *"Investigating microstructural changes that are background of model parameter values of macro-behaviour of clays",* Joint Summer School in Geotechnics, Technical University of Bari, 11-12th June 2015.

Co-author of oral presentations:

2016 | *"Microstructural changes in the background of the compression behaviour of clays",* F. Cotecchia, F. Cafaro, G. Mitaritonna, S. Guglielmi. 27th ALERT Workshop, Aussois, 2-5th October 2016.

2016 | *"Diagnosi dei meccanismi di frana a differenti scale di analisi"*, F. Cotecchia, F. Santaloia, C. Vitone, P. Lollino, G. Pedone, O. Bottiglieri, S. Guglielmi, F. Sollecito, R. Petti, G. Ruggieri, V. Tagarelli, presented by Prof. F. Cotecchia. Università della Basilicata, 27th May 2016, Potenza.

2015 | *"Microstructural changes in clays generated by compression and desaturation, explored by means of SEM and Image Processing",* F. Cotecchia, F. Cafaro, G. Mitaritonna, S. Guglielmi, presented by Prof. F. Cotecchia. 7th International

	Conference on Porous Media INTERPORE 2015, Padova, 18-21st May 2015.
2014	*"La diagnosi del meccanismo di frana nell'analisi del rischio"*, F. Cotecchia, F. Santaloia, C. Vitone, P. Lollino, G. Pedone, O. Bottiglieri, S. Guglielmi, R. Petti, presented by Prof. F. Cotecchia. LARAM Workshop 2014, Aula delle Lauree di Ingegneria – Campus dell'Università di Salerno, Fisciano (SA).

PUBBLICATIONS

2017	Guglielmi S., Cotecchia F., Cafaro F., A. Gens (2017). *Investigation of the microstructural evolution in compression and shear of a stiff clay".* Incontro Annuale dei Ricercatori di Geotecnica IARG 2017, 5th-7th July 2017, Matera.
2016	Cotecchia F., Cafaro F., Guglielmi S. (2016*). "Microstructural changes in the background of the one-dimensional compression behaviour of a stiff clay*", abstract. 27th ALERT Workshop, 3rd-5th October 2016, Aussois.
2016	Cotecchia F., Cafaro F., Guglielmi S. (2016). *"Microstructural changes in clays generated by compression explored by means of SEM and Image Processing"*. VI Italian Conference of Researchers in Geotechnical Engineering - Geotechnical Engineering in Multidisciplinary Research: from Microscale to Regional Scale, CNRIG2016, 22-23 September 2016, Bologna.
2015	Cotecchia F., Cafaro F., Guglielmi S. (2015). *"Microstructural changes in clays generated by compression and desaturation explored by means of SEM and Image Processing",* abstract. 7th International Conference on Porous Media, INTERPORE 2015, 18-21st May 2015, Padova.
in progress	Cotecchia F., Guglielmi S., Ruggieri G., Tagarelli V., Pedone G., Santaloia F., Trizzino R. *"Threshold climatic variables of reference in early warning systems mitigating landslide risk in the south-eastern Apennines"* (accepted).

in progress	Cotecchia F., Vaunat J., Casini F., Pedone G., Guglielmi S., Sollecito F. (in prep.). *"Modelling slope-atmosphere interaction through hydraulic and thermo-hydraulic approaches".*